Final Report

MEA and Stack Durability for PEM Fuel Cells

Cooperative Agreement No. DE-FC36-03GO13098

Submitted to

U. S. Department of Energy
Fuel Cells and Infrastructure Technologies Program

February 15, 2008

By
3M Fuel Cell Components Program
3M Company, St. Paul, MN 55144

Prime Contractor: 3M Company, St. Paul, MN 55144

Project Title: MEA and Stack Durability for PEM Fuel Cells

Principal Investigator: **Dr. Michael A. Yandrasits, 3M Fuel Cell Program**

Team Members: Plug Power
Case Western Reserve University
University of Miami

(This page left blank intentionally)

Foreword and Acknowledgements

This report documents the work performed by 3M Company and its subcontractors under the Cooperative Agreement No. DE-FC36-O3GO13098, “MEA and Stack Durability for PEM Fuel Cells”. The period of performance for this contract was from September 1 2003 to December 31 2007.

The principal objectives of this program were to develop membrane electrode assemblies (MEAs) and systems that are durable up to 40,000 hours under stationary power conditions and at the same time can be manufacture in high volume, commercial processes.

All MEA materials, process development work was carried out by 3M Co., at its St. Paul, MN, 3M Center campus and its Menomonie, WI, production plant. The 3M team included primarily members from the Fuel Cell Components Program, but significant assistance was received over varying periods of time from members of 3M’s Corporate Materials Rearch Laboratory, Process Technology Center, Analytical Technology Center, and Software Electronics and Mechanical Systems. Dr. Michael Hicks was the Principal Investigator and Technical Team Leader for the majority of the program and Dr. Michael Yandrasits was the Principle Investigator and Team Leader for the conclusion of the program. Dr. Judith Hartmann and Dr. Philip Miller were the Program Managers, and Mr.Steven Kays of 3M Government R&DContracts department was the contract administrator.

Significant recognition is due the 3M Fuel Cell Components Program technical team members who were most responsible for completing the work represented in this final report, including several who contributed major sections of this report. We are all very appreciative of the support of 3M management.

Subcontractors were Case Western Reserve University, Cleveland, OH; Plug Power, Lantham NY, and The University of Miami, Miami FL. From our subcontractors’ organizations we are particularly indebted to Prof. Thomas Zawodzinski and Dr. David Schiraldi, Dr. J Adin Mann, Mr. Vladimir Gurau and Uziel Landau of CWRU; Prof. Hongtan Liu of U. of Miami; Dr. William D. Ernst, Dr. Zhigang Qi, and Mr. Richard Gaylord of Plug Power.

This work was funded in part by the U. S. DOE, Energy Efficiency and Renewable Energy. DOE technical oversight of the project was provided by Technology Development Managers Kathi Epping, of the Dept. of Energy Hydrogen, Fuel Cells and Infrastructure Technologies Program, DOE Technical Advisor Thomas Benjamin (Argonne National Laboratory), and DOE Project Officer Reginald Tyler (Golden, CO).

Executive Summary

Proton exchange membrane fuel cells are expected to change the landscape of power generation over the next ten years. For this to be realized one of the most significant challenges for stationary systems is lifetime, where 40,000 hours of operation with less than 10% decay is desired. This project conducted fundamental studies on the durability of membrane electrode assemblies (MEAs) and fuel cell stack systems with the expectation that knowledge gained from this project will be applied toward the design and manufacture of MEAs and stack systems to meet DOE's 2010 stationary fuel cell stack systems targets.

The focus of this project was proton exchange membrane (PEM) fuel cell durability – understanding the issues that limit MEA and fuel cell system lifetime, developing mitigation strategies to address the lifetime issues and demonstration of the effectiveness of the mitigation strategies by system testing. To that end, several discoveries were made that contributed to the fundamental understanding of MEA degradation mechanisms. (1) The classically held belief that membrane degradation is solely due to polymer end-group "unzipping" is incorrect; there are other functional groups present in the ionomer that are susceptible to chemical attack. (2) The rate of membrane degradation can be greatly slowed or possibly eliminated through the use of additives that scavenge peroxide or peroxyl radicals. (3) Characterization of gas diffusion layer (GDL) using dry gases is incorrect due to the fact that fuel cells operate utilizing humidified gases. The proper characterization method involves using wet gas streams and measuring capillary pressure as demonstrated in this project. (4) Not all Platinum on carbon catalysts are created equally – the major factor impacting catalyst durability is the type of carbon used as the support. (5) System operating conditions have a significant impact of lifetime – the lifetime was increased by an order of magnitude by changing the load profile while all other variables remain the same. (6) Through the use of statistical lifetime analysis methods, it is possible to develop new MEAs with predicted durability approaching the DOE 2010 targets. (7) A segmented cell was developed that extend the resolution from ~ 40 to 121 segments for a 50cm2 active area single cell which allowed for more precise investigation of the local phenomena in a operating fuel cell. (8) The single segmented cell concept was extended to a fuel size stack to allow the first of its kind monitoring and mapping of an operational fuel cell stack.

An internal check used during this project involved evaluating the manufacturability of any new MEA component. If a more durable MEA component was developed in the lab, but could not be scaled-up to 'high speed, high volume manufacturing', then that component was not selected for the final MEA-fuel cell system demonstration. It is the intent of the team to commercialize new products developed under this project, but commercialization can not occur if the manufacture of said new components is difficult or if the price is significantly greater than existing products as to make the new components not cost competitive. Thus, the end result of this project is the creation of MEA and fuel cell system technology that is capable of meeting the DOEs 2010 target of 40,000 hours for stationary fuel cell systems (although this lifetime has not been demonstrated in laboratory or field testing yet) at a cost that is economically viable for the developing fuel cell industry. We have demonstrated over 2,000 hours of run time for the MEA and system developed under this project.

Table of Contents

List of Figures

List of Tables

List of Abbreviations

AC	alternating current
ATR	attenuated total reflectance
BET	Brunauer Emmette Teller (gas adsorption surface area)
BOL	beginning of life
CCB	catalyst coated backing
CCM	catalyst coated membrane
C	carbon
CI	counter ion
CO	carbon monoioxide
CS	chemically stable
CV	cyclic voltammograms
DENT	double edge notch tear
DF	difunctional
DI	deionozed
DMA	dynamic mechanical analysis
DMBE	duel microband electrode
DOE	Department of Energy
DSM	Dutch State Minning Sulupor™ vendor
ECOS	electro-chemical oxidative stability
ECSA	electrochemical surface area
EOL	end of life
EW	equivalent weight, polymer molecular weight per mol of acid groups
FC	fuel cell
FEP	fluorinated ethylenepropylene
FER	fluoride emission rate
FRR	fluoride release rate
FTIR	Fourier transform infrared spectroscopy
gsm	grams per square meter
GDL	gas diffusion layer
HF	hydrogen fluoride
HFR	high frequency resistance
HOR	hydrogen oxidation reaction
HPLC	high performance liquid chromatography
ICP	ion coupled plasma
IEC	ion exchange capacity
IIPS	ion induced phase separation
ISE	ion selective electrode
kPa	kilopascals
LC-MS	liquid chromatography – mass spectroscopy
LCP	liquid crystal polyester
MC	model compound
MEA	membrane electrode assembly
MF	monofunctional
MPL	micro pourous layer
MS	mass spectroscopy
m/z	mass to charge ratio
NMP	M-Methylpyrrolidinone
NMR	nuclear magnetic resonance
NSTF	nanostructured thin film catalyst
OCV	open circuit voltage
OFR	oxygen free radicals
ORR	oxygen reduction reaction

PA	poly(amide)
PDS	potentiodynamic polarization scan
PEFC	polymer electrolyte fuel cell
PEI	Poly(etherimide)
PEM	proton exchange membrane, polymer electrolyte membrane
PEMFC	proton exchange membrane fuel cell
PET	Poly(ethyleneterephthalate)
PFPA	pentafluoropropionic acid
PFSA	perfluorinated sulfonic acid
ppm	parts per million
PSf	Poly(sulfone)
PSS	potentiostatic scans
Pt	platinium
Pt/C	Pt on carbon catalysts
PTFE	poly(tetrafluoroethylene)
PVDF	poly(vinylidenefluoride)
REV	Resistive element volume
R2	least squares fitting parameter
RH	relative humidity
RHE	reversible hydrogen electrode
RRDE	rotating ring disc electrode
SCCM	standard cubic centimeters per minute
SEF	surface area enhancement factor
SHE	standard hydrogen electrode
TEM	transmission electron microscopy
TFA	trifluoroacetic acid
Tg	glass transition temperature
TGA	thermal gravimeteric analysis
TFE	tetrafluoroethylene
UV	ultraviolet
XRD	x-ray diffraction

Section 1. Introduction

1.1 Approach

The approach for increasing stationary fuel cell system lifetime involved two interacting paths: optimization of MEAs and subcomponents for durability and optimization of system operating conditions to minimize performance decay. Ex-situ accelerated component aging tests were used to age components and determine failure modes. Aged components were then assembled into MEAs for performance testing in comparison to virgin MEAs. In this manner, the effect of component aging on MEA performance was quantified and mitigation strategies were implemented. In addition, three dimensional (3D) modeling and novel experimental approaches were used to probe the loci of degradation/failure within an MEA. A total system approach was used to study the interactions between stack design/operation and MEA performance/durability. With this approach, the system (stack and MEA) was optimized for durability. Finally, since 40,000 hours of testing is not obtainable during this 4-year program, test data generated from both accelerated and normal MEA operation were used to predict MEA lifetime. All MEA development was based upon a new 3M proprietary perfluorinated sulfonic acid ionomer.

The project team consisted of 3M, Plug Power, Case Western Reserve University, and the University of Miami. 3M was primarily responsible for component development, MEA integration and accelerated testing with statistical lifetime analysis; Plug Power was primarily responsible for investigating system variables, MEA testing in modules and stacks, and stack development; Case was primarily responsible for the development of diagnostic tools, physical property characterization, and formulating an ionomer degradation model; and University of Miami was primarily responsible for investigating MEA non-uniformities via modeling. The approach and team assignments are shown graphically in Figure 1.

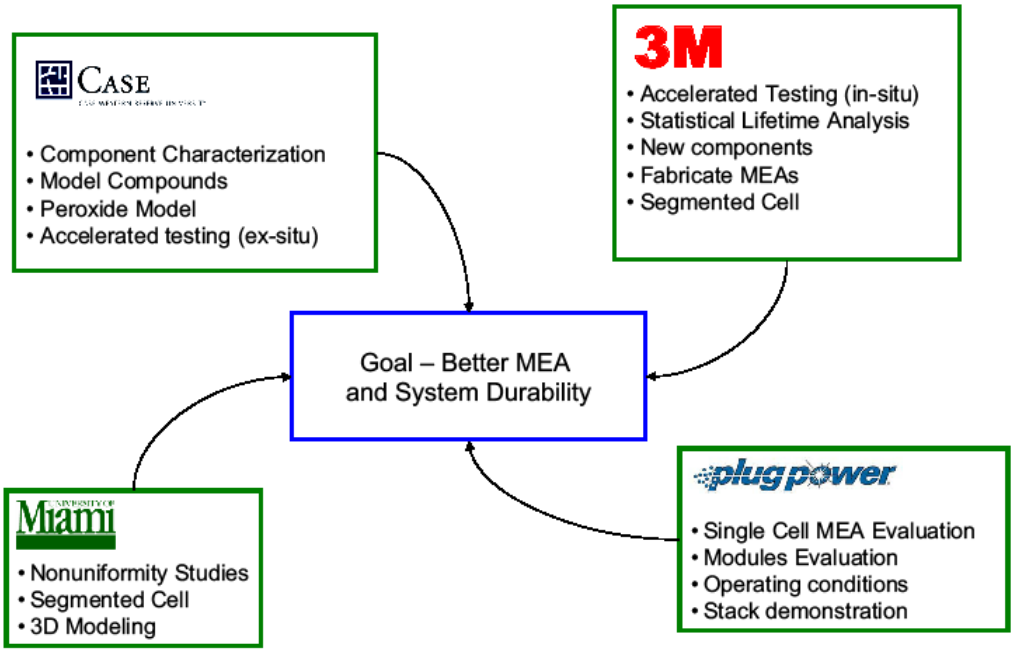

Figure 1. Project approach with assigned major activities

1.2 Description of Work Plan

The work plan for this project was broken into tasks depending on each team member's assignments. While this approach made it easy for writing the work plan (each team member was responsible for writing their own tasks), it was not an effective means to report progress as multiple team members worked on overlapping tasks. As a result, it was decided to report progress in terms of common areas like 'Component Development' or 'System Operation' instead of task number. In order to eliminate confusion regarding where results for a given task are located, the following summarizes the original tasks and cross-references which section of this report the results are located.

Task 1 - Generation of PEM and Electrode Structures Optimized for Performance and Durability, Using a New-to-the-World PFSA Ionomer

Task 1 focuses on MEA component development and optimization and is divided into three subtasks. Subtask 1.1 centers on the fabrication and characterization of new membranes based upon 3M's proprietary PFSA ionomer. The results from subtask 1.1 can be found in Section 2.1 of this report. Subtask 1.2 is directed at evaluating the effect of catalyst support, ink composition and electrode structure on durability and at studying the effect of GDL type and microlayer composition on durability. The results of subtask 1.2 can be found in Sections 2.2 and 2.3. Subtask 1.3 centers on controlled aging of MEAs to understand failure modes and estimate lifetime. The results of this subtask can be found in Section 5.

Task 2 - Determining optimum electrode structure in three dimensions

Task 2 investigates how nonuniformities within a cell affect failure modes. Task 2 is divided into two subtasks that cover both the theoretical and experimental investigations of nonuniformities. The focus of subtask 2.1, is mathematical models to investigate the impact of membrane, electrode or GDL nonuniformities on current distribution. The results of this subtask can be found in Section 3.1. Subtask 2.2 involves the development and fabrication of a highly instrumented segmented cell to experimentally quantify nonuniformities in an operating fuel cell. The results of this experimental work are covered in Sections 3.2 and 3.3.

Task 3 - Ex-situ characterization of MEAs

Task 3 is directed at structural and physical property characterization of MEAs and is divided into three subtasks. Subtask 3.1 centers on the development and validation of ex-situ analytical tools to study MEA chemical and structural properties. The analytical tools developed in subtask 3.1 are used to characterize aged MEAs in subtasks 3.2 and 3.3. The results of task 3 are found in Section 2.

Task 4 - Ex-situ aging and Characterization of MEA Material Components and Model Development

Task 4 focuses on ex-situ aging and characterization of MEA components. This task is divided into four subtasks which focus on the development of ex-situ aging test methods (see Sections 2.1.2, and 2.2.1); development of test methods to determine loci of chemical induced failure in a cell (see Section 3.2); development of component structure-property database to correlate ex-situ aging tests results to MEA lifetime tests (see Section 2.1.2); and the development of a l materials model of aging incorporating kinetics and component structure-property relationship (see Section 2.1.3).

Task 5 - MEA Single Cell Lifetime Characterization

Task 5 focuses on MEA performance and lifetime characterization in single cells. Task 5 consists of several subtasks which primarily center on understanding the impact of fuel cell operating conditions on MEA decay rate in order to determine the optimal operating conditions in terms of MEA lifetime. The results of task 5 are in Sections 5 and 6.

Task 6 - MEA Performance Characteristics in Stacks and Systems

Task 6 studies MEA performance and lifetime characterization in systems. Subtasks for task 6 include: analysis of field data for decay mechanisms, evaluation of contamination and transient effects, stack failure mode analysis, and a 2000 hour system demonstration. The results for task 6 can be found in Section 6 including the system demonstration.

Section 2: Component Development

2.1 Membrane

2.1.1 Introduction

Membrane durability is fundamental to MEA durability. We approached the task of improving the membrane by first studying the existing degradation mechanisms through ex-situ, in-situ, and model compound studies. Next, we attempted to address the deficiency in chemical resistance or mechanical strength properties through systematic development programs.

The majority of the membrane development work was based on two perfluorosulfonic acid (PFSA) polymers. The traditional Nafion™ polymer from DuPont was used in many degradation mechanism studies, as a control in most membrane experiments or as a fixed variable in non-membrane related experiments (catalyst evaluations for example). The newly developed 3M ionomer was chosen for the majority of the membrane development work. Figure 2 shows the structure of both the Nafion ™ ionomer and the 3M ionomer.

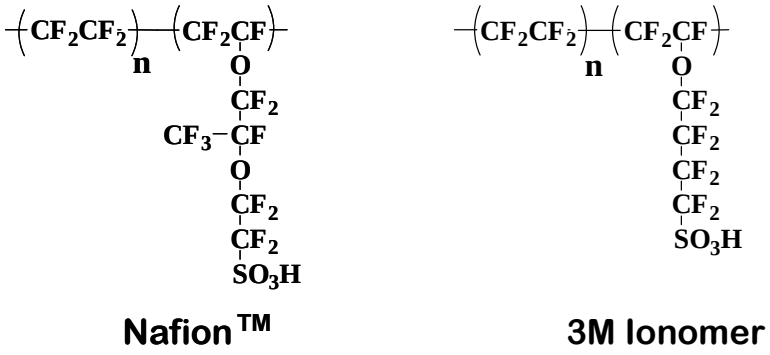

Figure 2. Chemical Structure of Nafion(TM) and 3M ionomer.

The 3M ionomer has a shorter side chain with just four carbons and lacks one ether linkage. Because of these differences the 3M ionomer typically has a higher “glass transition” or alpha transition temperature for the same equivalent weight. Another benefit of the shorter side chain is that the equivalent weight of the polymer is lower at the same copolymer ratio when compared to Nafion™. Finally, since 3M produces the monomer and polymer used in our membranes we

are able to change any aspect of the polymer such as the copolymer ratio (i.e. equivalent weight), molecular weight, end groups, and addition of other monomers.

Note: The following two sections *2.1.2 Thermochemical and Morphological Investigation of Nafion™ Membrane Degradation* and *2.1.3 Model Compound studies* represent contributions from Case Western Reserve University. The remaining sections represent contributions primarily from 3M researchers.

2.1.2 Thermochemical and Morphological Investigation of Nafion™ Membrane Degradation

CASE
CASE WESTERN RESERVE UNIVERSITY

Introduction

The ultimate life of PEMFCs is intrinsically related to the chemical stability of the membrane. In a PEMFC, one of the requirements of the membrane is to separate the fuel (hydrogen) and the oxidant (air or oxygen) from mixing with each other. However it has been observed that it is this membrane which often fails due to chemical degradation. One of the primary agents causing the degradation is thought to be hydrogen peroxide, H_2O_2, which can be chemically or electrochemically generated during PEMFC operation.[1] The normal electrochemical reactions occurring at the two cell electrodes of PEMFC lead to water being the only chemical product of the process. Idealized oxygen reduction reaction at the cathode results in water as the 4-electron reduction product. However, it is also possible to have an incomplete oxygen reduction process, which leads to the generation of H_2O_2 as the 2-electron reduction product, as indicated by the schematic in Figure 3.

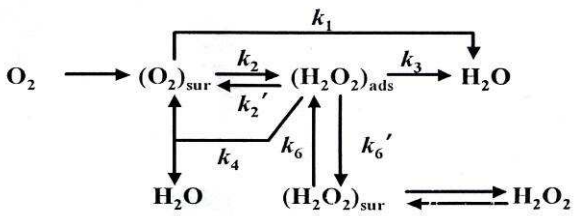

Figure 3. Scheme for ORR indicating routes for peroxide generation

The peroxide is generated at a low potential (0.67 V vs. RHE) which is well within the range in which a PEMFC operates. However, the reduction potential of peroxide is very high (1.77 V vs. RHE), a potential never attained in PEMFC single cell operation. Therefore the peroxide once generated remains within the MEA for the duration of cell operation. H_2O_2 is a highly oxidative compound and can chemically attack and degrade the MEA components.

Mechanism of Membrane Degradation by Peroxide

Besides the incomplete oxygen reduction occurring at the PEMFC cathode, generation of hydrogen peroxide is also possible by oxygen diffusion across the membrane from the cathode to the anode side, followed by incomplete reduction at the surface of the anode catalyst.[2,3,4] The peroxide can then either homolytically decompose or react with transition metals ions such as $Fe^{2+}$and Cu^{2+}, which are present as typical contaminants, to generate hydroxyl (•OH) and hydroperoxyl (•OOH) radicals.[5,6] The radical species then attack the membrane, especially the hydroxyl radical which is very reactive and has been shown to break the long perfluorinated chains of Nafion over long periods of time.[7] Rotating ring disk electrode (RRDE) studies have

confirmed the presence of hydrogen peroxide generated in fuel cell anodes operating on hydrogen/air.[8] Hydrogen peroxide concentrations have been found to increase with decreasing membrane thickness, supporting the notion of oxygen permeation to the anode as an operating mechanism for peroxide formation. By comparison peroxide generation at the cathode is very small.[9,10] Schlick and co-workers have confirmed the presence of (•OH) by electron spin resonance spectroscopy.[11] The key question still remains as to how these radicals actually attack the membrane. A widely discussed mechanism circulated in the PEMFC community is the generation of radicals through the 'Fenton's mechanism' carried out in Fenton's regent (aqueous solution of hydrogen peroxide mixed with ferrous ions):[12]

$$Fe^{2+} + H_2O_2 \rightarrow Fe^{3+} + \bullet OH + OH^- \quad (1)$$

$$Fe^{3+} + H_2O_2 \rightarrow Fe^{2+} + \bullet OOH + H^+ \quad (2)$$

Figure 4. Fenton's Mechanism

Fenton's reagent is a very strong oxidizing agent and can immediately decompose hydrogen peroxide to form radicals. Fenton's reagent is a well-known mimic for generating peroxide radicals at temperatures resembling fuel cell conditions. A highly cited mechanism of peroxide attack on Nafion membrane has been proposed by Curtin and co-workers from DuPont.[13] As per their mechanism, the radicals generated by the Fenton's mechanism can attack any COOH-containing terminal bond in the membrane, usually the COOH-containing endgroups of the Nafion™ mainchain. Equations 3-5 in Figure 5 illustrate the mechanism of radical attack on Nafion™ membrane terminating in carboxylic acid end groups: [13]

$$R_f - CF_2COOH + \bullet OH \rightarrow R_f - CF_2 \bullet + CO_2 + H_2O \quad (3)$$

$$R_f - CF_2 \bullet + \bullet OH \rightarrow R_f - CF_2OH \rightarrow R_f - COF + HF \quad (4)$$

$$R_f - COF + H_2O \rightarrow R_f - COOH + HF \quad (5)$$

Figure 5. End Group Degradation Mechanism

The net result of the sequence of reactions in Equations 3-5 is the loss of a fluorine atom from the mainchain of the membrane in the form hydrogen fluoride (HF). Consecutive cycles of these reactions lead to a continuous evolution of HF and the shortening of the Nafion polymer and is often called 'mainchain unzipping'. A number of groups have reported that the use of Fenton's reagent can liberate fluoride from PEMFC membrane at concentrations equivalent to or higher than those observed in operating fuel cell.[1] Researchers have detected fluoride ions in anode and cathode effluent water.[14] The fluoride generation has been found to generally increase with temperature and also increase linearly with Fe(II) levels until present in such excess as to become a pseudo zero order in metal ion.[1] The evolution of fluoride is accompanied by thinning of the membrane, an observation documented by Aoki et. al..[15] A possible solution towards arresting the evolution of fluoride has been the end capping of the Nafion membrane to reduce the concentration of – [COOH] groups, primarily fluorinating them. Such an exercise should reduce the fluoride emission to almost negligible levels once the concentration of carboxylic acid endgroups is minimized. However, plots of fluoride generation rates against decreasing concentrations of carboxylic acid content (Figure 6) have indicated a significant non-zero intercept: [16]

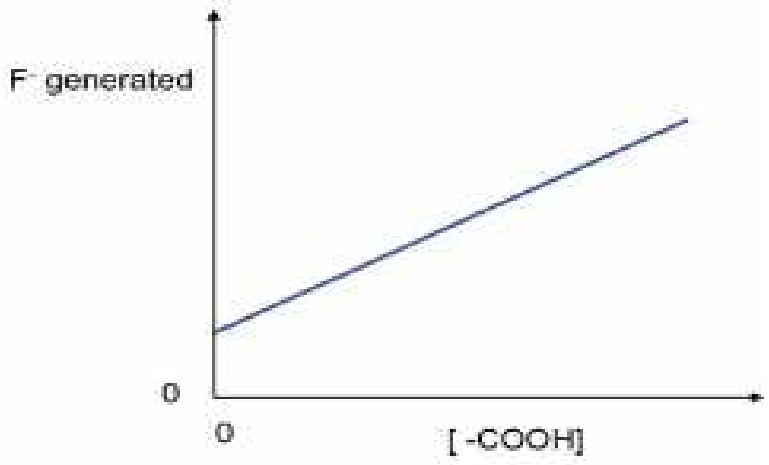

Figure 6. Effect of carboxylic acid end groups on fluoride evolution from Nafion membrane[17]

The non-zero intercept corresponding to almost 10% of the total fluoride generation, demands that there be an investigation into an additional route of membrane degradation, once which also accounts for the side chain degradation of Nafion™ membranes. This is especially important because low molecular weight organic compounds, related to degradation of side chains of PFSA membranes have been detected during fuel cell operation.[18]

Consequences of Membrane Degradation

Variations in temperature and humidity cause cyclic stresses which lead to dimensional changes. Coupled to these dimensional changes is the chemical attack due to degradation, which can eventually lead to mechanical defect formation in the membrane. [19] Huang *et al.* investigated mechanical failure of the membrane due to relative humidity variations and found catastrophic failure of the cell/stack due to rapid gas-crossover following a mechanical breach in the membrane.[20]

Objectives of Our Work

The objective of this work is to attempt to determine how chemical degradation affects the functioning of the membrane and what key membrane characteristics such as morphology, dimensions, mechanical strength, and thermomechanical properties are affected by the degradation process. Understanding the ramifications of Nafion™ membrane degradation from a morphological and thermomechanical point of view is quite a challenge because, the chemical changes in the membrane (as highlighted by the Fenton's mechanism), occur relatively slowly. Fluoride emissions in an operating fuel cell corresponding to a reasonable fraction of the membrane are detected over hundreds (and sometimes thousands) of hours of operation.[1] consequently, the Fenton's conditions have to be such that the degradation or aging process proceeds at an accelerated rate. Once an MEA has been fabricated and assembled within a single fuel cell (or in a stack) for testing purposes, it is very difficult to monitor where exactly the fluoride is generated during fuel cell testing. A detailed investigation into the exact location of fluoride generation and a division of the fluoride generated, between that in the membrane, and that in the electrode, is outside the scope of this chapter. This report focuses on degrading a commercially available Nafion™ membrane by a harsh Fenton's reagent under accelerated cyclic degradation or aging conditions. The ferrous and peroxide concentrations employed for degrading the membrane are much higher than what is possibly generated during PEMFC

operation (Typically 1 part Fe per 5-25 parts peroxide (w/w)).[7] The logic behind employing such a high concentration is to set an upper limit for intensity of the peroxide attack. Prolonged peroxide generation in certain areas of the membrane over a certain projected lifespan (say 5,000 hours), might lead to a similar degradation response in the MEA causing its failure.

Fluoride evolution from the degraded membrane has been determined using an ion-selective electrode. Dimensional changes and changes in membrane weight have been measured simultaneously at the end of the Fenton's aging cycle. Morphological characteristics of the membrane have been compared pre- and post- Fenton's aging. Influence of chemical aging on the thermal and dynamic mechanical of the membrane has been determined. Mechanical response of the membrane such as tensile strength has been compared before and after degradation. Fuel cell performance of the degraded membrane has been evaluated by fabricating an MEA and compared to a corresponding performance from a similar un-degraded membrane sample.

Experimental

Ex-situ Accelerated Fenton's Degradation

A 50 cm^2 piece of Nafion™ 117 (Aldrich, equivalent weight =1100) membrane was used for the degradation experiments. As a pre-treatment exercise, the membrane piece was soaked successively in 5 % H_2O_2 (two hours at 80℃), de-ionized water (one hour at 80℃), 0.5 M H_2SO_4 (two hours at 80℃) and de-ionized water (one hour at 80℃). Thereafter the membrane piece was dried at 70℃ for 72 hours in a vacuum oven. After the sample had dried, its thickness and weight were accurately measured. The protonated sample was then subjected to degradation or 'aging' in the form of the Fenton experiment. A schematic of the degradation regime is illustrated in Figure 7. Each degradation cycle involved initially ion-exchanging the Nafion™ 117 piece (in its protic state) in a 0.1 M solution $FeSO_4$ (Fisher) solution at 70℃. The ion exchange converted the acid form ionomers to Fe (II) form. After the ion exchange, the membrane sample (yellow in color) was removed and rinsed thoroughly with de-ionized water to clean up the residual ion-exchange solution and further blotted dry. The concentration of ferrous sulfate was chosen to target a 100 % Fe (II) loading.

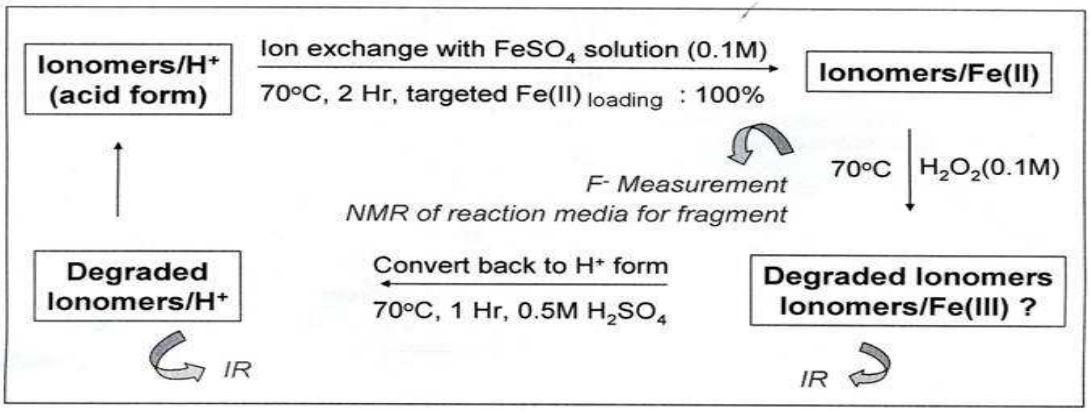

Figure 7. Schematic illustrating regime for accelerated chemical degradation of Nafion 117 membrane in Fenton's reagent

The next step in the degradation process involved was to transfer the Fe(II)-exchanged membrane sample to a de-ionized water bath solution in a three-necked flask and degas the solution for 15 minutes with dry nitrogen gas (to remove any oxygen that might react with the radicals created). The temperature of the solution was then raised to 80℃ and 0.1 M H_2O_2 was introduced into the flask through an addition funnel at the rate of 1 drop per second. After the

addition of the peroxide, the reaction mixture was held at 80℃ under nitrogen purge for different durations of time. After that, the flask was allowed to cool and 5 ml of the reaction solution was extracted from the flask for measurement of fluoride using a fluoride ion selective electrode (Mettler-Toledo). The corresponding value of fluoride release rate was calculated. The remaining solution was preserved in the flask for the next cycle of degradation. The degraded membrane sample (orange-brown in color) was re-protonated to acid form by immersing in 0.5 M H_2SO_4 at 70-80℃ for one hour.

Such a cycle was repeated twelve times, after the sixth degradation cycle, part of the degraded, re-protonated and dried membrane was cut off and removed for characterization studies. The remaining piece was used for further degradation. Six additional degradation cycles were carried out. The second, third and fourth cycle peroxide concentration was 1M, 2M and 3M respectively. The concentration was held at 3M for the remaining eight cycles. The peroxide content translated to an extremely harsh Fenton's environment subjected to the membrane. The thickness and weight of the membranes were accurately measured after the sixth and twelfth cycles.

Characterization of Degraded Membrane

Surface morphology of the aged Nafion™ was investigated by SEM. A small portion of the aged Nafion™ 117 piece (after six and twelve cycles of Fenton aging, protonation and drying) was cut. Preparation of the samples for electron microscopy involved dipping the cut piece in liquid nitrogen and then breaking off the quantity required for SEM analysis. Thereafter the membrane samples were sputtered coated with palladium and micrographs obtained using a PhilipsXL30 Environmental Scanning Electron Microscope (ESEM). The accelerating voltage employed for the electron beam was 20 kV. Images of the sample cross-section and surface were taken at various magnifications. Remaining portion of the aged Nafion™ 117 sample was preserved for next stage of Fenton treatment. The degraded membrane surfaces were also looked at using an optical microscope (Olympus BX60) with a SPOT digital camera for image capture.

Rectangular sample specimens (width 5-6 mm and length > 10 mm) were cut from the aged Nafion™ 117 sample and subjected to Dynamic Mechanical Analysis (DMA) using a Triton Instruments DMA. The test specimen was clamped in a tensile fixture and the sample chamber flushed with liquid nitrogen to cool the sample down to -100 ℃. Temperature was ramped at 3℃/min from -100 to 180℃ and an oscillatory stres s applied at a frequency of 1 Hz. Thermo-mechanical properties of the sample such as storage modulus, loss modulus and loss tangent-tan δ, were measured as a function of temperature. The focus of attention was a comparison of the glass transition temperature-T_g, which was obtained as the peak of the Tan δ plot against temperature.

Thermal stability of the undegraded and degraded Nafion™ samples was compared by decomposing the membrane samples (5-10 mg) under nitrogen flow in a thermogravimetric analyzer (TGA; TGA-SDTA 851e, Mettler-Toledo Instruments). The TGA measurements were carried out from 25 to 600ºC at a rate of 10ºC/min.

Room temperature (25℃) tensile measurements were p erformed on the membrane samples using a DMA (TA Instruments Q800) utilized as a tensile tester. The measurements were made in the controlled force mode. Sample dimensions were 5 to 6 mm wide and > 10 mm long. The samples were initially equilibrated at 25℃; therea fter the force applied was ramped from an initial pre-load value to 18 N at a rate of 0.5 N/min. The data generated was utilized to plot stress-strain curves for the samples.

To compare water uptakes, identical dry weights (W_{dry}) of undegraded and degraded membrane samples were soaked in de-ionized water at room temperature (25℃) for 24 hours. The wet weight (W_{wet}) was then measured after blotting off the surface water droplets. The water uptake of the membranes was calculated as:

$$Water-uptake(\%) = (\frac{W_{wet} - W_{dry}}{W_{dry}}) X 100 \quad (6)$$

Figure 8. Water Uptake Calculation

For ionic conductivity measurements, identical weights of two samples were equilibrated in 100% RH conditions for 4 days, then ionic conductivity measured by AC Impedance. The conductivity was calculated using the expression $\sigma = l/Rdw$, where *l* is the distance between the electrodes, *d* and *w* are thickness and width of the membranes, respectively, and R is the high frequency intercept Re(Z) axis for the Nyquist plot plotted from AC impedance measurements.

For electrochemical performance testing, the Nafion™ 117 membrane (after the twelfth degradation cycle) was employed to fabricate a MEA in conjunction with 0.3 mg/cm^2 electrodes prepared using the 20 % E-TEK^{sm} catalyst. A similar MEA was fabricated using the undegraded Nafion™ 117 membrane. Each MEA was assembled along with PTFE-coated fiberglass gaskets and 5cm^2 gas diffusion layers (GDL) (E-TEK High pressure GDL) in a single cell test fixture with stainless steel end plates and graphite collector channels. The single cell was then connected to a fuel cell test station (FCT 2000, Fuel Cell Technologies Inc., Albuquerque NM) which was coupled to a load box (Agilent Technologies, 6063 B, 250 W, 0-10 A, 3-240 V) and interfaced with a computer through a National Instruments Lab VIEW program. The test station was equipped with temperature control of the reactant gases and the cell hardware. Inlet gases to the cell were humidified by passing through bubblers containing water and their flow rates controlled using mass flow controllers. Backpressure regulators on the anode and cathode lines allowed regulation of inlet gas pressure.

Cathode and anode inlet fuel temperatures were set at 85ºC. Temperature of the humidified gas lines, hydrogen at the anode and the air at the cathode was kept at 10ºC higher than the fuel inlet temperature. This procedure prevented condensation as the fuel passed through the lines. Gas flow rates at both cathode and anode lines were maintained at 100 sccm; the temperature of the cell hardware was held at 80ºC. Regulating the back pressure valves a backpressure of 15 psi was applied to both inlet fuel lines. The cell was maintained at open circuit voltage (OCV) or no load conditions until the above mentioned temperature and pressure parameters were attained. Thereafter, a load of 0.6 V was applied to the cell from the load box and the measured current allowed to stabilize. This procedure was carried out to ensure complete hydration of the membrane. Reproducible *V-I* characteristics of the MEA were subsequently measured in the form of galvanodynamic polarization curves with data points recorded at current intervals of 50 mA. The polarization data for the undegraded and degraded Nafion™ membranes was compared.

Results and Discussion
Fluoride Evolution from Degraded Membrane

The cumulative loss of fluoride ions (F^-) as a function of exposure time to Fenton's reagent is presented in Figure 9. This fluoride release rate (g F^-/ cm^2 .hour) clearly indicates that with repeated degradation cycles, fluoride continuously leached out of the membrane. The data in Figure 10 provided information complementary to Figure 9. With repeated Fenton aging of the membrane, high ppm levels of fluoride evolved from the membrane. It must be kept in mind that after the sixth cycle, a portion of the 50 cm^2 membrane sample was cut and preserved for characterization purposes. Calculations yielded the surface area of the remaining membrane piece (which was now used for degradation cycles 6 through 12, to be 33 cm^2). In spite of a smaller sample being used for degradation (for cycles 6-12), the cumulative fluoride release rate never dropped indicating that the smaller membrane sample had a faster rate of fluoride generation. The fluoride release rates were in the ballpark with data reported in literature for Nafion™ and Gore Select™ mebranes[8,18].

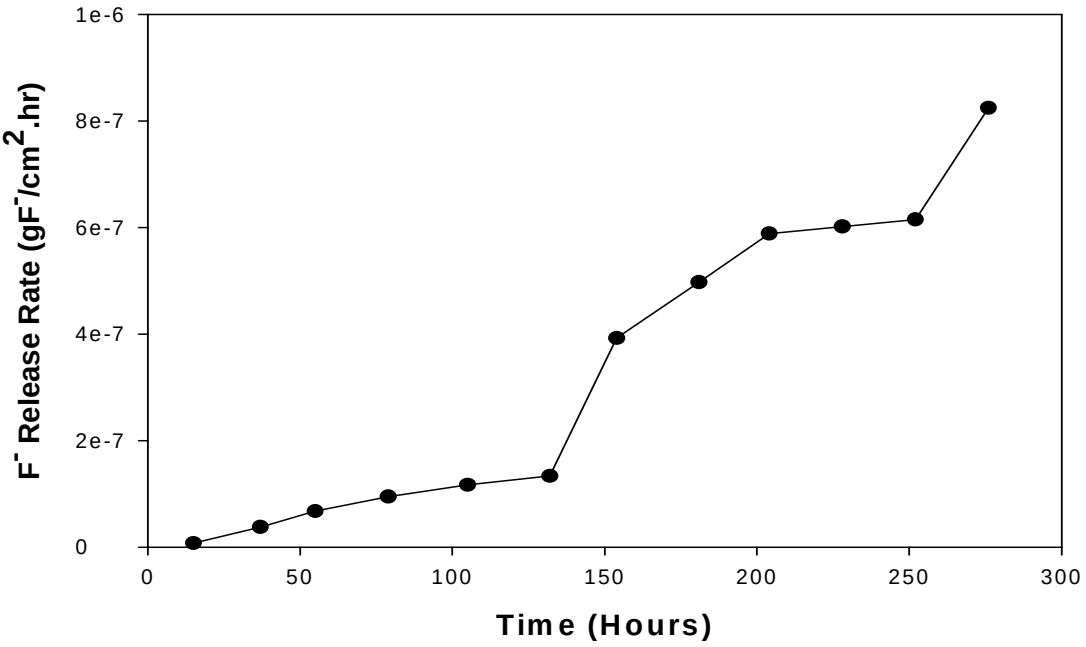

Figure 9. Cumulative Fluoride release rates (gm F-/cm2.hr) from Nafion™ 117 membrane during Fenton's degradation

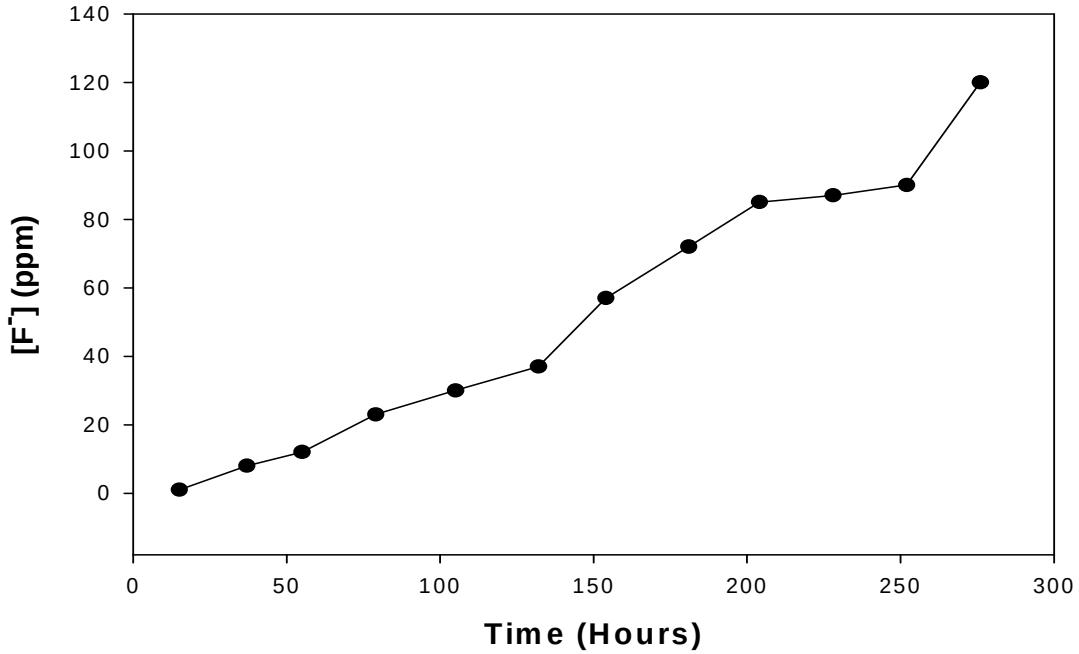

Figure 10. Cumulative Fluoride release rates (in ppm) from Nafion™ 117 membrane during Fenton's degradation

Morphological and Dimensional Analysis of Degraded Membrane

Table 1. compares the thickness and weight of the Nafion™ 117 sample prior to and after the completed degradation cycles. The data indicates that the membrane sample continued to lose weight and thickness over the period of Fenton's degradation. Even though the overall loss in thickness and weight compared to the starting material is only 8 % and 18%, respectively, the loss in dimensions and weight accompanied by an evolution of fluoride from the membrane indicates that over the lifespan of the MEA operation, the membrane will constantly erode. Such erosion, if unchecked over the duration of fuel cell operation will thin the membrane to the point where mechanical damage might occur, leading to membrane failure.

Table 1. Relative changes in weight and thickness of a 50 cm2 Nafion 117 piece after six and twelve cycles of Fenton's treatment.

	Nafion™ 117- '**As-received, Protonated**', dried for 72 hrs at 70℃	Nafion™ 117- Fenton degraded for **six** cycles, protonated, dried for 72 hrs at 70℃
Average Thickness for 50 cm^2 square piece	**0.177 mm**	**0.168 mm**
Average weight for 50 cm^2 square piece	**1.945 g**	**1.765 g**
Result	**5 %** loss in thickness and **10 %** loss in weight	

	Nafion™ 117- Fenton degraded for **six** cycles , dried for 72 hrs at 70℃	Nafion™ 117- Fenton degraded for **twelve** cycles, protonated, dried for 72 hrs at 70℃
Average Thickness for 50 cm^2 square piece	**0.168 mm**	**0.155 mm**
Average weight for 50 cm^2 square piece	**1.277 g***	**1.050 g**
Result	**8 %** loss in thickness sand **18 %** loss in weight (compared to starting material)	

***Note: Initial weight of sample is different for degradation cycles 6-12 because after the sixth cycle, part of the degraded membrane was cut and used for SEM/DMA/TGA analysis**

SEM photomicrographs in of the undegraded and degraded Nafion™ 117 surfaces are compared in Figure 11. and Figure 12. , indicating the surface and cross sectional morphology of the samples, respectively. For the unmodified Nafion™ 117 surface, there is no indication of bubble or crack formation and cracks reported by Moore *et al.* after their Fenton treatment of Nafion™.[21] In our work, after the sixth degradation cycle, the surface started to show imperfections appearing in the form of pits and dents (Figure 6). Comparing the surface images from the sixth and twelfth cycles, the surface indeed progressively gets riddled with the holes, some of which are 20-30 microns wide. An observation of the corresponding cross-sectional images (Figure 12.) clearly indicates the void formation which has been discussed by Moore *et al.* The voids appeared different from those observed by Moore, who observed bubble like formation in the degraded sample, akin to gas escaping and leaving behind voids. The membrane used in this work was extruded as opposed to the solution cast membrane used by Moore. The cross-sectional dimensions from the SEM images seem to be consistent with the thickness measurements (Table 1.). The surface damages and voids started to appear prominently after the sixth stage indicating that the degradation was starting to intensify between the sixth and twelfth degradation cycles.

Optical micrographs taken on the Nafion™ 117 membrane surfaces strengthen the SEM observations. From Figure 13., the surface of the degraded sample (after 12 cycles) appeared very rough when compared to the 'As-received, protonated' Nafion™ 117 surface due to imperfections, which were caused by the chemical degradation of the membrane.

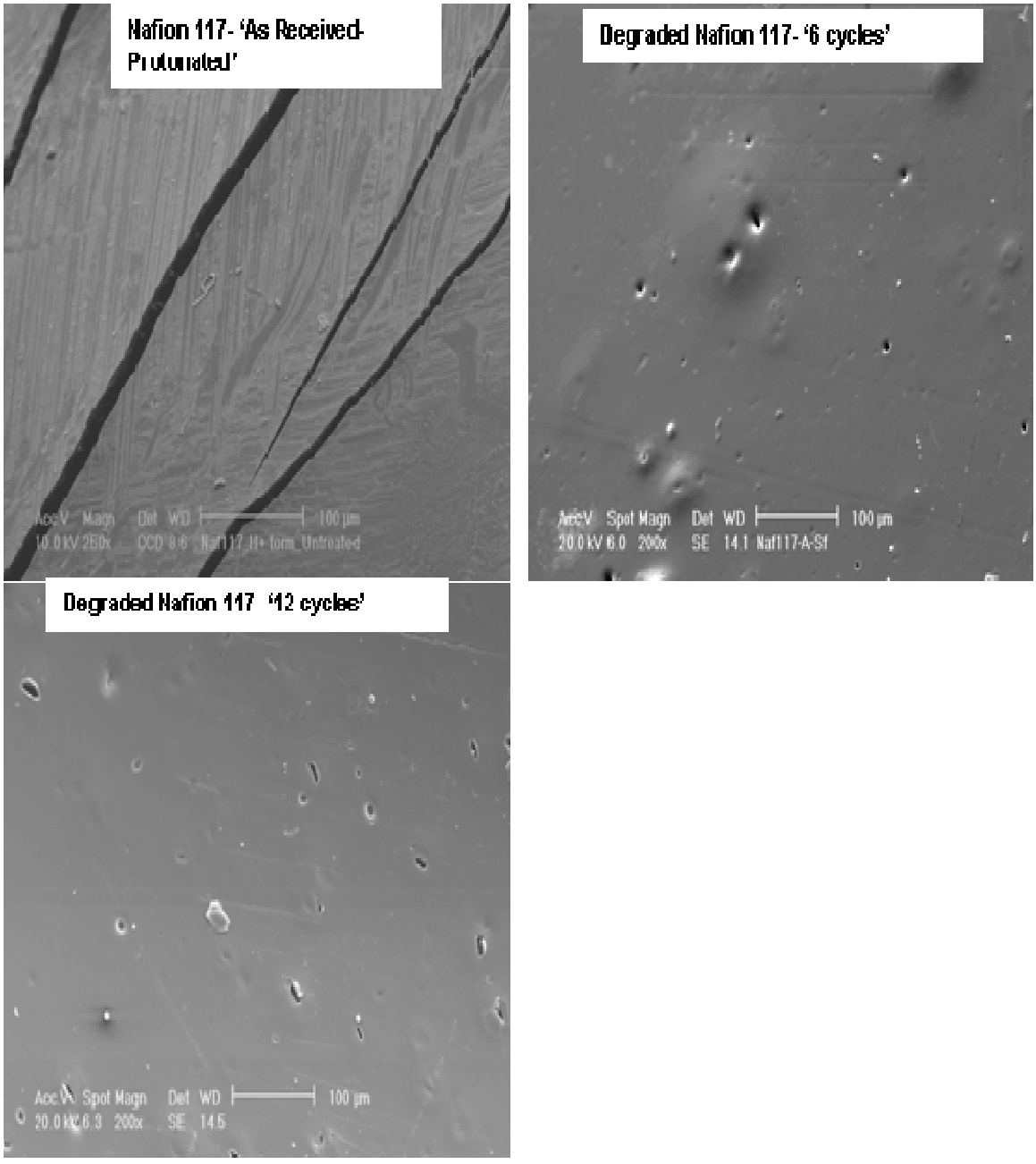

Figure 11. SEM images of Nafion 117 surface-'As-received, protonated' and after six and after twelve degradation cycles, respectively

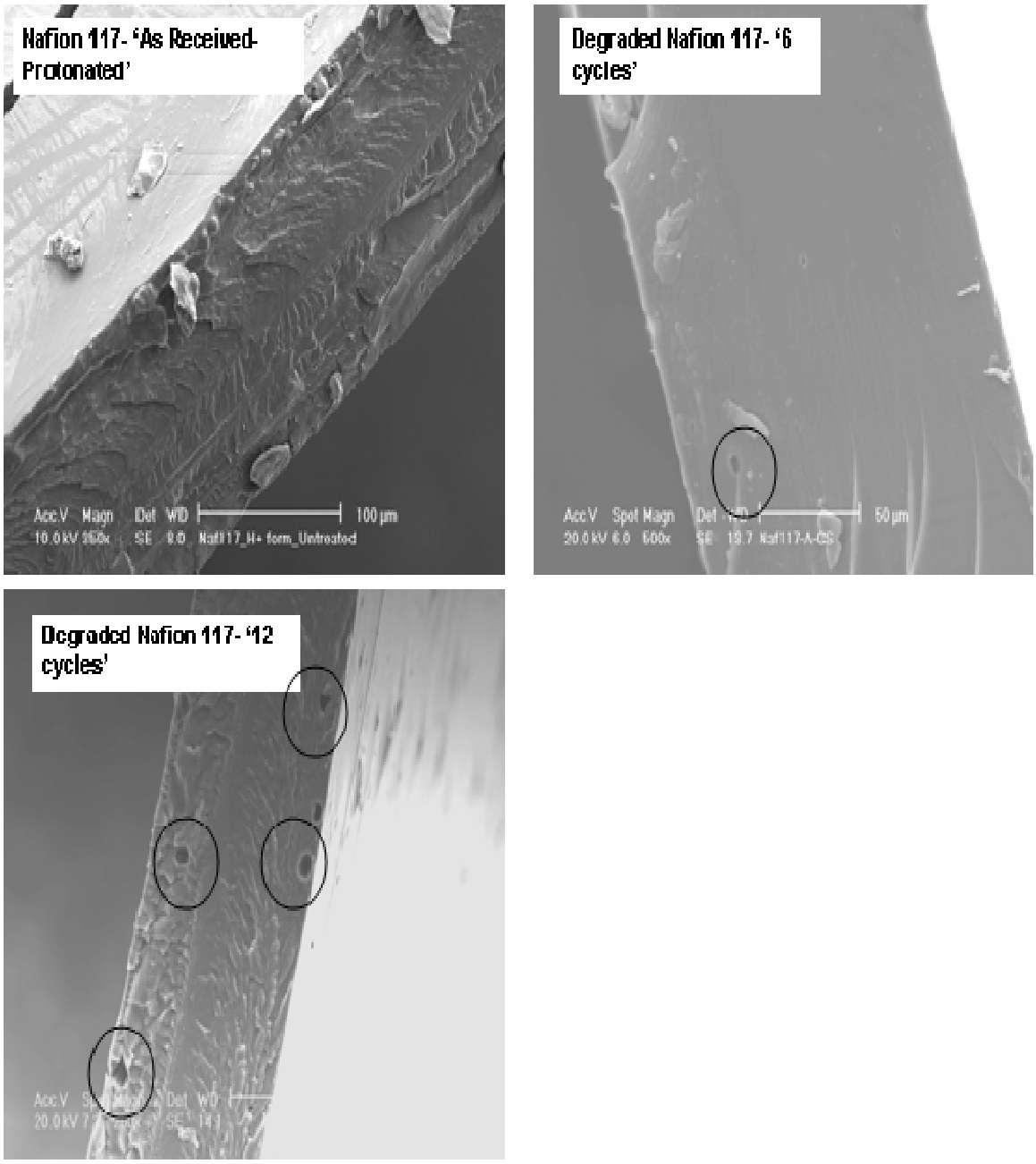

Figure 12. SEM images of Nafion™ 117 cross-section-'As-received, protonated' and after six and after twelve degradation cycles, respectively

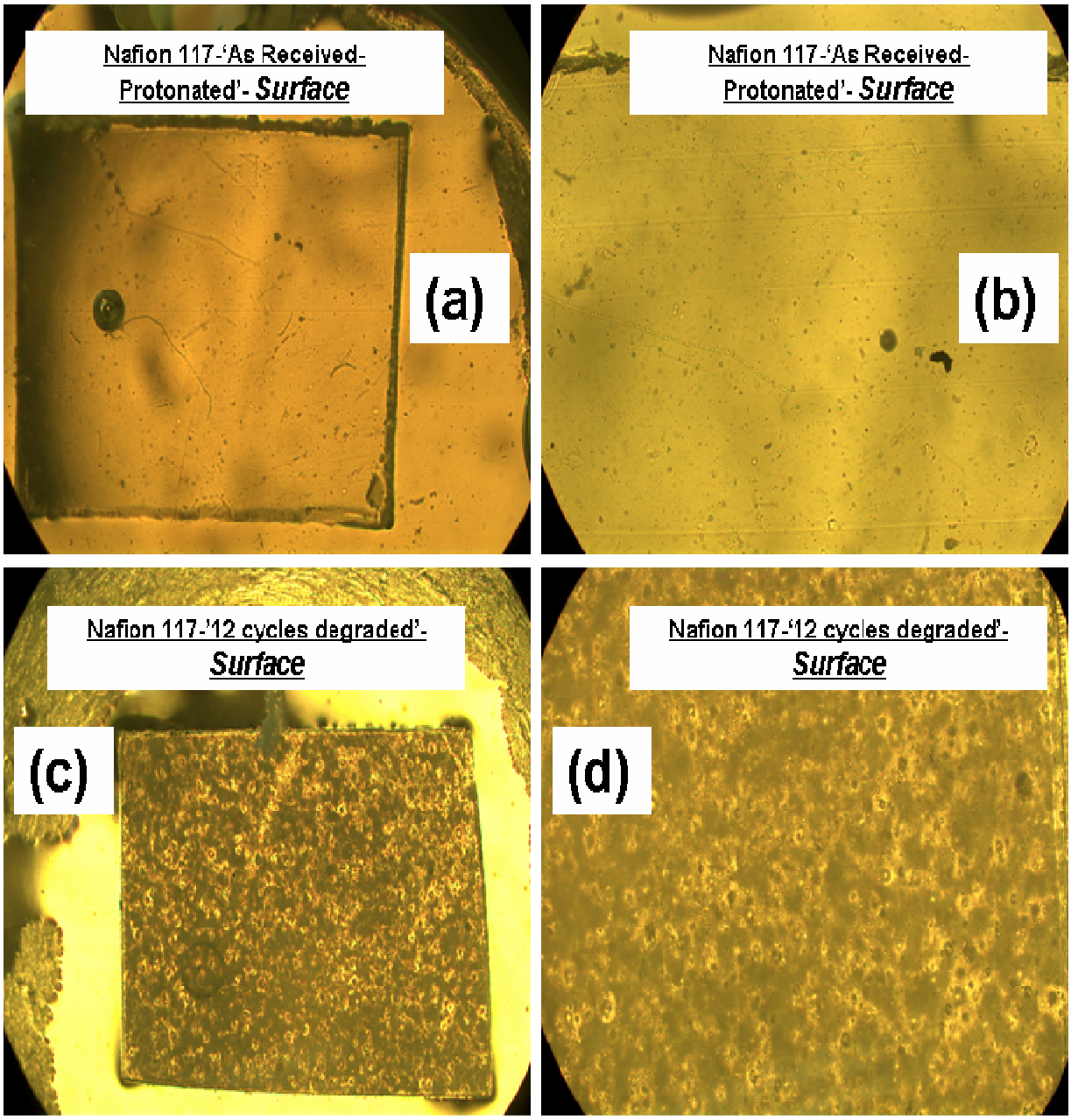

Figure 13. Optical micrographs of 'As-received, protonated' (a-b) and degraded Nafion™ 117 surfaces (c-d) after 12 degradation cycles indicating surface voids

Thermo-mechanical Analysis of Degraded Membrane

TGA thermograms of 'As-received, protonated' Nafion™ 117 membrane and membrane degraded for twelve Fenton's cycles are compared in Figure 14. As is common to the two curves, thermal decomposition of the samples started after 300℃ and the TGA curves were very similar to those measured by Kawano *et al.* for Nafion™ membranes in proton form.[22] Weight loss between 300 and 385℃ was attributed to the desulfonation of side chains in the Nafion™ membrane.[23] As reported by Kawano and Sun[22,23], final decomposition of the side chains and the PTFE backbone of Nafion™ began at 400℃, until 550° C, by when most of the mass was lost. TGA curve for the degraded Nafion™ 117 sample, for the most part, appeared to overlap that of

the unmodified membrane. The desulfonation of the backbone appeared to occur at a slightly faster rate for the degraded membrane. There were no drastic differences in the onset temperatures for various regions of thermal decomposition in the degraded Nafion™ sample (compared to the literature reported temperatures for virgin membrane) indicating that Fenton's degradation had not systematically altered the main chain or side chains of the Nafion™ sample.

Figure 15. presents a comparison of DMA data between the undegraded and degraded Nafion™ 117 samples in the form of a plot of loss tangent (tan δ) against temperature. The peak in the tan δ plot corresponds to the α-transition, which is attributed to the long range mobility of chains/sidechains in Nafion™ membrane (chain motions within a dynamic electrostatic network).[21] The low temperature β-transition corresponding to the onset of segmental motions of the polymer chains within a static electrostatic network was not visible in the DMA curve. Unlike the observations made by Moore *et al.*,[21] the α-transition did not shift to higher temperatures for the degraded sample, as is clear from Figure 10. In fact, Moore and co-workers found the α-transition of some degraded samples to have shifted while the others retained their position. They attributed this result to an inherent heterogeneity in their chemically stable (CS) membrane itself. From literature, it is known that above 115℃, the network of hydrophilic clusters, made up from the sulfonic groups, becomes mobile, before the clustered structure finally collapses.[22,24] In our work, the position for the α-transition, corresponding to the T_g did not shift at all. This indicated that after degradation there was no change in the molecular structure of Nafion™ 117 which would affect the mobility of the hydrophilic side chains. The difference in our observation with that of Moore may arise from the manner in which the membrane is fabricated (solution cast vs. extruded). The peak loss tangent values decreased for the degraded Nafion™ samples indicating that the membrane had become more elastic after degradation,[25] a result that was unclear.

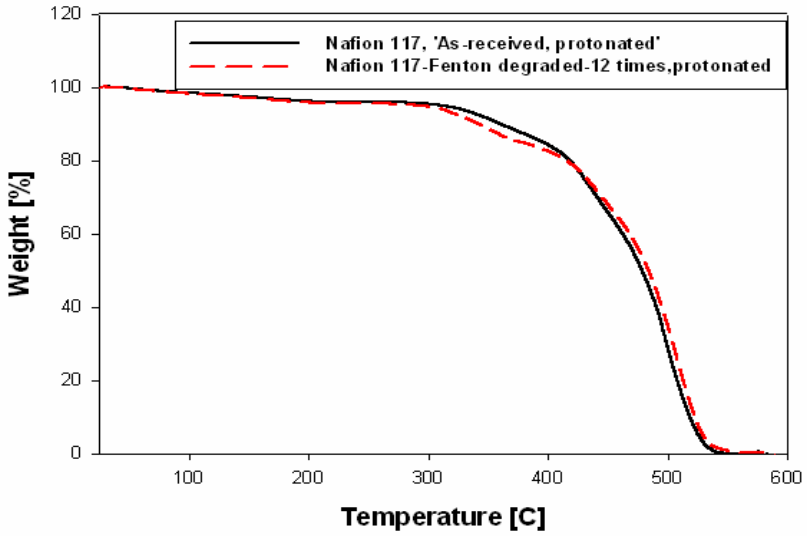

Figure 14. Comparison of TGA curves for Nafion™ 117 – 'as-received, protonated' and 'Fenton degraded, protonated' samples under nitrogen atmosphere

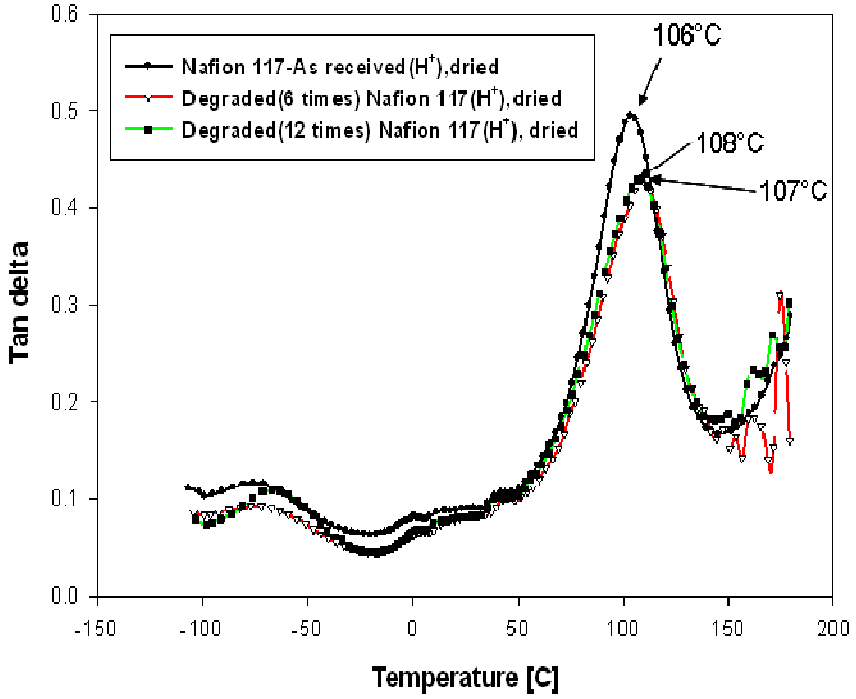

Figure 15. DMA-Comparison of Tan δ curves for Nafion™ 117 – 'as-received, protonated' and 'Fenton degraded, protonated'

Comparison of Water Uptake and Ionic -Conductivity

Hydration of the membrane is closely related to its ionic conductivity and mechanical stability. Water uptakes of the 'as-received, protonated' and Fenton degraded Nafion™ 117 samples, are given in Table 2. Ionic conductivities of the two samples are also compared in Table 2. The degraded membranes have a slightly high water uptake % than the undegraded membrane. The membrane water uptake values for the two samples were a close match to the numbers reported for Nafion™ membranes with an equivalent weight of 1100, at ambient conditions.[26] The ionic conductivity values were significantly lower than values reported in literature (0.085 S/cm),[27] and this may have been a result of insufficient equilibration of the membrane samples at 100% RH conditions. Because of the insufficient equilibration of the membranes, it was not possible to derive a clear conclusion based on the ionic conductivity data by itself. However, the equivalence in the water uptake indicates that the side chains of the degraded Nafion™ 117 membrane, which are responsible for hydration of the membrane, had not been affected by the harsh peroxide attack and still retain the ability to transport protons, similar to the undegraded sample.

Table 2. Water uptake and ionic conductivity comparison for undegraded and degraded Nafion™ 117 membrane samples

Sample	Water uptake (weight %)	Ionic conductivity at 25℃ (Siemens/cm)
Nafion™ 117- 'As received' [H^+]	21	0.0402
Degraded Nafion™ 117- '12 cycles' [H^+]	24	0.0345

Comparison of Tensile properties

Stress-strain curves of the Nafion™ 117-'as-received' membrane samples indicated a variability among the samples tested (Figure 11). For Nafion™ 117-'as-received, protonated' sample, linear deformation occurred at very low strains. The samples displayed a fairly low yield strain and high modulus. Some samples failed before reaching maximum load (#3 in Figure 16.) at the maximum load (18 N) while others continued to elongate (#1 and # 2 in Figure 16). Thus, the maximum strain and the maximum stress were variable. No necking phenomenon was observed. The shapes of the curves resembled those reported in literature for Teflon™ films.[28]

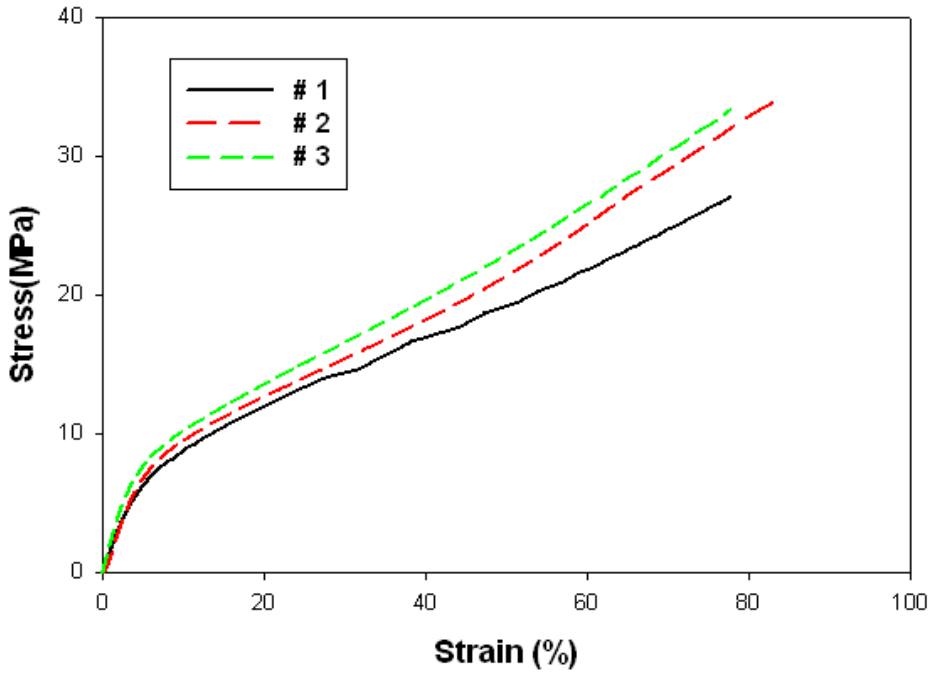

Figure 16. Comparison of stress-strain curves for Nafion™ 117 – 'As-received, protonated' samples

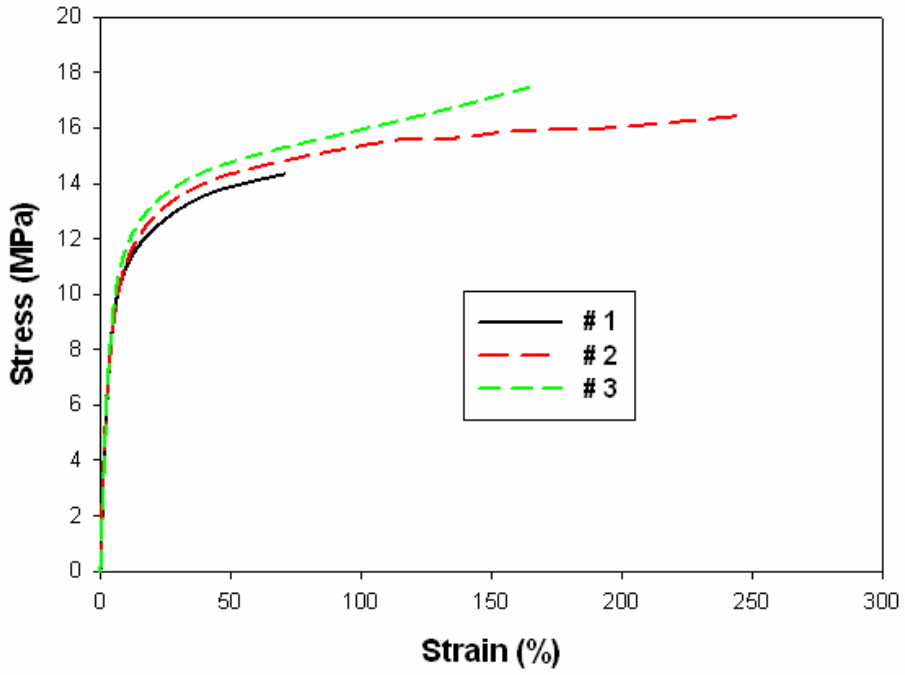

Figure 17. Comparison of stress-strain curves for Nafion™ 117 – 'Fenton degraded (12 cycles), protonated' samples

Stress-strain curves for the Fenton's degraded sample (12 cycles) are illustrated in Figure 17. A comparison of average tensile data between the undegraded and degraded samples is made in Table 3. As is clear from Figure 17., no catastrophic failure or drop in mechanical behavior resulted even after the harsh Fenton's degradation test. From Table 3, the degraded Nafion™ samples also displayed a fairly low yield strain but very high modulus, as was evident from the steep slope of the linear region.

The maximum strength dropped for the degraded sample and the yield strain indicated a high degree of variability, with one of repetitions elongating up to 240 % (Figure 17). No firm conclusions could be derived from the tensile data based on the variable values of ultimate strength and elongation at break.

Table 3. Comparison of tensile data for undegraded and degraded Nafion™ 117 membrane samples based on stress-strain curves in Figures 11-12

Sample	Yield Strain (%)	Ultimate Strength (MPa)	Elongation at Break (%)
Nafion™ 117- 'As received' [H^+]	4.3 ± 0.5	31.6 ± 4.0	80 ± 4
Degraded Nafion™ 117-12 cycles' [H^+]	3.9 ± 0.6	16.1 ± 1.6	160 ± 90

Proposed Mechanism for Membrane Failure

The results from the characterization of the chemically-degraded membranes indicated that the only change which was detected in the membranes post chemical degradation was fluoride evolution from the membrane, accompanied by a gradual thinning of the membrane sample and loss in weight. The morphology of the degraded samples was altered to some extent with the formation of voids on the surface and in the membrane cross-section. There was no significant impact on the thermo-mechanical, and tensile properties of the membrane indicating that the chemical structure of Nafion™ and its molecular arrangement had not been affected. The question now arises is, how does membrane failure actually occur? To speculate on the exact mechanism, a schematic for the probable cause of failure is illustrated in Figure 18. Fluoride measurements have clearly demonstrated that during chemical degradation, the membrane leaches out fluoride while it is being uniformly eroded. The variability in the thickness of the starting Nafion™ samples also indicates that there might be areas in the sample which are thinner and hence weaker than some other areas. Such areas can be termed as 'weak-spots' as shown in Figure 18. The weak spots can also be generated due to precipitation of metal ions (which start Fenton's degradation) inside the membrane.[29] Thus as the membrane is being attacked by peroxide and eroded, the erosion can be more profound at these weak spots. Such weak are spots are probably the voids which can be observed in the SEM images of the Nafion™ 117 membrane after twelve degradation cycles (Figure 11). Eventually after constantly thinning of the membrane, erosion at one of these weak spots might traverse across the membrane causing a pin-hole to form. The pin-hole formation most-likely occurs before the projected lifespan of the membrane. If the above theory holds true, as the membrane thins evenly due to the peroxide attack while leaching out fluoride, a thinner membrane such as Nafion™ 112 (thickness~ 60 µm) will develop a pinhole much faster. The mechanical, thermomechanical and hydration characteristics of the membrane degraded in our work have not been drastically affected, therefore it can be concluded that even after the harsh chemical degradation cycles, the membrane had not reached a point where pin-hole formation occurred, through SEM evidence started to indicate towards void formation.

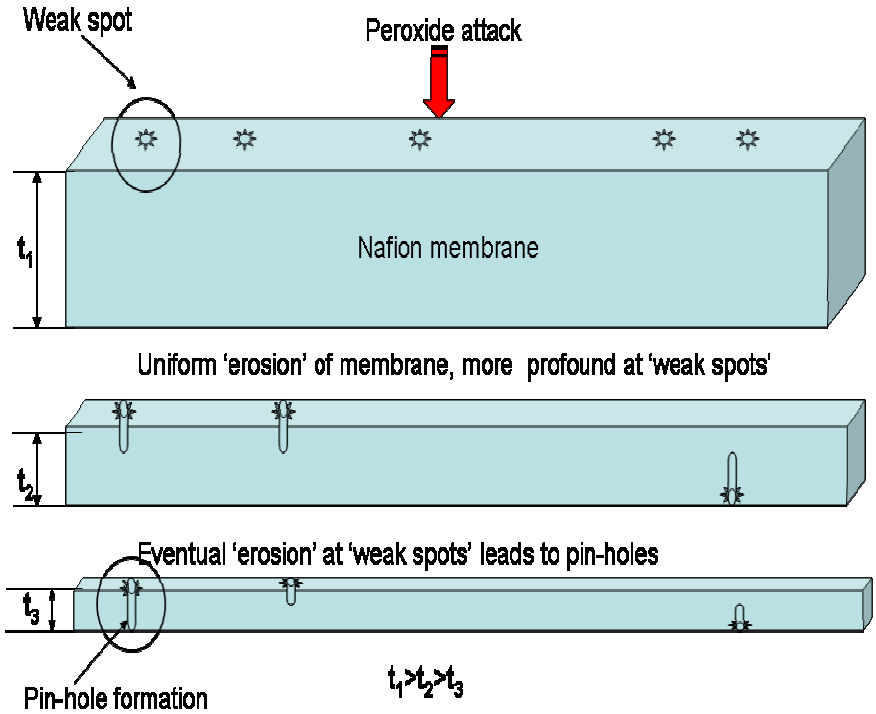

Figure 18. Schematic illustrating proposed mechanism of membrane thinning and pin-hole formation due to peroxide attack

Fuel Cell Performance of Degraded Membrane

A comparison of fuel cell performances of MEAs fabricated using the undegraded and Fenton's degraded Nafion™ 117 membranes are presented in Figure 19. Both the MEAs were fabricated using the commercial E-TEK catalyst as the electrodes (platinum catalyst loading on both anode and cathode was 0.3 mg cm^{-2}). From Figure 19., open circuit voltage of the MEA prepared using the degraded Nafion™ 117 sample is in the acceptable range (> 0.9 V) and equivalent to the corresponding value for the undegraded membrane MEA. The high value of open circuit voltage is a first indication that there is no breach in the degraded membrane. The fuel cell performance for the two MEAs also overlaps in the ohmic drop region, indicating that the hydration behavior and ionic conductivity of the Nafion™ 117 membrane has not been affected by the chemical degradation. The sturdiness of the Nafion™ 117 sample used in our work is clearly evidenced by these results. For the total time of degradation (~300 hours), the membrane retains its structural integrity as well as its characteristic properties, and exhibits a comparable performance to the undegraded sample. Long term degradation studies for hundreds (and if possible thousands of hours) of hours need to be carried out to before a noticeable change in fuel cell performance occurs.

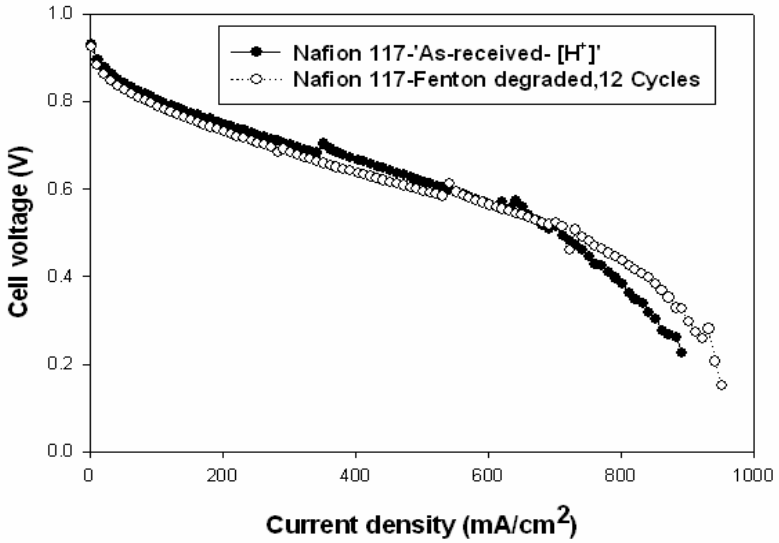

Figure 19. Cell polarization curves for MEAs prepared using undegraded Nafion™ 117 and Nafion 117 sample Fenton degraded for 12 cycles. Anode fuel- H2, cathode fuel – Air.

Conclusions and Outlook

The issue of membrane durability is a very important area in the field of PEMFC materials development. Our work has shown that Nafion™ 117 membrane does evolve fluoride, a result also observed by numerous other researchers. The fluoride evolution is accompanied by a slow but gradual erosion of the membrane surface, loss in weight and generation of voids within the membrane and on its surface. These voids pose the potential to generate pin-holes if the membrane continues to erode over its lifespan. However for the specific degradation mechanism carried out in our work, no pin-hole formation resulted, as evidenced by the acceptable fuel cell data for the degraded membrane sample. Also other properties of the membrane such as hydration, ionic conductivity, mechanical and thermomechanical response remained fairly similar to the undegraded membrane

The degradation regime in our work is extremely harsh and in real world conditions, concentration of the peroxide generated is probably small than the levels employed in our work. However, the rationale behind the use of such high concentrations is to accelerate the degradation process. The degradation of Nafion™ is appears to be a localized process with certain locations in the membrane degrading faster than others. One key finding would be to map the distribution of peroxide generated at various points in the membrane. Also, detailed electrochemical experiments need to be carried out to separate the total peroxide generated into the fraction at the electrode and that in the membrane. A detailed understanding into the exact chemical mechanism of the degradation, including the degradation of the side chains is being carried out[30] The findings need to be correlated with long term durability studies where the membrane is tested for thousands of hours in a fuel cell, with constant monitoring of Fluoride from the anode and cathode and measurement of dimensional changes. To verify the degradation mechanism, end capped Nafion™ membranes can also be tested for fuel cell performance and the generation of fluoride measured and compared with data for regular Nafion™ membranes without end capping.

2.1.3 Model Compound studies

CASE
CASE WESTERN RESERVE UNIVERSITY

Model Compound and Membrane Chemical Durability Studies

Knowledge of membrane degradation mechanisms can serve as important material design guidelines to improve stability and the service lifetime. Results of membrane deterioration, such as fluoride evolution in the effluent water, membrane thinning, and pin-hole or crack formation are frequently observed in the operating fuel cell systems[31,32,33].Various mechanical degradation modes have been proposed to explain such observations, including: fatigue-type behavior resulting when membranes are subjected to rapid dehydration/rehydration cycles that can be caused by rapid current density changes,[12, 14] and concentrated stress areas and localized heat spots caused by penetration of catalysts particles into membrane.[15, 16]

The chemical degradation of membranes is thought to play a critical role in the observed fuel cell failures, although the final failure may ultimately result from the interplay between different degradation routes within various fuel cell components. The current state of knowledge describing possible chemical mechanisms of degradation for PEM membranes was recently reviewed.[34,35] The majority of authors in the field attribute chemical degradation of PFSA membranes to be caused, at least in part, by exposure to peroxide and hydroxyl radicals known to be produced in these electrochemical devices *via* incomplete reduction (2 electrons) of O_2. Various membrane chemical structure changes were observed as a result of degradation. Schlick *et al*.[36] reported the observation of a polymeric radical where the unpaired electron is located on the tertiary carbon atom in Nafion™ backbone that is linked to the pendant side chain. Chain end radicals with structures like R_f-O-CF_2-CF_2• were also identified on the side chain radical by electron spin resonance (ESR), when Nafion™ membranes, saturated with metal counter ions, were exposed to UV radiation with the presence of H_2O_2. The reaction between the Fe(III) counter ions and sulfonic acid groups on the side chains was proposed to produce such chain end radicals: R-O-CF_2-CF_2-SO_3^- + Fe(III) → R-O-CF_2-CF_2-SO_3• + Fe(II), followed by rearrangement via elimination of SO_2 and O_2. Direct soaking of Nafion™ in 3% (v/v) aqueous H_2O_2 solution for up to 30 days resulted in the formation of S-O-S bond as determined by Fourier transform infrared spectroscopy (FTIR).[37] The S-O-S bond formation was thought to be the result of crosslinking of sulfonic acid groups on the side chains, which subsequently reduces the ductility and proton conductivity. In another study,[38] FTIR studies revealed trace amount of R-SO_2F or S-O-S formation when Nafion™ was degraded by H_2O_2/Fe(II) solutions; such reagents

are commonly known as Fenton's reagent, and are widely used to generate hydroxyl and hydroperoxyl radicals.[39] The authors also commented that the side chains were decomposed more easily than the main chain, based on the ^{19}F nuclear magnetic resonance (NMR) integral ratio changes of Nafion™ repeat units. FTIR[32], ^{13}C NMR[32], ^{19}F NMR[40], and mass spectroscopic (MS)[40] analysis of the degradation test solution exhibited fluorinated fragments with the structure largely resembling the derivated Nafion™ side chain structure.

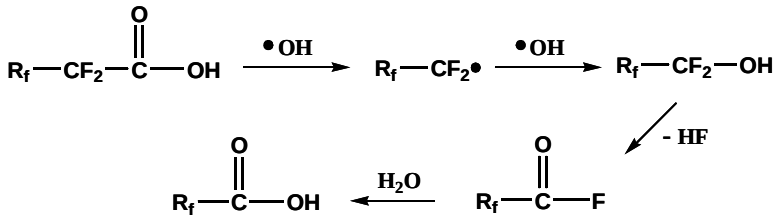

Figure 20. Chain end "un-zipping" degradation Mechanism

Despite valuable information revealed from the literature cited above, the detailed degradation mechanism(s) leading to the observed chemical structural changes is still poorly understood. One important mechanism was proposed by Curtin *et al*. to explain the fluoride generation pathway[41]. As shown in Figure 20, the degradation process starts from the carboxylic acid end groups (-COOH) that may be present in small concentrations. These end groups are unintentionally introduced from the manufacturing process of Nafion™ via the hydrolysis of the persulfate initiators used in the polymerization of Nafion™[42]. The degradation is proposed to proceed by a main chain unzipping mechanism: hydroxyl radicals abstract hydrogen atoms from -COOH, followed by decarboxylation to form primary perfluorinated radicals. These primary radicals then react with available hydroxyl radicals to form primary fluorinated alcohols, which are highly unstable and rapidly decompose to acyl fluorides with elimination of HF. Subsequent hydrolysis of acyl fluorides yields carboxylic acid ends to re-enter the degradation cycle, shortening the chain by one net carbon unit. Fluorination of end groups leads to the reduction of reactive end group contents, but the fluoride evolution was not eliminated even when the reactive end groups are reduced to be close to zero, as shown in Figure 21 [41,43]. A second degradation mechanism is therefore necessary to account for the significant, non-zero fluoride evolution observed when carboxylic acid end groups are eliminated, to explain the structures of degradation products identified as discussed above.

This chemical durability project addresses the need for the construction of a coherent model of PEM polymer degradation mechanisms. In order to gain the benefit of standard chemical methods generally not easily deployed when studying the intractable ionomers, a family of low molecular weight model compounds (MCs) with structural characteristics similar to moieties found in PFSAs was examined. Additionally, the degradation test and products analysis of MCs will enable the comparison of reactivity for different moieties toward degradation. The degradation of the benchmark PFSA membrane, Nafion™ and 3M ionomers was studied in parallel. Relative kinetics of fluoride generation, as well as characterization of degradation products were considered as mechanistic probes.

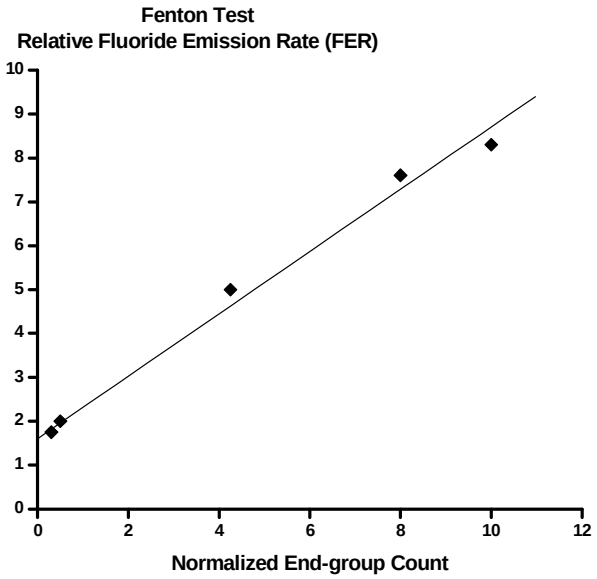

Figure 21. Plot showing relative fluoride emission rate (FER) from Fenton's test as a function of concentration of reactive end-groups (Figure recreated from reference 43)

Materials

The structures of model compounds (hereafter MC) considered in this work, along 3M and Nafion™ 117 (hereafter Nafion™) ionomers are given in Figure 22. The 3M ionomers and Nafion™ were provided by 3M. Extra Nafion™ was also purchased from Aldrich. MC1, perfluoro(2-methyl-3-oxahexanoic) acid, 97%, was purchased from Lancaster Synthesis. MC2, perfluoro(2-methyl-3-oxa-7-sulfonicheptanoic) acid, 96%, was provided by 3M. MC3, perfluoro(4-sulfonicbutanoic) acid, was provided by 3M. MC4, perfluoro-n-octanoic acid, 98%, was purchased from SynQuest Labs. MC5, nonafluorobutansulfonic acid, was purchased from SynQuest Labs. MC6, 1H,-perfluorooctane, was purchased from SynQuest Labs. MC7, perfluoro(3-oxahexanoic sulfonic) acid, and MC8, perfluoro(4-methyl-3-oxaoctanoicsulfonic) acid, were provided by 3M. All the MCs were used as received. Ferrous sulfate heptahydrate, 99%, was purchased from Fisher. Hydrogen peroxide solution, 30% (w/v), was obtained from Fisher. Total Ionic Strength Adjustment Buffer (TISAB II, with CDTA) solution was purchased from Thermal Orion. Acetonitrile and ammonium acetate, both HPLC grade, were purchased from VWR.

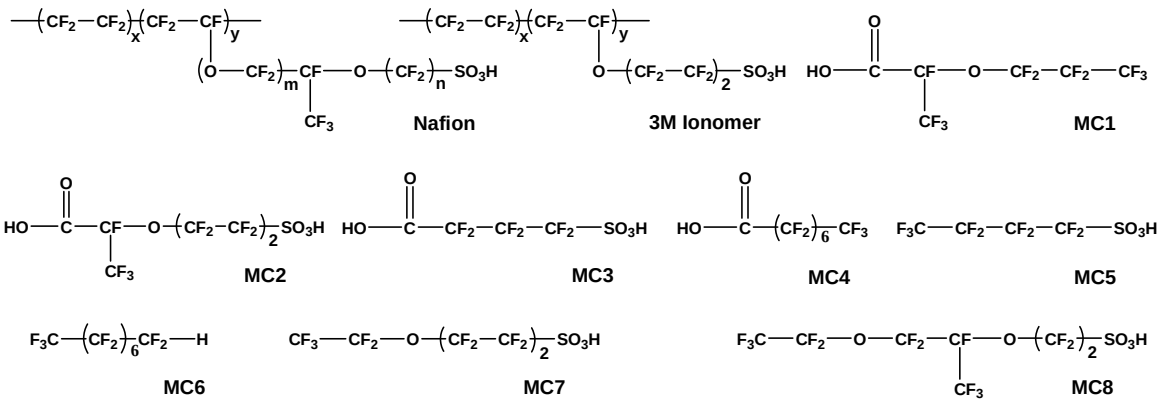

Figure 22. Structures of Nafion™ (upper left), 3M Ionomers (upper center), and various MCs

Characterization Methods and Experimental Procedures
Membrane Pretreatment Protocol

Membrane samples were converted to acid form by the following protocol prior to the degradation test: membrane in the form of film is cleaned by heating in a 1.5% v/v peroxide solution at 70^{o}C for 1 hour, followed by washing the membrane in a hot DI water bath (70^{o}C) for 1 hour. The membrane then was boiled in 1M sulfuric acid for 1 hour to convert to acid form. The whole process was completed by subsequent washing with 70^{o}C DI water for 1 hour.

Fenton's Degradation Procedure for Model Compound
Mild Condition Test

Fenton's reagent, a combination of H_2O_2 and a ferrous salt, is a very effective method to generate hydroxyl and peroxyl radicals. As mentioned above, these radicals are the most commonly attributed attacking species for the FC PEM. The decomposition of H_2O_2 is a very complicated system, but the major and generally-accepted reactions are: $H_2O_2 + Fe^{2+} \rightarrow Fe^{3+} + HO^{-} + HO^{\cdot}$, and $HO^{\cdot} + H_2O_2 \rightarrow HO^{\cdot} + H_2O$. It is known that many factors, such as stoichiometry and order of addition of reagent, can easily alter the products. In this study, known amount of H_2O_2 was slowly added to a well-stirred solution containing locally excess Fe^{2+} to minimize the consumption of hydroxyl radicals via reacting with hydrogen peroxide, i.e. the second reaction above, so as to maximize the generation of the highly reactive hydroxyl radicals to mimic the attacking species in the FC operation.
The concentrations of MCs and Fenton's reagents are tabulated in Table 4. The exact concentration of H_2O_2 formed in a real fuel cell is very difficult to measure, and is a function of many factors such as membrane thickness, but typical concentration was measured to be 10-20 ppm[44], which translates to approximately 0.5 mM. In this study, 11 mM concentration was used for accelerated degradation tests for mild test conditions.

Table 4. Concentrations of reagents used in degradation tests

	Reagents Concentrations
Fe(II)	1.25 mM (ca 70 ppm)
H_2O_2	11 mM
MC	100 mM
DI Water	50 ml (total)

Each MC was first mixed with a 40 ml aqueous solution containing 1.25 mM ferrous ions by dissolving ferrous sulfate heptahydrate in water (all the concentrations mentioned here are calculated based on the total volume, *i.e.* the final volume after all the reagents are introduced into the reactor), then the solution was bubbled with nitrogen dry gas for at least 10 minutes to remove the oxygen that might react quench radicals. The solution was subsequently heated to 70 ± 2º C. To the flask was added the hydrogen peroxide through an addition funnel at a slow dropping rate, typically 10 to 20 drops per minute. The reaction mixture was held at around 70ºC under purge of nitrogen for about 24 hours, followed by removing a 2 ml sample from the reactor for fluoride concentration measurement. The tests were continued by adding fresh ferrous ions and hydrogen peroxide to react by same procedure described above, and another fluoride measurement was carried out after an interval of 24 hours. The sample process was repeated for 5-6 times cycles, for a total of ca. 130 hours to complete the test. The data were presented by plotting the amount of fluoride detected as a function as accumulated degradation test time/intervals.

Harsh Condition Test

Solution of Fe^{2+} and MC were firstly mixed and stirred, with the N_2 bubbling for about 30 min. H_2O_2 was then slowly added into the well-stirred solution by addition funnel. The reaction temperature was adjusted to about 70^{o}C, and the reactor throughout the whole course is purged by dry N_2 gas. The average reaction time was controlled to be around 24 hours. Once the reaction was finished, the precipitates generated will settle down to the bottom after about 30 min without stirring, a F^- measurement was taken by removing a 2 ml sample from the solution. Subsequently, the solution was filtered through a glass filter, and the precipitates were washed by copious amount water and acetonitrile. Finally, water and actonitrile were taken out by a rotavapor, leaving the treated MC in the flask. This treated MC was used again to do the subsequent tests. Concentrations of reagents are tabulated in Table 5. Detailed schemes are shown as follows in Figure 23.

Table 5. Concentrations of reagents used in harsh condition degradation tests

	Reagents Concentrations
Fe(II)	400 mM
H_2O_2	400 mM
MC	100 mM
DI Water	50 ml (total)

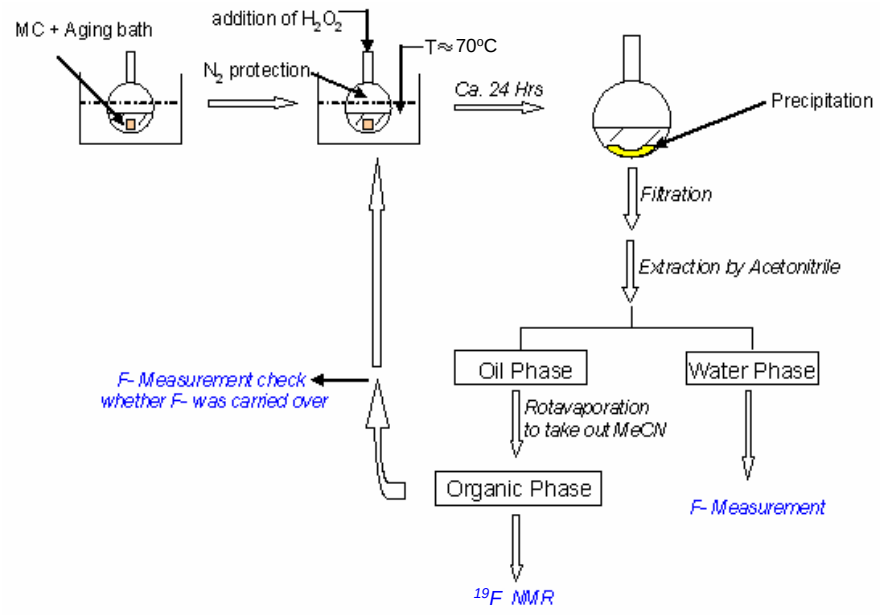

Figure 23. Schematic diagram showing harsh degradation test procedure for the model compounds.

Fenton's Degradation Procedure for Membrane Samples
Fenton's Degradation Test

Iron salt was dissolved in DI water. Membrane samples were then added into this solution. Subsequently, the flask was sealed by septum, and bubbled with Argon for one hour, followed by increasing the temperature to 70°C. H_2O_2 was added in by addition funnel when the temperature was constant. The system was bubbled with argon throughout the course of experiment in order to keep oxygen from reacting with the radicals.

Modified Fenton's Degradation Test

Degradation test procedure of Nafion™: The degradation test started with the acid form of Nafion™. The first step was to convert Nafion™ to its Fe(II)-saturated form by immersing the sample in a 0.1M $FeSO_4$ solution for 2 hours at 70℃. After the ion exchange, the sample was removed and rinsed with deionized water to remove the residual ion exchange solution from the membrane, and further blotted dry with paper towels. The samples appeared to be light yellow in color prior to the degradation test. The targeted Fe(II) loadings was quantitative relative to the concentration of sulfonic acids, which was calculated from the equivalent weight of Nafion™. The second step was to put the Fe(II) saturated Nafion™ into a deionnized water bath (which does not contain ferrous ions like in previous Fenton's degradation tests), then the solution was degassed with dry nitrogen gas for at least 10 minutes prior to the addition of H_2O_2. The solution was then heated to 70 ± 2℃ and hydrogen peroxide (concentration 0.1M based on the total volume of the reaction media, identical to the concentration used in the "harsh" Fenton's experiment) was slowly introduced into the flask to react through an addition funnel. The reaction mixture was held at 70℃ under purge of nitrogen for certain period of reaction time, typically *ca.* 35 hours. Subsequently, the fluoride concentration measurement was carried out by removal of 2ml aliquots from the reactor. The reaction media was not discarded but used in the following test (same amount of water 2 ml was added back to the reactor to balance the total volume along with the addition of hydrogen peroxide for the next round of degradation experiment). The third step was to convert the degraded sample (dark brown color) back to acid form (colorless) by

immersing in 0.5M H_2SO_4 at 70℃ for 1 hour. The next round of degradation test was then carried out by following the procedure described above.

UV H_2O_2 Photolysis Degradation Test

In parallel to the Fenton's reaction, UV photolysis of hydrogen peroxide was exploited as a clean source to study the effect of radical on MCs. An advantage of this approach is that it eliminates the iron ions present in Fenton's testing, but not present in such high concentrations under authentic fuel cell operation. Analytically, the absence of iron ions will potentially lead to more readily interpreted data. It is well known in literature that hydroxyl and peroxyl radicals are generated when hydrogen peroxide is exposed to UV radiation.[36, 45] The light source used was an Oriel standard 100W Mercury lamp with a wavelength from 200-2500nm. MCs were mixed with DI water (concentration is 100 mM, total volume of testing sample is 3 ml in a quartz cuvette) and then further exposed to the UV radiation for 1 hour at room temperature, with and without the presence of hydrogen peroxide (400 mM).

Table 6. Concentrations of reagents used in membrane degradation tests.

	Reagents Concentrations
Fe(II)	80 mM
H_2O_2	400 mM
Ionomers	5-10 grams
DI Water	250 ml (total)

Fluoride Concentration Measurement

Fluoride ion concentration in aqueous solutions was measured using an ion selective electrode (ISE) (Mettler-Toledo, ISE part # 51340510, meter model number MX300), which was calibrated over the range 0.01 – 1000 ppm fluoride using NaF aqueous solutions. The detection accuracy limit is at least 0.1 ppm (5.26×10^{-6} M), which still gives a satisfactory calibration curve fit when compared to the theoretical value using the Nernst equation. All the fluoride concentration data reported here were obtained by a direct measurement method against the calibration curve: the electrode was immersed into a solution containing 2 ml sample and 2 ml TISAB II solution (the solution was constantly stirred) and an potential reading of the meter was recorded after equilibrium was reached, typically 5-10 min. The electrode was checked daily by a solution of known fluoride concentration to ensure accuracy, and was re-calibrated whenever deviation was observed.

NMR Characterization

NMR spectra were obtained by a Varian AS600 600 MHz spectrometer. Acetonitrile-D_3 from Fisher was used as the solvent for MC treatment experiments; all the chemical shifts are referenced to $CFCl_3$ (defined as 0 ppm) as standard.

LC-MS Characterization

The LC-MS analysis was carried in a Thermo LC-MS system. Column used was HP/Agilent Zorbax column (Eclipse XDB-C18, 2.1mm X 15cm). HPLC grade ultra pure water was used to prepare mobile phases. Solvent A: Aqueous 6 mM ammonium acetate. Solvent B: 95/5 Acetonitrile/water containing 6 mM ammonium acetate. The solvent gradient started with constant 5%B for 5 minutes, then from 5% B to 100% B in 25 minutes, followed by holding at 100%B for 5 minutes. Sample injection volume was 2 μL, and the mobile phase flow rate was 0.25 mL/min. MS scanning: negative electrospray, Scan 50-1000 m/z.

FTIR Characterization

FT-IR spectroscopy was carried out on the original and degraded ionomer samples by a Perkin-Elmer spectrometer. Scanning wave number was from 400-4000 cm^{-1}. Typical acquisition is 32 scans.

Membrane Equivalent Weight Measurement

Membrane samples (fresh/aged, about 2X2 cm^2) were soaked in concentrated nitric acid (70% w/w) or H_2SO_4 (ca. 0.5 M) for an hour to convert to protonated forms. The sample in the solution was diluted and filtered through a filter paper (such as #2) to check the integrity of the film after soaking. Excess acids were washed away by rinsing with DI water thoroughly. The samples were then dried in vacuum oven (80^oC) overnight. Sample weights were taken after the drying. The dried sample was soaked in NaCl (1-3M) overnight to exchange Na^+ for H^+. The exchanged protons were titrated NaOH using phenolphthalein as an indicator. The equivalent weight data were averaged from three independent titrations.

Results and Discussion
Fluoride Generation
Model Compound: Fluoride Generation from Fenton's Degradation Test

Caution has been taken to ensure the accuracy of the fluoride concentration measurement by examining the effect of sample pH, ferrous ion concentration, and ferric ion concentration on measured readings. It was verified that the measurement was not affected by sample pH values when using TISAB II buffer solution to maintain the desired pH range and good ion background (control experiment data not shown for brevity). Note: when pH > 7, OH^- will interfere the electrode response to fluoride; and when pH < 5, the proton can complex a portion of fluoride in solution by forming the undissociated acid HF and the $(HF_2)^{-1}$ ions. It was also found that the presence of Fe^{2+} does not interfere with the measurement when TISAB II is used, while interference from Fe^{3+} was observed but could be eliminated by a serial sample dilution method, in which an accurate fluoride concentration can be obtained by diluting the sample to the point (typically 100 fold dilution) where the concentration of Fe^{3+} does not interfere while keeping measuring fluoride concentration well above the detection limit of the electrode. Therefore, if ISE is used to measure the concentration of fluoride, cautions have to be taken to correct the interference of Fe(III) ions to get reliable fluoride concentration data.

For mild degradation test, the fluoride evolution from MCs is plotted in Figure 24. The fluoride concentration is presented as the atomic percentage ratio of fluoride released relative to the total fluorine atoms from each model compound. MCs containing carboxylic acid groups showed significantly higher rates of fluoride generation than those without that functional group. The fluoride evolution of MC5, MC6, MC7 and MC8 shows the order: MC5 > MC7 ~ MC8 > MC6. The lowest fluoride generation of MC6 is expected due to the poor solubility in aqueous solution (phase separation was observed). The relatively higher fluoride release rate observed for MC5 may be due to the fact that MC5 contains less fluorine atoms (shorter chain than MC7 and MC8), which may increase the percentage of fluoride release. It is important to note that even for these least reactive model compounds (MC6, MC7, and MC8), the generated fluoride concentration was significant. This results strongly implies that fluoride release pathways from PFSAs other than the carboxylic acid end group degradation exist and are kinetically competitive. This point is highly relevant since MC8 is structurally a close analogue of Nafion™, while MC7 is the analogue of other popular commercial PFSAs (non-branch PTFE and perfluorovinylether sulfonic acid copolymers) manufactured by 3M and Dow. Carboxylic acid containing MCs exhibit the following fluoride generation rate order: MC3 > MC2 ~ MC4 > MC1. The overall trend is monotonic and relatively linear, accounting for as much as 2% of the total fluorine content of the starting materials. Shorter chain MC3 again shows higher fluoride release ratio. It is however not yet clear why the fluoride release from MC1 is the lowest.

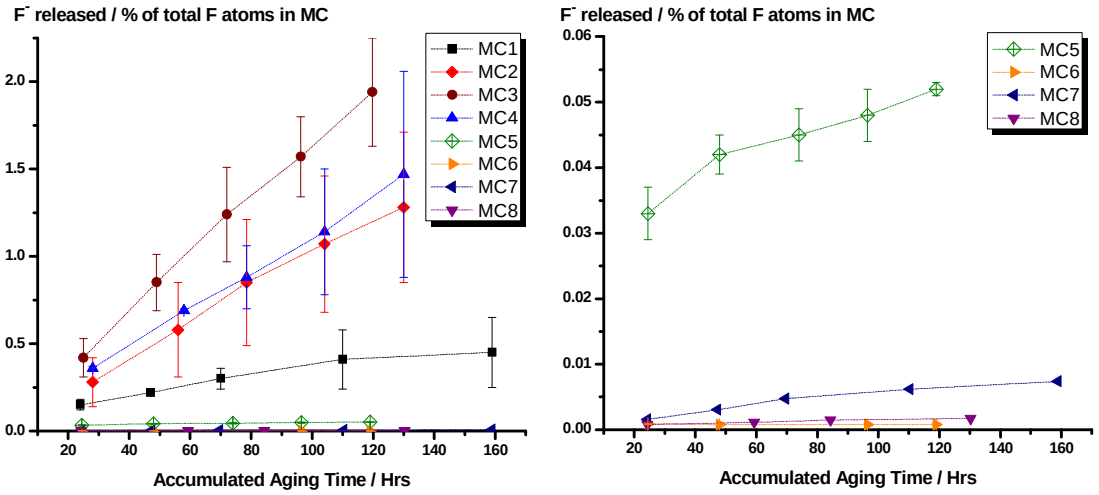

Figure 24. Fluoride evolution from MCs as a function of test time in mild degradation test

For harsh degradation test, the fluoride evolution from MCs is plotted in Figure 25. At the first glance, the results obtained under the two sets of Fenton's conditions are similar, but not identical. The harsh Fenton's conditions literally do not result in greater model compound decomposition than was observed under mild conditions. It may be the case that under the harsh conditions, much of the generated radical species are lost to self-recombination or other non-productive reactions. In each case, the model compounds possessing carboxylic acid groups degrade most rapidly.

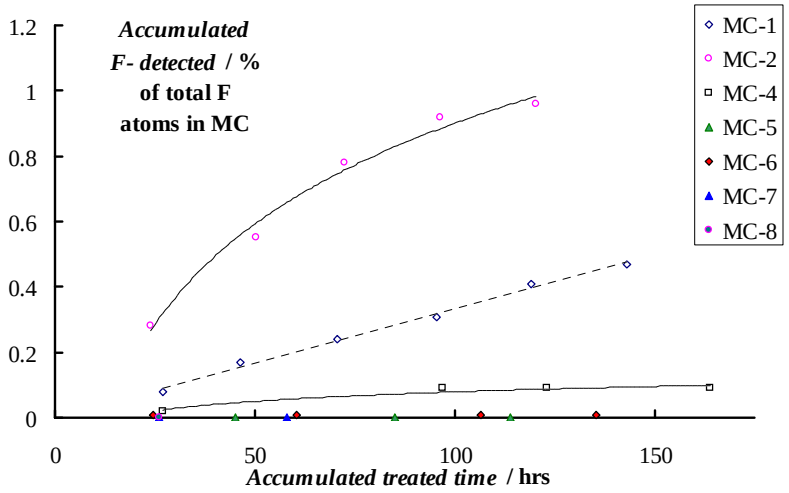

Figure 25. Fluoride evolution from MCs as a function of test time in harsh degradation tests

Model Compound: Fluoride Generation from UV H_2O_2 Photolysis Degradation Test

MC solutions were exposed to UV irradiation to degrade at room temperature, and the fluoride generation was measured. UV irradiation was carried out on two sets of samples: MC solutions without H_2O_2 as control experiment, and MC solutions with H_2O_2 added, as shown in Figure 26. For MCs containing carboxylic acid groups (MC1 - MC4), UV irradiations led to fluoride generation even without the presence of added H_2O_2, probably due to UV-facilitated decarboxylations that may further trigger structural changes[46]. Higher concentration of fluorides was generated when H_2O_2 was added to the MC solutions subject to UV irradiation. MC5 and MC6 were found to generate much less fluoride than the -COOH containing MCs, i.e. MC1, MC2, MC3 and MC4, even when UV irradiation was carried with H_2O_2 added. Overall, similar degradation trend was found to be in agreement with the Fenton's degradation test.

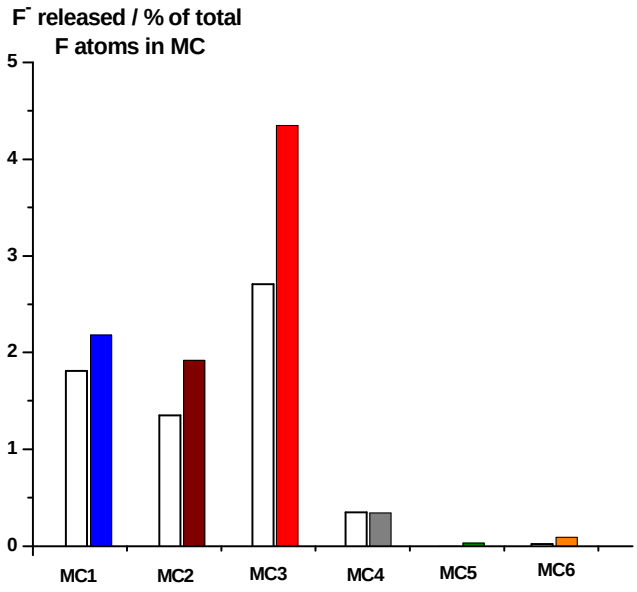

Figure 26. Fluoride evolution from MCs by 1 hour UV exposure. For each MC, blank column is fluoride generated from UV exposure without H_2O_2 added into the solution, filled column shows the fluoride generated from UV exposure with the presence of H_2O_2.

Membrane: Fluoride Generation from Fenton's Degradation Test

The fluoride generation from 3M-G1 and Nafion is shown in Figure 27. The released fluoride is normalized to the sample weight of ionomer samples used, showing a gradual increase of fluoride generation over the testing time. The estimated fluoride evolution rate in current accelerated degradation test is in the order of 1.0×10^{-6} g of fluoride/hr-cm^{-2}, which is two orders of magnitude higher than the fluoride release rate from actual running fuel cells.[11, 22] This result shows good validation of the accelerated degradation test method used in this work, *i.e*. Fe(II) ions are loaded into the membrane, and further addition of H_2O_2 can generate attacking radical species inside the membrane.

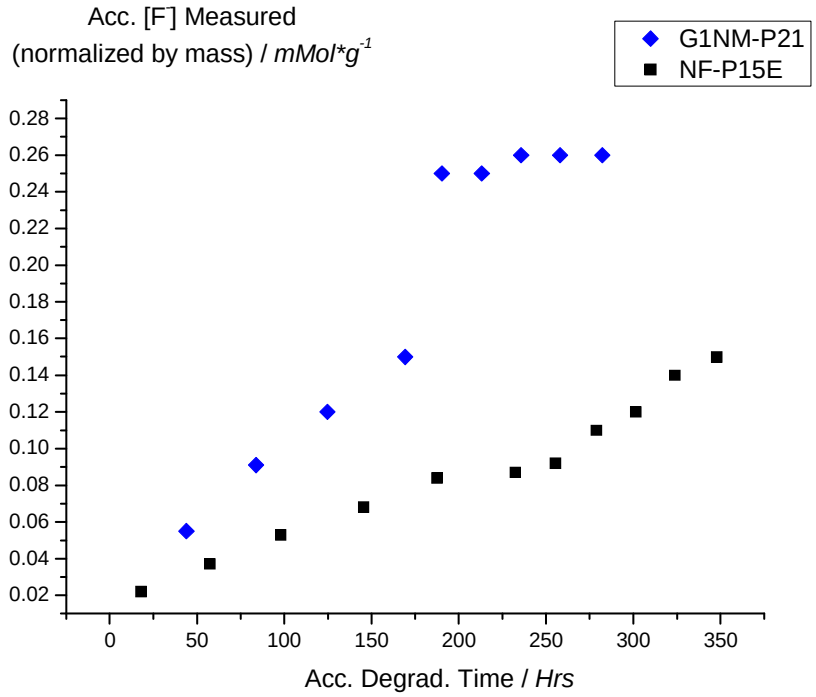

Figure 27. Fluoride evolution from 3M-G1 (Legend, G1NM-P21) and Nafion™ (Legend, NF-P15E) as a function of test time in modified Fenton's test for membrane samples

Compared with the original membrane Fenton's degradation data (shown in Figure 28), the modified degradation test yielded much higher fluoride generation than simply exposing the membrane to a solution containing both Fe(II) ions and H_2O_2, as the degradation might primarily happen on the surface.

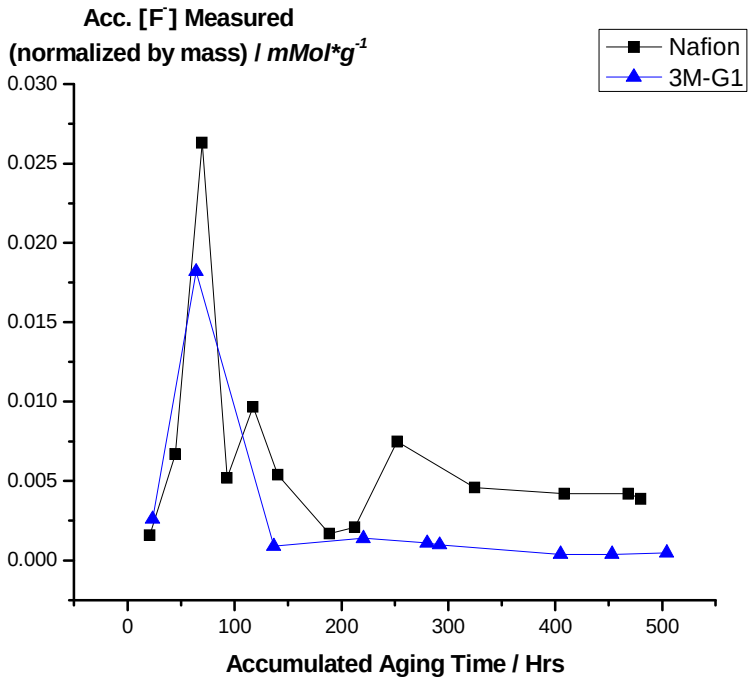

Figure 28. Fluoride evolution from 3M-G1 and Nafion™ as a function of test time in original Fenton's test for membrane samples

Degradation Product Analysis and Postulated Degradation Mechanisms
LC-MS of Model Compound Degradation Product

The chain end unzipping mechanism is widely accepted in the literature. However, the structure of the resulted degradation product has not been confirmed. Chain end unzipping mechanism products were verified by the degradation product analysis of MC4, a molecule that contains only a carboxylic acid group on a linear perfluorinated linear aliphatic chain (R_f-COOH). After the Fenton's test, LC-MS experiment was carried out on the reaction mixture of MC4. The data are shown in Figure 29 and Figure 30.

In Figure 29, the full chromatograph is shown on the top where it is very obvious that there are a series of peaks at different elution times. The full chromatography trace can be extracted by a specific ion molecular weight to show the relative ion intensity of that specific ion at different elution times, the resulted chromatography trace will be called extracted chromatograph hereafter. Such has been carried out on the full chromatograph of MC4 reaction mixture. Six ion molecular weight ranges were used to extract the full chromatograph: 412-413 Da, 362-363 Da, 312-313 Da, 262-263 Da, 212-213 Da, 162-163 Da, and the resulted extracted chromatographs are shown in Figure 29. The full chromatograph is accurately anatomized into six peaks at six elution times, and the MS spectrum of each peak at these six elution times were recorded and shown in Figure 10 with the designation of MS-1 to MS-6.

MS-1 in Figure 30 exhibits that the peak at this elution time is the intact MC4, where the 413 Da ion is assigned to be the parent ion by losing a proton and form a negative anion, and the 827 Da ion is assigned to an adduct ion of a molecule of MC4 and a parent ion of MC4. These two ions should serve as good signature ions for solving the MS spectrum with the structure similar to MC4. A close examination of the rest of MS spectra (MS-2 to MS-6) reveals that at those five

earlier elution times, the molecular weights of various parent ions differ by 50 Da, and the molecular weights of adduct ions differ by 100 Da, and therefore MS-2 is assigned to be the C_f6-COOH because the difference of this molecule and MC4 (C_f7-COOH) is a -CF_2- unit (50 Da). The difference of 100 Da (a net decrease of two -CF_2- units) for the adduct ions and a shorter elution time (a shorter elution time is expected for a molecule with shorter hydrophobic tail for the reverse phase C18 column used) both confirm this assignment. Similar analogues have also been observed for MC3 to MC6. The stepwise loss of CF_2 units, reforming another terminal carboxylic acid groups, is completely consistent with the unzipping degradation mechanism for degradation of molecules like MC4 under the testing conditions. Another degradation product, CO_2 gas, was trapped by bubbling the reactant gas into a tube containing phenolphthalein indicator. It was observed that the color of the test tube turned from pink to colorless within 1 hour upon the addition of H_2O_2 into the flask. ^{19}F NMR indicated that there were no fluorinated organic compounds in the trapping test tube to cause the observed color change, and the detection of CO_2 again supports the unzipping mechanism.

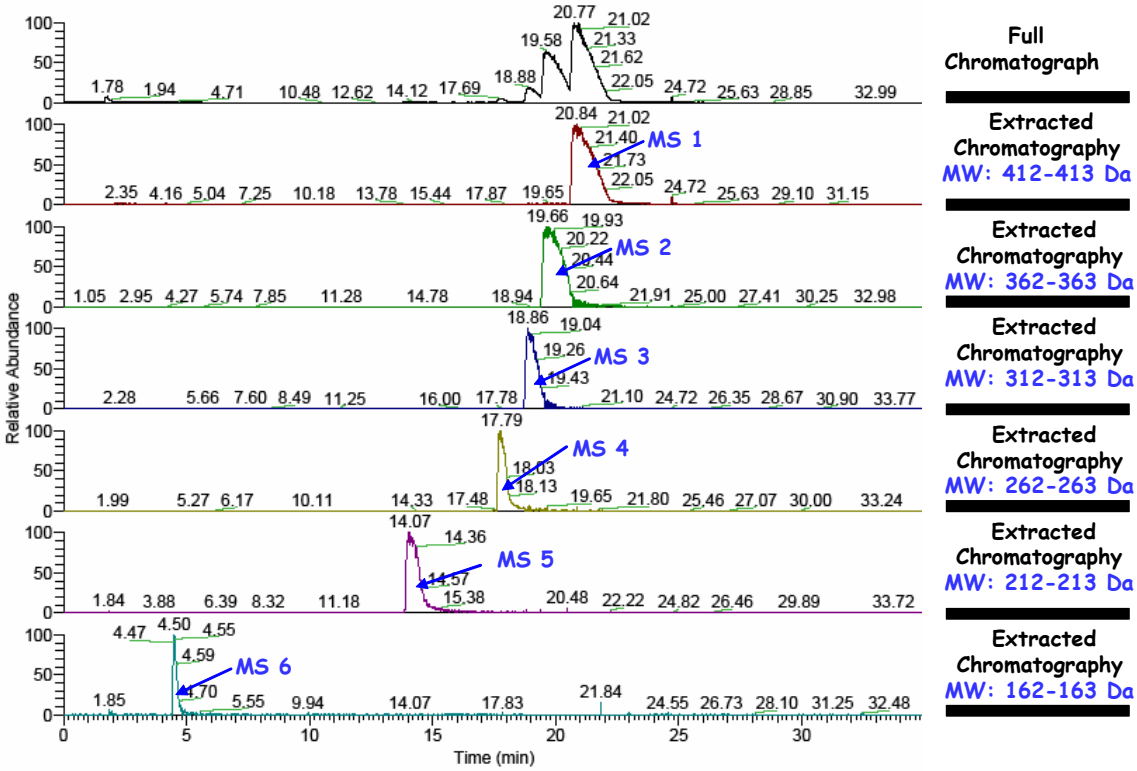

Figure 29. LC chromatographic trace of degraded MC4 reaction product mixture

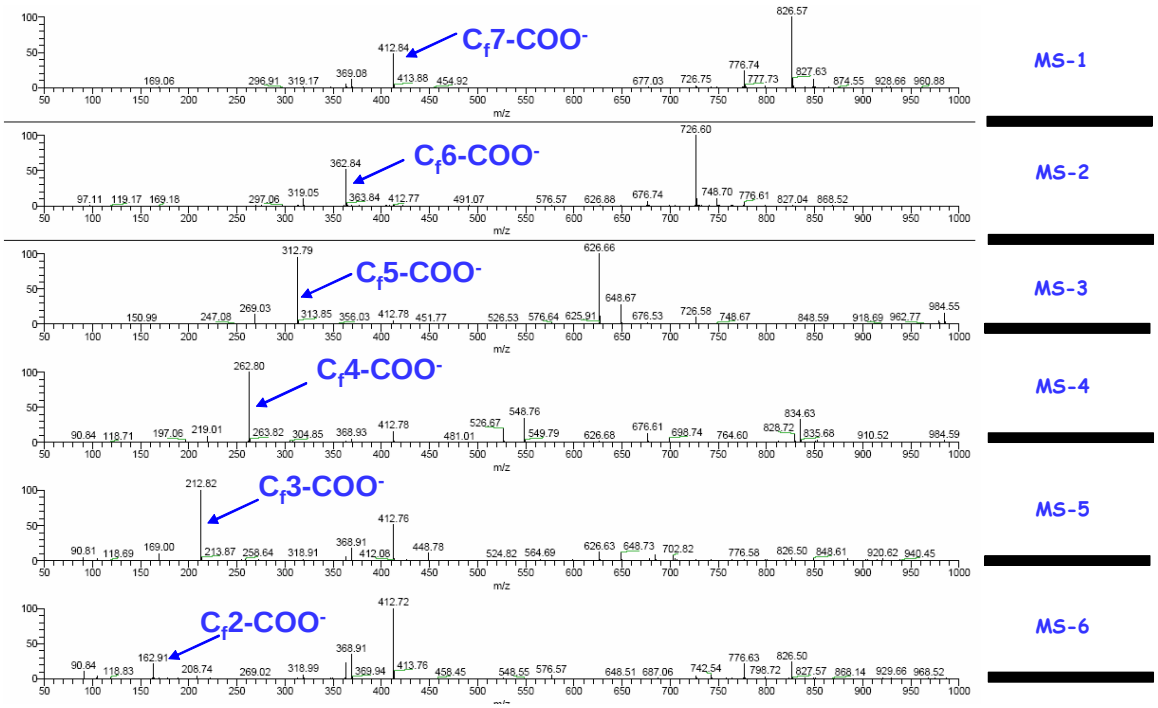

Figure 30. MS spectra of LC trace of a degraded MC4 reaction product mixture at various elution times

From fluoride evolution data and the degradation product analysis of MC4, it is clear that terminal carboxylic acid groups are very reactive toward radical attack. It is necessary to compare of relative reactivity of these carboxylic acid groups and other moieties such as ether linkages and tertiary carbons with the PEM membrane polymers and their model compounds. MC1 and MC2 are suitable for such a comparison, since both of them contain carboxylic acid, ether, and tertiary carbons. In addition, the degradation of MC1 and MC2 will potentially reveal the subsequent degradation fate of the side chains of Nafion, should they be cleaved from the polymer main chain. The LC-MS product analysis results of MC1 are shown in Figure 31 to Figure 34. LC-MS of degraded reaction mixture found intact MC1, trifluoroacetic acid (TFA) and pentafluoropropionic acid (PFPA). The parent ions and other corresponding adduct ions are tabulated inTable 7.

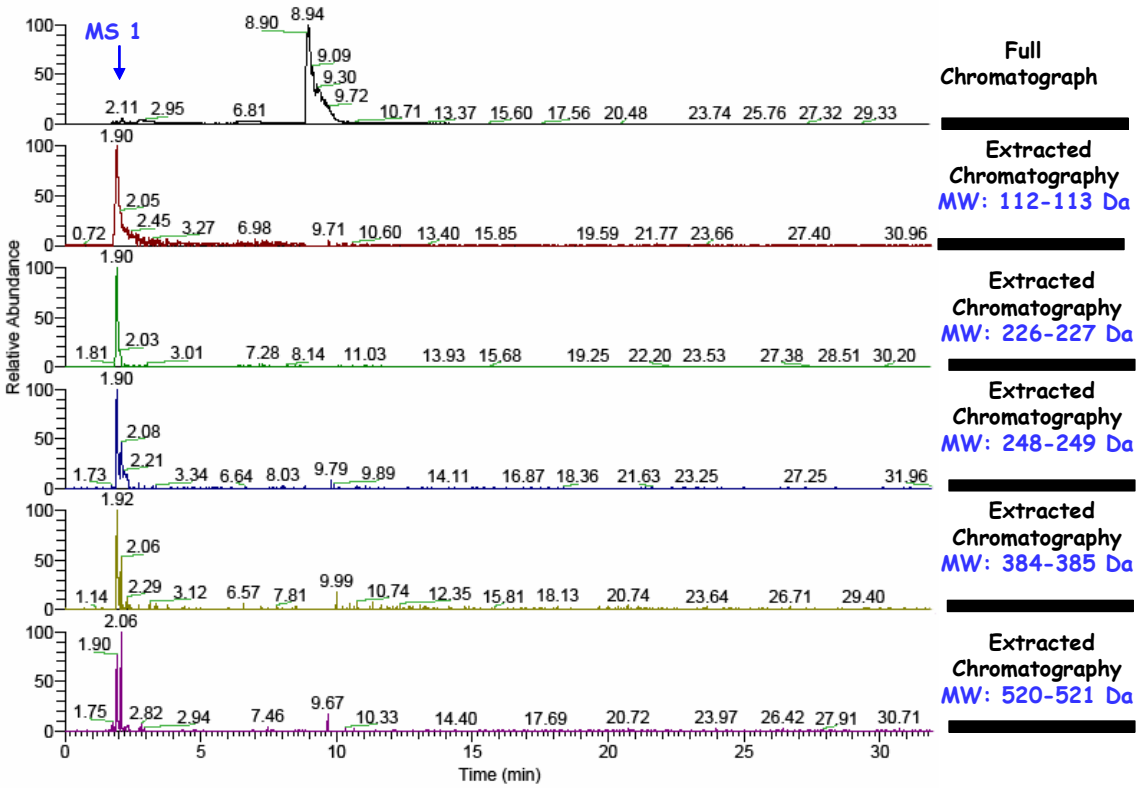

Figure 31. LC chromatographic trace of degraded MC1 reaction product mixture (top) LC traces (relative abundance) of selective ions from TFA (bottom five traces)

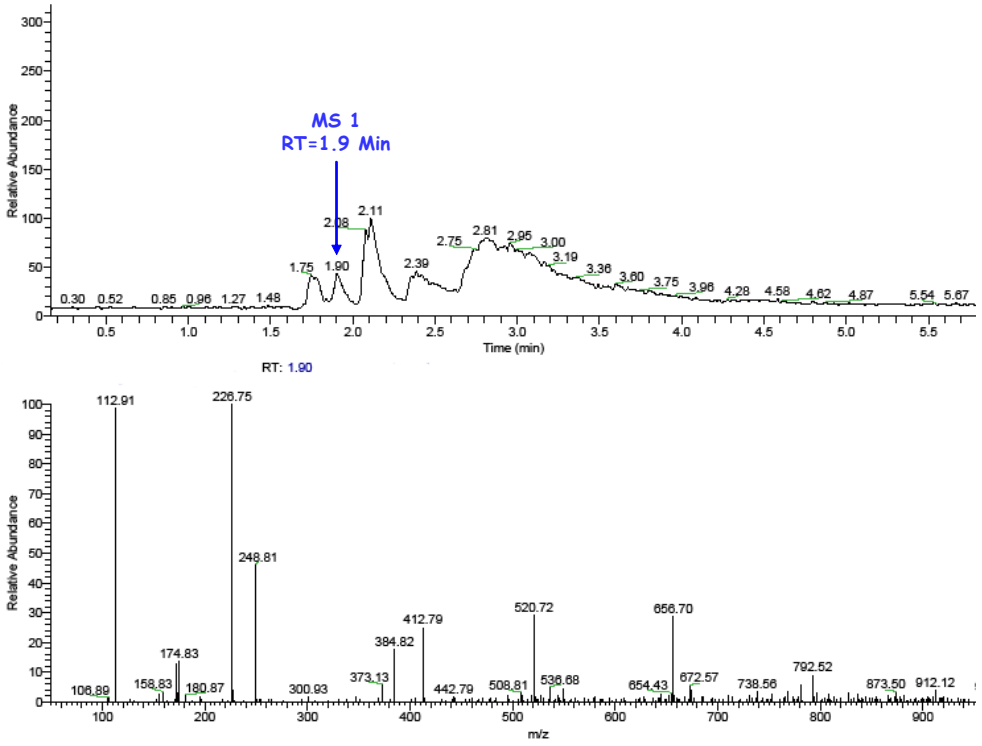

Figure 32. MC1 LC trace (top) and corresponding MS spectrum (bottom) at RT=1.9 min

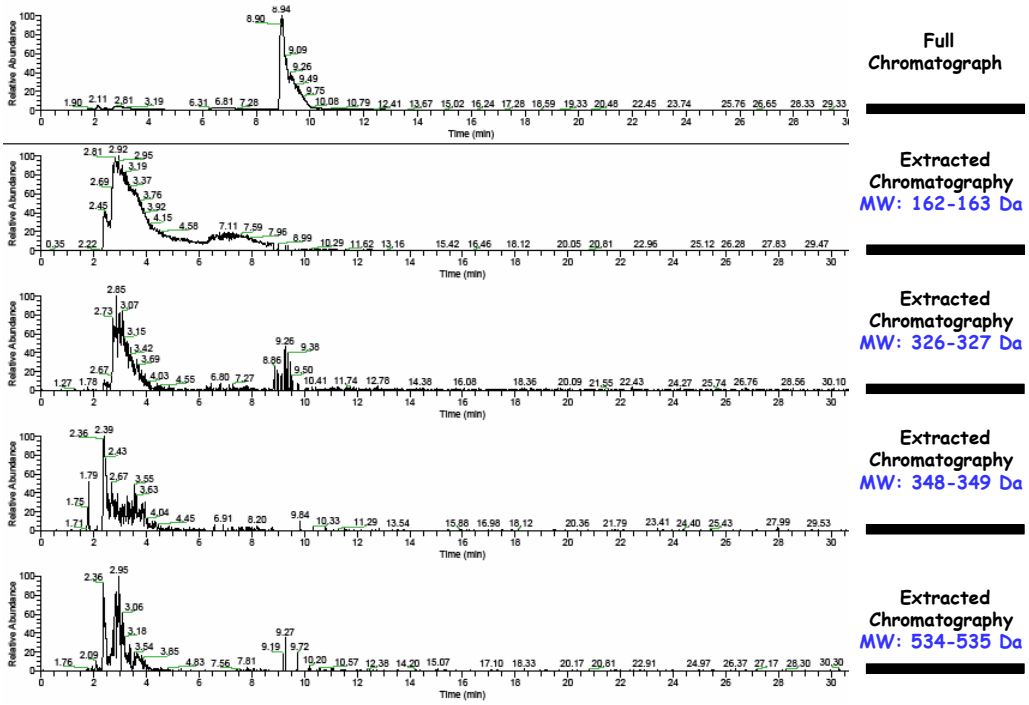

Figure 33. LC chromatographic trace of degraded MC1 reaction product mixture (top) LC traces (relative abundance) of selective ions from PFPA (bottom four traces)

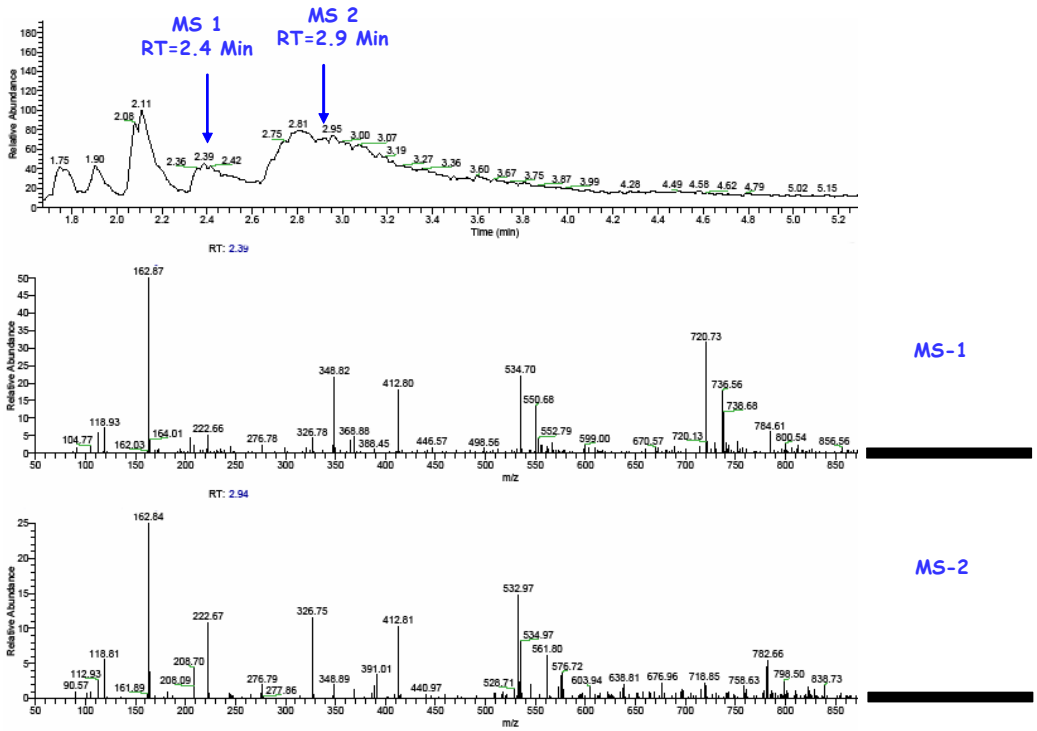

Figure 34. MC1 LC trace (top) and corresponding MS spectra (bottom) at RT=1.9 min and 2.9 min.

From the full LC trace of MC1 reaction mixture, the large peak at retention time *ca*. 9.0 min is the intact MC1 reagent. TFA peak shows up at about 1.9 min, and PFPA peak is a broader peak from 2.4 minute tailing to about 4.3 minute. It should be mentioned that the other peaks at 1.7 minute, 2.1 minute, and 6.8 minute are identified to be contaminants present in the starting MC1, and thus are excluded from the degradation products analysis. The concentration of these contaminants did not change measurably during the Fenton's and UV photolysis degradation experiments. Mobile phase empty checks in between data acquisition found similar ion patterns from those peaks, and the expected TFA and PFPA peaks were found from at least 3 independently degraded samples. The chromatographs extracted by expected ions from TFA are shown in Figure 31, in which the peaks of different ion molecular weights appear at very similar elution times. Similar trend is observed for Figure 33, although the peaks are considerably broader than those of TFA. MS spectra shown in Figure 32 and Figure 34 clearly exhibit the expected ions from TFA and PFPA tabulated in Table 7.

Table 7. Tabulated parent and adduct ions of TFA and PFPA

TFA	MW of Ions	PFPA	MW of Ions
CF_3-COOH	114	CF_3-CF_2-COOH	164
(TFA-H^+)	113	(PFPA-H^+)	163
TFA * (TFA-H^+)	227	PFPA * (PFPA-H^+)	327
(TFA-H^++Na^+) * (TFA-H^+)	249	(PFPA-H^++Na^+) * (PFPA-H^+)	349
2(TFA-H^++Na^+) * (TFA-H^+)	385	2(PFPA-H^++Na^+) * (PFPA-H^+)	535
3(TFA-H^++Na^+) * (TFA-H^+)	521	3(PFPA-H^++Na^+) * (PFPA-H^+)	721
4(TFA-H^++Na^+) * (TFA-H^+)	657		

^{19}F NMR analysis of these same reaction products supported the LC/MS assignments (TFA: -CF_3 at about -76 ppm; PFPA: -CF_3 at -82 ppm, and -CF_2- at 125 -ppm) as well as identifying small concentration of tetrafluoroethyl, heptafloropropyl ether (-CFH- at about 146 ppm as doublet of multiplets) as another product. Note that this new ether is not seen in LC-MS, probably due to the fact that in LC-MS the ion acquisition is set to be negative ion mode. We propose a mechanism which explains the observed reaction products for MC1 in Figure 35. In this mechanism, radical abstraction of a carboxylic acid hydrogen atom initiates decarboxylation of the model compound. The decarboxylated radical intermediate can then undergo electron transfer or atom abstraction to produce the observed ether. Capture of a second hydroxyl radical would be expected to produce perfluorinated propyl acetate; we have independently demonstrated that such perfluorinated alkyl acetates will rapidly hydrolyze to the perfluorinated acetic and propionic acids which were identified as MC1 reaction products.

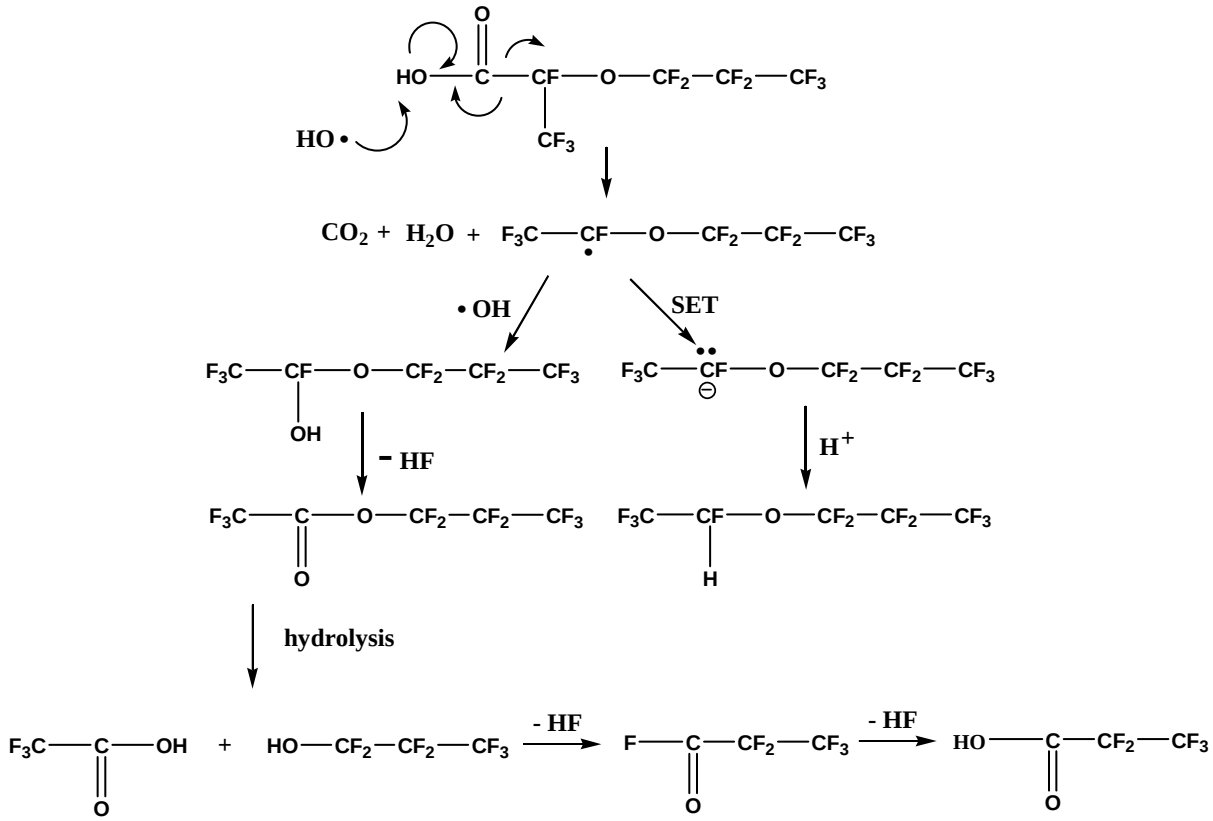

Figure 35. Proposed Mechanism for MC1 Degradation

MC8 was chosen as a small molecule analog to the Nafion™ polymer itself, substituting a perfluoroethyl group for the polymer backbone. LC/MS analysis of MC8 degradation products identified four significant species in addition to the starting material. LC traces and MS spectra (the expected parent and adduct ions of product 1-4 as tabulated in Table 5 are highlighted with circles) are presented in Figure 15 and Figure 16. The major product appeared to be a fluorinated carboxylic acid compound (MC8, Product 1), which could be expected to result from cleavage of the ether group near the methyl end. Three other structures (Product 2 to 4) were also identified as being the direct degradation products from MC8, or they might be resulted from further degradation product of product-1. One of these reaction products (product 3) corresponds to a MC1 degradation product as well.

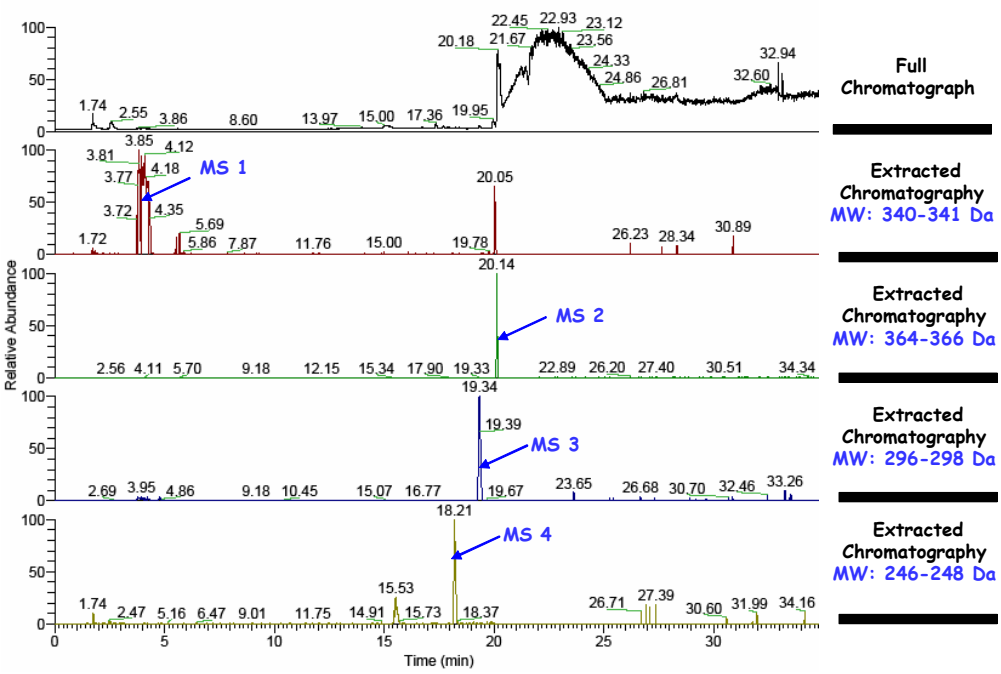

Figure 36. LC chromatographic trace of degraded MC8 reaction product mixture (top) LC traces (relative abundance) of selective ions from proposed products (bottom four traces)

Table 8. Proposed degradation products of MC8 with expect parent and adduct ions

MC8, Product 1 (MC8-PRDT1)

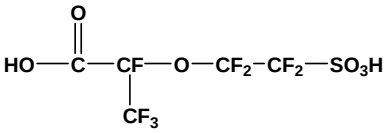

MC8-PRDT1	m/z
(MC8-PRDT1-H^+)	341
(MC8-PRDT1-H^+)-CO_2	297
(MC8-PRDT1-$2H^+$)	170
(MC8-PRDT1-$2H^+$)-CO_2F	277

MC8, Product 2 (MC8-PRDT2)

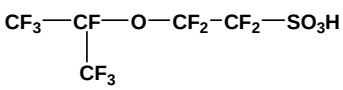

MC8-PRDT2	m/z
(MC8-PRDT2-H^+)	365
MC8-PRDT2 * (MC8-PRDT2-H^+)	731

MC8, Product 3 (MC8-PRDT3)

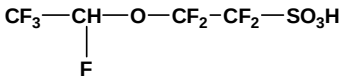

MC8-PRDT3	m/z
(MC8-PRDT3-H^+)	297
MC8-PRDT3 * (MC8-PRDT3-H^+)	595
(MC8-PRDT3-H^++Na^+) * (MC8-PRDT3-H^+)	617

MC8, Product 4 (MC8-PRDT4)

MC8-PRDT4	m/z
(MC8-PRDT4-H^+)	247
(MC8-PRDT4-H^++Na^+) * (MC8-PRDT4-H^+)	517

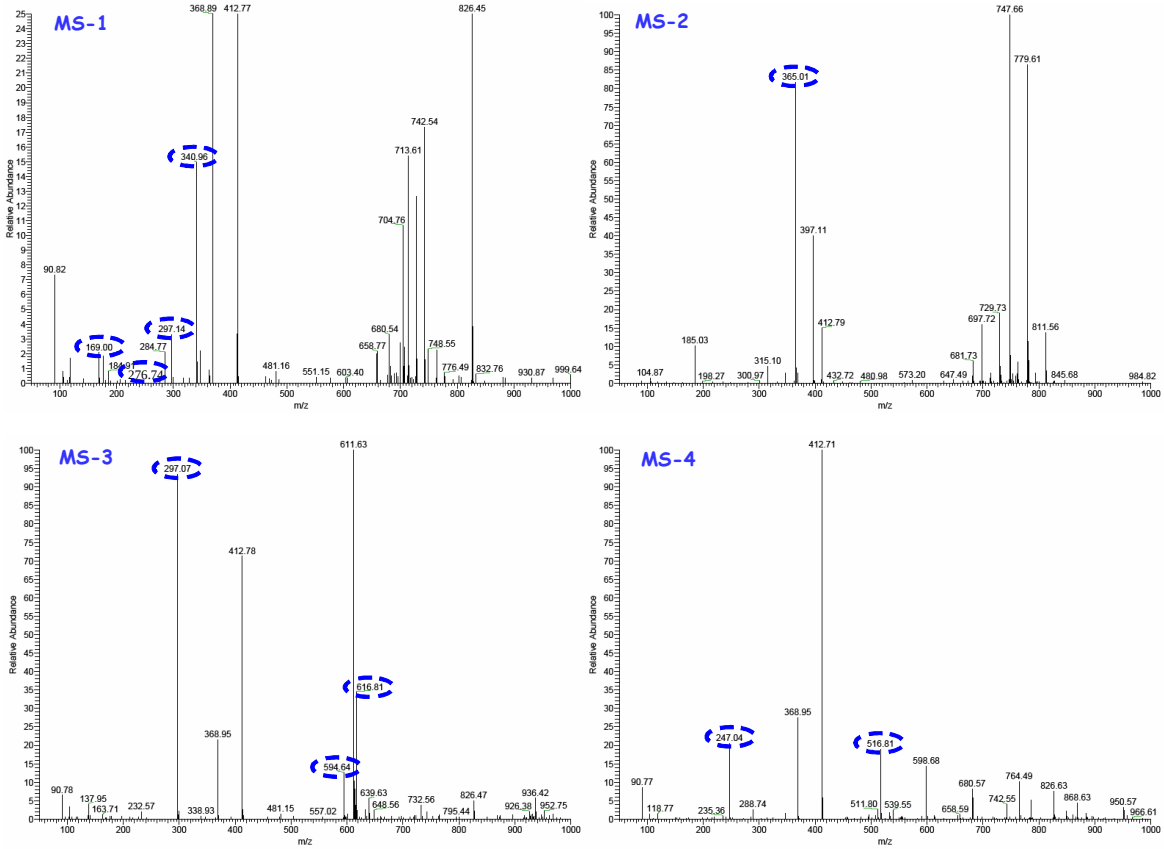

Figure 37. MS spectra marked as MS-1 to MS-4 in Figure 11: (top-left) RT=3.9 min, (top-right) RT=20.1 min, (bottom-left) RT=19.3 min, (bottom-right) RT=18.2 min

MC7 was selected as structural analogue to PFSAs with one ether linkage on the side chain, such as 3M and Dow membranes. LC-MS was also carried out to analyze the degradation products. The identified products and impurity compound are listed in Table 6. Putting the data from MCs degradation together, it is clear that degradation mechanisms other than the chain end unzipping mechanism are possible. Specifically for MC7 and MC8, structures without -COOH also underwent degradation, likely through an ether cleavage reaction.

Table 9. Proposed degradation products of MC7 based on LC-MS analysis

Designation, Molecular Weight	Structure
MC7, 416 Da	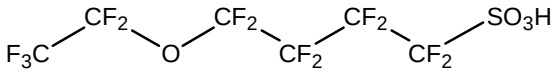
Impurity, 398 Da	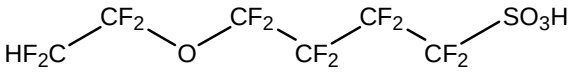
Product A, 276 Da	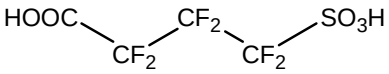
Product B (TFA), 114 Da	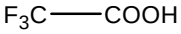
Product C, 392 Da	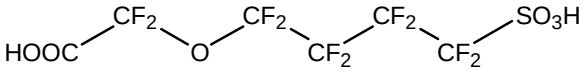
Product D, 300 Da	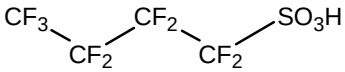

LC-MS of Nafion™ Degradation Product

The aqueous extract from Fenton's Reagent treatment of Nafion™ membrane was analyzed using the same LC/MS (Figure 38) and ^{19}F NMR (Figure 39) methods used for the model compounds. Among a number of products which have resisted identification to date, the major reaction product from Nafion™ degradation was identical to Product 1 shown in Table 8. Other than the expected ions listed in Table 6, the m/z value of 682 was assigned to an adduct ion consisting of a deprotonated parent ion and another intact product molecule. Identical degradation product resulted from Nafion™ degraded in running fuel cell testing was also independently reported by Healy *et al.*[40] This result strongly suggests that side chain cleaving in the polymer membrane occurs, just as is the case with its small molecule analogues.

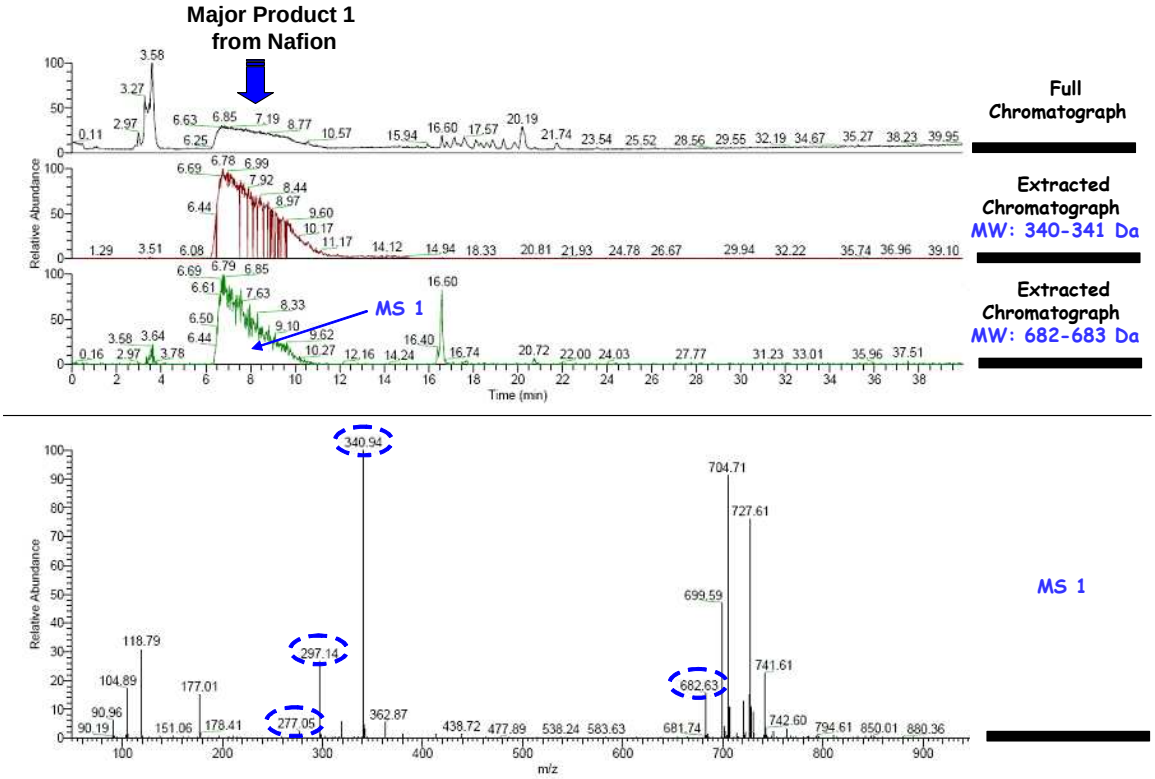

Figure 38. Nafion™ degradation product LC trace (top three, full and extracted chromatographs) and corresponding MS spectrum (bottom) at RT=7.7 min.

NMR Analysis of Nafion™ Degradation Product

The NMR spectrum of the Nafion™ degradation product is shown in Figure 39 with the peak assignments. The NMR spectrum confirms the structure postulated from the LC-MS data.

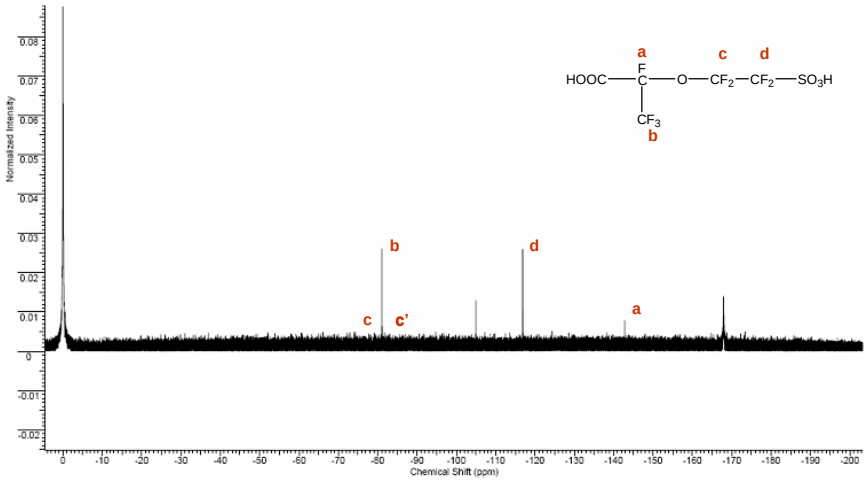

Figure 39. ^{19}F NMR of Nafion™ degradation major product from Fenton's degradation test solution

FTIR of Degraded Membrane Structure by Modified Degradation Test

Infrared spectroscopy (FTIR) was used to investigate chemical changes in the degraded membranes. These studies revealed possible crosslinking of sulfonic acid groups to form -S-O-S- bond. The samples investigated are listed in Table 10

Table 10. Summary of samples studied with FTIR

Sample ID	Description
NF CI Fe(II)	Nafion™ loaded with Fe(II) as counter-ion (CI)
NFFC	Identical Nafion™ sample for replica and Fuel Cell testing after degradation (larger size).
NF P15-E:	Fe(II) Fenton Degraded Nafion™ Sample
NF P11-#10-3	Original Fenton Degraded Nafion™ Sample
G1NM	3M first generation ionomer: 3M-G1-NM

Effect of having Fe(II) as counter Ion and drying history.

All the IR spectra presented below were not normalized by intensity, and were used as obtained. Sample designations in the IR curves below are:

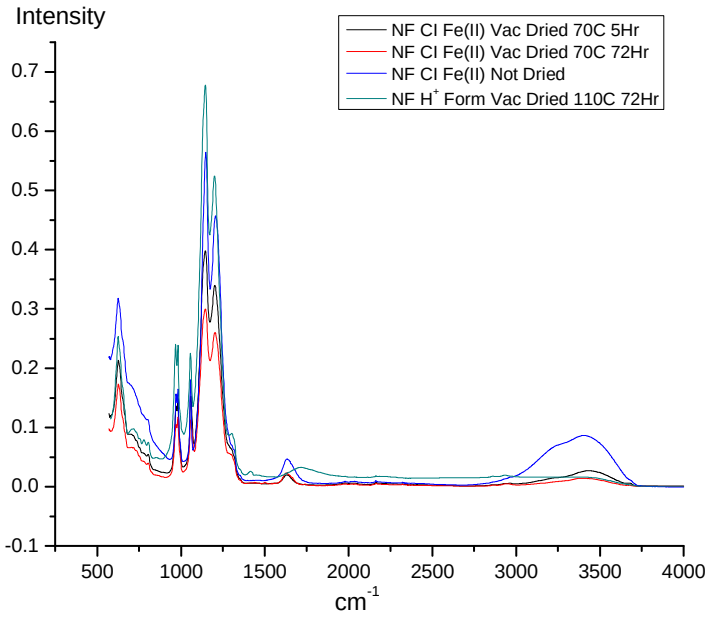

Figure 40. Effect of drying history for Nafion™ samples with Fe(II) as counter ion (CI) (full spectrum)

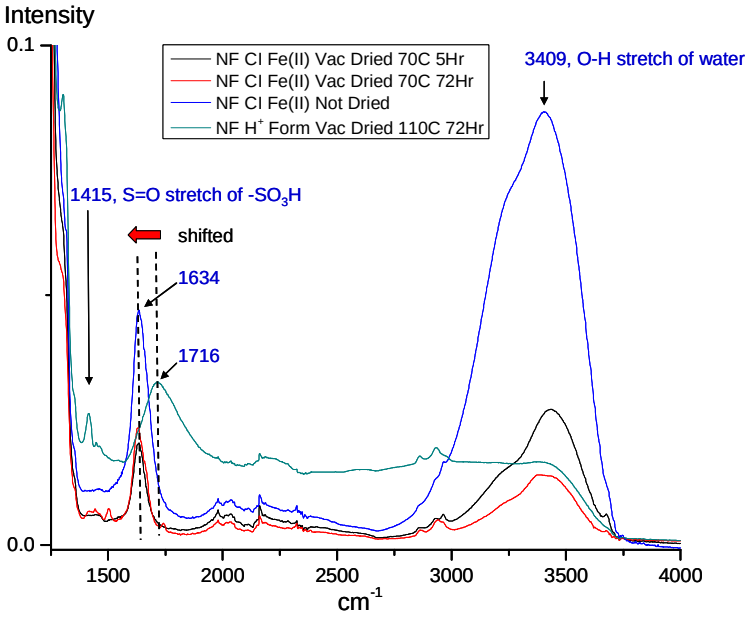

Figure 41. Effect of drying history for Nafion™ samples with Fe(II) as counter ion (Cl) (enlarged)

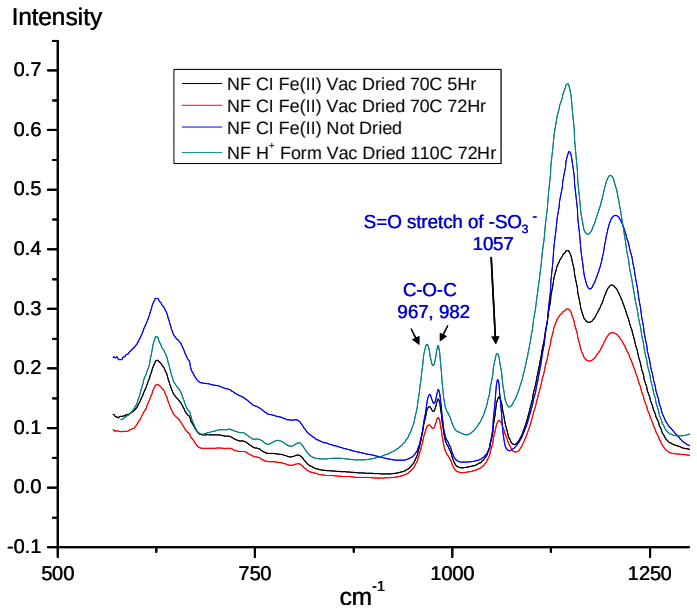

Figure 42. Effect of drying history for Nafion™ samples with Fe(II) as counter ion (Cl) (enlarged)

Peak assignments were made from the spectra in Figure 40,Figure 41, and Figure 42. A table of the peak location and assignment is shown below (

Table 11).

Table 11. FTIR peak assignments

Peak	Assignment
3409 cm^{-1}	O-H stretching of water
1415 cm^{-1}	S=O stretching of $-SO_3H$
1057 cm^{-1}	S=O stretching of $-SO_3^-$ bonded to water (H_2O)
967 and 982 cm^{-1}	C-O-C stretching
1716 cm^{-1}	Not yet assigned
1634 cm^{-1}	Not yet assigned

Very obvious decrease of water peak at 3409 cm^{-1} is observed for samples going from "wet" to "dry", although for most rigorous drying (110^{o}C, vac., 72 Hr) there are still water present because the peak at 1057 cm^{-1}, assigned to S=O stretching of $-SO_3^-$ bonded to water (H_2O), is clearly seen. The peak at 1415 cm^{-1}, S=O stretching of $-SO_3H$, decreases rapidly as the water content (hydration) increases because less free $-SO_3H$ groups are around. The peak at 1716 cm^{-1} in acid form Nafion™ sample (for Nafion™ exchanged with Fe(II), it shifts to 1634 cm^{-1} and becomes sharper) has not been assigned yet. There are two possible assignments: it can be the bending vibration of out side of the acidic water regime (H_3O^+ / $H_5O_2^+$); or it can be the vibration peak of -C=O from possible end group although it is too broad for a -C=O vibration. Other than the changes associated with water/drying history, the most obvious spectral change upon loading of Fe(II) is the shifting from 1716 to 1634 cm^{-1}, which is not understood yet.

Spectral changes of Fe(II) Exchanged Fenton degraded Nafion™ samples.

The spectral reproducibility seems quite good when the spectra of two replicas, NF (red) and NFFC (blue) in Figure 43, Figure 44, and Figure 45 are compared. Similar to the discussion in previous section, the peak at 1415 cm^{-1}, S=O stretching of $-SO_3H$, decreases rapidly as the water content increases (water content% of 70^{o}C 72 Hr Vac. Dried > 110^{o}C 72 Hr Vac. Dried). Additionally, the peak at 1057 cm^{-1}, S=O stretching of $-SO_3^-$ bonded to water (H_2O), shifts slightly higher wave number as the water content increases (more $-SO_3^-$ bonded to acidic water, eg. H_3O^+).

As seen in Figure 44, the peak at 1716 cm^{-1} shifts to 1698 cm^{-1}. Seen also are two small should peaks at 1668 cm^{-1} shifts to 1790 cm^{-1}. Another obvious spectral change is the development of two peaks for degraded sample, at around 1453 cm^{-1} and 1523 cm^{-1}. These few new peaks and important changes have not been assigned.

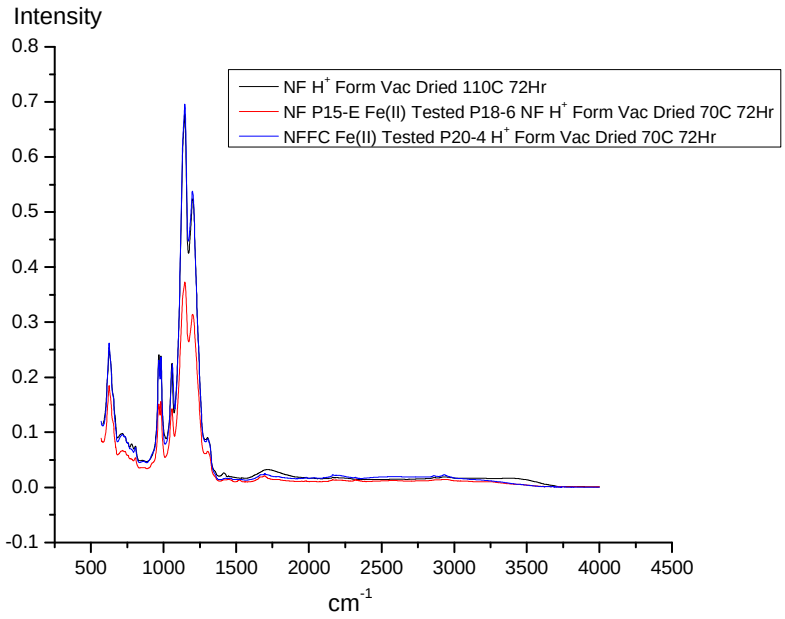

Figure 43. Nafion™ Fe(II) Fenton degraded sample (NF) and another replica (NFFC) (full spectrum)

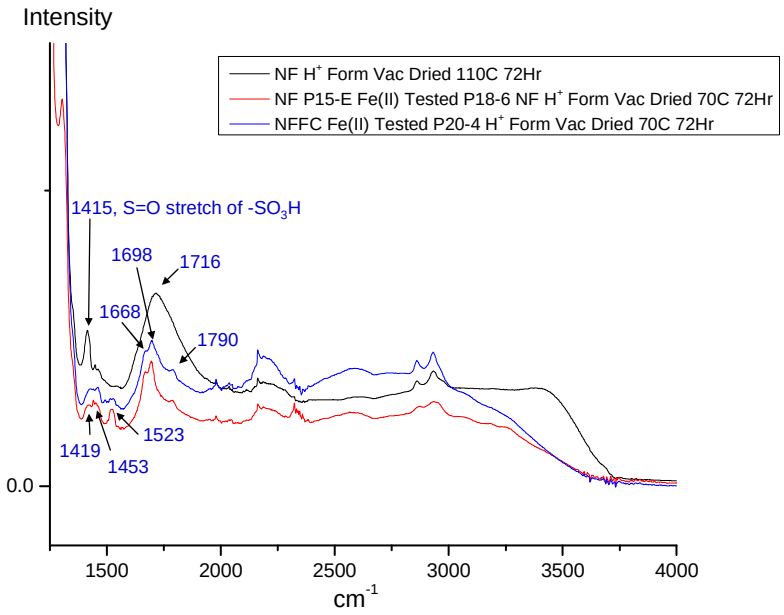

Figure 44. Nafion™ Fe(II) Fenton degraded sample (NF) and another replica (NFFC) (enlarged)

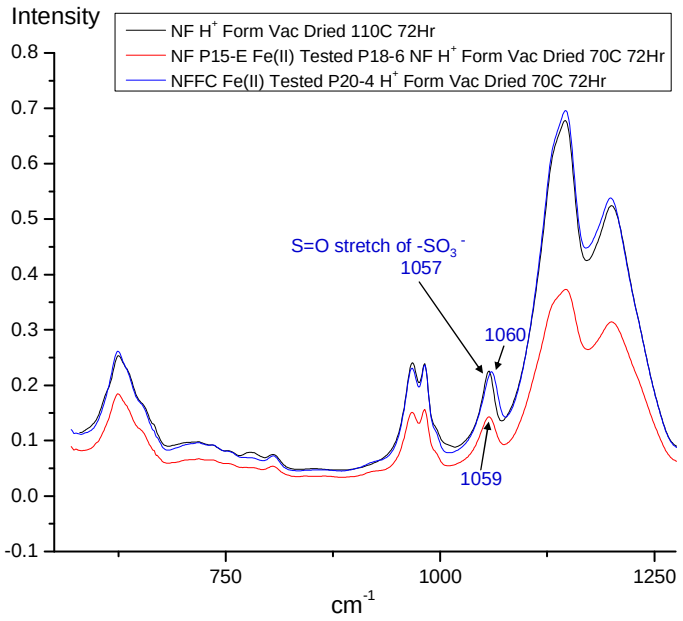

Figure 45. Nafion™ Fe(II) Fenton degraded sample (NF) and another replica (NFFC) (enlarged)

Spectral comparison of Fe(II) Exchanged Fenton and Original Mild Fenton degraded Nafion™ samples.

The major new peaks for Fe(II) Exchanged Fenton degraded sample (1453, 1523, and 1698 cm^{-1}) seem similar to those of Mild Fenton degraded sample (1441, 1518, and 1685 cm^{-1}). Similar shifting is also found for the peak at 1716 cm^{-1} in the untreated sample to 1683 cm^{-1}. Peak assignment is discussion below.

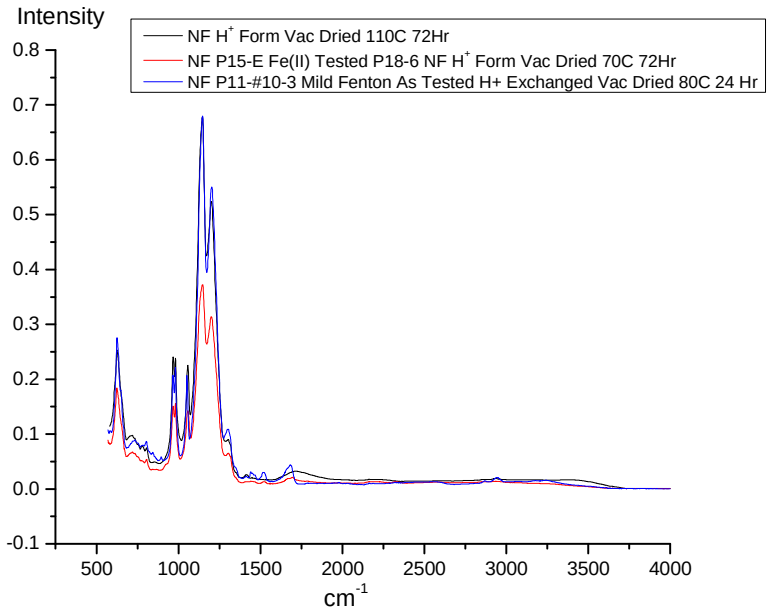

Figure 46. Fe(II) Fenton degraded sample (NF P15-E) and mild Fenton degraded sample (NF P11-#10-3) (full spectrum)

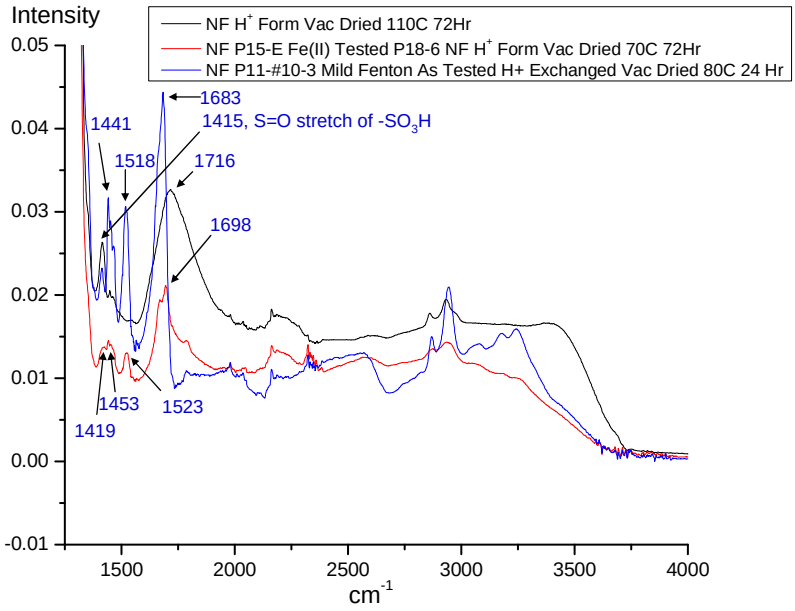

Figure 47. Fe(II) Fenton degraded sample (NF P15-E) and mild Fenton degraded sample (NF P11-#10-3) (enlarged)

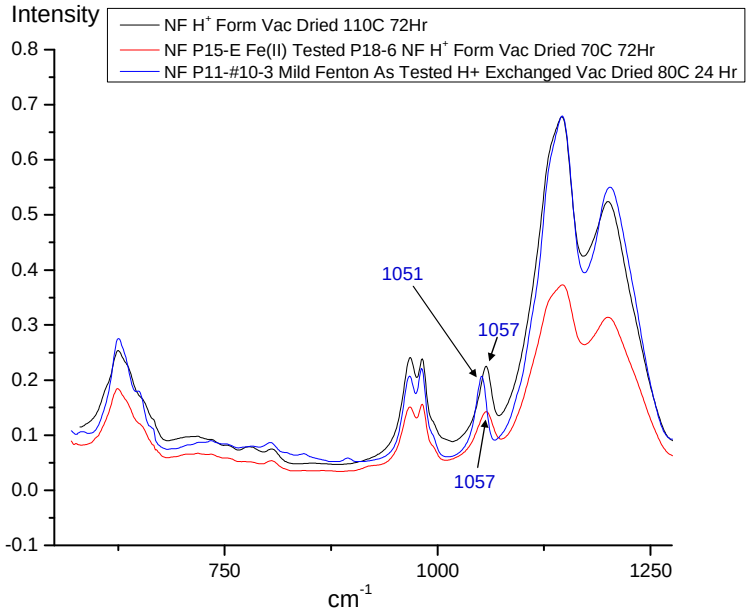

Figure 48. Fe(II) Fenton degraded sample (NF P15-E) and mild Fenton sample (NF P11-#10-3) (enlarged)

Spectral changes of Fe(II) Exchanged Fenton degraded 3M-G1-NM samples.

Albeit the background noise level is quite large for the above-shown ATR spectra of 3M-G1-NM samples, Figure 51 shows two major spectral changes between dried Fe(II) degraded G1-NM sample (blue) and the untreated sample (black): 1) the shifting of the peak at 1716 to 1693 cm^{-1}; two emerging peaks at 1455 and 1521 cm^{-1}.

Since the differences in chemical structure between G1 and Nafion™ are the lacking of C-O-C and no further branching (tertiary carbon) on side chains, the resemblance of spectral changes after degradation might suggest common attacking sites. In a recent report[37], Nafion™ membrane degraded by Fenton's test showed similar IR spectral changes. The New peaks emerged at about 1440 cm^{-1} is therefore assigned to the formation of -S-O-S- bond (the crosslinking of between sulfonic acid groups on side chains), and the shifted peaks at about 1670 cm^{-1} are attributed to the change of water band due to the crosslinking of side chains.

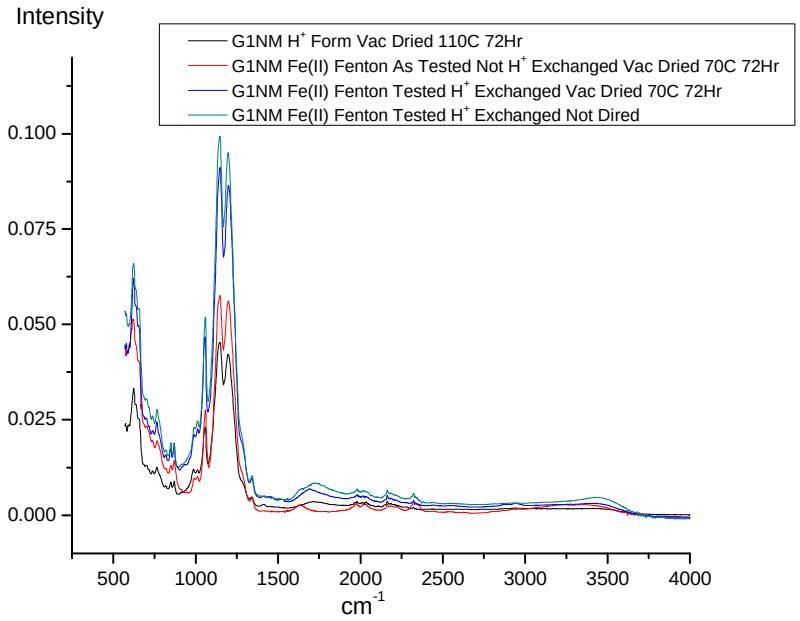

Figure 49. 3M-G1-NM Fe(II) Fenton degraded sample (G1NM) and effect of drying history (full spectrum)

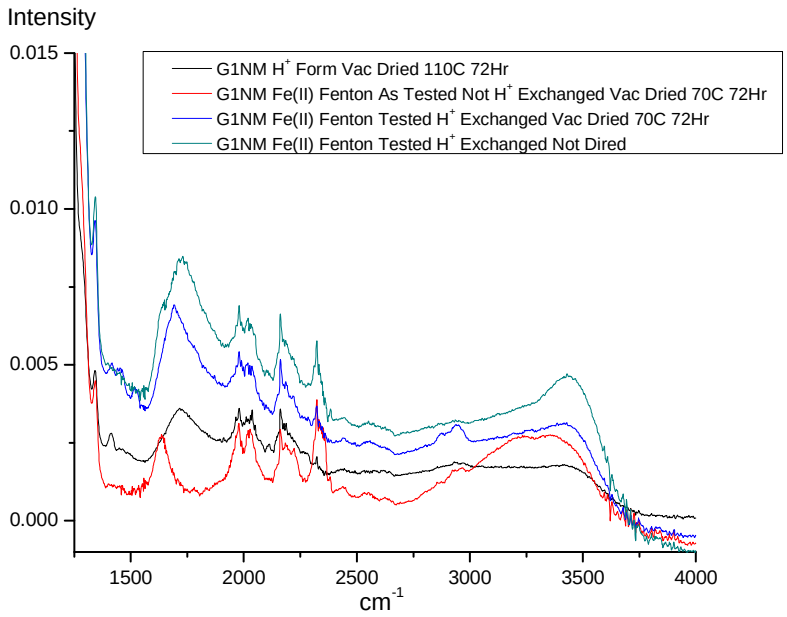

Figure 50. 3M-G1-NM Fe(II) Fenton degraded sample (G1NM) and effect of drying history (enlarged)

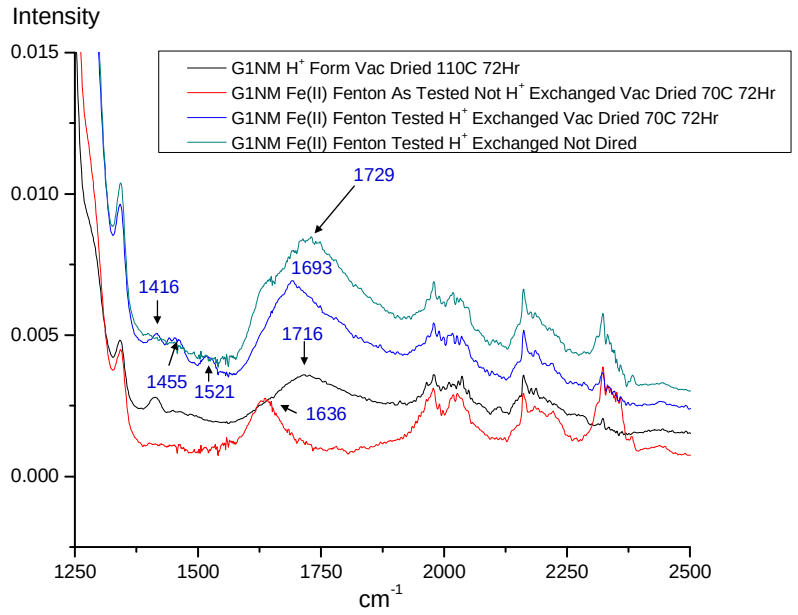

Figure 51. 3M-G1-NM Fe(II) Fenton degraded sample (G1NM) and effect of drying history (enlarged)

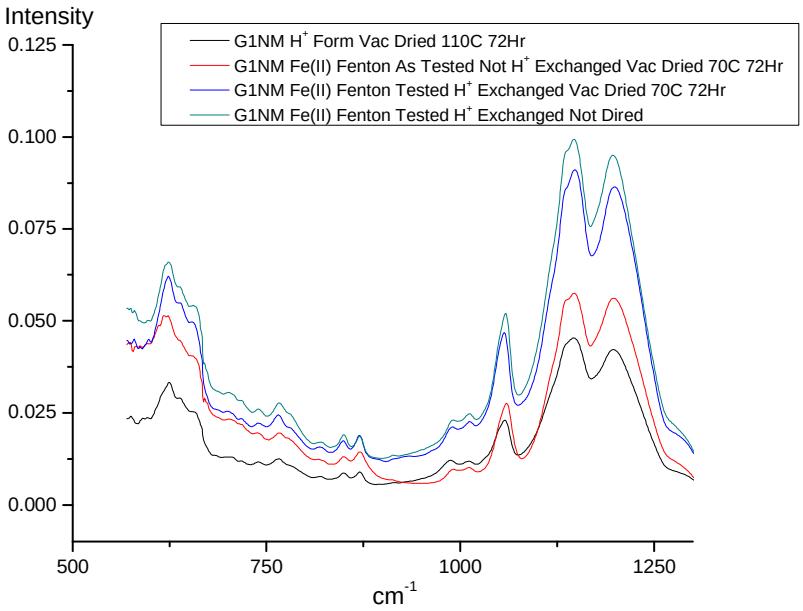

Figure 52. 3M-G1-NM (Fe(II) Fenton degraded sample (G1NM) and effect of drying history (enlarged)

The following table summarizes the major spectral changes for various degraded samples.

Table 12. Spectral chages for various samples

Samples	**Shifted Peak** / cm^{-1}	**New Peak 2** / cm^{-1}	**New Peaks** / cm^{-1}
Nafion Fe(II) Fenton Degraded Sample	1698	1523	1453
Nafion Mild Fenton Degraded Sample	1685	1518	1441
3M-G1-NM Fe(II) Fenton Degraded Sample	1693	1521	1455

Conclusions

Combining these product analyses with the relative fluoride generation rates in this study, and the published results correlating fluoride generation with carboxyl chain ends in Nafion™, a viable model presents itself:

- To the extent that backbone carboxylic acid groups exist in a PEM membrane, those groups will serve as the preferred sites of attack.
- Ether linkages, which connect the ionic groups to PTFE chains, might also be viable points of attack for peroxide radicals, and can lead to side chain cleavage.
- While the rate of reaction at carboxylic acid end groups appears to be larger than that of ether cleavage, in a commercial product which contains minimal carboxylate end groups, the overall rate of side chain ether attack may become significant, consistent with the previously published non-zero fluoride intercept data for membrane with highly modified end groups.
- IR study of the degraded membrane samples shows the possible formation of -S-O-S-, indicating the crosslinking of sulfonic acid groups on side chains.

Note: The remaining sub sections represent work primarily from 3M Researchers

2.1.4 Membrane Characterization

MEA fabrication and testing

Throughout the course of this project a great number of tests and evaluations were performed. Often the tests were designed for a specific experimental objective. In these cases the test is described in the text for that section of the report. However, several tests were conducted over the course of the project and used in multiple sections. The single cell saturated testing and single cell accelerated testing protocols will be described in this section and referred to in other sections where membranes were fuel cell tested. Similarly, mechanical property testing using a humidity controlled environment is also described in this section and used throughout the project in particular the double notch tear (DENT) test method.

The durability test most often used for screening membrane candidates is referred to at the “90/60/60 test”. These conditions were chosen since lifetime durability testing is costly and the short term testing at 90/60/60 ℃ (90° cell temp, 6 0° anode and cathode dew point) provides a relative idea of membrane durability that can be extracted from the fluoride release data collected after only 20-50 hours of accelerated testing.

The test conditions and MEA materials for the 90/60/60 screening are as follows:

- Flexible carbon paper gas diffusion layer (3M 2950)
- Decal laminated catalyst onto membrane

- Anode- carbon dispersed catalyst 0.4 mg/cm^2 Pt/C
- Cathode- carbon dispersed catalyst 0.4 mg/cm^2 Pt/C

- Teflon/Glass gaskets, 20% cell compression target

All samples tested were 50 cm^2. The catalyst electrodes were coated on a decal form using catalyst ink cathode and the electrodes were laminated using a rotary laminator at elevated temperature and pressure. The membrane electrode assemblies were statically bonded using the same time, temperature, and pressure and a 20% compression target.

The MEAs were loaded into a standard 50cm^2 cell test hardware with quad serpentine flow fields and connected to a Fuel Cell Technologies Inc Test Station. The samples were conditioned overnight and measured for crossover and short. Accelerated testing was run at 90℃ cell temperature with anode and cathode dew points at 60℃. The pressure was set to 15 psig on the anode and 7 psig on the cathode respectively and the load was cycled between 0.01, 0.2, and 0.5 A/cm^2. Water collections were made during the accelerated test to characterize the fluoride ion release of the particular membrane.

The saturated test conditions are identical to those listed above with the cell temperature set to 70℃ and both anode and cathode dew points set to 7 0℃. In these cases the test is referred to as “saturated conditions” or “70/70/70”.

In a small number of instances a cell was not able to run at 90/60/60, usually due to very high impedance at these conditions. In those cases the dew points were raised to 70℃ while leaving the cell temperature ay 90℃. This condition is re ferred to as “90/70/70” and is noted in the title or caption of the presented data.

Mechanical Testing in Humidity Chamber

One of the key needs in any material development program is the ability to measure mechanical properties under the same temperature and humidity conditions found in the actual use environment. Prior to the start of this project 3M purchased a humidity chamber for the purpose of making such measurements. A load frame was fabricated and software developed to measure simple puncture strength values for membrane samples. The capability of this equipment was increased during the course of the project to make measurements in three different tensile modes; load vs. displacement, load vs. time, and displacement vs. time. The humidity chamber can operate from room temperature to 80℃ with rela tive humidity ranges of approximately 30% up to 100%. A photograph of the load from is shown in Figure 53.

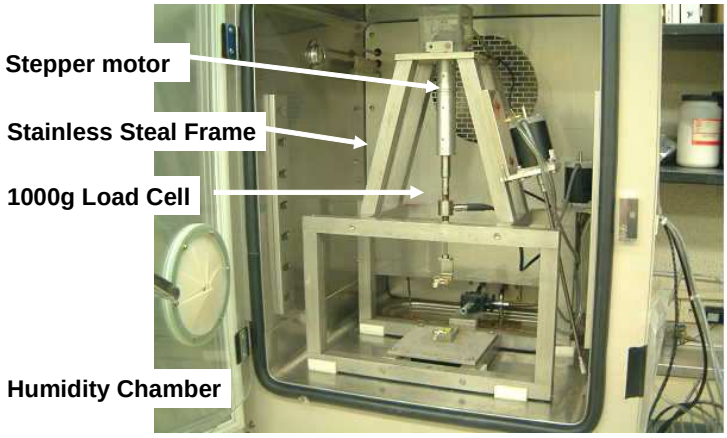

Figure 53. Humidity Chamber with Load Cell

This equipment was used for a variety of tensile and tear tests. One test typically run is the double edge notch tear test (DENT). The test is described in detail by Mospach et. al. [47] with an example of typical data shown in Figure 54. As expected, the tear strength decreases with increasing humidity. Interestingly, the extruded Nafion™ 112 sample had differing tear strength in the cross web vs. down web directions. The new 3M ionomer showed higher tear strength values as compared to the similarly prepared cast Nafion™ . When this test was used for comparison between experimental samples the conditions of 50℃ and 50% RH were the only conditions run.

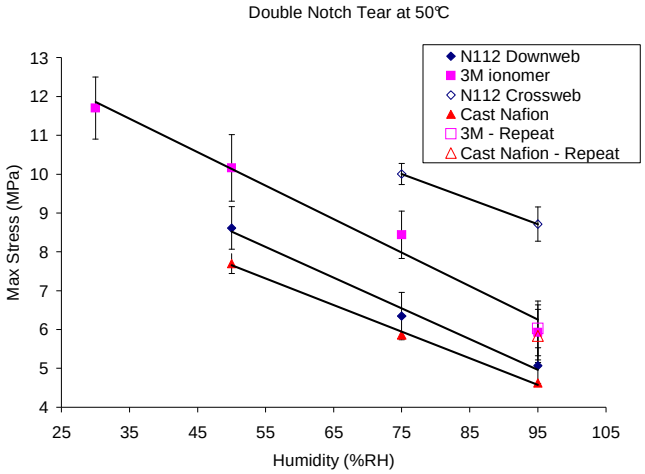

Figure 54 Tear Strength vs. % RH at 50℃ for select membranes

2.1.5 End Group Modification

The chain end groups for fluoropolymers are typically carboxylic acid groups. These groups are known to be unstable to heat[48] and, in the case of PFSA membranes, hydrogen peroxide[49]. One

proposed mechanism was discussed in section 2.1.2 Thermochemical and Morphological Investigation of Nafion™ Membrane Degradation and reproduced in Figure 55.

$$R_f - CF_2COOH + \bullet OH \rightarrow R_f - CF_2 \bullet + CO_2 + H_2O \quad (3)$$

$$R_f - CF_2 \bullet + \bullet OH \rightarrow R_f - CF_2OH \rightarrow R_f - COF + HF \quad (4)$$

$$R_f - COF + H_2O \rightarrow R_f - COOH + HF \quad (5)$$

Figure 55. Fenton's Mechanism

Regardless of the exact mechanism it is apparent that the end groups participate in oxidative degradation. And because of this strategies that reduce or eliminate the carboxylic acid end groups and replace them with stable groups such as –CF3 should improve the overall durability of the membrane. Various methods have been developed in order to convert unstable carboxylate end groups to a stable functionality. One of the most common methods is to expose the polymer to fluorine gas at elevated temperatures. This method was first reported by researchers at DuPont [49] and has since been used in a variety of fluorinated polymers. During the course of this program several methods were investigated for modifying the end groups such that the unstable carbonyl functionality was no longer part of the polymer. The methods investigated included; exposure to fluorine gas, initiator structure during polymerization, heat treatment, and others.

One of the most common methods for quantifying the concentration of end groups in fluoropolymers is by infrared spectroscopy. The carbonyl (C=O) stretch at about 1775 cm-1 is easy to detect and integrate in the sulfonyl fluoride form of the ionomer. Unfortunately, the technique is significantly more difficult when the polymer is in the acid (proton) form due to overlapping with water absorptions of hydronium and other ions. The infrared spectra of an ionomer before and after one of these treatments are shown in Figure 56. In this case the peaks at 1775 and 1807 cm-1 have been all or mostly eliminated indicating successful conversion of the end groups.

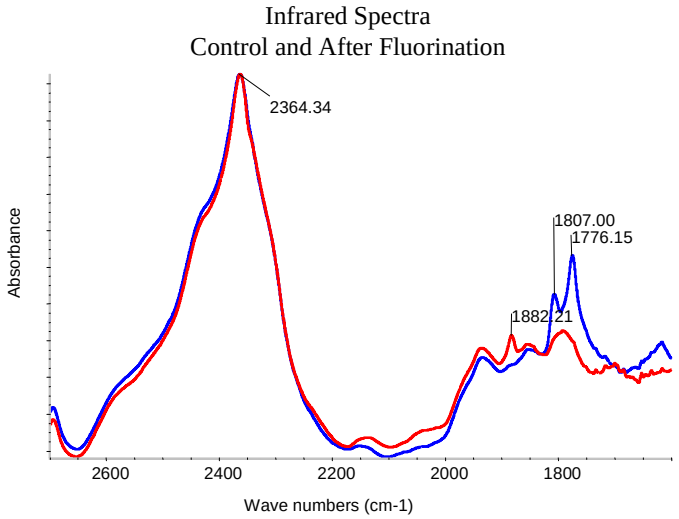

Figure 56. FTIR spectra of a typical ionomer before (blue) and after (red) end group modification.

After the polymer end groups were successfully modified they were converted into membrane films by pressing in a hot press followed by hydrolysis of the suflonyl fluoride and subsequent acidification or by typical dispersion and casting methods. The films were then subjected to the well known Fenton's test. The results of one of these experiments is shown in Figure 57 where the fluoride ion release rate over time was significantly lower for two different end group modification conditions as compared to the non-modified control.

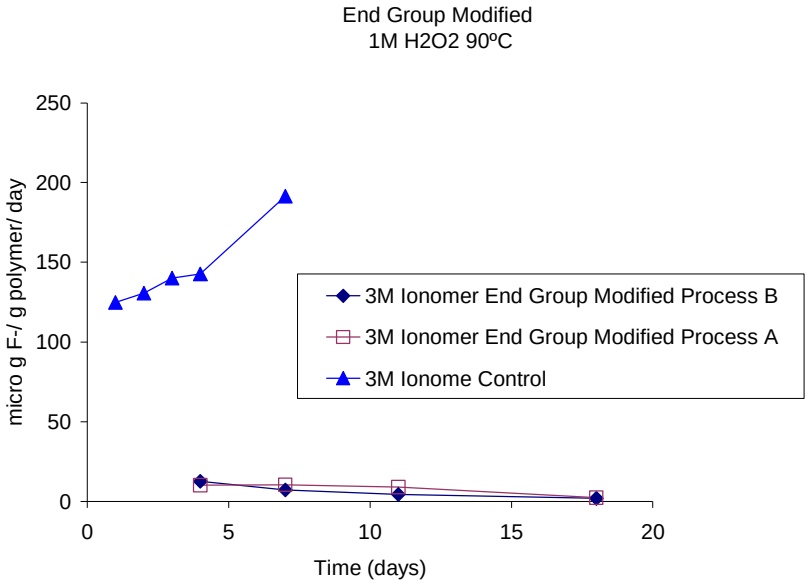

Figure 57. Fluorine release rate as a function of time in 1M H2O2

These data are consistent with the result found in the model compound section of this report where small molecule perfluoro carboxylic acid compounds decomposed at a significantly higher rate than non carboxylate materials. Interestingly, the fluoride generation rate is non-zero even for fully modified polymers perhaps indicating a secondary mechanism of side chain attack as suggested by the perfluor ether model compounds. (see section 2.1.3 Model Compound studies)

Performance in a fuel cell is the test that is ultimately the most meaningful. Both accelerated and non-accelerated test results showed a reduction in the level of fluoride ion released for end group modified polymers as compared to non-modified controls. Typical accelerated durability test results are shown in Figure 58. The fluoride ion released in the effluent water is significantly higher for the control (blue) as compared to the end group modified sample (magenta). The lifetime as defined by the point where the OCV goes below 0.8 V is longer for the modified polymer. This can be seen in the example in Figure 58 but more importantly determined in a statistical analysis where 31 MEAs made with unmodified membrane were compared to 8 MEAs run in the same test using membrane modified to have low levels of unstable end groups (Figure 59). In this experiment the mean lifetime was 209 hours for the control compared to 395 hours for the more stable membranes.

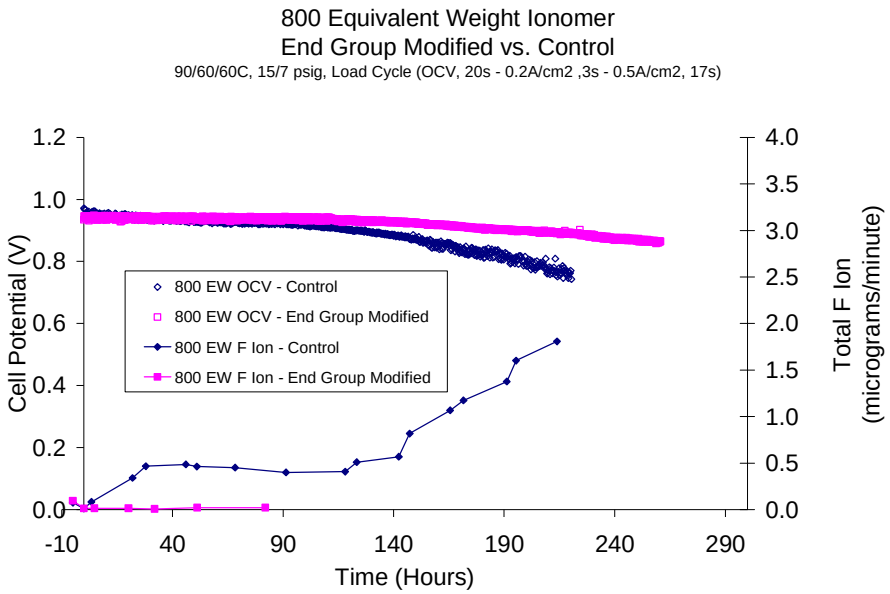

Figure 58. Potential at OCV vs. time for a typical durability test comparing end group modified membrane and a control.

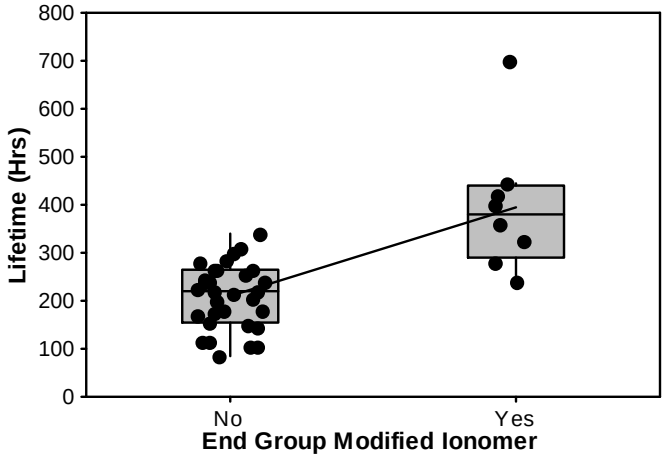

Figure 59. Statistical comparison of lifetimes between membranes with and without end group modification.

Conclusions

A strategy of chemically modifying the end groups of the PFSA polymer membrane was employed during the course of this program. Several methods were investigated and one was chosen to be implemented for 3M ionomer production. The reduction of the carboxylate end groups was determined by infrared spectroscopy and the stability of the membrane was demonstrated in ex-situ and in-situ durability testing.

2.1.6 Reinforced Membrane

Reinforced Membrane Development

Mechanically reinforcing the weak proton exchange membrane (PEM) of the fuel cell is expected to increase the useful lifetime of the fuel cell by absorbing the stresses a membrane has to endure due to thermal, humidity, and pressure cycling during its operation. This is especially important in the latter part of the membrane life when chemical degradation of the membrane has further reduced its ability to withstand failure.

There are a large number of potential supports for PFSA membranes. One of the most popular is expanded PTFE used by W.L. Gore[50] and DuPont[51]. These supports are often filled with ionomer solution then dried to form the supported membrane. This technology has been demonstrated to work and is the subject of significant research at those two companies as well as others[52].

One objective of this program was to model the stresses expected on a membrane in a typical fuel cell MEA. The results of this analysis were used to help identify the mechanical requirements necessary for a successful supported membrane. To evaluate the effects of these stresses, a humidity cycle test was implemented as an in-situ way of evaluating stresses in a cell. This test was able to provide complimentary data to the ex-situ tensile and tear testing described in a previous section.

A second objective was to survey a variety of potential support structures in an effort to identify a system that could improve both the mechanical strength of the membrane and the durability of an MEA under both accelerated then real time durability tests. Candidate supports were categorized based on construction or method of manufacturing (Table 13).

Table 13. Support materials considered for reinforced membrane development.

Category	Support Material
Nonwoven	Glass
	Aromatic polyester (LCP)
Woven	Glass
	Ceramic
	Polyester
Porous Membrane	PTFE
	PVDF
	Polyethylene
Multilayer	PSf
	PEI

There are many challenges to developing an effective supported membrane. The support itself has to be both hydrolytically and oxidative stable. The overall conductance of the membrane needs to be similar to that of a neat (unsupported) membrane and the support cannot leach contaminants such as cations that will compromise the proton conductivity. The support also needs to be strong enough to improve the mechanical strength properties such as tear or tensile strength. And the interface between the ionomer and support cannot fail resulting in a breach of the membrane and gas cross over. Evaluations of candidates were conducted with these considerations in mind.

MEA stress field due to bipolar plate compression:

The MEA is compressed between the bipolar plates as the fuels cell stack is assembled. This compression is essential to get good electrical contact and proper sealing in the stack. However,

the compressive forces in the MEA are not uniform. The MEA is compressed significantly under the lands but experiences little or no compression under the channels. This leads to a complex stress field in the MEA in the vicinity of the lands.

Finite elements models were developed to simulate the stress fields induced in the MEA due to this compression by the bipolar plates. Some of the stress fields that are calculated by these models are shown in Figure 60.

This study resulted in the following findings:

1. Tensile stress fields are formed in the MEA.
2. GDL penetrates into the gas flow channels, by almost as much at the MEA is compressed.
3. GDL and the catalyst layer may separate from the membrane.

Formation of the tensile stresses in the membrane may lead to failure of the MEA, possibly under the lands where the maximum tensile stresses are observed. In addition, the tensile stress field in the MEA may lead to the separation of the catalyst layer from the GDL and/or the membrane. This may form a small gap between these layers in the vicinity of the lands. This separation reduces the performance of the fuel cell by rendering those areas ineffective.

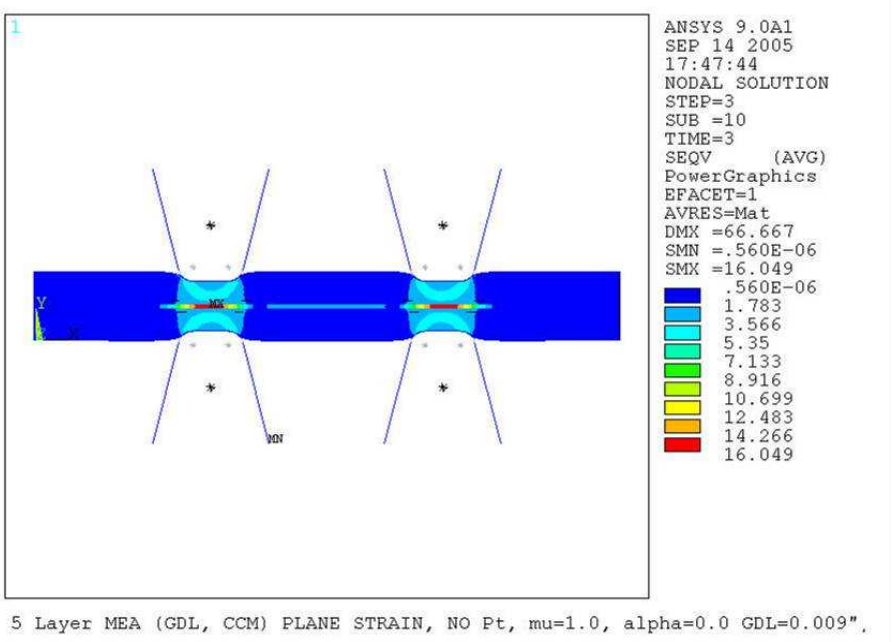

Figure 60. EQV stress field in an MEA, formed by Nafion™ membrane (30 micron), catalyst, and a 230 micron GDL. Bipolar plates compress the GDL by 1/3 of its original thickness. Stresses are in MPa.

Humidity Cycle Testing

A test method was developed in order to evaluate mechanical failure of membranes in the absence of chemical decomposition. The objective of the test is to subject membranes to fatigue by rapidly cycling between wet and dry humidity conditions. A similar test has been reported by researchers at GM[53] and modified for this program. A complete cycle from approximately 0% to 150% relative humidity takes about 6 minutes. A table of the test conditions is shown below (Table 14)

Table 14. Humidity cycle test conditions

• 80℃ cell temperature
• 120° gas injector temperature
• 2000 sccm air on both sides (anode and cathode flow fields)
• Humidity change from 0% to 150% RH
• 2.5 minutes at 150% RH, 3.5 minutes at 0% RH
• Ambient pressure (~0 psig) during operation
• Pressurized one side to 9 psig twice a day to leak check membrane
• Failure defined as 10 sccm leak rate

A typical set of data is shown in Figure 61 where two samples where measured with three repeats each. In this data set the same membrane was compared using GDLs that contained a microspores layer (MPL) and a bare (no MPL). It is clear from the data that the leak rate increased rapidly in the case where the GDL does not contain a micro layer.

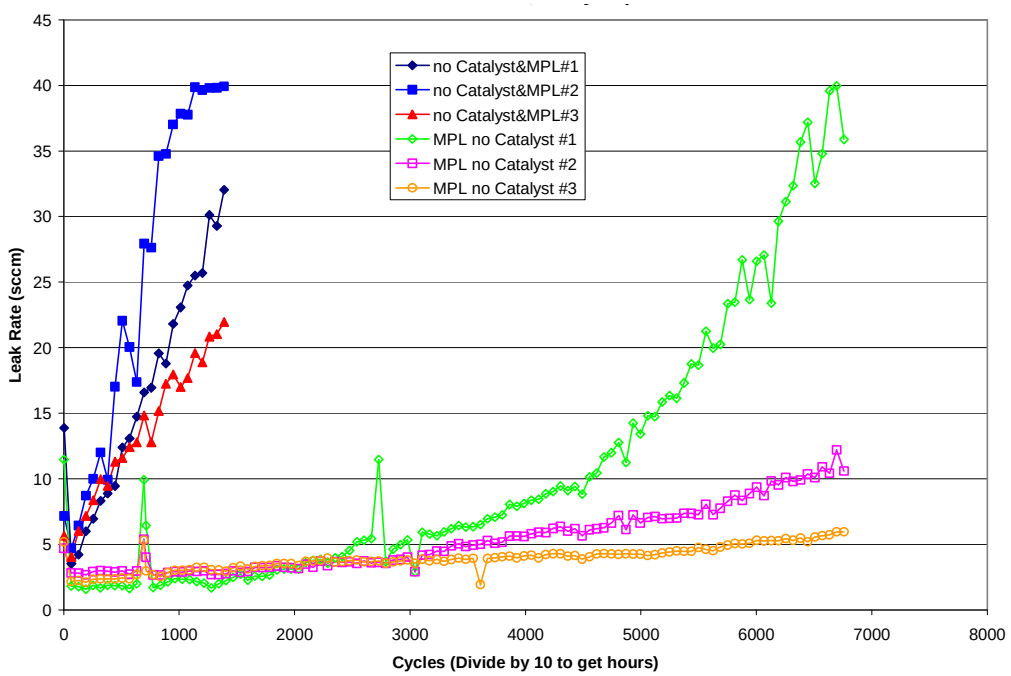

Figure 61. Leak rate for two sets of samples with and without MPL.

Table 15 shows data for several MEA and membrane constructions.

Table 15. Typical humidity cycle test results for different MEA and membrane constructions

Sample	Cycles to failure
Production MEA (Nafion™ inonomer)	>1300
Production MEA (Nafion™ inonomer)	>1300
Production MEA (Nafion™ inonomer)	>1300
GDL and membrane only (no catalyst or MPL)	218
GDL and membrane only (no catalyst or MPL)	355

GDL and membrane only (no catalyst or MPL)	444
GDL with MPL and membrane (no catalyst)	4554
GDL with MPL and membrane (no catalyst)	6381
GDL with MPL and membrane (no catalyst)	7520

This test was then used to evaluate a variety of membranes, MEA constructions and experimental reinforced membranes. One of the main purposes of this test is to evaluate the potential for leaks when a fibrous support is used in combination with a PFSA ionomer. If the ionomer delaminates from the support due to the expansion and contraction associated with humidity changes then one would expect a breach in the membrane followed by and increased leak rate. Table 16 shows an example set of data for one of the proprietary reinforced membranes studied compared to two controls.

Table 16. Leak Rate for one reinforced membrane and two control membranes

Sample	Cycles to failure
Reinforced membrane example	2661
Reinforced membrane example	2031
Reinforced membrane example	2947
Nafion 111	1547
Nafion 111	1192
Nafion 111	3045
3M Ionomer	6600
3M Ionomer	6682
3M Ionomer	2250

In this example the reinforced membrane failed with an average time of 2,546 hours as compared to and average 1,928 hours for the commercially available Nafion ™ 111 and 5,177 hours for an unreinforced 3M ionomer sample. No reinforced membrane consistently outlasted a comparable neat (unsupported) membrane in this test.

Support evaluation based on expanded PTFE

The use of a porous polytertafluoroethylene (PTFE) support to reinforce PFSA membranes has been well known in the industry for years. Publication form W.L Gore[54,55] and others[56,57,58] detail the fabrication and testing of these membranes. The primary purpose for the reinforcement is to improve the durability of an MEA by preventing mechanical failures such as tears or pinholes in the membrane over time. PTFE is an excellent choice for support material due to its excellent thermal and chemical stability, in particular stability in the presence of hydrogen peroxide.

As part of this program we investigated filling a commercially available expanded PTFE support with 3M PFSA ionomer. The support was obtained from Tetratec Corp., Ivyland, Pa and filled with ionomer solution using various coating and drying techniques. Accelerated fuel cell testing using the 90/60/60 protocol (Figure 62) shows an improvement in membrane durability in this accelerated test.

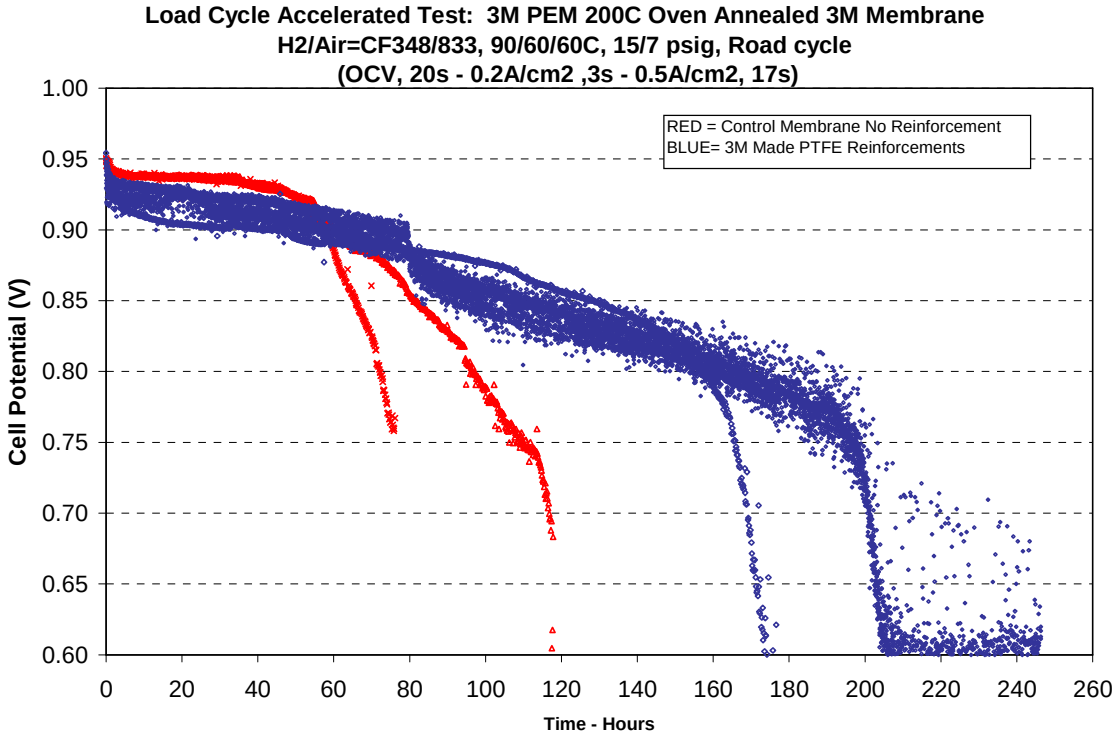

Figure 62. Example of fuel cell durability testing comparing control membranes (red) to membranes reinforced with TetraTec expanded PTFE (blue)

Even though PTFE based supports have been used successfully as fuel cell membrane supports we chose to limit our investigations in this area due to the relatively large amount of work already conducted with this support by , W.L. Gore, DuPont, and others.

Support evaluation based on PVDF

Another fluoropolymer candidate for a membrane support is polyvinylidiene fluoride (PVDF). This polymer has the advantage of chemical inertness greater than most hydrocarbons but somewhat less than PTFE. A proprietary process was used to fabricate a porous membrane using a PVDF polymer. These membranes were then filled with ionomer and evaluated for mechanical properties and fuel cell performance. In most cases membranes made with this support showed unacceptably low proton conductivity while exhibiting only modest strength improvements.

Support evaluation based on Polyethylene support

Polyethylene porous films were also considered as support materials for PFSA membranes. Even though aliphatic hydrocarbons are not generally considered oxidatively stable enough to be a membrane polymer, the high degree of crystallinity and water insolubility may allow the polymer to be used as a support. A high density polyethylene support sold under the trade name Solupor™ was obtained from DSM Solutech. This material was coated with 733 EW ionomer resulting in a 28 micron thick film. An MEA was made from this membrane and tested in a fuel cell for performance and conductivity (hydrogen pump or AC impedance). Hydrogen-pump and impedance values of about 69 $m\Omega.cm^2$ were measured and compared favorably to control impedance values of about 45 $m\Omega.cm^2$.

Electron microscope images show that this membrane was not void free and may not have bonded well with the polyethylene support. Figure 63 and Figure 64 show electron microscope

images of cross-sectioned samples of this membrane. It can be seen that unfilled voids exist in the center of the membrane, presumably as a result of poor ionomer filling in these areas or possibly delaminating of the ionomer from sections of this support.

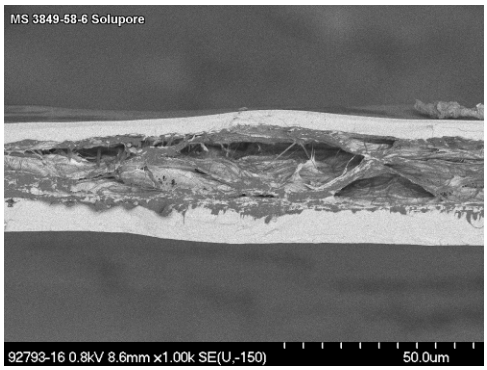

Figure 63. Solupor™ coated (compositional SEM)

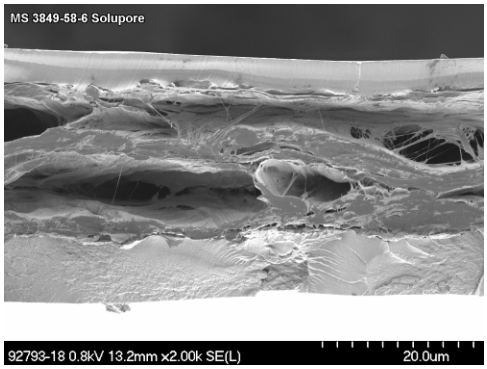

Figure 64. Solupor™ coated (compositional SEM) higher magnification.

This membrane was fabricated into an MEA for accelerated durability testing. The following graph (Figure 65) shows a comparison between the polyethylene supported membrane and a control in a 90/60/60 single cell test. In this case the lifetime was improved over the control.

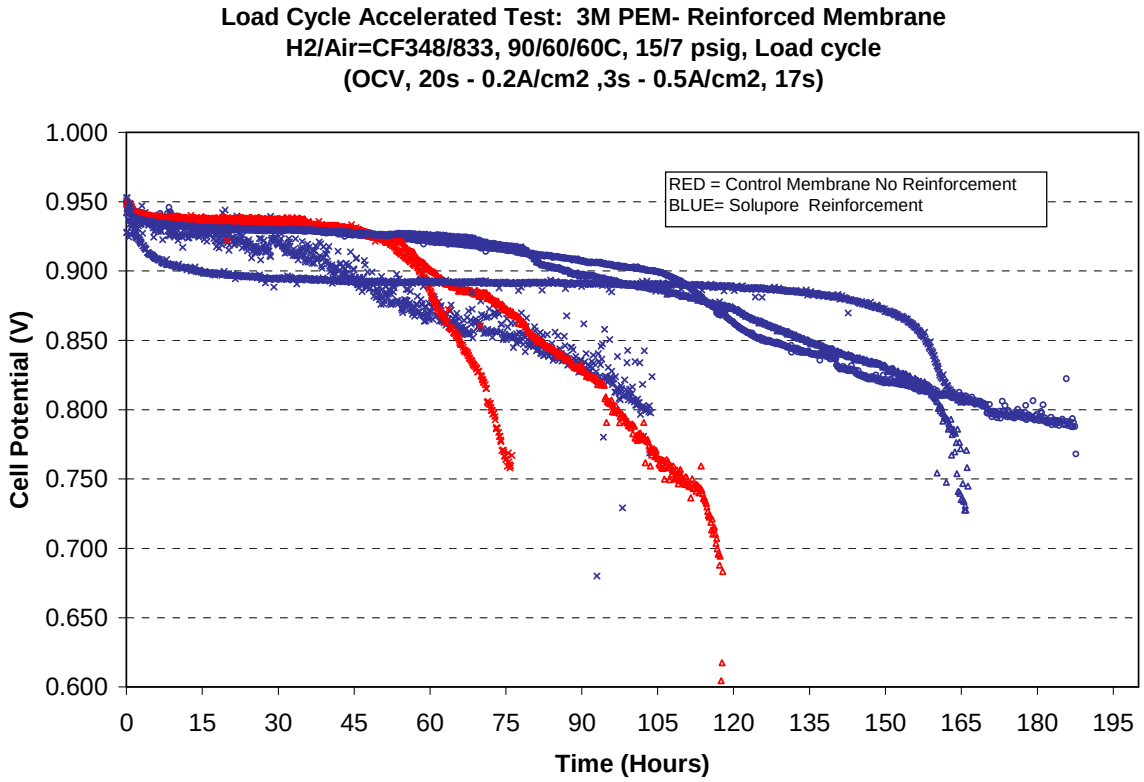

Figure 65. Comparison between HDPE support and control membrane in an accelerated lifetime test. (90/60/60)

One of the most significant draw backs of a polyethylene support is the low melting point of this polymer (~130℃). Not only does this present problems in drying and annealing of the ionomer that is used to fill the support 120°C is likely not possible. For these reasons and the somewhat modest increase in lifetime in an accelerated test we discontinued work in this area.

Support evaluation based on glass / ceramic woven Fabric

Glass fibers were considered at a membrane support. Like PTFE, glass can be very strong, hydrolytically and oxidatively stable, and be relatively thin. Woven fabric made from E-glass with a density of 17 g/m^2 (WF-002 from Aerospace Composite Products, Livermore, CA) and nominal thickness of 25 µm was successfully coated in the lab and in a 3M pilot scale coating line. Mechanical test data on this material showed marked improvements to the membrane properties. Values increased for both a tear test (6x improvement) and creep testing (13x improvement) over a neat control at 50℃ and 100% RH.

Fuel cell performance data however showed significant loss in performance, particularly in the initial fuel cell test stages. Membrane resistance measured by hydrogen pump was consistently higher than the resistance as measured by AC impedance. Various root causes for the high H-pump values for the glass reinforced PEM were investigated. The initial studies on metal extractable as a possible source of decreased performance of the PEM was considered by comparing extractable levels with nitric acid (HNO_3) using the fabric material (E-glass) and a ceramic fiber support know for its low impurity levels, 3M's Nextel™ 610.

Table 17. Nitric acid extraction of E-Glass and 3M's Nextel™ 600 support.

conc. (ppm)	E-Glass Cloth	Nextel 610 Roving
Ca	635	8
Al	334	
Na	165	7
K	133	5
Mg	101	
B	52	
Si	43	7
Fe	25	9
Cu	9	
Ti	7	
Zn	<5	
TOTAL	1504	36

As can be seen in Table 17, the E-glass sample had significantly higher levels of cations. This prompted the more thorough investigation of extractables with HNO_3 of 6 different types of glasses (other than E-glass) and as a function of time.

Figure 66 shows the total extractable metal content for six candidate reinforcing fibers. Four of the samples were Nextel™ ceramic and two glass fibers. Figure 67 shows iron level data for the same six samples. The effect of these extractables on membrane performance was tested using a membrane prepared with chopped fibers rather than in a woven or nowoven support. A typical procedure would be to mix 20% by volume of chopped Nextel™ 610 fibers with an ionomer solution then coat and dry to form a membrane.

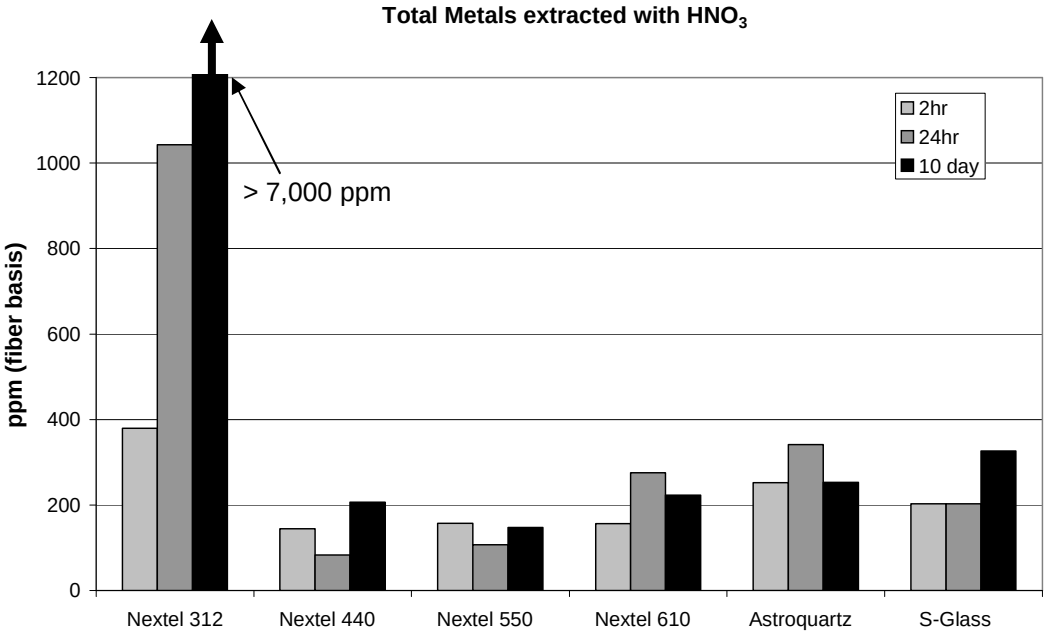

Figure 66. Total metals extracted with nitric acid for 6 candidate inorganic fibers. Data for 2 hrs, 24 hrs, and 10 days is shown.

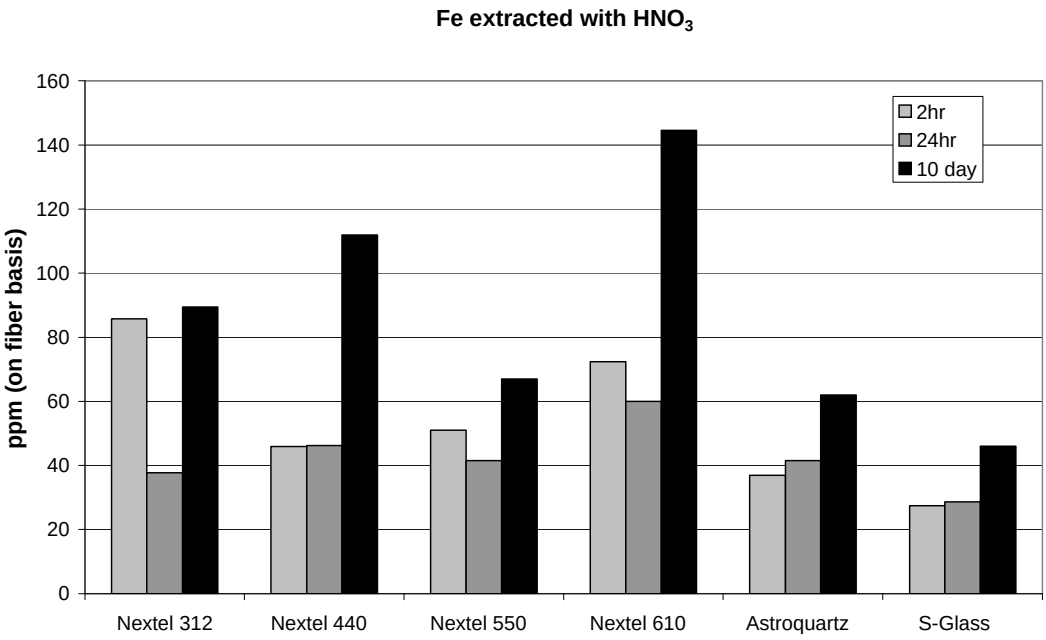

Figure 67. Total iron extracted with nitric acid for 6 candidate fibers. Data for 2 hrs, 24 hrs, and 10 days is shown.

Membranes with hammer-milled Astroquartz™ were also prepared at 5, 10 and 15% loading. All three membranes were tested and had acceptable H-pump values. For example the 5% Astroguarts™ has a resistance of 70 $m\Omega.cm^2$ for a 47 μm thick membrane. These tests indicate that the performance difficulties with the glass are related to the acid leachable components.

Work was then focused mitigating the effect of these impurities from woven glass supports. Three strategies pursued were to; extract the E-glass support with nitric acid prior to use in a membrane, protect the E-glass with a coating, and to change to an S-glass based support.

E-glass fabric, style# 101, with a basis weight of 17 gsm, was sent out to Intec Products Inc., Anaheim, for leaching. The samples were then fabricated into membranes and tested. Standard PDS scans are used as a measure of performance loss due to leached contaminants. The graphs in Figure 68 show that there is no evidence of performance loss with the leached glass when compared to the un-leached E-glass fabric. However, the leached E-glass fabric had virtually no strength and could easily be pulled apart. The leached E-glass fabric density was measured to be about 7.5 gsm, corresponding to about 50 wt% loss due to the leaching process. Since E-glass is typically 52 – 56 wt% SiO_2, it is expected that the leached E-glass fabric was essentially SiO_2. This approach proved not to be viable due to the low strength of the leached E-glass.

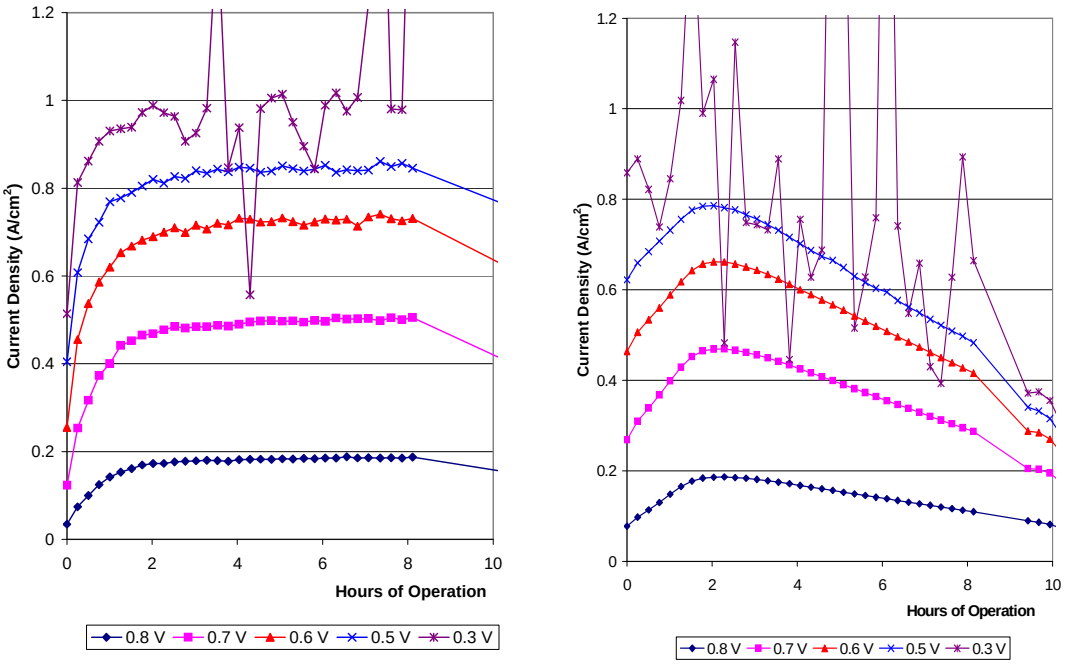

Figure 68. Current density vs. time for two glass reinforced membranes. The sample on the left was fabricated with 'pre-leached' glass; the right sample used the as received glass.

A second strategy was to protect the E-glass against leaching. One of the approaches investigated was the use of a fluorosilane coating on the surface of the E-glass fabric. For this purpose an E-glass fabric was obtained from Hexcel-Schwebel that did not have a surface modifier treatment. This style fabric (#104) was thicker and heavier than a style #101. The thickness of the fabric was about 32 micron and the basis weight about 19 gsm. The silane was applied from a dilute solution in alcohol followed by drying at elevated temperatures. The fluorosilane treated fabric was then coated with an 850 EW ionomer solution to form a membrane. Figure 69 shows the PDS plots for this reinforcement, again compared to a style #101 E-glass reinforced membrane. It is evident that the fluorosilane treatment did not help with the performance loss due to leachables.

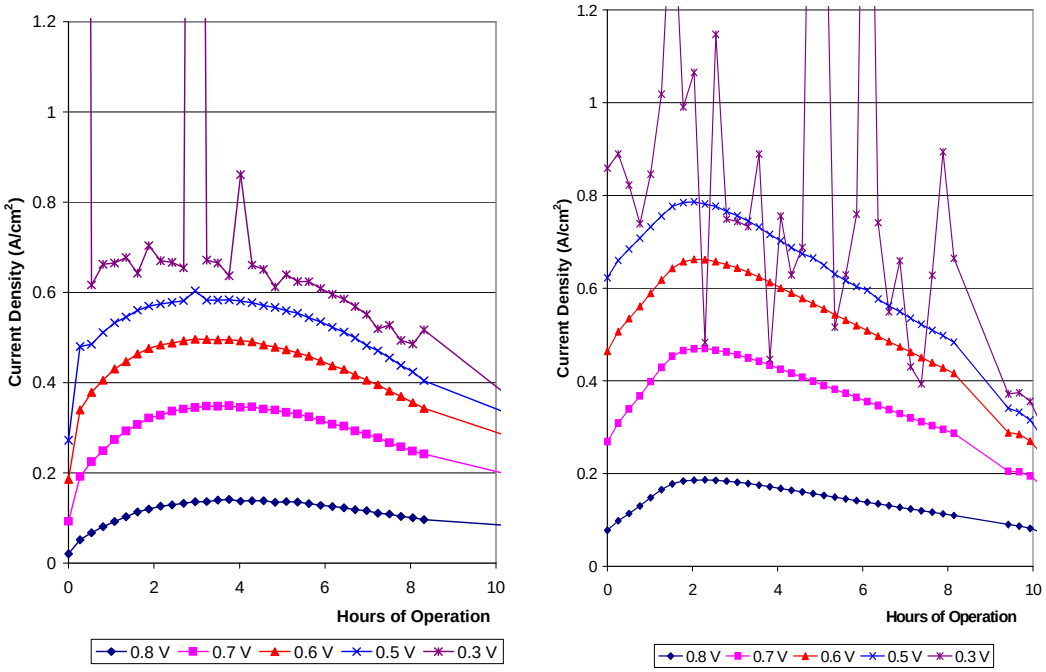

Figure 69. Current density vs. time for two glass reinforced membranes. The sample on the left was fabricated with fluorosilane treated glass; the right sample used the as received glass.

The last strategy used to mitigate the effect of cationic impurities from glass was to use an S-glass woven fabric. Currently there is no woven fabric commercially available using this glass type in a thickness less than about 60 µm. This is because yarns of S-glass are not available with less than 220 filament counts. As a result, the woven fabric has a basis weight of 48 gsm. The E-glass fabric style #101, by comparison, has a basis weight of 17 gsm and a nominal thickness of 25 micron. A study was conducted that looked at the effect of warp and weft counts on the final fabric thickness by taking published data and looking at thickness trends within a class of yarns. It can be reasonably concluded from this that it would not be possible to make a S-glass fabric of less (or close to) a 25 micron thickness by taking existing S-glass yarns and making a more open weave without significantly compromising the integrity of the fabric.

A special order run of 51 filament yarn would have to be made for us to get a fabric of 25 micron or less. This was not pursued due to the cost involved. Instead, the thinnest commercial S-glass fabric (WF-15A, from Aerospace Composite Products) was used to investigate the effect on performance of an S-glass supported membrane.

The S-glass fabric was coated using an 850 EW 3M ionomer solution. The final average membrane thickness was 52 micron, which is less than the uncoated fabric (60 micron). Weight measurements were used to calculate the filling as 30% ionomer, 70 wt% glass (66 vol%). Considering this, it is expected that the performance of this membrane would be compromised compared to the bare, unreinforced, membrane. This can be seen in the PDS plots in Figure 70. The PDS plots also show that there is no obvious problem with acid leaching of compounds from the glass.

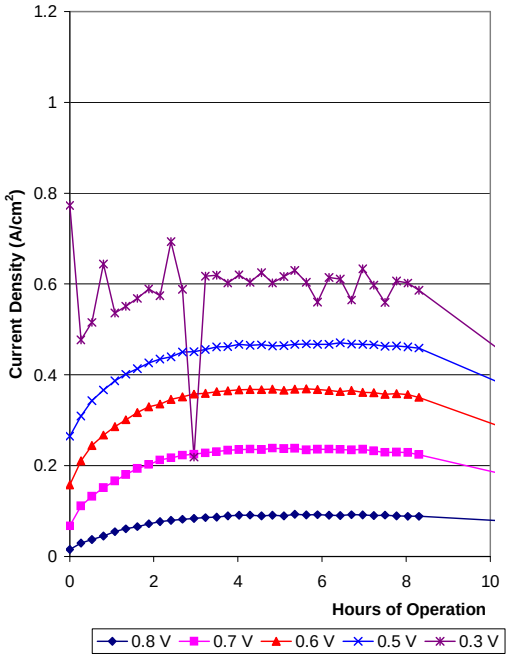

Fig 3.1(e) S-Glass with 33vol% ionomer

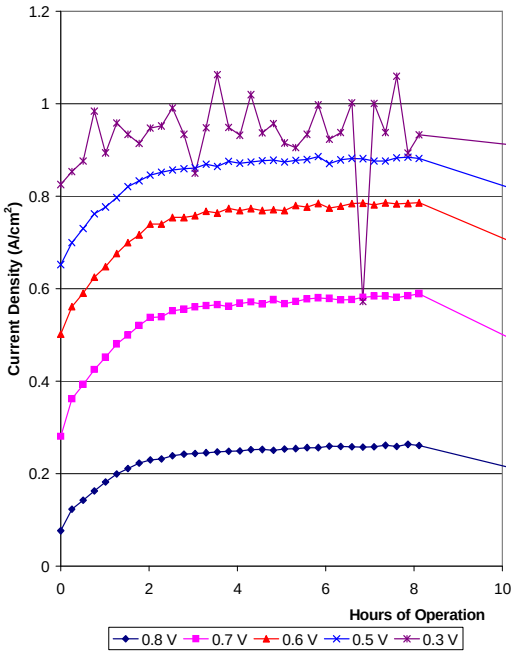

Fig. 3.1(f) 850 EW bare ionomer

Figure 70. Current density vs. time for an S-glass reinforced membrane (left) and unreinforced control (right). The low performance is attributed to the low fraction of ionomer in combination with the thickness.

S-glass was also more difficult to coat than E-glass due to the high number of filaments. This can be seen in the SEMs below in Figure 71.

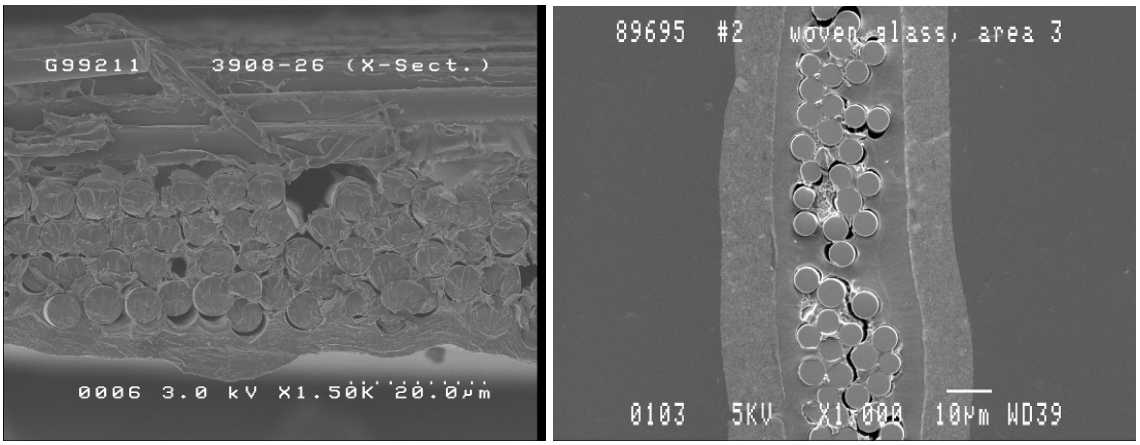

Figure 71. SEM cross sections of S-glass filled with ionomer. Incomplete filling and poor interfacial adhesion can be seen.

Glass fabric was evaluated as a potential support for PEM membranes. Cations that are leached from and E-glass support are detrimental to performance and a mitigation strategy determined. Three approached were studied; pre-leaching the E-glass, coating with a fluorosilane, and changing to the cleaner S-glass. The pre-leaching proved effective at removing impurities but resulted in a significantly weakened support. The silane coating was ineffective at preventing the

cations from contaminating the membrane. And the S-glass, while having reduced impurities, was not commercially available in the density or thickness desired for fuel cell membranes.

Supports based on woven PET and PA netting

Polyethylene terephthalate (PET) and polyamide (PA) netting were evaluated as possible reinforcing materials for a PFSA based membrane. These materials are not generally viewed as hydrolytically stable enough to serve as a durable support. However, the insights into the strength and performance of membranes fabricated with these supports were considered instructive.

Woven PET netting was obtained from Vestegaard-Frandsen, a Danish company that specializes in mosquito netting. The thinnest netting available is about 45 microns thick with an open area of only 45%. More open fabrics are available, but are >60 microns in thickness, which are not viable candidates for PEM reinforcement.

A membrane was prepared and tested in a single cell test. The hydrogen-pump and AC impedance measurements were 80 and 82 mOhm.cm^2, respectively. These numbers are high, but when considering that the coated membrane was about 60 microns thick, compare very well with neat membrane at the same thickness: 80 and 73 mOhm.cm^2, respectively. However, the membrane failed when a differential pressure was placed across the membrane during testing. Post mortem analysis revealed an embrittlement of the PET fibers which lead to edge tears.

SEM analysis of the membrane showed some areas with good bonding of the PEM to the PET, while other areas with some delaminating, as shown in (Figure 72).

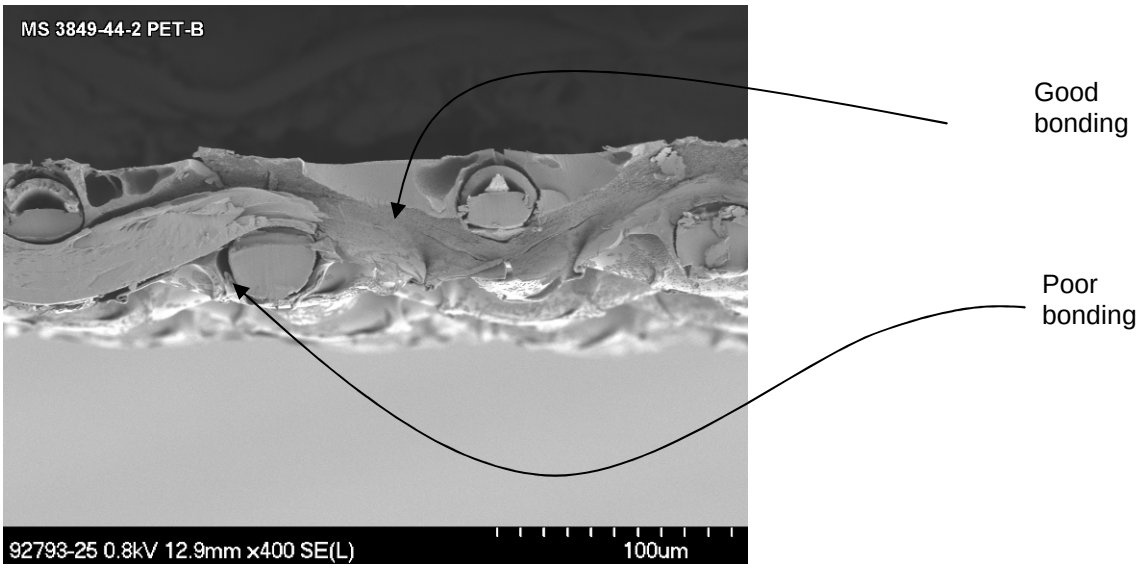

Figure 72. SEM cross-section of a woven PET fabric reinforced PEM.

Further attempts of producing PET reinforced membranes for single cell testing failed. The major issue encountered with PET was microscopic evidence of de-wetting of the PET strands

Use of a polyamide netting material from SAATI (PA 70/49) provided similar results. This netting had a thickness of 54 μm and a basis weight of 17.2 g/m^2 .

The fuel cell test showed a high H-Pump of 108 mΩ.cm^2 which is expected for a 76 μm sample, but the sample failed to perform in the harsher 90/60/60 protocol, More importantly, the H_2 crossover current of 4.2 mA/cm^2 is very high, especially for a thick membrane This suggests a

poor interface between the ionomer and support or breach of the membrane under fuel cell conditions.

Work was halted for both approached due to the lack of suitably thin starting support structures and the poor interfacial adhesion leading to high gas crossover.

Supports based on multilayer coating

A unique approach to fabricating a reinforced membrane was developed during this program. A multilayer membrane can be fabricated using a multiple cavity die during a solution casting process. The proper choice of support polymer and solvent can result in a phase inversion of the non-conductive polymer to form a support structure. A schematic is shown in Figure 73. The process consists of using a multilayer extrusion die to cast 3M's perfluorosulfonic acid copolymer formulation on both sides of a non-iononic polymer such as polysulfone (PSf) or polyetherimide (PEI) solution in N-methylpyrolidone (NMP). Upon contact with the perfluorinated ionomer dispersion, the nonionic polymer coating undergoes a phase inversion via ionomer-induced phase separation (IIPS). During this process, the ionomer dispersion acts as the coagulant interpenetrating the micropores, and upon further solvent evaporation, the ion-conductor becomes locked within the micro-infrastructure of the non-ionic support.

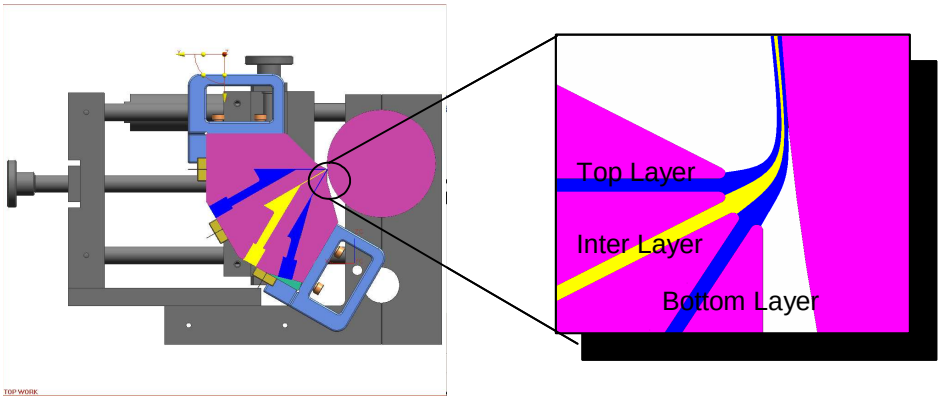

Figure 73. Schematic illustration of the multilayer extrusion/casting process

The primary advantages of this reinforcement approach can be summarized as follows:

- The thermal and dimensional stability characteristic of high temperature polymers like PSf or PEI allows the support to maintain its micro-porous structure, even during post-drying annealing operations at 180-200℃.

- NMP is a good solvent for the support polymer and coalescing agent for the ionomer dispersion. This provides sufficient pore volume to quickly remove residual solvents, thus reducing the likelihood of blister defects during the drying/annealing process.

- The multilayer coating scheme presents a unique method for processing reinforced proton-exchange membranes (PEMs).

- In a single coating step the support is covered by an ion-transport skin on both the anode and cathode sides of the membrane.

- This method differentiates itself from the common reinforcement approach of imbibing pre-formed porous supports. As a result the manufacture of thinner (13 μm) reinforced PEMs is possible.

The PSf-reinforced PEM development took place on a pilot line in 3M's corporate research and process development laboratory. The ionomer dispersions (lower/upper slots) and non-ionic polymer coating solutions (middle slot) were fed to a three cavity die by means of syringe pumps. A 3-zone convection oven was used to optimize the phase inversion followed by solvent drying. All coating formulations were multilayer extruded on a 2 mil polyimide substrate (Kapton™). Volumetric flow rates were optimized to yield good quality 12 – 30 micron reinforced PEM's. It was found that thinner 3-layer composites gave better coating quality and better conductivity due to enhanced ionomer interpenetration in the polymer support layer. The SEM micrographs in Figure 74 show typical multilayer membranes made by this technique.

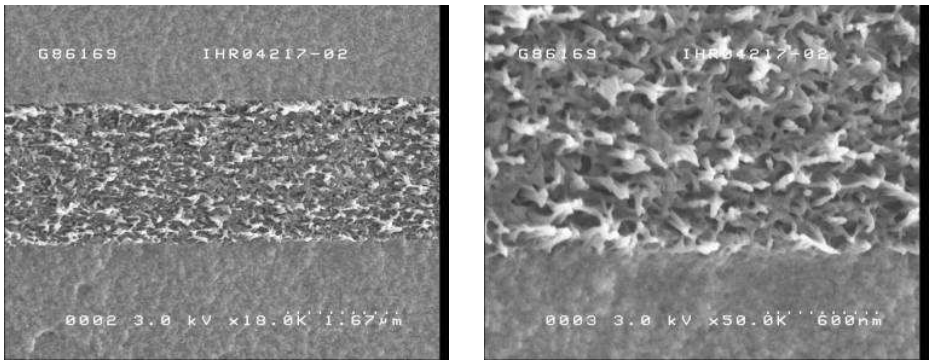

Figure 74. SEM micrographs of 15 micron thick PSf-reinforced membrane.

This sample consists of a 2.5 micron interpenetrated PSf support sandwiched between two-7 micron thick proton-exchange membranes of 1000 EW. Pore size measurements indicated an average of 98 nm with a standard deviation of 30 nm.

Fuel cell performance tests on this sample gave excellent proton conductivity characterized by a hydrogen pump value of 68 ohm-cm2 and an AC impedance of 64 mOhm-cm^2.

Lifetime durability was measured using the time for the OCV to cross 0.8V as the criteria. A PSf reinforced PEM compared favorably with neat membrane. (Figure 75).

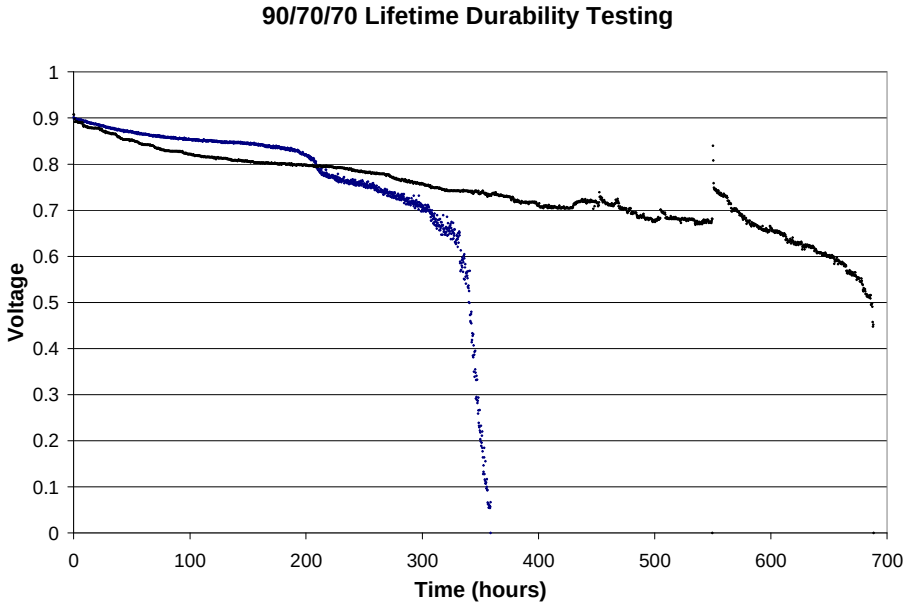

Figure 75. 90/70/70 durability testing of PSf reinforced membrane

Experiments showed feasibility of coating high and low EW ionomer dispersions in the same 3-layer composites. Lower EWs (800) gave superior conductivity as compared to higher EW counterparts without compromising mechanical strength.

Two support polymers were investigated during this program. Both the PSf and PEI were chosen for there desirable chemical and mechanical properties. Unlike the PSf shown in Figure 74, SEM analysis of the PEI-reinforced PEM's indicates severe delaminating at the ionomer-porous PEI interface and a general lack of ionomer interpenetration in the interlayer. As shown in the micrographs below (Figure 76) the PEI interlayer supports showed delaminating and poor ionomer interpenetration.

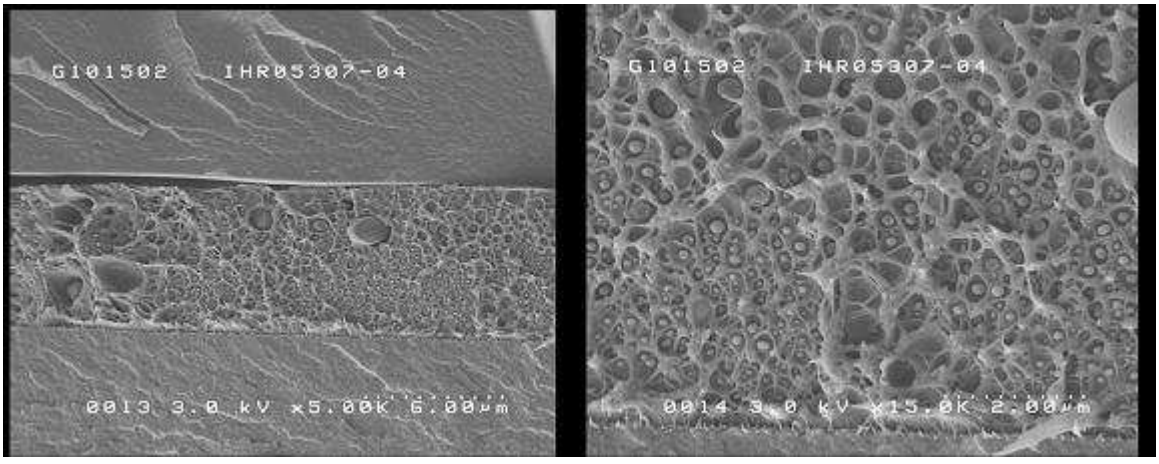

Figure 76. SEM micrographs of PEI-reinforced membrane.

The polymer solution viscosity was measured in an effort to determine the differences between the two polymers behavior in this process. As illustrated in the viscosity chart in Figure 77, the

NMP-based PEI coating formulation had a lower viscosity than the PSf counterpart solution. This did not allow good phase inversion and ionomer penetration at typical process conditions. Attempts to reduce interlayer thickness by reducing the volumetric flow rates caused flow instabilities at the extrusion die lips.

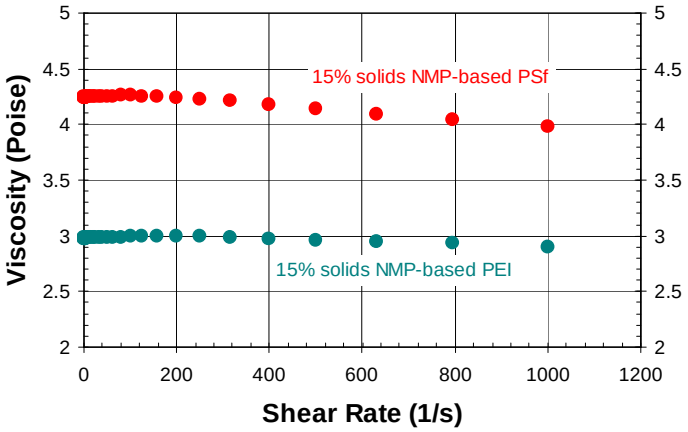

Figure 77. Viscosity vs shear rate for PSf and PEI polymer solutions in NMP

The balance between improved mechanical properties and proton conductivity is always a primary concern with reinforced PEMs. The graph in Figure 78 of conductivity (hydrogen pump) and tear strength measurements for the PSf-reinforced PEM samples is one way to view this balance. In this analysis, samples were not separated due to either different interlayer formulations or different multilayer construction.

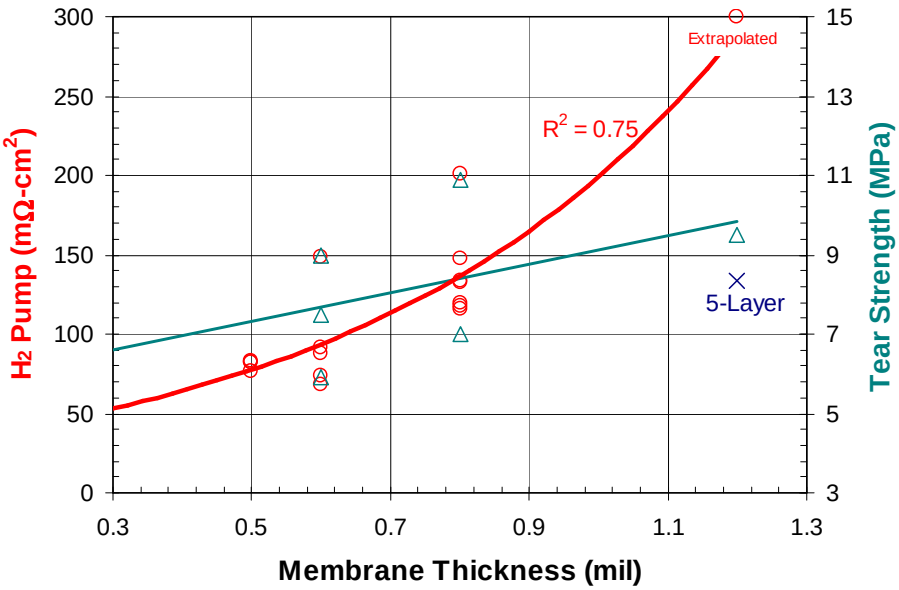

Figure 78. Conductivity and tear strength as a function of total membrane thickness in multilayer PFs supported PEMs.

Based on the above analysis the conclusion was made that the fuel cell performance of PSf-reinforced PEMs is limited by the overall thickness of the composite. Very thin reinforced PEMs (about 8 microns) are required to attain the desired H_2 pump values in the vicinity of 50 mOhm*cm^2.

Supports based on LCP Non-Woven

Non-woven porous support materials were evaluated throughout this program. Typical fibers are polyethylene, polypropylene, or certain polyesters. The thermal stability of most of these polymers would not be suitable for the coating and drying temperatures needed for typical PFSA ionomers. One polyester was investigated due to its high thermal transitions. Liquid crystal polyester (LCP) is a wholly aromatic polyester based on a copolymer of p-hydroxybenzoic acid and p- hydroxynapthoic acid. This polymer has a liquid crystal phase at elevated temperatures and can be formed into very strong, highly aligned fibers. And even though polyesters are know to be hydrolytically unstable, it was speculated that the high degree of crystallinity would restrict the absorption of water and therefore the bulk hydrolysis of the polymers used in the fiber. A non-woven mat of this material was obtained from Crane Paper Company for evaluation.

Crane LCP HM090 liquid crystal polyester Type B is 30 +/- 8 micron thickness with areas with little inter-fiber bonding. Non-woven materials are often uneven in thickness and this LCP sample had areas of thickness as high as 50 microns. Membranes in this thickness range often have unacceptably high resistance regardless of the support. In addition, defects were assumed to arise from thick zones. The goal of the project was to improve bonding, and thickness uniformity while retaining porosity of the webs. Major improvements to processing Crane HM090 LCP paper were obtained by applying pressure after a 204℃ treatment of the paper. Coating webs with ionomer was accomplished with a 2-layer hand-spread coater. The coating quality of these PEM composites was often not acceptable due to numerous wrinkles developed during the coating process. Despite these wrinkles, excellent hydrogen pump values were measured.

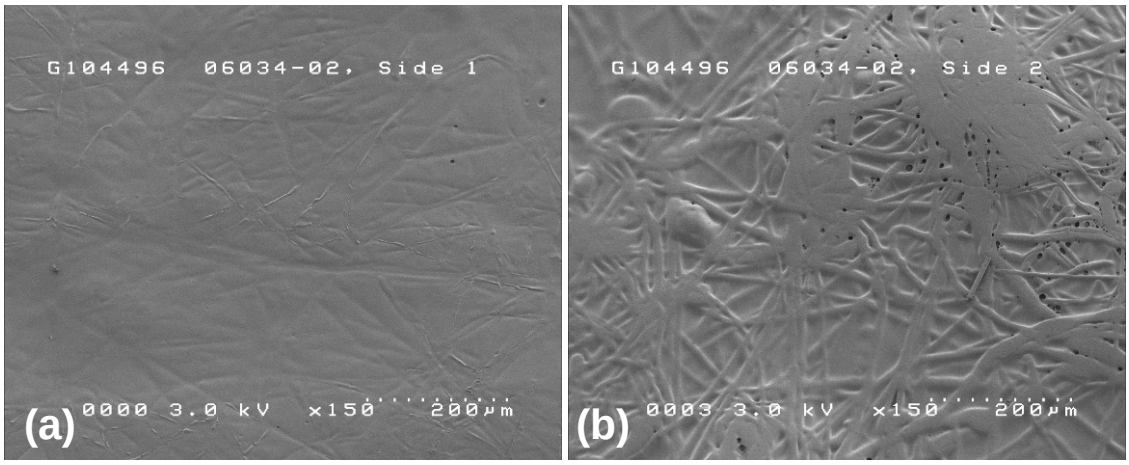

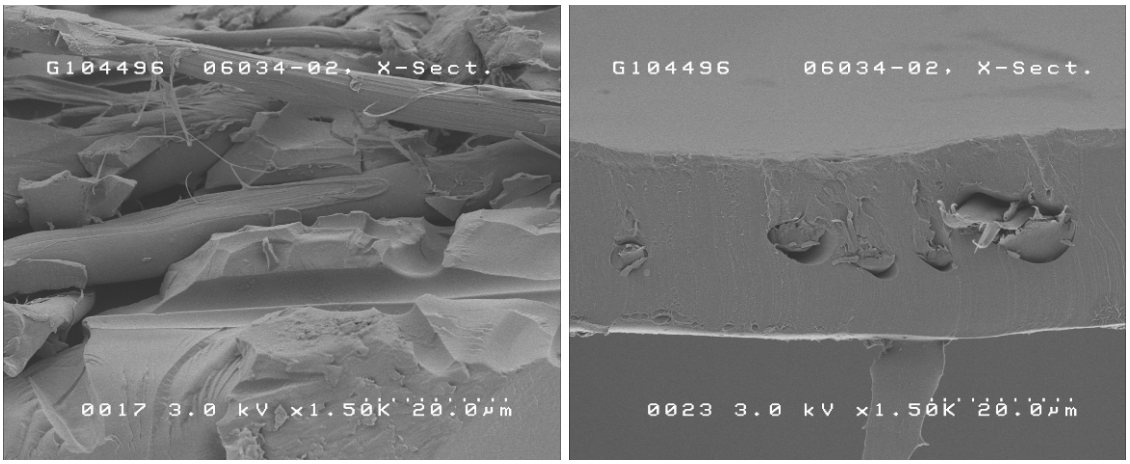

Figure 79. Electron micrograph of LCP supported membrane. (a) liner side (b) air side (c) fractured in liquid N2 (d) cut with bladed after cooling with dry ice

The adhesion of the LCP to the ionomer is potentially a problem. The SEM in Figure 79 (c) shows a fiber and its imprint in the ionomer. The next SEM (d) shows fibers of LCP being pulled away from the ionomer, presumably due to the cutting action. However there is no evidence of adhesion of the ionomer to the fibers.

Two membranes from were submitted for accelerated lifetime durability testing under the 90/60/60 fuel cell condition. The results indicated that the samples may have had a hole in them from early stages of the test. The data in Figure 80 shows the plots of two LCP membranes compared to two control (un-reinforced) membranes.

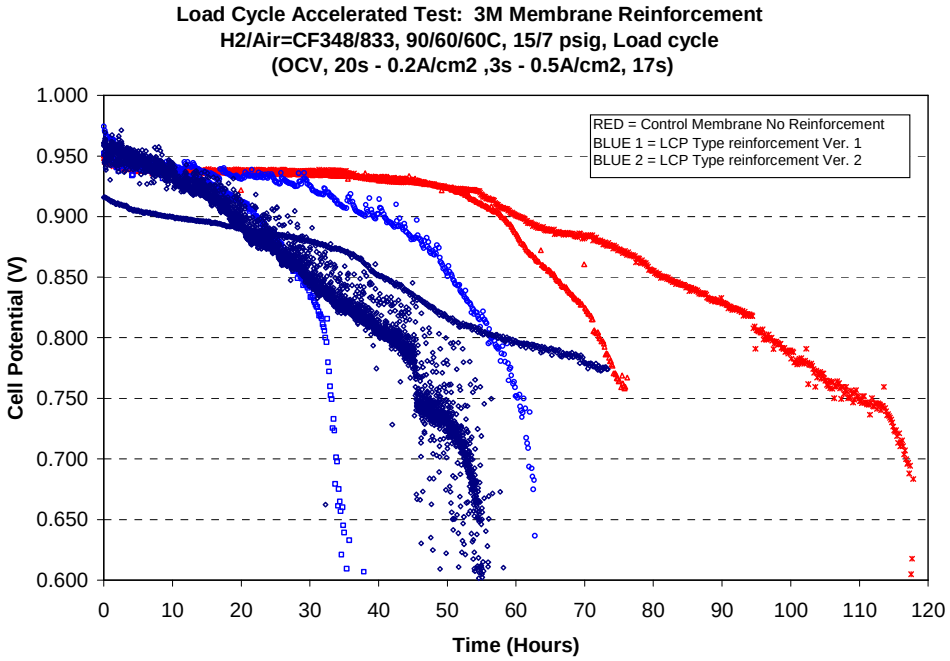

Figure 80. Durability test for two versions of LCP reinforced membranes (two samples each). Red symbols show control membranes in the same test.

Table 18. Membrane resistance and crosso over values for two LCP reinforced membranes

Sample	H-Pump (mohm-cm2)	Impedance (mOhm-cm2)	H2 crossover(mA/cm2)
1	82	83	0.0033
2	74	71	0.0014
3	119	115	0.0012
4	75	71	0.0106

The results on these membranes looked quite good for samples 2 and 4. However, some membrane breach is evident with the high H_2 crossover value for sample 4.

Two approaches were investigated to improve the adhesion of the LCP to the ionomer. One consisted of plasma treatment of the LCP using the following 3 plasma treatment environments:

- O_2
- Silane + O_2
- Ammonia

SEMs (not shown) of the treated LCP membranes showed no differences in adhesion between fibers and matrix.

Sulfonation of the LCP was also attempted with the idea of introducing sulfonic acid groups onto the aromatic polyester as has been done for polyether ether ketones and similar polymers. Literature suggests that a fuming sulfuric acid solution would be the most effective in sulfonating the surface of the LCP, while minimizing the possibility of acid catalyzed hydrolysis of the ester. The LCP was oven dried at 120^{o}C for at least 1 hour before use. The addition of the fuming sulfuric acid to the LCP resulted in dissolution (or degradation) of the LCP within seconds. This result indicated surface sulfonation was not possible with this support.

The LCP non-woven support was not able to overcome the difficulties in thickness variations, support adhesion, and durability testing. For these reasons this approach was abandoned

Reinforced membrane summary

A variety of supports were evaluated as reinforcing materials for a PFSA membrane. While fuel cell durability is the ultimate objective, most materials were evaluated through ex-situ mechanical tests or, when possible, simple fuel cell performance tests. The two key criteria used to determine whether a candidate should be advanced to an accelerated durability are the proton conductivity and tear resistance. These two criteria can be easily visualized by plotting hydrogen pump versus tear strength (double notch tear). Figure 81 shows a plot of several membranes tested during this project. Only the woven glass, LCP, and multilayer coatings were considered suitable for durability testing.

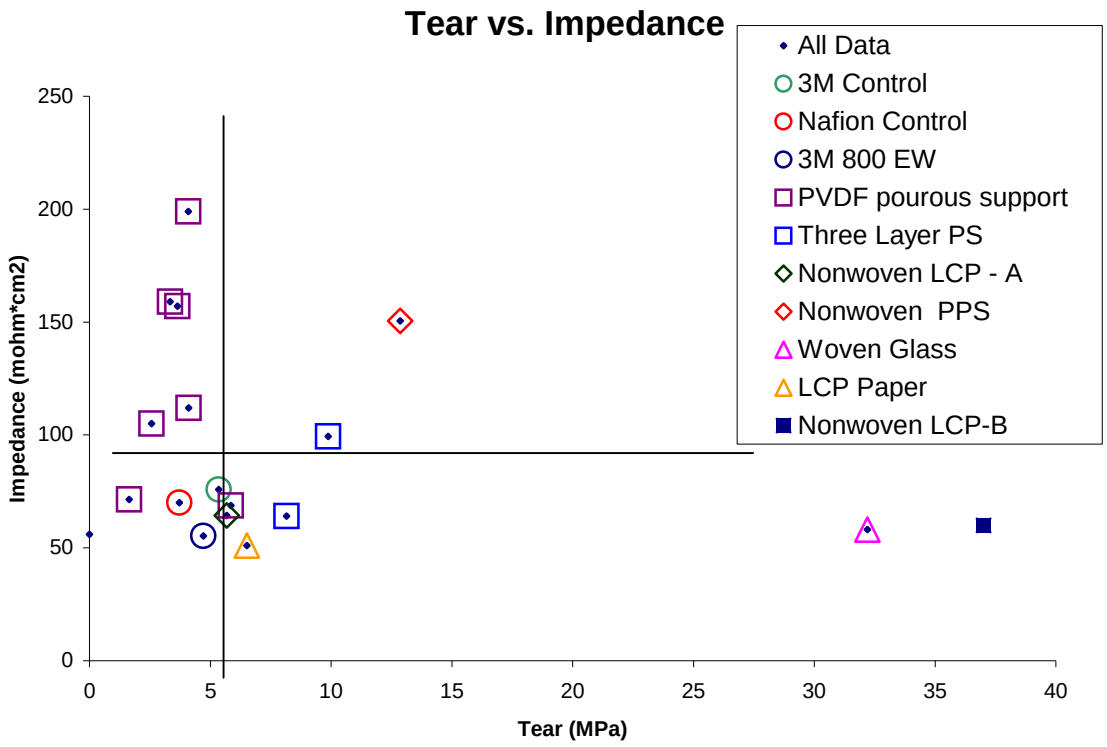

Figure 81. Impedance versus tear strength for a variety of reinforced membrane candidates. Only samples in the lower right quadrant were considered suitable for advanced testing.

Even when the strength was greatly improved the durability was typically lower than that of a control. Many factors may contribute to this result including; coating quality, support adhesion, oxidative stability, and others. It was determined that the role of oxidative degradation of the ionomer – supported or homogeneous – was a more significant factor in determining ultimate lifetime in accelerated fuel cell testing.

Edge Protection

Introduction

The necessity of protecting the membrane edge has long been recognized by MEA suppliers and stack manufactures. Although this topic does not show up in the academic literature often[59], there are numerous patents and patent applications[60] disclosing methods of protecting the membrane edge from damage and thereby increasing the lifetime of the MEA in a durability test or under actual use conditions. Regardless of the protection strategy, the method must be applicable to high volume manufacturing methods in order to be truly viable in the industry. In this program we explored and developed a method of applying a liquid coating to the membrane that could be ultraviolet (UV) light cured to form a durable, thin film, protective layer. Additional methods were investigated such as adhesive backed films but not fully developed under this program.

Design

The main objective of this work was to protect the membrane from damage near the GDL edge. A cartoon cross section is shown in Figure 82 depicting the subgasket layers on the membrane with a small degree of underlap (~1-5 mm) into the GDL.

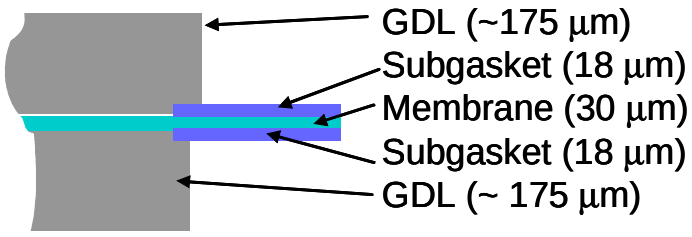

Figure 82. Cartoon showing location of subgasket layer (note catalyst and microporous layer not shown).

Since this protective coating needs to be applied to the membrane around the entire perimeter of the active area a method of pattern coating is required. Screen printing was chosen as the method best suited for this application due to its simplicity, flexibility in pattern shape and size, and the low cost of screens which allow for many different sizes and shapes of MEAs. Initial lab trials were conducted on a table top screen printing device. Once the idea was demonstrated to be feasible a rotary screen printing station was installed on existing process equipment.

The thin membrane proved to be a poor substrate for coating and curing due to the extreme dimensional instability of this material under different humidity, line tension, and temperature conditions. A process was developed where the coating is printed on the membrane while it is still on the polyester liner used when casting the ionomer. Once one side is coated and cured, a temporary liner is laminated to the air side of the subgasket coated membrane and the coating (first) liner is removed. The second side of membrane is printed with the UV resin and cured in the same fashion as the first. At the end of this process the membrane is ready to be laminated into an MEA by applying catalyst to the membrane “window” followed by GDL attachment. A simpler assembly is to laminate a catalyst coated GDL to the membrane window frame. A

photograph of a typical subgasketed MEA is shown in Figure 83. Note that the blue color is a pigment added in order to help facilitate alignment of the two sided coating using optical sensors.

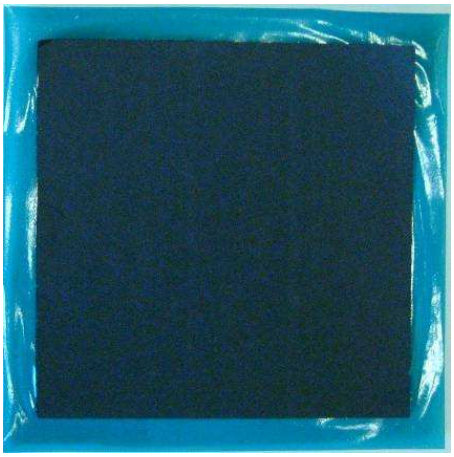

Figure 83. Photograph of subgasketed MEA.

While cartoons like the one shown in Figure 82 are helpful in describing the concept of the subgasket in relation to other layers in the fuel cell, images of real MEAs provide the best view of the various layers. Figure 84 shows an optical microscope cross section of the active area of a typical MEA with each of the layers labeled.

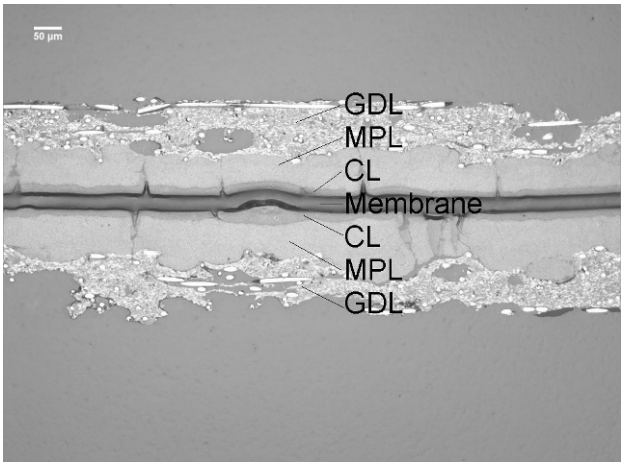

Figure 84. Typical cross section of experimental MEA with layers noted

Another image is shown in Figure 85 of the edge of the MEA where the subgasket layers are labeled. It can be seen in this image that the subgasket layer provides a thin film barrier between the membrane and the rough edges of the GDL.

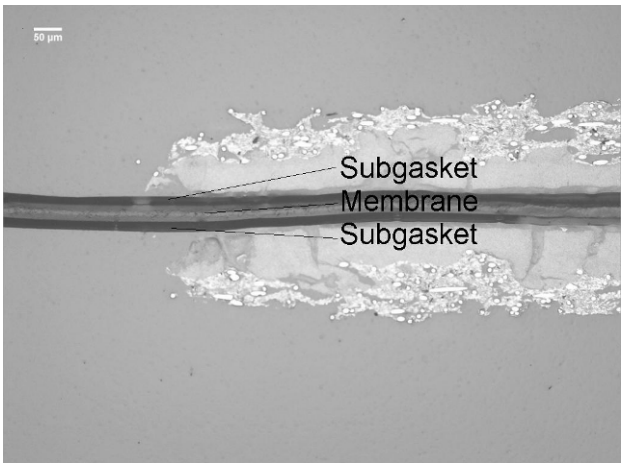

Figure 85. MEA Edge with subgasket and membrane noted

The last image in the set is shown in Figure 86 where the subgasket inner edges are labeled. This is the region where the protected edge transitions into the active area. It can bee seen in this image that the subgasket layers have a tapered edge due to the nature of the coating method and provides a gradual reduction in stress on the membrane in this region.

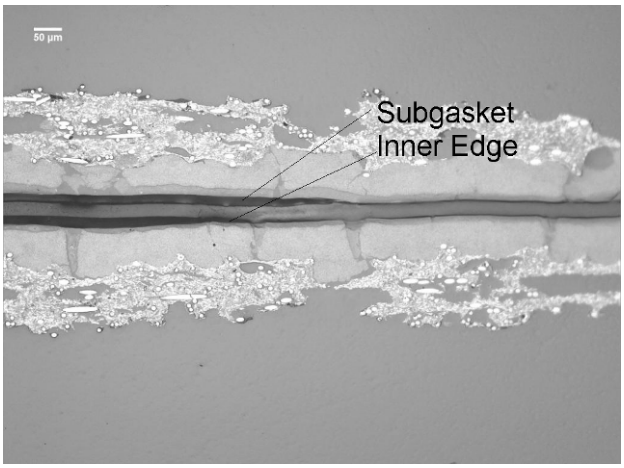

Figure 86. Subgasket inner edges

Resin Development

The properties required of the subgasket resin coating can be divided into categories needed in order to have a robust process and properties required for use in an operating fuel cell. The following Table is a brief summary of these various properties;

Table 19. UV Subgasket Requirements

Process Requirements:
- Low Viscosity
- Rapid Cure
- Adhesion to membrane
- Color contrast with membrane for optical sensor alignment
- Safety

Fuel Cell Environment Requirements
- Protect membrane edges
- Hydrolytic stability
- Low levels of extractable materials
- Low defect coating (high coating uniformity)
- Good membrane adhesion

There are a nearly infinite number of resins, monomers, initiators, and additives to choose from when designing a coating for this type of application. The initial work was focused on identifying a suitable base resin for the coating. The objective was to use a base polymer that was known to be; water stable, oxidativly stable; have low extractables and be able to make a strong coating. The category of urethane acrylates were chosen for this purpose since they typically meet these basic requirements. Several varieties of urethane acrylate resins were screened in a simple test formulation with the best performing material chosen for further development. In these initial screening experiments the photoinitiator was held at a constant level to keep the number of mixture permeations manageable. Next, the identified resin was formulated with several co-monomers in an effort to develop a formulation that meet as many of the process and use requirements as possible. Two monofunctional monomers, one low glass transition temperature (MF1) and one glass transition temperature (MF2), were chosen along with a difunctional monomer (DF) for formulation screening. A four component mixture design was run with mixture levels as shown graphically in Figure 87.

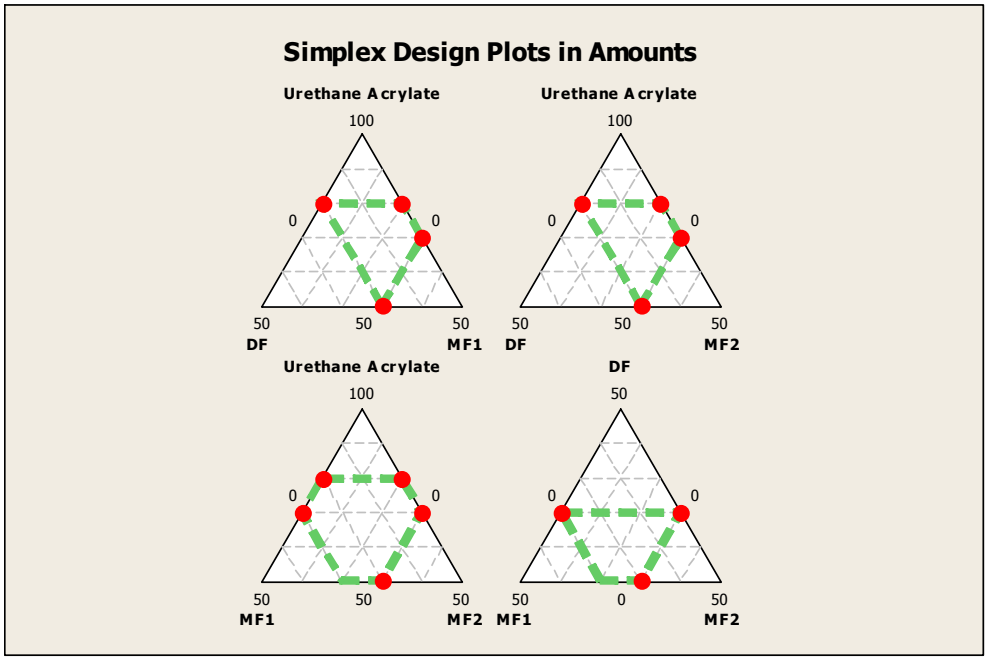

Figure 87. Screening mixture design with urethane acrylate, difunctional monomer (DF), monofunctional monomer 1(MF1) and monofunctional monomer 2(MF2)

The formulation was evaluated for viscosity, coating quality, tensile strength and tensile elongation. It was determined from the screening experiment that only one of the monofunctional monomers was necessary (MF1) which reduced the number of reactive components to the three used in the final optimization. The final formulation was chosen based on the results of the design shown in Figure 88.

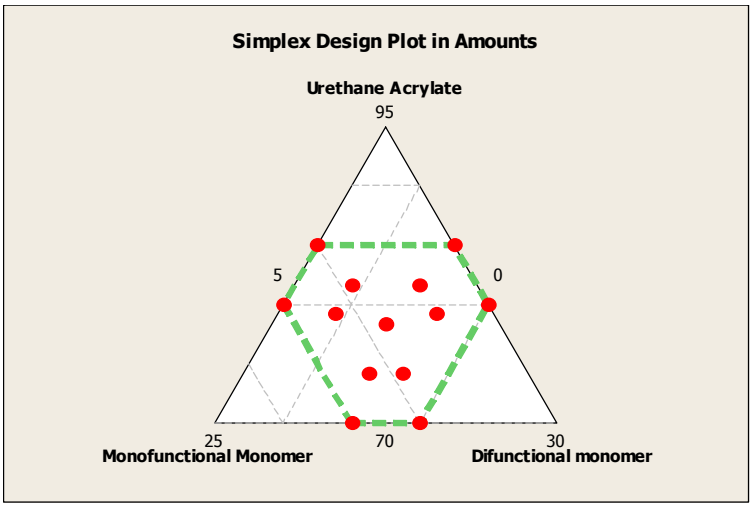

Figure 88. Mixture design to optimize subgasket formulation.

Once the main components were identified through the various down selecting experiments the initiator and leveling agents were optimized. Several levels and types of photo initiators were chosen and tested for cure speed, percent cure, and material properties. This work was completed on the process equipment installed in our factory using the actual coating and curing conditions that would likely be used in production. From this work an initiator and type and level were chosen. The blue pigment was used at the recommended level and was not subjected to any optimization efforts.

The coating quality was the last phase of the subgasket development work. An optical microscope image of a typical experimental coating is shown in Figure 89. The colors in this image depict thickness variations on the coating surface.

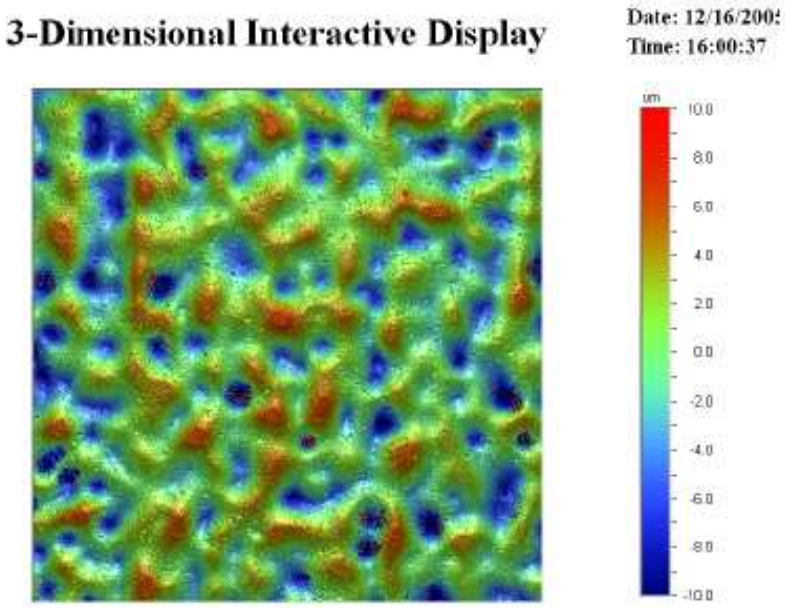

Figure 89. Optical micrograph of typical subgasket surface (note: colors represent variation in coating thickness)

The uneven coating quality was not acceptable for strength or membrane protection purposes. A series of leveling agents were evaluated for coating quality and strength. The smoothness of the surface was evaluated by using a simple hand held gloss meter. While this method was somewhat indirect is allowed for simple evaluations prior to the more time consuming microscopy measurements. From this evaluation a leveling agent was chosen and implemented in subsequent formulations. The photograph in Figure 90 shows the quality of a typical film with optimized leveling agents. While the coating is not 100% defect free, it is of suitably high quality to meet the functional objectives of the subgasket.

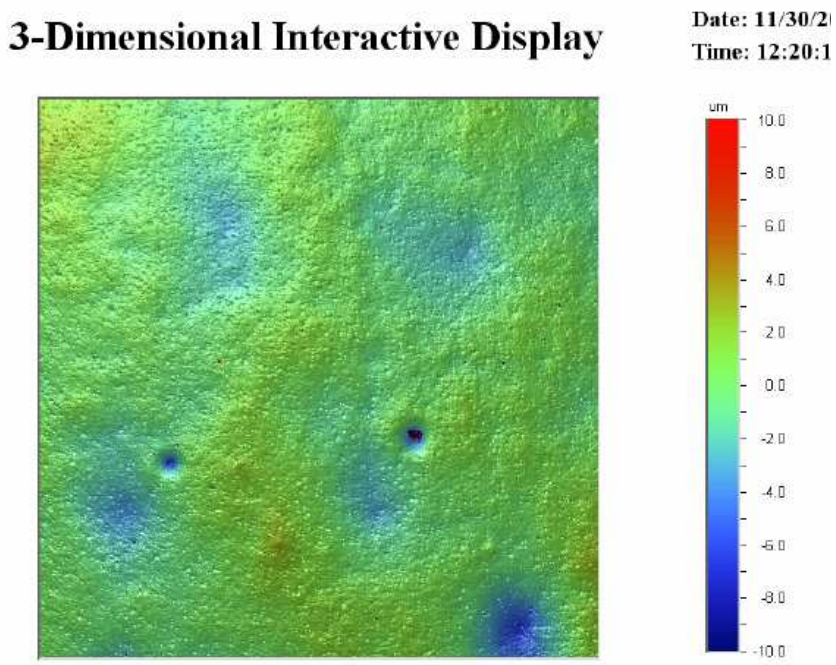

Figure 90. Optical micrograph of subgasket surface after leveling agent optimization (note: colors represent variation in coating thickness)

Durability Demonstration

The last phase of development of the UV cured subgasket formulation was a demonstration of the coating durability and functional performance. A short, six cell stack was constructed using existing 3M hardware. The MEAs used are the same as shown in Figure 83. The protocol was chosen with the objective of stressing the membrane edges by subjecting the MEAs to a series of wet/dry cycles. This was accomplished two ways, first through load cycling at 0.2, 0.4, and 0.6 amps/cm2 for 20 minutes at each condition then back down (0.6, 0.4, and 0,2 A/cm2). Second the dew point of the inlet gasses was varied from 60℃ (dry) to 75℃ (wet) for 2 hours and one hour respectively while keeping the stack temperature at a constant 70℃. Once daily the stack was allowed to run at OCV for 1 minute with a hydrogen inlet pressure of 12 kPa higher than the cathode air pressure. If a breach in the membrane (edge failure or active area) were to occur the OCV would rapidly decrease. A graphical representation of a typical 24 hour cycle is depicted in Figure 91.

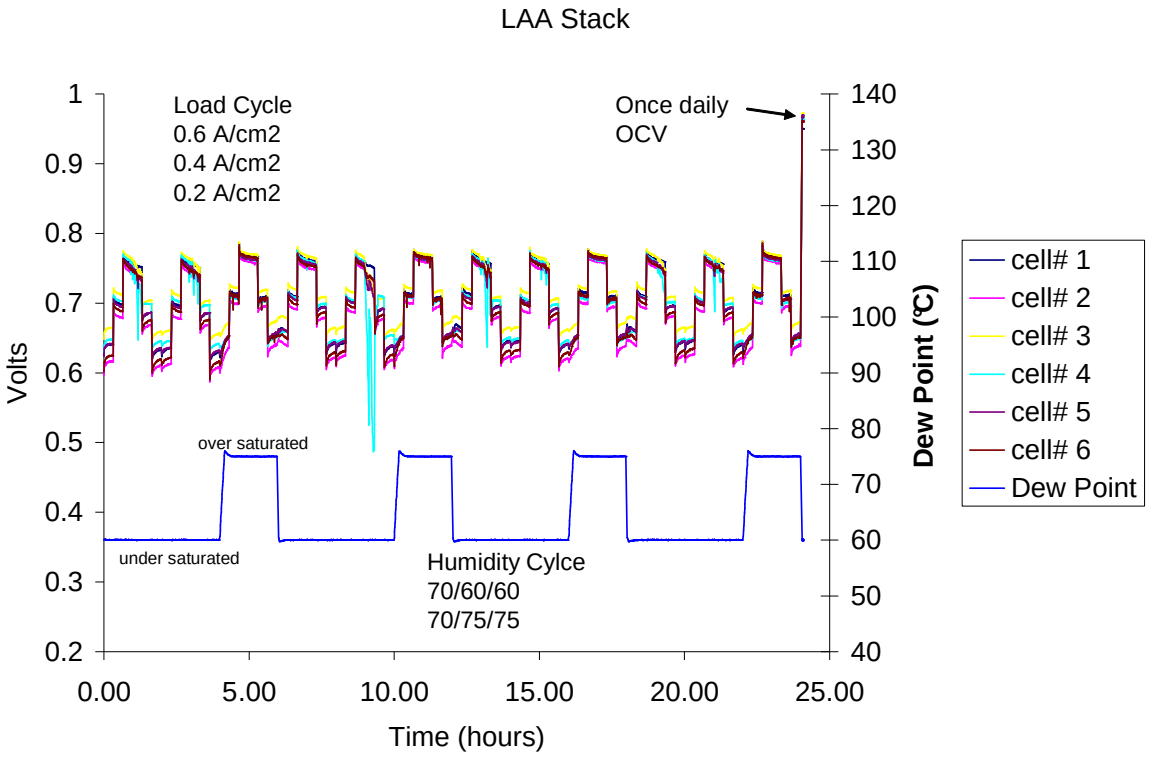

Figure 91. Load cycle and dew point cycle for subgasket durability test.

This protocol was run continuously for 1800 hours (75 days) with ten unplanned shut downs due to system and control issues. Water was periodically collected during this period and analyzed for fluoride ion as another measure of membrane failure. The potential at OCV was plotted for all six cells as a function of time along with the fluoride ion release rate in Figure 92.

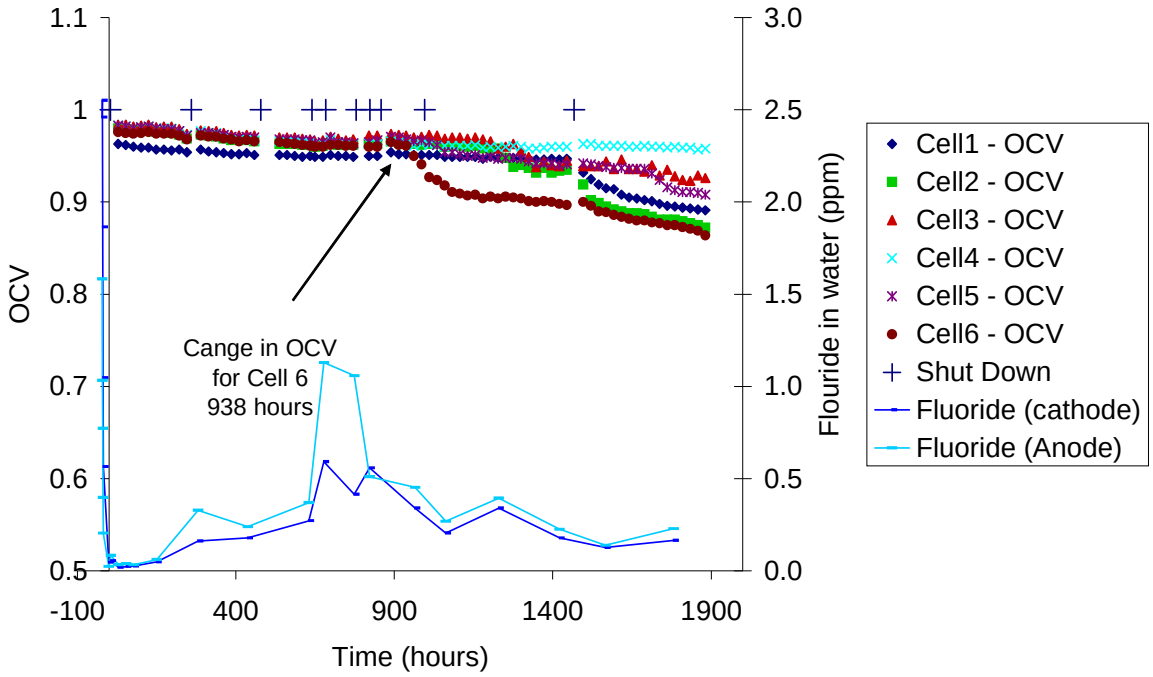

Figure 92. Durability test with UV subgasket construction.

It can be seen from this graph that the OCV is quite stable for the first 900 hours. At about 968 hours the OCV at cell six began to decline. Typically the OCV continues to decline when there has been a membrane breach (recall the hydrogen pressure is 12 kPa higher than the air pressure) but in this case the OCV returned to a somewhat stable, although lower, value. The spike in the fluoride ion emission is likely due to the series of unplanned shut downs that occurred in that tome period. Post mortem analysis did not show signs of edge failure in any of the six cells.

Subgasket Summary

The objective of this work was to develop a functional edge protection that is easily applied to MEAs assembled in high volume. The method of rotary screen printing a UV cured resin was developed and demonstrated to be feasible in production and in a short stack fuel cell test. This type of subgasket is suitable for many applications but may not fit all fuel cell constructions or operating conditions. Exploratory work was conducted using adhesively attached polyester subgakaskets as part of this program.

2.1.7 Peroxide stabilizing membrane additives

Background

Research carried out under this project, DOE DE-FC36-03GO13098 ("DOE IV"), included identification and optimization of stabilizing membrane additives. This work was a continuation of research originated under DOE DE-FC04-02AL67621 ("DOE III"). Accordingly, this contribution to the final report for DOE IV begins with a background section that includes a brief review of the major findings under DOE III, as well as repetition of some other background information that can

be found in the related contribution to the DOE III final report. Work carried out under DOE III resulted in two patent applications.[61,62]

As has already been discussed substantially in the present report, the lifetime of PEMFC's is largely determined by their operating conditions and the chemical stability of their material components. In fact, lifetime can vary over orders of magnitude for operating conditions that might at first seem remarkably similar. For example, the same fuel cell design might survive for over 10,000 hours while operating at 70℃ and with saturated gas streams, but fail in only a few hundred hours while operating at 80℃ and with 70℃ dew point gas streams. At the same time, there is significant motivation from a system design standpoint to raise the temperature of operation and reduce the humidification requirements for the cell. At present stationary powder applications typically consider a reasonable target to be 40,000hrs of operation at 70℃ with saturated gas streams. An automotive target often cited is 5000 hours lifetime with load-cycle operation at 80-90℃ and 60-70℃ dew point gas stre ams (or less humidification, preferably). These targets are considered a "first node" in the widespread commercialization of fuel cells for continuous stationary power or fuel cell powered automobiles.

There are several contributors to the declining performance of PEMFC's over time. While the gradual decay in performance largely derives from changes that occur in the catalytic electrode layers, the source of catastrophic failure is generally the membrane. Essentially, chemical degradation and/or mechanical stress eventually lead to the development of a tear or pinhole in the membrane. The mechanical challenge can be met through MEA design, crosslinking of the ionomer, and/or the use of reinforcement materials in the membrane (e.g., membrane can be a perflurosulfonic acid ionomer impregnated within a porous expanded PTFE matrix). The objective of the durability-related research for this part of the program was the chemical durability of the conductive ionomer itself. After decades of research, it is widely held that membrane degradation occurs as a result of attack by hydrogen peroxide which is formed as a byproduct during fuel cell operation.. Further complicating the picture, the prevailing view also includes the idea that hydrogen peroxide alone is not sufficient to degrade a perfluorinated ionomer membrane. Rather, it is primarily through the action of transition metal cations like Fe^{2+} on the hydrogen peroxide which form hydroxyl radical according to Fenton's reaction that ionomer degradation actually occurs. Notwithstanding the general acceptance of a role for oxidative radicals in membrane degradation, as well as a significant research that has been carried out over many years, a complete understanding of PEMFC membrane degradation is not yet established.[63] Accordingly, the additive development effort described here followed significant screening work on many candidate additives, largely without regard for possible mechanisms of stabilization.

Under DOE III, a methodology was developed for identifying additives for possible stabilization properties. A brief summary of that work is given now. More complete details can be found in the final report for DOE III. The methodology included three stages of experimentation: i) ex-situ peroxide soak-testing; ii) accelerated MEA testing, with fluoride ion collection; iii) long-term MEA testing to failure. A very clear finding from the DOE III work was that MEA degradation is very poorly correlated with ex-situ hydrogen peroxide soak testing, at least with respect to the impact of many candidate additives. Although certain additives showed positive results for both types of testing (e.g., manganese- and cerium-based membrane additives), many others gave "false positive" results in the soak test (e.g., platinum and ruthenium-based membrane additives)--at least with respect to MEA test conditions that have been used to date. Interestingly, Mn- and Ce-based additives, although favorable, were not as effective in the ex-situ testing as Pt- and Ru-based additives. Despite the lack of correlation between tests, the discovery of the beneficial impact of Mn- and Ce-based additives led to considerable additional work on those materials. Under DOE III, a soluble manganese salt and a commercial manganese dioxide powder were studied extensively with MEA lifetime testing. Also under DOE III, a soluble cerium salt (ceric ammonium nitrate) was identified as an effective stabilizing additive, with that work producing positive initial MEA durability testing results.

Under DOE IV, the studies on Ce-based additives were expanded to include: i) other sources of cerium; ii) a transmission electron microscopy study on membranes with Ce-based additives; iii) screening of other rare earth -based candidate additives; iv) a study of the effects of additions of Mn- and Ce-based additives together; and v) a comparison of the different Mn and Ce sources with regard to their trade-offs between durability enhancement and performance reduction. The remainder of this section is focused on these five areas of investigation.

Screening of different cerium sources

Without knowledge of the exact mechanism of stabilization that resulted from ceric ammonium nitrate ($(NH_4)_2Ce(NO_3)_6$) additions to PFSA membrane casting dispersions under DOE III, a study was undertaken to determine whether different behavior would be observed for other sources of cerium, including Ce^{3+} salts and cerium oxides. The ex-situ peroxide soak test was selected for screening the other cerium-based additives. Table 20 below lists the additives that were studied. As noted in the table, most of the additives appeared to dissolve into the casting dispersion at first, but eventually led to turbidity. The appearance of turbidity in the casting dispersions prompted the transmission electron microscopy study described in the next section.

Table 20. Membranes with cerium based additives. All membranes contain 500 ppm added Fe.

Sample	meq Ce/g polymer	Turbity (1=low, 5=high)
3M ionomer 800 EW control	**n/a**	**n/a**
CeO2 colloid	**0.031**	**5**
Ce(SO4)2	**0.020**	**4**
Ce2(CO3)3-nH2O	**0.024**	**2**
Ce(OOCCH3)3-1.56 H2O	**0.018**	**3**
Ce(OH)4	**0.022**	**3**
Ce(NO3)3-6H2O	**0.022**	**1**

Ex-situ hydrogen peroxide soak test for different cerium sources

An ex-situ hydrogen peroxide test was developed and used to screen the stabilizing effect of the various additives. A piece of cast membrane measuring approximately 35 – 50 microns and 0.05-0.1g was weighed and then placed into glass jar containing 50g of 1M hydrogen peroxide. The jar is capped and then placed into an oven at 90℃ for five days. After five days, the membrane film is removed, dried, and weighed. In order to increase the weight loss "signal" for PFSA membranes, ferric nitrate ($Fe(NO_3)_3$-$9H_2O$) is fully dissolved into all casting dispersions (control dispersion, as well as dispersions with candidate stabilizing additives) at a level of 500ppm Fe (by weight, Fe in the final membrane). In order to remove the effect of a difference in relative humidity during initial and final weighings (day 0 vs. day 5), a separate piece of PFSA film for every sample type (that is not soaked) is weighed. The mass changes for the latter pieces of film (unsoaked) lead to correction factors for the soaked pieces of film, thereby allowing the mass change associated with the soaking itself to be isolated. Finally, two sample replicates were tested for each candidate additive. Figure 93 below gives weight loss results for the membranes. The data show conclusively that a range of different cerium sources, including Ce^{3+} and Ce^{4+}containing salts and oxides, are effective in improving the resistance of iron contaminated PFSA membranes to attack by hydrogen peroxide. Similar results were obtained for an experiment using a submicron cerium oxide powder (Rhodia Polishing Opaline, also refered to as Rhone-Poulenc Polishing Opaline).

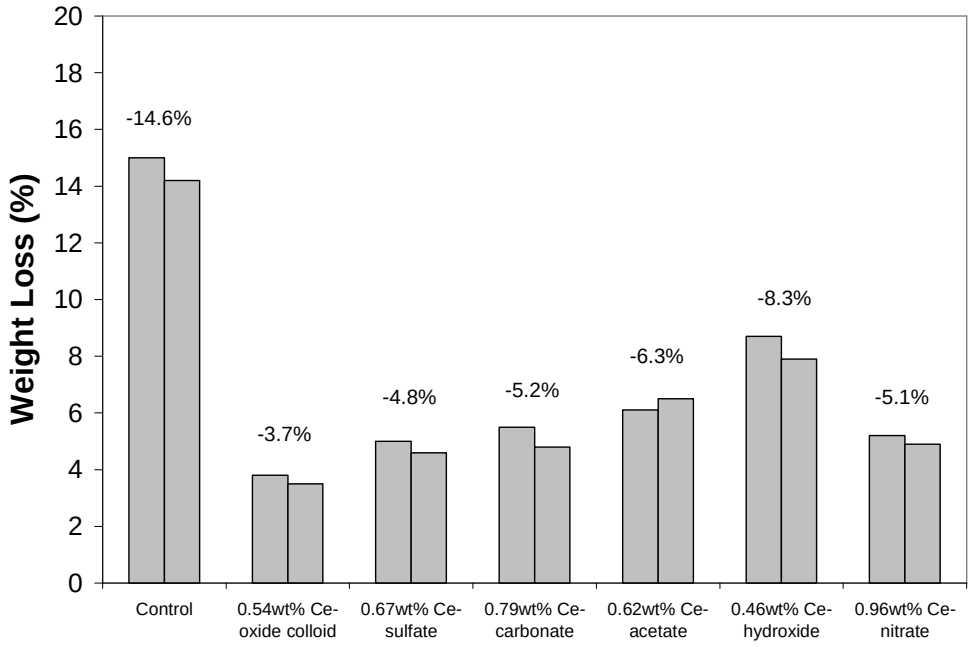

Figure 93. Weight loss during ex-situ soak test for 800EW 3M PFSA membranes containing various cerium-based additives. Note that all membranes in the figure also include 500ppm Fe by weight, added as ferric nitrate.

Transmission electron microscopy study of PFSA membranes with cerium-based additives

The turbidity that was observed after a period of apparent good solubility for various cerium sources in PFSA membrane casting dispersions motivated a closer investigation of the membranes produced by those dispersions. In particular, there was interest to determine whether a new solid phase containing cerium was precipitating out of solution. Therefore, diffraction contrast imaging and electron diffraction were carried out, using the transmission electron microscope (TEM - JEOL 200CX @ 200 kV). Thin sections of film were examined with typical images shown in Figure 94 and Figure 95. In Figure 94, the particles of CeO_2 powder that were added directly (Rhodia Polishing Opaline) are illustrated. In Figure 95, an interesting result related to the addition of a soluble cerium salt to the casting dispersion is illustrated. Specifically, the addition of ceric ammonium nitrate to the casting dispersion led to the appearance of CeO_2 particles in the finished membranes. In is unknown what fraction of the cerium was converted to cerium oxide. Membranes prepared with the other initially soluble sources of cerium were not investigated by TEM.

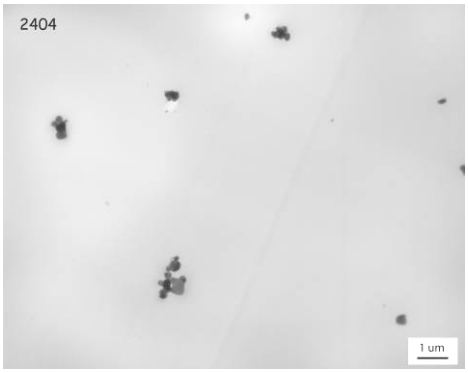

Figure 94. Bright field TEM photomicrograph of a PFSA membrane containing particles of CeO2, added as submicron Rhodia Polishing Opaline.

a)

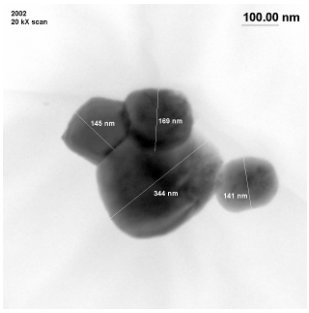

b)

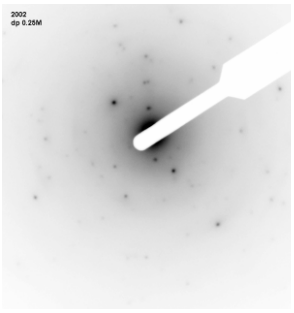

Figure 95. Bright field TEM photomicrograph (a) of a PFSA membrane containing particles of CeO2, apparently converted from (NH4)2Ce(NO3)6 added to the casting dispersion; electron diffraction pattern (b) taken from the particles.

Screening of other rare earth based candidate additives

The favorable results for a number of cerium-based additives prompted the investigation of other rare earth-based candidate additives. In identical fashion to the experiment described above for different Ce-based additives, a variety of other rare-earth-based additives were screened using the ex-situ peroxide soak test. The other rare-earth-based additives included selected rare earth salts and rare earth oxides. Figure 96 and Figure 97 give the results of the screening experiments. As shown in the figures, cerium is distinguished from the other rare earths in its activity as a stabilizer against oxidative attack by hydrogen peroxide and Fe.

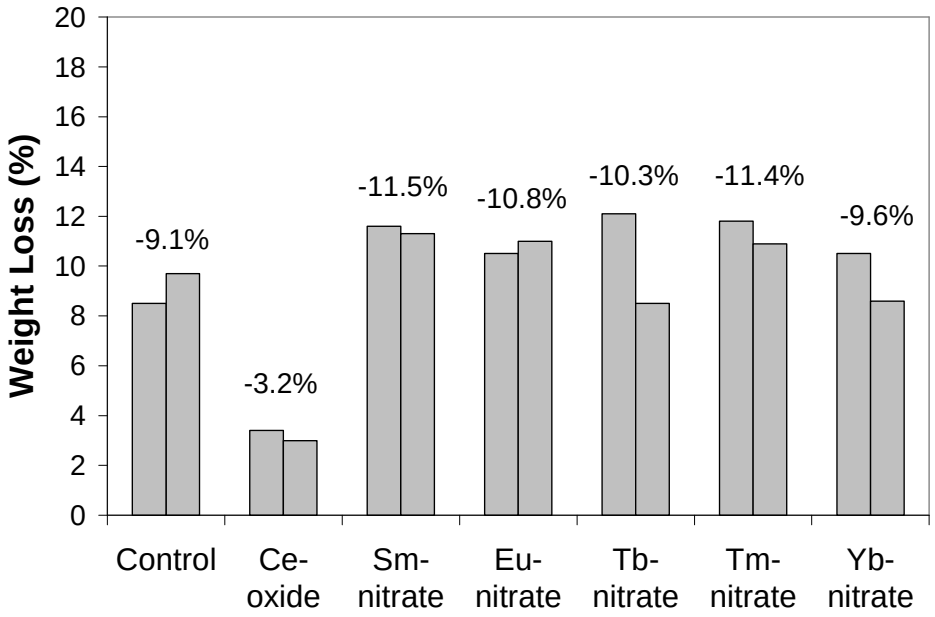

Figure 96. Weight loss during ex-situ soak test for 800EW 3M PFSA membranes containing various rare-earth-based additives. Note that all membranes in the figure also include 500ppm Fe by weight, added as ferric nitrate.

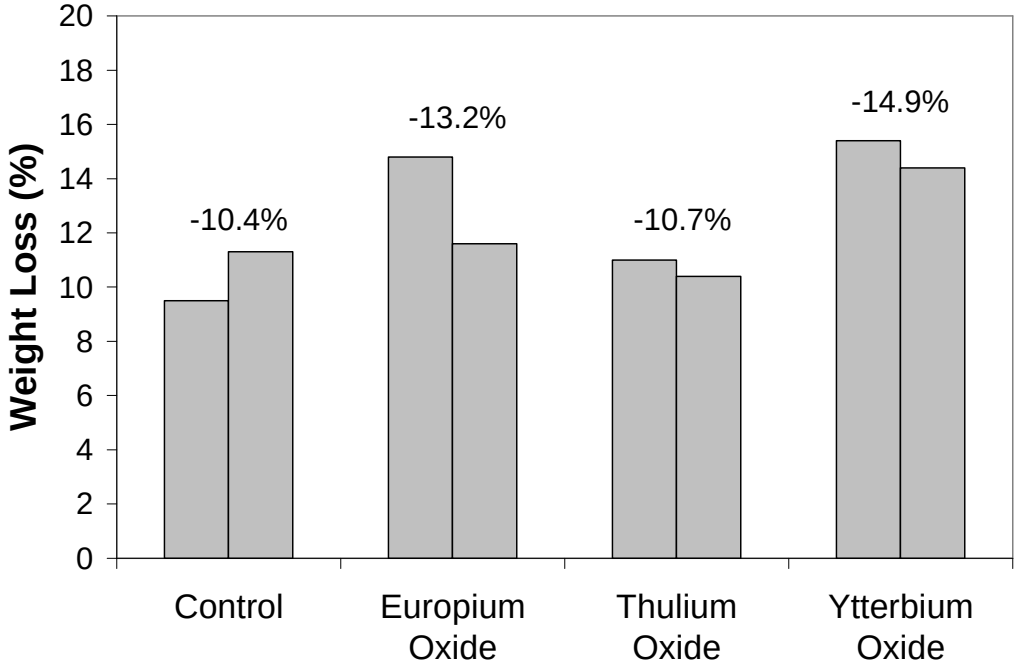

Figure 97. Weight loss during ex-situ soak test for 800EW 3M PFSA membranes containing various rare-earth-based additives. Note that all membranes in the figure also include 500ppm Fe by weight, added as ferric nitrate.

Stabilization of PFSA-based MEA's with combination of Mn and Ce

With Mn and Ce identified as useful elements generally for addition to PFSA-based MEA's, an experiment was carried out to determine whether the use of both elements in combination would yield further improvement. To this end, MEA's with membranes containing both Mn and Ce (added as soluble manganese nitrate (50wt% in water), J. T. Baker Cat. No. 2544-01 and particulate Rodia Polishing Opaline CeO_2 to the casting dispersion) were compared with MEA's containing only the Mn-based additive, only the Ce-based additive, or containing no additive at all. Table 2 below gives the formulations of the four membrane samples. The additives were combined with a 3M PFSA ionomer
membrane casting dispersion with stirring. The control membrane measured 853 equivalent weight by titration. Membranes were cast on glass, dried, and annealed.

The fluoride release results in Table 21 show that the different additives and the combination have improved fluoride over the control but that they are not significantly different from each other. In most cases one or two of the 4 samples tested had a significantly higher fluoride release. These outliers can be attributed to several sources, but often when testing MEAs that comprise a handspread-cast membrane, variability in the data can occur due to the coating quality of the membranes. Fluoride ion measurements can give "falsely" high readings if there is a small pinhole, bubble, or other defect in the membrane. Additionally the first samples in a sample set often had the best fluoride results, because the first samples in each case are fabricated using the regions of membrane having the best visual appearance.

Table 21. Fluoride release data collected for the Mn and Ce combination series of membrane additives. The fluoride release is the range (low and high) represents the total fluoride collected from both the anode and cathode.

Sample	# of samples	Fluoride release (micrograms/min) at 50 hours	
		Low value	High Value
Mn	4	0.002	0.028
CeO2	4	0.003	0.035
Mn + CeO2	4	0.002	0.030
Control (no addative)	4	0.009	0.121

Trade-off between durability and performance for various Mn- and Ce based additives.

A key area of importance in the use of durability-enhancing additives is in managing their negative impact on fuel cell performance. Accordingly, an initial experiment was undertaken to determine whether there are appreciable differences between various Mn- or Ce-based additives, with respect to stabilizing effects for a given level of performance loss. In order to probe this question, an experiment was undertaken wherein a series of membranes with approximately the same measured equivalent weight (with additive, measured by titration) were converted to MEA's and tested for fuel cell performance and accelerated degradation. In pre-work to the actual experiment, the impact of the various additives on measured EW was determined. This pre-work allowed for additive levels to be determined which would yield approximately the same EW for the eventual MEA sample series. Table 22 gives the formulations for the final series of membranes in this study. All membranes were derived primarily from the same batch of 3M PFSA membrane casting dispersion had an ion exchange capacity of 1.144 meq/g (EW874). The additives listed in Table 22 were stirred into the 3M PFSA membrane casting dispersion. For Control 1, another batch of similarly low EW 3M PFSA casting dispersion, except partially neutralized with alkali ions, was blended with the main PFSA source. For Control 2, another batch of 3M PFSA casting dispersion, except with higher EW (ca. 1000) by virtue of its polymerization formulation, was

blended with the primary PFSA batch in order t hit the target IEC. All membranes were cast on glass, dried and annealed. Table 22 includes results of titrations carried out on the membranes to determine their effective equivalent weight (with additives). The values in the table are essentially the same with only a 2% total spread in effective ion exchange capacity. This series of membrane samples, and their associated MEA samples, are referred to herein as the "fixed-equivalent weight series."

Table 22. Formulations for membrane casting dispersions with various Mn- and Ce-based additives, all targeting the same equivalent weight; measured effective ion exchange capacity and associated equivalent weight for the cast membranes (by titration).

Sample	Additive	IEC	EW
Control 1	1000 EW polymer with Na ions	1.108	902
Mn oxide	MnO powder	1.104	906
Mn nitrate	Mn(NO3)2 (aq)	1.119	894
Ce oxide	CeO2 powder	1.115	897
Ce oxide colloid	CeO2 colloid 20%	1.099	910
Ce nitrate	Ce(NO3)3-6H20	1.113	898
Control 2	1000 EW polymer	1.108	903

The MEA testing results are summarized in Table 23 where the fluoride release data is the average of the number of samples given. There were two control sample sets and five different additives. In most cases, attempts were made to obtain results for at least three replicates of each sample. The membranes were prepared by handspread technique which can sometimes lead to small defects and more variability. In some cases an outlier was observed with a lower OCV under pressurized conditions suggesting a small hole was present. In this case the outlier sample(s) was removed before averaging the data.

The performance metrics shown in Table 23 are a typical performance mark at the beginning of an air utilization test that is run at 70℃, 100%RH , 0.6A/cm^2 and 2.5 cathode stoich. Also the performance of the fuel cell under accelerated conditions 0.5A/cm^2 at 90/60/60℃ gives a good comparison under dry conditions.

Table 23. Fluoride and performance data collected for the fixed equivalent weight series of membrane additives. The fluoride release average represents the total fluoride collected from both the anode and cathode.

Sample ID	# Samples	Average F- at 50 hrs (micrograms/min)	Performance at 70℃ 100% RH and 0.6 A.cm2		Performance at 90/60/60 and 0.6 A/cm2	
			Ave Voltage	Std Dev (V)	Ave Voltage	Std Dev (V)
Control 1	3	0.065	0.658	0.008	0.366	0.026
Mn oxide	2	0.010	0.642	0.007	0.388	0.008
Mn nitrate	2	0.004	0.624	0.009	0.377	0.006
Ce Oxide	3	0.013	0.658	0.013	0.368	0.085
Ce Oxide colloid	3	0.020	0.609	0.022	0.354	0.069
Ce nitrate	3	0.033	0.611	0.030	0.360	0.048
Control 2	3	0.123	0.662	0.001	0.405	0.016

The data suggest the $Mn(NO_3)_2$ additive gives the best combination of fluoride release and performance. In general the Ce additives produced good fluoride release as compared to the control and within close range of the Mn containing samples. The performance was also similar for Ce containing samples. The main difference between the Ce and Mn additives was in their variability. While the sample sizes were small (2 or 3) for all of these sets, it does appear the standard deviation in performance for the Ce containing samples is higher than for the Mn containing samples.

Conclusions for the additive work

The addition of a peroxide scavenging additive has proven to increase the oxidative stability of a PFSA membrane in both ex-situ testing and in fuel cell testing. The fluoride release rates are significantly lower for membranes made with both manganese or cerium ions and compounds. The work completed under this program built off of the observations made in a previous Department of Energy Contract (DE-FC04-02AL67621) and the additive chosen for the final durability testing was based on a manganese compound.

2.1.8 Conclusions for the membrane sections

A large amount of testing and development work was complete as part of this project. Model compound studies lead to the realization that the carboxylic acid end groups of the membrane polymer were no the only functionality subject to degradation in the presence of hydrogen peroxide. The ether linkages in the polymer could also be degraded at a slower, but measurable, rate.

The 3M ionomer was used as the basis for developing a new membrane that has; stabilized end groups, peroxide decomposing additives, a UV cured subgasket edge protection, and low equivalent weight (~800 EW). Significant amount of research was completed in the area of reinforced membrane development, however, little or only modest benefit was realized. It was determined that a more oxidatively stable membrane was the best choice for the required durability improvements.

2.1.9 References for Membrane Section

[1] Schiraldi, D.A. *J. Macro. Sci. Part C. Poly. Rev.*, **2006**, 46, 315

[2] LaConti, A.B.; Hamdan, M.; MacDonald, in *Handbook of Fuel Cells-Fundamentals, Technology and Applications Vol.3.*, Vielstich, W.; Gasteiger, H.A.; Lamm, A.,(Eds.), John Wiley and Sons: New York, **2003**, pp 647

[3] Buchi, F.N., Gupta, B.; Haas, O.; Scherer, G.G. *Electrochimica Acta*, **1995**, 40, 345

[4] Wang, H.; Capuano, G.A. *J. Electrochem. Soc.*, **1998**, 145, 780

[5] Inaba, M. *Degradation Mechanism of Polymer Electrolyte Membrane Fuel Cells*, 14th International Conference on Properties of Water and Steam, Kyoto Japan, 395

[6] Pozio, A.; Silva, R.F., De Francesco, M.; Giorgi, L. *Electrochimica Acta*, **2003**, 48, 1543

[7] Maletzky, P.; Bauer, R.; Lahnsteiner, J.; Pouresmael, B. Chemosphere, **1999**,10, 2315

[8] Liu, W.; Zuckerbrod, W. *J. Electrochem. Soc.*, **2005**, 152, A1165

[9] Paulus, U.A.; Schmidt, T.J., Gasteiger, H.A.; Behm, R.J. *J. Electroanal. Chem.*, **2001**, 495, 134

[10] Antoine, O.; Durand, J. *J. Appl. Electrochem.*, **2000**, 30, 839

[11] Kadirov, M.K.; Bosnjakovic, A.; Schlick, S. *J. Phys. Chem. B.*, **2005**, 109, 7664

[12] Walling, Cheves; Kato, S. *J. Amer. Chem. Soc.*, **1971**, 93, 4275

[13] Curtin D.E.; Lousenberg, R.D.; Henry, T.J.; Tangeman, P.C.; Tisack, M.E. *J. Power Sources*, **2004**, 131, 41

[14] Mittal, V.O.; Kunz, H.R.; Fenton, J.R. *Electrochem. Solid State Lett.*, **2006**, 9, A299
[15] Aoki, M.; Asano, N., Miyatake, K., Uchida, H., Watanabe, M. *J. Electrochem. Soc.*, **2006**, 153, A1154
[16] Schwiebert, K.; Raiford, K.; Nagarajan, G.; Principe, F.; Escobedo, G. " *Startegies to improve the durability of perfluorosulfonic acid membranas for PEM fuel cells*", KFTCA Internacional Symp., Washington, D.C. **2005**
[17] Schwiebert, K.; Raiford, K.; Nagarajan, G.; Principe, F.; Escobedo, G. " *Startegies to improve the durability of perfluorosulfonic acid membranas for PEM fuel cells*", KFTCA Internacional Symp., Washington, D.C. **2005**
[18] Healy, J.; Hayden, C.; Xie, T.; Olson, K.; Waldo, R.; Brundage, M.; Gasteiger, H.A.; Abbott, J. *Fuel Cells*, **2005**, 5, 320
[19] Liu, W.; Ruth, K.; Rusch, G. *J. New. Mater. Electrochem. Syst.*, **2001**, 4, 227
[20] Huang, X.; Solasi, R.; Zou, Y.; Feshler, M.; Reifsnider, K.; Condit, D.; Burlatsky, S.; Madden, T. *J. Poly. Sci. B. Polym. Phys.*, **2006**, 44,2346
[21] Moore, R.B.; Mauritz, K.A. *Characterization of PEMFC Membrane Durability*, DOE Annual Merit Review Proceedings, **2006**
[22] de Almeida, S.H.; Kawano, Y., *J. Thermal Anal. and Cal.,* 1999, 58 , 569
[23] Sun, L.; Thrasher, J.S.; *Poly.Deg. and Stability.*, **2005**, 89,43
[24] Alberti, G.; Casciola, M.; Massinelli, L.; Bauer, B. *J. Memb. Sci.*, **2001**, 185, 73.
[25] Jalani, N.H.; Dunn, K.; Datta, R. *Electrochimica Acta*, **2005**, 51, 553.
[26] Doyle, M.; Lewittes, M.E.; Roelofs, M.G.; Perusich, S.A. *J. Phys. Chem. B.*, **2001**, 105, 9387
[27] Hickner, M.A.; Pivovar, B.S. *Fuel Cells*, **2005**, 5,213.
[28] Kawano, Y.; Wang, Y.; Palmer, R.A.; Aubuchon, S.R. *Polímeros*, **2002**, 12, 96
[29] Paul , MRS Sym. Proc. **2006**, 927
[30] Zhou, C.; Zawodzinski Jr., T.A.; Schiraldi, D.A. *Macromolecules*, submitted, **2007**
[31] Liu, W.; Ruth, K.; Rusch, G., Membrane Durability in PEM Fuel Cells. *Journal of New Materials for Electrochemical Systems* **2001,** 4, (4), 227-232.
[32] Tang, H.; Peikang, S.; Jiang, S. P.; Wang, F.; Pan, M., A degradation study of Nafion proton exchange membrane of PEM fuel cells. *Journal of Power Sources* **2007,** 170, (1), 85-92
[33] Aoki, M.; Uchida, H.; Watanabe, M., Decomposition mechanism of perfluorosulfonic acid electrolyte in polymer electrolyte fuel cells. *Electrochemistry Communications* **2006,** 8, (9), 1509-1513
[34] Collier, A.; Wang, H.; Yuan, X. Z.; Zhang, J.; Wilkinson, D. P., Degradation of polymer electrolyte membranes. *International Journal of Hydrogen Energy* **2006,** 31, (13), 1838-1854.
[35] Schiraldi, D. A., Perfluorinated polymer electrolyte membrane durability. *Polymer Reviews* **2006,** 46, (3), 315-327.
[36] Kadirov, M. K.; Bosnjakovic, A.; Schlick, S., Membrane-Derived Fluorinated Radicals Detected by Electron Spin Resonance in UV-Irradiated Nafion and Dow Ionomers: Effect of Counterions and H2O2. *Journal of Physical Chemistry B* **2005,** 109, (16), 7664-7670
[37] Qiao, J. L.; Saito, M.; Hayamizu, K.; Okada, T., Degradation of perfluorinated ionomer membranes for PEM fuel cells during processing with H2O2. *Journal of the Electrochemical Society* **2006,** 153, (6), A967-A974.
[38] Kinumoto, T.; Inaba, M.; Nakayama, Y.; Ogata, K.; Umebayashi, R.; Tasaka, A.; Iriyama, Y.; Abe, T.; Ogumi, Z., Durability of perfluorinated ionomer membrane against hydrogen peroxide. *Journal of Power Sources* **2006,** 158, (2), 1222-1228.
[39] Walling, C., Fenton's reagent revisited. *Accounts of Chemical Research* **1975,** 8, (4), 125-31.
[40] Healy, J.; Hayden, C.; Xie, T.; Olson, K.; Waldo, R.; Brundage, M.; Gasteiger, H.; Abbott, J., Aspects of the chemical degradation of PFSA ionomers used in PEM fuel cells. *Fuel Cells (Weinheim, Germany)* **2005,** 5, (2), 302-308.
[41] Curtin, D. E.; Lousenberg, R. D.; Henry, T. J.; Tangeman, P. C.; Tisack, M. E., Advanced materials for improved PEMFC performance and life. *Journal of Power Sources* **2004,** 131, (1-2), 41-48.
[42] Bro, M. I.; Sperati, C. A., End groups in tetrafluorethylene polymers. *Journal of Polymer Science* **1959,** 38, 289-95.

[43] Escobedo, G., Strategies to improve the durability of perfluorosulfonic acid membranes for PEM fuel cells. *KFTCA International Symposium* **2005 , December 8-9**, (Presentation data).
[44] Liu, W.; Zuckerbrod, D., In situ detection of hydrogen peroxide in PEM fuel cells. *Journal of the Electrochemical Society* **2005,** 152, (6), A1165-A1170.
[45] Hubner, G.; Roduner, E., EPR investigation of HO. radical initiated degradation reactions of sulfonated aromatics as model compounds for fuel cell proton conducting membranes. *Journal of Materials Chemistry* **1999,** 9, (2), 409-418.
[46] Chen, J.; Zhang, P.-y.; Liu, J., Photodegradation of perfluorooctanoic acid by 185 nm vacuum ultraviolet light. *Journal of Environmental Sciences (Beijing, China)* **2007,** 19, (4), 387-390.
[47] Maspoch et. al. *Polymer Testing* **19** (2000) 559-568
[48] Pianca, M. et. al., "End Groups in Fluoropolymers", *J. Fluorine Chem*. **95** (1999) 71-84
[49] GB 1210794
[50] W. Liu , K. Ruth, and G. RuschJ. New. Mat. Electrochem. Systems 4, 227-231 (2001)
[51] DuPont Press release, November 16, 2006 "*DuPont Fuel Cells Introduces New Extended Life Membrane*"; http://www.dupont.com/fuelcells/news/index.html
[52] S.Hommura, Y. Kunisa, I. Terada and M. Yoshitake, *Journal of Fluorine Chemistry* Volume 120, Issue 2, April 2003, Pages 151-155
[53] T. Greszler "Membrane Performance and Durability Overview for Automotive Fuel Cell Applications", U.S. Department of Energy Hydrogen, Fuel Cells and Infrastructure Technologies Program, 2006 High Temperature Membrane Working Group Meeting, September 14, 2006, San Francisco, California
[54] Bahar, B.; Honson, A.; Kolde, J.; US patent 5,599,614
[55] Cleghoren, S.;Kolde, J. and Liu, W. "Catalyst coated composite membranes" *Handbook of Fuel Cells – Fundamentals, Technology and Applications*, John Wiley & Sons, Vol 3, Part 3, pp 566-575.
[56] Liu, F.; Yi, B.; Xing, D.; Yu, J, and Zhang, H. "Nafion/PTFE composite membranes for fuel cell application" *J. Membrane Sci.* 212 (2003) 213-223.
[57] Denton, J.; Gascoyne, J.; Hards, G.; and Ralph, T.; US patent 6,042,958
[58] Stone, C.; Summers, D.; US patent 6,689,501
[59] Put in anything you can find
[60] Mekala and Stegink, Gore, GM
[61] M. H. Frey, D. M. Pierpont, and S. J. Hamrock, "High durability fuel cell components with cerium oxide additives," U. S. Patent Application No. US20070099052 A1.
[62] M. H. Frey, D. M. Pierpont, and S. J. Hamrock, " High durability fuel cell components with cerium salt additives," U. S. Patent Application No. US20070099053 A1.
[63] V. O. Mittal, H. R. Kunz, and J. M. Fenton, "Membrane Degradation Mechanisms in PEMFCs," *J. Electrochemical Soc.* **154** [7] B652-B-656 (2007).

2.2 GDL Development

Like any of the MEA components, GDL durability is critical to overall MEA durability. If the GDL degrades over time, the MEA performance decreases due to flooding. In order to improve GDL durability, we first developed test methods to characterize the important GDL properties. Once the characterization methods were established, we developed accelerated screening tests and aged GDLs to determine the impact of GDL degradation on MEA performance.

2.2.1 Characterization Methodology

Introduction

In an MEA, the gas diffusion layer (GDL) has several roles: (1) It serves as the electron conductor between the electrode and the flow field, (2) it promotes the even distribution of gases to the electrode and (3) it transports or wicks water away from the electrode and into the flow field but at the same time must help retain water in the membrane to avoid drying out the MEA. Due to the high carbon content of the GDL, it can easily serve as the electron conductor and, as a result, we did not attempt to characterize this property. Instead, our focus was on characterizing the water and gas transport properties because, during durability studies, these GDL properties change over time. We utilized four techniques - internal contact angle (Table 24), in-plane permeability, through-plane permeability and water capillary pressure - to characterize the transport properties of the GDL.

Internal Contact Angle

GDL internal contact angle was chosen over the more common external contact angle for determining hydrophobicity because the external does not capture the hydrophobicity of the internal GDL pore structure and the surface of the GDL is not smooth, thus the external measurements are not very accurate. Furthermore, it is believed that GDL flooding begins when the internal pores fill with water. The following summarizes the methodology used to measure GDL internal contact angle and the results are found in Table 24.

Table 24. GDL internal contact angle data

GDL Sample	Capillary Constant x10^{-6} *[cm^5]*	Owens-Wendt-Mann				Least Squares			
		Q_{H2O} *[°]*	γ_s	γ_s^d	γ_s^p	Q_{H2O} *[°]*	γ_s	γ_s^d	γ_s^p
GDL 1	0.25 ± 0.04	100	14.8	4.5	10.3	-	-	-	-
GDL 8	1.78 ± 0.08	104	13.4	3.2	10.1	-	-	-	-
GDL 2	0.015 ± 0.004	115	12.2	0.6	11.6	-	-	-	-
49-031125-MC	4.6 ± 0.2	84	25.9	17.2	8.7	-	-	-	-
50-031125-MC	3.6 ± 0.3	99	25.1	23.6	1.5	-	-	-	-
109-040113-MC	6.1 ± 0.9	109	16.3	15.4	0.9	-	-	-	-
112-040113-MC	6 ± 1	105	16.0	14.1	1.9	-	-	-	-
115-040113-MC	6.6 ± 0.7	114	17.1	16.9	0.2	-	-	-	-
51-031125-MC	1.3 ± 0.1	121	15.0	15.0	0.0	-	-	-	-
52-031125-MC	5.3 ± 0.7	126	11.4	11.4	0.0	-	-	-	-
53-031125-MC	5 ± 1	120	13.3	13.3	0.0	-	-	-	-
56-031216-MC	11.9 ± 0.7	104	16.7	14.6	2.1	-	-	-	-
57-031216-MC	11.1 ± 0.7	98	16.8	11.9	4.8	-	-	-	-
27-031007-MC	19.9 ± 0.7	106	15.4	13.5	1.9	-	-	-	-
28-031007-MC	11.4 ± 0.5	105	14.7	12.5	2.2	-	-	-	-
29-031007-MC	9.91 ± 0.03	112	13.8	13.1	0.7	-	-	-	-
55-031216-MC	1.00 ± 0.06	107	13.9	12.0	1.9	-	-	-	-
134-040302-MC	10.7 ± 0.3	124	12.6	12.6	0.0	122 ± 5	14± 1	14 ± 1	0
218-041119-MC	8.4 ± 0.4	107	16.1	14.7	1.4	107 ± 4	16± 2	15±2	1.4±0. 7
219-041119-MC	9.1 ± 0.8	106	16.1	14.4	1.7	107 ± 4	15± 2	13±1	1.6±0. 7
220-041119-MC	9.6 ± 0.7	103	16.7	14.4	2.2	101 ± 7	17± 3	14±2	3±2
249-050713-MC	6.1 ± 0.2	108	15.2	13.8	1.4	107 ± 3	15± 1	13.1±0. 9	1.7±0. 7
250-050721-MC	6.8 ± 0.4	109	15.7	14.7	1.0	110 ± 6	15± 2	14±1	0.9±0. 8
251-050722-MC	6.3 ± 0.6	N/A	N/A	N/A	N/A	89.9± 0.1	N/A	N/A	N/A
253-060118-MC	6 ± 1	N/A	N/A	N/A	N/A	N/A	N/A	N/A	N/A
254-060118-MC	6.9 ± 0.3	115	13.4	13.0	0.4	115 ± 5	13± 1	13±1	0.3±0. 5
255-060118-MC	6.5 ± 0.3	108	15.0	13.7	1.3	110 ± 7	15± 2	14±2	0.9±1
256-060118-MC	6.1 ± 0.4	N/A	N/A	N/A	N/A	N/A	N/A	N/A	N/A
297-061212-MC	8.9 ± 0.4	105	19.6	18.4	1.1	106 ± 8	20± 3	19±3	1±1
298-061212-MC-1	9.3 ± 0.7	104	19.3	18	1.4	102 ± 10	20± 4	19±3	1±2
298-061212-MC-2	8.9 ± 0.2	102	19.4	17.6	1.8	105 ± 8	20± 3	19±2	1±1
299-061212-MC-1	9.2 ± 0.7	98	20.2	17.3	2.9	101 ± 8	21± 3	19±2	2±2

299-061212-MC-2	8.8 ± 0.08	99	20.6	17.9	2.6	101 ± 9	21± 4	19±3	2±2

Experimental

A Krüss (Hamburg, Germany) K100 Processor Tensiometer was used to measure the hydrophobicity of the GDL samples. A schematic of a tensiometer, an instrument that employs the Washburn method for automated wetting studies, is shown in Figure 98. The gas diffusion layer is held by a metal clamp, which is attached to a very sensitive balance. The test liquid is on platform on a precise screw-type motor. The motor slowly raises the test liquid until the balance detects the contact of the diffusion layer material to the liquid surface. A computer records the mass of liquid absorbed by the GDL as a function of time.

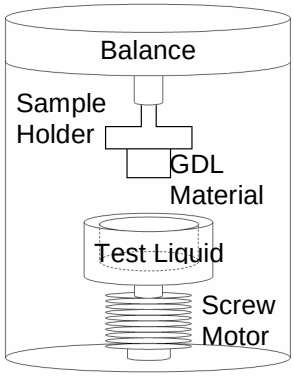

Figure 98. Test apparatus for wettability measurements

Summary of Test Method

First, the capillary constants for at least four samples of each GDL are measured using the Washburn method with n-hexane. Next, contact angles against at least four different wetting liquids are measured using the tensiometer and predetermined capillary constants. Lastly, an Owens-Wendt plot is constructed to determine the GDL surface energy and the contact angle against water.

Washburn Method for Wettability Measurement

The Washburn method described below is the first step of the analysis and is used to determine the material capillary constant and the internal contact angle of water to the material. If a porous solid is brought into contact with a liquid, the rise of liquid into the pores of the solid due to capillary action is governed by the following equation first described by Washburn:

(1) $$t = Am^2$$

(2) $$A = \frac{\eta}{c\rho^2\gamma_{LV}\cos\theta}$$

Combining Equations (1) and (2) yields Equation (3), which is the useful form of Washburn's equation.

(3) $$\cos\theta = \frac{m^2}{t}\frac{\eta}{c\rho^2\gamma_{LV}}$$

If a liquid with known density, viscosity and surface tension are used in a Washburn experiment a plot of the mass of liquid squared versus time is produced yielding two unknowns: the contact angle of the liquid on the solid and the solid material capillary constant. However, if a liquid that is known to have a contact angle of 0º on the porous solid is used, then the solid material capillary constant *c* can be calculated. N-hexane is usually a good choice as the liquid for determining material capillary constant because of its low surface tension (18.4 mN/m) at room temperature.

Once the solid material capillary constant has been determined for a porous solid, other liquids can be tested for wettability. Using the capillary constant and mass squared versus time data the contact angle of a liquid on a solid can be calculated from Equation (3). The material capillary constant for a porous solid is given by:

(4)
$$c = \frac{1}{2}\pi^2 r^5 n^2$$

Thus, two pieces of the same porous material would have the same material constants only if they were exactly the same size. If they were exactly the same size, the number of capillaries would be equal. Additionally, the two samples must be held relative to the surface of the test liquid in the same configuration. Otherwise, their material capillary constant will be different because the average capillary radius and number of capillaries will appear different from the point of view of the test liquid.

Owens-Wendt Calculation of Surface Free Energy and Contact Angle to Water and Mann Modification[64, 65, 66]- The surface free energy (γ_S) of a solid is equal to the sum of the dispersion (γ_S^d) and polar (γ_S^p) components:

(5)
$$\gamma_S = \gamma_S^d + \gamma_S^p$$

The following relation has been used:

(6)
$$\gamma_{SL} = \gamma_S + \gamma_L - 2\left[\left(\gamma_S^d \gamma_L^d\right)^{1/2} + \left(\gamma_S^p \gamma_L^p\right)^{1/2}\right]$$

where γ_{SL} is the free energy relating to the interface between the solid and the probe liquid, γ_L is the free energy of the liquid, and γ_L^d and γ_L^p are the dispersion and polar components of the surface free energy of the liquid, respectively. Combining Equations (5) and (6) with Young's equation (7) yields the following expression:

(7)
$$\gamma_L \cos\theta = \gamma_S - \gamma_{SL}$$

(8)
$$\gamma_L(1+\cos\theta) = 2\left[\left(\gamma_S^d \gamma_L^d\right)^{1/2} + \left(\gamma_S^p \gamma_L^p\right)^{1/2}\right]$$

where θ is the contact angle between the probe liquid and the surface of the solid. Two unknowns (γ_s^d and γ_s^p), occurring in Equation (8) can be determined from the measurements of the contact angles of different liquids with known values of γ_L^d and γ_L^p. Rearrangement of Equation (8) yields:

(9)
$$(1+\cos\theta)\left(\gamma_L \Big/ 2\sqrt{\gamma_L^d}\right) = \sqrt{\gamma_S^d} + \sqrt{\gamma_S^p \gamma_L^p / \gamma_L^d}$$

A plot of $(1+\cos\theta)(\gamma_L/2(\gamma_L^d)^{0.5})$ versus $(\gamma_L^p/\gamma_L^d)^{0.5}$ for different liquids yields γ_s^d (square of the y-intercept), γ_s^p (square of the slope) and consequently γ_s from Equation (5). The plots for the same solid and different liquids are situated on a straight line, therefore for known values of $(\gamma_L^p/\gamma_L^d)^{0.5}$

for water, the contact angle between water and solid may be calculated from the ordinate after interpolation. Alternatively, varying the values of γ_s^d and γ_s^p in a least squares fit analysis of contact angle data will yield the dispersive and polar components of the surface free energy of the solid and consequently γ_s from Equation (5). This last method was proposed by Dr. J.A. Mann.

Method of Least Squares[67,68]

An alternative to the graphical Owens-Wendt Method is the Method of Least Squares, which provides in addition the standard deviation of the estimated parameters.
The physical law (8) is rewritten as:

(10)
$$y = \sqrt{a_1 x_1} + \sqrt{a_2 x_2}$$

or as a functional relationship between the dependent and independent variables:

(11)
$$y = f(a_1, a_2, x_1, x_2)$$

where the dependent variable is y = (γ_L/2)(cosθ+1), the independent variables are $x_1 = \gamma_L^d$, $x_2 = \gamma_L^p$ and the unknown parameters are $a_1 = \gamma_S^d$ and $a_2 = \gamma_S^p$

The residuals are defined as the difference between the measured and calculated values of the dependent and independent variables respectively:

(12)
$$R_{y_i} = Y_i - y_i$$
$$R_{x_{j,i}} = X_{j,i} - x_{j,i} \qquad j = 1, 2$$

The weights are defined as the reciprocal of the squares of the measurement uncertainties (standard deviations):

(13)
$$w_{y_i} = \frac{1}{\sigma_{y_i}^2}$$
$$w_{x_{j,i}} = \frac{1}{\sigma_{x_{j,i}}^2}$$

The method of least squares consists in determining the values of parameters a_1 and a_2 which minimize the weighted sum of the squares of residuals:

(14)
$$S = \sum_{i=1}^{n} \left(w_{y_i} R_{y_i}^2 + \sum_{j=1}^{3} w_{x_{j,i}} R_{x_{j,i}}^2 \right)$$

The conditional function is defined as:

(15)
$$F^i = y_i - f(a_1, a_2, x_1, x_2)$$

The initial guess of the unknown parameters is a_1^0 and a_2^0. The initial value of the conditional function is estimated from measurements and the initial guess of the unknown parameters:

(16)
$$F_0^i = Y_i - f(a_1^0, a_2^0, X_1, X_2)$$

The weight factor for each measurement is defined as:

(17)
$$L_i = \frac{\left(\frac{\partial F^i}{\partial y}\right)^2}{w_{y_i}} + \sum_{j=1}^{2} \frac{\left(\frac{\partial F^i}{\partial x_{j,i}}\right)}{w_{x_{j,i}}}$$

The optimized values of the unknown parameters are calculated as:

(18)
$$A = C^{-1}V$$

where:

(19)
$$A = \begin{bmatrix} a_1^0 - a_1 \\ a_2^0 - a_2 \end{bmatrix}$$

$$C = \begin{bmatrix} \sum_{i=1}^{n} \frac{\frac{\partial F^i}{\partial a_1}\frac{\partial F^i}{\partial a_1}}{L_i} & \sum_{i=1}^{n} \frac{\frac{\partial F^i}{\partial a_1}\frac{\partial F^i}{\partial a_2}}{L_i} \\ \sum_{i=1}^{n} \frac{\frac{\partial F^i}{\partial a_1}\frac{\partial F^i}{\partial a_2}}{L_i} & \sum_{i=1}^{n} \frac{\frac{\partial F^i}{\partial a_2}\frac{\partial F^i}{\partial a_2}}{L_i} \end{bmatrix}$$

$$V = \begin{bmatrix} \sum_{i=1}^{n} \frac{\frac{\partial F^i}{\partial a_1} F_0^i}{L_i} \\ \sum_{i=1}^{n} \frac{\frac{\partial F^i}{\partial a_2} F_0^i}{L_i} \end{bmatrix}$$

The standard deviations for the unknown parameters are:

(20)
$$\sigma_{a_k} = \left(\frac{S}{n-2}\right)^{1/2} \cdot \left(C_{kk}^{-1}\right)^{1/2}$$

The procedure for determining a_1 and a_2 is the following:

1. Collect the data measurements Y_i, X_1, X_2 and the standard deviations σ_{y_i}, $\sigma_{x_{j,i}}$;
2. Make the initial guess for the unknown parameters a_1^0 and a_2^0;
3. Using the initial guess for the unknown parameters and the measurements, calculate the conditional function (16) and its partial derivatives from (15);
4. Calculate the weight factors (17);
5. Calculate the elements of matrix *C* and vector *V* (19);
6. Invert matrix *C*;

7. Calculate vector *A* (19) and a_1 and a_2;
8. Use newly calculated a_1 and a_2 as the initial guesses for step 2;
9. Continue steps 2 to 8 until the change in a_1 and a_2 is less than a prescribed value;
10. Calculate the standard deviations for a_1 and a_2 (20)

Method for In-plane Permeability

In-plane permeability is an important measure of gas transport in a GDL. Low in-plane permeability means that gas will not be able to diffuse to the electrode located under the flow field lands and instead all the reaction will take place in the electrode located under the flow field channels. Table 25 contains the in-plane permeability results.

Table 25. GDL in-plane (x-y) and through-plane (z) permeability

Sample ID	x-y viscous (m^2) x E-11	z-axis viscous (m^2) x E-12	z-axis inertial (m) x E-8
GDL 1	1.9	1.36	
GDL 8		6.54	
GDL 2	0.5	0.37	
30-031107-MC		2.07	
31-031107-MC		1.88	
32-031107-MC		3.05	
33-031107-MC		2.30	
34-031107-MC		2.40	
35-031107-MC		3.22	
36-031107-MC		2.15	
37-031107-MC		1.88	
38-031107-MC		0.44	
39-031107-MC		0.18	
40-031107-MC		0.22	
51-031125-MC	2.94		
52-031125-MC	0.49	1.56	
53-031125-MC	1.86	29.8	
57-031216-MC		4.3	
55-031216-MC	0.3		
134-040302-MC	1.02	0.06	
218-041119-MC		3.39	0.36
219-041119-MC		3.32	0.289
220-041119-MC		6.55	0.64
226-041210-MC		4.87	44
226-041210-MC		8.9	8.2
234-050222-CM		0.080	0.7
235-050222-CM		3.11	3.68
249-050713-MC	0.5	0.0266	0.16
250-050721-MC	0.8	0.8	0.16
252-050722-MC	1.1	8.99	109
253-060118-MC		75	43
254-060118-MC		4.2	9.0
255-060118-MC		1.7	1.91
256-060118-MC		1.4	1.5

Apparatus

The apparatus is presented in Figure 99. The annular GDL sample is clamped by an upper and a lower fixture. An amount $\boldsymbol{Q}$ of preconditioned test gas enters the upper fixture through an inlet opening. The gas flow rate is controlled by a flowmeter situated upstream of the inlet opening. The gas is forced through the GDL into the atmosphere in a radial direction. A pressure gage and a temperature sensor measure the pressure $\boldsymbol{P_1}$ and the temperature $\boldsymbol{T_1}$ upstream of the sample. A second temperature sensor measures the temperature $\boldsymbol{T_0}$ of the surrounding atmosphere. The upper and lower fixture assembly is placed between the platens of a press. The compression force and the deformation of the sample are measured with a load cell and a strain sensor attached to the upper platen through a support. The equipment used to condition the gas (heater and humidifier) is not described here.

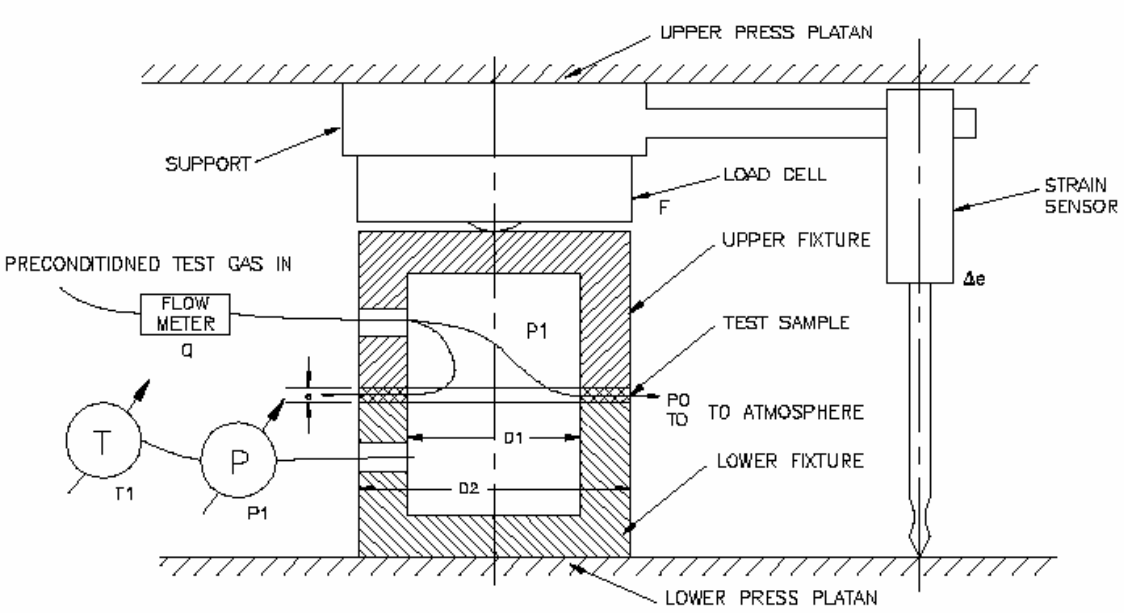

Figure 99: Test apparatus for in-plane permeability measurements

Summary of Test Method

The thickness, *e,* of each GDL samples was measured in five points using a digital micrometer. The apparatus correction was determined by measuring the pressure drop in the fixtures without GDL sample, for the required interval of flow rates and for different space ***e*** between fixtures. At different compression levels, we measured the compression force ***F***, the GDL deformation ***De***, the pressure P_1, and the temperatures T_1 and T_0 upstream and downstream the test fixture for different flow rates ***Q***.

Calculations - Average gas pressure and temperature through GDL sample:

(21)
$$T = \frac{T_1 + T_0}{2}$$

(22)
$$P = \frac{P_1 + P_0}{2}$$

Flowmeter reading corrections:

(23)
$$Q = C_f \frac{P_1}{P} \frac{T}{T_1} Q_{measured}$$

where C_f is the correction factor.

With T and P obtain density ρ [kg/m^3] and dynamic viscosity μ [Ns/m^2].

Darcy-Forchheimer equation for flow through porous media:

(24)
$$\frac{dP}{dr} = \frac{\mu}{k_V} V + \frac{\rho}{k_i} V^2$$

where the velocity V is

(25) $$V = \frac{Q}{A}$$

(26) $$A = 2\pi re$$

Introducing (25) and (26) in (23) and rearranging:

(27) $$dP = \frac{\mu}{k_V}\frac{Q}{2\pi e}\frac{dr}{r} + \frac{\rho}{k_i}\frac{Q^2}{4\pi^2 e^2}\frac{dr}{r^2}$$

integrating equation (27) one obtains:

(28) $$\Delta P = \frac{\mu}{k_V}\frac{Q}{2\pi e}\ln\left(\frac{D_2}{D_1}\right) + \frac{\rho}{k_i}\frac{Q^2}{2\pi^2 e^2}\frac{D_2 - D_1}{D_1 D_2}$$

or

(29) $$y = \frac{1}{k_i}x + \frac{1}{k_V}$$

where*:*

(30)

$$y = \frac{\Delta P}{\mu}\frac{2\cdot\pi\cdot e}{Q}\frac{1}{\ln\left(\frac{D_2}{D_1}\right)}$$

$$x = \frac{Q\cdot\rho}{\pi\cdot \mathrm{e}\cdot\mu}\frac{D_2 - D_1}{D_1\cdot D_2}\frac{1}{\ln\left(\frac{D_2}{D_1}\right)}$$

For each flow rate Q and corresponding pressure difference $\Delta P = P_1 - P_0$ calculate x and y from (30). Plot the values x and y on a linear graph paper and obtain the straight line that best fits the points. Intercept of this line on the y-axis is $(1/k_v)$. The slope of the line is $(1/k_i)$.

Note: If the flow is laminar, the inertial permeability coefficient, k_i is negligible small.

List of Symbols

A	Cross-sectional area *[m^2]*
C_f	Flowmeter correction factor
D_1	Inner chamber diameter *[m]*
D_2	Outer chamber diameter *[m]*
e	GDL sample thickness *[m]*
Q	Flow rate *[m^3/s]*
P_1	Pressure upstream test fixture *[N/m^2]*
P_2	Pressure downstream test fixture *[N/m^2]*
P	Average pressure in GDL sample
T_1	Temperature upstream test fixture *[K]*
T_2	Temperature downstream test fixture *[K]*

T	Average temperature in GDL sample
V	Gas velocity *[m/s]*
k_V	Viscous permeability coefficient $[m^2]$
k_i	Inertial permeability coefficient *[m]*
ρ	Gas density $[kg/m^3]$
μ	Dynamic viscosity $[N.s/m^2]$

Method for Through-Plane Permeability

Through-plane permeability is an important measure of gas transport in a GDL. Low through-plane permeability results in excess mass-transport resistance which correlates to a reduction in fuel cell performance. Table 25 contains the through-plane permeability results.

Apparatus

The GDL samples are clamped between an upper and a lower fixture (Figure 100). The test gas (dry air) enters the upper fixture through an inlet opening. The upper and lower fixtures consist each of an inner and outer chamber. The inner and outer chambers of the upper fixture communicate through a number of ports. The inner-upper chamber provides path for an amount Q of air to pass through the tested GDL material. The inner-lower chamber is connected to a flowmeter. The outer-upper chamber is pressurized to prevent side leakage (in-plane) from the inner chamber. The outer-lower chamber leads to atmosphere through an adjustable pressure-equalizing valve. A pressure-differential gage measures the pressure drop between the inner-upper chamber and the inner-lower chamber (P_1-P_2). A second pressure-differential gage measures the pressure difference between the inner-lower and the outer-lower chambers (P_3-P_2). The pressure-equalizing valve is adjusted to equalize pressures P_3 and P_2. An additional pressure gage is used to measure the pressure P_2 in the inner-lower chamber. Two temperature sensors are used to measure the gas temperature upstream T_1 and downstream T_2 *of* the test fixture.

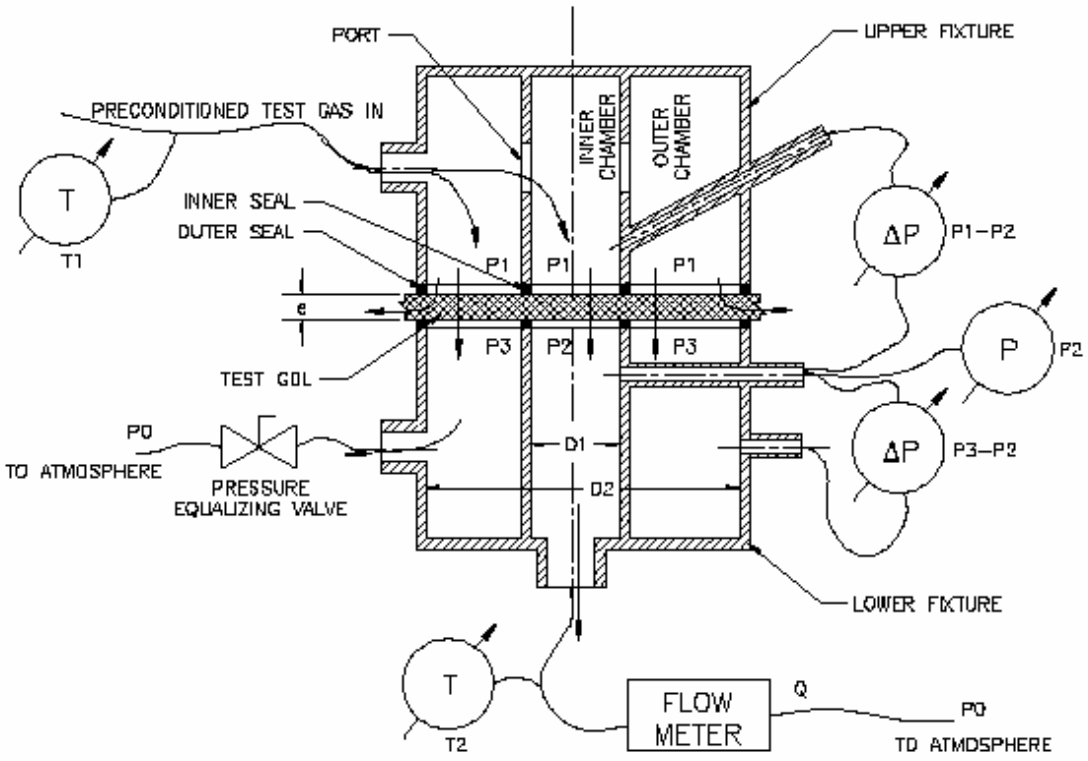

Figure 100. Test apparatus for through-plane permeability

Summary of Test Method

The thickness, *e,* of each GDL sample is measured in five points using a digital micrometer. With the GDL sample set in the fixture, the pressure drop P_1-P_2, the pressure P_2 and the temperatures T_1 and T_2 are measured for approximately twenty different flow rates. For each measurement the pressure-equalizing valve is adjusted so that $P_2 = P_3$.

Calculations

The average gas pressure and temperature through the GDL sample are calculated as:

(31)
$$T = \frac{T_1 + T_2}{2}$$

(32)
$$P = \frac{P_1 + P_2}{2}$$

The flow meter reading corrections are:

(33)
$$Q = C_f \frac{P_2}{P} \frac{T}{T_2} Q_{measured}$$

where C_f is the correction factor.

With T and P obtain density ρ [kg/m^3] and dynamic viscosity μ [Ns/m^2].

Darcy-Forchheimer equation for flow through porous media:

(34)
$$\frac{\Delta P}{e} = \frac{\mu}{k_V} v + \frac{\rho}{k_i} v^2$$

where the velocity V is

(35)
$$v = \frac{Q}{a}$$

Method of Least Squares[67,68]- The physical law (4) is rewritten as:

(36)
$$y = a_1 x_1 x_2 + a_2 x_1^2 x_3$$

or as a functional relationship between the dependent and independent variables:

(37)
$$y = f\left(a_1, a_2, x_1, x_2, x_3\right)$$

where the dependent variable is $y = \frac{\Delta P}{e}$, the independent variables are $x_1 = V$, $x_2 = \mu$, $x_3 = \rho$ and the unknown parameters are $a_1 = \frac{1}{k_V}$ and $a_2 = \frac{1}{k_i}$.

The residuals are defined as the difference between the measured and calculated values of the dependent and independent variables respectively:

(38)
$$R_{y_i} = Y_i - y_i$$
$$R_{x_{j,i}} = X_{j,i} - x_{j,i} \qquad j = 1, 2, 3$$

The weights are defined as the reciprocal of the squares of the measurement uncertainties (standard deviations):

(39)
$$w_{y_i} = \frac{1}{\sigma_{y_i}^2}$$
$$w_{x_{j,i}} = \frac{1}{\sigma_{x_{j,i}}^2}$$

The method of least squares consists in determining the values of parameters a_1 and a_2 which minimize the weighted sum of the squares of residuals:

(40)
$$S = \sum_{i=1}^{n} \left(w_{y_i} R_{y_i}^2 + \sum_{j=1}^{3} w_{x_{j,i}} R_{x_{j,i}}^2 \right)$$

The conditional function is defined as:

(41)
$$F^i = y_i - f\left(a_1, a_2, x_1, x_2, x_3\right)$$

The initial guess of the unknown parameters is a_1^0 and a_2^0. The initial value of the conditional function is estimated from measurements and the initial guess of the unknown parameters:

(42)
$$F_0^i = Y_i - f\left(a_1^0, a_2^0, X_1, X_2, X_3\right)$$

The weight factor for each measurement is defined as:

(43)
$$L_i = \frac{\left(\frac{\partial F^i}{\partial y}\right)^2}{w_{y_i}} + \sum_{j=1}^{3} \frac{\left(\frac{\partial F^i}{\partial x_{j,i}}\right)}{w_{x_{j,i}}}$$

The optimized values of the unknown parameters are calculated as:

(44)
$$A = C^{-1}V$$

$$A = \begin{bmatrix} a_1^0 - a_1 \\ a_2^0 - a_2 \end{bmatrix}$$

$$C = \begin{bmatrix} \sum_{i=1}^{n} \frac{\frac{\partial F^i}{\partial a_1}\frac{\partial F^i}{\partial a_1}}{L_i} & \sum_{i=1}^{n} \frac{\frac{\partial F^i}{\partial a_1}\frac{\partial F^i}{\partial a_2}}{L_i} \\ \sum_{i=1}^{n} \frac{\frac{\partial F^i}{\partial a_1}\frac{\partial F^i}{\partial a_2}}{L_i} & \sum_{i=1}^{n} \frac{\frac{\partial F^i}{\partial a_2}\frac{\partial F^i}{\partial a_2}}{L_i} \end{bmatrix}$$

$$V = \begin{bmatrix} \sum_{i=1}^{n} \frac{\frac{\partial F^i}{\partial a_1}F_0^i}{L_i} \\ \sum_{i=1}^{n} \frac{\frac{\partial F^i}{\partial a_2}F_0^i}{L_i} \end{bmatrix}$$

(45)

The standard deviations for the unknown parameters are:

(46)
$$\sigma_{a_k} = \left(\frac{S}{n-2}\right)^{1/2} \cdot \left(C_{kk}^{-1}\right)^{1/2}$$

The procedure for determining a_1 and a_2 is the following:

1. Collect the data measurements Y_i, X_1, X_2, X_3 and the standard deviations σ_{y_i}, $\sigma_{x_{j,i}}$;

2. Make the initial guess for the unknown parameters a_1^0 and a_2^0;
3. Using the initial guess for the unknown parameters and the measurements, calculate the conditional function (42) and its partial derivatives from (41);
4. Calculate the weight factors (43);
5. Calculate the elements of matrix *C* and vector *V* (45);
6. Invert matrix *C*;
7. Calculate vector *A* (45) and a_1 and a_2;
8. Use newly calculated a_1 and a_2 as the initial guesses for step 2;
9. Continue steps 2 to 8 until the change in a_1 and a_2 is less than a prescribed value;
10. Calculate the standard deviations for a_1 and a_2 (46)

List of Symbols

a	Cross-sectional area $[m^2]$
a_k	Unknown parameters $(k = 1, 2)$
A	Vector in equation (15)
C_f	Flowmeter correction factor
C	Matrix in equation (15)
D_1	Inner chamber diameter [m]
D_2	Outer chamber diameter [m]
e	GDL sample thickness [m]
f	Functional relationship between dependent and independent variables
F	Conditional function
k_V	Viscous permeability coefficient $[m^2]$
k_i	Inertial permeability coefficient [m]
L	Weight factor
n	Number of measurements
Q	Flow rate $[m^3/s]$
P_1	Pressure upstream test fixture $[N/m^2]$
P_2	Pressure downstream test fixture $[N/m^2]$
P	Average pressure in GDL sample
R	Residuals
S	Weighted sum of the squares of residuals
T_1	Temperature upstream test fixture [K]
T_2	Temperature downstream test fixture [K]
T	Average temperature in GDL sample
v	Gas velocity [m/s]
V	Vector in equation (15)
w	Weights
x_j	Calculated independent variable $(j = 1, 2, 3)$
X_j	Measured independent variable $(j = 1, 2, 3)$
y	Calculated dependent variable
Y	Measured dependent variable
ρ	Gas density $[kg/m^3]$
μ	Dynamic viscosity $[N.s/m^2]$
σ	Standard deviation

Method for Measuring Capillary Pressure as a Function of GDL Saturation

Introduction

Water management is a critical issue in PEMFC performance. High water content in the ionomer-phase of the catalyst coated membrane (CCM) determines high protonic conductivity, which is a key factor in insuring high fuel cell performance. Liquid water in the gas diffusion layer and

catalyst layer pores hinders the oxygen ability to reach the reaction sites, but proves beneficial for PEMFCs operating in dry conditions.

Catalyst layers are being optimized for increased catalytic activity, selectivity and durability but inherently, lack the flexibility to control the amount of water that would accumulate in its pores during fuel cell operation. Nevertheless, if well designed, the GDL may promote or inhibit water flow from the catalyst layer into the GDL in a desired, controlled fashion. Thus the GDL takes the role of water content regulator in the adjacent catalyst layer. The amount of water that will reside in the catalyst layer pores is determined at steady-state by the saturation equilibrium at the GDL - catalyst layer interface. Most likely, the two porous regions are characterized by different drainage / imbibition curves. At this interface, the gas-phase and liquid-phase pressures, and therefore the capillary pressure, are continuous, which implies that the water saturation must have a discontinuity (Figure 101). For a catalyst layer with a known capillary pressure – saturation relationship, a GDL may be designed such that a desired amount of water will be present in the catalyst layer pores during fuel cell operation. Because of its central nature, tailoring the GDL provides an opportunity: once we master the details of GDL structure and composition, we will have a powerful and as yet untapped design tool for fuel cells optimization. The determination of capillary pressure as function of saturation in GDLs is a condition *sine qua non* for achieving this goal.

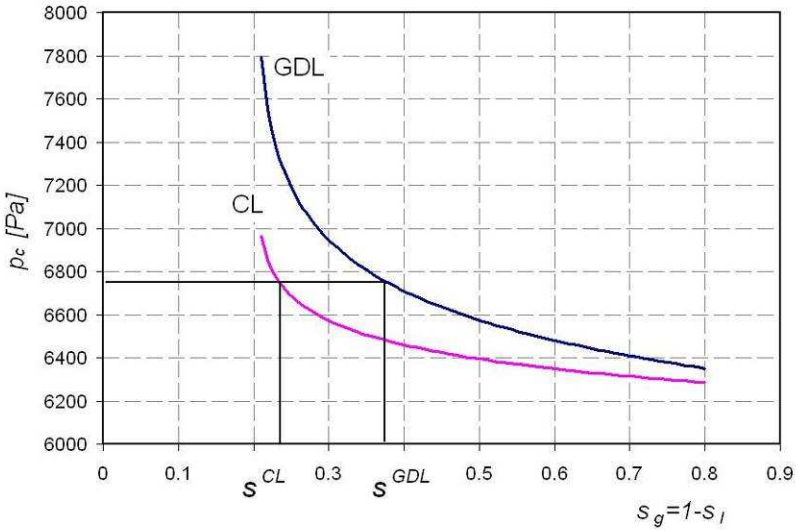

Figure 101. Liquid Saturation Discontinuity at GDL – Catalyst Layer Interface

Typical GDLs for PEM fuel cells consist of a macro-porous back-bone for structural rigidity and one or more micro-porous layers aimed to optimize the electrical conductivity and the water transport *within* the GDL and *between* the GDL and the catalyst layer.

Typically, micro-porous layers of GDLs are mixtures of a carbon or graphite powder and polytetrafluoroethylene (PTFE). The carbon matrix generally consists of carbon grains (20-40 nm) which form agglomerates of 200-300 nm size (Figure 102). The carbon – PTFE porous structure is therefore characterized by a bi-modal pore size distribution, with primary pores of 20-40 nm inside the agglomerates between the carbon grains, and secondary pores of 40-200 nm between the agglomerates. The effect of the PTFE content on the pore-size distribution affects the inter-agglomerate space (secondary pores) but not the intra-agglomerate space (primary pores). The volume of the secondary pores increases with the PTFE wt%. PTFE, due to its molecular size, cannot penetrate the intra-agglomerates, but exists in the inter-agglomerate space.

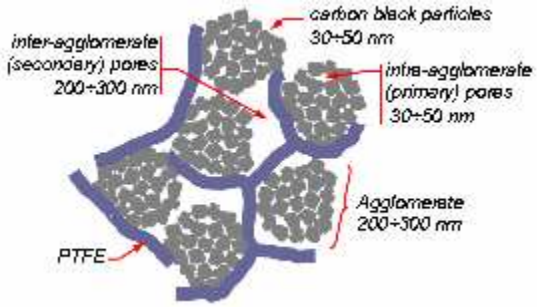

Figure 102. Typical Structure of Micro-Porous Layers for GDLs

The capillary pressure, p_c depends locally on the nature of the solid matrix and on the degree of saturation, s_l. There have been attempts to express the capillary pressure as a function of the saturation level

(47) $$p_c = p_c(s_l)$$

for groundwater flow based on dimensional analysis using the Leverett *J*- function[69]. The *J*-function is being mistakenly used in the literature related to GDLs[70] as a generally valid expression. It has been shown however that the *J* – function is successful in correlating pressure data originating from specific lithologic type of porous media within the same formation, but is not of general applicability[71]. One of the main limitations of the Leverett *J* – function lies in the fact that the square root of the porosity – permeability ratio, $\sqrt{\frac{\varepsilon}{k}}$ is an inadequate scale factor that is incapable of accounting for the individual differences between the pore structures of various samples[72]. It is necessary therefore to be able to determine the capillary pressure – saturation relationship for GDLs and catalyst layers experimentally.

Experimental methods used today for determination of $p_c = p_c(s_l)$ involve the displacement of the wetting fluid (air) by the non-wetting one (water), when the pressure of the non-wetting fluid is progressively increased (drainage). When water is injected in the porous GDL, it will initially invade the largest (secondary) pores (Figure 103a). As the water pressure is further increased, the air - water interface retreats into successively smaller (primary) pores (Figure 103b).

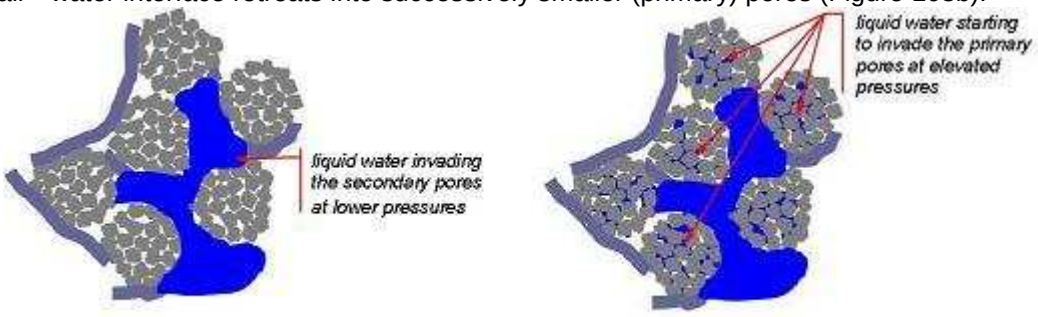

(a) (b)

Figure 103. Illustration of water filling the (a) secondary pores and (b) primary pores.

During the imbibition process, as the water pressure is decreased, the air - water interface advances back towards successively larger (secondary) pores. Each step requires that the capillary pressure and the amount of water residing in the GDL sample are measured only after the equilibrium is established (after water is uniformly distributed throughout the GDL sample).

There have been reported recently some partially successful attempts to determine $p_c = p_c(s_l)$ for hydrophobic GDLs by the group at University of Kansas using the volume displacement method[73]. Based on the expectation that water does not imbibe spontaneously into porous materials with neutral wettability[74,a], Nguyen *et al.*[73] attempted to determine the capillary pressure for a 5% wet proof SIGRACET® 10BA GDL by filling and draining water into the sample and measuring the volume of water displaced. The sample was filled and drained with water by varying the liquid water pressure at the water-sample interface. The procedure requires waiting until equilibrium is reached (steady-state condition), when water fills uniformly the entire sample. The measurement proved unsuccessful, since the irreducible air saturation decreased, and the water residual saturation increased from one scan to the next, and there was no clear distinction between the primary (envelope) curves and the scanning curves, but rather the curves shifted in time towards higher water saturation levels. The drawback of the method consists in the difficulty to determine when equilibrium conditions are reached. Laboratory experiments have often shown that it may take as long as days, or even years for a liquid to penetrate uniformly into a finite porous sample. We have also shown recently using tensiometry, that water imbibes spontaneously into partially wet-proofed GDLs. The mass of water imbibed in the GDL sample (Figure 104) increased in time over ten hours of experiment.

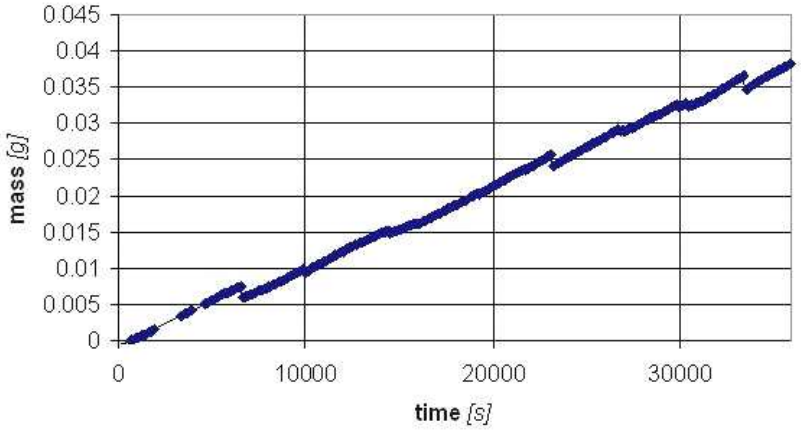

Figure 104. Mass of Water Imbibed Spontaneously into a Partially Wet-Proofed GDL During an Experiment Using the Wilhelm Method (Specific Isons and Rheons are Clearly Noticed).

It is expected that all the experimental methods which are based on measuring $p_c = p_c(s_l)$ at equilibrium (steady-state) will suffer of the same drawbacks as the volume displacement method. Here we present a practical method which allows the determination of the $p_c = p_c(s_l)$ relationship during the drainage, imbibition and scanning processes. The method requires monitoring a single representative elementary volume (REV) of the GDL sample using the Neutron Imaging Technique and eludes the requirement of reaching equilibrium steady-states before each measurement is taken.

[a] GDLs are commonly manufactured of carbon or graphite, having a contact angle to water of approx 80^o mixed with polytetrafluoroethylene (PTFE), having a contact angle to water of approx 105^o. Materials such as carbon and PTFE, having contact angles to water between of 75^o and 105^o to 120^o are classified as systems with neutral wettability.

Materials and Method

The proposed method consists in monitoring simultaneously the liquid-phase pressure and the saturation in a representative elementary volume (REV) of the GDL sample, when water is injected in the sample.

The GDL sample is annular (1.5" OD and 1.0" ID) which confers axial symmetry to the phenomenon being studied (1-dimension). The GDL sample consisted of a 3M micro-porous layer (2.1-2.8 mils thick) dispersed on a polyimide ring. The sample porosity was measured by weighting the sample before and after being immersed in n-hexane which is assumed to spread into the GDL pores (zero internal contact angle).

To simplify the method, only an REV representing the inner boundary is monitored. At this boundary, the liquid pressure inside the GDL pores is equal to the liquid pressure measured in the inner cavity of the annular sample. Since micro-porous layers are homogeneous structures, it is assumed that all REVs are characterized by the same porosity and pore-size distribution.

In Figure 105, the annular GDL sample (1) is compressed between two aluminum (6061-T6) compression plates (2, 3) using tierod – nut assemblies (4) equally displaced around the sample. Liquid water is injected in the inner cavity of the annular GDL sample using a screw-actuated micrometer syringe (5). Liquid pressure in the inner cavity of the annular sample is monitored using a (0-55 in water) pressure gage (6). The air trapped in the inner cavity of the annular sample, tubing and pressure gage is eliminated through a vent (7) before the measurements starts. A cadmium shield ring (8) surrounds the outer edge of the GDL sample.

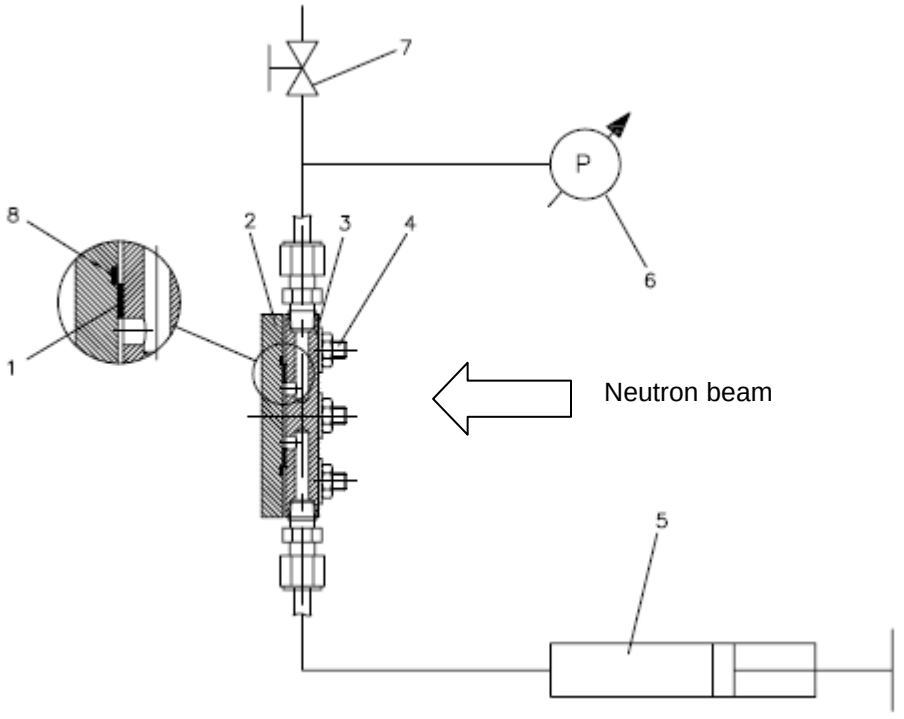

Figure 105. Setup for Capillary Pressure Measurements

After being dried, the sample is clamped into the fixture. Liquid water is injected into the inner cavity formed between the annular GDL sample and the compression plates. All air trapped in the cavity, lines and pressure gage is purged through the valve, then the valve is closed. Liquid saturation is monitored in an REV situated at the interface with the inner cavity (GDL inner

boundary) using Neutron Imaging. Liquid water is injected in small incremental amounts (not required to be monitored), until it penetrates the REV. The corresponding pressure is the threshold pressure.

Optical density images of the sample and the liquid pressure are recorded with a frequency of 1Hz over a time period of twenty minutes for each measurement. The recorded pressure is averaged and the optical density images are summed over this time interval. The saturation in the REV is calculated from the resulted optical density image of the sample.

Water is injected in small incremental amounts until no further saturation increase is noticed in the REV. The recorded pressures and saturations determine the drainage curve. To determine the spontaneous imbibition curve, water is no longer injected. Liquid water accumulated in the REV pores start retreating from the smallest (primary) pores into the larger (secondary) pores and advances through the largest pores in radial direction, towards the external boundary, as the liquid water pressure decreases. To determine the forced imbibition curve, the water is extracted with the syringe. Water remaining in the smaller pores after the first spontaneous drainage is forced into the largest pores and then exits the GDL sample. The method is repeated in order to determine the scanning curves.

Results

To prove the feasibility of the method, only a single measurement was taken after water was injected in the sample at a pressure of 55 in H_2O. The sum of the optical density images over twenty minutes is shown in Figure 106. The water thickness in an REV situated at the inner boundary of the sample is shown in Figure 107.

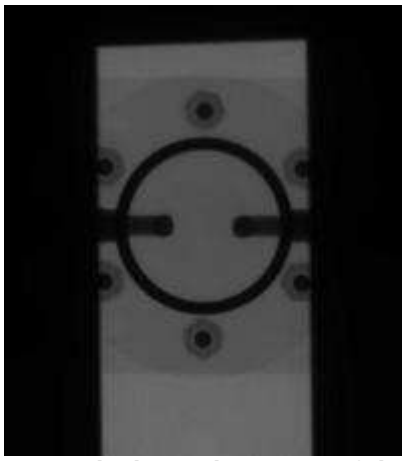

Figure 106. Optical Density Image of the Sample

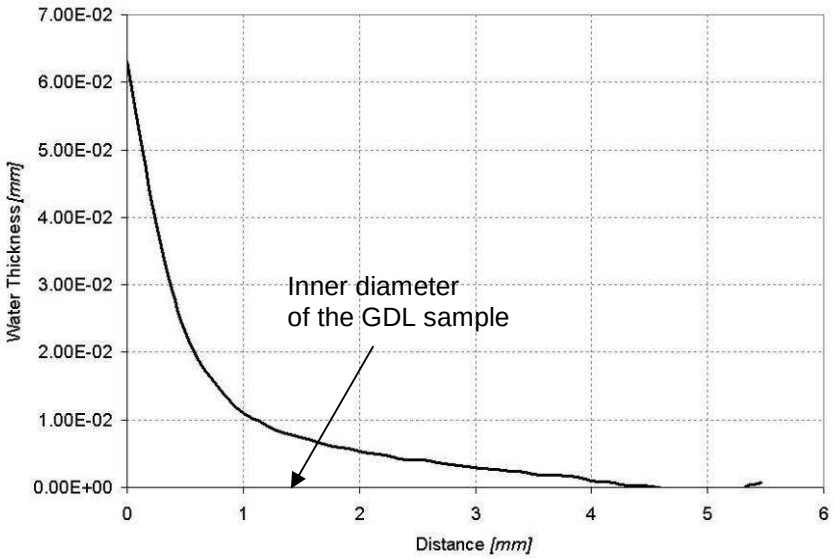

Figure 107. The Water Thickness in the GDL Sample in an REV at the Inner Diameter of the Sample

Conclusions

We have demonstrated the feasibility of a method for the determination of capillary pressures as function of saturation for the hydrophobic GDLs. The method requires monitoring a single representative elementary volume (REV) of the GDL sample using the Neutron Imaging Technique and eludes the requirement of reaching equilibrium steady-states before each measurement is taken.

To complete the determination of the capillary pressure as function of saturation for the GDL sample, the measurement must be repeated at other pressures during the drainage, imbibition and scanning processes.

2.2.2 Accelerated Screening Tests

3M

Screening tests are typically *ex-situ* component tests designed to quantify incremental improvements during component development. Screening tests are very useful in determining the relative durability of one component design to another. For the GDL development, three screening tests were used evaluate electrochemical and chemical stability. The three tests were voltage cycling test, constant voltage test, and peroxide stability test.

Voltage Cycling Aging
Test Method Development and Implementation - Electro-Chemical Oxidative Stability (ECOS) of GDL materials test was developed. The equipment is shown and Figure 108 and the experimental setup was:

The electrolyte: 0.5 M Sulfuric Acid
Reference electrode: SCE
Counter electrode: Pt wire

Active sample area ~ 12 cm^2
Potentiostatic (PS) scan for five minutes
AC impedance and CVs between potentiostatic scans as diagnostics
PS scan voltage is incremented by 0.1V and procedure repeated through a series of voltages (often 0.9 V to 2.0 V)

For the ECOS test, the current density is metric of interest and is plotted versus applied potential. The current density is a measure of the corrosion of the carbon; the lower the current, the more stable the material. Thus, a low current density is a desired property and represents a stable component.

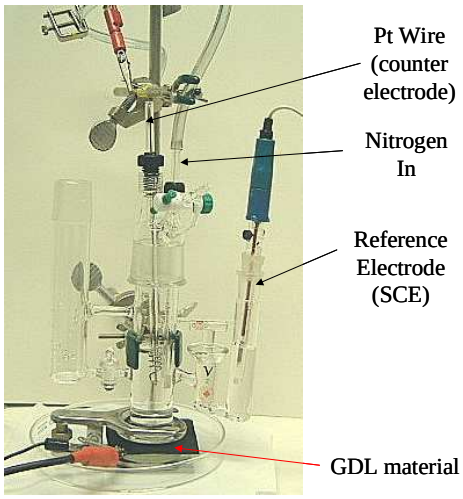

Figure 108. Experimental set-up for voltage cycling aging of GDL material

Constant Voltage Aging

A cell, similar to the one shown in Figure 108, but larger with the ability to hold ~ 100 cm^2 GDL samples was constructed. Just like the voltage cycle tests, 0.5M H_2SO_4 was used as the electrolyte. Unlike the voltage cycle tests, in the constant voltage aging, the voltage is held constant for a period of time. After the aging, the sample can be characterized. Because of the large sample size, a 50 cm^2 sample can be cut from the aged sampled and assembled into an MEA. In this manner, the effect of GDL aging on fuel cell performance can be determined.

Peroxide Aging

A third test method for oxidizing samples was developed. Unlike the previous two methods which measured electro-chemical stability, this technique measured chemical stability. Samples were subjected to 15% H_2O_2 at elevated temperatures (180℉). The peroxide so lution was mixed with a 1M H_2SO_4. Since H_2O_2 degradation was present, the H_2O_2 concentration was monitored by titration and the bath was periodically changed in order to keep the H_2O_2 concentration close to 15 weight percent. Samples were exposed to the solution for various time periods. In this test, oxidative resistance was measured in terms of weight loss; the lower the weight loss, the more oxidatively stable the material.

2.2.3 Selection of GDL Composition

GDL Backing

Using the ECOS test, two different virgin backings were screened for oxidative stability (Figure 109).

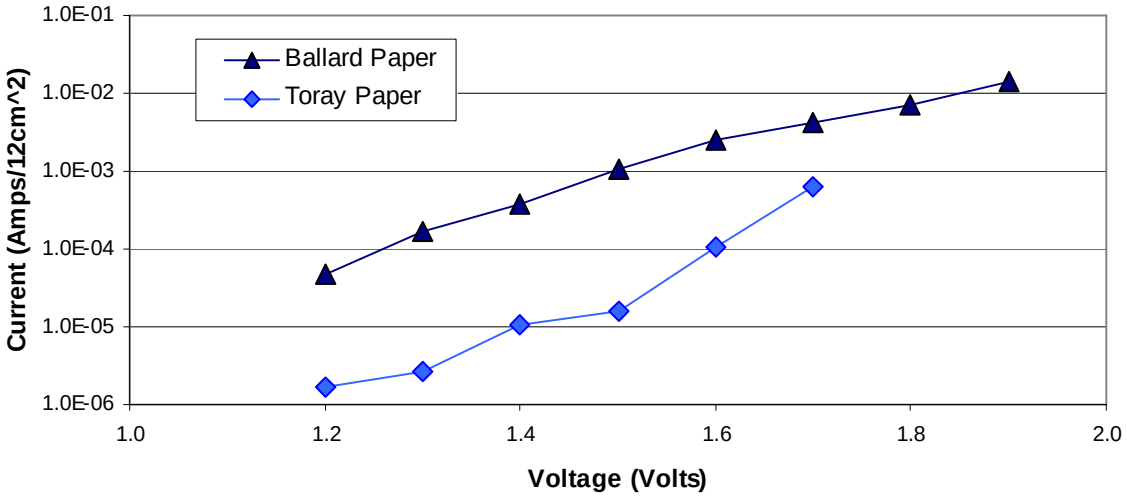

Figure 109. ECOS screening of virgin GDL backing.

At all voltages scanned, the Toray Paper resulted in a lower current density. At 1.5 volts Toray carbon paper is reacting 100 times slower than the Ballard non-woven. A large difference in the static contact angle was also observed. The Toray paper retains a high contact angle unlike the Ballard (Table 26).

Table 26. Comparison of ECOS Testing of Virgin GDL Backings

Sample ID	Current Density @ 1.5 Volts (A/cm^2)	Contact Angle @ highest Voltage scanned (Degrees)
Toray	$1.31 * 10^{-6}$	111.5
Ballard	$8.67 * 10^{-5}$	0.0

Traditionally GDLs contain a flouropolymer as a non-wetting agent. ECOS test were done on the two backings where the binder loading was also varied. Figure 110 is an example using PTFE as the binder and Ballard's backing. Table 27 compares Toray and Ballard .

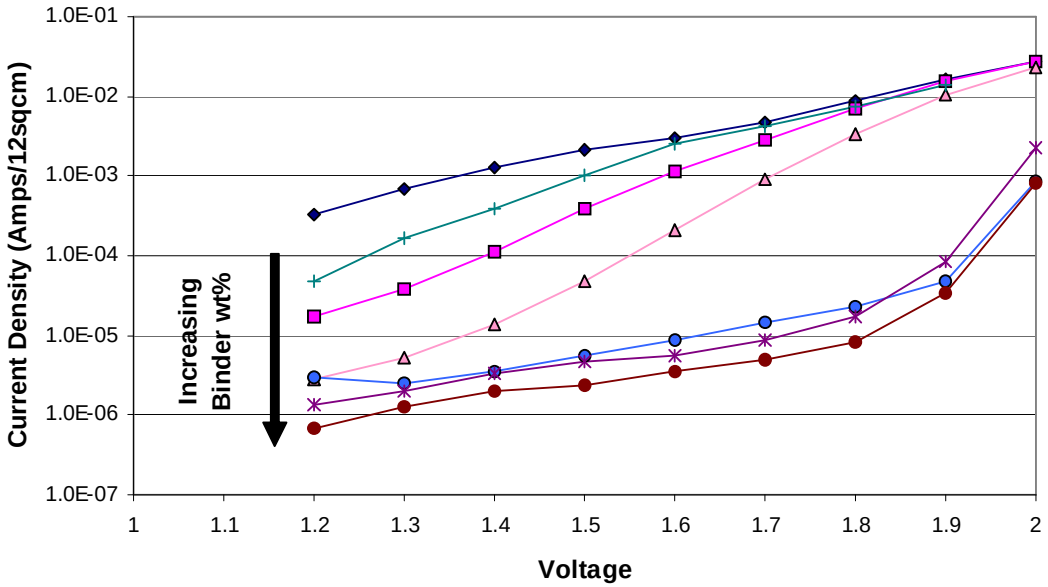

Figure 110. Influence of binder content on stability of BMP backing.

Table 27. Comparison of Toray and backings with various binder levels.

Sample ID	Current Density @ 1.5 Volts (A/cm^2)	Contact Angle @ highest Voltage scanned (Degrees)
Toray 0.00% PTFE	$1.31 * 10^{-6}$	111.5
Toray 0.10% PTFE	$4.53 * 10^{-7}$	129.0
Toray 0.25% PTFE	$1.50 * 10^{-7}$	134.2
Toray 0.50% PTFE	$1.57 * 10^{-7}$	134.1
Toray 1.00% PTFE	$9.18 * 10^{-8}$	135.9
Toray 2.50% PTFE	$6.87 * 10^{-8}$	133.3
Toray 6.00% PTFE	$8.15 * 10^{-8}$	132.0
Ballard 0.00% PTFE	$8.64 * 10^{-5}$	0.0
Ballard 0.10% PTFE	$1.80 * 10^{-4}$	0.0
Ballard 0.50% PTFE	$3.26 * 10^{-5}$	0.0
Ballard 1.00% PTFE	$4.06 * 10^{-6}$	36.7
Ballard 2.50% PTFE	$4.58 * 10^{-7}$	136.1
Ballard 5.00% PTFE	$2.93 * 10^{-7}$	132.8

From the results, it was concluded that the Toray material was more stable. In both cases, it is clear that the binder material protects the carbon from being oxidized. Higher binder loadings offer more protection to the backing. However, having a high binder loading in the backing fills the porous structure of the backing and thus adversely affects performance. The PTFE loading for Toray paper should be at least 0.25% to prevent a change in surface energy by oxidation. The PTFE loading for Ballard should be at least 2.50% to prevent a change in surface energy by oxidation. Ballard with 5% PTFE was chosen as the standard backing while examining different GDL constructions and is used in the GDL 3 design.

Substrates were also oxidized using the peroxide aging test. Six different electrode backings were screened for their resistance to oxidation. The six materials were submerged in a bath of 1M H_2SO_4 with 15 wt% H_2O_2 at 180℉. The samples were weighed before and after aging the material for 240 hrs. The results are shown in Figure 111. The rates of oxidation are greatly reduced when a hydrophobic treatment is applied to the electrode backing.

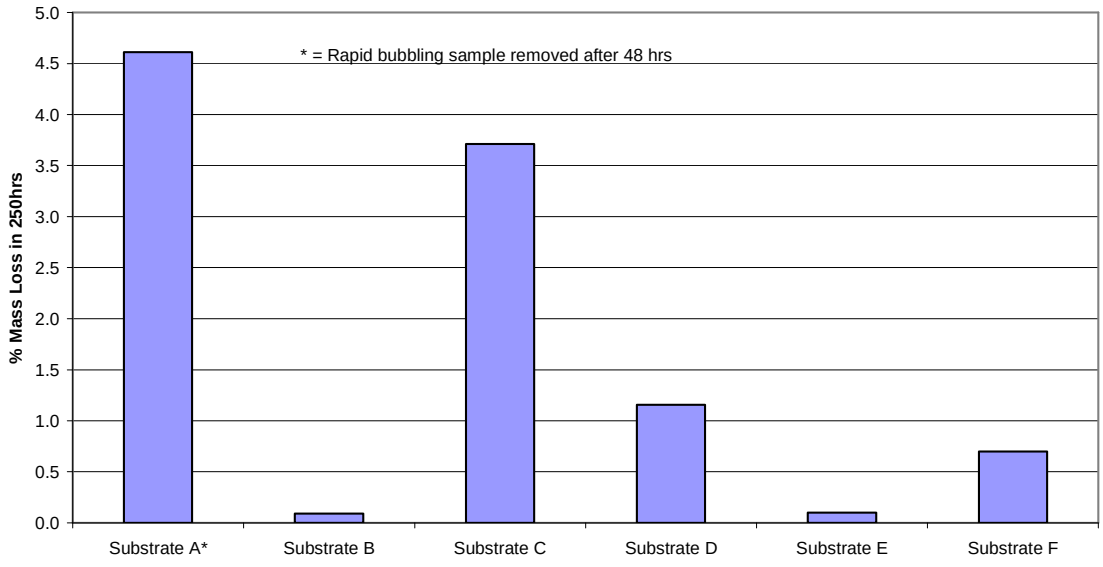

Figure 111. Chemical aging of virgin substrates.

Carbon Blacks for the Micro Layer

3M screened 12 different carbon blacks for oxidative stability. ECOS tests were performed on materials that used different carbon blacks. The samples were made by applying a micro layer that contained 1% binder (PTFE) and 99% carbon black. The low PTFE level was selected in order to reduce the influence of the binder on oxidative stability. The micro layer was coated onto Ballard treated with 5% PTFE. The material was then sintered at 380°C for 10 minutes. Figure 112 contains the results of the various carbon types as a function of voltage and Table 28 summaries the data at 1.5 Volts.

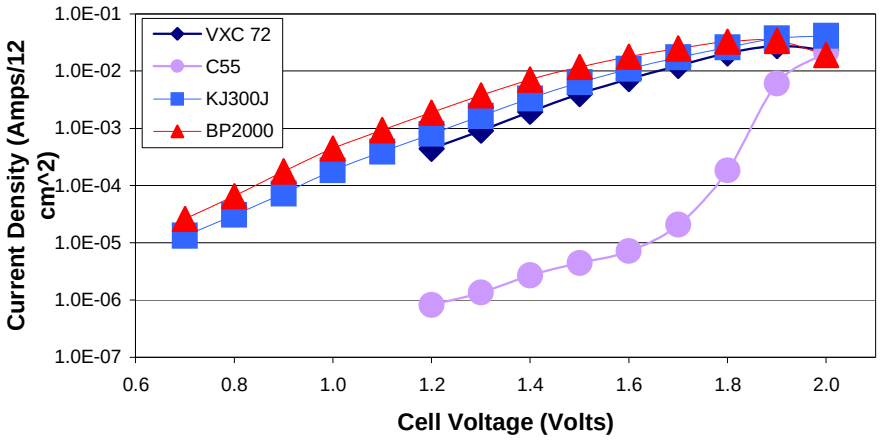

Figure 112. ECOS testing of selected carbon types in micro porous layer. Ballard GDL with MPL consisting of 99% carbon and 1% PTFE.

Table 28. Impact of carbon type in micro porous layer on ECOS current at 1.5 volts

Carbon Type	ECOS Current at 1.5 Volts (A/cm^2)
Vulcan X72	3.33E-04
C55, AB	3.70E-07
Ketjen 300J	5.30E-04
BP2000	9.85E-04
Graphitized Vulcan X72	1.32E-07
Graphitized C55, AB	1.30E-06
Timcal KS4	1.32E-06
Raven Black 14	4.68E-06
Vulcan P	8.02E-06
Sterling C	5.63E-05
Timcal 250	4.09E-05
Timcal 350	7.68E-04

The selection criteria used to select the carbon black to be used in the micro porous layer included: mass loss after 24 hours in 15% H_2O_2 @ 180°F, static contact angle after H_2O_2 aging, commercial availability, process experience, and current density at 1.5 Volts. Based on these criteria, Cheveron's C55 Acetylene Black (highlighted in Table 28) was chosen as the carbon type to pursue. GDL 3 uses C55 carbon on Ballard's with 5% PTFE.

The peroxide aging test was also used to characterize carbon black stability. The test used Ballard GDLs with 5% PTFE in the backing. The binder content in the micro layer was only 1%. This was done to minimize the effects of the binder. The samples were then subjected to 180℉ 15% H_2O_2 in 1M H_2SO_4 for 24 hours. The samples were weighed before and after the aging. The lower the mass loss, the more stable the carbon to oxidation. The results are shown in Figure 113.

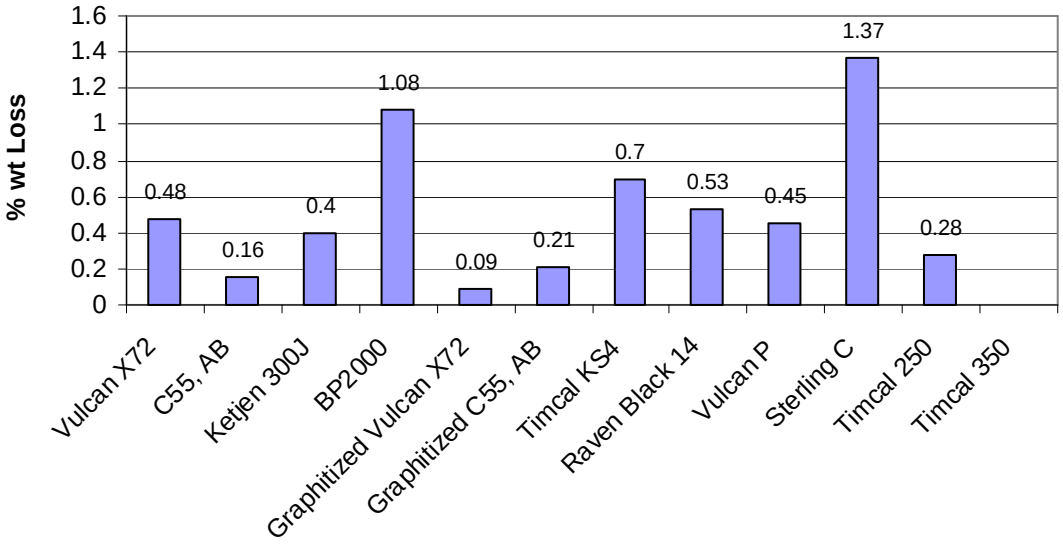

Figure 113. Peroxide aging of carbon blacks.

The four best carbons were C55, Graphitized Vulcan VXC, Graphitized C55, and Timcal 350. This data was used in the decision matrix for carbon selection for future GDL designs. C55 was chosen as the carbon type to move forward with for GDL 3 and GDL 4.

Binder Type and Loading in the Micro Layer

Three different binders; PTFE, FEP, and PFA where investigated for oxidative resistance in the micro layer. ECOS tests where done using the three binders. A poor carbon, Vulcan XC72, was chosen in order to ensure that a response could be measured between the different binders. The binder loading in the micro layer is 20% wt. The backing of the material was Ballard with 5% PTFE. The use of different binders does play a roll in offering an improved resistance to oxidation as shown in Figure 114 and summarized in Table 29. FEP gives the best level of protection. FEP was selected for the GDL 4 design.

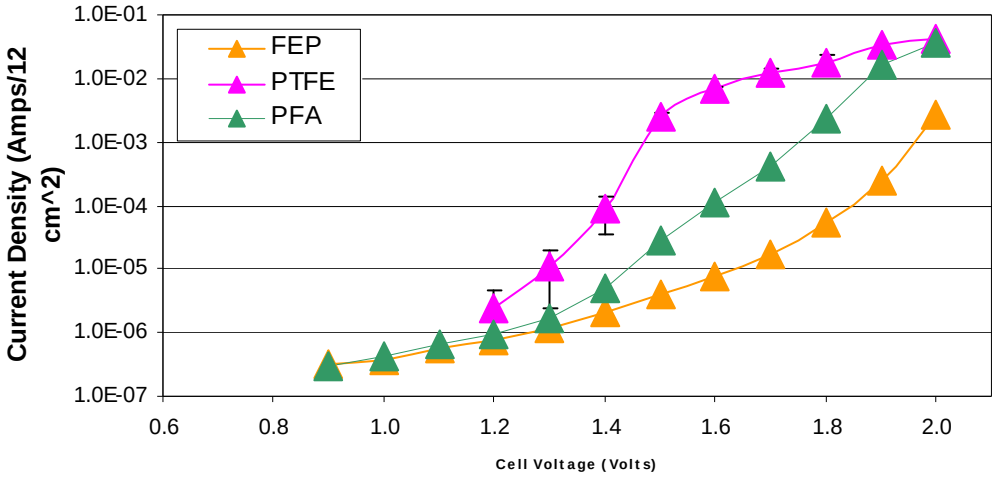

Figure 114. Impact of micro porous binder type in ECOS testing

Table 29. Summary of ECOS binder testing

Sample ID	Current Density @ 1.5 Volts (A/cm^2)	Contact Angle @ highest Voltage scanned (Degrees)
PTFE	$2.07 * 10^{-4}$	84.2
PFA	$2.32 * 10^{-6}$	92.0
FEP	$3.37 * 10^{-7}$	109.6

Similar to the backing, the binder loading in the micro porous layer will play a roll in the oxidative stability. The % binder was systematically investigated. The carbon chosen for the experiment was Cabot's VXC-72 and the backing was Ballard's with 5% PTFE. The PTFE weight percent was changed from 1 to 70 wt% as shown in Figure 115. A comparison of the impact of the PTFE versus FEP is shown in

Table 30.

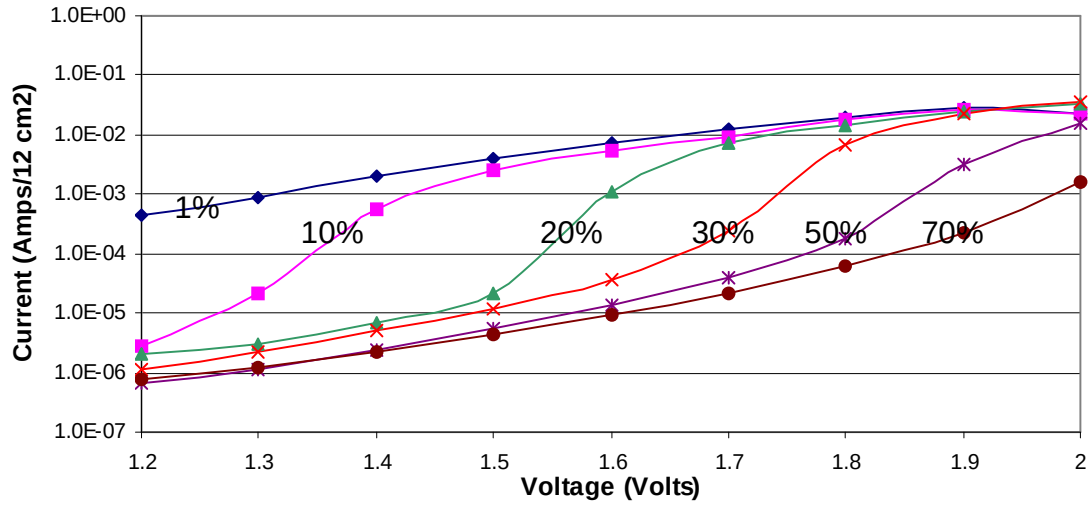

Figure 115. Impact of PTFE binder level in micro porous layer during ECOS testing.

Table 30. Comparison of PTFE versus FEP in micro porous layer binder level.

Sample ID	Current Density @ 1.5 Volts (A/cm^2)	Contact Angle @ highest Voltage scanned (Degrees)
PTFE 1%	$3.33 * 10^{-4}$	43.6
PTFE 10%	$2.17 * 10^{-4}$	62.2
PTFE 20%	$1.78 * 10^{-6}$	84.2
PTFE 30%	$1.02 * 10^{-6}$	101.9
PTFE 50%	$4.59 * 10^{-7}$	113.3
PTFE 70%	$3.73 * 10^{-7}$	114.2
FEP 1%	$3.63 * 10^{-4}$	53.4
FEP 10%	$7.53 * 10^{-5}$	104.2
FEP 20%	$3.37 * 10^{-7}$	109.6
FEP 30%	$4.65 * 10^{-7}$	112.4
FEP 50%	$1.84 * 10^{-7}$	130.0
FEP 70%	$1.85 * 10^{-7}$	126.4

Here the use of FEP over PTFE becomes clear. At all binder loadings, the FEP performance is superior to PTFE. FEP was selected as the binder in the micro porous layer for the GDL 4 design.

Impact of Micro Layer Dispersion Composition and Quality

Additional areas of interest are the micro layer dispersion composition and quality. Different processes allow for the binder to become more or less homogeneous. A well-dispersed binder should give a more stable micro layer. Two dispersions were made using Vulcan XC-72 carbon and PTFE. The end composition between the two micro layers is the same. The first was a non-water based dispersion and the other was a water-based dispersion. Figure 116 contains micrographs of the two micro layers.

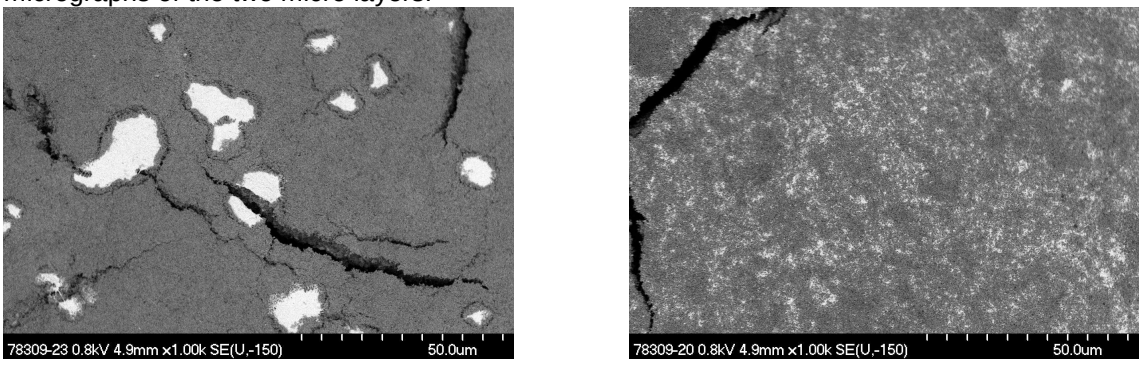

Figure 116. Micrograph of non aqueous (left) and aqueous (right) based PTFE micro layer dispersions.

In the non-water-based dispersion, the binder is poorly distributed as evidenced by the large clumps of PTFE (white areas). The use of a water-based dispersion method has greatly improved the PTFE dispersion quality. The PTFE agglomerates are much smaller and have a higher level of homogeneity.

The use of a new binder, FEP instead of PTFE, will once again change the processing of the micro layer dispersion. Figure 117 is a micrograph of a water-based dispersion using FEP. At a magnification level of 1000x, the micro layer appears to be homogeneous and perfectly

dispersed. We then investigated the oxidative stability of the PTFE and FEP dispersions via the ECOS test (Figure 118). There is a difference in the stability which reinforces the need to have a well-dispersed binder in the micro layer.

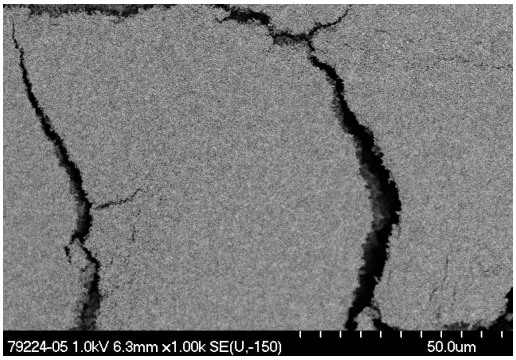

Figure 117. Micrograph of aqueous based FEP dispersion.

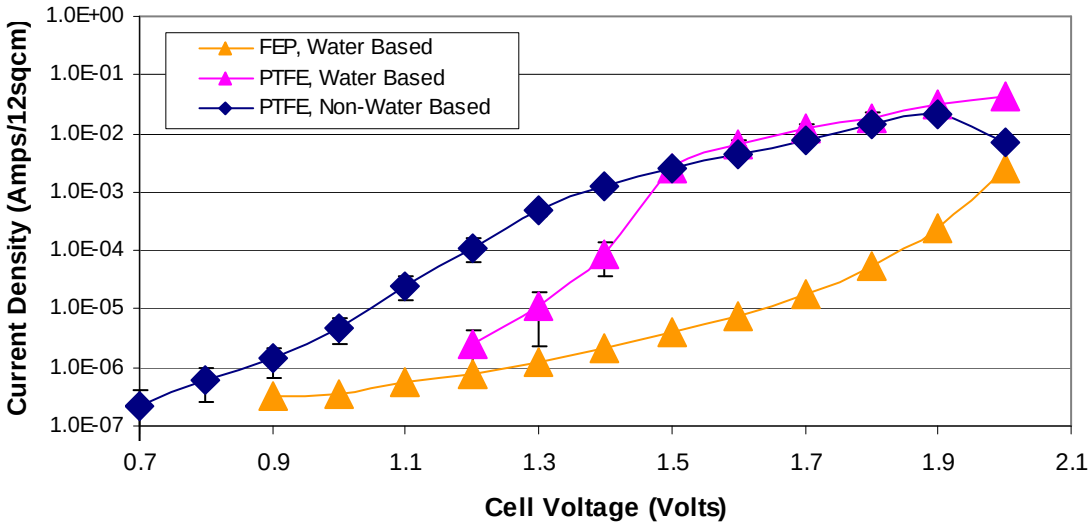

Figure 118. ECOS test of aqueous and non-aqueous micro layer dispersions.

The use of a well-dispersed binder resulted in slowing of the rate of corrosion (oxidation) by approximately 1000x at 1.5 volts. The water-based process was selected for the GDL 3 and GDL 4 designs.

Impact of GDL Aging on Fuel Cell Performance

Various GDL designs were aged either electrochemically or chemically and then assembled into MEAs with a unaged GDL on the anode and an aged GDL on the cathode. In this manner, the impact of GDL aging on fuel cell performance could be identified. The results for electrochemical GDL aging are shown in Figure 119 to Figure 121 and the results for chemical aging are shown in Figure 122 to Figure 124.

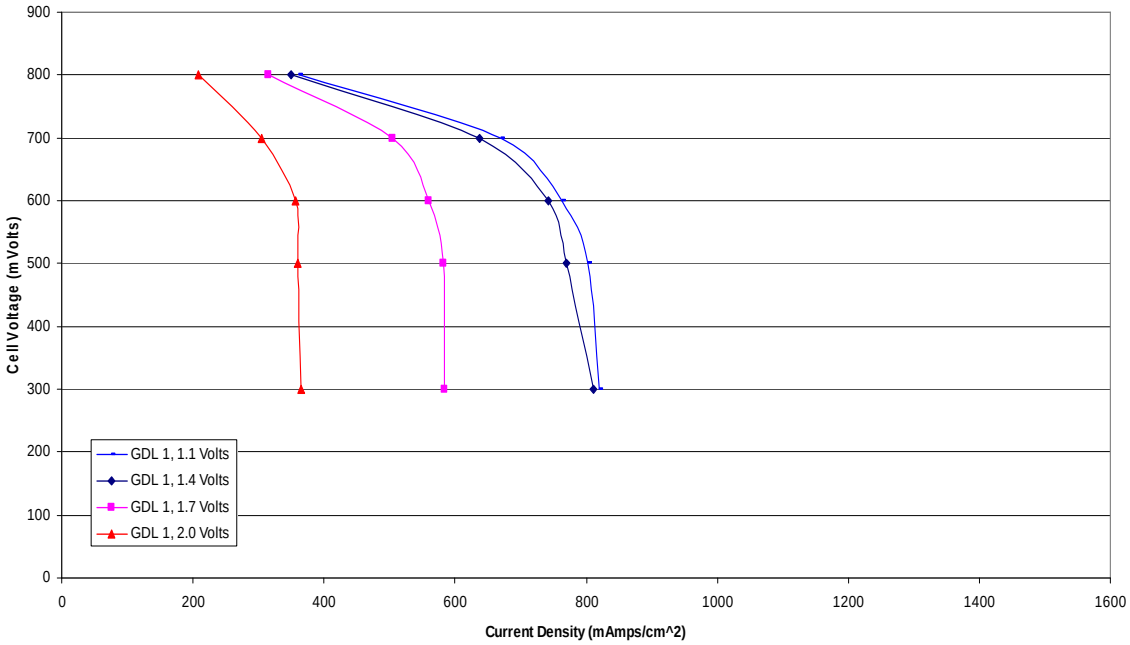

Figure 119. Impact of electrochemical aging GDL 1 on fuel cell performance.

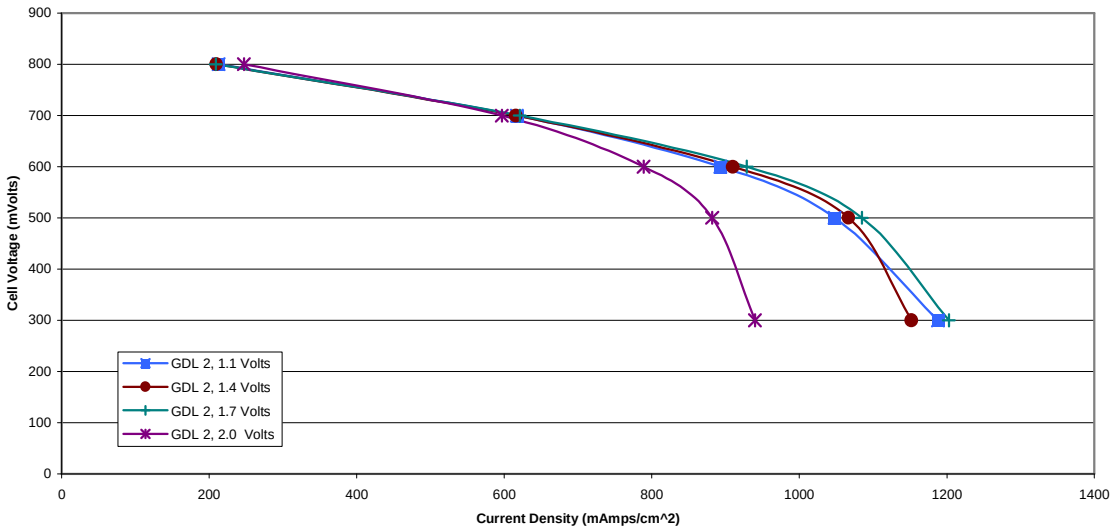

Figure 120. Impact of electrochemical aging GDL 2 on fuel cell performance.

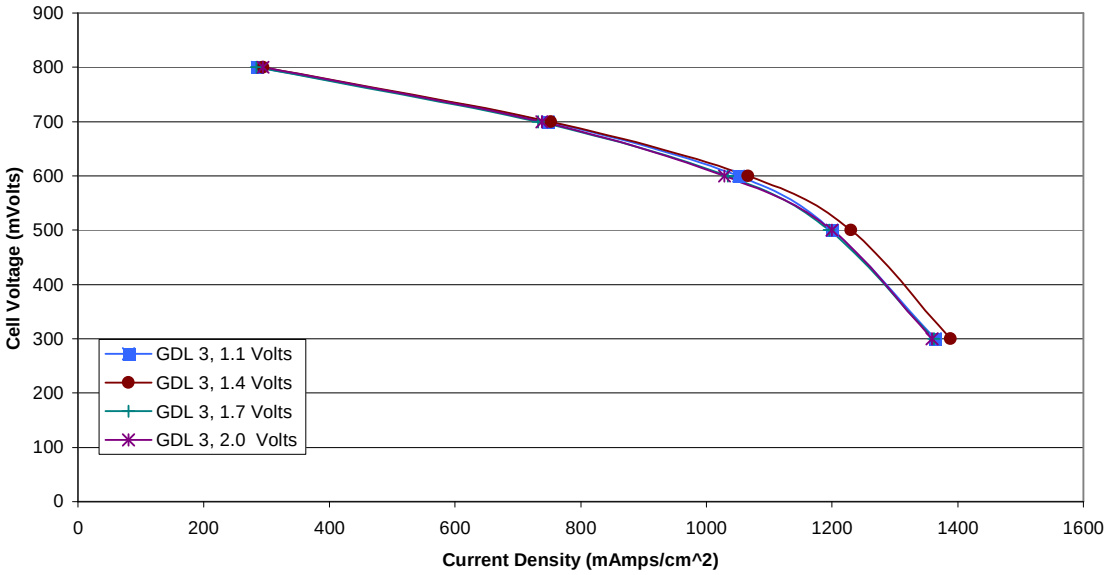

Figure 121. Impact of electrochemical aging GDL 3 design on fuel cell performance.

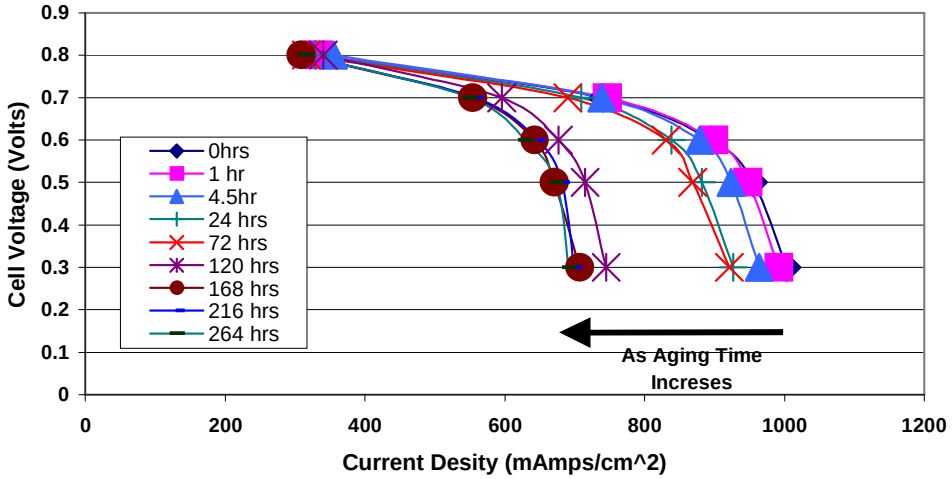

Figure 122. Impact of chemical aging on GDL 1 fuel cell performance.

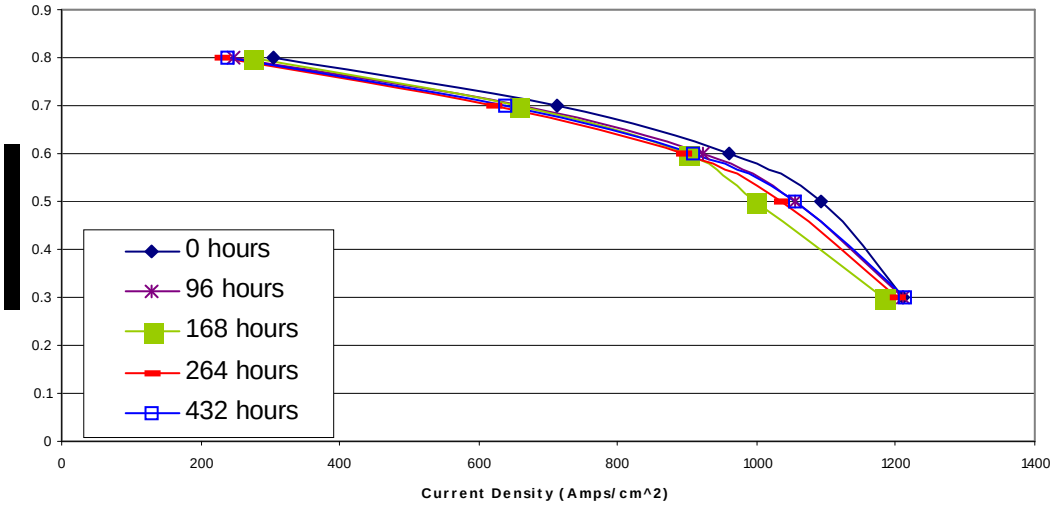

Figure 123. Impact of chemical aging on GDL 2 fuel cell performance.

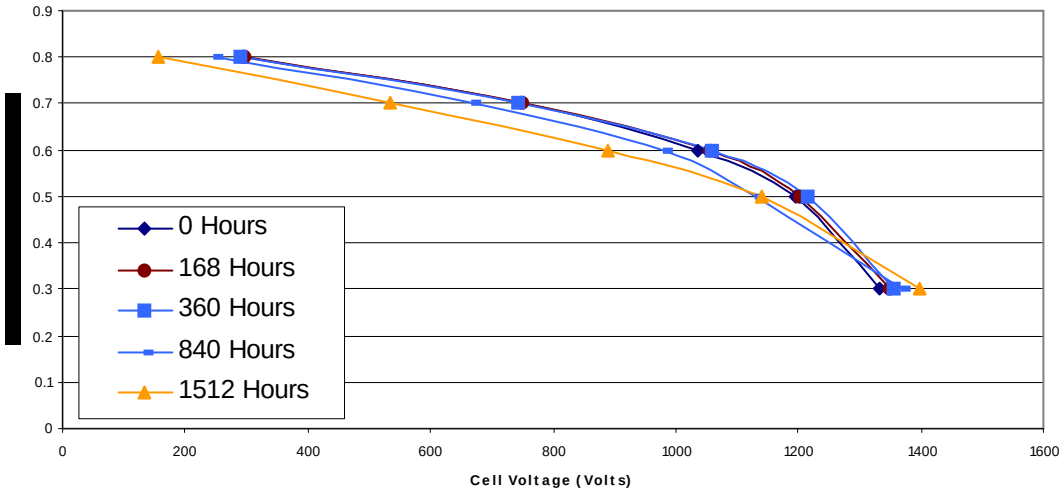

Figure 124. Impact of chemical aging GDL 3 design on fuel cell performance.

In all cases, the aged GDL had a negative impact on fuel cell performance although the degree of impact greatly depends on the GDL design. The improvements seen between GDL 1 and GDL 2 is due to a more uniform micro layer. The GDL 1 design clearly developed a severe mass transport problem as the GDL is oxidized. The improvement between GDL 2 and GDL 3 was due to a raw material change. A more stable carbon black was used in the micro porous layer for the GDL 3 design. The GDL 3 design retained its properties and did not become as oxidized as the GDL 1 and GDL 2 GDLs.

2.2.4 Selection of Final GDL Design

Comparison of Different GDL Designs

Several GDLs were developed during this project. The following summaries the aging tests performed on the GDLs which guided the selection of the final GDL design. The ECOS test was performed on two baseline designs, GDL 1 and GDL 2, and a more durable designed developed under this project, GDL 4. The results of the ECOS test are shown in Figure 125

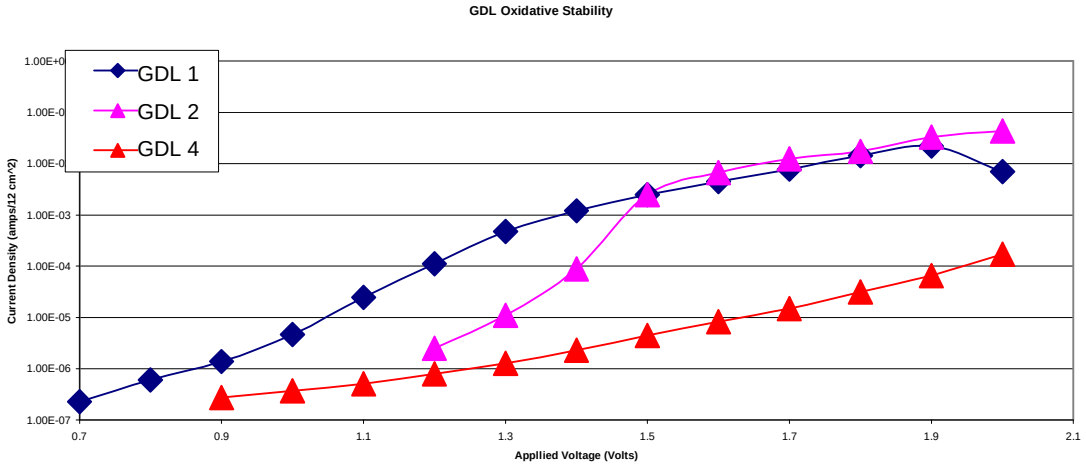

Figure 125. ECOS testing of various GDL designs.

The oxidation resistance of GDL 4 is greater than two orders of magnitude over the GDL1 or GDL 2 at high potentials. Even at low voltages, GDL 4 is more stable. As a result, an additional experiment was setup to look at voltages that occur during normal operation of a fuel cell stack. Cyclic voltamograms were ran from 0.3 Volts to ~ 0.9 Volts. The test was performed on GDL 1 (Figure 126) and GDL 4 (Figure 127). The data indicates that GDL 1 has oxygen adsorption / desorption peaks indicating that the GDL is being oxidized. On the other hand, GDL 4 does not show an oxygen adsorption / desorption peak. Contact angles were also measured for the two GDLs during the ECOS testing as a function of number of cycles (Figure 128). The change in the contact angle resulted from different levels of oxidation of the micro layer. GDL 1's contact angle fell under 90 degrees which corresponds to the poor performance in the mass transport region of the polarization curves. GDL 4 design did not show a change in surface energy within the first 100 cycles.

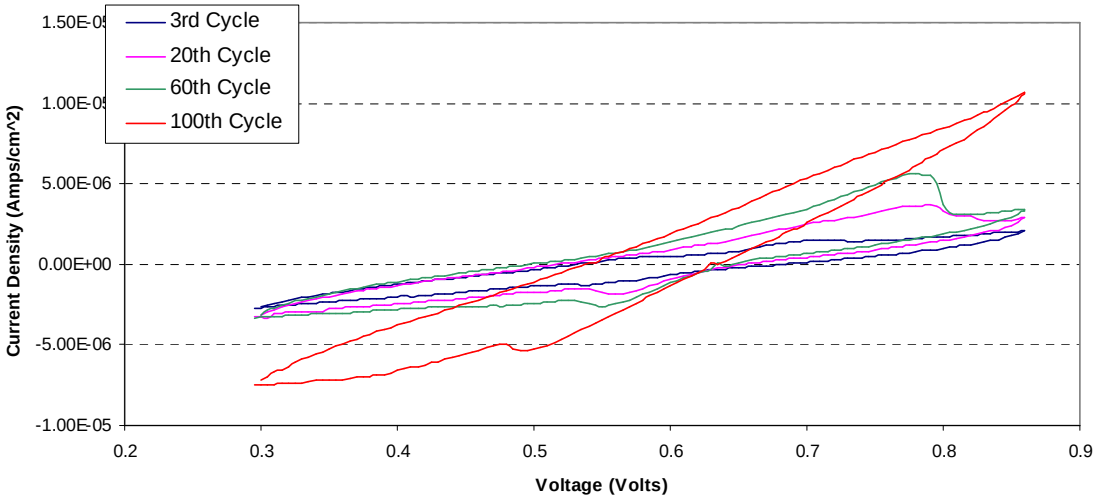

Figure 126. ECOS testing of GDL 1 at fuel cell potentials.

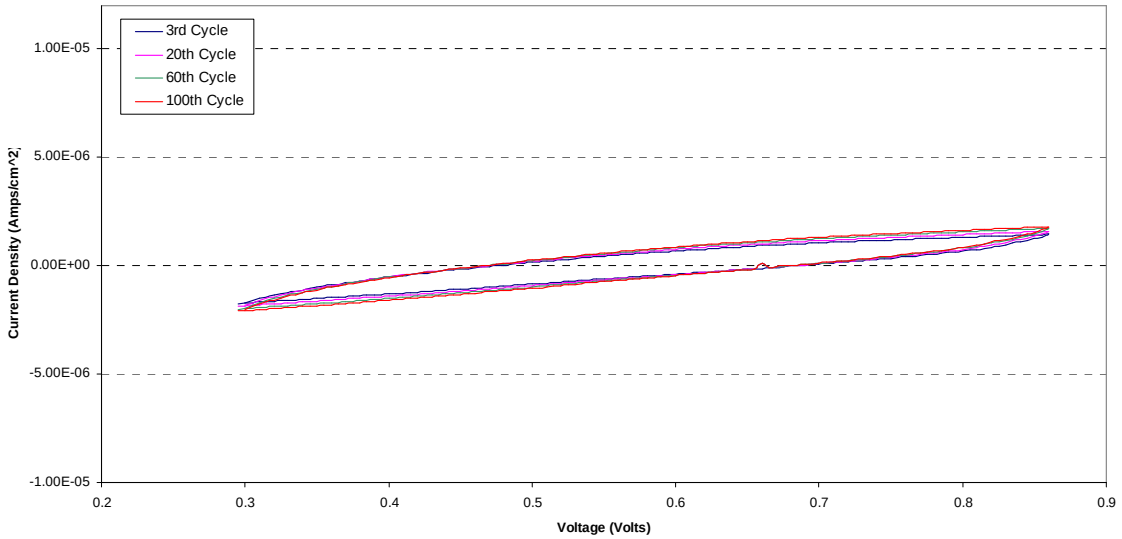

Figure 127. ECOS testing of GDL 4 at fuel cell potentials.

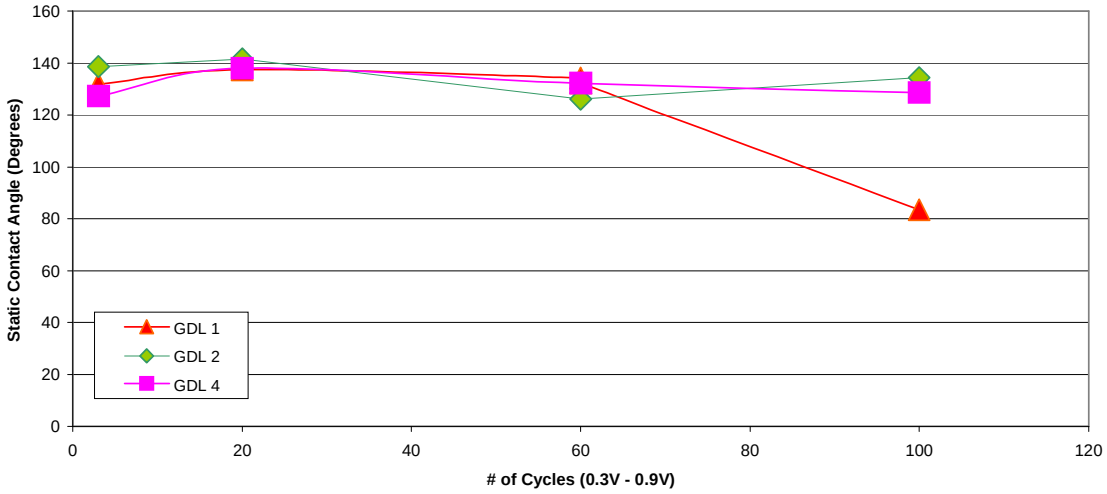

Figure 128. Contact angle as a function of ECOS cycle number

Additional experiments utilized constant voltage aging tests to differentiate between GDL designs. Each sample was repeated four times. The voltages examined were 0.8, 1.4, 2.0, and 2.6 volts. Each voltage was held for 1, 10, 100, 1000 minutes. We measured the contact angle, mass gain, electrical resistance and fuel cell performance of GDL 1 and GDL 4 as a function of aging.

GDL 1 experienced the greatest contact angle change. Originally the micro layer of GDL 1 had a contact angle of ~ 135 degrees. The contact angle fell to as low as 50 degrees under the most severe conditions (Figure 129). GDL 4 did not undergo the same level of change as GDL 1. In fact GDL 4's contact angle remain relatively constant during the test (Figure 129).

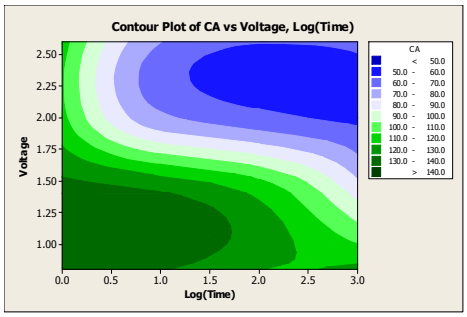

(A)

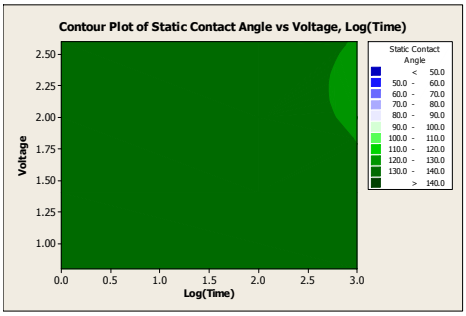

(B)

Figure 129. Contour plots of contact angle as a function of constant voltage aging. (A) GDL 1; (B) GDL 4.

The data suggests that GDL 1 has become oxidized and hydrophilic, while GDL 4 remained hydrophobic. In order to tell whether or not GDL 4 was oxidized the mass gain was also examined (Figure 130).

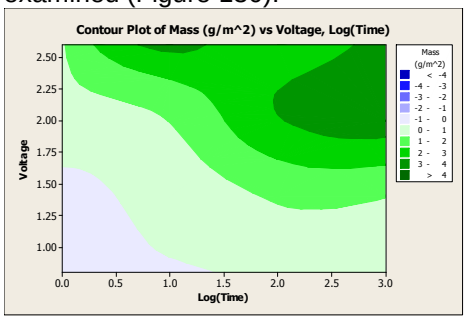

(A)

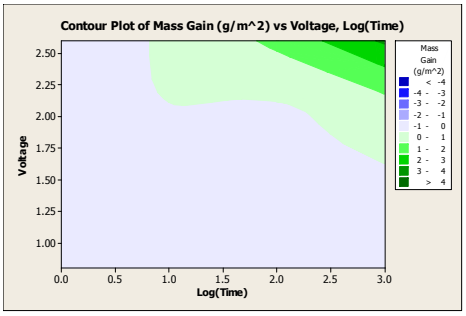

(B)

Figure 130. Contour plots of weight gain as a function of constant voltage aging. (A) GDL 1; (B) GDL 2.

Both GDLs experienced mass gain, although GDL 4 only had a high mass gain at very severe conditions. The mass gain is due to surface oxidation of the carbon in the micro layer. In addition to having a different carbon, GDL 4 uses a different binder and process in the dispersion preparation. As a result, a more uniform distribution of binder in the micro layer occurs in GDL 4. The uniform distribution keeps the GDL hydrophobic even though the carbon has been oxidized. The binder used in GDL 1 is not evenly distributed in the micro layer and thus become hydrophilic as the carbon oxidizes. Figure 131 shows backscattered SEM images which highlights the distribution of binder in the micro layer.

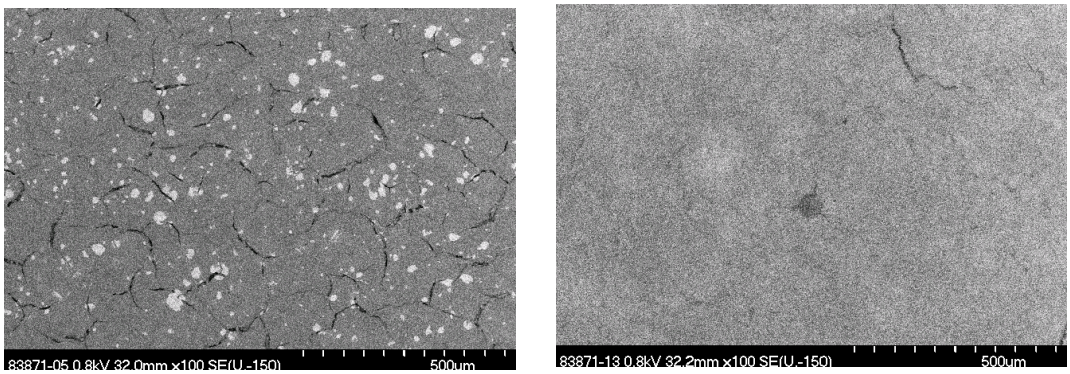

(A) (B)

Figure 131. SEM images of GDL 1 (A) and GDL 4 (B) microlayer.

The electrical resistance was also measured on the aged GDLs. An increase in the electrical resistance was seen as a function of time and voltage (Figure 132). This fact again shows that a surface oxidation exists on the GDL surface. Both GDLs are oxidizing at very high voltages and long times, although GDL 1 starts to oxidize at lower voltages and shorter times than GDL 4.

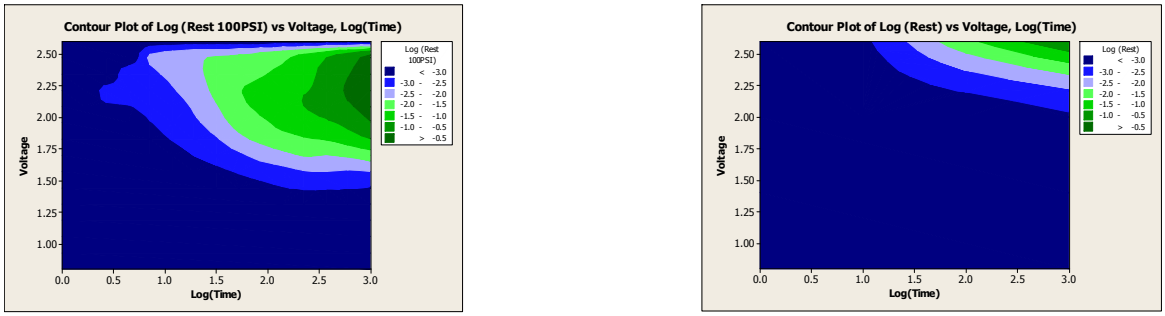

(A) (B)

Figure 132. Contour plots of electrical resistance as a function of constant voltage aging. (A) GDL 1; (B) GDL 4.

Fuel cell performance was measured at the different oxidation levels on GDL 1 and 4. The testing was done at 70℃ using H_2 and Air at ambient pressures as fuel. The flow rates were 800 sccm on the anode and 1800 sccm on the cathode. Both flows were fully saturated. From the polarization curves, the limiting current density was recorded at 0.3 volts. The limiting current density of GDL 1 changed from approximately 900mA/cm^2 to 400mA/cm^2 (Figure 133). The reduction of the limiting current density is a direct consequence of increasing the mass transport resistance. Oxidation of the micro layer is responsible for the increase in mass transport resistance. In contrast, the limiting current density of GDL 4 changed from approximately 1100mA/cm^2 to 1000mA/cm^2 (Figure 134). As the sample was aged, the oxidation stability of GDL 4 yielded superior MEA performance.

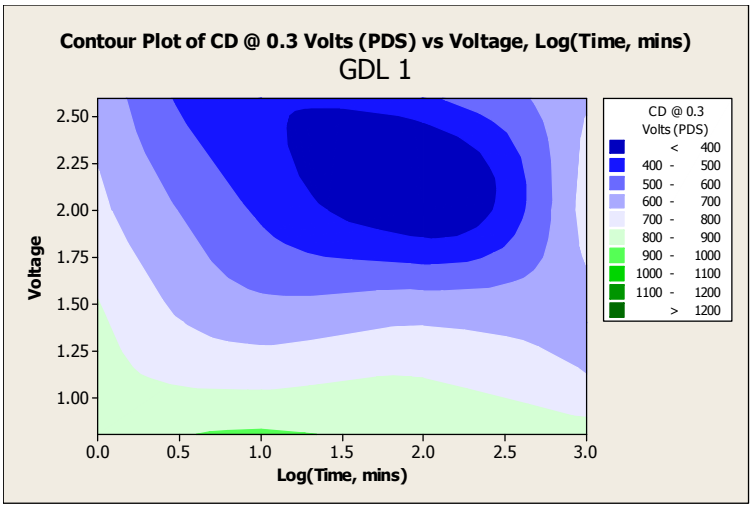

Figure 133. Contour plot of current density at 0.3 V as a function of constant voltage aging for GDL 1.

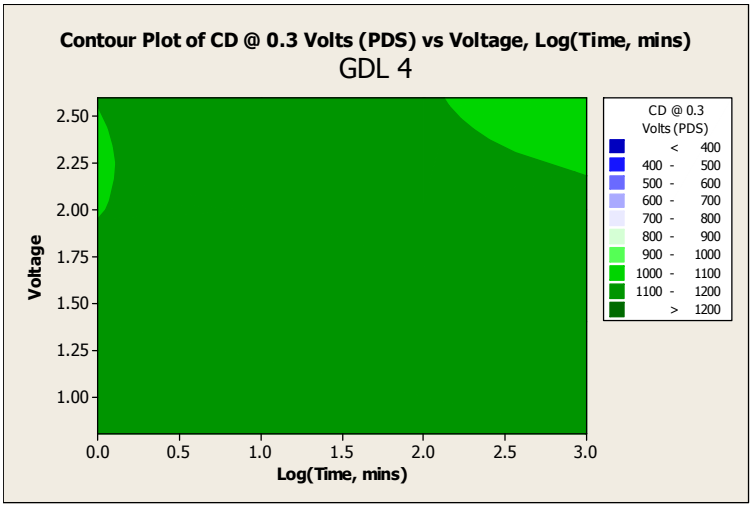

Figure 134. Contour plot of current density at 0.3 V as a function of constant voltage aging for GDL 4.

GDL oxidation is one mechanism for MEA performance decay. A function between applied voltage and time was related to micro layer oxidation. The level of oxidation was measured by two different methods, contact angle and the number of corrosion coulombs. The time to reach a certain level of corrosion coulombs at a set voltage can be used to describe the failure point/oxidation level of the GDL One method to quantify the lifetime of the GDL is to look at how the contact angle changes during oxidation. A decline in the contact angle has been correlated to fuel cell performance, in particular as the contact angle falls the mass transport resistance of the MEA increases (see Figure 129 and Figure 133). The static contact angle of GDL 1 shows a sudden change in hydrophobicity of the micro layer once the sample has experienced approximately 50 coulombs (Figure 135). The onset of the hydrophobicity change was selected as the failure point for the micro layer. In order to define the relative stability of one GDL to another, a stability factor was defined as the time for GDL A at a given voltage X to reach 50 coulombs divided by the time for GDL 1 at a given voltage X to reach 50 coulombs or mathematically as:

Stability Factor = Time to 50 Coulombs $_{GDL\ A,Volts}$ / Time to 50 Coulombs $_{GDL\ 1,Volts}$.

The stability factor for GDL 4 is shown in Table 31. The data in Table 31 clearly indicates the oxidative stability superiority of GDL 4 compared to GDL 1. In essence, the data indicates that GDL 4 is over 631 times more stable than GDL 1 at 2.0 Volts. As a result of its inherent stability, GDL 4 was selected as the final GDL design.

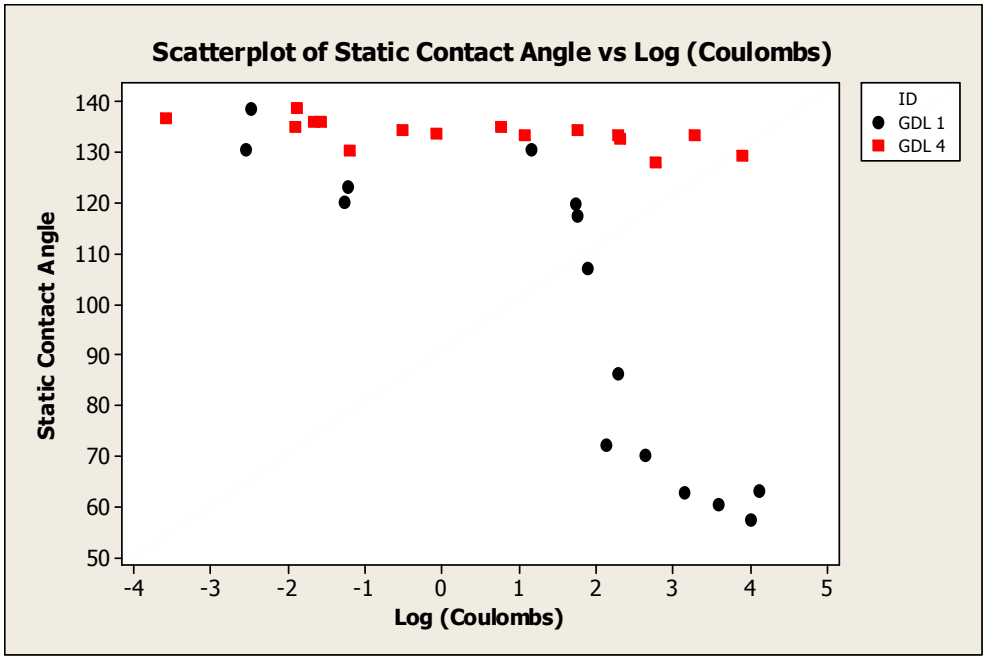

Figure 135. Contact angle versus coulombs.

Table 31. Stability factor of GDL 4.

Applied Voltage (Volts)	Stability Factor
2.6	12
2.0	631

Optimization of Final GDL Design

GDL 4 was selected as the final GDL design for this project, based upon its inherent durability in comparison to other designs. Once selected, a design of experiments was performed on the GDL 4 binder loading in the backing and micro porous layer thickness to determine if performance of the GDL could be increased without sacrificing durability. Fuel cell results were collected at the following conditions 70℃ cell, 10 0%/100% RH, 0/0psig, 1.25/2.5 stoichiometry. As the current density increased a shift between the dominant variable occurred. Figure 136 shows the response at 0.2 A/cm^2. At low current densities, 0.2 A/cm^2, the micro layer thickness was the key parameter that dictated the performance. Thinner micro layers improved performance. An optimum micro layer thickness was not revealed in the design space examined. As the current density increases, both the micro layer thickness and the backing treatment level influence the performance of the MEA, at 0.6 A/cm^2 (Figure 137). At 1A/cm^2, backing treatment level became the dominate parameter (Figure 138). As a result of the DOE, GDL 4 design was locked. The micro layer thickness was set to 250 (roll speed %) and the % FEP in the backing was set at 5%.

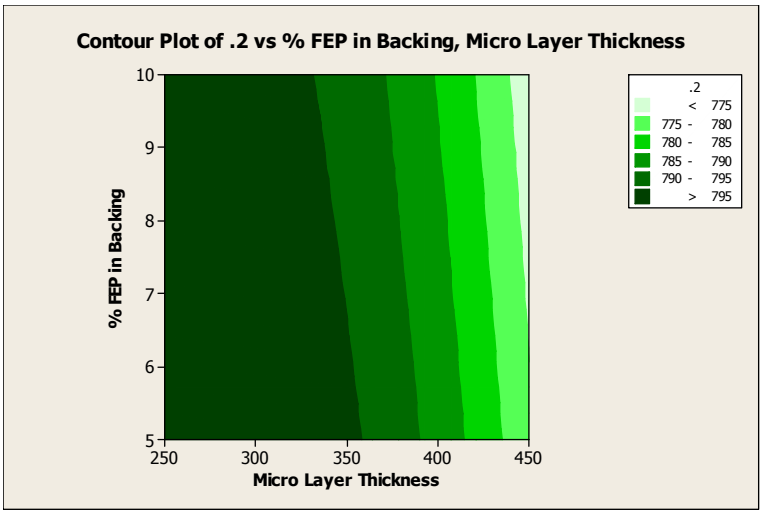

Figure 136. Results of GDL 4 Optimization DOE - fuel cell performance versus binder level in backing and micro porous layer thickness at 0.2 A/cm^2.

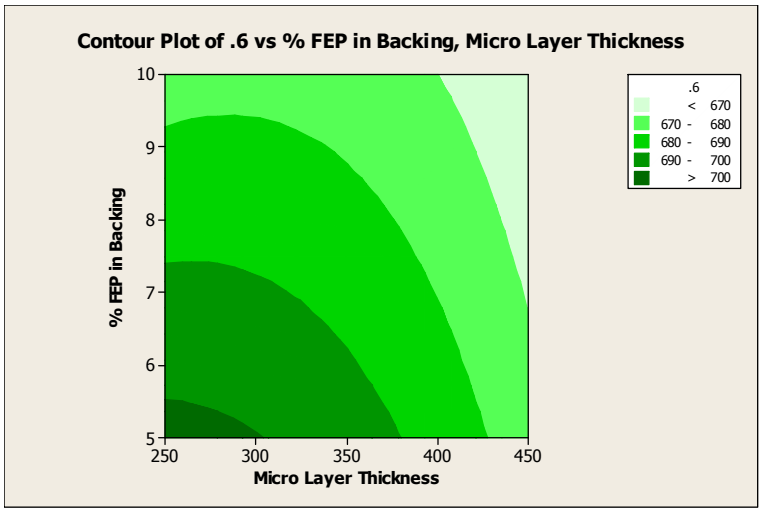

Figure 137. Results of GDL 4 Optimization DOE - fuel cell performance versus binder level in backing and micro porous layer thickness at 0.6 A/cm^2.

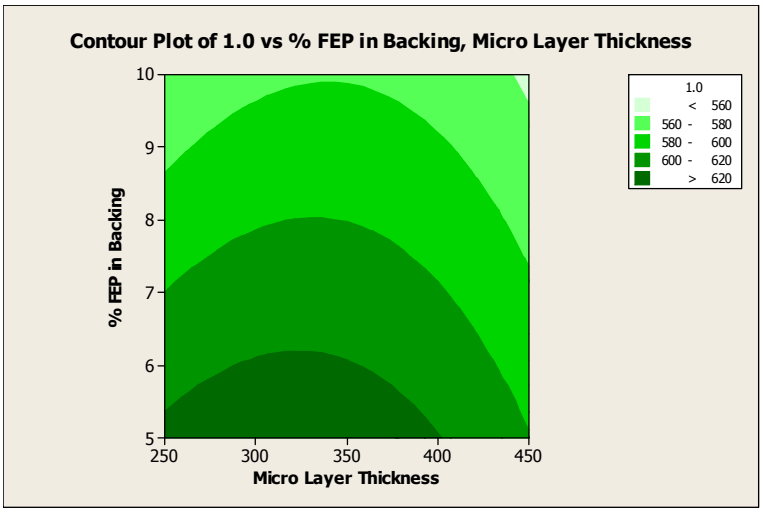

Figure 138. Results of GDL 4 Optimization DOE - fuel cell performance versus binder level in backing and micro porous layer thickness at 1.0 A/cm^2.

GDL 4 has improved oxidative stability and good fuel cell performance. However, physically bonding GDL 4 to a CCM proved to be impossible with standard bonding parameters due to low surface energy of the GDL and reduced surface roughness. The samples bonded initially, but in a short time the bond fails. GDL 4 needed improvement if a fully bonded MEA is desired. In a previous design, GDL 2 used binder A in the micro layer. GDL 2 was able to bond to a CCM without issues. GDL 4's micro layer used binder B. A new GDL design (GDL 5) was created to address the bonding issue and it uses a mixture of binder A and B in the micro layer. Laboratory samples were made to prove the feasibility. The resulting MEAs bonded. GDL 5 is very oxidative stable, as shown in Table 32.

Table 32. Stability factor of GDL 5

Applied Voltage (Volts)	Stability Factor
2.6	4
2.5	6
2.4	8
2.3	13
2.2	21
2.1	36
2.0	87
1.9	134
1.8	288
1.7	654
1.6	1549

Initial fuel cell results show no difference between GDL 4 and GDL 5 (Figure 139). MEA fabrication was different for GDL 4 and 5. The same procedure was used, but different results were obtained – GDL 4 did not bond, but GDL 5 did bond. Thus, GDL 5 formulation was selected as the final GDL design to be used in the final system test MEAs.

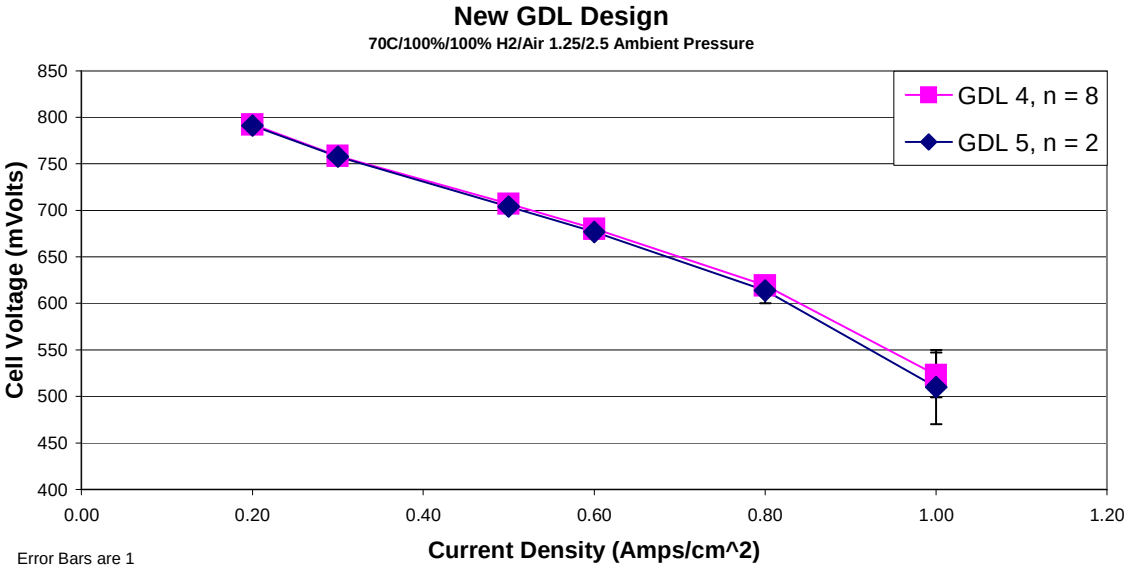

Figure 139. Fuel cell performance of GDL 4 and GDL 5.

Summary

A varity of accerated test methods were used to identify an optimized GDL. Approximately 650 ft of GDL 5 have been manufactured in 3M's Stillwater, MN manufacturing plant. These GDL were then used for the remainder of the program for material evaluations and durability studies

A patent application was filed on the use of a melt-processible and non-melt processible binder in the micro layer.(US2006-0222840-A1)

2.2.5 GDL References

[64] D. K. Owens and R. C. Wendt, *J. Appl. Polym. Sci.* **13**, 1791 (1969).
[65] D. H. Kaelble, *J. Adhesion* **2**, 66 (1970).
[66] D. H. Kaelble, *Physical Chemistry Adhesion*. Wiley, New York (1971).
[67] J. A. Mann, Jr.: "Digital-Computer-Oriented Numerical Analysis in Surface Chemistry" in E. Matijjevic, R. J. Good (Eds) "Surface and Colloid Sciences", vol. 13.
[68] J. R. Wolberg: "Prediction Analysis" D. Van Nostrand Company, Princeton, New Jersey, 1967.
[69] M. C. Leverett, in Trans. A.I.M.E., 142, pp. 341-358 (1941).
[70] Z. H. Wang, C. Y. Wang and K. S. Chen, in Journal of Power Sources, 94, pp. 40 –50 (2001).
[71] H. W. Brown, in Trans. A.I.M.E., 192, pp. 262 (1956).
[72] F. A. L. Dullien: "Porous Media; Fluid Transport and Pore Structure", Academic Press, 1979.
[73] T. V. Nguyen *et al*. in ECS Transactions, 3 (1), pp 415-423 (2006).
[74] W. G. Anderson, in Journal of Petroleum Technology, pp.1283-1299 (1987).

2.3 Catalyst/Electrode Development

Introduction

Unlike the previous two sections on membrane and GDL, the focus of this section is not the development of new catalysts for fuel cell operation. Instead the focus of this section is the characterization of commercially available catalysts to determine which offers the best durability and performance combination for use under this project. To the first approximation, the performance of a MEA is proportional to the catalyst geometric surface area, also referred to as the SEF or surface enhancement factor. SEF is defined as the catalyst surface area divided by the geometric active area (cm^2/cm^2) where the catalyst surface area is measured by an integration of the crossover, electronic short and double layer corrected hydrogen adsorption-desorption currents of the cyclic voltammetry. In order to minimize performance decay, it is important to maintain the initial catalyst surface area. There are a number of mechanisms that can lead to catalyst surface area loss – support oxidation, catalyst agglomeration, catalyst poisoning and catalyst dissolution. Additionally, catalyst can impact membrane durability via peroxide formation. In that respect, the role of the catalyst induced membrane degradation will be examined as observed by changes in the fluoride concentrations found in the effluent water.

2.3.1 Cathode Electrodes

Support Oxidation

One of the major issues facing Pt/C catalysts is the instability of the carbon support in the fuel cell environment[75]. The carbon is thermodynamically unstable in the presence of Pt at elevated temperatures. In fact, the Pt catalyst catalyzes the combustion of carbon to carbon dioxide in the presence of oxygen via a chemical process. Platinum can also electrochemically oxidize carbon to carbon dioxide at elevated potentials (> 0.9 V) where the potential can depend on the carbon type. While these potentials do not exist in a fuel cell under normal steady state operation, the conditions of start/stop or fuel starvation can result in local potentials where the cathode potential is > 1.0 V versus the standard hydrogen potential. As a result, it is necessary to evaluate different cathode catalysts to determine their oxidative stability. To this end, we developed a 1.2 V test to evaluate the oxidative stability of commercially available catalysts supports.

The 1.2 V test utilizes a $50cm^2$ MEA under H_2/N_2 at 250/500 sccm, and 80^oC dew points. During the test, the cell temperature is held at 80°C. The testing is done using a potentiostat to make potentiostatic measurements at 1.2 volts vs. the hydrogen reference electrode for five hours at a time. Between the five hour scans, cyclic voltammetric (CV) scans are carried out at 100 mV/s from 20 mV less than open circuit voltage to 1.2 V. From the CV scans, Figure 140, the electrochemical surface area is determined. Notable features in the CVs are the rise of a small peak at about 0.57 volts vs. SHE related to carbon oxidation and the initial large change in the double layer capacitance which then stays at about a constant amount despite further decreasing catalyst surface area. The double layer capacitance should decrease with decreasing surface area as they are directly proportional. The increasing double layer capacitance and carbon peak in the CV are unique to this mechanism of catalyst surface area loss. In this manner, the surface area is plotted versus time to determine the stability of the carbon support. In addition, MEA fuel cell performance was periodically measured under H_2/Air at 800/1800 sccm, 80°C cell temperature and 100% inlet gas relative humidity. An initial survey of ten catalysts of different carbon support, metal loading and vendor in shown in Figure 141. The data clearly indicate that the oxidative stability is dependent on support type. The fuel cell performance of three of the

catalysts is shown in Figure 142. As expected, catalyst J, which is the most stable catalyst in Figure 141, has the least fuel cell performance decay in the Figure 142. In order to confirm the validity of the 1.2 V test, two of the catalysts, A and J, were tested for 500 hours in a fuel cell. At the end of the 500 hour test, catalyst A had lost 25% of its surface area while catalyst J had only lost 5% of its surface area. Further, the performance degradation for the more stable catalyst support was half that of the less stable support. It must be noted that there was a large difference in initial performance however an extrapolation of the 500 hour test data would show the more stable catalyst J's performance surpassing catalyst's A performance at about 1000 hours.

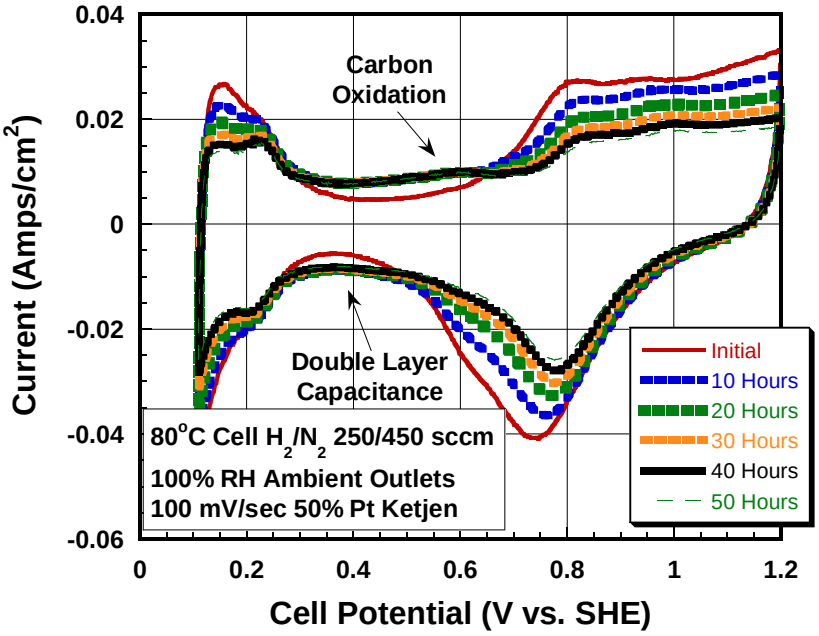

Figure 140. Cyclic voltammetry scans carried out between 5 hour constant 1.2 volts scans at 80°C cell temperature.

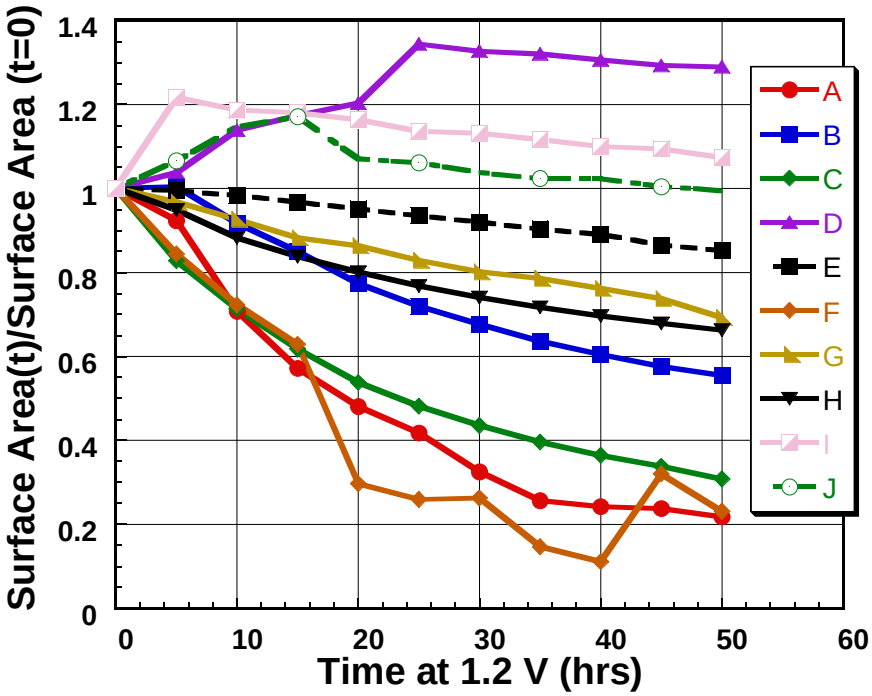

Figure 141. Impact of catalyst type (vendor, metal loading and support) on catalyst oxidative stability.

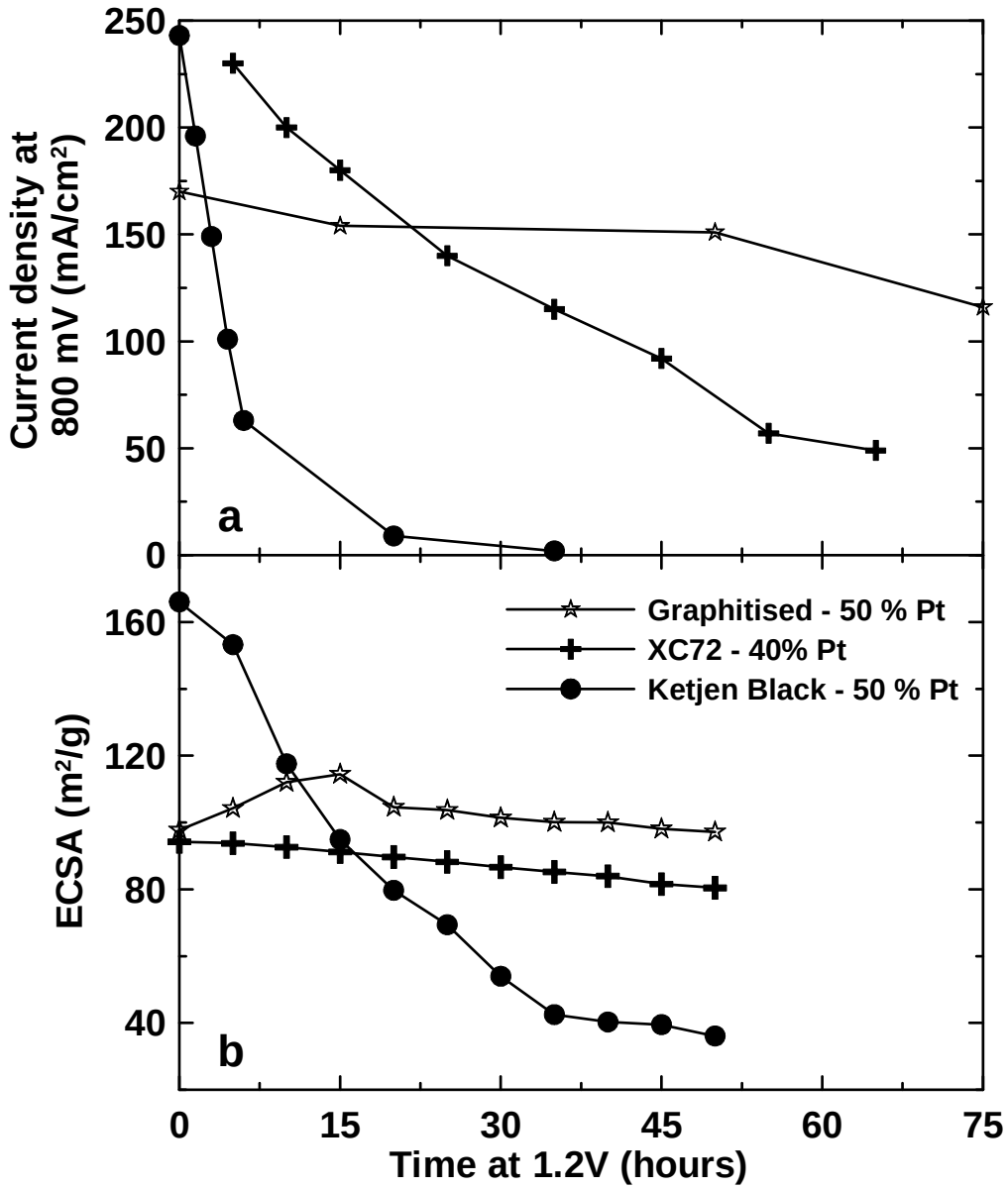

Figure 142. The fuel cell performance (a) and catalyst surface area loss of catalyst A (Graphitized), E (XC72), and J (Ketjen) between 1.2 V accelerated test scans.

The results from the first survey indicated that catalyst support type was likely the most important variable. However, since the catalysts from the first survey were made by different vendors and contained different Pt/C loadings and carbon supports, it was unclear if that was indeed the case. As a result, two additional surveys were completed. For these surveys, a vendor supplied six catalysts on different carbon supports at the same 50% Pt/C loading and a second vendor supplied different metal loadings on the same carbon type. The results of 1.2 V test for the different carbon supports at constant metal loading is shown in Figure 143 and the results for the variable metal loading on the same carbon are shown in Figure 144. From Figure 143 it is clear that carbon support has a major impact of catalyst oxidative durability. As the support surface area is reduced, the oxidative stability of the catalyst is increased. However, this does not mean that he best catalyst for fuel cells should use the lowest surface area catalyst support. A negative impact of the lower carbon support is lower fuel cell performance. As a result, one most balance the durability requirements and the performance requirements of the fuel cell application. From

Figure 144 it is clear that lowering the catalyst metal loading decreases the oxidative stability. Although this result was unexpected, it can easily be explained. At low catalyst metal loadings, the Pt particles are very small and well dispersed across the surface of the carbon. As the metal loading is increased, the Pt particle size increases due to agglomeration and the Pt is not well dispersed. As a result, at higher metal loadings there is less Pt surface area in contact with the carbon support in comparison to low metal loadings. Since Pt is responsible for the catalytic oxidation of the carbon, less Pt surface area in contact with the carbon results in less carbon oxidation. In order to understand our accelerated test and the mechanisms behind it we also selected one catalyst and looked at the loss of SEF as a function of the working electrodes gas humidification level. What we observed can be seen in Figure 145. There is a clear trend that increasing working electrode gas humidification leads to faster catalyst surface area loss. This result is not unexpected as the source of oxygen for the catalyst/support oxidation is water at these potential.

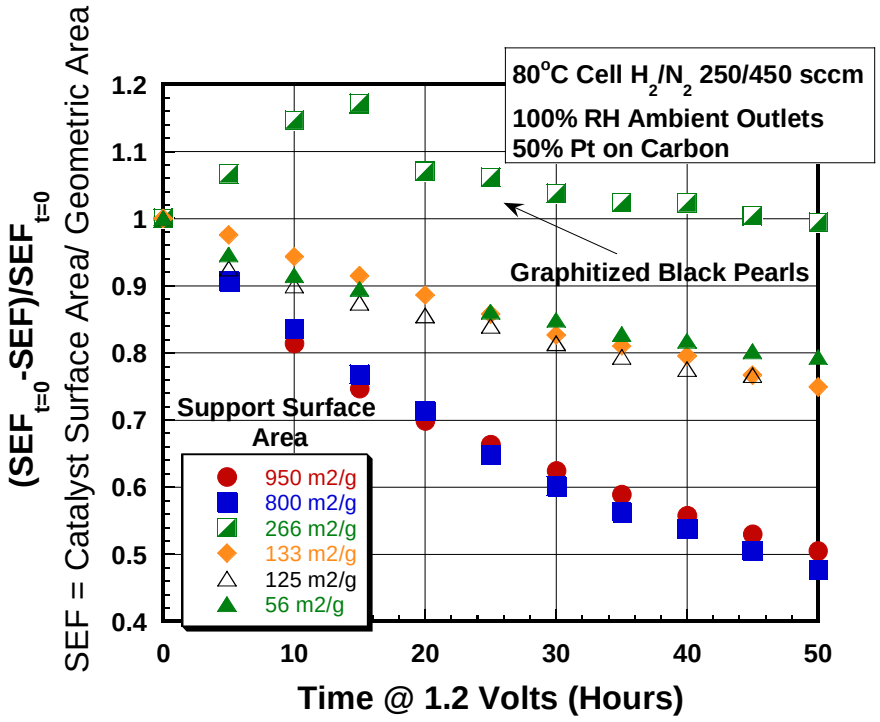

Figure 143. Impact of catalyst support type on oxidative stability for 50% Pt/C catalyst.

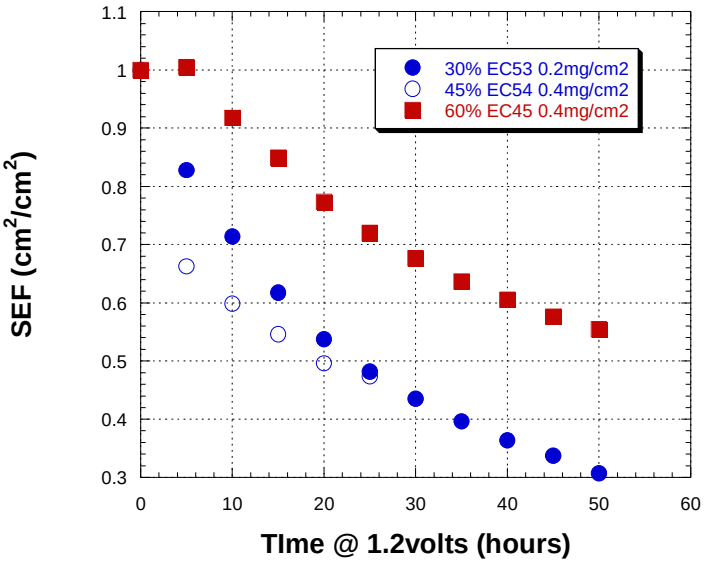

Figure 144. Impact of catalyst metal loading on oxidative stability.

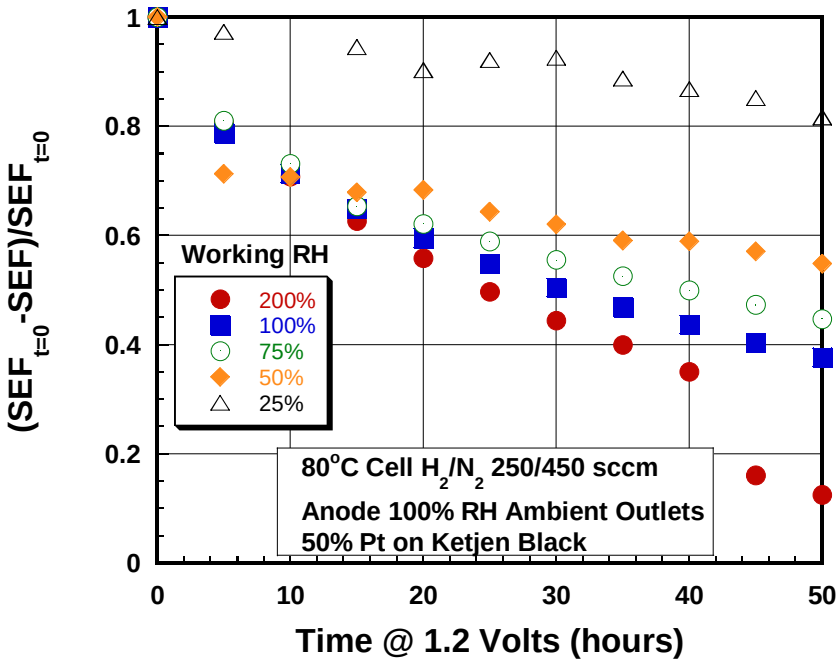

Figure 145. Catalyst surface area loss for one catalyst as a function of the working electrode relative humidity.

Cycling Stability

It is well known in the literature that platinum dissolution due to voltage cycling is a cause of platinum surface area loss[76,77]. In our survey of catalysts we examined different variables that might affect this outcome. Using our accelerated test, which is modeled after Gastieger's[76], we explored variables such as gas humidification, crystallite size, alloys, and carbon support to see how they affected the catalyst surface area loss mechanism. The protocol used had an aging script of 0.6-1.0 Volts vs. SHE with a 25 mV/sec sweep rate for 500 cycles carried out ten times. Between each set of 500 aging cycles, diagnostic CVs were made sweeping at 100mV/sec between 0.1 and 1.0 volts vs. SHE in order to determine the surface area.
Figure 146 shows the diagnostic CVs carried out between sets of cycles for a 50% Pt on a Ketjen carbon while Figure 147 shows the aging cycle progression. Note that unlike the 1.2 volt steady state, here the double layer does not increase nor does the peak associated with carbon oxidation become resolved. Figure 148 best illustrates the differences in the changes in the double layer capacitance as a function of test time for the two protocols and the same electrode configuration. Each data point represents 5 hours for the potentiostatic and 500 cycles for the potentiodynamic. In the potentiodynamic scanning the double layer capacitance decreases at first though not as much as it should given the large surface area loss while the steady state 1.2 volts scans has a precipitously

Studies were carried out looking at the effects of crystallite size, working electrode gas humidification, catalyst support type, and cell temperature. The strongest response seen was to that of catalyst crystallite size (as determined by vendor from XRD).
Figure 149 shows these results. Larger crystallites are less susceptible to platinum dissolution which is not surprising based on geometric and thermodynamic factors. Geometrically, larger crystallites have less exposed catalyst surface per total catalyst amount so they will be less reactive. Thermodynamically, larger crystals are more energetically stable. In this study some alloys were evaluated and they appeared more stable generally because of their larger crystallite size, however, there could be other factors that also contributed to their increased stability in this accelerated test protocol. The effect of the working electrode relative humidity was examined using the cycling protocol as it was with the steady state 1.2 volt test. This time, as Figure 150 shows, there was no significant difference in catalyst loss as a function of working electrode RH. It is surprising that a water based dissolution process would show no change in catalyst loss with changing RH.

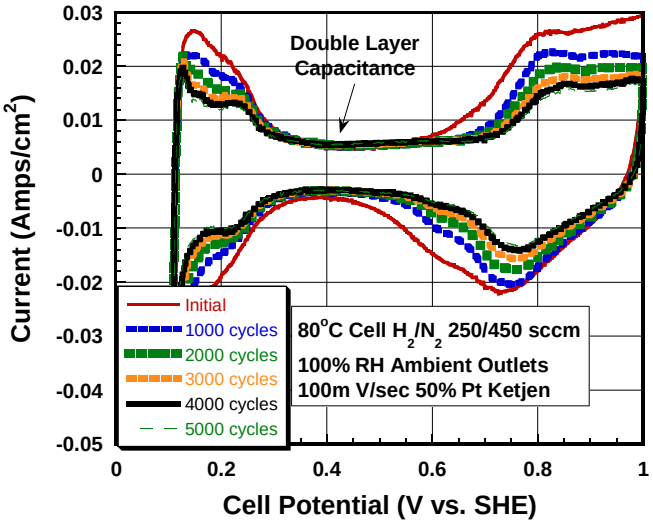

Figure 146. Example of the impact of the voltage cycling test on catalyst surface area stability.

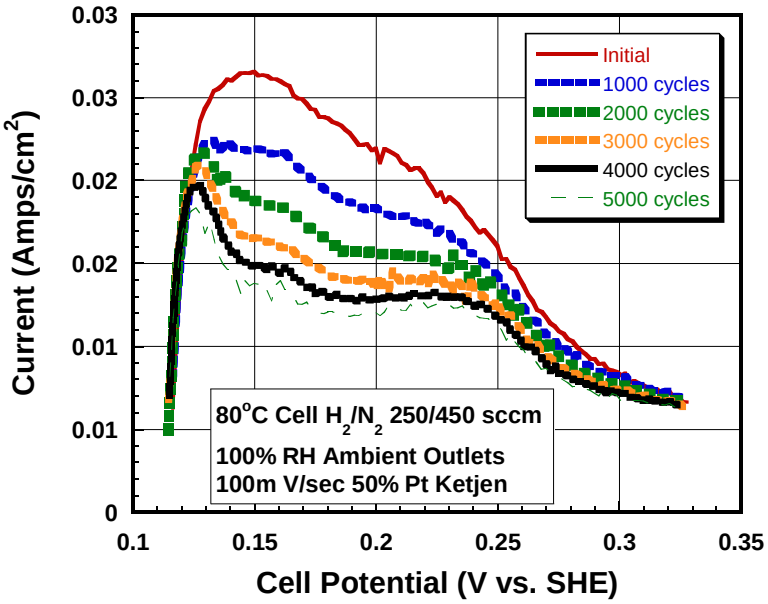

Figure 147. Blow-up of Figure 146 highlighting the loss of Pt surface area.

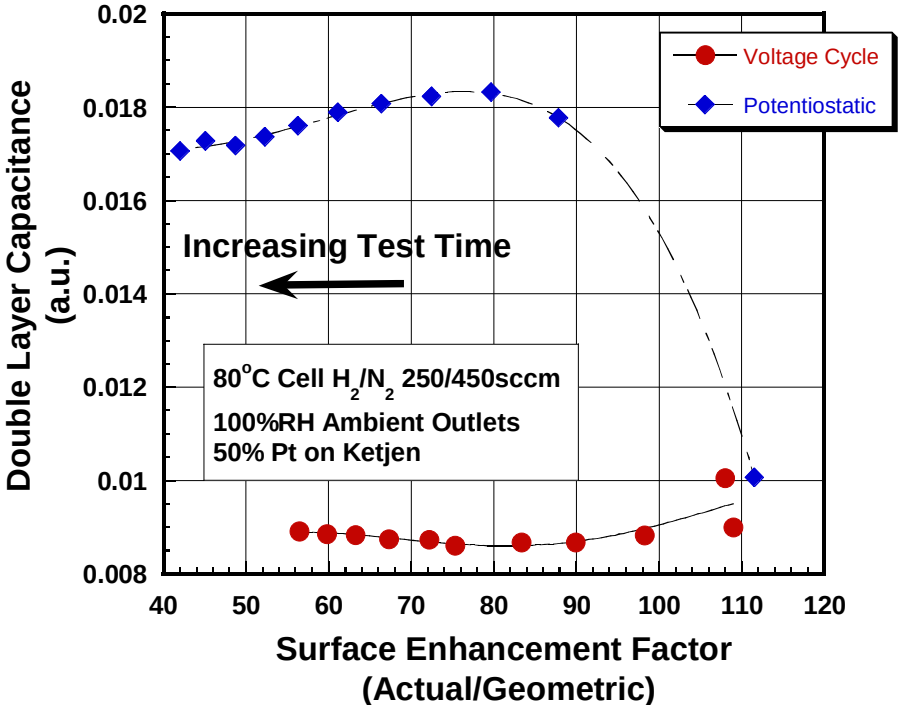

Figure 148. Comparison between potentistatic and potential cycle aging tests.

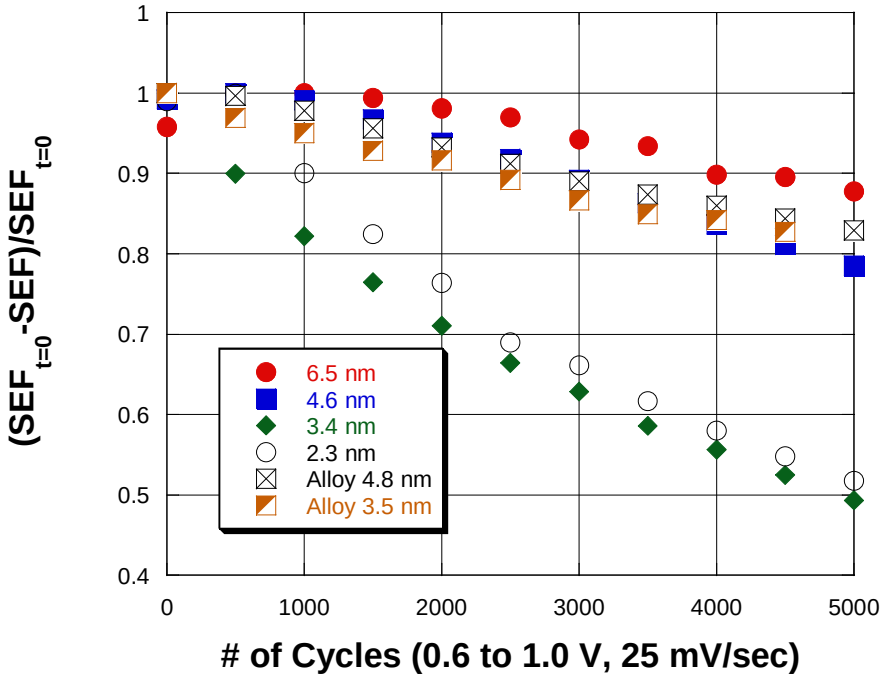

Figure 149. Impact of Pt crystallite on catalyst stability in voltage cycling test.

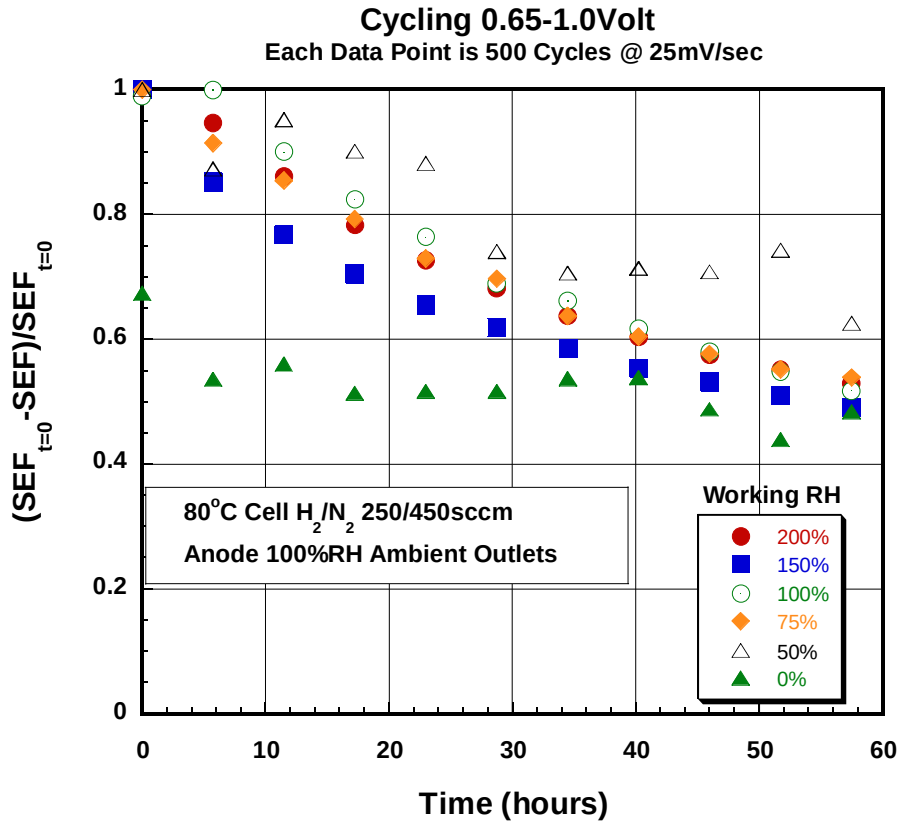

Figure 150. Impact of relative humidity on catalyst stability in voltage cycling test.

Fuel Cell Testing Verification of Accelerated Testing

In order to validate the accelerated test protocols, fuel cell testing was carried out on one lot of catalyst CCB (catalyst coated backing) to look at the loss of catalyst surface area as a function of test conditions. The first series of tests were carried out as a function of cell temperature at either constant voltage of 750mV or voltage cycling. The voltage cycling consisted of looping a series of one minute long potentiostatic scans at 750, 810, and 875 mV. All experiments for this series were carried out with fully saturated inlet gas streams with H_2 and air flows of 250/833 sccm. Cell outlet gas pressure was increased with increasing cell temperature to maintain inlet saturation and a fixed gas water content. Electrochemical surface area (ECSA) measurements were carried out periodically during fuel cell operation to determine the surface area. ECSA measurements were carried out in a series of three measurements at 40°C cell temperature and 70°C gas inlets. The first in the series went from 0.1 to 0.65 volts vs. SHE, the second from 0.1 to 1.2 volts vs. SHE and then the third repeated the first. The purpose behind this was to derive a cathode surface area before and after electrochemically cleaning it by oxidizing likely contaminants by going to 1.2 volts. The last ECSA represents best the true catalyst surface area. It was observed that the difference between the third and first surface areas decreased with increasing test time and decreased faster for higher cell temperatures. The loss of surface area under fully saturated test conditions was generally linear with time. This surface area loss rate is plotted as a function of 1/T for both test conditions – steady state and voltage cycle in Figure 151. In general, the higher the cell temperature the faster the catalyst surface area loss for both the steady state and the cycled potential. Voltage cycling for this catalyst had approximately an order

of magnitude surface area loss, though the difference in rates decreases with increasing temperature. The loss of performance tracked well with the rate of catalyst surface area loss. All the effluent water was collected and fluoride emission rates (FER) increased slightly with increasing temperature but showed little to no difference between operating conditions.

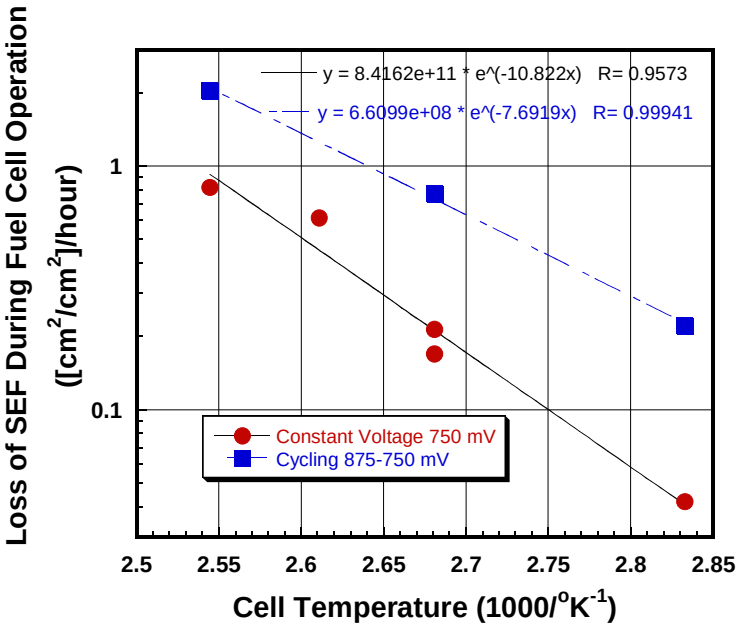

Figure 151. Arrhenius plot of surface are loss versus temperature.

Analysis of the shape of the CVs generated after the fuel cell tests is consistent with the accelerated tests used for probing each of the different mechanisms – support oxidation and platinum dissolution. Figure 152 highlights this showing the same differences in CV that we saw in the accelerated tests for the steady state potential - increased double layer and peak at 0.57 vs. SHE. The cycled CV does not show these features but does show larger relative changes in different platinum hydrogen absorption peaks in the CV.

Figure 153 Figure 153 demonstrates this showing with the cycling larger changes in (100) and (110) then the (111) facets. This result is consistent with the accelerated cyclic observations. What was perhaps not consistent with the accelerated test is the effect of humidification level on the loss of cathode surface area. Only two samples were tested as fuel cells at a reduced humidity under the potentiostatic 750mV test protocol. Figure 154 shows that the SEF decrease far more rapidly then the fully humidified samples but seemed to reach a plateau in SEF loss, one that we have not observed in fully saturated testing. The changes in double layer capacitance, Figure 155 may offer a clue, as the abrupt increase in the double layer capacitance seems to correlate with the plateau in surface area loss for the reduced humidity samples.

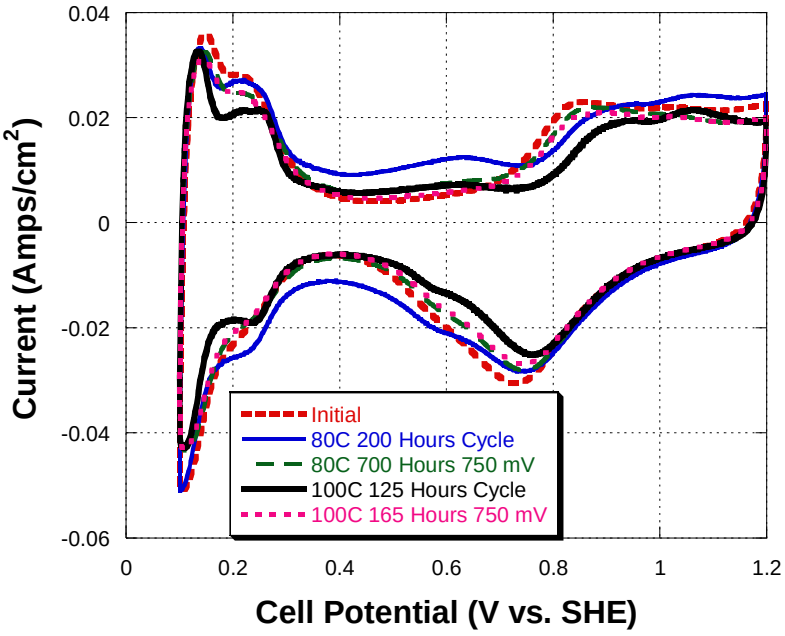

Figure 152. Cyclic voltamograms after fuel cell testing.

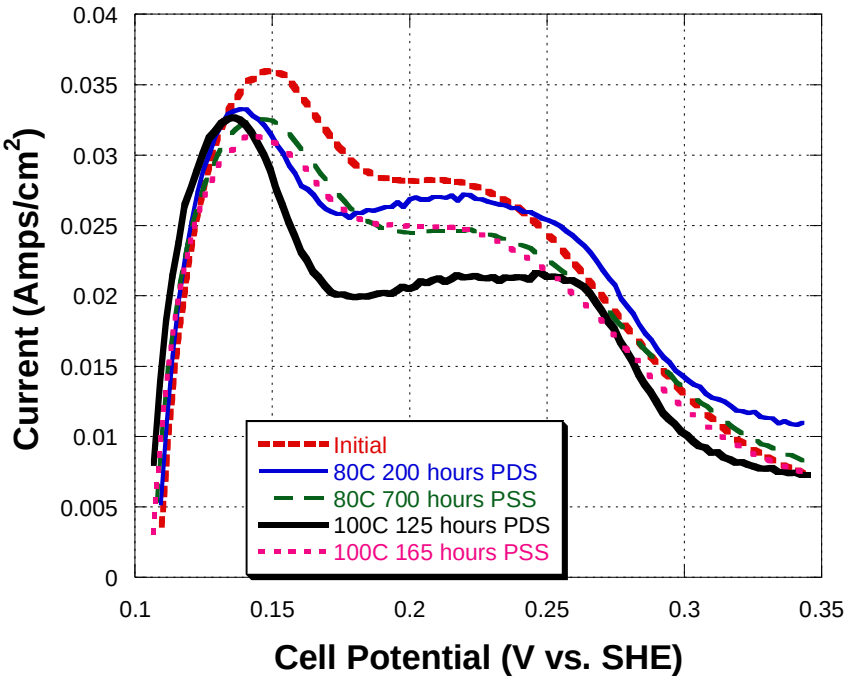

Figure 153. Cyclic voltamograms after fuel cell testing – Hydrogen adsorption region.

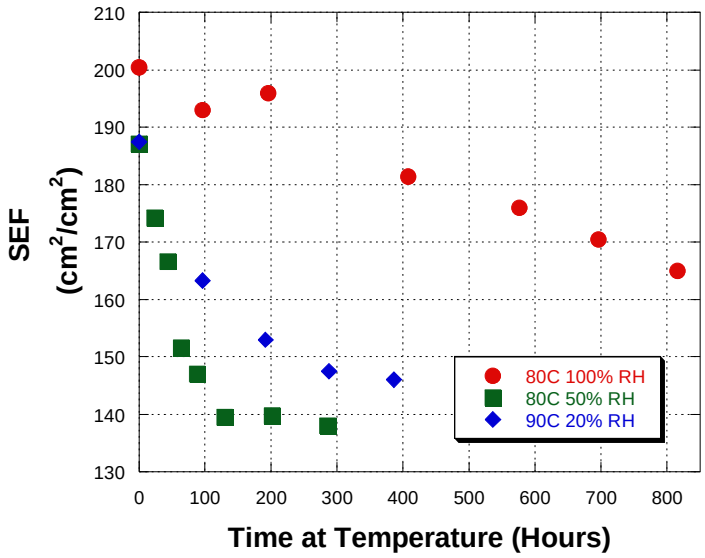

Figure 154. Plot of loss of surface area as a function of test time at various cell temperatures and relative humidities run at steady state 750mV.

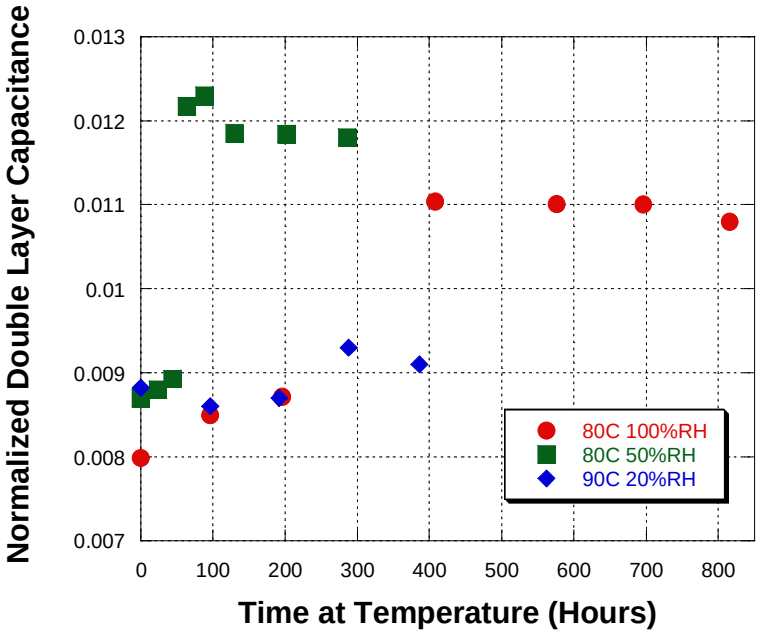

Figure 155. Plot of double layer capacitance as a function of test time at various cell temperatures and relative humidities.

Electrode Formulation

There are many factors that go into electrode formulation such as ionomer/carbon ratio, ionomer type and equivalent weight, use of surfactants/co-solvents, additives for peroxide mitigation, loading and most importantly processing. Many of these factors were explored for their influences on catalyst stability, performance and startup time. The first factor looked at was the I/C ratio applying both accelerated tests. No difference in degradation rate was observed over I/C ratios 0.4, 0.6, 0.8, and 1. In addition, we looked at CCBs and CCMs of the same catalyst type in both accelerated and fuel cell testing and saw no difference in the loss rate of catalyst.

An important factor in electrode formulation is the use of surfactants and additives to improve coating properties and perhaps catalyst utilization. The use of catalyst ink surfactants to facilitate coating consistency can have a strong impact on a number of different performance factors but they can have their strongest impact on MEA startup as not all of the surfactant is removed in drying and it or its byproducts need to be washed out of the MEA or oxidized by the cathode.

Figure 156 shows the impact on startup and final performance for a three different surfactants. It should be noted that this is the kinetic region of the polarization curve. Initial fuel cell testing of inks made with these additives indicated that there could be higher fluoride ion release with some of the additives but a later more thorough study showed no correlation with surfactant level.

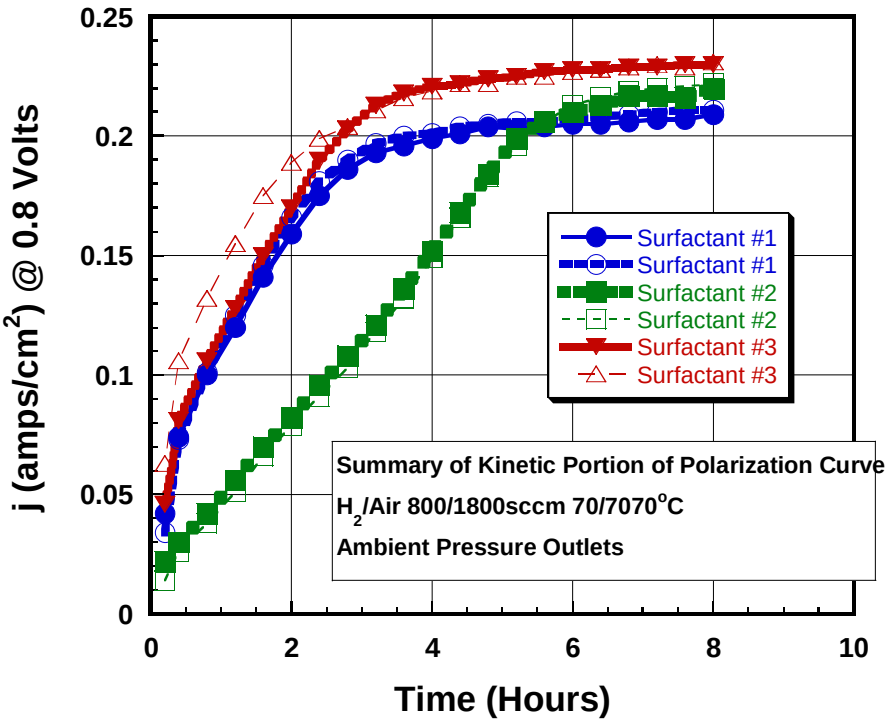

Figure 156. This plot shows the performance start up differences for three different catalyst ink surfactants as manifest by the measured current at 0.8 volts from a polarization scans taken at 70℃ cell operation.

Summary of Cathode Electrodes

In summary we developed accelerated cathode catalyst durability tests to probe the different mechanisms of catalyst surface area loss and verified that they were consistent with long term fuel cell durability test observations. Using these accelerated tests we explored a large number of commercially available carbon supported catalysts from five different vendors. Further, one

vendor supplied us with special catalysts to explore carbon supports with a fixed crystallite size and metals loading. What was observed was that the most stable catalysts would be those with the highest degree of graphitization and the largest crystallite size. The graphitization minimizes the support degradation and the large crystallite size minimizes the platinum dissolution with voltage cycling. Both of these solutions however have a negative impact on fuel cell performance so the selection of our cathode catalyst for durability testing had fuel cell performance as its counterbalance.

2.3.2 Anode Electrodes

Ruthenium Stability

The main durability issue facing anode catalysts is CO tolerance or more specifically, the loss of CO tolerance over time. The CO tolerance of Pt is improved by alloying Pt with Ru. The PtRu alloy is the industry standard for addressing CO tolerance however the long term stability is unknown. Numerous customers have reported the apparent loss of CO tolerance for MEAs/stacks that have run for several thousand hours[78]. In order to evaluate the stability of the PtRu alloy, three accelerated tests were developed. The first test involved holding the anode at greater than 1.3 V versus the standard hydrogen electrode. It is interesting to note that extended testing under 1.2 volts had no impact on the catalyst or the support. The second test involved operation at 10% air bleed (percent of total flow) and 1 A/cm^2 load for a cell operating in reformate pump mode. The third test involved continuous reformate pump at 0.5 amps/cm^2 with no air bleed and a 10ppm CO challenge. For all the accelerated tests, CO stripping voltammograms were periodically taken to monitor the change in the PtRu alloy. For the second and third tests anode overpotential as a function of time was also measured as a performance indicator.

From work prior to the start of this project, two anode catalysts were selected for evaluation based upon their performance under a variety of conditions. Both catalysts A and B performed similarly under air bleed test conditions, but catalyst B outperformed catalyst A under no air bleed with low levels of CO (< 10 ppm). The results of the 10% air bleed reformate pump for catalyst A is shown in Figure 157. Catalyst B showed no change in over 200 hours. Figure 158 for two different anode catalysts. Both catalysts exhibit loss of CO tolerance over time as evidenced by the reduction of the CO stripping peak and the shifting of the CO peak potential to more positive potentials. Both of these results indicate that the catalyst is becoming more ‘Pt like” indicating that Ru is being oxidized and transported into the membrane. In the beginning of the test both had the same initial anode overpotential but by the end of the test the catalyst with the large change in CO stripping voltammogram could no longer hold current while the other catalyst had less than a 50mV change in anode overpotential.

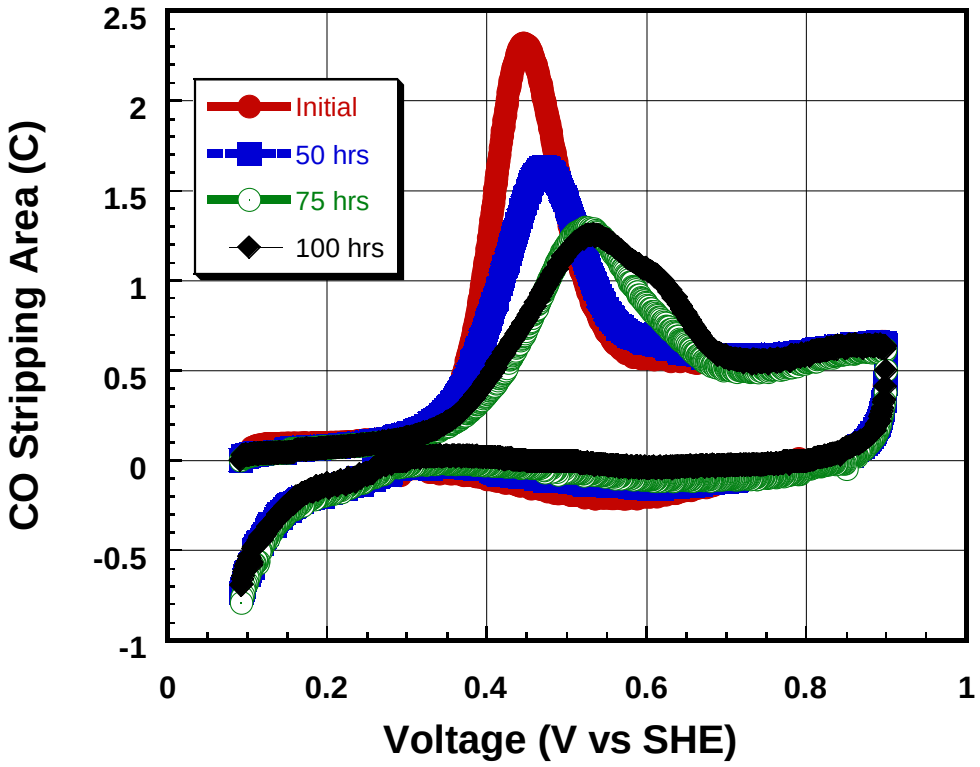

Figure 157. CO stripping results for anode catalyst A after reformate pump testing under a 10% air bleed challenge.

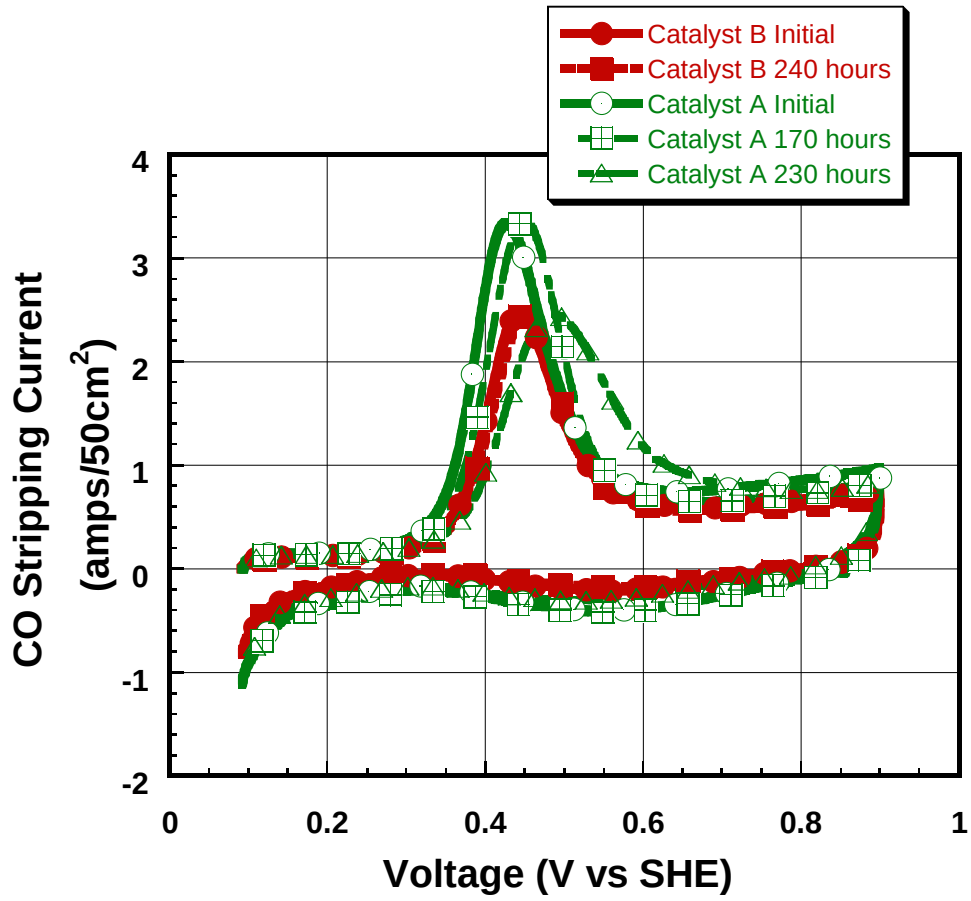

Figure 158. CO stripping results for anode catalyst B after reformate pump testing.

Typical results for the constant voltage test are shown in Figure 159. The results show that the catalyst is stable for extended periods of times at 1.2 V, but rapidly losses its CO tolerance as the potential is increased to 1.3 and 1.4 volts. Again, the reduction of the CO stripping peak and the shift of the CO stripping peak to more positive potentials are indications that the catalyst is losing Ru and becoming more 'Pt like'.

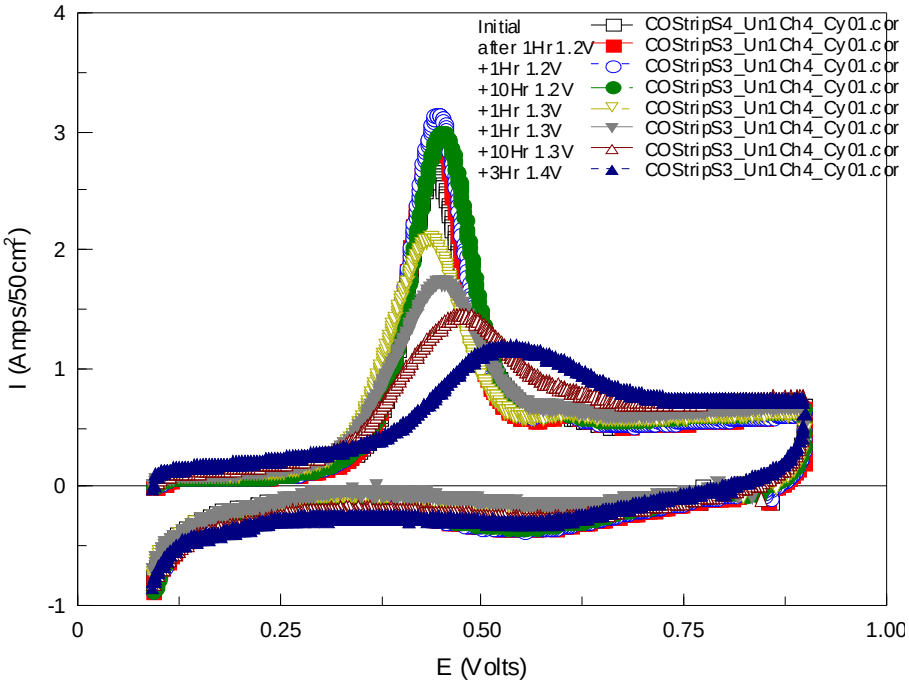

Figure 159. CO stripping results for anode catalyst A after accelerated constant potential testing.

Electrode Formulation

Far less time was involved in the study anode electrode formulation effects on durability then was spent on the cathode formulation. It was clear from the onset the most important challenges for durability had to do with cathode catalyst stability. Many of the lessons learned in the cathode development were applied to the anode with out testing as a matter of prioritization. Surfactants used in the anode ink coating process most often made their way to the cathode and caused the issues related to slow startup

.

Anode Summary

In summary, we evaluated two platinum-ruthenium based electrodes for use in the anode catalyst. The CO tolerance decreased over time under accelerated testing due to ruthenium dissolution resulting in a more “platinum like” catalyst surface. Two candidates performed similarly under air bleed conditions. However, catalyst B outperformed catalyst A under in the absence of air bleed and at lower air bleeds and showed far less susceptibility to Ru loss under accelerated testing protocols.

2.3.3 Catalyst’s Role in Membrane Degradation

Platinum is known to be a source of peroxide and also a peroxide decomposer. There are three mechanisms that have identified whereby peroxide is formed at a platinum site. The first mechanism has do to with gas crossover, where oxygen that permeates through the membrane and comes into contact with absorbed hydrogen on the surface of the anode platinum catalyst can make peroxide, this is also pertinent to the use of air bleed on the anode for increase CO tolerance with reformate. The second mechanism occurs at the cathode when the cell potential is less than 0.6 volts. This mechanism is thought to be exacerbated by contaminates on the

catalyst surface. The third mechanism is an offshoot of the first, where platinum has dissolved from the electrodes and migrates into the membrane where it serves as a center for peroxide formation with the adsorption of hydrogen and oxygen. All three mechanisms are most likely present at all times but their relative contributions vary with operating conditions and, to a certain extent, MEA construction.

An initial focus of the project involved collaboration between CASE University and 3M to explore the role of the cathode catalyst in peroxide production and fluoride emission rate (FER) during fuel cell operation. A matrix of catalysts were explored to examine the variable space of support type and metals loading. CASE examined the peroxide production for a number of catalysts via RRDE electrode studies. At the same time, the same catalysts were incorporated into MEAs and tested in fuel cells to determine the FER. An example of the RRDE data generated by CASE can be seen in Figure 160. The well known increase in the peroxide generated with potentials less than 0.6 volts is observed.

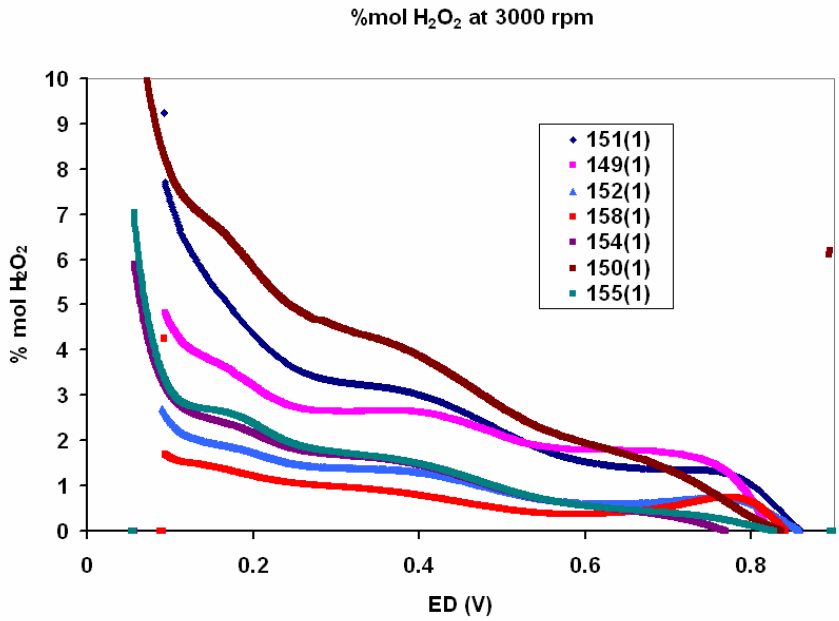

Figure 160. RRDE curves of seven different catalysts looking at % mole H_2O_2 as a function of metal's percentage on one carbon and a fixed metal's percentage on different surface area carbons.

No clear trend was observed for the catalyst in terms of mole% H2O2 in regards to catalyst metals loading or catalyst support type. Support BET surface areas were varied from 50 to 900 m^2/gram and metals percentage on one carbon was varied from 30 to 40 to 50%. If a trend was observed it was that the mole % of H_2O_2 may be a function of the catalyst surface area tested, Figure 161. This can be explained by platinum's role as a peroxide decomposer, where the larger the surface area the more platinum surface the peroxide has to sweep over in the RRDE.

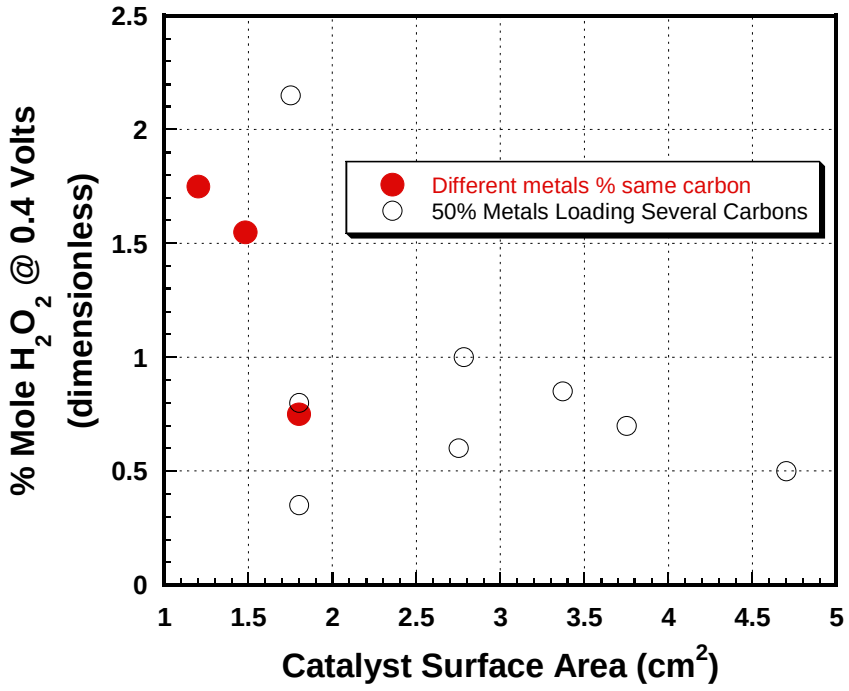

Figure 161. RRDE results for mole % H2O2 detected at the ring electrode as a function of the measured surface area of the disk electrode for each of the samples tested in Figure 160.

This would be consistent with the model of peroxide being decomposed by platinum, as the higher the surface area the more catalyst surface area the peroxide has to navigate through before it hits the ring. The same set of catalysts was tested as MEAs at 80/7070°C constant voltage 0.4 volts test conditions where the effluent water was collected and FER was determined. The experiments showed no clear trends and the results were most likely colored by the poor performance of some of the catalysts which led to variable cell outlet RH and the differences in surface area. Unfortunately surface areas were not measured in the experiment. Based on subsequent studies, a surface area was found to be one of the more important factors. The first results to hint at that were studies of the FER as a function of voltage for two different catalyst types. The results of that early study are plotted with Plug Power test results in Figure 162.

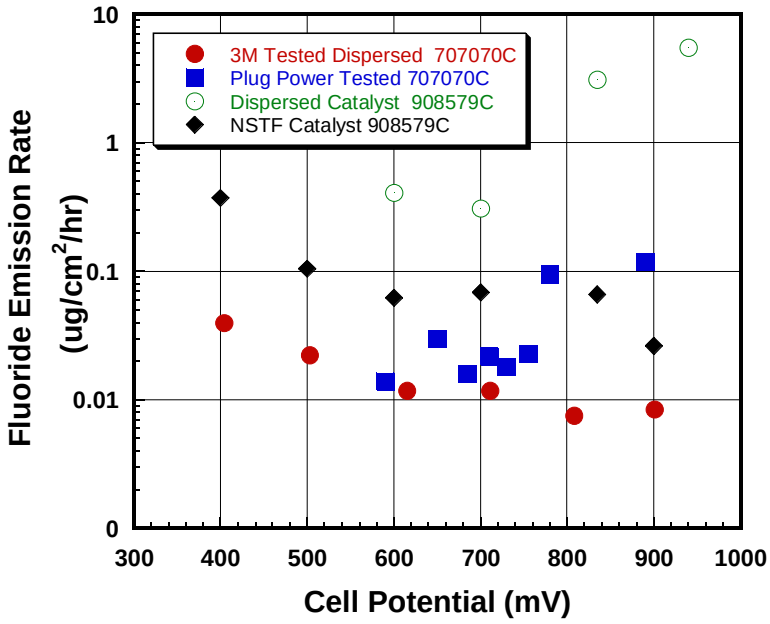

Figure 162. Voltage dependence of Fluoride Emission Rate (FER) as a function of test condition and catalyst type.

At cell voltages less than 700mV the results are very consistent with the increase in peroxide generated observed in the RRDE study. The lower FER of 3M's NSTF (nano structured thin film) catalyst could be explained by its higher activity and/or its lower surface area. The inconsistency of the highest potential FER most likely is related to the test protocol,

The possible relationship between catalyst surface area and FER was first hinted at in a study designed to look at voltage stability as a function of cathode loading. We tracked the effluent water fluoride ion concentration as a function of time during the study. The results are plotted in Figure 163. By eye, the relationship looks weak but by the Minitab™ analysis gave a Pearson coefficient of 0.19 which is significant.

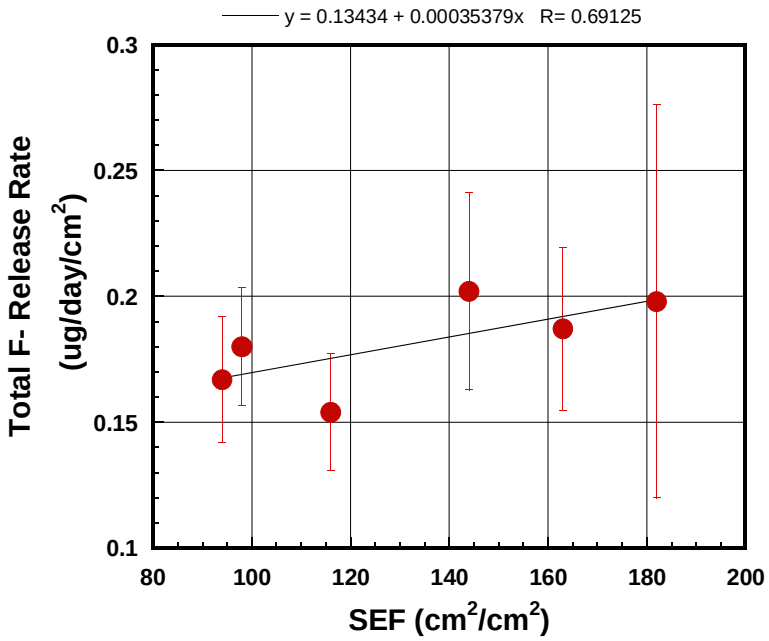

Figure 163. Fluoride emission rate vs. cathode catalyst beginning of test SEF.

The test was not very aggressive since the cells were run fully saturated at constant current with voltages above 0.5 volts. Further testing at the most aggressive conditions showed a stronger relationship (Figure 164). The more aggressive conditions are based on protocols recommended by the US Fuel Cell Council[79]. In these tests, the cell temperature is elevated to 90^{o}C, the cathode is oxygen, the sample is at OCV, and the RH of the inlet gasses is 30%.

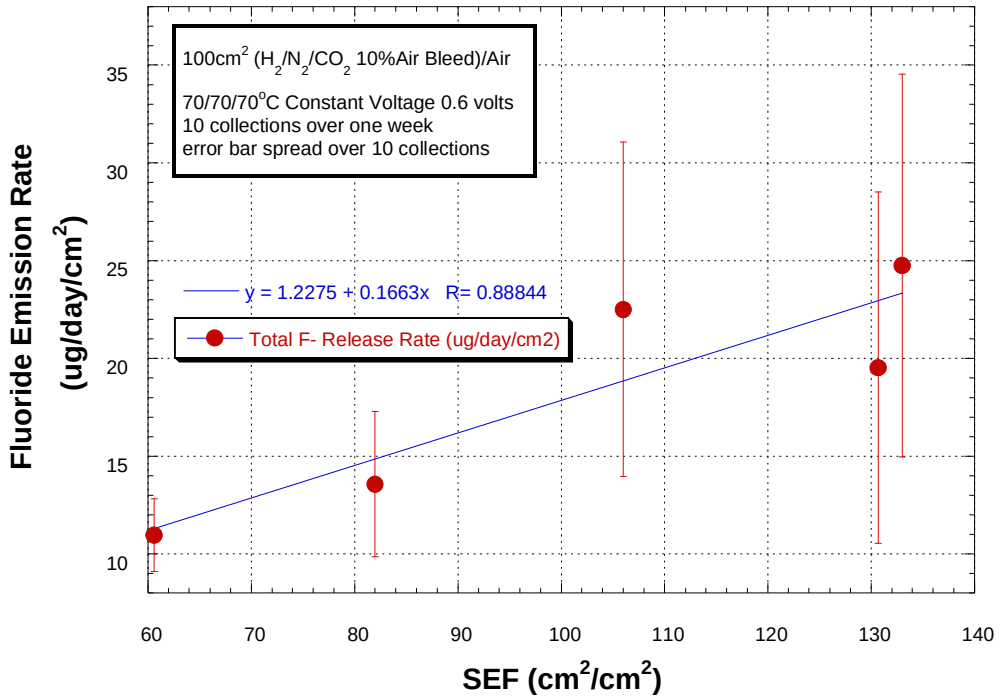

Figure 164. Fluoride emission rate as a function of Platinum anode surface area testing under high air bleed testing.

Figure 165 represents the results of the FER studies as a function of MEA construct[80]. The baseline in the figure represents the typical amount of fluoride flux going through the cell from the 1 ppb fluoride of our DI water supplies. The most dramatic results are between the low SEF (about 9cm^2/cm^2) NSTF platinum and the relatively high SEF (about 180 cm^2/cm^2) dispersed carbon supported catalyst.

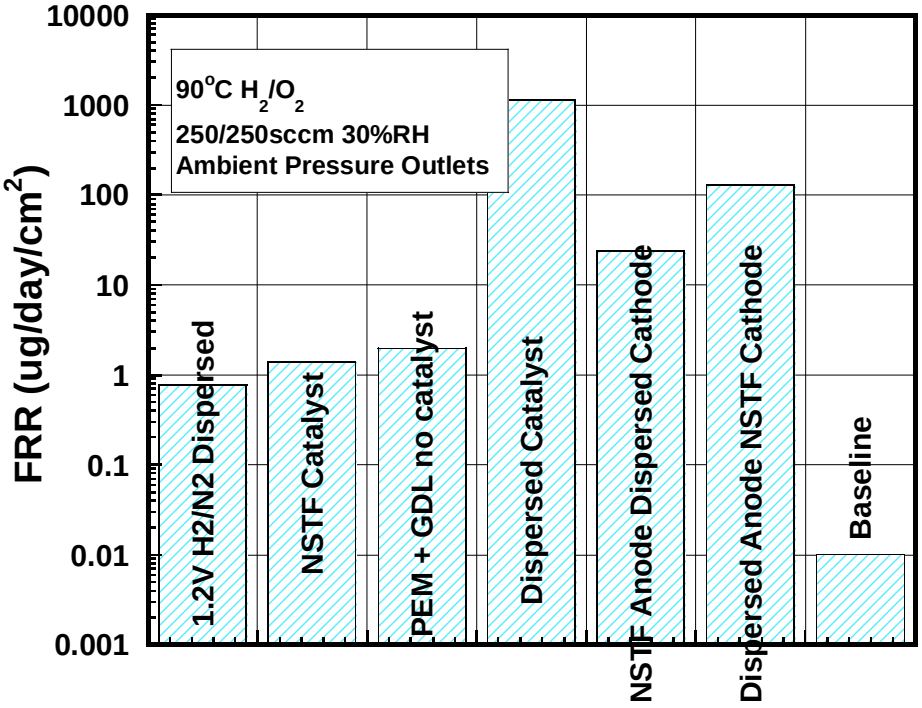

Figure 165. Fluoride ion emission rates (FER) for different MEA constructions

The FER of the dispersed catalyst is over two orders of magnitude higher than the NSTF catalyst. The NSTF has approximately the same FER as PEM + GDLs, the PEM alone, and the dispersed MEA under H_2/N_2. It is not understood why yet that the FER was so much higher than the background for the samples that had no catalyst or did not have oxygen present. Another interesting feature in Figure 165 is the change in FER depending on the location of NSTF catalyst. It is not surprising that having the anode be a low SEF and the cathode a high SEF would give the lower FER than the inverse as at OCV it is thought that the predominate peroxide formation mechanism would be oxygen crossover to the anode forming peroxide and that would be dependent on the number of catalyst sites available. It is surprising that low/high anode/cathode SEF is more than an order of magnitude higher FER than the low/low anode/cathode SEF combination implying that even at OCV there is a contribution to the peroxide production from the cathode. As a follow up to this study, we did a study of the FER for a variety of different anodes under our standard load cycle Shiva test conditions (see *2.1.4 Membrane Characterization*). What we found was that generally independent of catalyst type the FER was proportional to the SEF of the anode catalyst, Figure 166.

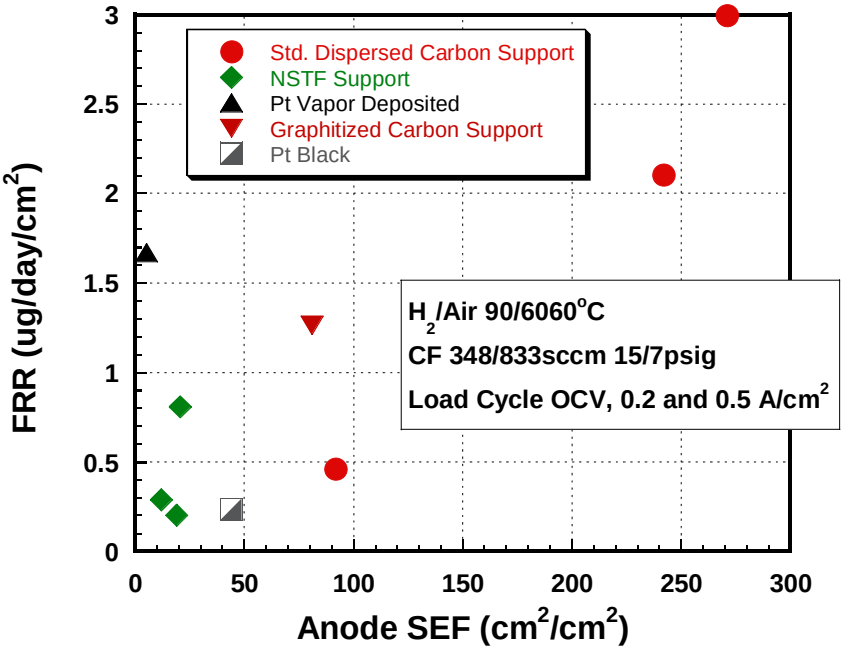

Figure 166. Fluoride emission rate as a function of anode surface area

It is important to note the diversity of catalyst types tested here from carbonless NSTF to two types of dispersed carbons to platinum blacks and ebeam deposited platinum on the PEM. The exception to the FER being proportional to the SEF is the ebeam deposited platinum directly on the PEM, where it is conjectured that either there was some thermal damage done to the PEM by that process or that metallization was more susceptible to dissolution and precipitation somewhere in the PEM.

In addition to these studies we also examined the role of air bleed and catalyst type in FER. An anode loading study was carried out to look at the performance decay under high air bleed. The anode gas composition had no CO in it and consisted of H2, N2 and CO2 with a 10% of total flow air bleed. This is much higher then would be used in a standard cell. The first series of samples was done with a platinum catalyst (Figure 167).

Figure 167. Fluoride emission rate (FER) over time for different Pt and PtRu loadings shows the difference in FER between the platinum anode series, the use of a PtRu anode and the initial cathode loading series. What is observed is a much higher FER for platinum then PtRu anode catalyst under the same air bleed. Further, the effect of this extremely high air bleed increases the FER by only a factor of about 3 over an MEA with no air bleed. The contribution to the FER of a more normal 1% air bleed with a PtRu catalyst at these conditions would be minimal.

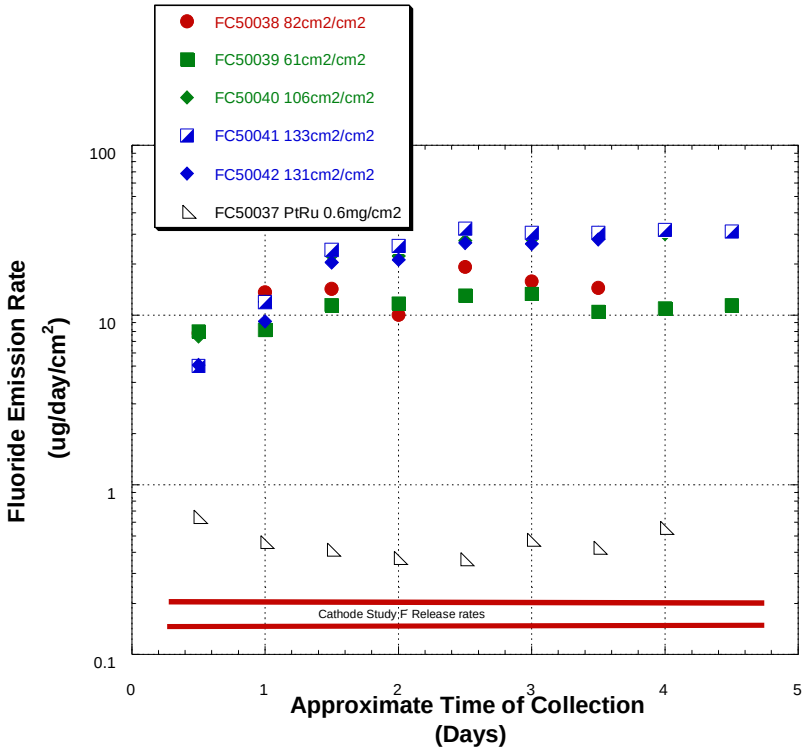

Figure 167. Fluoride emission rate (FER) over time for different Pt and PtRu loadings

Catalyst's Role in Membrane Degradation Summary

We have identified a number of factors and non factors in catalyst's role in membrane degradation. To the first order, SEF is the most important factor related to the catalyst in FER. Increasing SEF on both the anode and the cathode is related to increasing FER. The magnitude of the proportionality of SEF to FER is magnified by the oxygen partial pressure and the dryness of the test conditions. There may be differences in the peroxide production rate for different catalysts and support types but that is very small in comparison to the effect of the SEF. In addition, we explored the effect of high air bleed as a function catalyst type and loading and observed an order of magnitude gain in going from PtRu to Pt catalysts. FER was found to be function of catalyst surface area and metals composition with air bleed study, where the use of PtRu on the anode as opposed to Pt had a nearly two orders of magnitude reduction in FER.

2.3.4 References

[75] D.A. Stevens, M. T. Hicks, G. M. Haugen and J.R. Dahn, "Ex Situ and In Situ Stability Studies of PEMFC Catalysts, Effect of Carbon Type and Humidification on Degradation of the Carbon," *J. Electrochem. Soc.* **152** (12) A2309-A2315 (2005).
[76] H. Gastieger, S. Kocha, B. Sompalli, F. Wagner. Appl. Cata. B: Env. 56 (2005) 9-35
[77] R.M. Darling and J.P. Meyers, J. Electrochem. Soc. 152 (1) (2005) A242-A247.
[78] Conversations with system integrators.
[79] US Fuel Cell Council, http://www.usfcc.com/resources/technicalproducts.html#form
[80] G.M. Haugen et al, ECS Presentation, 212th ECS Meeting, Washington D.C.

Section 3: System Operation – How System Operating Conditions Effect Durability

3.1 Nonuniformity Studies - Modeling

Membrane durability is fundamental to MEA durability. We approached the task of improving the membrane by first studying the existing degradation mechanisms through ex-situ, in-situ, and model compound studies. Next, we attempted to address the deficiency in chemical resistance or mechanical strength properties through systematic development programs.

The main objective of this modeling research is to study the effects of nonuniformities in PEM fuel cell. The modeling research is divided into five distict groups investigating the effects of nonuniformities in (1) the electrode (catalyst layer), (2) the GDL, (3) the membrane, (4) system cooling and (5) flow distribution. The modeling geometry is shown in Figure 168.

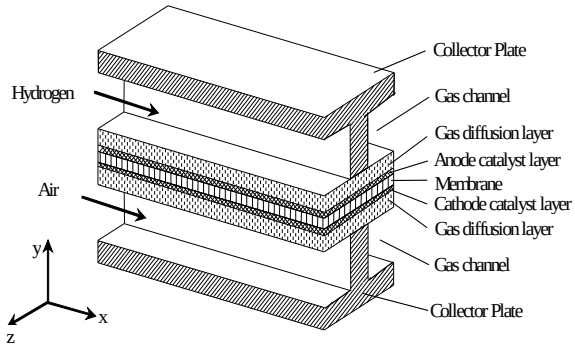

Figure 168. Model Geometry

3.1.1 Electrode Modeling

Catalyst Loading

By varying the product of specific active catalyst surface area and the exchange current density (ai_0) in the modeling equations, we have simulated the non-uniformities in catalyst loading or the specific active catalyst surface area along the gas flowing direction in the channel in the form of $ai_0 = a + bx$. The coefficients a and b are obtained for different operation conditions when the current distribution in the membrane is approximately even along the gas flowing direction. For the model, this 'uniformity' condition corrsponds to an overpotential = 0.2, pressure = 3 atm, relative humidity of reactant gases = 100%, hydrogen flow rate = 567 sccm, air flow rate = 1800 sccm, and cell temperature = 50, 60 or 70ºC. Figure 169 to Figure 172 shows the distribution of local current density with different values of a and b at cell temperature = 70ºC

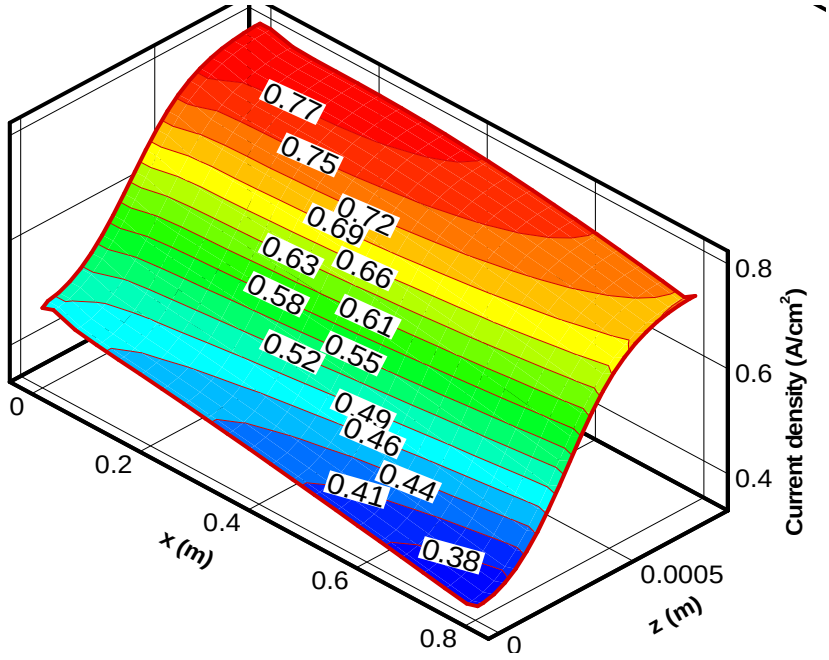

Figure 169. Current density in the membrane with a=264, b=200

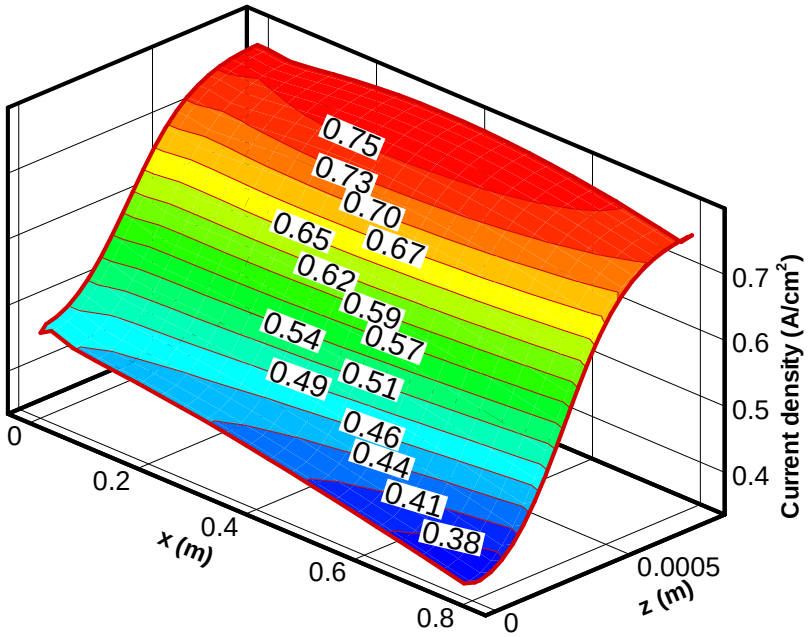

Figure 170. Current density in the membrane with a=243.9, b=250

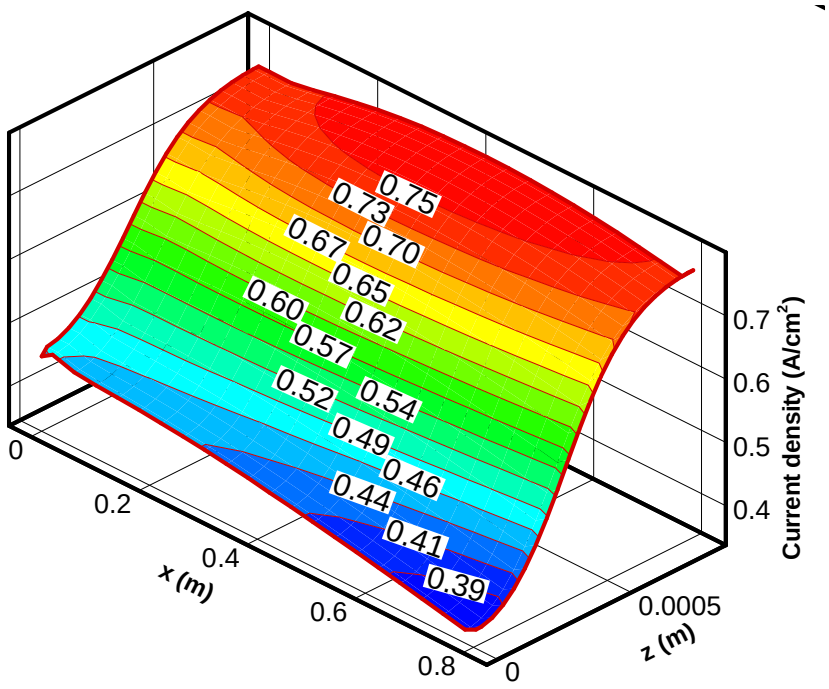

Figure 171. Current density in the membrane with a=233.9, b=275

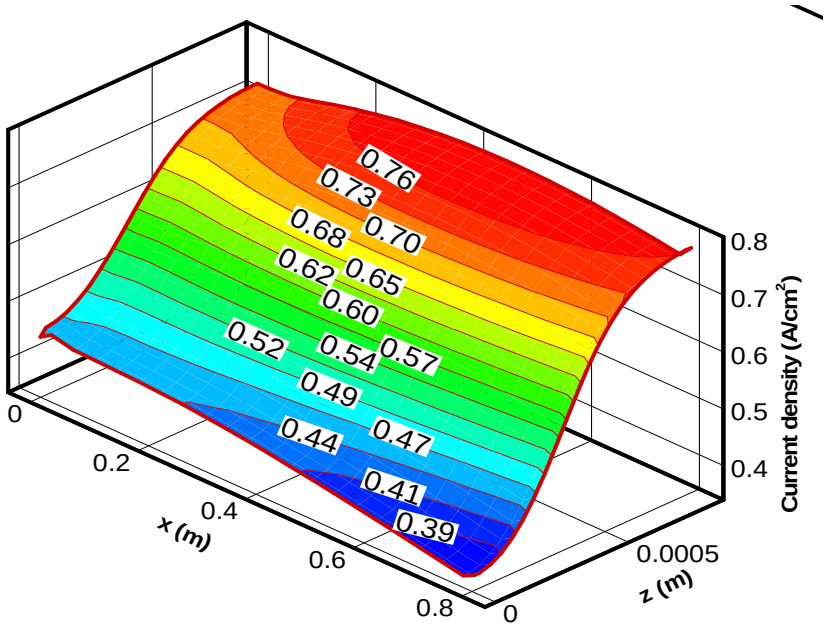

Figure 172. Current density in the membrane with a=223.8, b=300

The power output of the fuel cell with different linear catalyst distributions and the same total catalyst loading are compared in Table 33. It is observed that the power output is essentially the same for all conditions studied.

Table 33. Fuel cell power output as a function of catalyst loading distribution.

a	b	i	V	P
264	200	0.616	0.758	0.467
243.9	250	0.614	0.777	0.477

233.9	275	0.613	0.777	0.476
223.8	300	0.612	0.760	0.465

Conclusions

An increase in the local catalyst loading will lead to change in local current density. However, if the total catalyst loading does not change from one case to another, the power output will remain approximately equal for all cases.

Ionic Conductivity

Inside the catalyst layer, the ionic conductivity of the catalyst layer (CL) changes along x-direction according to one of five senarios::

a. Ionic conductivity is constant constant (CL ionic 1)
b. Ionic conductivity increases linearly with the largest CL ionic conductivity increased by 5 times (CL ionic*5) compared to the baseline
c. Ionic conductivity decreases linearly with the smallest CL ionic conductivity reduced by half (CL ionic*1/2) compared to the baseline
d. Ionic conductivity increases at one location with a sine function and the largest CL ionic conductivity is increased by five times (CL bell ionic*5) compared to the baseline
e. Ionic conductivity decreases at one location with a sine function and the smallest CL ionic conductivity is decreased by one-half (CL bell ionic*1/2) compared to the baseline

Figure 173 to Figure 175 illustrate the ionic conductivity profiles, the resulting polarization curves and the temperature distribution inside the fuel cell, respectively

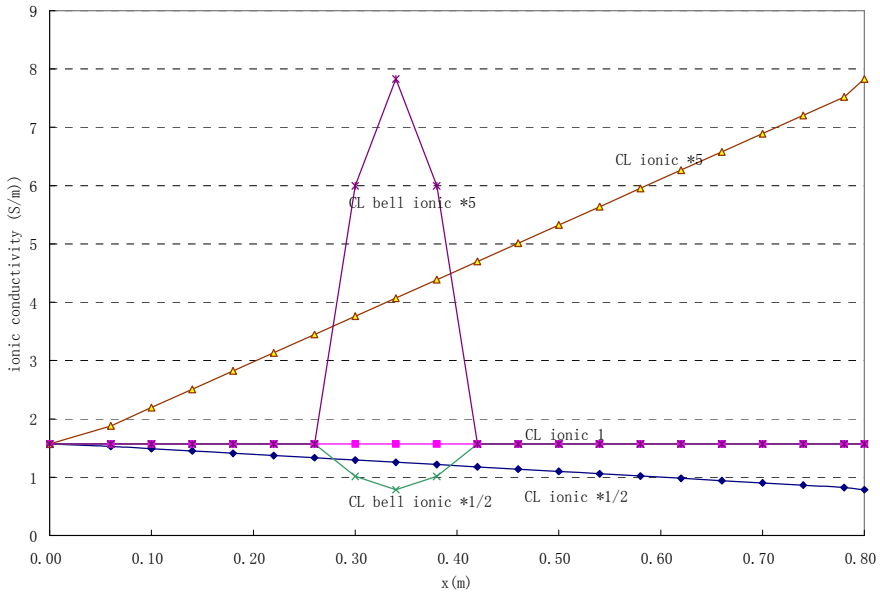

Figure 173. The catalyst layer ionic conductivity profiles

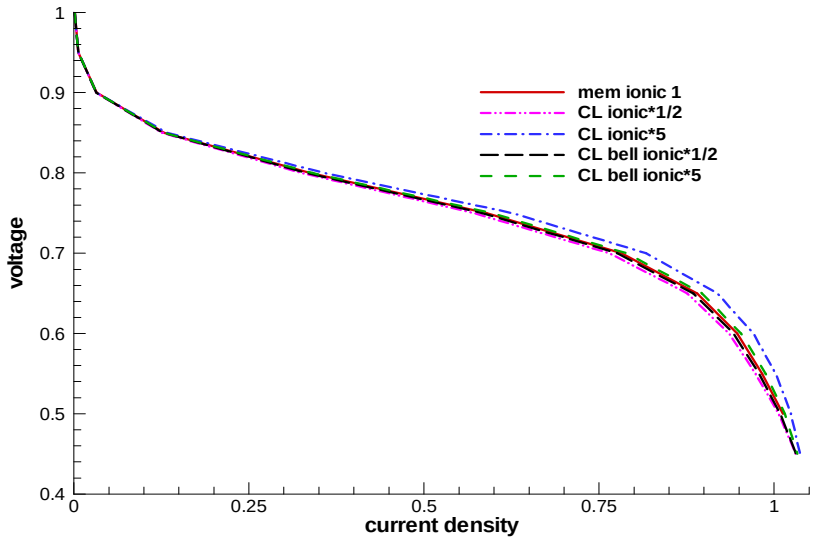

Figure 174. Figure 1.2b: The polarization curves

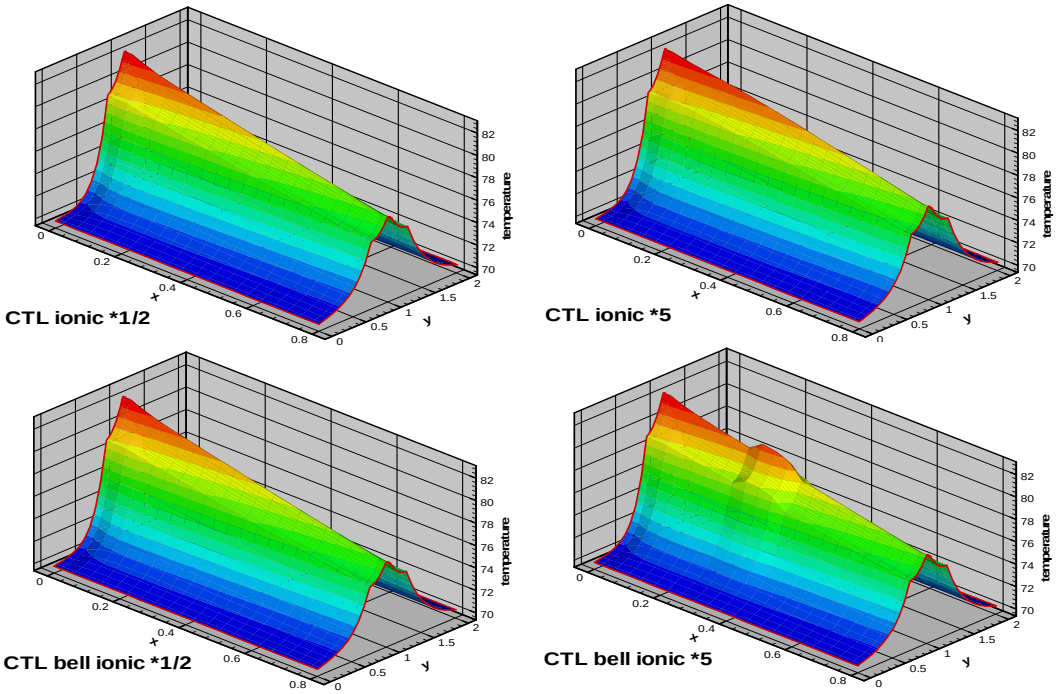

Figure 175. The local temperature distributions at cell voltage=0.70 v. The current densities for the four cases are: 0.7647 A/cm^2, 0.8170 A/cm^2, 0.7757 A/cm^2 and 0.7895 A/cm^2.

Conclusions

The change of catalyst layer ionic conductivity affects power output. Larger ionic conductivity leads to less ohmic loss and larger power output. here is no obvious influence by the CL ionic conductivity on the mass transfer.

The ionic conductivity affects temperature in two aspects: 1) the distribution of the local current density and 2) the heat generation rate. As heat generation rate is inversely proportional to the

ionic conductivity, large ionic conductivity leads to less heat generation. But large ionic conductivity also leads to an increase in the current density and thus an increase in heat generation. The overall effect in an increase in ionic conductivity leads to an increase in current density and a higher operating temperature

Liquid Water Distribution in the Catalyst Layer

Inside the fuel cell the CL saturation changes along x-direction:

a. Saturation increases linearly and the largest saturation is 1 at the end of the channel (CL sat+1)
b. Saturation increases linearly and the largest saturation is 0.5 at the end of the channel (CL sat+0.5)
c. Saturation changes with sine distribution at one location and the largest saturation is 1 (CL bell sat+1)
d. Saturation changes with sine distribution in at one location and the largest saturation is 0.5 (CL bell sat+0.5)

Figure 176 to
Figure 178 illustrate the catalyst saturation profiles, the resulting polarization curves and the temperature distribution inside the fuel cell, respectively

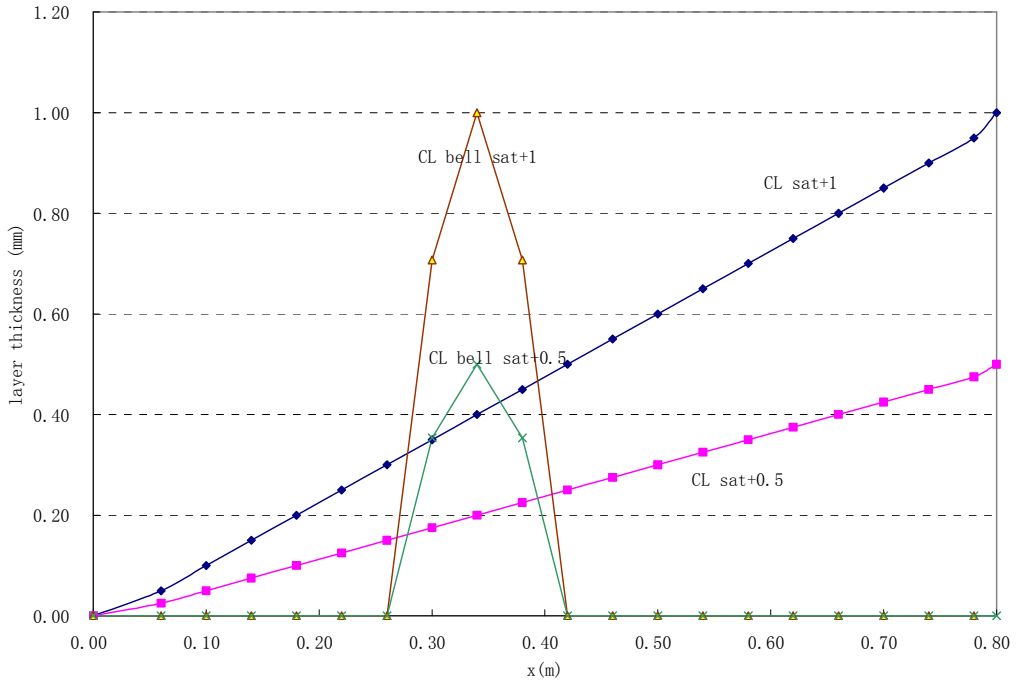

Figure 176. Catalyst layer saturation profiles

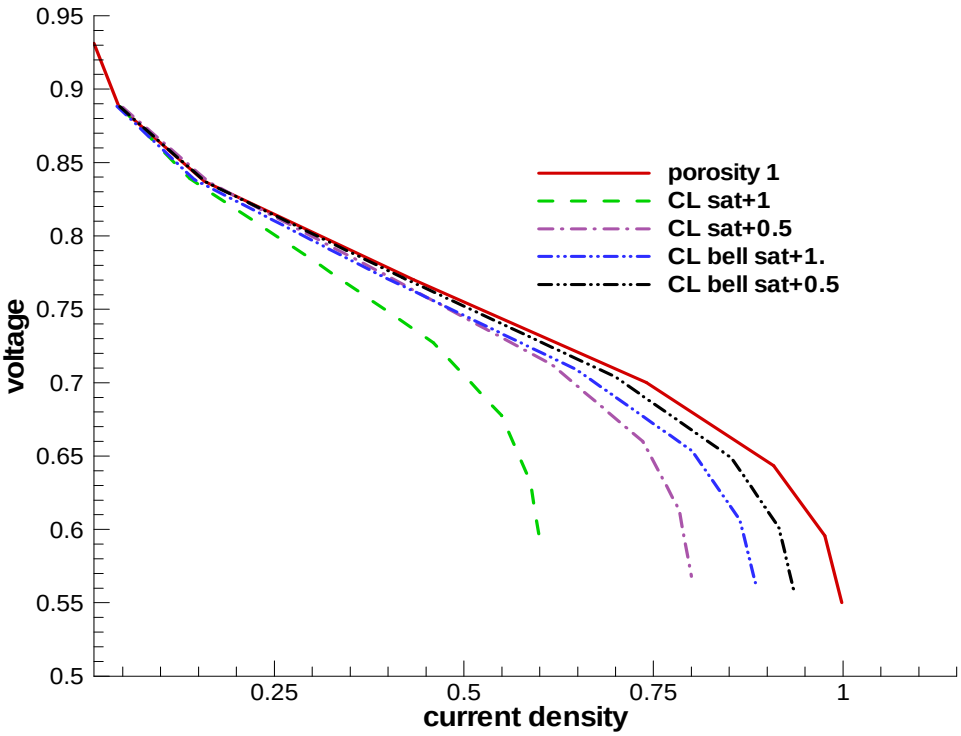

Figure 177. The polarization curves

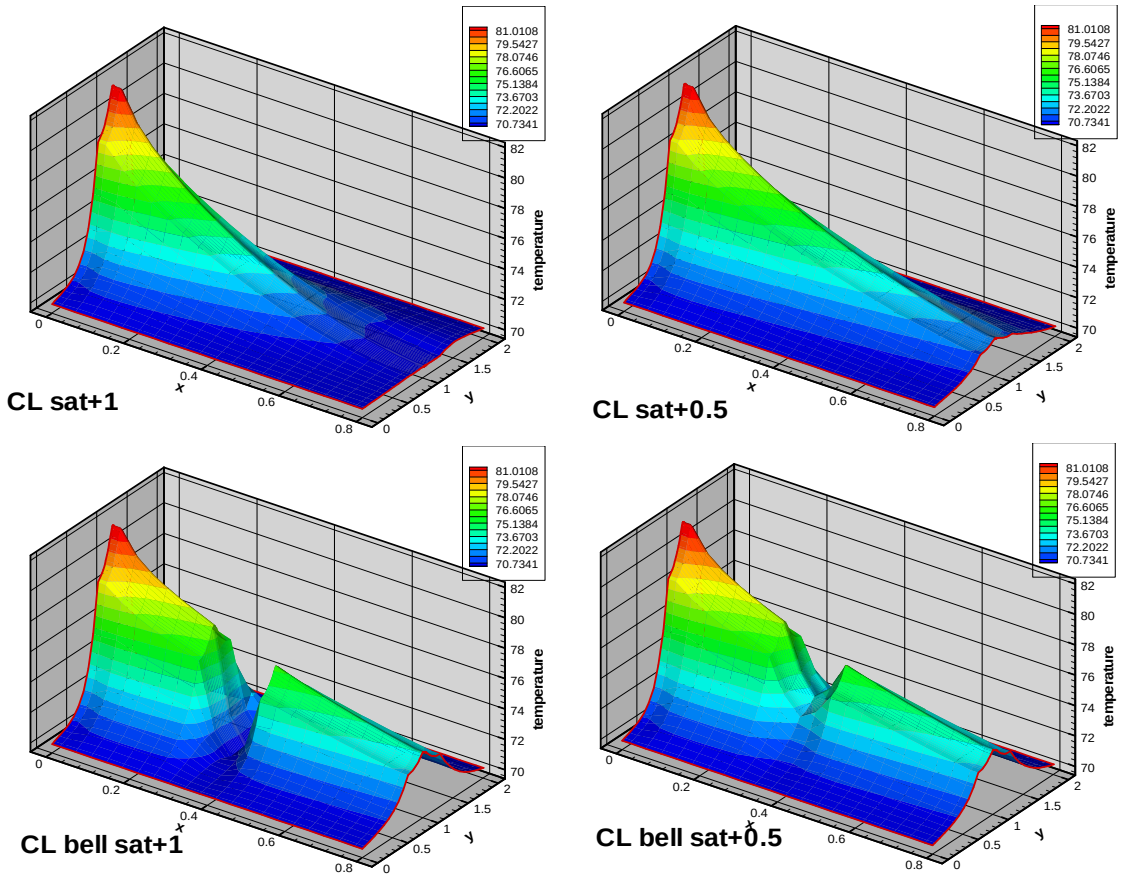

Figure 178. The local temperature contours, overpotential =0.32 v.

Conclusions

The change of CL saturation changes the mass transfer resistance: as the saturation increases so does the mass transfer resistance. The base case has the largest power output and the largest limiting current density. For other cases when additional saturation is considered, the power output and the limiting current densities are reduced. Where the local current density is reduced, the local temperature is reduced as well.

Thickness of the Catalyst Layer - Linear Distribution

In these experiments, the catalyst layer thickness changes linearly along x-direction, but total thickness of CTL+GDL remains constant. Thus, the layer thickness of GDL is changed accordingly, either compressed or expanded.

a. CL thickness increases lineally and at the end the thickness is two times larger than the initial (CL 2)
b. CL thickness increases lineally and at the end the thickness is four times larger than the initial (CL 4)
c. CL thickness decreases lineally and at the end the thickness is 1/2 times smaller than the initial (CL 1/2)
d. CL thickness decreases lineally and at the end the thickness is 1/4 times smaller than the initial (CL 1/4)

Figure 179 shows the grids with the changing catalyst layer thickness. Figure 180 shows the polarization curves. Figure 181 is an example of the local temperature contours.

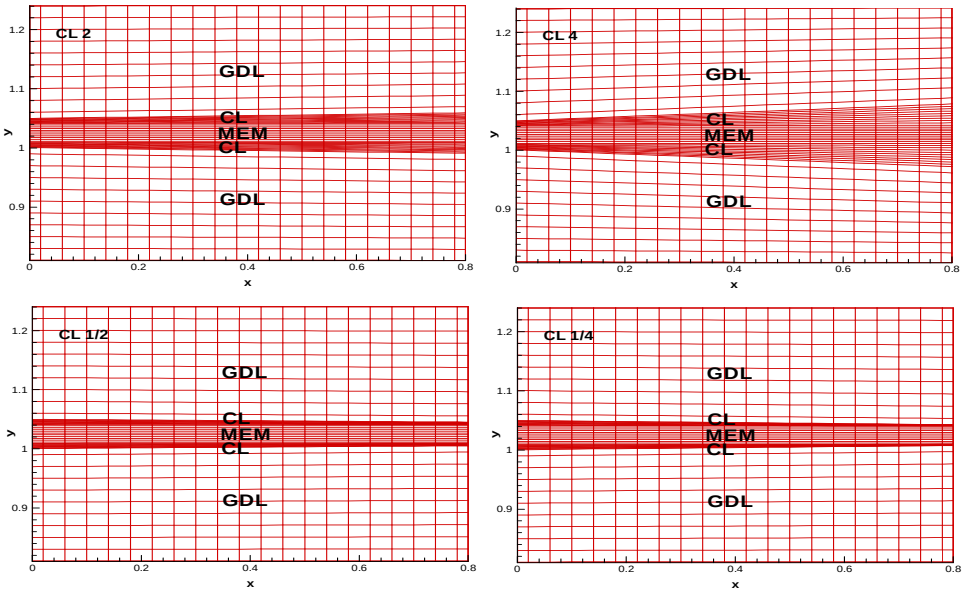

Figure 179. The grids

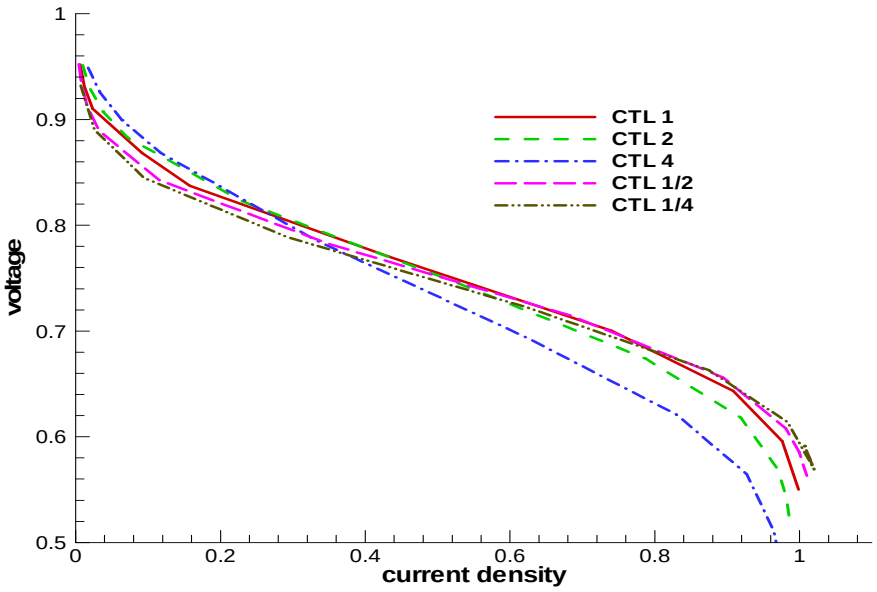

Figure 180. The polarization curves

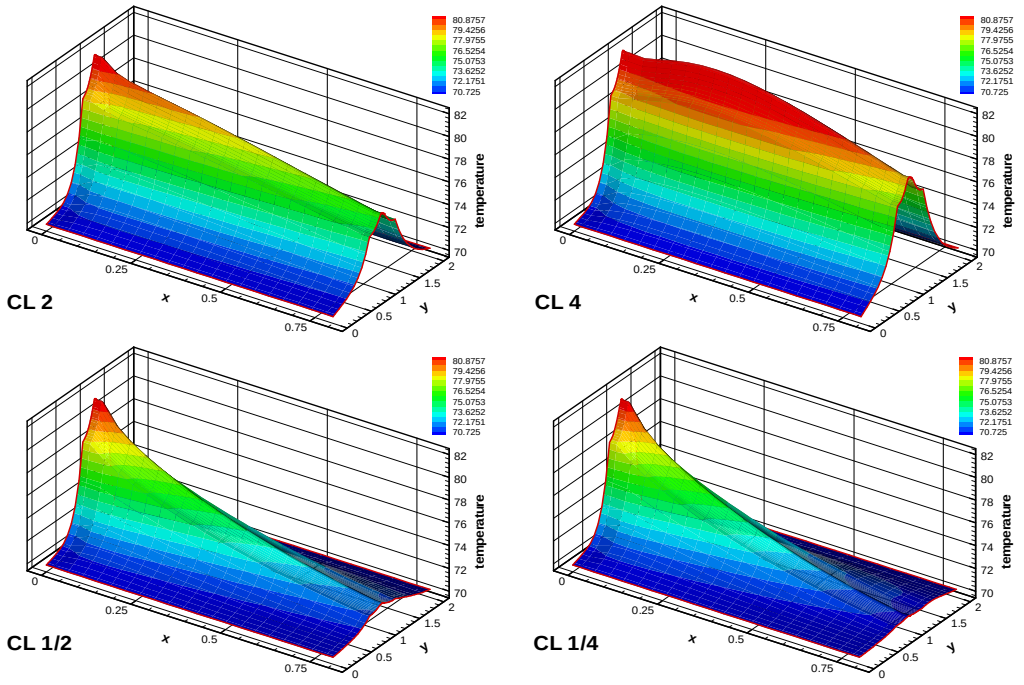

Figure 181. The local temperature contours at overpotential =0.32v. The current density for the four cases: 0.9190 A/cm^2, 0.9270 A/cm^2, 0.8945 A/cm^2, 0.8748A/cm^2.

Conclusions

The change of catalyst layer (CL) thickness while maintaining a constant CL + GDL thickness has two effects: it affects the mass transfer resistance and the ohmic resistance . As the total thickness of GDL+CL remains constant in this study, when CL thickness is increased, GDL thickness is reduced. Since the GDL has larger pores than CL, the mass transfer resistance is increased.. When CL thickness increases, ohmic loss also increase. Overall, non-uniformity in CL thickness has negative effects on cell power output and it may also lead to hot spots inside the fuel cell.

Thickness of the Catalyst Layer - Bell Distribution

Inside the fuel cell, in one place the catalyst layer thickness changes with sine distribution along x-direction, but CTL+GDL total thickness remains constant. Thus, the layer thickness of GDL is changed accordingly, either compressed or expanded.

a. CL thickness increases and the largest CL thickness is increased one time (CL +1)
b. CL thickness increases and the largest CL thickness is increased three times (CL +3)
c. CL thickness decreases and the smallest CL thickness is reduced 1/2 (CL -1/2)
d. CL thickness decreases and, the smallest CL thickness is reduced one time, thus the smallest CL thickness is zero (CL -1)
e. The thickness is constant (CL 1)

Figure 182 shows the grids with the changing catalyst layer thickness. Figure 183 shows the polarization curves. Figure 184 is an example of the local temperature contours.

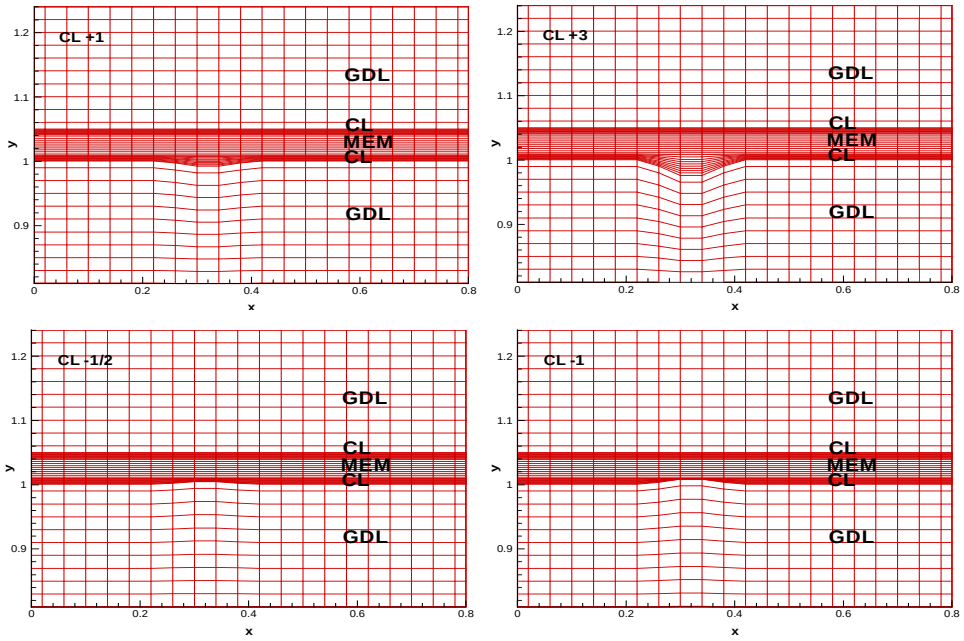

Figure 182. The grids

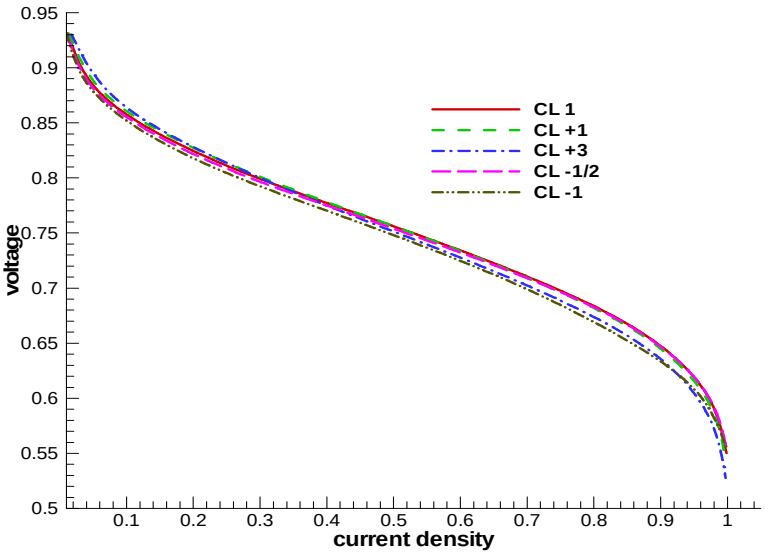

Figure 183. The polarization curves

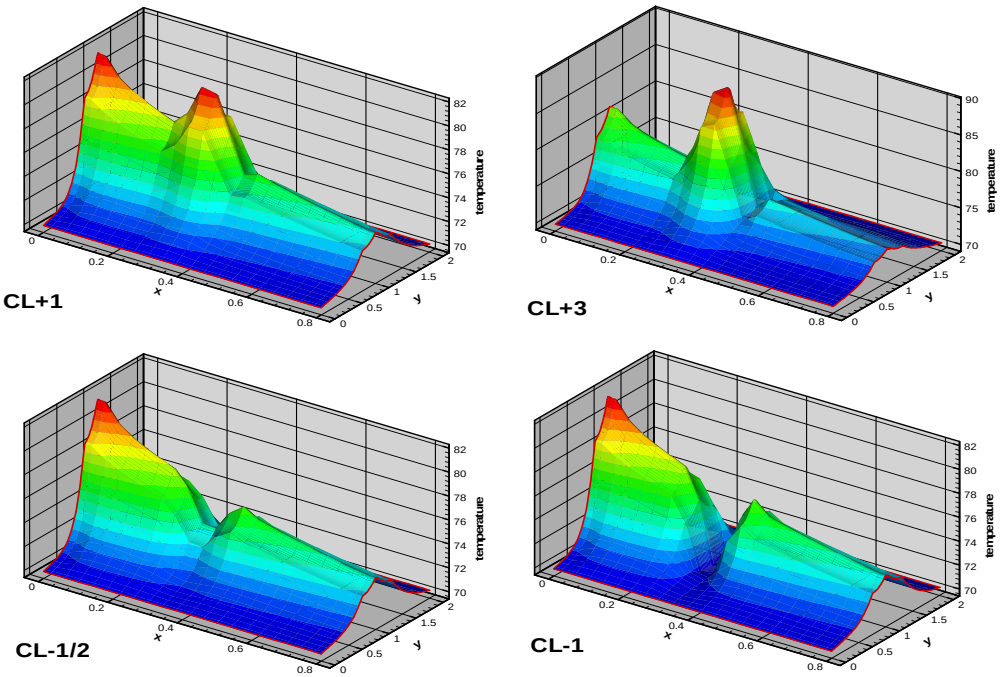

Figure 184. The local temperature contours at overpotential =0.32v. The current density for the four cases: 0.9128 A/cm^2, 0.9164 A/cm^2, 0.9030A/cm^2, 0.8568 A/cm^2.

Conclusions

Non-uniformity in CL thickness has a negative effects on cell power output. It may also lead to hot spots inside the fuel cell.

Porosity - Linear Distribution

Inside the fuel cell, in one place the porosity of the catalyst layer changes linearly along x-direction.

a. Porosity is constant (CL porosity 1)
b. Porosity increases and the largest porosity is increased by 0.2 (CL por+0.2)
c. Porosity decreases and, the smallest porosity is reduced by 50% (CL bell por-0.5)
d. Porosity decreases and, the smallest porosity is reduced by 90% (CL bell por-0.9)

Figure 185 to Figure 187 illustrate the porosity profiles, the resulting polarization curves and the temperature distribution inside the fuel cell, respectively

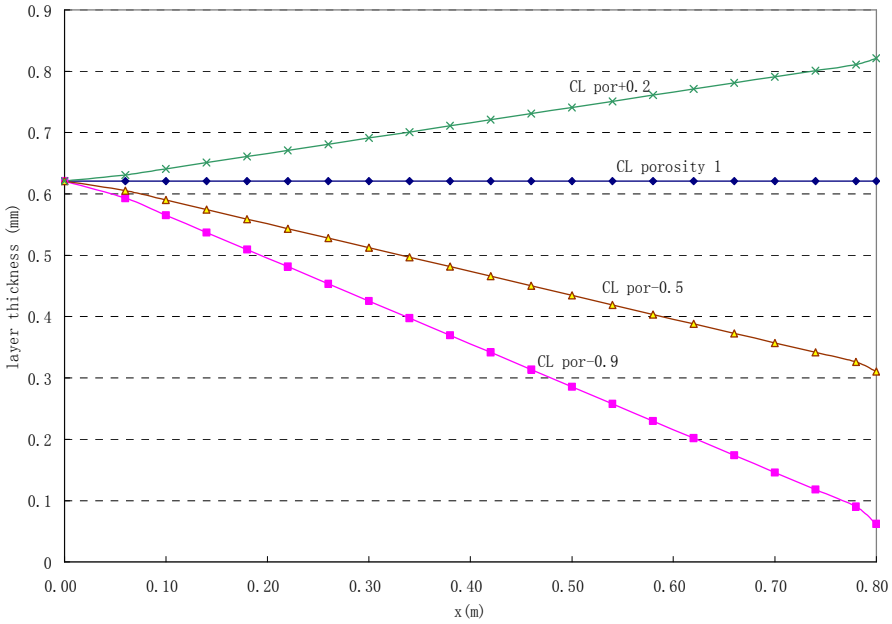

Figure 185. The change of CL porosity along x-direction

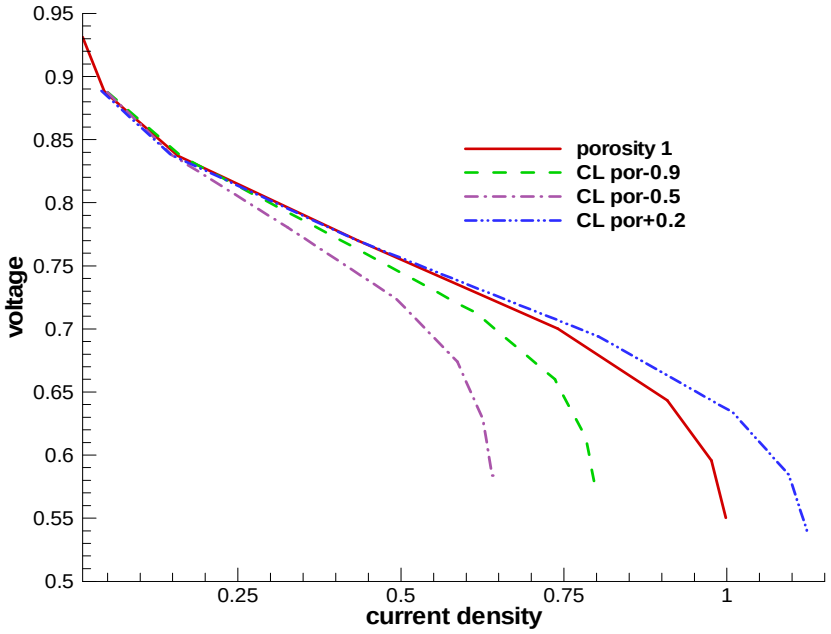

Figure 186. The polarization curves

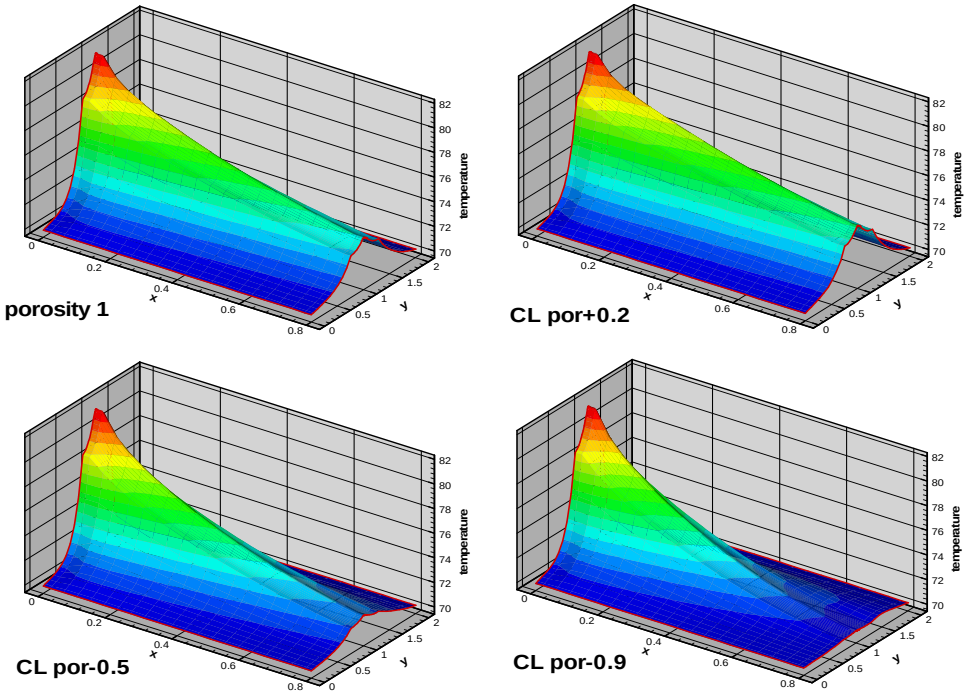

Figure 187. The local temperature distributions at overpotential =0.32 v

Conclusions - The change of the CL porosity leads to change of mass transfer resistance, and as a result, the power output is changed. Case “CL por+0.2” has the largest porosity and largest power out. Its limiting current density is also the largest. Case “CL por-0.9” has the smallest porosity, the lowest power output and the smallest limiting current density. Where local current density is increased, the local temperature is also increased.

Porosity - Bell Distribution

Inside the fuel cell, in one place the porosity of the catalyst layer changes with bell function along x-direction.

a. Porosity is constant (CL porosity 1)
b. Porosity increases and the largest porosity is increased by 0.2 (CL bell por+0.2)
c. Porosity decreases and the smallest porosity is reduced by 50% (CL bell por-0.5)
d. Porosity decreases and the smallest porosity is reduced by 90% (CL bell por-0.9)

Figure 188 to illustrate the porosity profiles, the resulting polarization curves and the temperature distribution inside the fuel cell, respectively

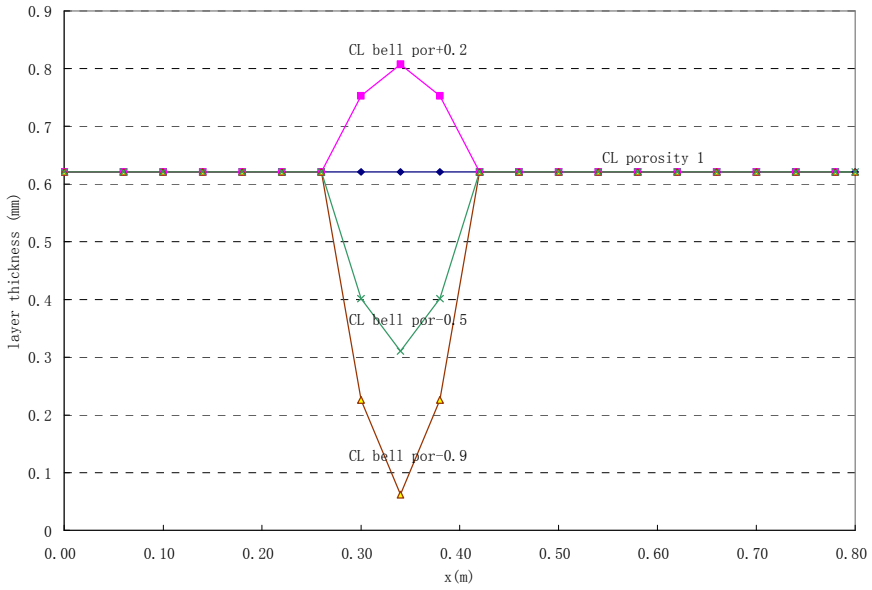

Figure 188. The change of porosity along x-direction

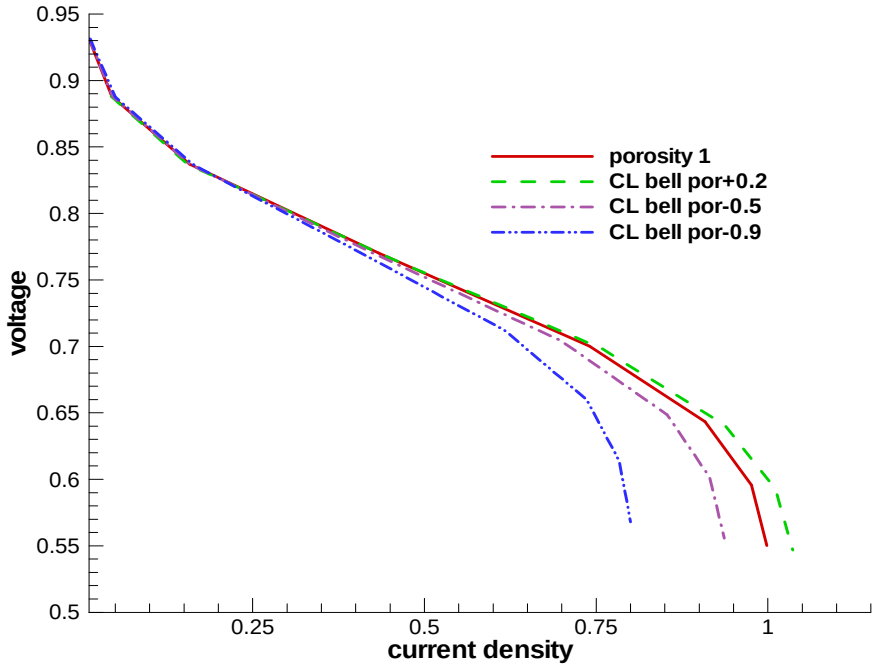

Figure 189. The polarization curves

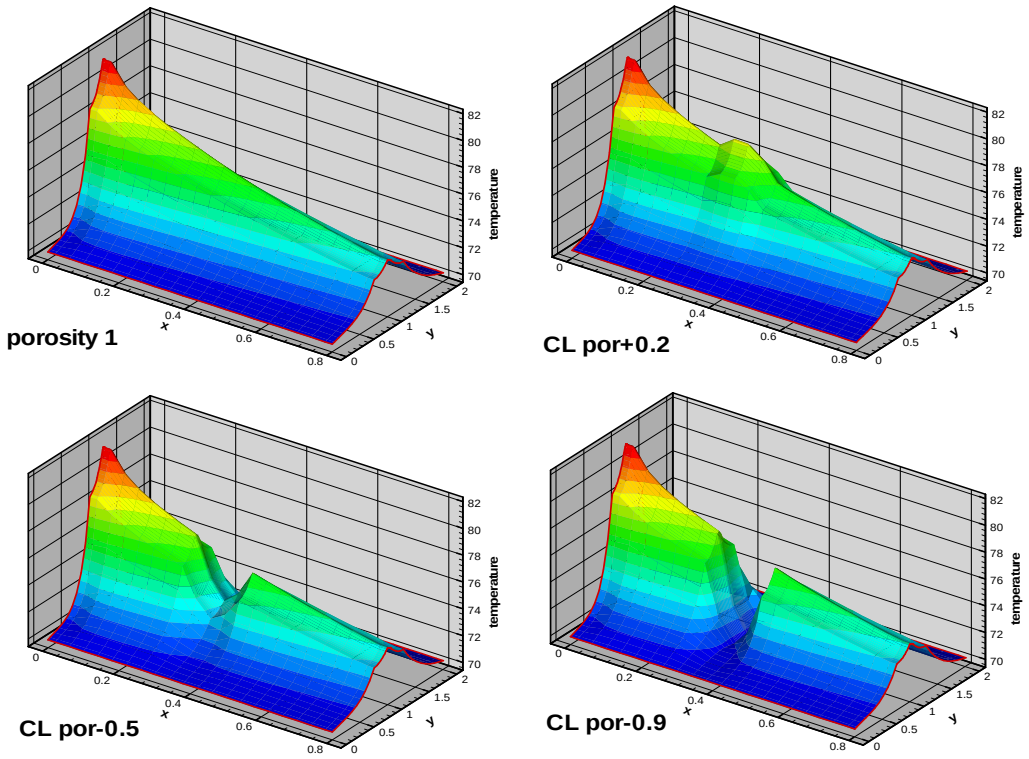

Figure 190. The distribution of temperature, overpotential =0.32 v.

Conclusions:

Same conclusion as “Catalyst Porosity - Linear Distribution” section - namely the power output increases with increasing porosity

3.1.2 GDL

Modeling practices have been carried out to study the effects of non-uniform distribution/variations in (1) porosity, (2) water distribution and (3) thickness.

Porosity - Linear Distribution

Inside the fuel cell, the porosity of GDL changes linearly with x,

a. at the end of the channel, the porosity increases by 0.1 (GDL por+0.1)
b. at the end of the channel, the porosity increases by 0.2 (GDL por+0.2)
c. at the end of the channel, the porosity is 0 (GDL por-0)
d. at the end of the channel, the porosity decreases to one-half (GDL por-1/2)

Figure 191 to Figure 193 the porosity profiles, the resulting polarization curves and the temperature distribution inside the fuel cell, respectively.

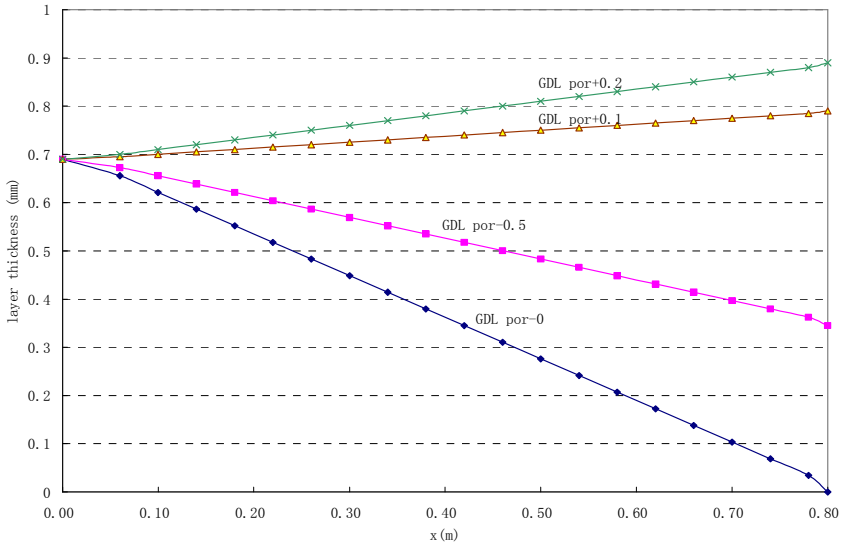

Figure 191. GDL porosity profile

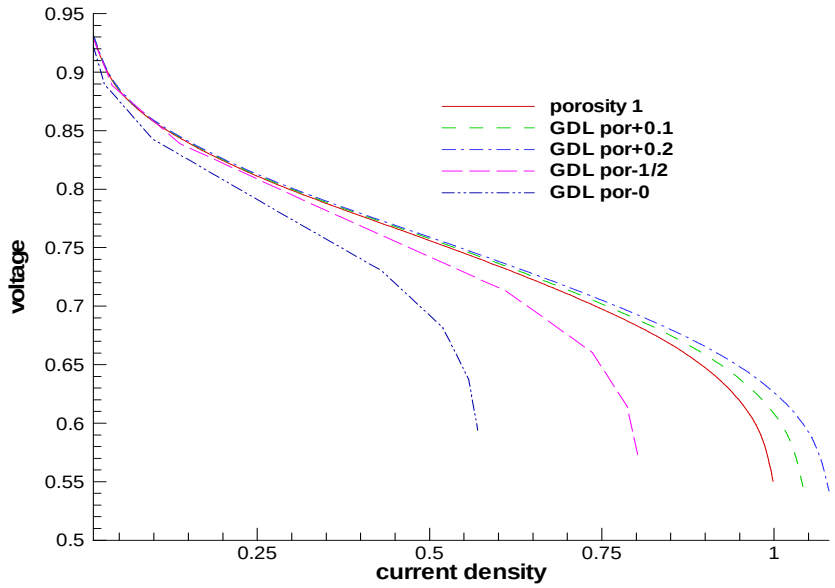

Figure 192. The polarization curves

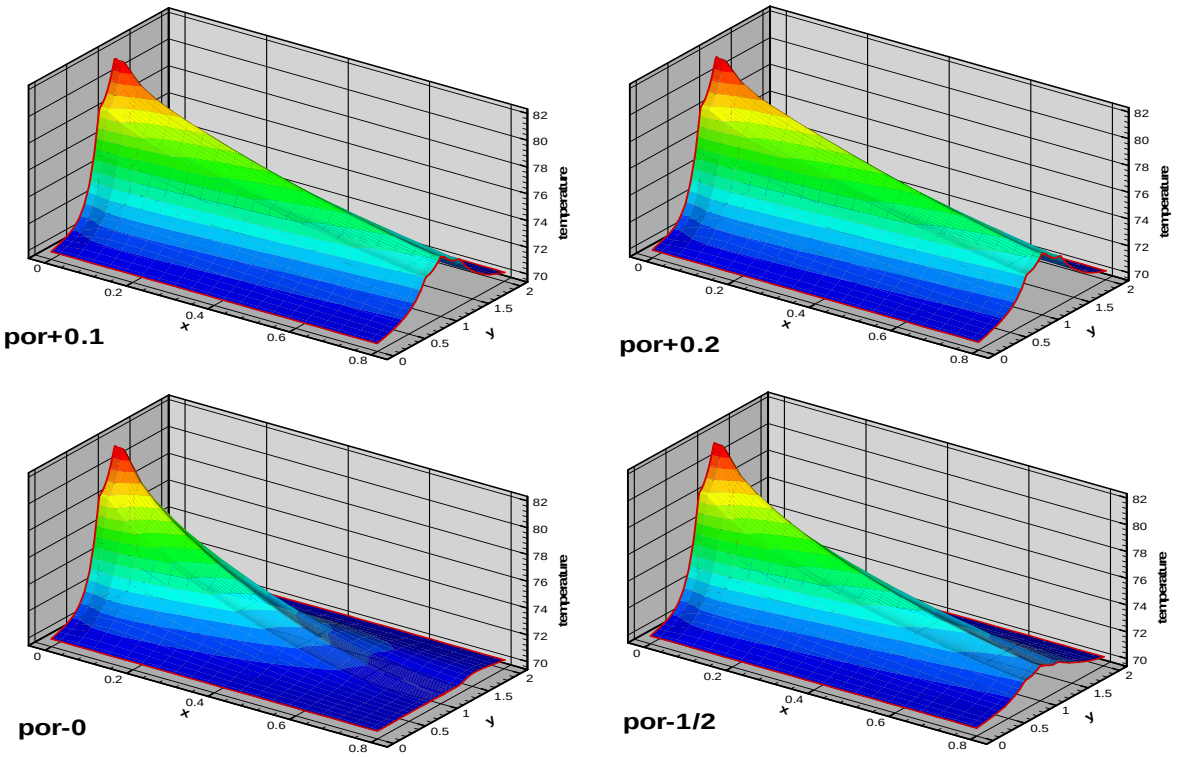

Figure 193. The local temperature distributions at overpotential =0.32 v

Conclusions

The change of GDL porosity causes changes in the mass transfer resistance: as the GDL porosity increases, the mass transport resistance is reduced and the performance is increased. The distribution of local temperature follows the same pattern as the local current density.

Porosity - Bell Distribution

Inside the fuel cell, the porosity of GDL changes along x-direction with sine distribution at one place,

a. Porosity increases and the largest porosity is increased by 0.1 (GDL bell por+0.2)
b. Porosity increases and the largest porosity is increased by 0.2 (GDL bell por+0.1)
c. Porosity decreases and the smallest porosity is reduced to 0 (GDL bell por-0.)
d. Porosity decreases and the smallest porosity is reduced by half (GDL bell por-1/2)

Figure 194 to Figure 196 illustrate the porosity profiles, the resulting polarization curves and the temperature distribution inside the fuel cell, respectively.

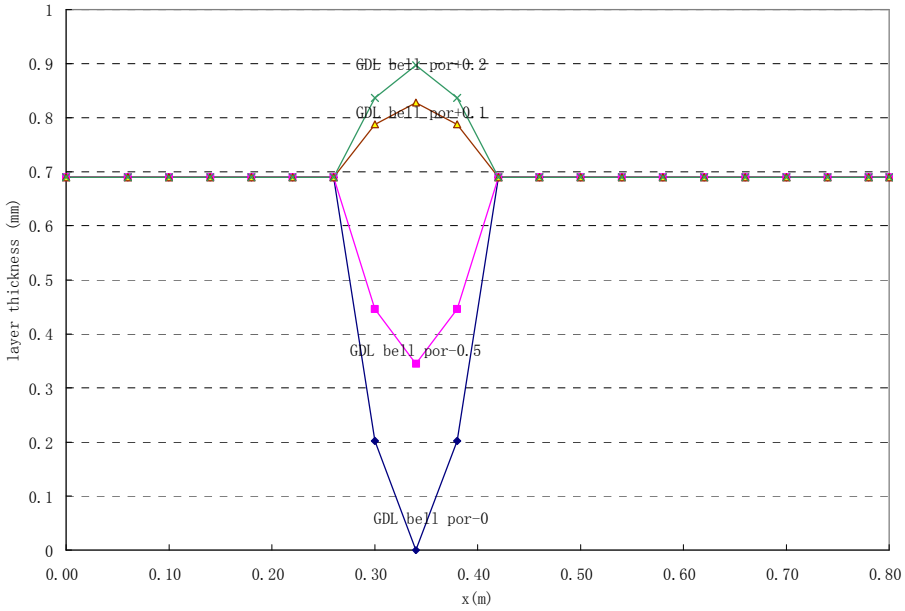

Figure 194. GDL porosity profile

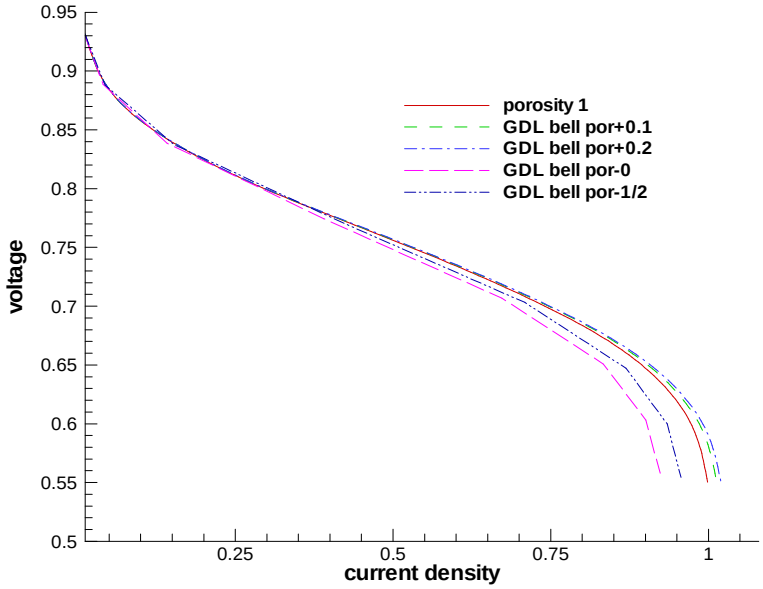

Figure 195. The polarization curves

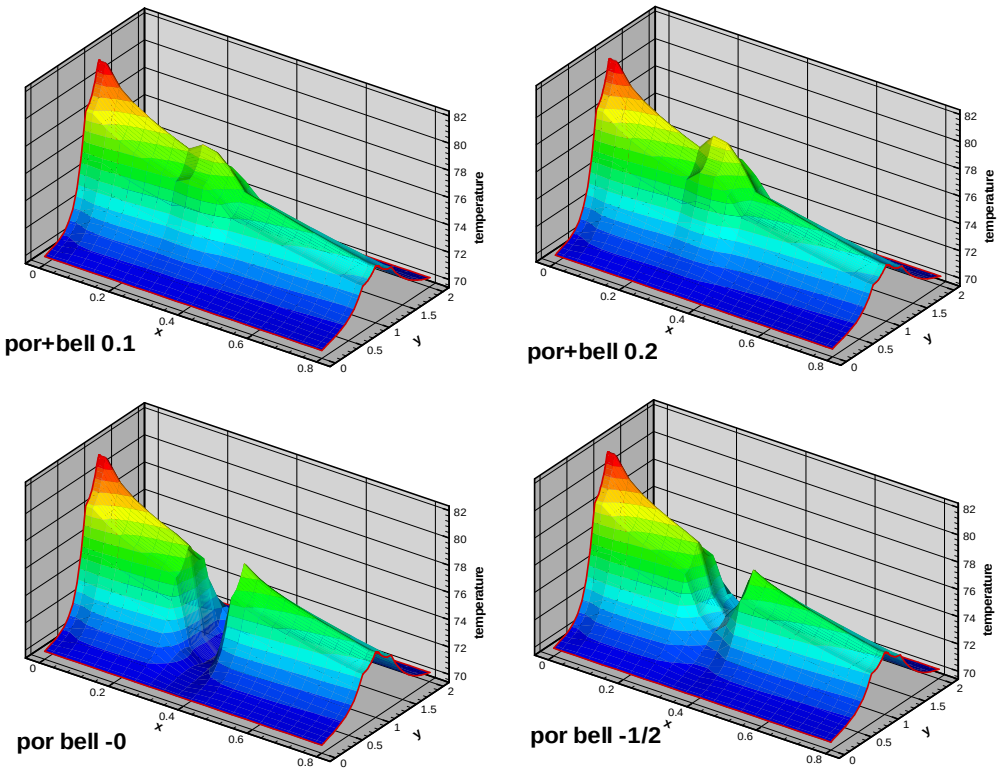

Figure 196. The local temperature distributions at overpotential =0.32v.

Conclusions - Same as "GDL Porosity - Linear Distribution", namely as the GDL porosity increases, the mass transport resistance is reduced and the performance is increased.

Varied Liquid Water Distribution in the Pores of GDL

Inside the fuel cell, in one place the GDL saturation changes along x-direction,

a. Saturation increases linearly and the largest saturation is 1 at the end of the channel (GDL sat+1)

b. Saturation increases linearly and the largest saturation is 0.5 at the end of the channel (GDL sat+0.5)

c. Saturation changes with sine distribution in one place and the largest saturation is 1 (GDL bell sat+1)

d. Saturation changes with sine distribution in one place and the largest saturation is 0.5 (GDL bell sat+0.5)

Figure 197 to Figure 199 illustrate the GDL saturation profiles, the resulting polarization curves and the temperature distribution inside the fuel cell, respectively

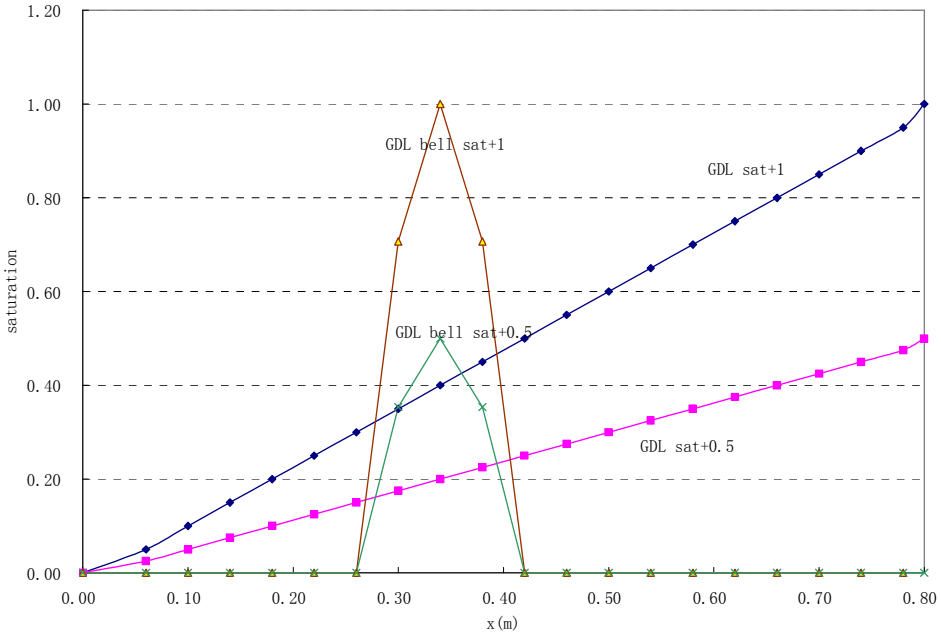

Figure 197. GDL saturation profiles

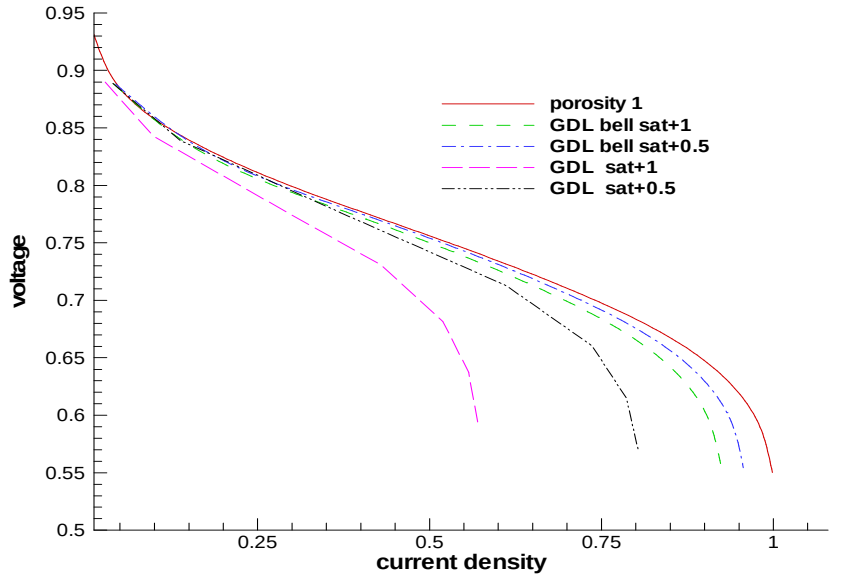

Figure 198. The polarization curves (Case porosity 1 is the base case)

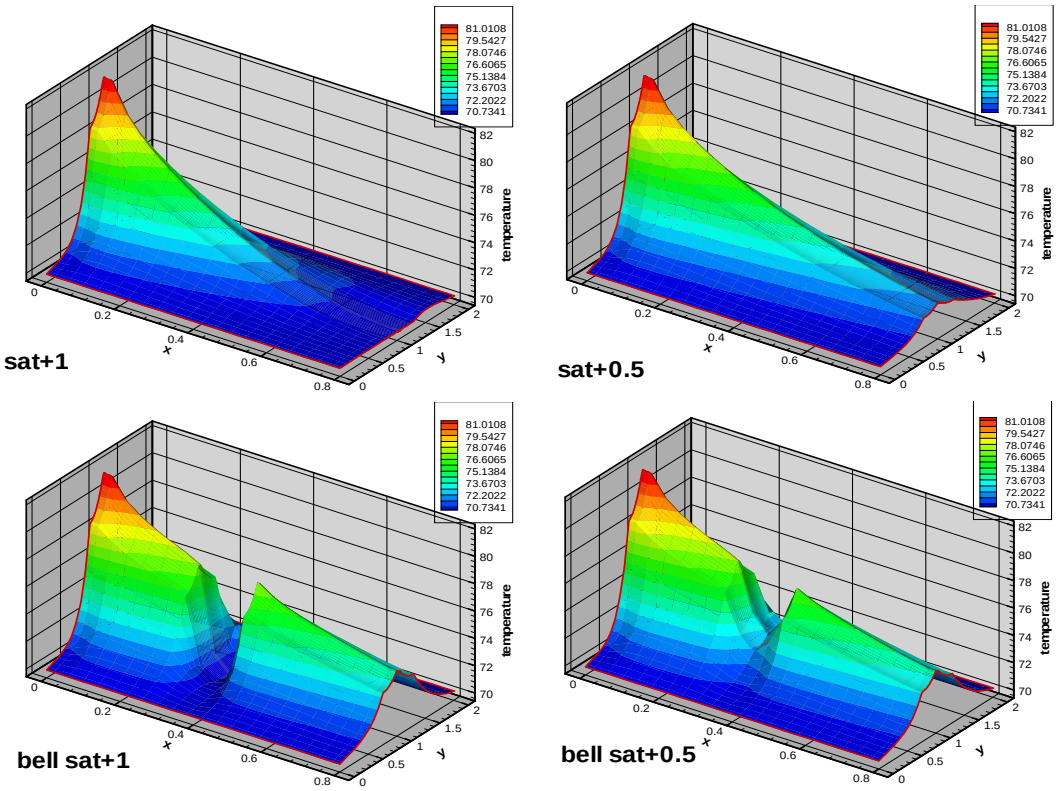

Figure 199. The local current density changes along z direction, overpotential =0.32 v.

Conclusions

Changing GDL saturation changes the mass transfer resistance: the larger the GDL saturation, the larger the mass transfer resistance. As a result, the power output and limiting current is reduced. Where the local current density is reduced, the local temperature is reduced too.

GDL Thickness - Linear Distribution

GDL thickness changes linearly along x-direction, but the total thickness of GDL+channel remains constant. Thus, the layer thickness of the gas channel is changed accordingly, either reduced or increased.

a. GDL thickness increases lineally and at the end the thickness is two times larger (GDL 2)
b. GDL thickness increases lineally and at the end the thickness is four times larger (GDL 4)
c. GDL thickness decreases lineally and at the end the thickness is two times smaller (GDL 1/2)
d. GDL thickness decreases lineally and at the end the thickness is four times smaller (GDL 1/4)

Figure 200 shows the grids used when the GDL thickness is changed. Figure 201 shows the polarization curves. Figure 202 is an example of the local temperature contours.

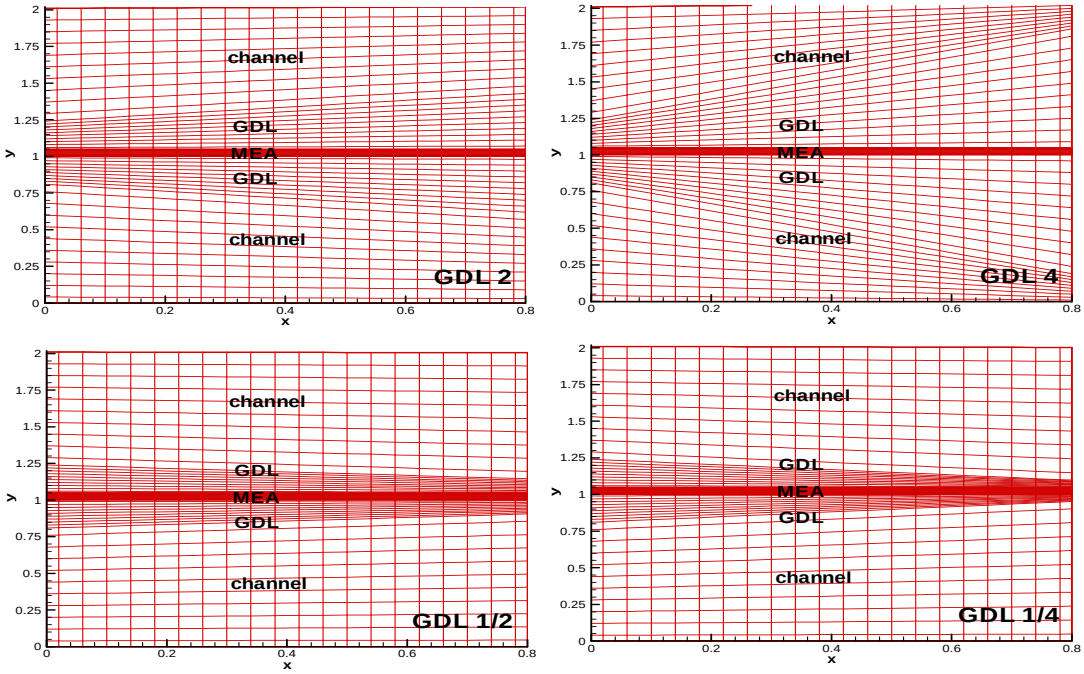

Figure 200. The computational grids

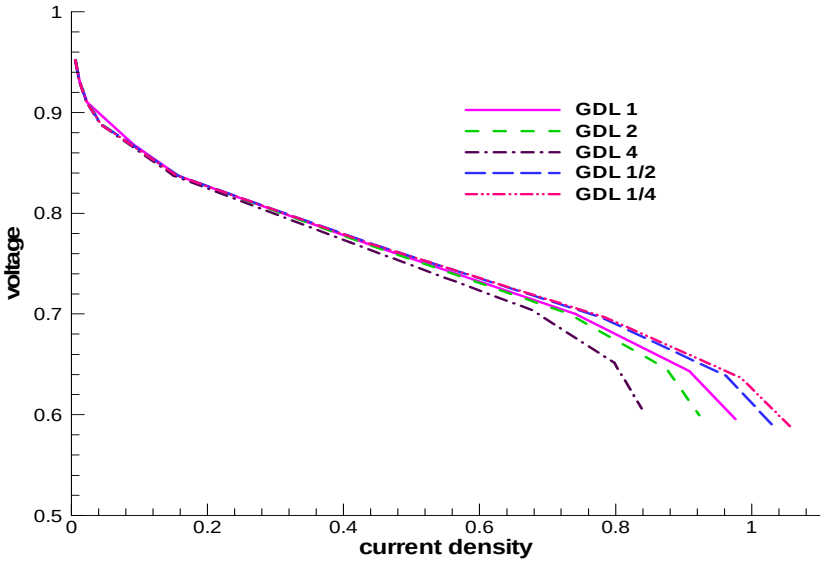

Figure 201. The polarization curves

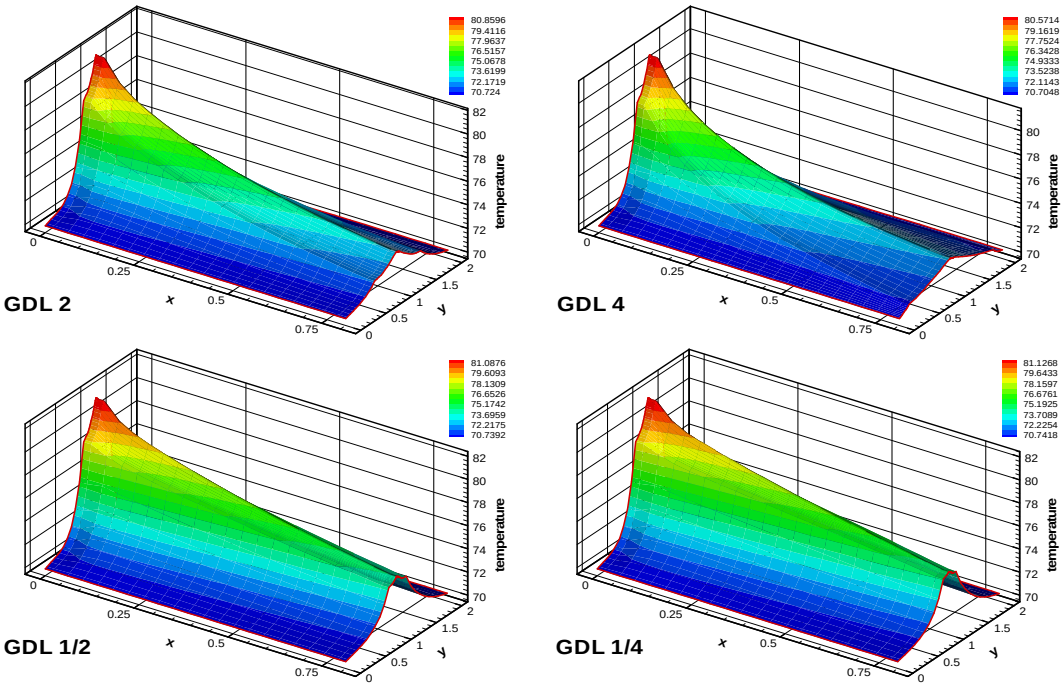

Figure 202. The local temperature contours at overpotential =0.32v. The current density for the four cases: 0.8747 A/cm^2, 0.7981 A/cm^2, 0.9624 A/cm^2, 0.9839 A/cm^2.

Conclusions - An increase in GDL thickness leads to the increase in mass transfer resistance. Thus, cases GDL 2 and GDL 4 have reduced power output and liming current densities. Where the local current density decreased, the local temperature is also decreased.

GDL Thickness - Bell Distribution

Inside the fuel cell, in one place the GDL thickness changes with sine distribution along x-direction, but the total thickness of GDL+channel remains constant. Thus, the layer thickness of channel is changed accordingly, either increased or reduced.

a. GDL increases and the largest GDL thickness is increased one half times CL+1/2)
b. GDL increases and the largest GDL thickness is increased one time (CL+1)
c. GDL decreases and the smallest GDL thickness is reduced 1/2 (GDL-1/2)
d. GDL decreases and the smallest GDL thickness is reduced one time, thus the smallest GDL thickness is zero (GDL-1)

Figure 203 shows the grids used when the GDL thickness is changed. Figure 204 shows the polarization curves. Figure 205 is an example of the local temperature contours.

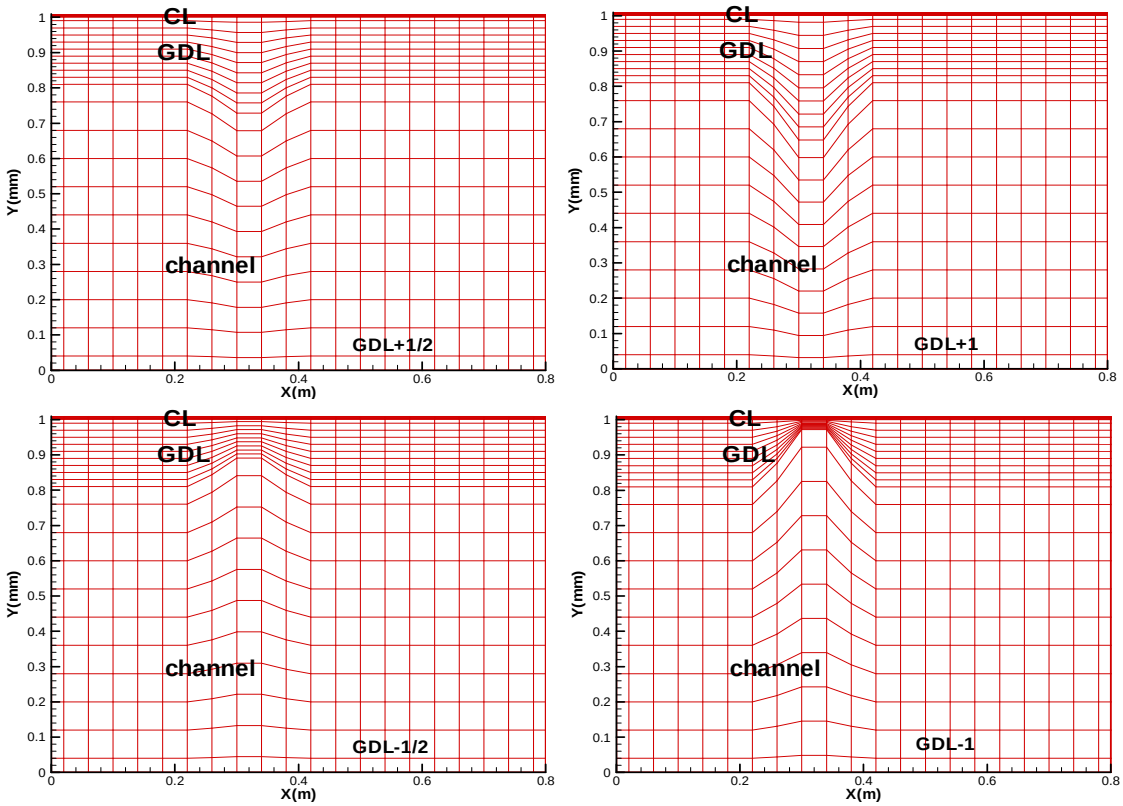

Figure 203. The computational grids

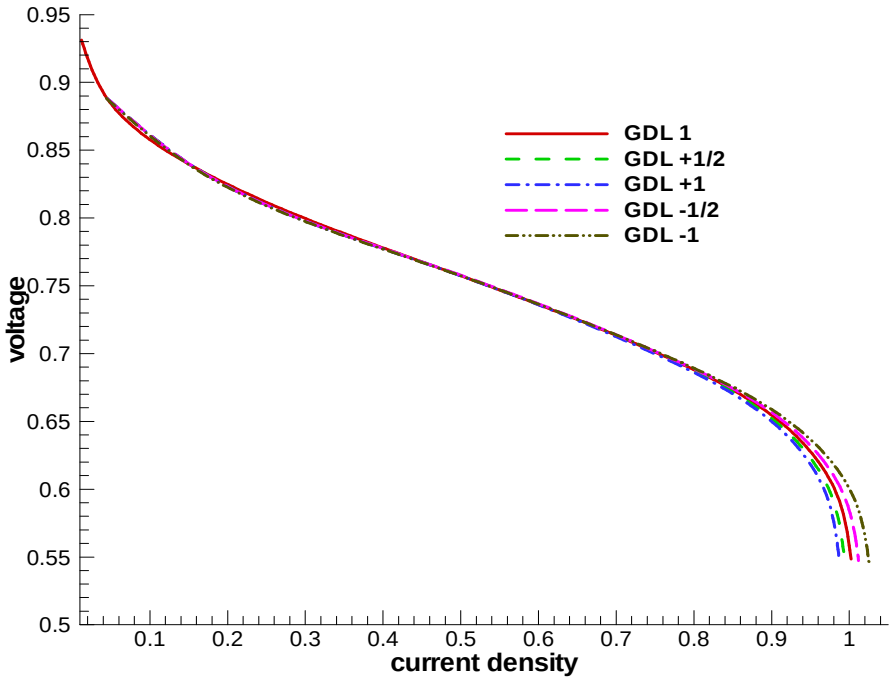

Figure 204. The polarization curves

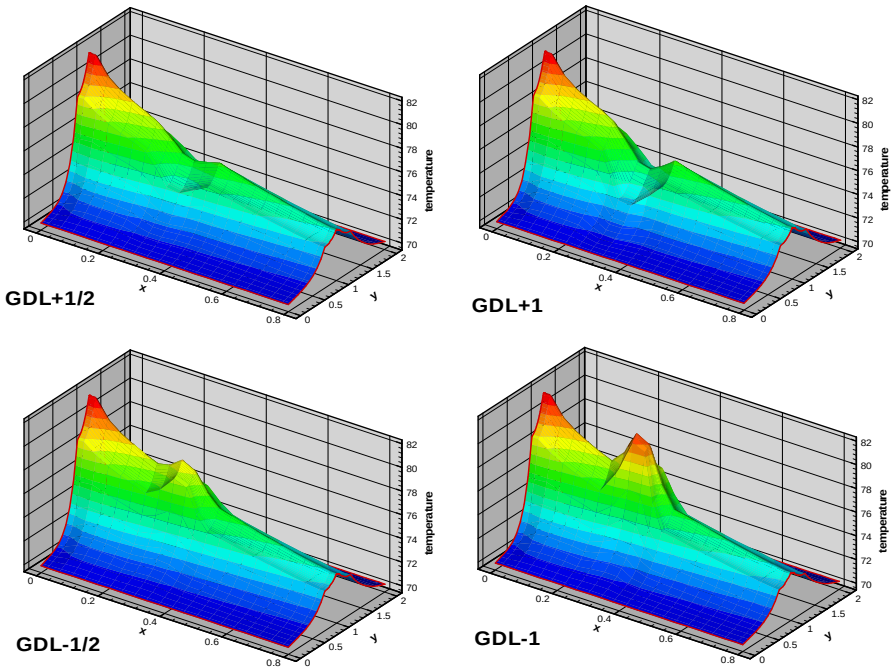

Figure 205. The local temperature contours at overpotential =0.32v. The current density for the four cases: 0.9204 A/cm^2, 0.9142 A/cm^2, 0.9345 A/cm^2, 0.9433 A/cm^2.

Conclusions

Same as " non-uniform thickness of GDL" section, namely an increase in GDL thickness leads to the increase in mass transfer resistance and reduced power output.

3.1.3 Membrane

Modeling practices have been carried out to study the effects of non-uniformities in the membrane due to: (1) thickness and (2) ionic conductivity

Membrane Thickness - Linear Distribution

Catalyst layer thickness changes linearly along x-direction, but the total thickness of MEM+CL remains constant. Thus, the membrane thickness is changed accordingly, either compressed or expanded.

a. CL thickness is constant (CL1-MEM)
b. CL thickness changes lineally and at the end the CL thickness is two times larger (CL 2-MEM)
a. CL thickness changes lineally and at the end the CL thickness is 1/2 times smaller (CL 1/2-MEM)

Figure 206 shows the grids used when the membrane thickness is changed. Figure 207 shows the polarization curves. Figure 208 is an example of the local temperature contours.

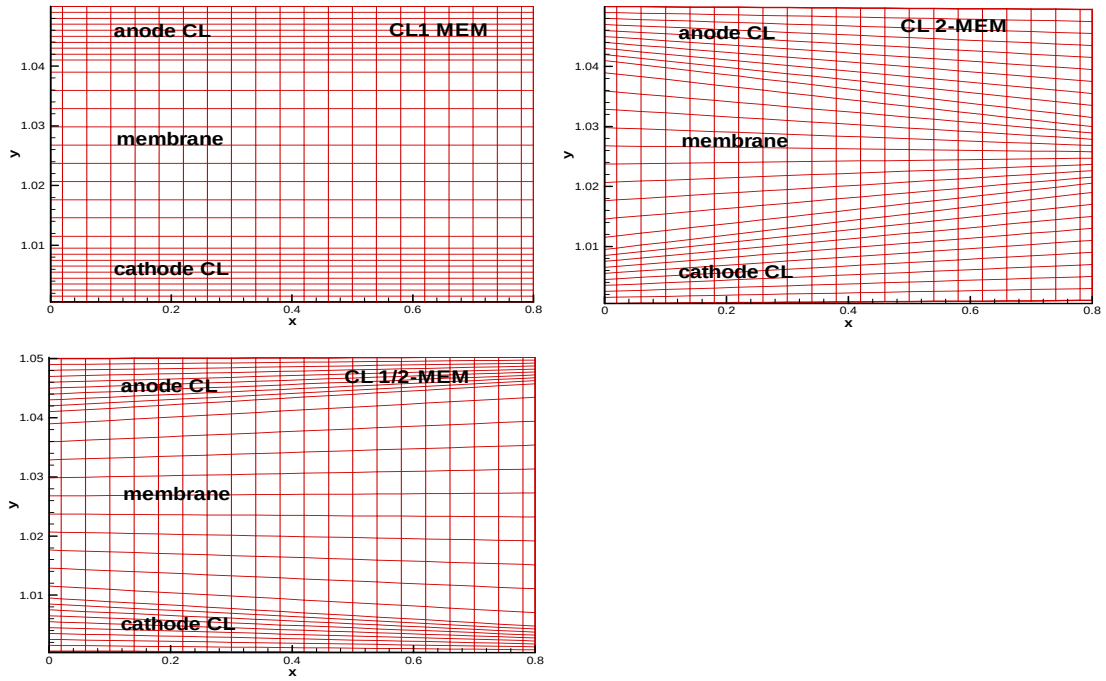

Figure 206. The computational grids

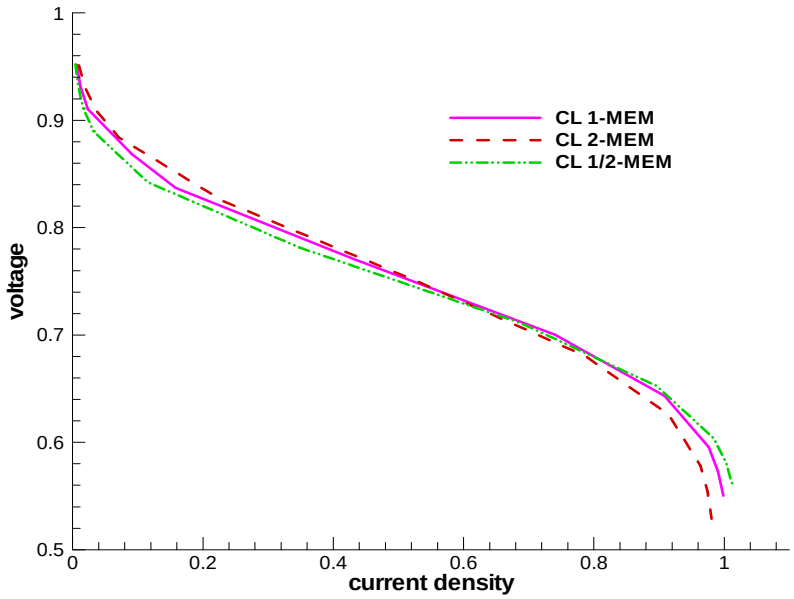

Figure 207. The polarization curves

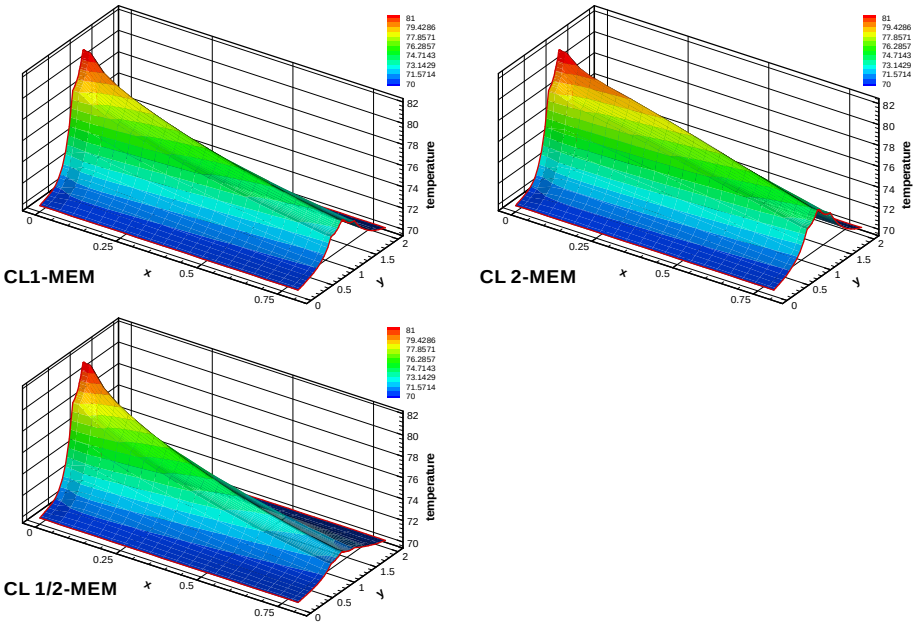

Figure 208. The temperature contours at overpotential =0.32v. The current density for the four cases: 0.9085 A/cm^2, 0.9147 A/cm^2, 0.8965 A/cm^2.

Conclusions

The change of CL thickness has two effects: it affects the mass transfer resistance and ohmic resistance. Thinner CL leads to smaller mass transfer resistance. But the reduction of ohmic loss within the catalyst layer is compensated by the increase in ohmic loss in the membrane, as the total thickness of MEM+CL remains constant.

CL1/2 –MEM: at low current densities, when there is enough oxygen, reduction of the CL thickness causes reduction of active area. Thus, power output is lower. But near the limiting current density, the power output becomes larger because of the reduction of mass transfer resistance..

CL 2-MEM: at low current densities, when there is enough oxygen, thicker CL thickness leads to larger power output because of the larger active area. At larger current densities, as mass transfer resistance increases, the power output gets lower.
Overall, the non-uniformities in CL thickness has negative effects on cell power output.

Membrane Thickness - Bell Distribution

Inside the fuel cell, in one place the catalyst layer thickness changes with sine distribution along x-direction, but CTL+MEM total thickness remains constant. Thus the layer thickness of MEM is changed accordingly, either compressed or expanded.

a. CL increases and the largest CL thickness is increased by oneCL+1 MEM)
b. CL increases and the largest CL thickness is increased by two (CL+2 MEM)
c. CL decreases and the smallest CL thickness is reduced by one-half (CL-1/2 MEM)
d. CL decreases and the smallest CL thickness is reduced by one resulting in zero CL thickness (CL-1 MEM)

Figure 209 shows the grids used when the membrane thickness is changed. Figure 210 shows the polarization curves. Figure 211 is an example of the local temperature contours.

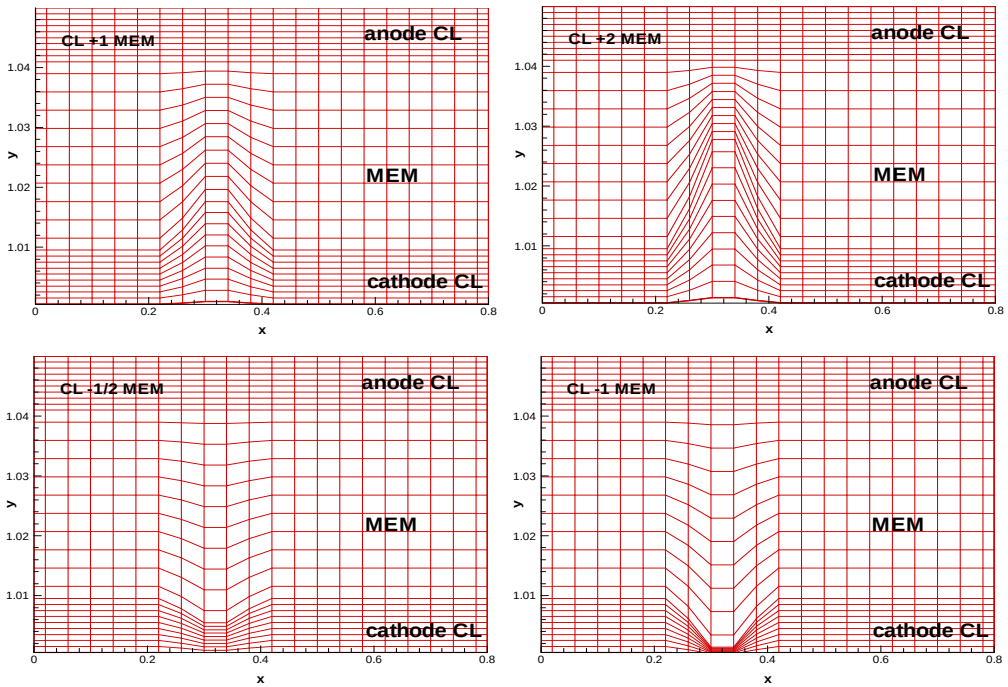

Figure 209. The computational grids

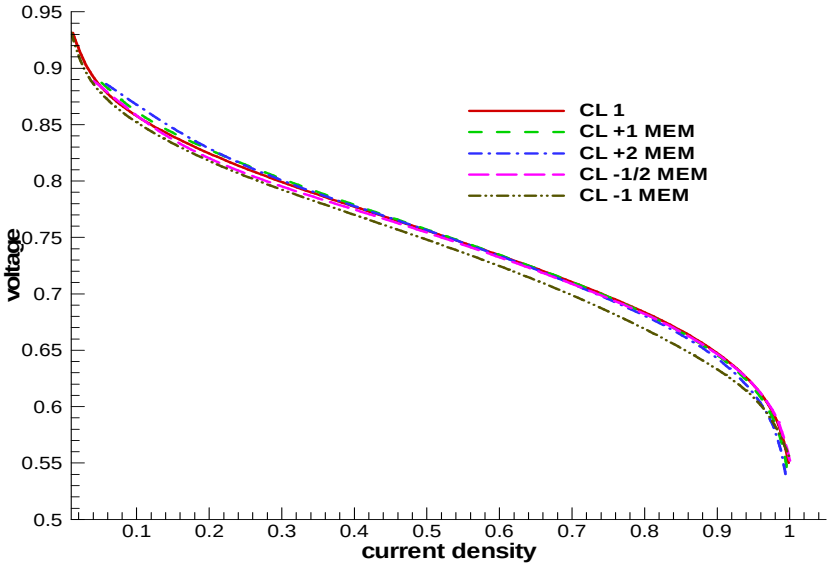

Figure 210. The polarization curves

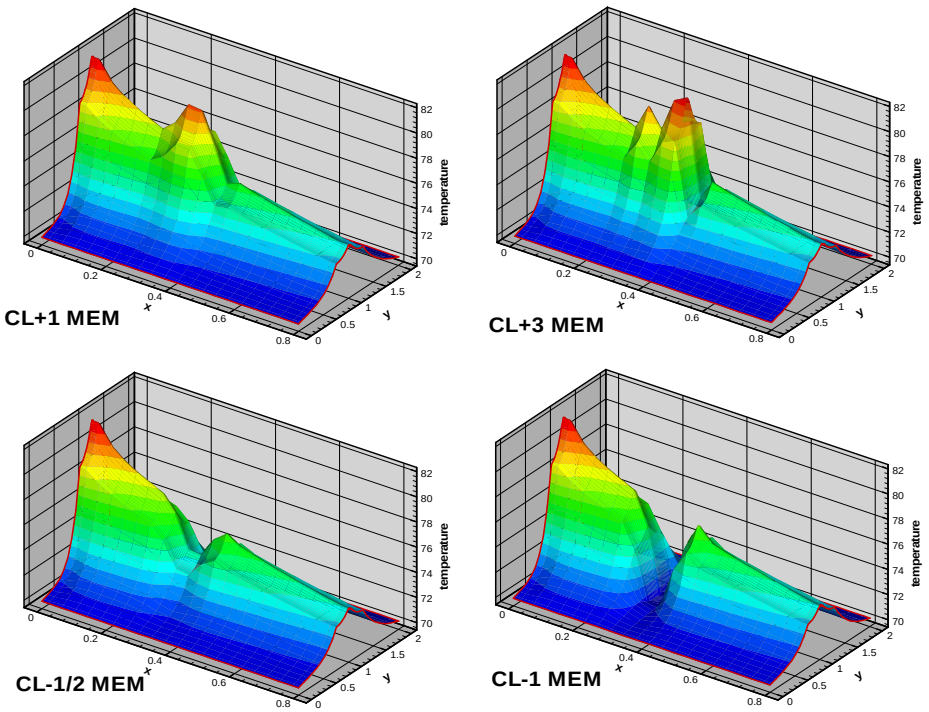

Figure 211. The local temperature distributions at overpotential =0.32v. The current density for the four cases: 0.91101 A/cm^2, 0.907461 A/cm^2, 0.903977 A/cm^2, and 0.861003 A/cm^2.

Conclusions - Reduced CL thickness leads to reduced activation area and reduced mass transfer resistance. Thus, case "CL -1 MEM" has reduced power output, but increased limiting current density. Case "CL+2 MEM" has larger power output at low current density, but smaller limiting current density. Temperature 'hot spots' may result from the changing layer thickness.

Variable Ionic Conductivity of the Membrane

Inside the membrane, the ionic conductivity of the membrane changes along x-direction:

a. Ionic conductivity constant (MEM ionic 1)
b. Ionic conductivity increases linearly and the largest MEM ionic conductivity is increased by five times (MEM ionic*5)
c. Ionic conductivity decreases linearly and the smallest MEM ionic conductivity is reduced by half (MEM ionic*1/2)
d. Ionic conductivity increases at one place with a sine function and the largest MEM ionic conductivity is increased by five times (MEM bell ionic*5)
e. Ionic conductivity decreases at one place with a sine function and the smallest MEM ionic conductivity is decreased by one-half (MEM bell ionic*1/2)

Figure 212 to Figure 214 illustrate the membrane conductivity profiles, the resulting polarization curves and the temperature distribution inside the fuel cell, respectively.

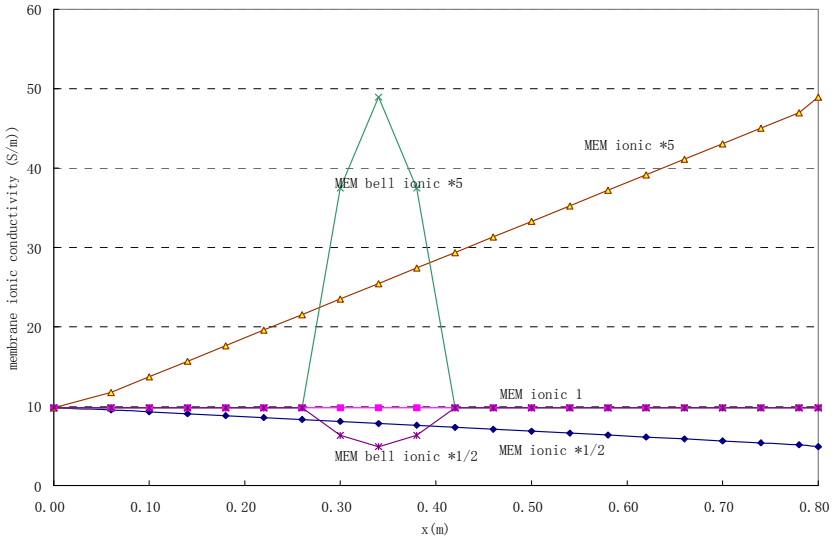

Figure 212. Membrane ionic conductivity profiles

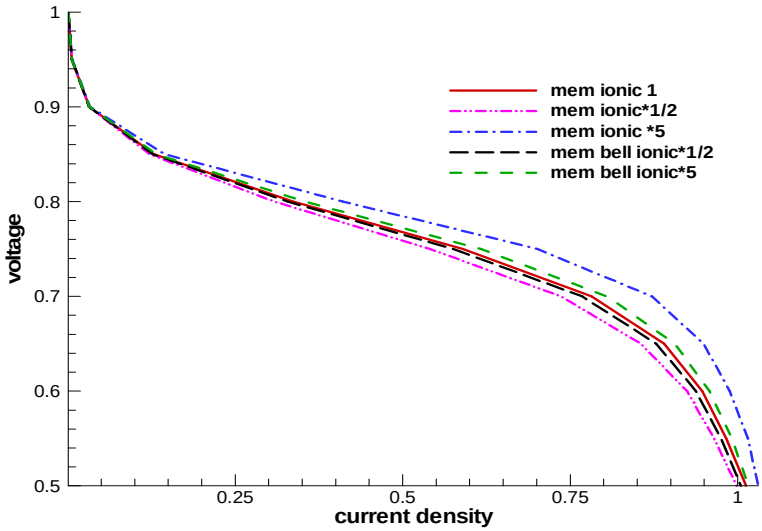

Figure 213. The polarization curves

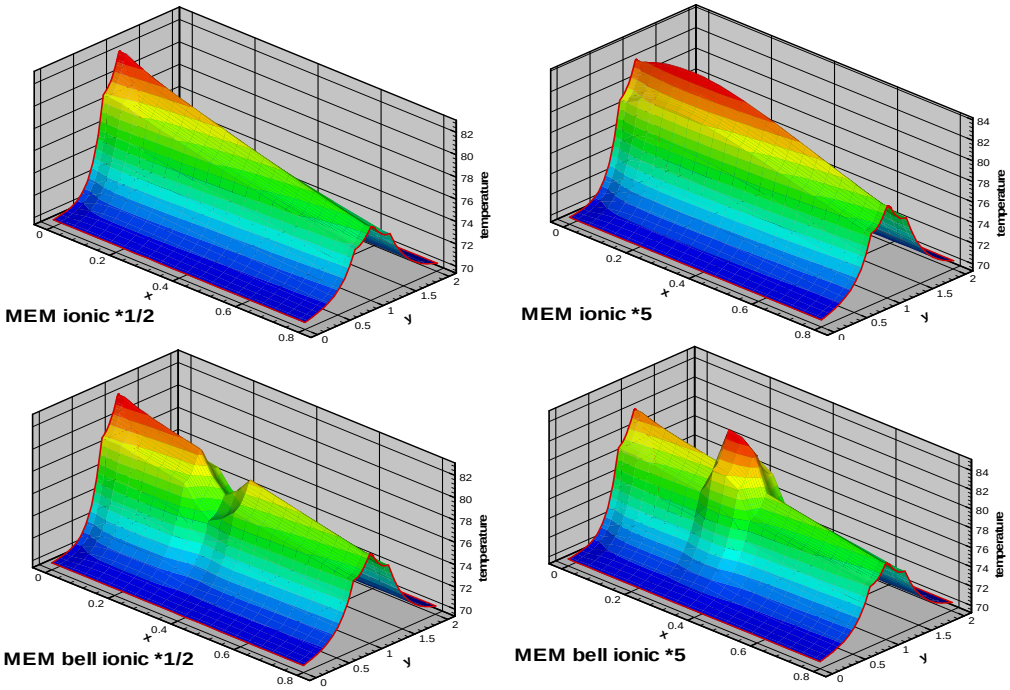

Figure 214. The local temperature distributions at cell voltage=0.70 v. The current densities for the four cases are: 0.7361 A/cm^2, 0.8719 A/cm^2, 0.7678 A/cm^2 and 0.8051 A/cm^2.

Conclusions

The change of MEM ionic conductivity affects power output. Larger ionic conductivity leads to less ohmic loss, and larger power output. There is no obvious influence by the MEM ionic conductivity on mass transfer. The most obvious influence is on the distribution of current density.

The ionic conductivity affects temperature in two aspects: 1) the distribution of local current density and 2) the heat generation rate. As theheat generation rate is inversely proportional to the ionic conductivity, increasing ionic conductivity leads to decreasing heat generation. But increasing ionic conductivity also leads to increasing current density and thus increasing heat generation. The overall result is a temperature increase with increasing conductivity.

3.1.4 Heat Transfer Properties

Wall Temperature

Inside the fuel cell, the wall temperature changes along x-direction.

a. Temperature increases linearly and the largest temperature at the end of the channel is 10C higher (temp +10)
b. Temperature increases linearly and the largest temperature at the end of the channel is 15C higher (temp +15)
c. Temperature increases linearly and the largest temperature at the end of the channel is 10C lower (temp -10)
d. Temperature increases linearly and the largest temperature at the end of the channel is 20C lower (temp -20)

Figure 215 to Figure 217 illustrate the wall temperature profiles, the resulting polarization curves and the temperature distribution inside the fuel cell, respectively.

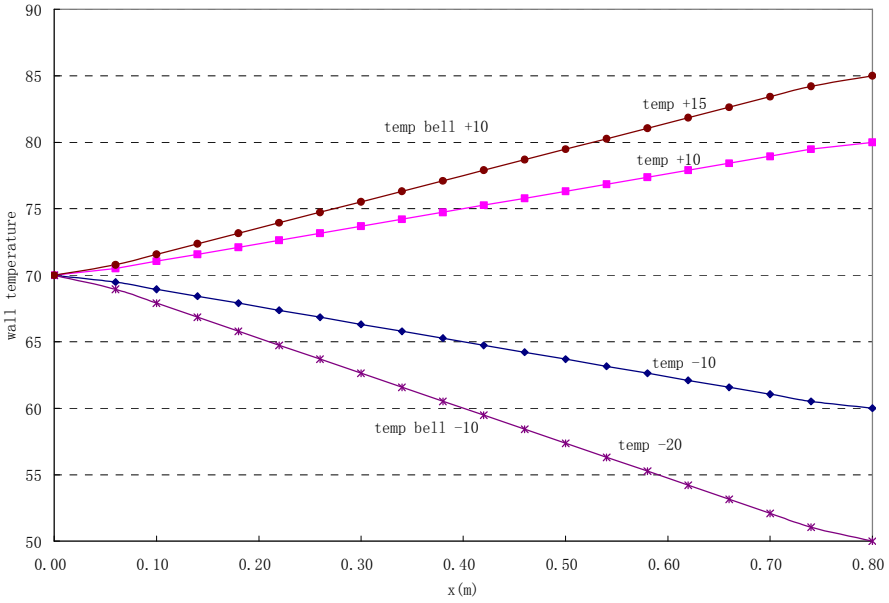

Figure 215. Wall temperature profiles

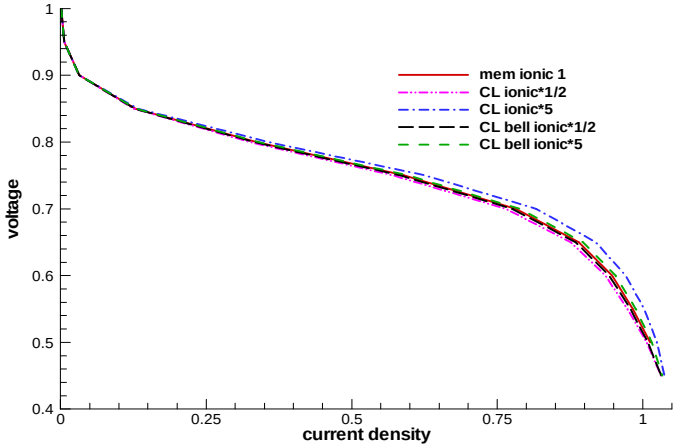

Figure 216. The polarization curves (Case porosity 1 is the base case)

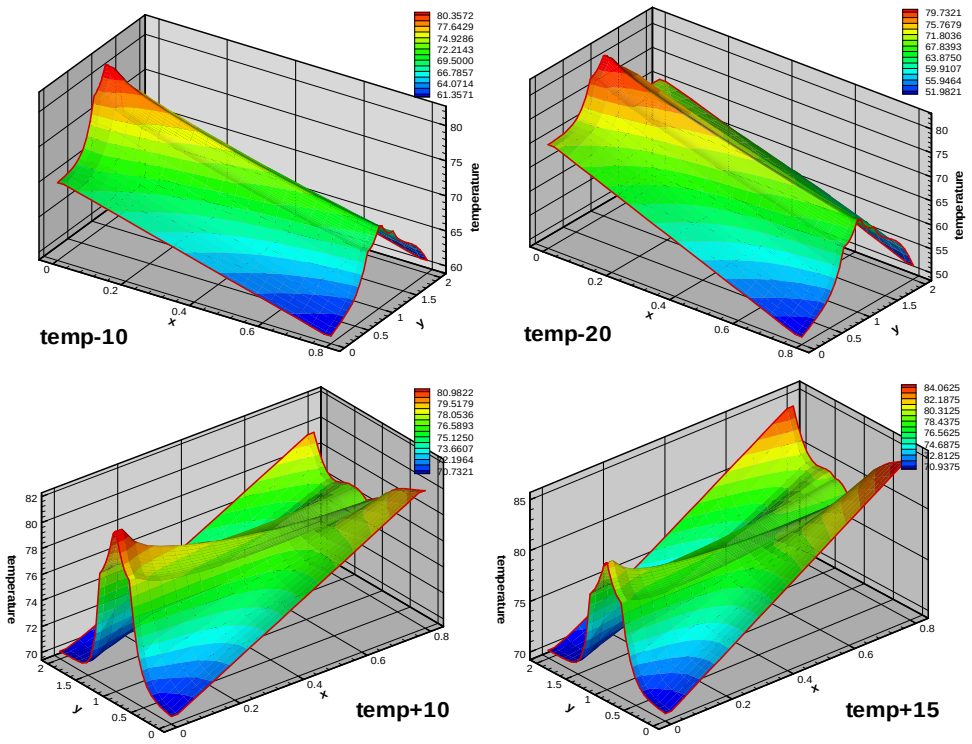

Figure 217. The temperature contours at overpotential =0.32 v.

Conclusions –

Changing the wall temperature changes the power output. Higher wall temperature leads to a small decrease in power output. Lowing wall temperatures near the exit can help reduce the core temperature.

Prandtl Number

Inside the fuel cell, the Prandtl number changes along x-direction. The Prandtl number is defined as**Error! Objects cannot be created from editing field codes.**

a. The Prandtl number increases linearly along x direction, and the largest Prandtl number is 10 times larger

b. The Prandtl number decrease linearl along x direction, and the smallest Prandtl number is 1/10

c. The Prandtl number increases at one place with sine function along x direction and the largest Prandtl number is 10 times larger

d. The Prandtl number decrease linearly at one place with sine function along x direction and the smallest Prandtl number is 11/10

Figure 218 to Figure 220 illustrate the Prandtl number profiles, the resulting polarization curves and the temperature distribution inside the fuel cell, respectively

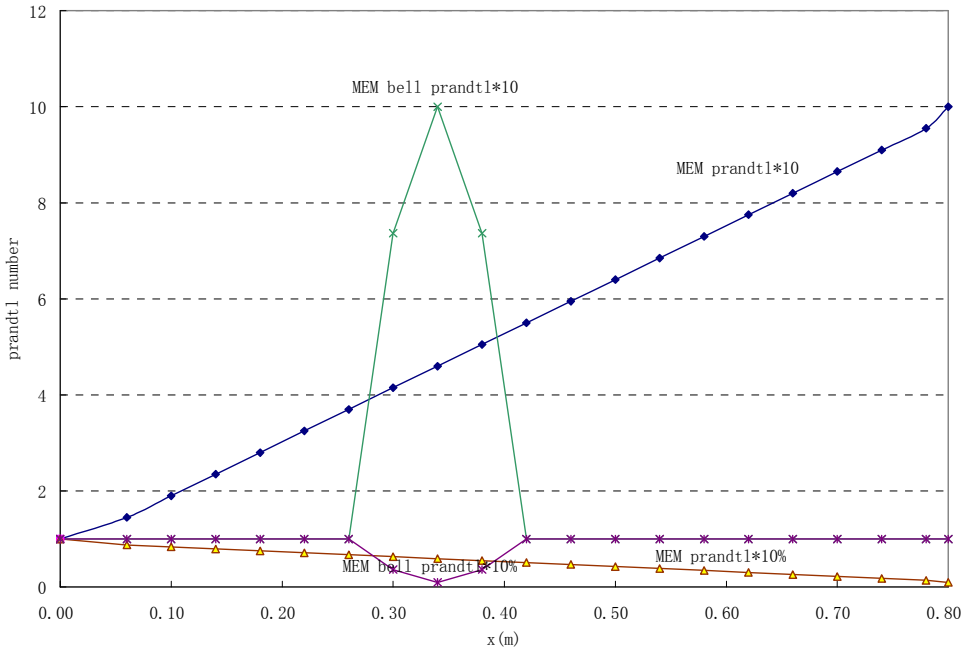

Figure 218. Prandtl number (Pr/Pr_0) profiles along x-direction

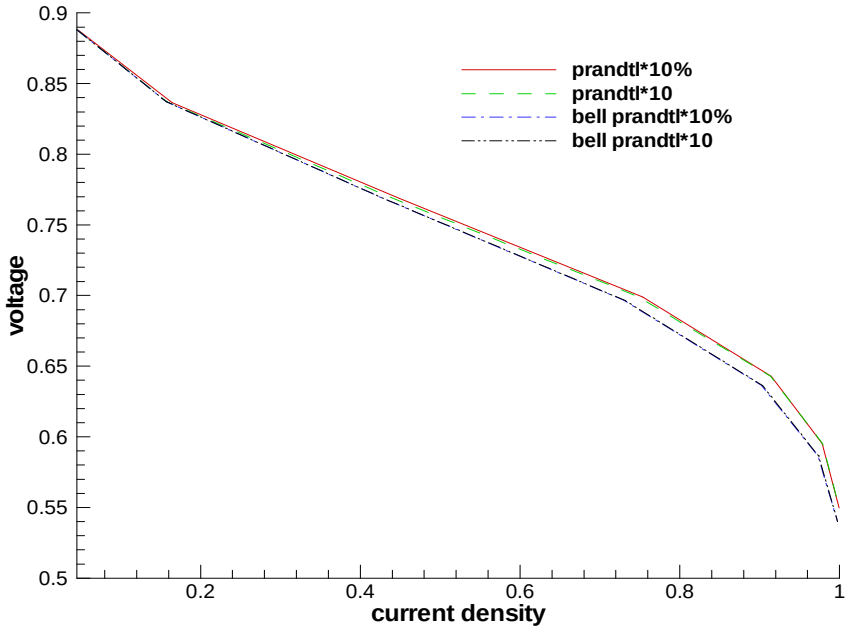

Figure 219. The polarization curves (Case porosity 1 is the base case)

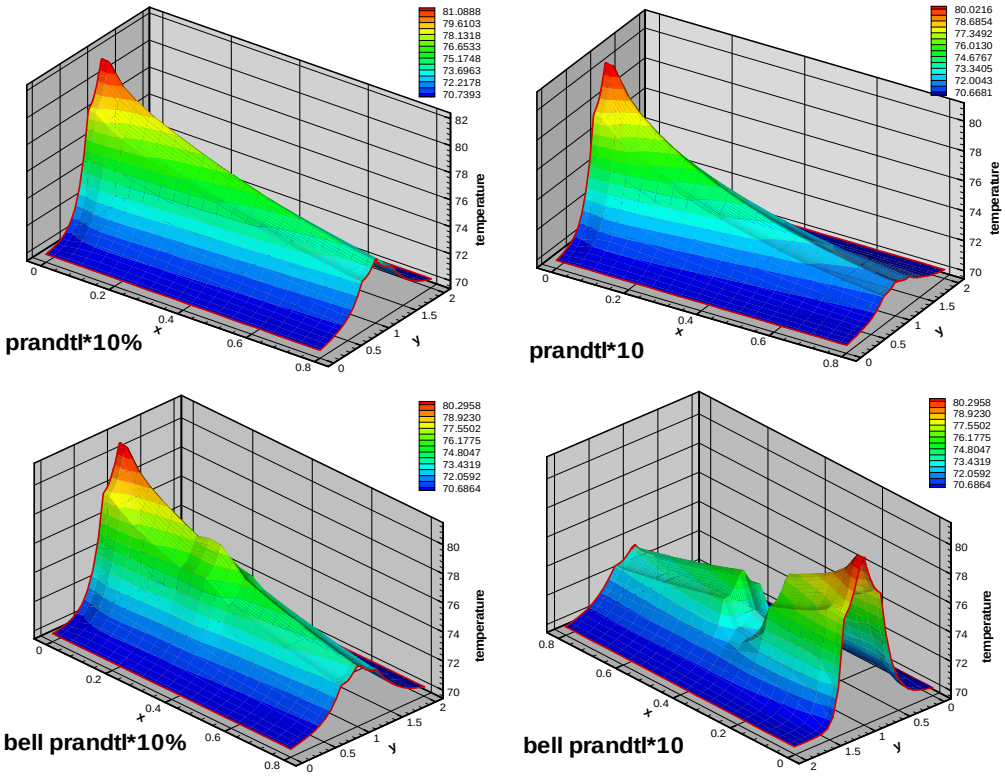

Figure 220. The temperature contours at overpotential =0.32 v.

Conclusions

Changing the Prandtl number affects the core temperature. As the Prandtl number is increased, the core temperature is reduced. At high core temperature, the power output is reduced.

3.1.5 Flow Distributions

The Base Case

In the base case, two channels have same inlet velocities, pressures, and oxygen concentrations

Figure 221 shows the flow field when two channels are studied. Figure 222 shows the oxygen concentrations (OXZ plane) inside GDL.

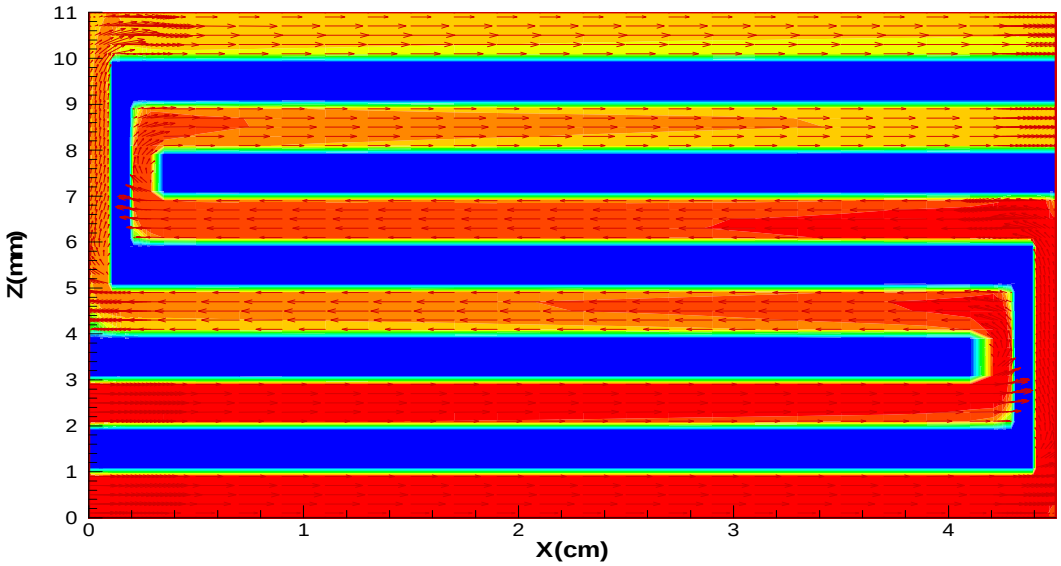

Figure 221. The flow field

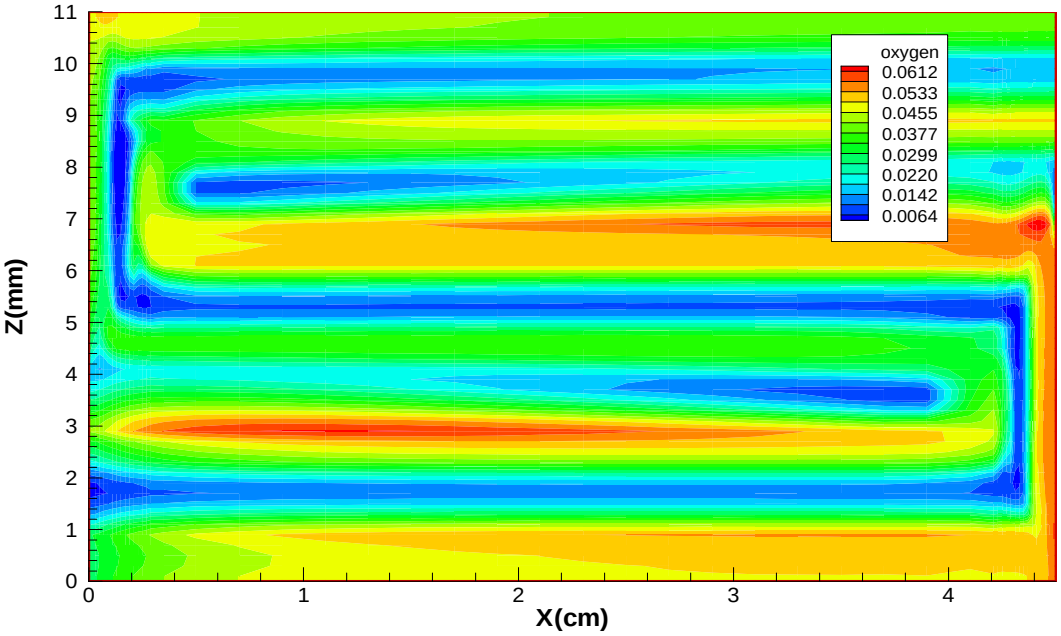

Figure 222. The oxygen concentrations (OXZ plane) inside GDL

Oxygen Concentration Reduced by 1/2

Figure 223 shows the flow field when the oxygen concentration in the 2nd channel is reduced by 1/2. Figure 224 shows the polarization curves.

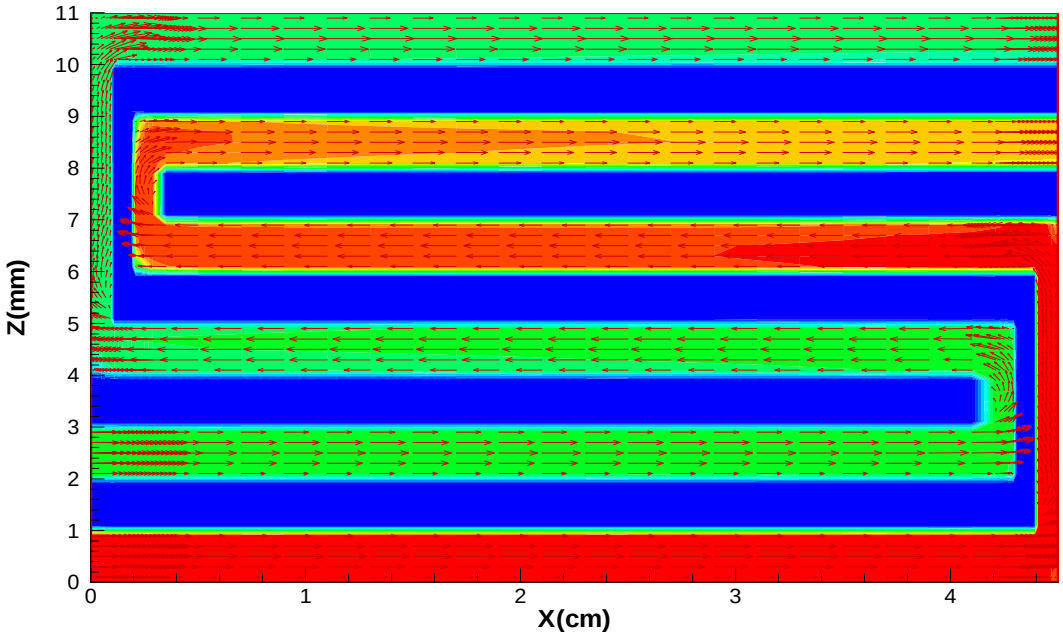

Figure 223. The flow fields

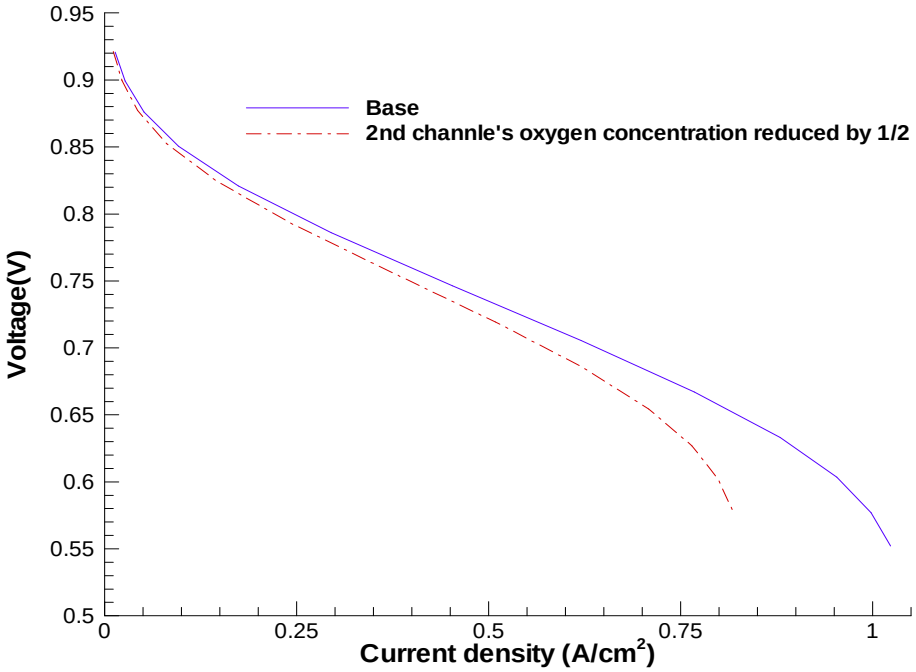

Figure 224. The polarization curves

The Inlet Velocity Reduced by 1/2

Figure 225 shows the flow field when the velocity in the 2nd channel is reduced by 1/2. Figure 226 shows the polarization curves.

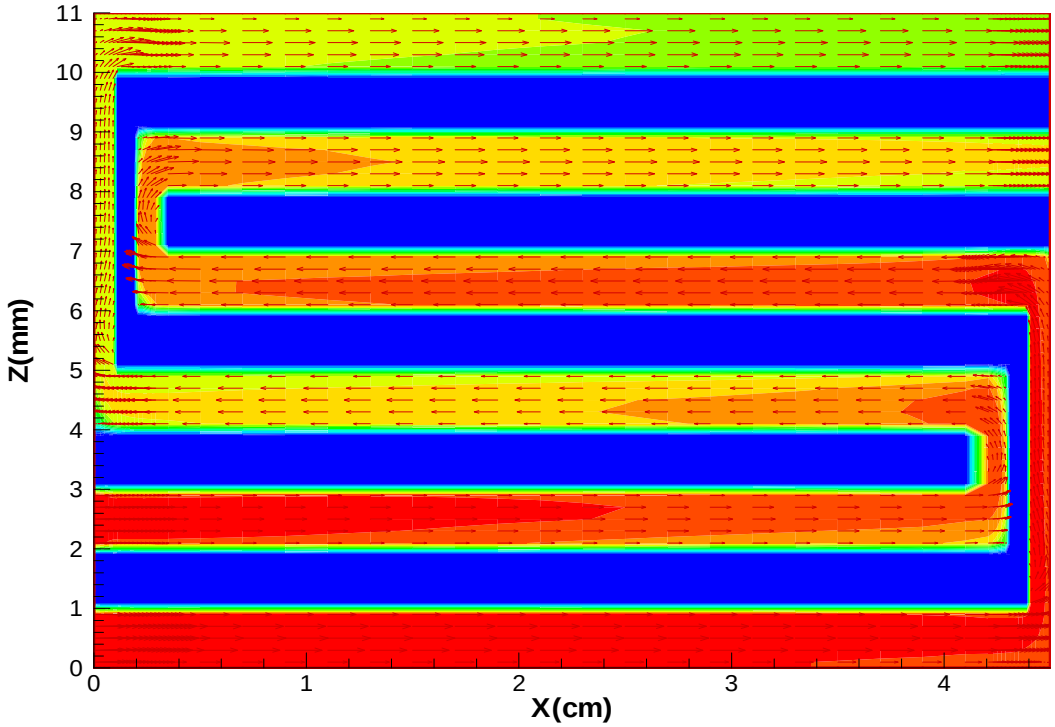

Figure 225. The flow fields

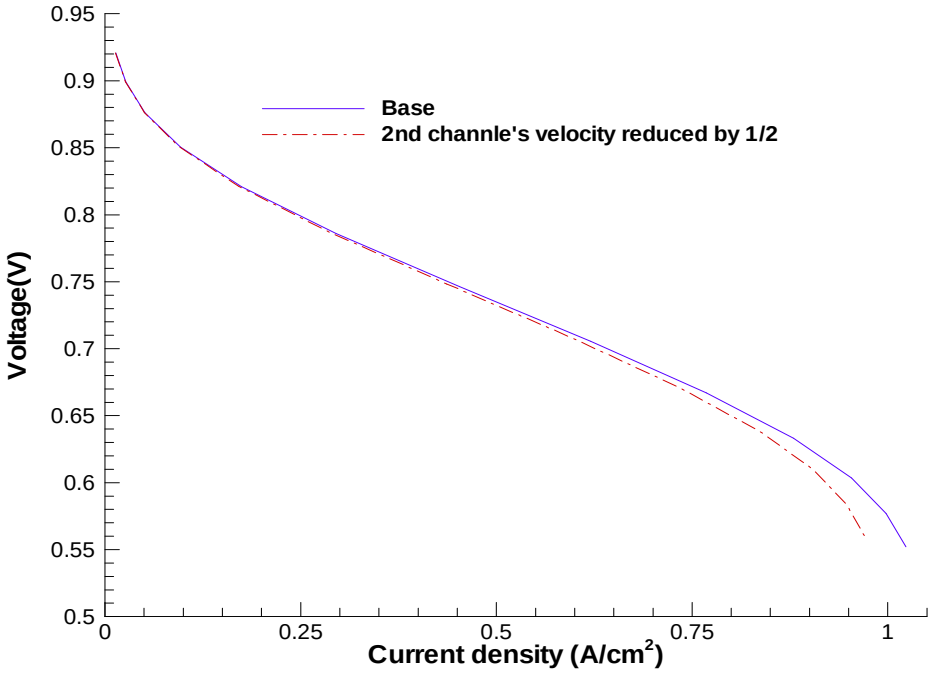

Figure 226. The polarization curves

The Pressure is Doubled

Figure 227 shows the polarization curves when the pressure in the 2nd channel is doubled. Figure 228 shows the oxygen concentrations (OXZ plane) inside GDL. When the 2nd channel's pressure is doubled, there is more oxygen fed to the channel.

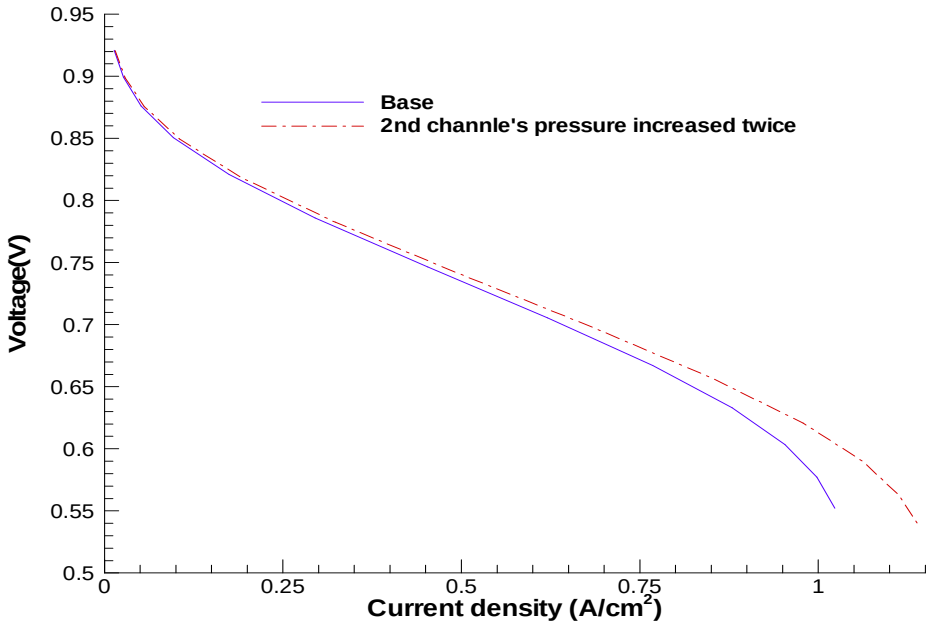

Figure 227. The polarization curves

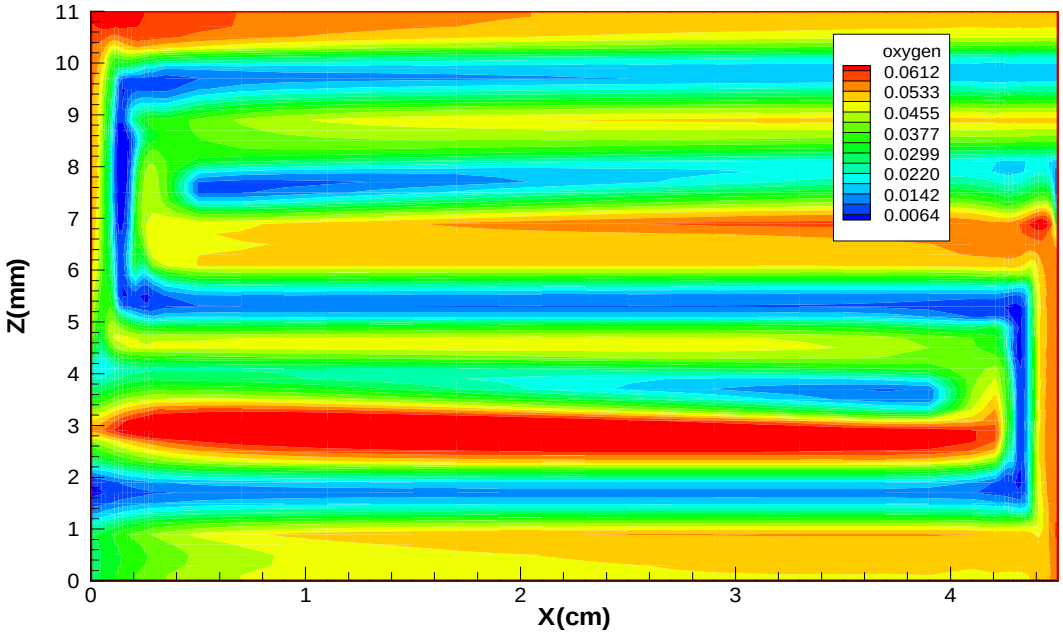

Figure 228. The oxygen concentrations (OXZ plane) inside GDL

3.2 Nonuniformity Studies – Experimental 50cm^2 Cell

3.2.1. Segmented Cell

Introduction

Mapping of the current distribution in an operating fuel cell could be critical to understanding MEA durability. A highly non-uniform current distribution may result in excessive local stresses in the MEA resulting in premature MEA failure. Several mathematical PEM fuel cell models have predicted non-uniform current distributions under a variety of operating conditions (1 - 3). However, experimental techniques have yet to provide sufficient data to confirm the modeling results.

Several approaches have been used to experimentally map current distribution in an operating fuel cell. Arrays of passive resistors[4], Hall sensors[5,6], segmented current collector/flow field or channel[3,7-11], and segmented MEA[7], [12] have been employed to measure current distribution. While all of these techniques offer advantages, they also have disadvantages such as poor spatial resolution, poor real-time measurement capabilities and MEA segmentation (*i.e.*, segmenting the MEA into electrically isolated geometric shapes). This work aims to extend the printed circuit board (PCB) approach employed by Brett et al[5] from monitoring current distribution in a single flow channel to monitoring current distribution in a full 50-cm2 quad-serpentine flow field.

The purpose of this section is to present a new, segmented cell design for *in-situ* monitoring of current distribution and demonstrate its performance during PEM fuel cell operation. The section investigates the effects of load setting, cathode flow rate and GDL design on current distribution uniformity for a quad-serpentine flow field. Early measurements were made with each of the 11 segments defined as a single pass down the quad-serpentine flow field. Once a 121 multi-channel load was completed, the spatial resolution of this segmented cell design increased by an order of magnitude, as each 'single pass segment' was divided into 11 smaller segments.

Segmented Cell Construction

The segmented electrode is a four-layer PCB made from FR4, a standard epoxy/fiberglass composite used in the circuits industry. The total thickness of the four-layer circuit board is 1.57 mm. PCB technology was utilized to fabricate a circuit consisting of 121-segments (11 by 11 matrix) in the shape of a 50-cm^2 quad-serpentine flow field (Figure 229). Each of the 121 segments consists of three rectangular electrodes and two rhombus shaped electrodes with a total area of ~ 0.41cm^2. The segments can be individually addressed as needed for testing through two 64-pin header connectors. Additionally, each segment has the capability for local impedance and temperature measurements.

Each circuit layer was constructed by etching a 36 μm thick Cu layer to the specification of the circuit design for that layer. Through holes were then drilled to provide for electrical connections between the segments and circuit layers. The through holes were etched and Cu plated to ensure electrical conductivity. To prevent gas leakage, the holes were filled with Cu and then top plated with Cu. A nominally 0.81 mm width by 0.76 mm depth serpentine gas flow channel with 0.81 mm channel separation was milled into the top layer of the FR4 epoxy/fiberglass composite to make a 50-cm2 quad-serpentine flow field. After milling, a 5.1 μm Ni barrier was applied to all

of the Cu surfaces followed by a hard plating of 18.3 µm of Au. A cross-section of the circuit board is shown in Figure 230.

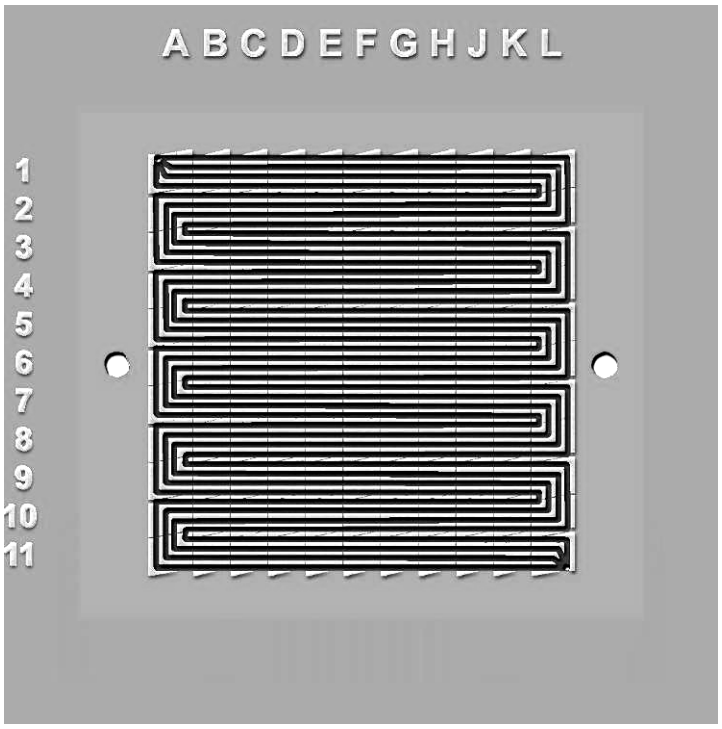

Figure 229. Drawing of segmented circuit board quad-serpentine flow field. Each segment consists of three rectangular electrodes and two rhombus electrodes. Total area of segment is ~ 0.41 cm^2 while total area of cell is 50 cm^2.

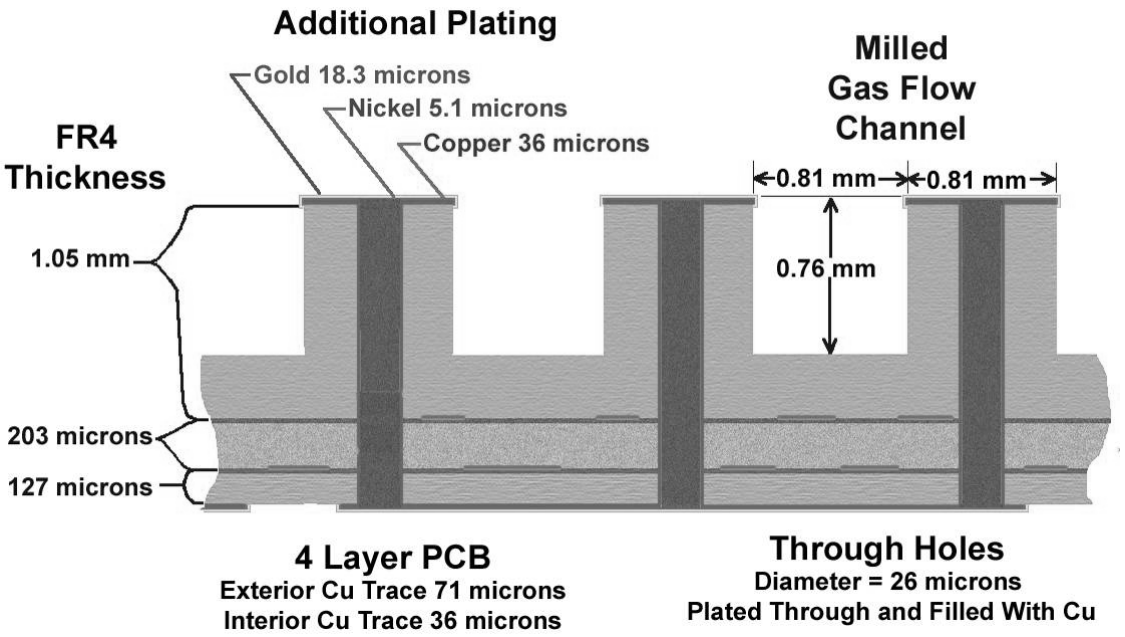

Figure 230. Cross-sectional drawing of printed circuit board construction.

Validation of Segmented Cell Design

As a first step to prove that the segmented cell design and fabrication was not influencing the test results, the resistance of the eleven segments was measured. Resistance measurements were made with only the flow fields present and with a GDL sandwiched between the flow fields. In both cases, the segment-to-segment resistance variation was less than 0.02 Ω. Additionally, the presence of the GDL resulted in a random distribution indicating that there is not a resistance bias in the down channel direction.

Figure 231 offers further proof that the segmented cell is operating correctly. Figure 231 plots the total current obtained by summation of the measured current from the eleven individual segments and the total current measured when the segments are shorted to function as one electrode in a fuel cell test. The data from the two experiments is in excellent agreement except for the 100 sccm air flow data for which the total current for the shorted cell is greater than the total current of the segmented cell at cell voltages less than 0.75 V. The discrepancy in the data resulted from the inability of the air MFC in the Fuel Cell Test Station to control the air flow at the 100 sccm set-point, i.e., the actual air flow rate was closer to 150 sccm.

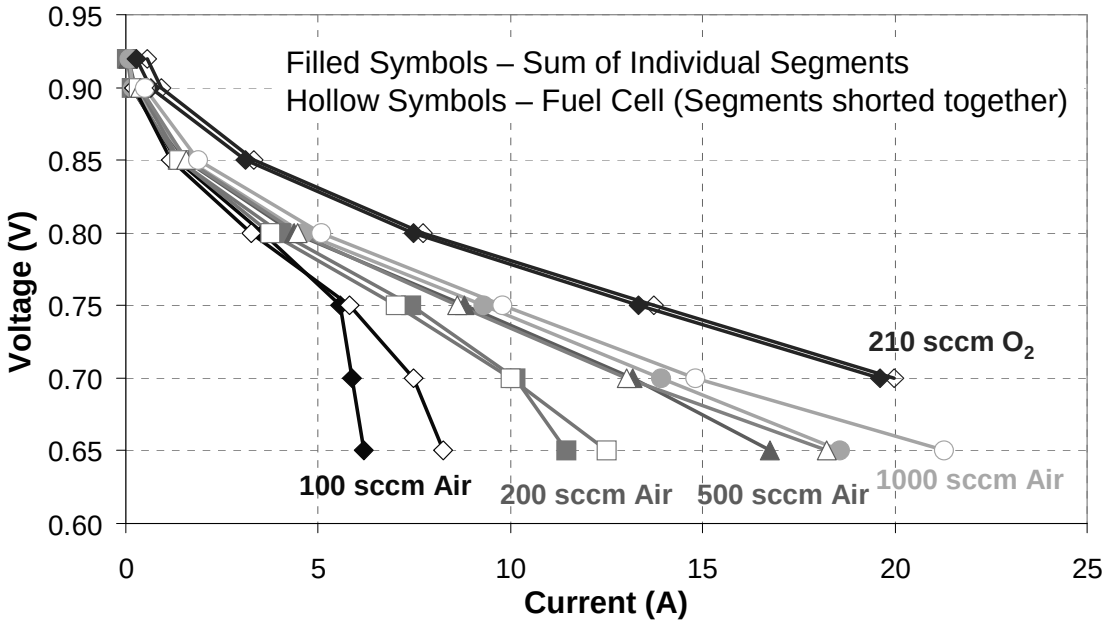

Figure 231. Comparison of total current obtained by summation of the measured current from the eleven individual segments to total current measured when the eleven segments are shorted to function as one electrode in a fuel cell test. Test conditions: 500 sccm H_2/variable sccm Air, 75ºC cell, 90% inlet gas RH and ambient pressure.

3.2.2 Impact of GDL Type on Current Uniformity

Experimental
Experimental Set-up

The membrane electrode assemblies (MEAs) tested consisted of a 30 μm cast Nafion® 1000 EW membrane with a 0.4 mg Pt/cm2 electrode on both sides of the membrane. The active area of the electrodes is 50 cm2 and PTFE reinforced glass gaskets were used for all experiments. Three different gas-diffusion layer (GDL) backings were evaluated: (1) a rigid paper, (2) a flexible non-woven and (3) a flexible woven. All of the GDLs have the same microlayer composition.

Testing was conducted under H2/Air or H2/O2 at 75ºC cell temperature, ambient pressure and 90% inlet gas relative humidity. Additionally, the gas streams were configured in co-flow orientation and the H2 flow was fixed at 500 sccm while the cathode feed stream varied from 100 to 1000 sccm of air or 210 sccm of O2.

Segmented Cell Configuration

The MEA was mounted into a 50-cm2 Fuel Cell Technologies test cell with a whole, quad-serpentine graphite flow field on the anode and a segmented, quad-serpentine PCB flow field on the cathode. The test cell bolts were tightened to 110 in-lbs. Gas was delivered to the segmented cell via Brooks Series 5850S mass flow controllers (MFCs). The gas was humidified using steam injectors supplied with deionized water (~ 18 MΩ·cm resistance) by a Shimadzu model LC-10AT VP HPLC pump. LOVE Electronics model 1600 temperature controllers controlled both the cell and the steam injector temperature. The segmented cell was shorted from 121 segments to 11 larger segments of ~ 4.5 cm2. The larger segments represent one pass down the quad-serpentine flow field (rows 1 to 11 in Figure 1). The segmented cell was controlled by two Solartron 1470A Multistats and CorrWare® software.

Fuel Cell Configuration

The configuration for the fuel cell testing is the same as the segmented cell configuration except for the following: (1) all segments in the segmented, PCB cathode flow field were shorted together to make one electrode; (2) Lab Alliance model 1 pumps were used to supply the deionized water to the steam injectors; (3) a Fuel Cell Technologies Fuel Cell Test Station with a Hewlett-Packard model 6050A electronic load was used to discharge the fuel cell; and (4) all functions of the fuel cell test station were computer controlled via 3M-developed Fuel Cell Testing Software.

Resistance Measurements.

A 1 Ω resistor was place in series between the segmented cell and the 1470A multistat. The 1470A multistat was used to set the voltage at 0.1, 0.25 and 0.5 V and measure the corresponding current. The resistance was then calculated via linear regression of the data set with the intercept set to zero.

Results and Discussion
Effect of Load Setting

The effect of load setting on the current distribution is shown in Figure 232 for 200 sccm of air. The difference between the minimum and maximum segment current increases as the total current is increased. In general, the current decreases from inlet to outlet. However, the highest current is not observed at the inlet; it is observed in the second segment from the inlet. Cleghorn et al. have proposed that the catalyst layer or the membrane is insufficiently humidified near the inlet thereby resulting in lower currents (7). Further evaluation of this occurrence is planned with the full 121-channel electrode.

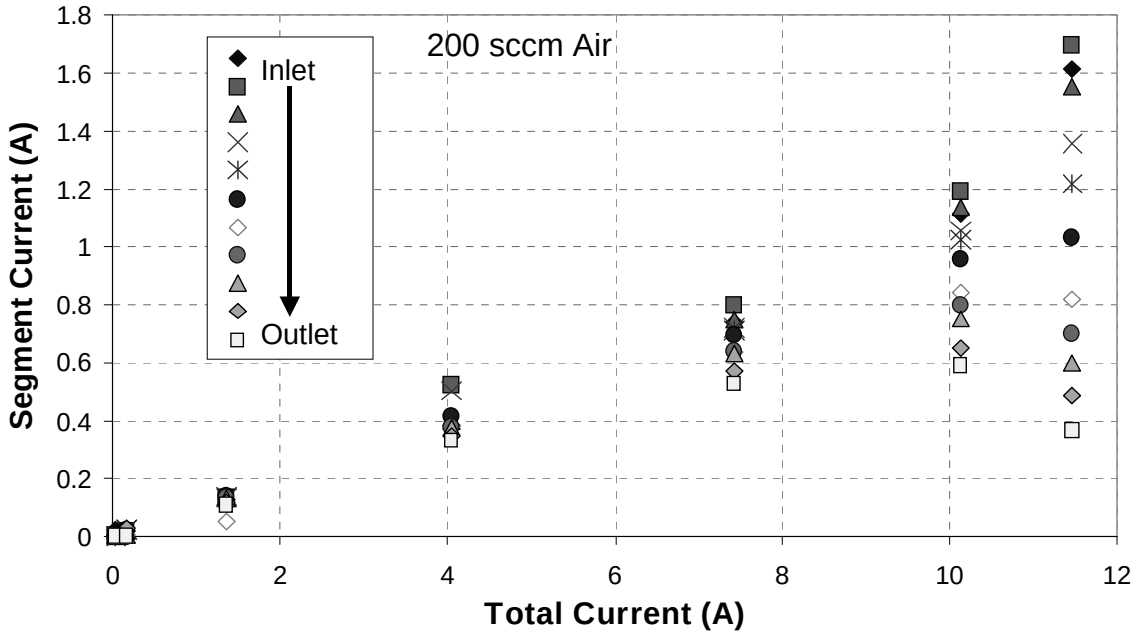

Figure 232. Effect of total current setting on current density distribution for 200 sccm of air on cathode. Test conditions: 500 sccm H_2/200 sccm Air, 75ºC cell, 90% inlet gas RH and ambient pressure.

Effect of Gas Flow Rate

For these experiments, the cathode gas flow rate was varied to determine its effect on current distribution uniformity. A total of four flow rates were investigated: 100, 200, 500 and 1000 sccm of air. The results of the experiments are shown in Figure 233. For comparison purposes, the air utilization for each flow rate is provided on the Figure and the dashed line represents a uniform current distribution. At high air utilizations (100 sccm air flow), the current distribution is highly non-uniform with the first three segments accounting for ~ 63% of the total current compared to ~ 3% in the last three segments. However, as the utilization is decreased, the current distribution becomes more uniform. For example, at an air utilization of 56% (500 sccm), the first three segments account for 32% of the total current which is close to target of 27% for a completely uniform current distribution.

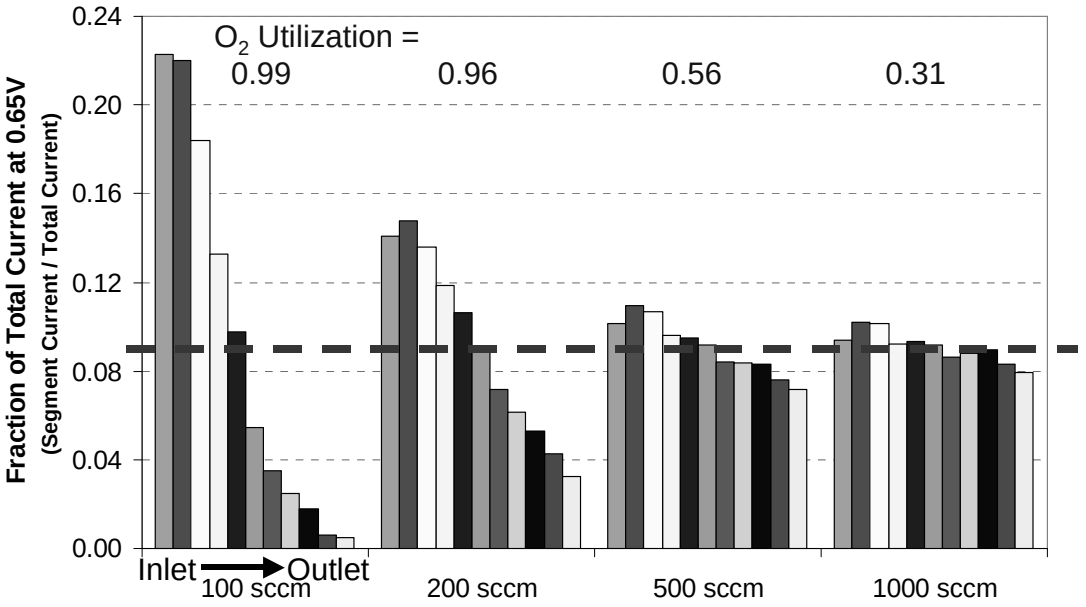

Figure 233. Effect of air flow rate on current density distribution. Test conditions: 500 sccm H_2/variable sccm Air, 75ºC cell, 90% inlet gas RH and ambient pressure.

Effect of GDL Backing

Three different GDLs were investigated for their effect on current distribution uniformity. Each GDL had the same micro-layer applied to a different backing – (1) flexible non-woven, (2) rigid non-woven paper and (3) flexible woven. Data for the different backings is presented in Figure 234 and Figure 235 for 200 and 500 sccm of air, respectively. At 200 sccm, the air utilization for the three GDL types varies from 0.95 to 0.99 indicating that the total current is approximately the same for each GDL even though the current distribution is different. Of the three different GDLs, the GDL made from the rigid, non-woven paper offers the best uniformity. At the higher flow rate of 500 sccm (0.58 average air utilization), the effect of GDL type is greatly diminished. At this utilization, the rigid, non-woven paper and the flexible woven result in very similar, uniform current distributions.

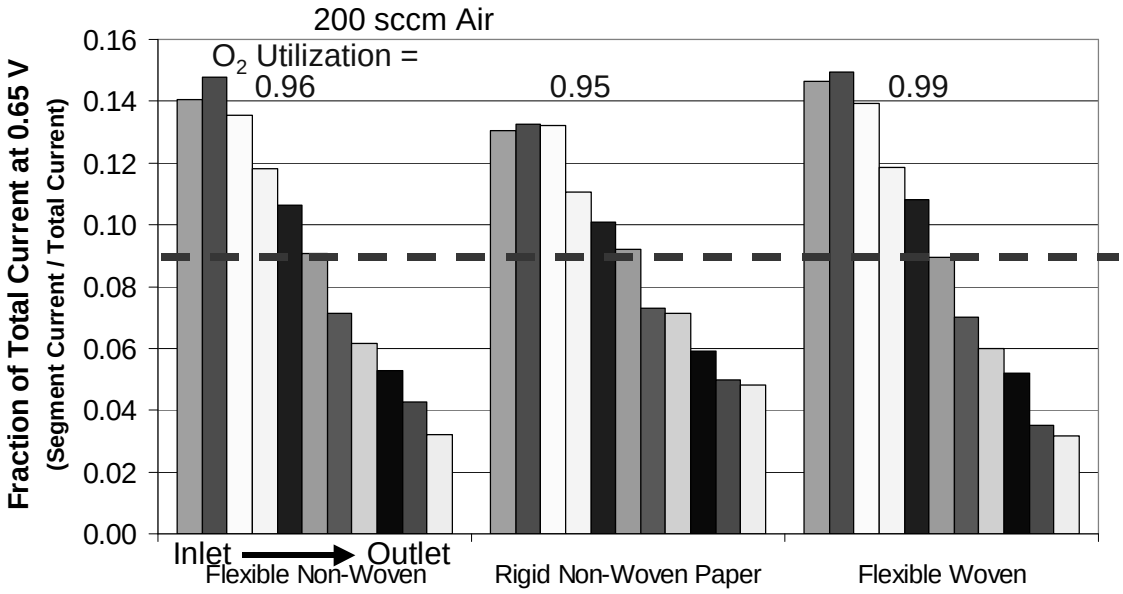

Figure 234. Effect of GDL backing on current density distribution for 200 sccm of air. Test conditions: 500 sccm H_2/200 sccm Air, 75ºC cell, 90% inlet gas RH and ambient pressure.

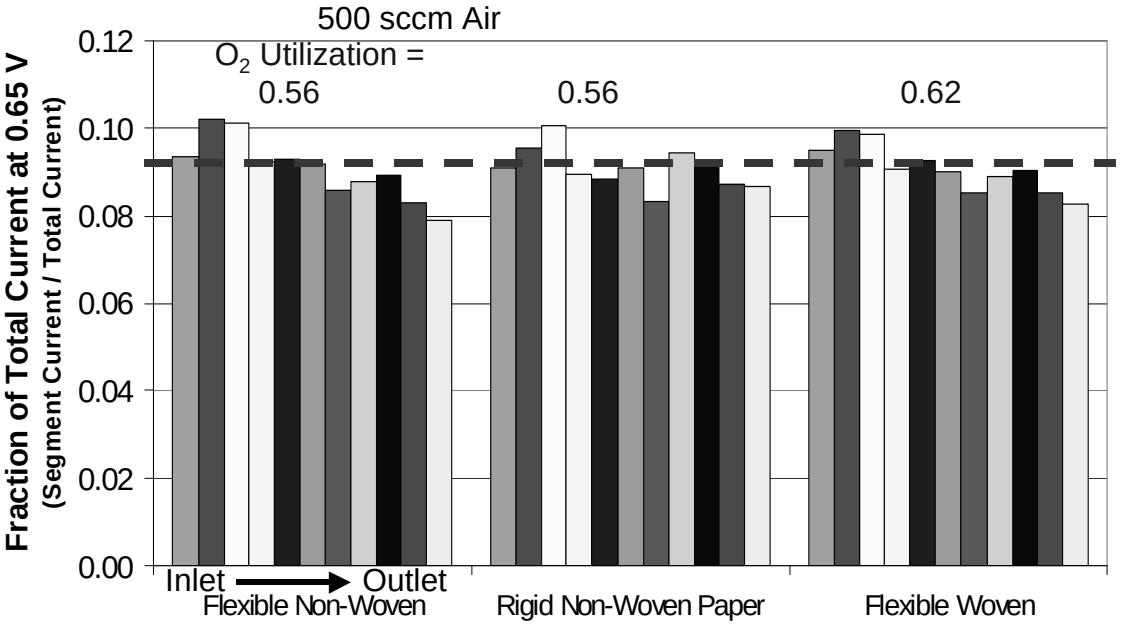

Figure 235. Effect of GDL backing on current density distribution for 500 sccm of air. Test conditions: 500 sccm H_2/500 sccm Air, 75ºC cell, 90% inlet gas RH and ambient pressure.

Summary

A 121-segment (11 x 11 matrix) segmented cell was developed utilizing PCB technology. Although equipment constraints limited the use of only 11 larger segments (the 11 segments in a row were shorted to make one larger segment), significant differences in the current distribution were observed. A more uniform current distribution can be obtained by reducing the total current

or by decreasing the air utilization (increasing the air flow) at a given current. The GDL backing also has an effect on the current distribution, although this effect appears to be a secondary effect since it is dominated by air utilization. Since the second or third segment from the inlet, not the first, typically resulted in the highest current, there is a need for more data at significantly higher spatial resolution in order to accurately map the current distribution. To that end, more detailed data using all 121 segments of the segmented cell are forthcoming.

3.2.3 Impact of Gas Flow Rate, Gas Relative Humidity and Flow Configuration on Current Uniformity

Segmented Cell Load Construction

The load for controlling the 121 channel segmented cell was developed internally at 3M. It consists of 11 proprietary circuit boards that each contain 11 individual loads. The loads can be operated in either a constant potential of current mode. Each load's set point can be controlled individually, i.e., it is possible to set the load of channel one to 0.3 V and the load of channel 2 to 0.5V for example. Labview™ based software was written to control the load. The user interface set-up is shown in Figure 236 and Figure 237 and the real-time results are displayed in Figure 238.

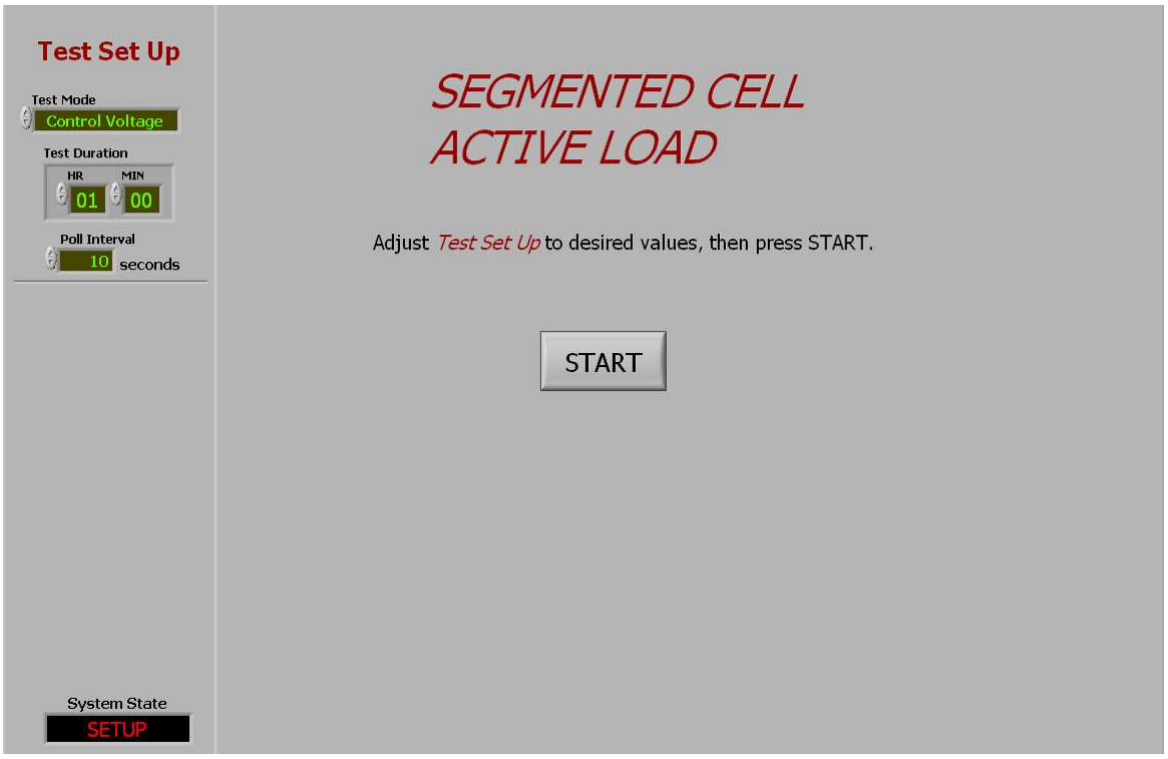

Figure 236. Screen shot of segmented cell load set-up user interface – Set control mode.

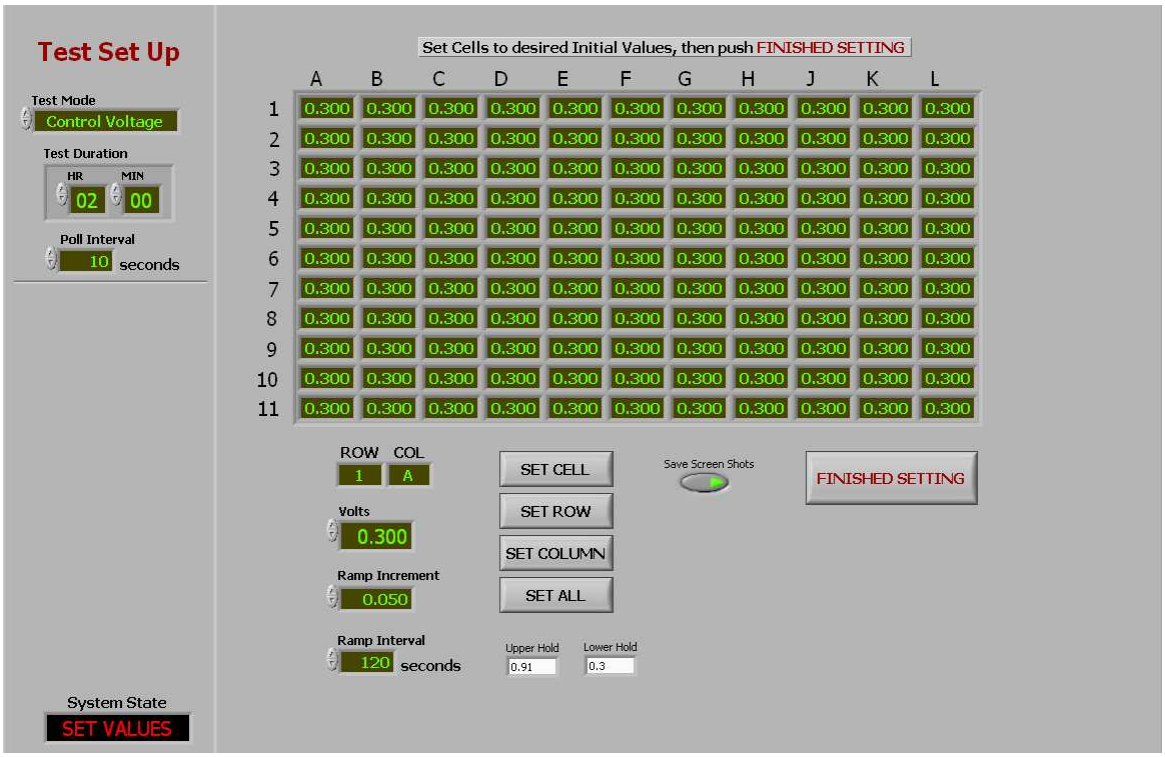

Figure 237. shot of segmented cell load set-up user interface – Setting load set points.

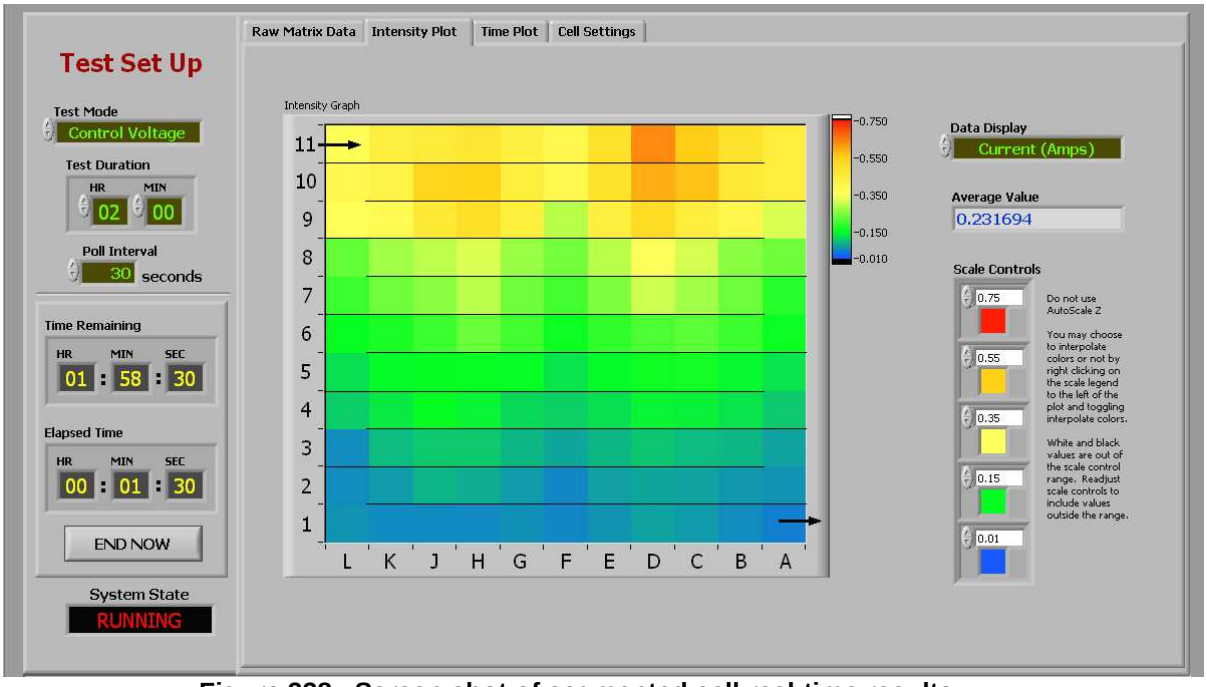

Figure 238. Screen shot of segmented cell real-time results.

Experimental
Experimental Set-up

The membrane electrode assemblies (MEAs) tested consisted of a 30 μm cast Nafion® 1000 EW membrane with a 0.4 mg Pt/cm2 electrode on both sides of the membrane. The active area of

the electrodes is 50 cm2 and PTFE reinforced glass gaskets were used for all experiments. A rigid paper was used as the gas-diffusion layer (GDL). Testing was conducted under H2/Air at 75ºC cell temperature, ambient pressure and the H2 flow was fixed at 500 sccm while the cathode feed stream was set to either 500 or 1000 sccm of air . The gas streams relative humidity was set to either 25% or 100%. Additionally, the gas streams were configured in co-flow orientation or counter-flow configuration.

Segmented Cell Test Configuration - The MEA was mounted into a 50-cm^2 Fuel Cell Technologies test cell with a whole, quad-serpentine graphite flow field on the anode and a segmented, quad-serpentine PCB flow field on the cathode. The test cell bolts were tightened to 110 in-lbs. Lab Alliance model 1 pumps were used to supply the deionized water to the steam injectors. A Fuel Cell Technologies Fuel Cell Test Station was used to control the cell temperature and gas flow rates to the fuel cell. All functions of the fuel cell test station were computer controlled via 3M-developed Fuel Cell Testing Software. The 3M proprietary 121-channel load was used to control the load of the 121-channel segmented cell.

Results and Discussion
Effect of Gas Relative Humidity

The effect of gas relative humidity is shown in Figure 239 to Figure 242. At low relative humidity and high current density (Figure 239), hot spots are found near the inlet of the cell. In fact, the first third of the cell is substantially more active than the rest of the cell and the last third is nearly unused. As the current is reduced (Figure 240), the hot spots move from the inlet to the outlet. The movement is a result of water concentration. At low current density and low inlet relative humidity, there is not enough water to properly humidify the membrane at the inlet and as a result the performance is reduced. However, since water is generated in the cell, the outlet is more humidified than the inlet resulting in higher local fuel cell performance. In comparison, at 100% inlet relative humidity, the hot spots remain in the first quarter of the fuel cell even as the current density is decreased (Figure 241 and Figure 242). Regardless of the inlet relative humidity, at near OCV operation, only a few random segments are operational (Figure 243).

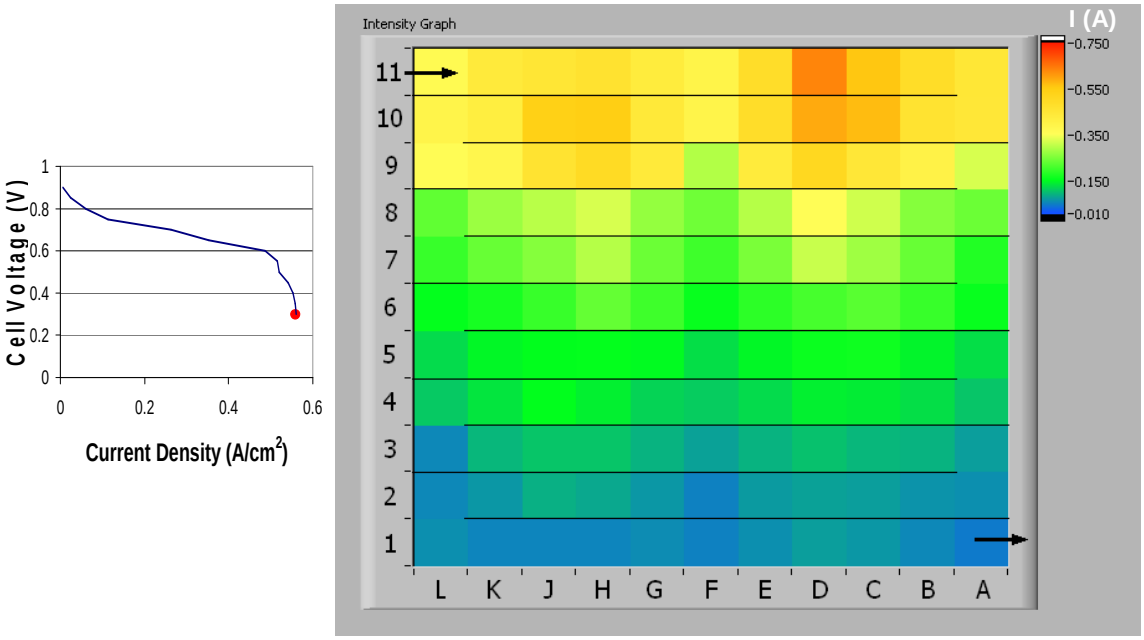

Figure 239. Segmented cell current distribution – 25% relative humidity; 500 sccm air; co-flow operation; nominally 0.57 A/cm^2.

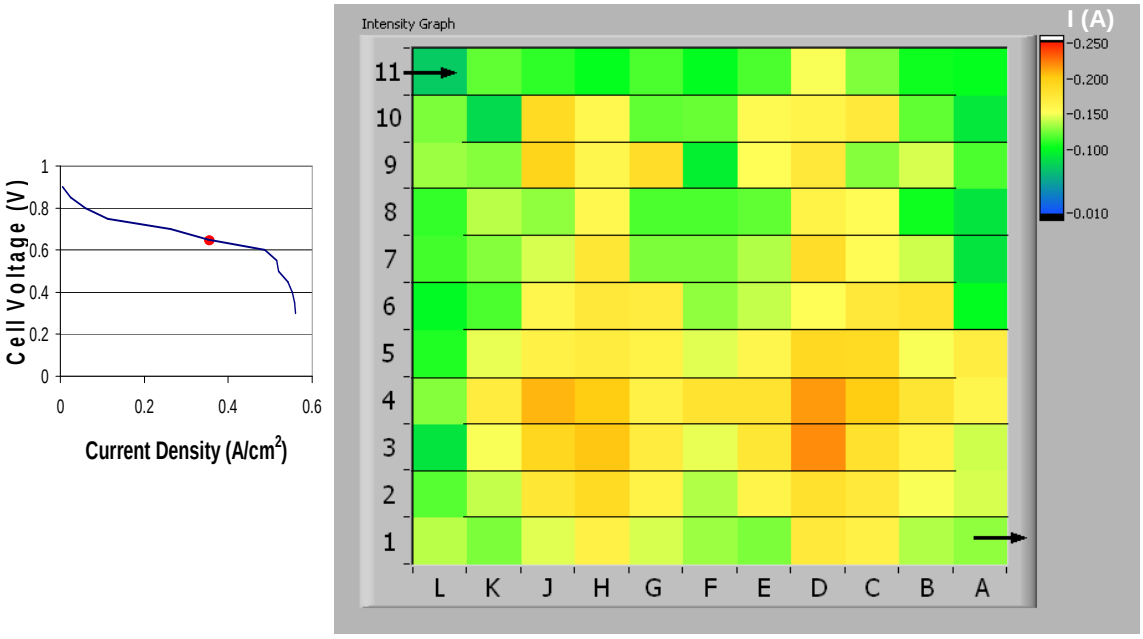

Figure 240. Segmented cell current distribution – 25% relative humidity; 500 sccm air; co-flow operation; nominally 0.36 A/cm^2.

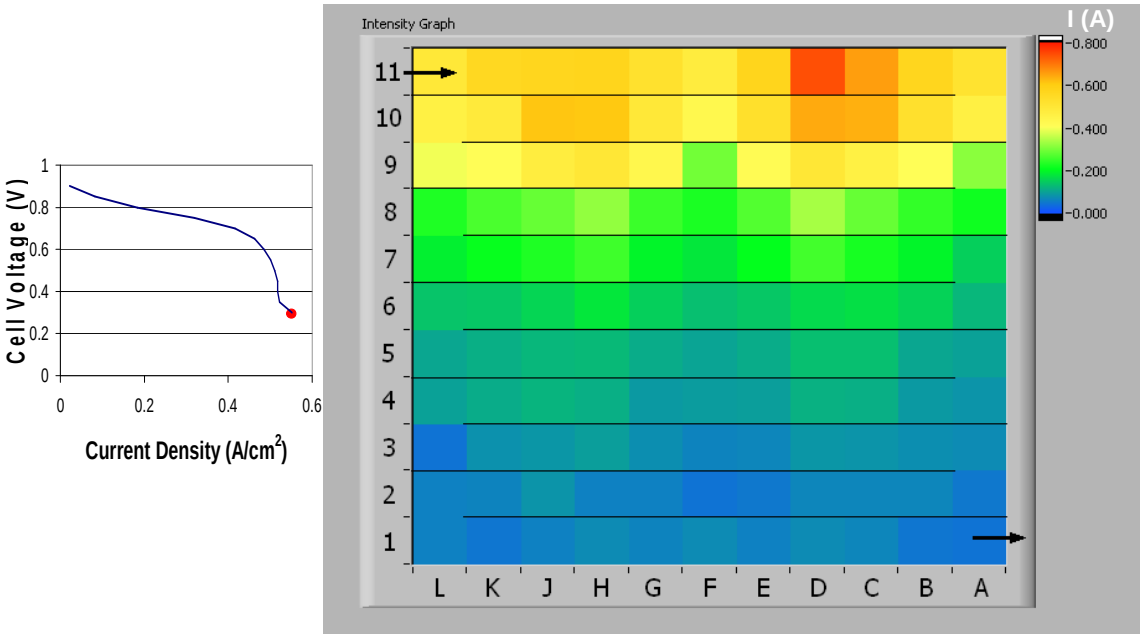

Figure 241. Segmented cell current distribution – 100% relative humidity; 500 sccm air; co-flow operation; nominally 0.57 A/cm^2.

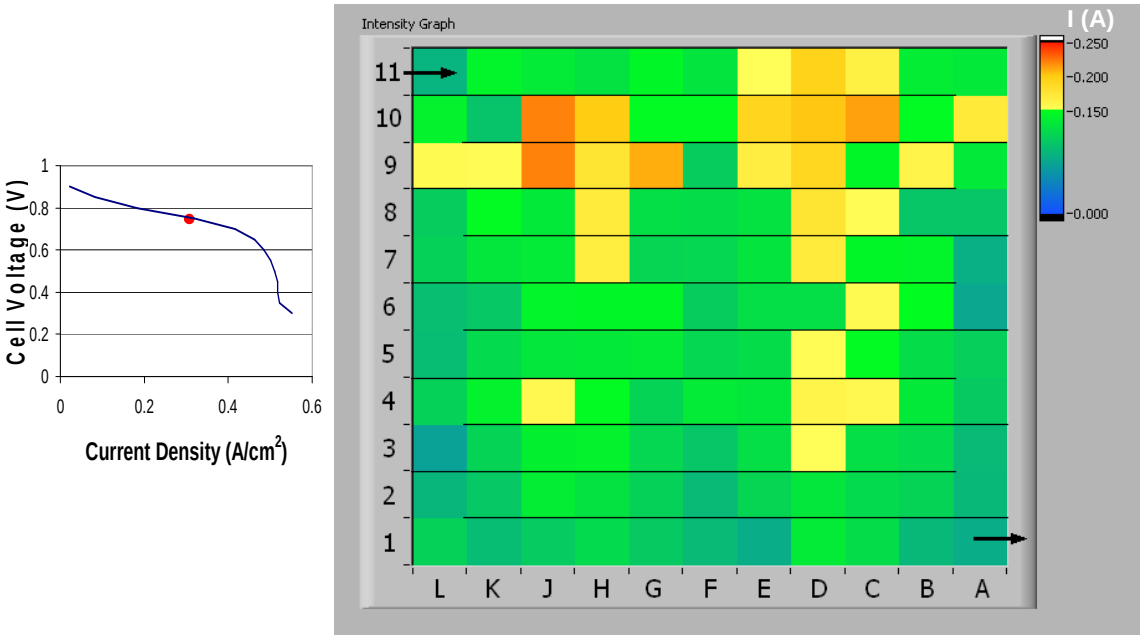

Figure 242. Segmented cell current distribution – 100% relative humidity; 500 sccm air; co-flow operation; nominally 0.3 A/cm^2.

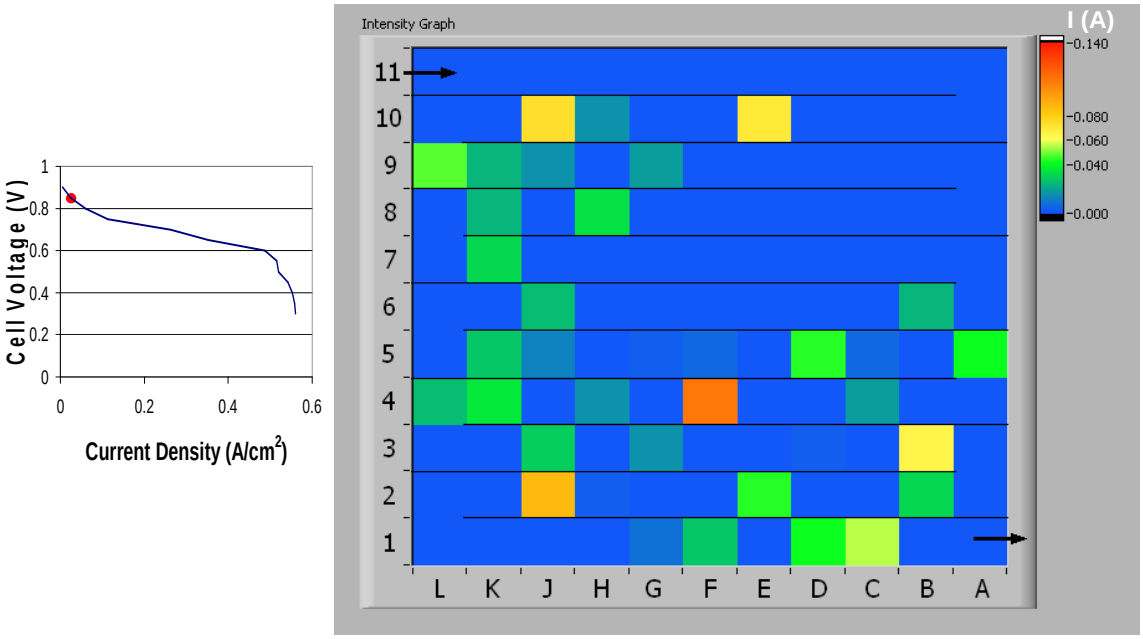

Figure 243. Segmented cell current distribution – 25% relative humidity; 500 sccm air; co-flow operation; nominally 0.05 A/cm^2.

Effect of Gas Flow Rate

At a low gas flow rate of 500 sccm air, approximately half of the cell is inactive in comparison to the inlet (Figure 241). The first third of the fuel cell is where all the activity takes place. When the air flow rate is increased to 1000 sccm, the first third of the fuel cell is still the dominant area for

activity (Figure 244). However, unlike the 500 sccm case, the outlet of the fuel cell is more active and the cell is more uniform overall.

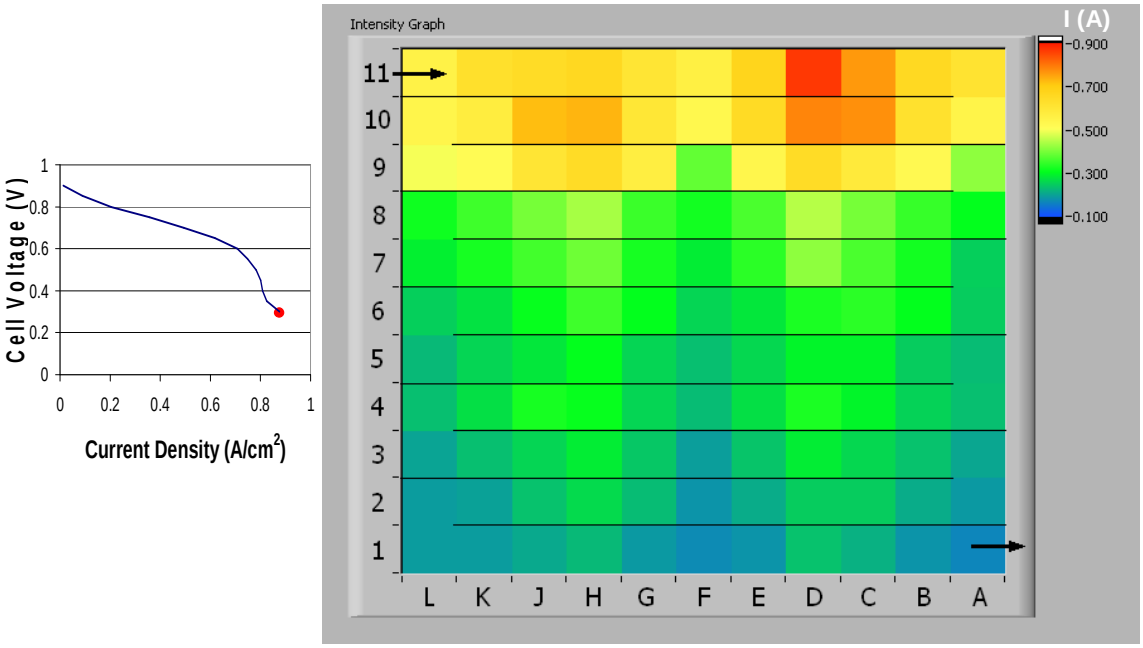

Figure 244. Segmented cell current distribution – 100% relative humidity; 1000 sccm air; co-flow operation; nominally 0.9 A/cm^2.

Effect of Gas Flow Configuration

When the cell is operated in counter-flow configuration, the hot spots are located near the inlet of the cathode gas stream (Figure 245). However, the current distribution uniformity of the counter-flow operation is significantly more uniform than that of co-flow operation. In co-flow operation, hot spots exists where the current is three times the nominal value. In the counter flow operation, the hot spot is only two time the nominal current and there are no dead zones of little or no activity.

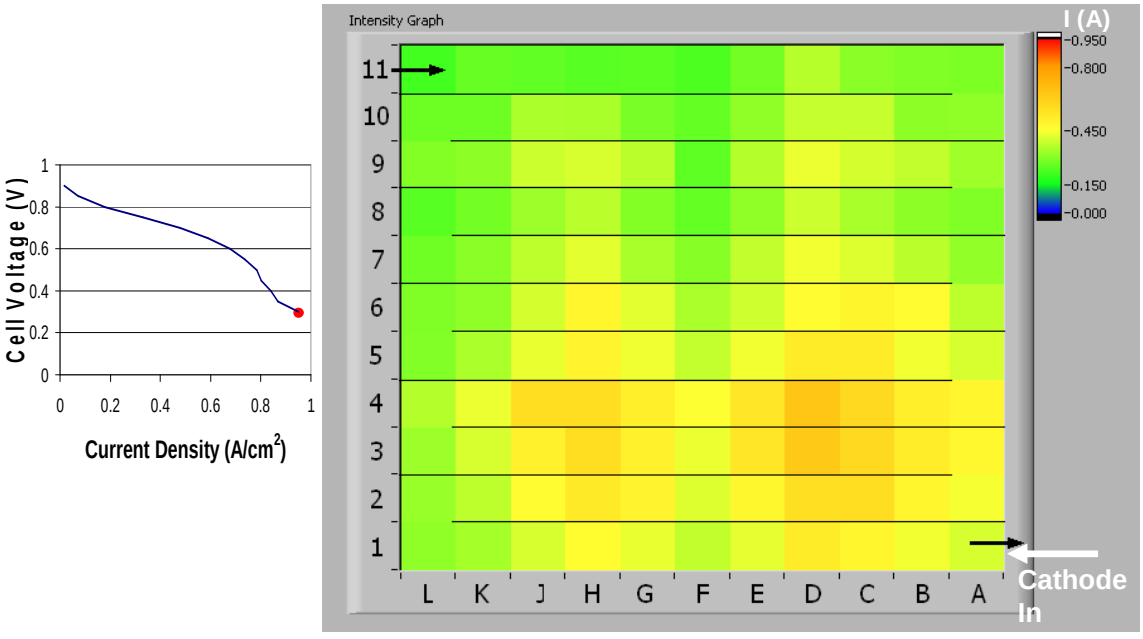

Figure 245. Segmented cell current distribution – 100% relative humidity; 1000 sccm air; counter-flow operation; nominally 0.95 A/cm^2

Summary
A 121-segment (11 x 11 matrix) segmented cell was tested using an 121-channel load. Inlet relative humidity, cathode gas flow rate and gas flow configuration were evaluated. Non-uniform current distributions were found to exist in operating fuel cells. Local current densities up three times the average current density were measured under co-flow, 500 sccm cathode gas flow rate and 100% relative humidity. In general, outlets tend to be under utilized in co-flow operation. Counter-flow operation results in higher current distribution uniformity in comparison to co-flow. Lastly, it was determined that the 'hot spots' location changes depending on load setting.

3.3 Nonuniformity Studies – Experimental 200cm^2 Cell

Segmented Cell Construction

Large scale 200 cm^2 segmented cell was built based upon the PCB concept of the 50 cm^2, 121-channel segmented cell. The 200 cm^2 cell was divided into 52-channels following the Plug Power flow field design. Figure 246 shows a cartoon depicting the location of each segment within the flow field area. The flow field channels are machined into the plate after the segments are fabricated. .

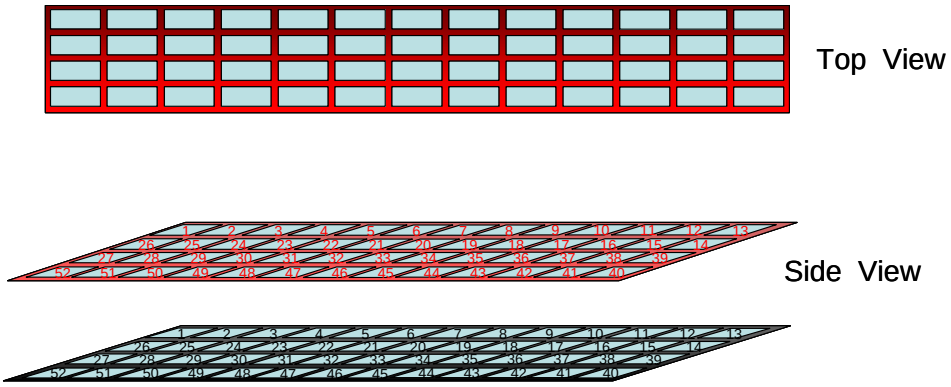

Figure 246. Top and side view schematic of segmented cell layout.

Unlike the 121-channel segmented cell which only segmented the cathode, the 52-channel segmented cell segmented both the anode and cathode and is more like a bipolar plate. Figure 247 shows the concept behind the bipolar plate with segments on the anode side of one cell and the cathode side of the neighboring cell.

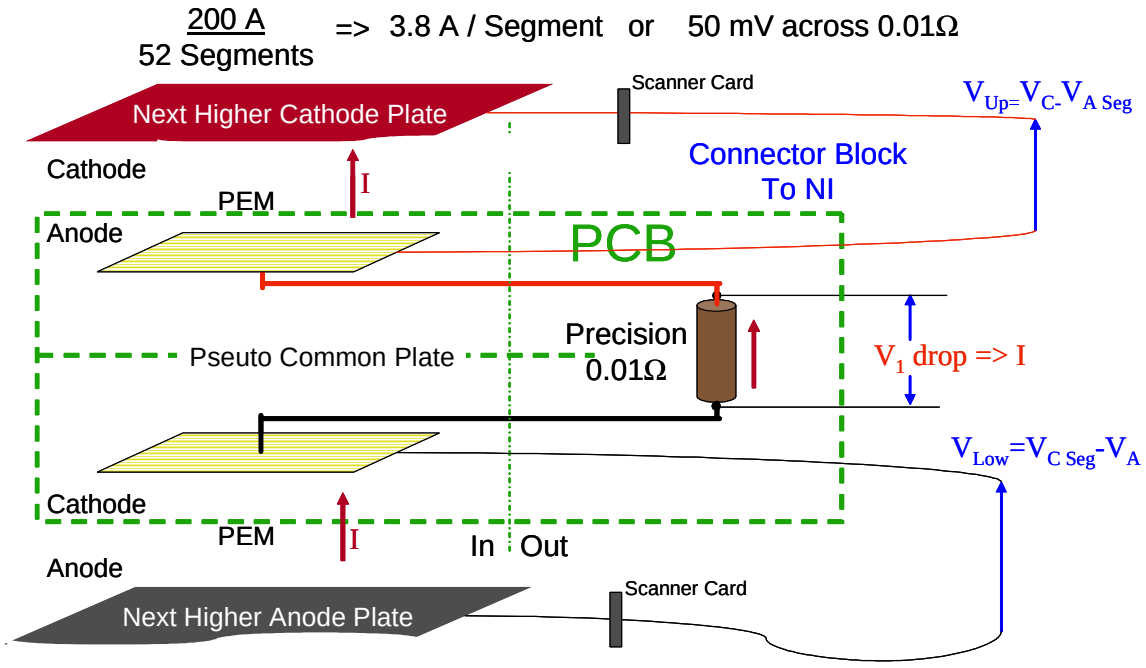

Figure 247. Schematic showing anode and cathode connections to form "bipolar" segmented cell

With this bipolar plate design, the 52-channel segmented cell can be placed within an operating fuel cell stack. By assembling the 52-channel segmented cell in different locations within test stack, a true 3D view of current density will be generated under real operating conditions. Figure 248 depicts a schematic of a stack with the segmented cell placed in one location.

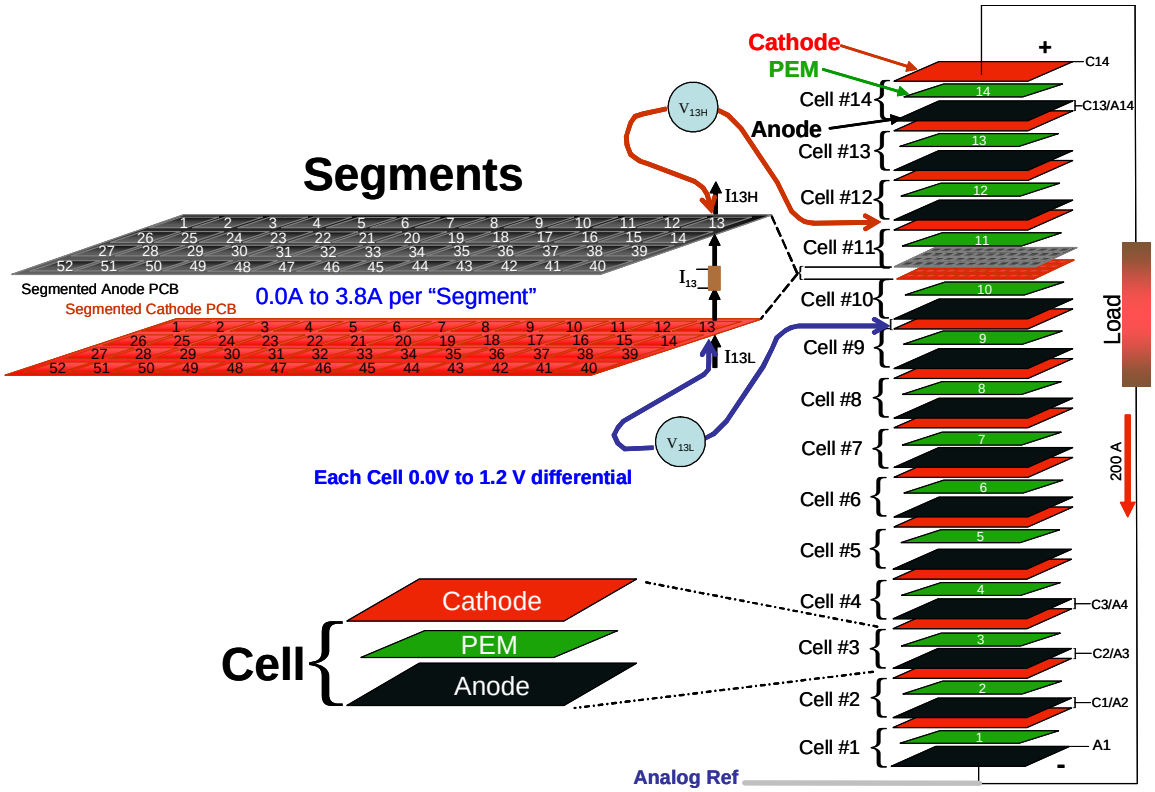

Figure 248. Schematic depicting the segmented cell in a full sized stack.

Segmented cell summary

A full sized, 52 segment, cell was fabricated and instrumented to operate in a full or sub sized stack. The design, assembly, and software development were all completed at 3M. The finished cell was shipped to Plug Power where it was successfully demonstrated in an operating substack. Refer to section *6.2.4 Segmented Cell Tool Development* for data generated using this equipment.

3.4 References

1. V. Gurau, H. Liu and S. Kakac, *AIChE J.,* 44, 2410 (1998).
2. J. Newman, "Investigating Failure in Polymer Electroyte Fuel Cells," 2005 DOE Hydrogen, Fuel Cells & Infrastructure Technologies Review, Washington, D.C. May 2005.
3. A. Hakenjos, K. Tüber, J.O Schumacher, and C Hebling, *Fuel Cells,* 4, 185 (2004).
4. J. Stumper, S. Campbell, D. Wilkinson, M. Johnson, and M. Davis, *Electrochim. Acta,* 43, 3773 (1998).
5. Ch. Wieser, A Helmbold and E. Gülzow, *J. Appl. Electrochem*., 30, 803 (2000).
6. G. Bender, M. Wilson and T. Zawodzinski, *J. Power Sources,* 123, 163 (2003).
7. S. Cleghorn, C. Derouin, M. Wilson and S. Gottesfeld, *J. Appl. Electrochem*., 28, 663 (1998).
8. D. Brett, S. Atkins, N. Brandon, V. Vesovic, N. Vasileiadis and A. Kucernak, *Electrochem. Commun*., 3, 628 (2001).
9. M. Mench, C. Wang and M. Ishikawa, *J. Electrochem. Soc*., 150, A1052 (2003).
10. M. Mench and C. Wang, *J. Electrochem. Soc*., 150, A79 (2003).

11. M. Noponen, T. Mennola, M. Mikkola, T. Hottinen, P. Lund, *J. Power Sources,* 106, 304 (2002).
12. N. Rajalakshmi, M Raja, K.S. Dhathathreyan, *J. Power Sources,* 112, 331 (2002).

Section 4: Studies of Peroxide Production, Transport, Reaction and Effects on Gas Diffusion Layers in Fuel Cells

Summary

In this project, Zawodzinski's group at Case performed work in several areas, briefly summarized below. First, we performed studies of peroxide generation at electrodes. As part of this activity, we used rotating ring disk electrodes coated with catalyst particles to estimate the typical percent of the ORR that proceeded only to hydrogen peroxide as a function of potential. Since those experiments were performed in aqueous solution, we sought a separate measure that would allow us to obtain similar data under fuel cell conditions—i.e. humidified from the vapor phase only. To this end, we developed the 'Dual Microband Electrode' approach. We used a patterned microelectrode array consisting of a generator electrode surrounded by collector electrodes (analogous to disk and ring in RRDE studies). This microfabricated array could be coated with a polymer electrolyte to allow solution-free operation. This was only a partial success because of microfabrication difficulties. At the close of the project, we were attempting a new design of experiment to eliminate the need for microfabricated electrodes. The outcome of all of this activity is that we have an estimate of the peroxide generation rate, albeit for flooded conditions.

Second, we developed the necessary transport experiments and model to describe the concentration of peroxide throughout the cell. Once again, several approaches were applied to this problem. First, we attempted to repeat and extend work first reported by W.L. Gore in which multilayer sandwich cells were prepared with a membrane inserted between half-MEAs and one microelectrode inserted between the anode half-MEA and a membrane and a second microelectrode inserted on the cathode side. However, this led to inconclusive results since the current associated with hydrogen cross-over was much higher than that arising from peroxide at the microelectrode. Second, the rate of diffusion of peroxide in a membrane layer was estimated from rotating disk electrode experiments analyzed with a thin-film model. A third battery of tests was developed to probe peroxide transport and its rate of reaction in various layers of the cell. Various combinations of electrode and membrane layers were arranged to systematically isolate each component of the cell and determine appropriate reaction and transport parameters.

Third, we developed and applied methods for the study of gas diffusion media. Methods to estimate in-plane and through-plane gas permeation were deployed. A method for estimating an average contact angle associated with the inside pores of the micro- and macro-porous layers were deployed. These were applied to aged GDLs. A final method under development as the program end allowed estimation of the capillary pressure needed to force liquid through the GDL. (see section *2.2.1 Characterization Methodology)*

Finally, we developed a mathematical modeling framework to assess the production, transport and reaction of peroxide in the cell.

4.1: Ex Situ Studies of Peroxide Generation, Transport and Reaction

Hydrogen peroxide formed as a result of incomplete oxygen reduction is suspected of degrading the performance of polymer electrolyte membrane fuel cells. The objective of this study is to investigate the effects of Pt loading and the type of carbon support on the catalytic activity of oxygen reduction catalysts in acidic solution. A thin-film rotating ring-disk electrode (RRDE) was used to determine the fraction of hydrogen peroxide production[81, 82] .

It is well-established that oxygen reduction in aqueous acidic media can occur by both a direct four electron path and two electron path. The latter of these paths, the two electron reduction, results in H_2O_2 as a product[83]. In acid solution, the direct four-electron path is:

$$O_2 + 4H^+ = 4e^- \rightarrow 2\ H_2O$$

with a thermodynamic reversible potential E_0 = 1.229V vs. NHE. The two-electron, or peroxide path, is given as:

$$O_2 + 2H^+ + 2e^- \rightarrow H_2O_2$$

with a thermodynamic reversible potential of E_0 = 0.67V vs. NHE.

It should be kept in mind that realistic PEMFC conditions employ, vapor-equilibrated electrolyte. It was a major aim of this work to develop a test methodology for studying H_2O_2 production under these realistic conditions. However, current research efforts rely almost entirely on the use of aqueous, acidic ionic conducting media to study the fundamentals of the ORR. These studies routinely employ the thin film rotating-ring-disk electrode methodology (thin-film RRDE)[84,85]. Factors limiting the thin-film RRDE experiment's ability to mimic the fuel cell interfacial environment include modification of the pre-exponential coverage dependent term in Butler-Volmer type rate expressions, interfacial water management and the further reduction or decomposition that H_2O_2 can undergo. In an aqueous ionic conducting media, further reduction of the H_2O_2 intermediate can occur according to:

$$H_2O_2 + 2\ H^+ + 2e^- \rightarrow 2H_2O$$

with a thermodynamic reversible potential of E_0 = 1.77V vs. NHE. The decomposition of peroxide can also occur via a disproportionation reaction:

$$2H_2O_2 \rightarrow 2H_2O + O_2$$

Several studies on peroxide production for high surface area Pt/C catalysts have been conducted recently. Paulus *et al.*[82] analyzed Pt alloyed with Rh and Fe for peroxide production using RRDE and found no significant differences between alloy catalysts and pure Pt in term of peroxide generation. In their study of Fe based fuel cell catalysts using both RRDE and single membrane electrode assemblies (MEAs) for the cathode, Lefevre and Dodelet[86] found loss of catalytic activity which they interpreted to be due to the detrimental effect of H_2O_2 released during ORR.

Antoine and Durand[87] studied the effect of Pt particle size on H_2O_2 formation and found that the fraction of peroxide produced increased as the platinum particle size decreased. However, in their Pt/C samples, the Pt mass ratio decreased along with the Pt particle size, such that both factors, viz. decrease in Pt active area and decrease in Pt particle size, might cause increased peroxide production. In another RRDE study on Pt/C catalysts in alkaline media, Genies *et al.*[88] have shown that the two electron pathway is significant on carbon as compared to Pt and that the ORR is predominantly governed by the activity of Pt particles dispersed on the carbon support. Other related studies, which do not address peroxide formation, but discuss Pt agglomeration were presented by Stonehart[89] and Watanabe *et. al* [90].

In spite of these studies on peroxide formation, it is still unclear as to what are the extent of contributions from the Pt and the C species to the formation and/or decomposition of peroxide during the ORR in the potential range of interest. We present here a systematic study of peroxide production on (i) Pt/C catalysts with varying Pt mass ratio on the same carbon support, keeping the Pt particle sizes constant to reveal the effect of the Pt active area, (ii) Pt/C catalysts with varying carbon support surface area, maintaining the same platinum mass ratio and same Pt particle size in order to characterize the dependence of peroxide formation on the carbon support and (iii) the carbon support by itself in order to measure the peroxide formation on carbon as compared to the Pt/C catalyst. Regarding item (ii) above, it will be subsequently shown that it is difficult to separate the effects due to the carbon support from those due to the Pt active area because both are coupled.

Key questions that we attempted to address by this work include:

1. How much peroxide is produced as a side-reaction of the ORR?
2. How does the above depend on catalyst type?
3. How much peroxide is produced on carbon?
4. How does this depend on environmental conditions?
5. How rapidly does peroxide diffuse through a thin film?

4.1.1: Studies of Filmed RRDE Electrodes

Hydrogen peroxide formed during the oxygen reduction reaction (ORR) on high surface area platinum on carbon (Pt/C) catalyst was measured using a rotating ring disk electrode (RRDE) coated with a thin film of catalyst. Catalyst samples with varying Pt content (30%-50%) on the same carbon support and catalysts with varying carbon support surface area (56-950 m^2/g) and the same platinum mass ratio (50% Pt) were analyzed. The peroxide generation decreased with increase in the platinum active area on all Pt/C samples. Carbon support sample without platinum showed negligible peroxide generation in the typical fuel cell operating region (0.5-0.75 V). The measured Pt active area increased with the carbon support active area, even for same Pt mass ratio and same sized Pt particles. It is hypothesized that enhanced agglomeration of Pt particles on low surface area carbons might cause the lower active area of platinum on the smoother carbon substrates. This loss in the Pt active area and the subsequent generation of extra, difficult to access edges by the Pt agglomerates on which the oxygen is adsorbed less reversibly, might be causing an increase in peroxide generation on low surface area carbon supports.

EXPERIMENTAL PROCEDURE: Studies of Filmed RRDE Electrodes

Schmidt *et al.* [1] first developed the method of attaching finely dispersed catalyst powder on a glassy carbon electrode via a thin Nafion® film for electrochemical characterization using RDE. This method was modified slightly to suit our experimental conditions: 2 mg of Pt/C catalyst (as received; provided by 3M) was ultrasonically blended for 15 minutes with 4 ml of distilled water (Millipore SuperQ System; resistivity: 18 MΩ cm). 25 µl of this solution was pippeted on the glassy carbon disk electrode (5 mm dia.) to obtain a catalyst loading of 44 $\mu g_{cat}/cm^2$. After drying in air, a 25 ml of diluted Nafion® solution (10 µl of Nafion® (5 wt% Fluka) + 90 µl of ethanol + 900 µl of distilled water) ultrasonically blended for 5 minutes, was put over the catalyst layer. The thickness of this Nafion® film was estimated to be around 0.1 – 0.15 µm, which has been shown to offer negligible film mass transfer resistance [1]. This procedure of thin film electrode preparation was kept the same for the experiments performed in this work so that the catalyst loading was kept nearly constant throughout.

After preparation, the electrode was immersed in deaerated (ultra high purity N_2, Praxair) 0.5 M H_2SO_4 solution (Fisher) in a standard three electrode cell. A luggin capillary with platinum gauze over which hydrogen was produced via electrolysis and maintained during the experiment, served as the reference electrode (NHE) and a platinum wire in a glass tube with fritted glass end served as the counter electrode. To eliminate effects due to possible contamination from the Nafion® film, the electrode was cycled several times between 0.05 V and 1.2 V to produce clean surfaces. The electrochemical active area was measured by integrating the charge in the hydrogen desorption region and normalizing it by the hydrogen adsorption-desorption charge on platinum (210 $\mu C/cm^2$).

In order to perform the ORR experiments, the electrolyte was purged with pure O_2 (ultra high purity, Praxair) for 20 minutes prior to every run to achieve saturation and a cathodic linear sweep was performed on the disk from 0.9 V to 0.05 V (vs NHE) at a scan rate of 10 mV/s under O_2 atmosphere. The ring was held at 1.15 V during the ORR runs and both the ring and the disk currents were recorded using a bi-potentiostat (Pine Instruments, Model: AFCBP1). The ORR runs were performed at 3 to 5 different speeds between 500 rpm and 3000 rpm. Before every ORR run, the capacitive (or the background) current was obtained for both the disk and the ring by sweeping the disk between the same potential limits at the same scan rate of 10 mV/s in deaerated solution. The background polarization currents obtained in the absence of oxygen were then subtracted from the polarization curves under O_2 to obtain the true faradaic currents.

RESULTS: Studies of Filmed RRDE Electrodes

Typical disk and ring currents for cathodic potential sweeps at different rotation speeds are shown in Figure 249. The background (or capacitive) currents obtained for both the disk and the ring in deaerated solution are also shown in Figure 249 (a) and (b). The theoretical collection efficiency (N) for the ring current (N = 0.2395), was used to calculate the % mol H_2O_2 [82,86,87]:

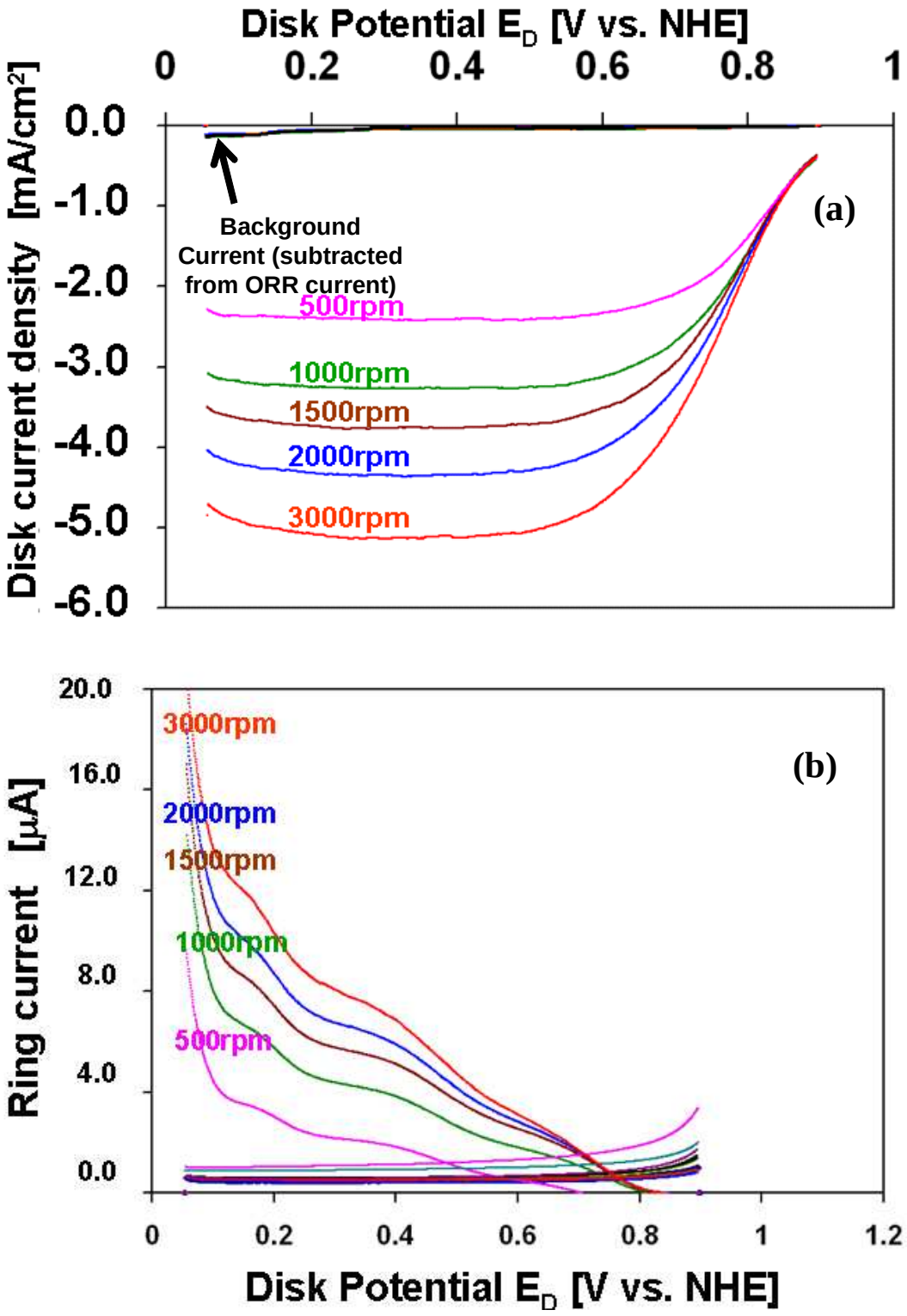

Figure 249. (a) Current-potential curves for O2 reduction on 40% Pt/C catalyst in a thin film; (b) peroxide re-oxidation on Pt ring electrode in 0.5 M H2SO4 saturated with pure O2. ER = 1.15 V (vs NHE). Scan rate: 10 mV/s.

Several researchers[82,83,84] have found the actual collection efficiency to be within 5 - 10% of the theoretical collection efficiency value by carrying a $Fe(CN)_6^{4-}/Fe(CN)_6^{3-}$ redox reaction at the glassy carbon disc. Since all catalyst samples were compared here for peroxide production at the same rotation speed of 3000 rpm at the same catalyst and Nafion® loading, the theoretical collection efficiency (N) was considered an adequate estimate.

Pt/C Samples with the Same Carbon Support and Different Pt Loading:

Pt/C samples with the same carbon support (carbon active area = 266 m^2/g) and varying Pt content (30, 40 and 50 wt% Pt) were analyzed for peroxide production. The % mol peroxide generated by these electrodes as a function of the disk potential is shown in Figure 250. For convenience, the % mol H_2O_2 produced in different samples are compared at one potential (0.675 V) mid-way in the potential region of typical fuel cell operation (0.5 V - 0.75 V).

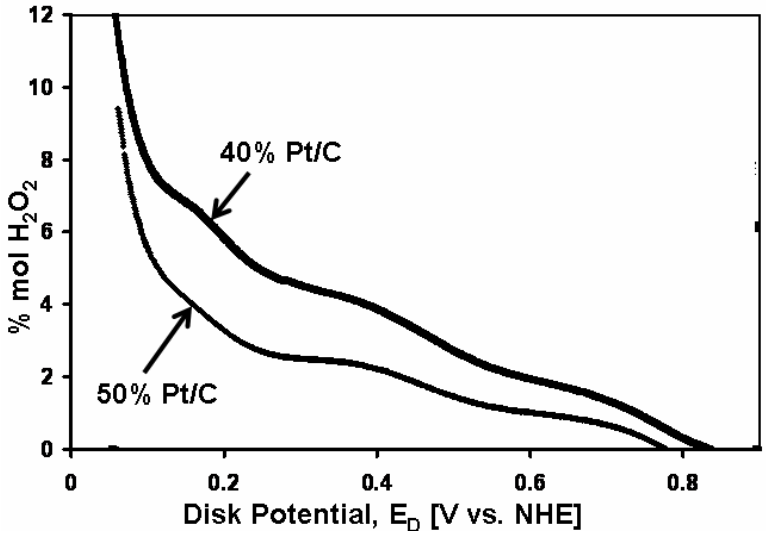

Figure 250. % mol H2O2 formed at on thin film electrode at disk rotation speed of 3000 rpm as a function of the disk potential for Pt/C catalysts with different Pt mass ratios at the same catalyst loading of 44 µgcat/cm2 (all parameters are the same as in Figure 249)

Table 34 provides the details of the platinum active area, the mean Pt particle sizes, % mol peroxide and the total moles of peroxide formed at 0.675 V at the same catalyst loading of 44 $\mu g_{cat}/cm^2$.

Table 34. Pt/C samples with varying Pt content on 266 m2/g carbon support

% wt Pt in Pt/C	Pt loading (mg_{Pt}/cm^2)	Active Area (cm^2)/ (m^2/g)	% mol H_2O_2 at 0.675 V	Total mol H_2O_2 (mol) at 0.675 V	Pt size[9] (nm)
30	0.0132	18/725	1.77	5.04×10^{-11}	2.3
40	0.0176	22/663	1.54	4.54×10^{-11}	2.3
50	0.0220	9/217	0.79	2.25×10^{-11}	2.4

The variation in the platinum active area with different Pt mass ratios is shown in Figure 251

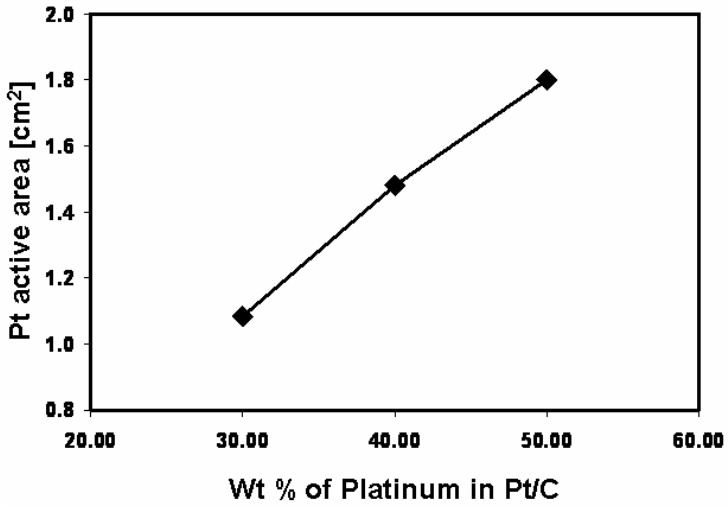

Figure 251. Variation in Pt active area with Pt mass ratio under constant Nafion® and catalyst loading of 44 µgcat/cm2 (all other conditions are the same as in Figure 249).

It is observed that peroxide formation in terms of both the total moles formed and % mol H_2O_2 decreases with increase in Pt loading (Figure 252(a)). The total moles and % mol peroxide values normalized by the platinum active area (cm^2) and platinum loading (mg_{Pt}/cm^2) are plotted in Figure 252 (b) and (c), respectively. These normalized values, which indicate the extent of H_2O_2 formation at the given platinum loading, also show an almost linear decrease in H_2O_2 production with increase in Pt loading.

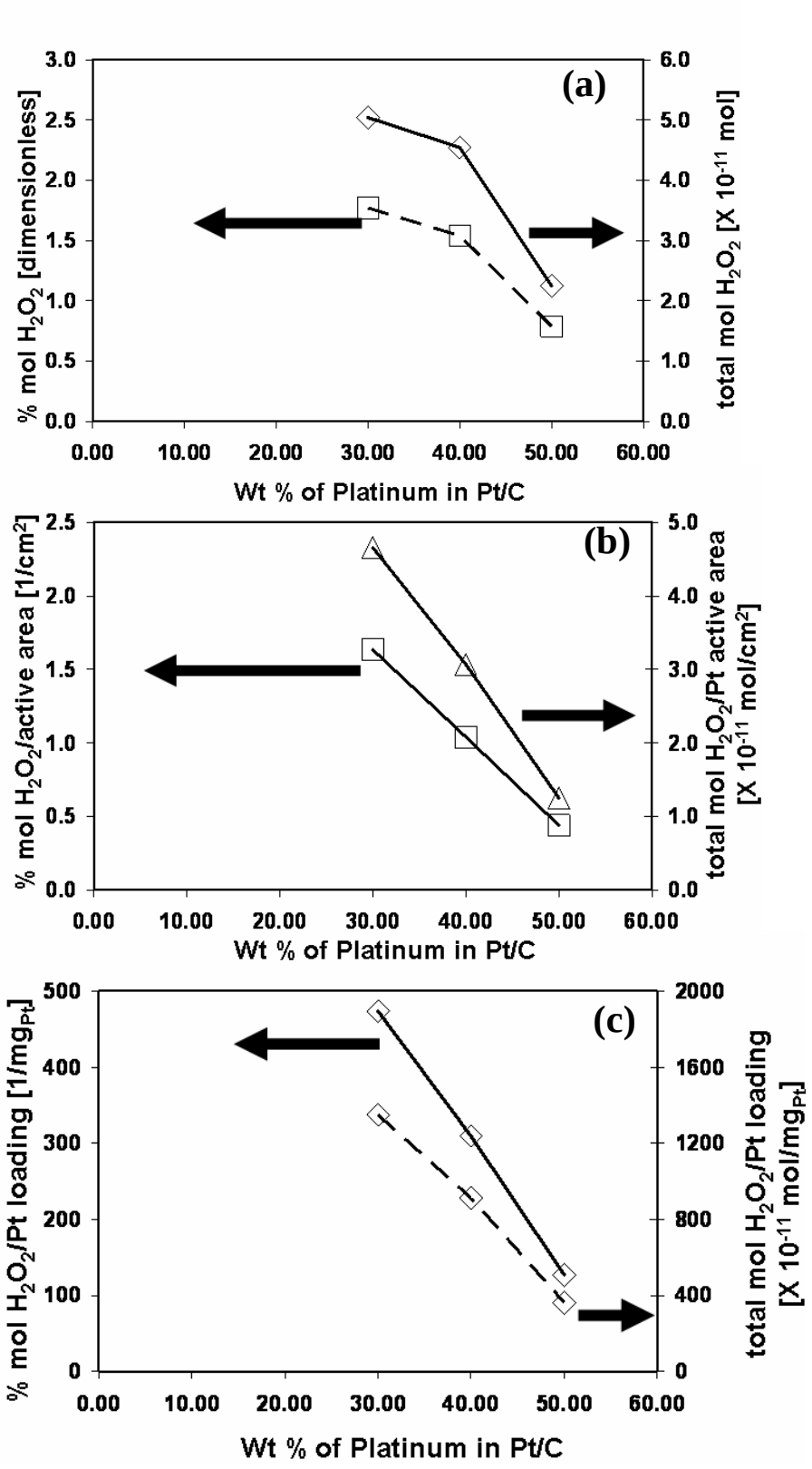

Figure 252. Peroxide generation at 0.675 V and at disk rotation speed of 3000 rpm as a function of % Pt mass ratio on same carbon support (266 m2/g) under same catalyst

loading of 44 µgcat/cm2 and same Nafion® loading in terms of (a) % mol H2O2 and total mol H2O2

Figure 253 shows the variation of the % mol peroxide generation and the inverse of active area with the platinum mass ratio.

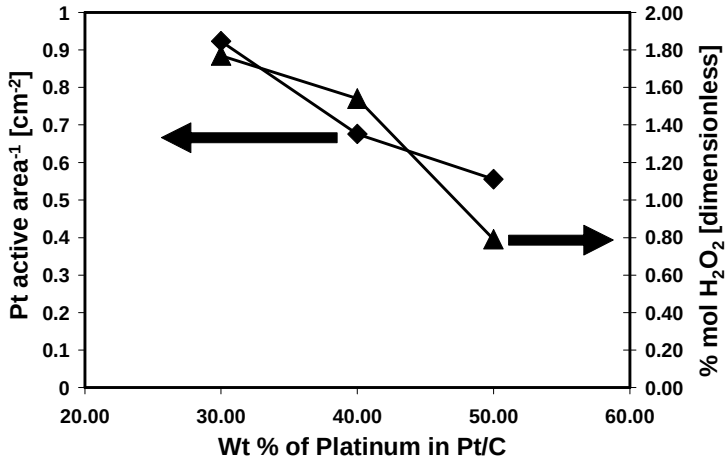

Figure 253. Variation of the % mol peroxide generation and the inverse of active area with the platinum mass ratio under constant Nafion® and constant catalyst loading of 44 µgcat/cm2 (all other conditions same as in Fig. 1).

Pt/C Samples with the Same Pt Loading and Different Carbon Support:

Pt/C samples with the same Pt loading (50 wt% Pt) having varying carbon supports providing different carbon surface area (56 - 950 m^2/g) were analyzed for peroxide generation. The variation in the Pt active area with the carbon support surface area is shown in Figure 254

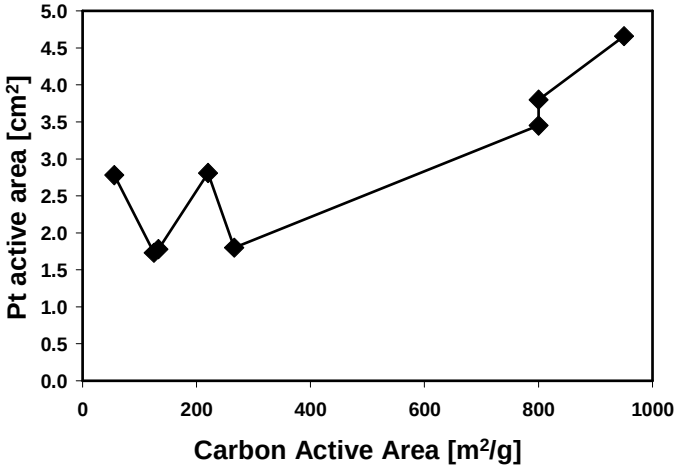

Figure 254. Variation in Pt active area as a function of the carbon support surface area for catalysts with 50% Pt mass ratio catalysts under constant Nafion® loading and catalyst loading of 44 µgcat/cm2 (all other conditions are the same as in Fig. 1).

The values of % mol peroxide and the total moles of peroxide at a disk potential of 0.675 V are plotted as a function of the surface area of carbon support in Figure 249(a). Table 35 provides the details of the carbon surface area, Pt active area, mean Pt particle sizes, % mol peroxide and total moles of peroxide formed at 0.675 V with the same catalyst loading of 44 $\mu g_{cat}/cm^2$. The total moles and % mol peroxide values normalized by the platinum active area is plotted in Figure 255(b).

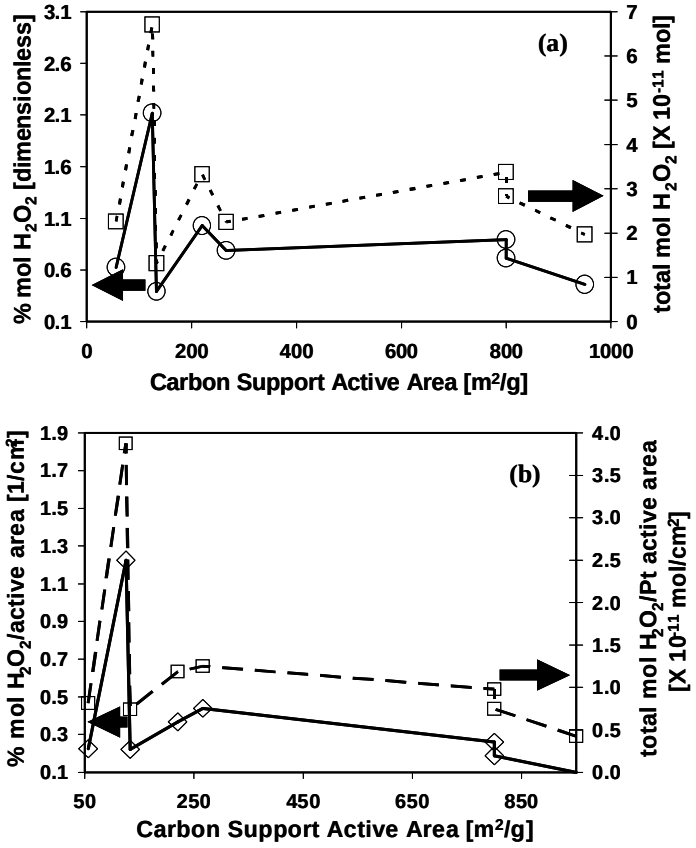

Figure 255. Peroxide generation at 0.675 V and at disk rotation speed of 3000 rpm as a function of the active area of the carbon support (m2/g) for 50% Pt mass ratio under the same catalyst loading of 44 µgcat/cm2 and the same Nafion® loading in terms of (a) % mo

Table 35. 50% Pt/C Samples with Varying Carbon Support

Active Area of Carbon (m^2/g)	Pt loading (mg_{Pt}/cm^2)	Active Area (cm^2)/ (m^2/g)	% mol H_2O_2 at 0.675 V	Total mol H_2O_2 (mol) at 0.675 V	Pt size[9] (nm)
56	0.0220	10/241	0.625	2.26 X 10^{-11}	2.3
125	0.0220	29/699	2.120	6.71 X 10^{-11}	2.2

133	0.0220	10/241	0.393	1.32×10^{-11}	2.4
220	0.0220	32/771	1.030	3.33×10^{-11}	2.2
266	0.0220	9/217	0.790	2.25×10^{-11}	2.4
800	0.0220	23/554	0.895	3.37×10^{-11}	2.4
800	0.0220	19/458	0.715	2.83×10^{-11}	3.2
950	0.0220	41/988	0.461	1.97×10^{-11}	2.6

The trends show an increase in Pt active area with increase in carbon support surface area (Figure 254) and also a corresponding decrease in peroxide production (Figure 256).

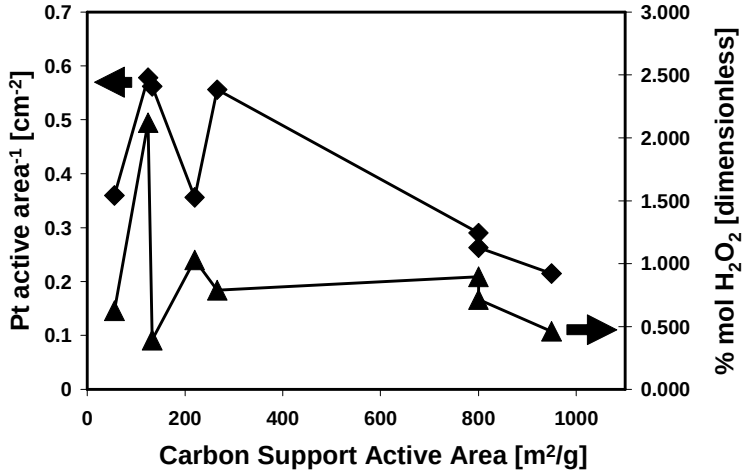

Figure 256. Variation of the % mol peroxide generation and the inverse of active area with the carbon support surface area for 50% Pt/C catalysts under constant Nafion® loading and catalyst loading of 44 µgcat/cm2 (all other conditions are the same as in Figure 249).

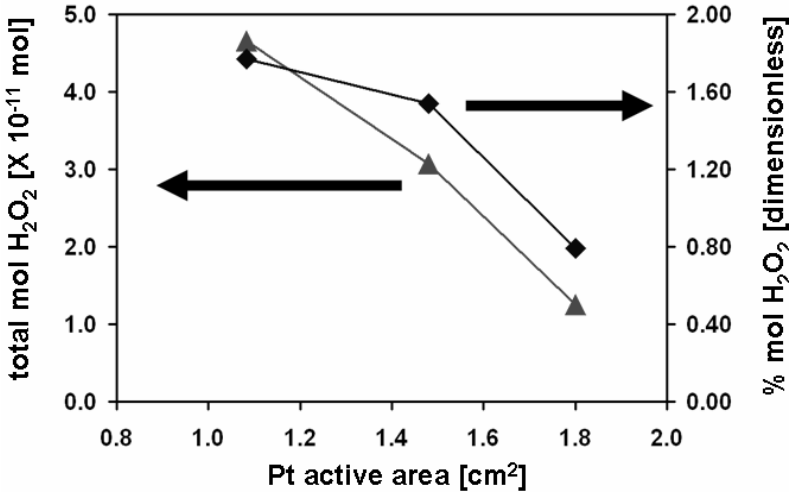

Figure 257. Platinum active area decreases with a decrease in the carbon support surface area for the same overall Pt weight. This may be due to increased Pt agglomeration which correlates with increased peroxide production

H_2O_2 Formation on Carbon Support:

Peroxide formation on carbon support with a surface area of 266 m^2/g was analyzed at different loadings (22 - 66 $\mu g_{carbon}/cm^2$) on the disk. Typical disk and ring currents on cathodic potential sweeps for carbon at different rotation speeds are shown in Figure 258.

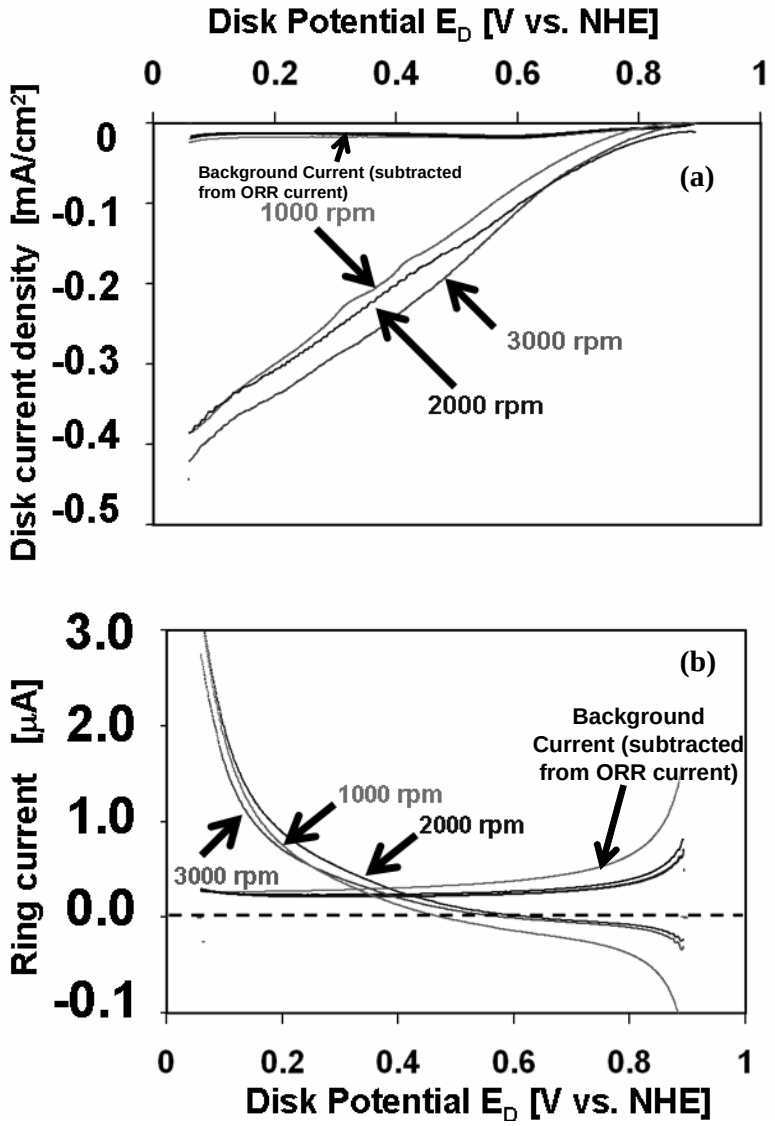

Figure 258. (a) Current-potential curves for O2 reduction on 266 m2/g carbon support in a thin film; (b) peroxide re-oxidation on Pt ring electrode in 0.5 M H2SO4 saturated with pure O2. ER = 1.15 V (vs NHE). Scan rate: 10 mV/s.

No mass transport limited region is noticed since the disk current density curves, as well as the ring current curves do not show a variation based on rotation speeds. The ORR current density is at least an order of magnitude lower than for any of the Pt/C samples. The % mol peroxide for different carbon loadings as a function of disc potential are shown in Figure 259

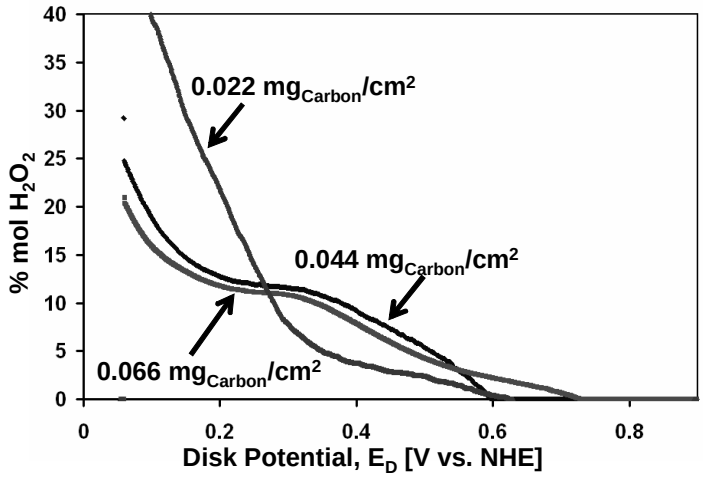

Figure 259. % mol H2O2 formed on the thin film electrode at disk rotation speed of 3000 rpm as a function of the disk potential for different loadings of Carbon support (266 m2/g) (all other conditions are the same as in Figure 249)

DISCUSSION: Studies of Filmed RRDE Electrodes

The observations based on peroxide production studies on the Pt/C samples can be summarized as follows:
(i) Peroxide production decreases with increase in platinum active area,
(ii) Peroxide production on carbon is negligible compared to that on Pt/C catalyst and
(iii) Platinum active area decreases with a decrease in the carbon support surface area for the same overall Pt weight. This may be due to increased Pt agglomeration which correlates with increased peroxide production.

Decrease in Peroxide Production with Increase in Platinum Active Area:
In our RRDE tests with Pt/C samples we notice that the peroxide generation is inversely proportional to the active area of platinum available for the reaction, under conditions of constant catalyst and Nafion® loading Figure 257, also Figure 253 and Figure 256 and for the same overall electrode area. The active area of Pt, plotted as a function of wt% Pt in Figure 251, shows an increase with the Pt content in the catalyst. The mol% peroxide production and the inverse of the Pt active area as a function of % wt Pt on same carbon support, plotted in Fig. 5, shows a decrease in peroxide production with increase in active area. In the case of Pt/C samples having same Pt mass ratio but varying carbon support surface area, we observe an increase in Pt active area with increase in carbon support area (Figure 254) Figure 256, depicting the inverse of Pt active area and mol % peroxide formed, as a function of the carbon support surface area also shows a similar trend in peroxide production with Pt active area. The original Pt particle sizes for all these Pt/C samples are almost equal (2.2-2.6 nm)[89]. This indicates that the net peroxide generation is less favorable on Pt, on which the ORR reaction proceeds mainly by the 4 electron

transfer pathway[81,82,87,91]. Tests conducted on carbon support without any Pt indicate that peroxide production on carbon is negligible at potentials positive to 0.4 V. This suggests a greater decomposition of peroxide, (which is formed on the Pt particles due to possible end-on non-dissociative oxygen adsorption on the edge atoms), when a greater platinum active area is available for the reaction[87,91].

Peroxide production on Carbon is negligible:

Runs with 22 $\mu g_{carbon}/cm^2$ and 44 $\mu g_{carbon}/cm^2$ produced negligible amount of peroxide at potentials positive to 0.5 V Figure 259. At potentials cathodic to 0.3 V, however, there is a large increase in % mol H_2O_2 production on carbon as compared with Pt/C samples. The ring current I_R, which indicates the total moles of H_2O_2 formed on carbon as a function of the disc potential, is lower than that on the corresponding Pt/C samples with the same carbon support (Figure 260).

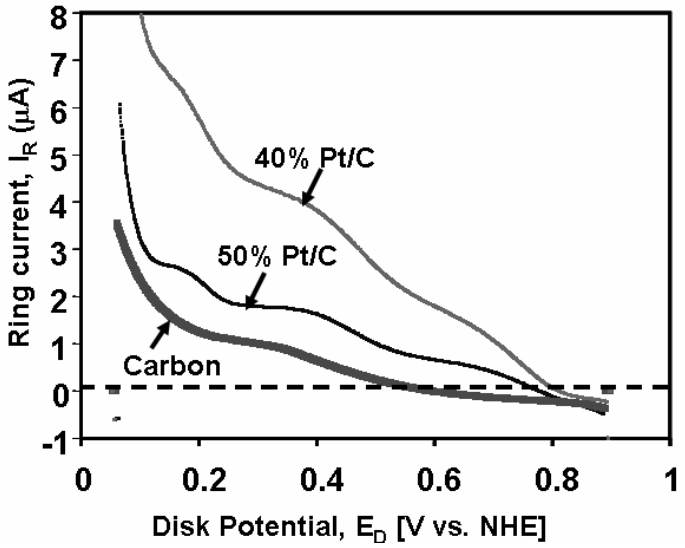

Figure 260. Comparison of Peroxide current (or Ring current, IR) obtained as a function of disk potential at 1000 rpm between bare carbon support and Pt/C catalysts with same carbon support

This indicates that, although peroxide formation during ORR is more favorable on carbon at potentials cathodic to 0.3 V, it is not a significant contributor to the net H_2O_2 formed in the potential range 0.5 V and 0.75 V where fuel cells are typically operated.

Decrease in Pt Active Area with Decrease in Carbon Support Surface Area:

Pt/C samples having the same platinum mass ratio (50% Pt) exhibit an increase in platinum active area as the surface area of carbon increases (Figure 254). In these samples, the catalyst loading, the Pt particle sizes and the Nafion® loading were kept constant. The original Pt particle sizes in all these samples were in the range of 2.2-2.4 nm. However, the active area of Pt plotted as a function of the carbon support surface area in Figure 254, shows an increase in Pt active area with increase of the carbon support surface area. Thus, although the carbon support may not be generating significant amount of peroxide in the potential range of interest, it has an impact

on the net peroxide produced on the Pt/C sample by possibly causing a variation in the Pt active area.

Equivalent Pt particle sizes were calculated based on the active area obtained from the hydrogen adsorption/desorption charge calculations and the known weight of catalyst loaded on the disc, assuming that the particles are individual spheres distributed on the carbon support. These radii were then compared with the sizes provided by the catalyst vendors (Table 36 and Ref. 89).

Table 36. Particle Size Calculation for 50% Pt/C Samples with Varying Carbon Support

Active Area of Carbon (m^2/g)	Pt loading (mg_{Pt}/cm^2)	Active Area (cm^2)/ (m^2/g)	Pt size {calculated} (nm)	Pt size {given}[9] (nm)
56	0.0220	10/241	4.2	2.3
125	0.0220	29/699	6.7	2.2
133	0.0220	10/241	6.5	2.4
220	0.0220	32/771	4.1	2.2
266	0.0220	9/217	6.5	2.4
800	0.0220	23/554	3.4	2.4
800	0.0220	19/458	3.1	3.2
950	0.0220	41/988	2.5	2.6

The calculated sizes are in agreement with the vendor data for only very high surface area carbon support (800-950 m^2/g) Pt/C catalysts. For low surface area carbons (56-266 m^2/g), the calculated sizes are much larger than those indicated by the vendor. The loss in Pt active sites due to the Nafion® loading was determined experimentally on bare and Nafion® coated polycrystalline platinum disk to be of the order of 30%, and was accounted for in the equivalent Pt particle size determination. The increase in average particle size and loss in Pt active area in low surface area carbon support leads us to the hypothesis that there is enhanced agglomeration of Pt particles on the relatively lower surface area carbon. This can be due to (i) the greater equivalent proximity (based on actual [not projected] carbon area) of Pt particles to each other on low surface area carbons (Table 37) and (ii) the relatively smooth substrate offering low “friction” which promotes lateral particle movement leading to their agglomeration.

Table 37. Calculation of Distance between Pt particles on Carbon Support

Pt/C Sample	High Surface Area Carbon Support	Low Surface Area Carbon Support
Mass ratio of Pt [%]	50	50
Carbon surface area (CSA) [m^2/g]	950	125
Pt loading on Disk [mg_{Pt}/cm^2]	0.022	0.022
Carbon loading [mg_C/cm^2]	0.022	0.022
Pt particle size (d) [nm]	2.6	2.2

No. of Pt particles (assuming spherical shape, no agglomeration) N = Pt loading*disk Area/(ρ_{Pt}*πd^3/6)	3.2 X 10^{-12}	5.2 X 10^{-12}
Surface Area of carbon available for Pt particles [cm^2] A = Carbon loading*Disk Area* CSA	59.2	7.8
Distance between Pt particles (D) [nm] ($N\pi D^2/4 = A$); $D = \{A/(\pi N/4)\}^{1/2}$	48.5	13.8

By contrast, the high surface area more convoluted carbon will tend to "lock" the Pt particles in place. A similar observation has been reported by Stonehart[89] and Watanabe *et. al* [90], who measured the Pt particle sizes as a function of the carbon surface area using TEM, CO adsorption and H_2 adsorption. They report that the specific activity for ORR decreased with the average distance between the agglomerated particles. The authors, however, did not measure or consider peroxide formation.

Considering an agglomerate of N particles formed on the carbon support from n initial particles, n/N such agglomerates are generated. We assume a disk-like agglomerate particle, where only the top area is completely exposed to reaction, while the regions of contact between particles are inaccessible for the ORR. A schematic representation of such an agglomerate is shown in Figure 261

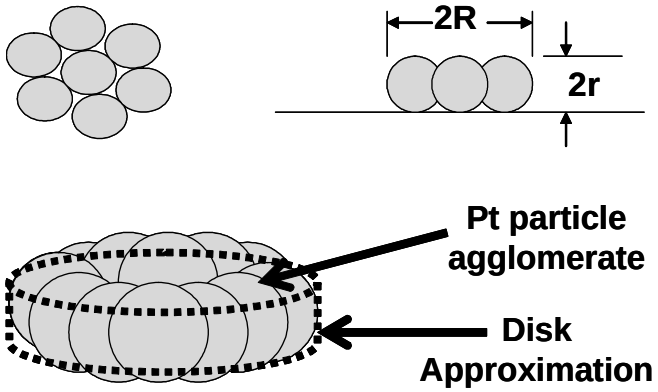

Figure 261. Schematic representation of a single layer (disk-like) agglomerate (of radius R) comprising of a fixed number of Pt particles (each of radius r)

Let r be the radius of each Pt particle and R, the radius of the agglomerate disk.

$$\pi R^2 \approx N^* \pi r^2$$

Equation 48

$$R = N^{1/2} r$$

Equation 49

In Equation 48 we neglect the area due to voids between the closely packed spheres, since this area is only a small fraction of the total area for closely packed spheres. The actual (non-projected) surface area of the agglomerate disk (consisting of N Pt particles) with radius R is:

Area = (sum of hemispherical area exposed at top face) + (area along perimeter)

$$\text{Area} = 2N\pi r^2 + 2\pi N^{1/2} r^2$$

Equation 50

The ratio of the total Pt active area corresponding to such agglomerates to the true active area in the event of no agglomeration gives a factor of ***X*** for the loss of active area of the platinum in the Pt/C catalyst due to agglomeration, i.e.,

$$\text{Measured Pt area} = X * (\text{True Pt area})$$

Equation 51

A more realistic model is to assume that once the number of agglomerated particles increases beyond, about 4-8 Pt particles, they are likely to form a multilayer structure, as shown schematically in Figure 262

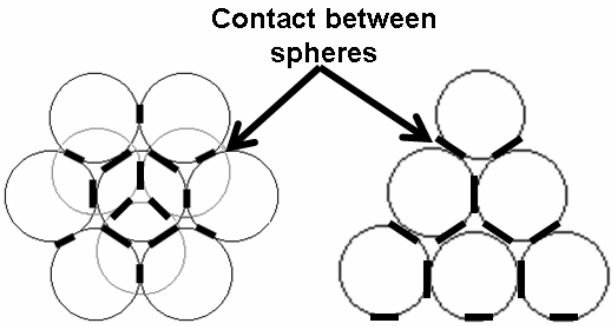

Figure 262. Schematic representation of a multilayer agglomerate comprising of a fixed number of Pt particles (each of radius r).

The exposed area of such an agglomerate was estimated and compared to the cumulative surface area of the total number of single Pt particles. The area reduction associated with agglomerates for both single layer (disk-like) agglomerates and multilayer structures is shown in Figure 263.

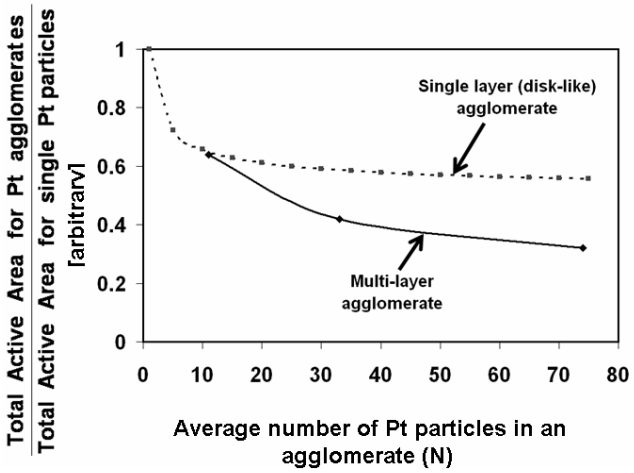

Figure 263. Decrease in active area of Pt particles (plotted as the ratio of measured area to the true area) with increase in number of Pt particles in an agglomerate.

Although, there is a loss in active area of Pt as the average number of particles in an agglomerate is increased, Figure 263 indicates that the multilayer agglomerate particle model provides a larger loss in the active area and hence a better agreement with the experimental results. Such a spherical model, which is only likely for agglomerates involving a larger number of Pt particles in an agglomerate, seems to be consistent with TEM studies.

The numbers of particles (N) in Pt agglomerates of different carbon supports were estimated by taking a ratio of the measured Pt active area to the true Pt area and obtaining the corresponding value of N indicated in Figure 263 These values of N when plotted against the carbon support surface area show an increased agglomeration on lower surface area carbon (Figure 264).

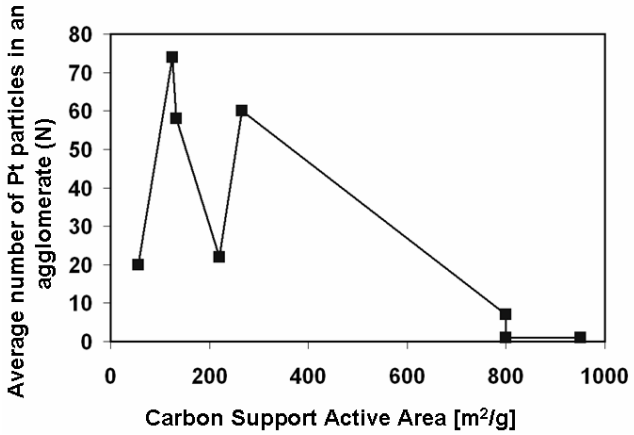

Figure 264. Average number of Pt particles in an agglomerate (calculated from measured active area of Pt) as the function of the carbon support surface area for experimentally analyzed Pt/C samples.

It is observed that when the Pt loading on the same carbon substrate (carbon surface area = 266 m^2/g) is increased, the Pt active area per unit weight of Pt, i.e. (Pt active area)/(Pt wt.) in m^2/g_{Pt}, remains substantially the same (Table 34). This may indicate that under those conditions, viz.

same carbon support and same Pt particle size, the degree of agglomeration is independent of the Pt mass ratio

Of particular interest to the peroxide formation issue is the presence of limited accessibility regions, such as grain boundaries formed due to contact between individual Pt particles and between the Pt particles and the carbon support. Previous researchers[87,91] have suggested that the peroxide formation is due to end-on oxygen adsorption on the platinum edge atoms, leading to production of O_2H^- species which are not dissociative. This mechanism of peroxide generation is hypothesized to take place on the low coordination number edge atoms of Pt, since the bulk surface is covered by the oxygenated intermediate species. In order to find out whether Pt agglomeration increased the edge regions, we approximate the relative perimeter regions for agglomerated Pt and compare it to the edge region in non-agglomerated single spherical particles.

We arbitrarily approximated that the radius of the circumference of the contact region formed by a single spherical particle sitting on a high surface area carbon support is of the order of $1/10^{th}$ of the radius of the particle (Figure 265).

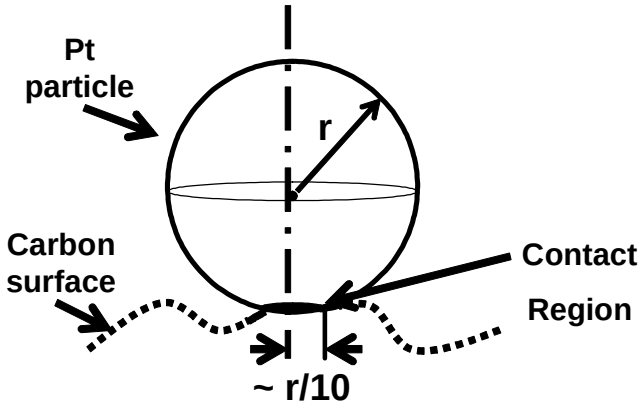

Figure 265. Schematic representation of the edge formed by a single Pt particle attached to the carbon substrate (the contact region is approximated by an area of 1/10th the radius of the Pt particle).

As depicted in Figure 262, the stacking or agglomeration of individual Pt particles will give rise to creation of additional edges due to increased contact regions formed between the single particles. Assuming that each inter-particle contact also gives rise to a region of circumference corresponding to $1/10^{th}$ the radius of the particle, the ratio of the edge regions of the disk-like ($N < 7$) or multilayer agglomerates ($N > 7$) to the sum of all the single particles was calculated and plotted in Figure 266.

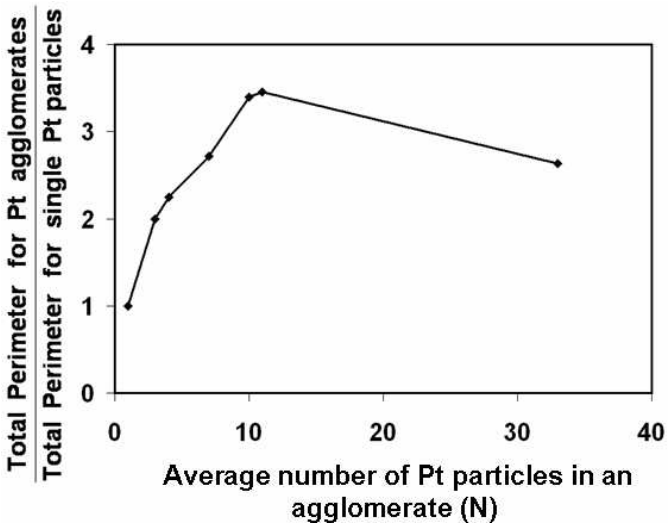

Figure 266. Increase in contact (edge) area of Pt agglomerates (plotted as the ratio of agglomerate contact perimeter to the sum of contact perimeter regions for individual Pt particles) with increase in number of Pt particles in an agglomerate.

It is observed that agglomerated Pt/C samples provide a greater edge region (where peroxide generation is hypothesized to be favored) as compared to non agglomerated Pt particles based on the same amount of Pt and the same original (non-agglomerated) Pt particle size. Agglomeration of Pt particles leading to low overall Pt active area accompanied by an increase in the edge regions might be collectively responsible for increased peroxide generation on Pt/C catalysts supported by low surface area carbon (Figure 256). Thus, although the carbon support might not be generating peroxide in the potential range of interest, it has an impact on the net peroxide produced on the Pt/C sample by varying the Pt active area.

The large variability that is noted in peroxide formation and in the calculated degree of agglomeration for low surface area carbons (left hand side of Figure 255, Figure 256, Figure 253) may be due to experimental inaccuracies. However, this variability may also be associated with actual fluctuations in the degree of agglomeration for Pt particles on relatively smooth carbon where agglomeration is expected to be high. This high agglomeration may depend on factors such as the type of carbon support, and the shape of the agglomerate, which was assumed to be a disk but actually may be spheroid.

The degree of faceting in the Pt particles may also somewhat affect the peroxide formation[92]. However, in our study, all the Pt samples were generated similarly and therefore the faceting is likely to remain constant for all tested samples, hence the effects we are reporting should be independent of this factor.

*CONCLUSIONS: Studies of Filmed RRDE Electrode**s***

Peroxide production studies using RRDE for different Pt/C samples revealed an inverse relationship between the Pt active area of catalyst and the peroxide produced. Peroxide production was observed to decrease with increasing Pt active area for the same catalyst loading and the same electrode area. A carbon support material tested for peroxide generation showed

negligible peroxide formation in the typical potential range of fuel cell operation (0.5-0.75 V). Pt/C samples with same Pt mass ratio but different carbon support surface areas revealed a dependence of Pt active area on carbon support surface area. It is hypothesized that agglomeration of Pt particles due to greater relative proximity between Pt particles on low surface area carbons might cause a loss in Pt active area, and hence, lead to a corresponding increase in production of peroxide. An approximate model indicating the extent of this agglomeration based on the measured Pt active area supports this hypothesis and reveals the generation of more edge regions by Pt agglomerates, which might bring about an increase in the peroxide production by end-on oxygen adsorption.

4.1.2: Peroxide Transport and DMBE Studies

With the limitations of the most common research methodology for examining ORR concerns in mind, it is clear that the development of a test method for detecting H_2O_2 produced as the result of the ORR under realistic fuel cell conditions is desirable. The motivation of the work being discussed here is the development of a test method that can be used to examine fundamentals associated with the ORR, in particular H_2O_2 production, under the most realistic fuel cell conditions. However, it is necessary to study H_2O_2 detection and transport in order to design such a test method. Two major initial tasks in the development of the new test method will be highlighted here. The first such task is the assessment of H_2O_2 diffusivity in polymer films. The second task is the testing of so-called dual microband electrodes (DMBE). These devices will eventually serve as a new test methodology for examining fundamental ORR concerns employing only a vapor-equilibrated polymer electrolyte. Liu demonstrated that a single microband electrode could be used under such conditions to obtain kinetic parameters and O_2 transport parameters that are comparable to a Pt/phosphoric acid system[93].

EXPERIMENTAL: Peroxide Transport and DMBE Studies

Measurement of H_2O_2 Oxidation Currents

The oxidation waves for dilute, acidic H_2O_2 solutions were measured via rotating-disk electrode (RDE) voltammetry. A bare and polymer (Nafion) filmed Pt RDE were used to measure the oxidation waves for 1 mMol H_2O_2 in 0.5 M $HClO_4$. The solutions were prepared from 11.7 N $HClO_4$ (70%) and 30 % unstabilized H_2O_2 obtained from Fisher Scientific. Ultra high purity (UHP) Ar and N_2 gases were obtained from Praxair and used to purge/ blanket the solution. It should be noted that unstabilized H_2O_2 was used because the stabilizing molecule, sodium stannate, may have an affinity to adsorb to the Pt electrode. The stock H_2O_2 solution concentration was determined via titration by potassium permanganate, which was standardized with oxalic acid. The concentration of peroxide in 30 wt % H_2O_2 is approximately 10 M. Therefore, 25 µL of the stock solution was diluted to a final volume of 250 mL with 0.5 M $HClO_4$ in order to prepare peroxide solutions for study.

Prior to the experiment, 0.5 M $HClO_4$ was de-aerated with UHP Ar and blanketed with UHP N_2. The bare Pt electrode was then potential cycled between 1.4 and 0.05 V vs. RHE for about 1 hr. Filmed RDE's were produced by rotating the RDE in the range of 500 – 1000 RPM for 5 min after pipetting about 25 µL of a 5% Nafion solution, obtained from Fisher Scientific. The Nafion solution was pipetted onto the RDE immediately after cold storage. The filming procedure is

essentially that developed by Porchet et al [94]. After allowing the filmed electrode to dry for 12 hr, it was immersed in 0.5 M $HClO_4$ for 1 hr, at which point the electrode was potential cycled between 1.4 and 0.05 V vs. RHE. The potential cycling described here corresponds to recording the cyclic voltammogram of the electrode in acid solution. The potential was swept at 50 mV/sec between the sweep limits given above.

After verification that the electrode surface was not undergoing any further changes, the solution was changed for the dilute H_2O_2 solution described above. Once the bare or filmed Pt RDE was introduced to the dilute H_2O_2 solution, the solution was de-aerated with UHP Ar and blanketed with UHP N_2 for 20 min. This procedure was followed for every oxidation wave measurement, except only 5 min was used between each measurement. This methodology was used in order to drive dissolved O_2 out of the H_2O_2 solution in order to prevent any significant electrochemical response due to the H_2O_2/O_2 couple. The measurement of H_2O_2 oxidation was carried out by sweeping the potential from 1.3 to 0.8 V vs. RHE at 5 mV/sec. 3 measurements of each oxidation wave were measured at each electrode rotation frequency. Electrode rotation frequencies in the range of 200 – 3600 RPM were examined.

DMBE Fabrication and Testing

DMBE devices were fabricated by common photolithographic, metal thin film deposition techniques in the Electronics Design Center (EDC) at Case. Approximately 200 nm of Pt was deposited on a Pyrex substrate. Prior to aqueous testing, the devices were cleaned by immersing them in 1 M HNO_3 and 30 wt % H_2O_2 for 5 min at 80˚C, respectively. Liu et al fabricated single microband electrodes that served as a design basis for the DMBE devices[95].

A proof of principle demonstration of the DMBE device was performed in 0.5 M $HClO_4$. Cyclic voltammetry was performed on the microband electrodes to assess the quality of the Pt electrode. These experiments were conducted after the acid electrolyte was purged with UHP Ar and blanketed with UHP N_2, as above. The potential was scanned at 50 mV/sec between 1.4 and 0.05 V vs. RHE.

After an initial assessment of the cyclic voltammetry of the DMBE device in 0.5 M $HClO_4$ was carried out, the device was operated in generator/collector mode, analogous to a RRDE experiment. The inner and outer bands were independently potentiostated.

The potential of the inner band of the electrode was swept from 0.85 to 0.2 V vs. RHE at 5.3 mV/sec. This was done in order to use the inner band as the generator electrode at which the ORR was taking place. The potential of the outer band was held constant at 1.2 V vs. RHE in order to collect any products formed, and having a long enough lifetime to reach the outer electrode of the device. The inter-electrode spacing used was 20 μM.

After performing the cyclic voltammetry of the DMBE device as described above, the 0.5 M $HClO_4$ solution was saturated with O_2 (obtained from Praxair) for 20 min. After the 20 min period expired, the O_2/0.5 M $HClO_4$ solution was then blanketed with O_2 for 5 min while allowing the bulk solution to experience no disturbance. At the end of this 5 min period the gas supply for the blanket was shut off. Careful attention to saturation and blanketing procedure was paid. This procedure was developed on the basis that even very small mechanical disturbances in and

above the solution significantly affected the ORR current value and stability in the region of mass transport control during operation of the DMBE device.

RESULTS AND DISCUSSION: Peroxide Transport and DMBE Studies

H_2O_2 Diffusivity

The oxidation waves for H_2O_2 in 0.5 M $HClO_4$ were measured for various electrode rotation frequencies and are depicted in Figure 249. The disk voltammograms offered in Figure 267 have three important features that are immediately obvious.

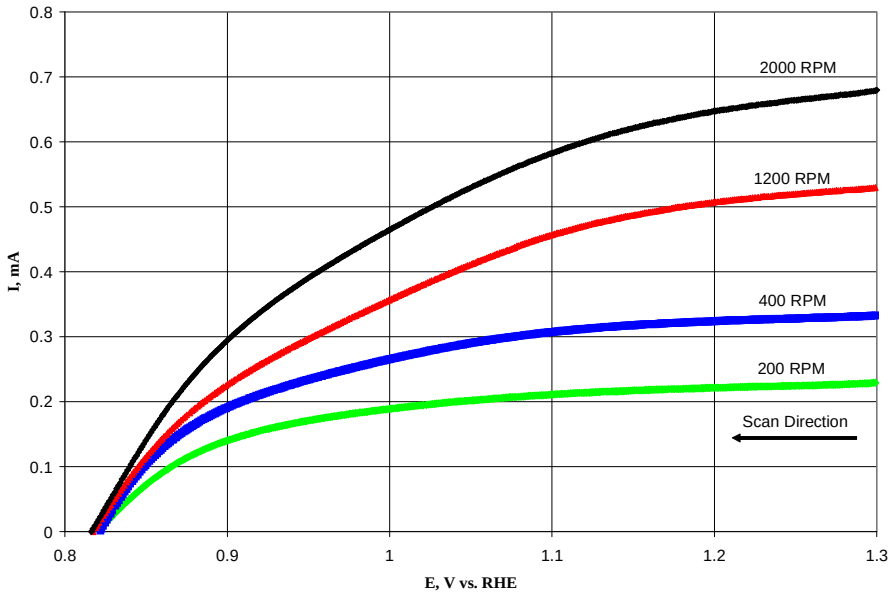

Figure 267. Voltammogram depicting the oxidation behavior of 1 mM H2O2 in 0.5 M HClO4. The potential was swept from positive to negative at 5 mV/sec. T = 25˚C.

An apparent limiting current plateau seems to emerge at disk potentials more positive than 1.2 V vs. RHE. This point will be explored more thoroughly later. Another feature of the voltammograms in Figure 267 is that they appear to be characteristic of a complicated, sluggish electrochemical process. This observation is based on the fact that the current does not appear to drop rapidly with decreasing potential, and a pre-anodic limiting current feature that seems to occur around 0.90 V vs. RHE. Westbroek and Temmerman[96] also observed an additional anodic wave feature, which they attributed to two peroxide oxidative mechanisms that operate simultaneously. Their work utilized a glassy carbon RDE to oxidize dilute, basic H_2O_2 solutions. The third feature of the voltammograms is that they converge on a zero-current value of the potential of about 0.82 V vs. RHE. This zero-current value of the potential is about 150 mV larger than the thermodynamic reversible potential, 0.67 V vs. RHE, given in Equation 48 The potential observed may be larger than the thermodynamic reversible potential due to the deviation of peroxide oxidation from a reversible, Nernstian process, or the dominance of one particular electrochemical couple in a mixed potential scenario.

In Figure 268 the total current, I, at 1.2 and 1.3 V vs. RHE is plotted against the square root of the electrode rotation frequency, $\omega^{1/2}$. A linear plot of I vs. $\omega^{1/2}$ indicates that the current is mass transfer limited and the slope can be used to obtain the peroxide diffusivity, according to the Levich equation:

$$I = 0.62nFAD^{2/3}\nu^{-1/6}C_b\omega^{1/2}$$

Equation 52

Where n (= 2 e^- in this work) is the number of electrons transferred, F (= 96,485 C/mol) is Faraday's constant, A (= 0.196 cm^2) is the electrode area, D is the species diffusivity, v (= 0.01 cm^2/sec)is the solution kinematic viscosity, C_b (1 x 10^{-6} mol/cm^3) is the solution species concentration, and ω (rad/sec) is the electrode rotation frequency. Figure 268 shows that the current at 1.2 and 1.3 V is indeed linear in $\omega^{1/2}$. Besides the linearity of the plots in Figure 268, the negligible y-intercept demonstrated indicates that I is related to $\omega^{1/2}$ by Equation 52 Using the slope of the plot for I at 1.2 V vs $\omega^{1/2}$ yields D = 1.1 x 10^{-5} cm^2/sec.

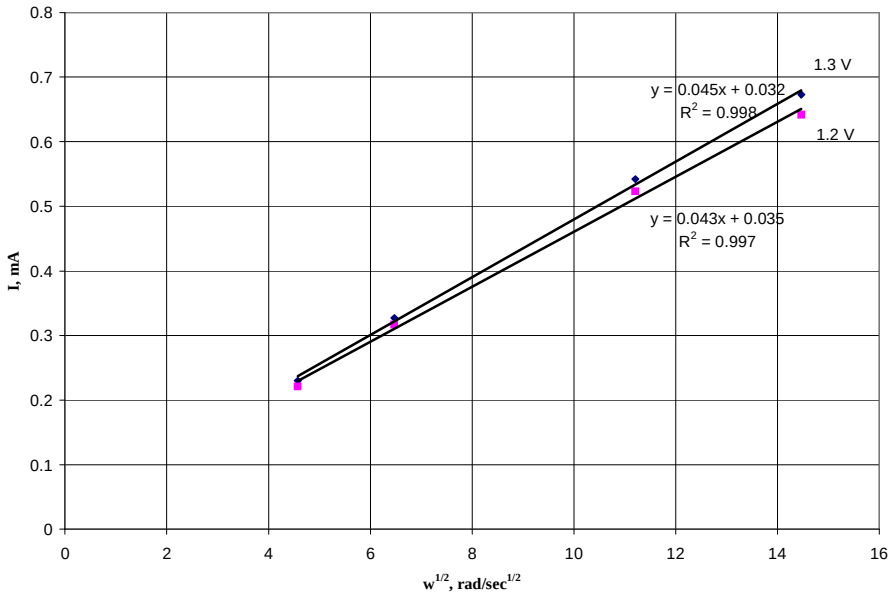

Figure 268. Levich plot of the current at 1.3 and 1.2 V vs. RHE (from figure 1)showing that the current at high oxidative potentials is strongly dominated by mass transport control.

Figure 269 presents a more detailed analysis of the anodic currents measured via RDE voltammetry for a bare Pt disk electrode from Figure 249 and a polymer filmed RDE.

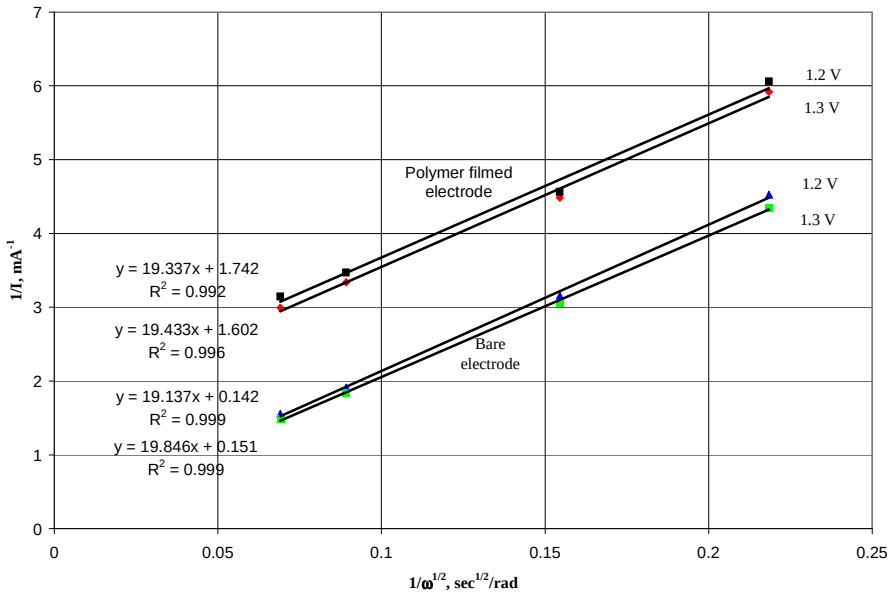

Figure 269. Koutecky-Levich and membrane model analysis of the current obtained at 1.2 and 1.3 V for a bare and polymer filmed Pt RDE.

The plots were constructed in a Koutecky-Levich fashion, where the inverse of I was plotted vs. the inverse of $\omega^{1/2}$ at 1.2 and 1.3 V vs. RHE. For both cases, bare and polymer filmed RDE, straight line plots resulted. In the case of the bare RDE the straight line relationship that is evident is of the following form:

$$\frac{1}{I} = \frac{1}{I_{l,a}} + \frac{1}{I_K} = \frac{1}{0.62nFAD^{2/3}\nu^{-1/6}C_b\omega^{1/2}} + \frac{1}{I_K}$$

Equation 53

I is the total current at the respective voltage and electrode rotation frequency, $I_{l,a}$ is the mass transfer dominated anodic current, and I_k is the current that would flow in the absence of mass transfer limitations. In the case of the bare RDE the straight line plot in Figure 251 gives a slope that also yields a peroxide diffusivity of 1.1 x 10^{-5} cm^2/sec in acidic solution. However, it is evident that the current at these large anodic potentials is under mixed control. This conclusion is drawn from the value obtained for I_k, which is the current that would flow in the absence of mass transfer limitations. The extrapolated value of I_k is 7.1 mA, corresponding to the current at infinite electrode rotation frequency. Examination of the straight line plots for the polymer filmed RDE in Figure 269suggest that the data follows the membrane model:

$$\frac{1}{I} = \frac{1}{I_{l,a}} + \frac{1}{I_F}$$

Equation 54

$I_{l,a}$ is the mass transfer dominated anodic current due to reactant diffusion in solution and I_F is the reactant diffusion current due to mass transfer in the polymer film. The diffusivity of H_2O_2 can be determined from the film diffusion current, which has the following form:

$$I_F = \frac{nFADκC_b}{\delta_F}$$

Equation 55

is the partition coefficient and δ_F is the polymer film thickness. In this work it is assumed that mass transfer of H_2O_2 into the polymer film from the solution is negligible. This means that it is assumed that κ =1, which would imply that the concentration just inside the polymer film takes on its greatest value, κC_b. This value of the concentration inside the polymer film is also indicative of mass transfer in the solution being negligible, which would occur at infinite electrode rotation frequency. A calculation of peroxide diffusivity in the polymer film using this model is dependent on the film thickness being known accurately and κ = 1. The thickness of the polymer film was determined using the empirical correlation of Porchet and Javet[94]. Using δ_F = 0.4 µm, the diffusivity of H_2O_2 in a film of Nafion 117 was calculated to be 6.0 x 10^{-7} cm^2/sec. The calculated value of the H_2O_2 diffusivity in a polymeric material is extremely sensitive to the degree to which δ_F is known. Further work will include a simultaneous, in-situ measurement of the film thickness.

DMBE Testing

Figure 270shows a schematic representation of the DMBE device. The DMBE used for testing in 0.5 M $HClO_4$ had an inter-microband electrode spacing of 20 µm.

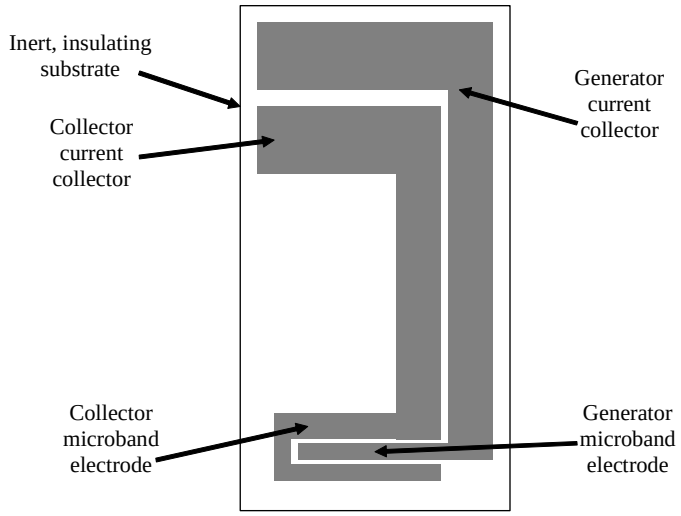

Figure 270. Representation of the DMBE device.

Figure 271 depicts cyclic voltammograms recorded for both generator and collector microband electrodes. In general, the cyclic voltammograms shown in Figure 271 exhibit the features expected for a Pt electrode in acid.

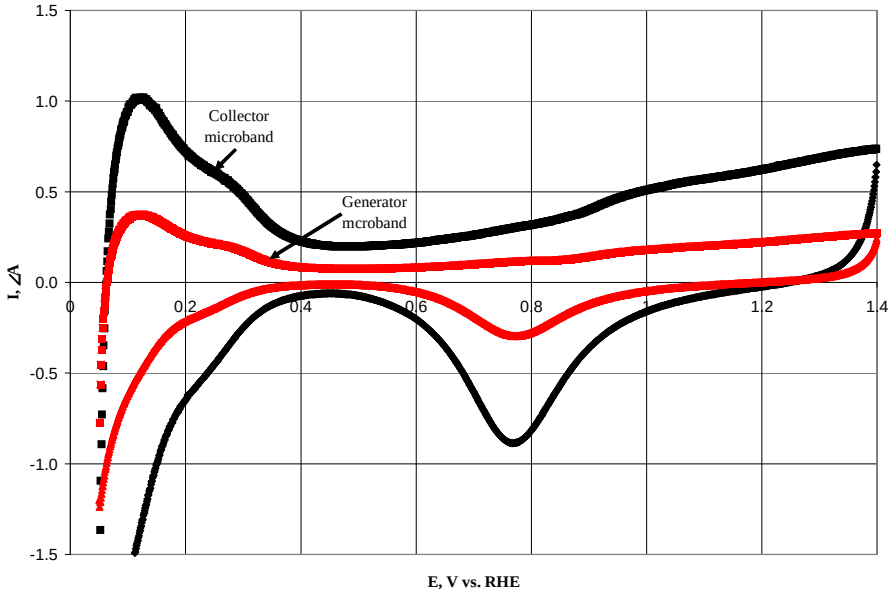

Figure 271. Cyclic voltammograms of the generator and collector microband electrodes in

A typical cyclic voltammogram for a Pt electrode exhibits regions of oxide formation and reduction, as well as H^+ adsorption/desorption. This behavior is evident in Figure 271, but some differences are apparent. It was necessary to take the generator microband electrode out to 1.4 V vs. RHE , well into the region of surface oxide formation, in order to observe a large surface oxide reduction peak, near 0.8 V vs. RHE. This behavior may be the result of introduction of organic matter to the microband electrode by the application of Kapton tape to protect it during its preparation for test. The onset of H^+ adsorption at potentials lower than 0.4 V vs. RHE, during the scan from positive to negative, that usually appears as two large H^+ adsorption peaks is not evident. Furthermore, the three H^+ desorption features that occur between 0 and 0.4 V vs. RHE, during the scan from negative to positive, are not well defined. The two latter deviations from ideal Pt in acid cyclic voltammetry have caused it difficulty in determining the true area of the generator and collector microband electrodes. After correcting for the 90 nA background current associated with double layer charging, the current corresponding to H^+ desorption was integrated with respect to time in order to compute the electrode surface area. The generator microband area was computed to be 6×10^{-3} cm^2, which is about 33% larger than its geometric area, 4×10^{-3} cm^2. It is not understood at this point if the discrepancy is due to electrode morphology or its electrochemical behavior.

After performing basic cyclic voltammetry, the ability of the DMBE to operate in generator/collector mode was examined. The operation of the DMBE in generator/collector mode is analogous to the RRDE experiment, with one marked difference. In the DMBE experiment the ability of the collector electrode to detect any by-products due to an electrochemical process at the generator relies on diffusion. This would assume that quiescent solution conditions exist. The well-defined hydrodynamics of the RRDE experiment utilize forced convection of the generated species to the collector electrode. So, in the DMBE test in O_2 saturated 0.5 M $HClO_4$ any by product detected at the collector electrode must have diffused across the 20 μm gap.

Figure 272 shows the linear sweep voltammetry behavior for the DMBE generator microband in both de-aerated and O_2 saturated 0.5 M $HClO_4$.

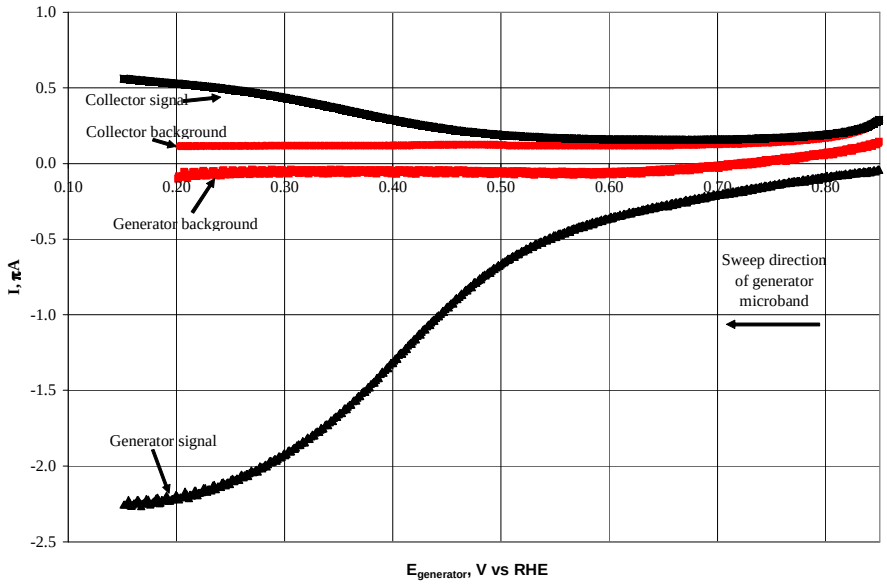

Figure 272. Voltammograms showing the generator-collector behavior of the DMBE in O2 saturated 0.5 M HClO4.

The linear sweep voltammogram recorded in de-aerated solution served as a measurement of the background current for the generator microband electrode. The collector microband electrode was potentiostated while its current was recorded for both de-aerated and O_2 saturated 0.5 M $HClO_4$. The measurement of the current for the potentiostatic control of the collector microband electrode in de-aerated solution served to establish its background current. These background currents may be attributed to double layer charging and the oxidation/reduction of solution impurities and the Pt surface. It is evident from examining this figure that the background current is quite low for both the generator and collector microband electrodes. Most of the background current for the generator microband electrode is due to some reduction process, and is on the order of -5 nA. The background current at the collector microband electrode was on the order of 120 nA. The initial spike in the generator background current may be due to the stripping of adsorbed hydrogen, and then is dominated by another oxidation process.

The linear sweep voltammogram recorded for the generator microband electrode in O_2 saturated 0.5 M $HClO_4$ is quite significant in comparison to its background current. It seems that the current is approaching mass transfer limitation at potentials less than 0.3 V vs. RHE. This mass transfer limited current is reproducible employing cell conditions described in the experimental section of this work, and approaches -2.25 μA. The DMBE experiment is very sensitive to the state of the solution, and area above it. That is, the voltammetry of the generator microband electrode, especially in the mass transfer limited regime of the curve, depends greatly on a quiescent solution and no disturbance of the solution surface by the flow of blanketing gas. A limiting current plateau does not occur for a wide potential window. This may be explained by a slow

growth of the O_2 depleted region next to the generator microband electrode which relies only on reactant diffusion.

Another interesting feature of Figure 272 is the signal obtained at the collector microband electrode, which is held at 1.2 V vs. RHE, when the potential of the generator microband electrode is swept. It is well understood that a prevalent side product of the ORR is H_2O_2. This may occur by reaction in Equation 48 If H_2O_2 desorbs and does not undergo further reduction via the reaction in Equation 49, it could diffuse across the inter-electrode gap of the DMBE and be oxidized. This oxidation should occur according to the reaction in Equation 50. It is clear that the collector microband electrode is detecting an ORR side product. This is based on the current obtained while holding the collector microband potential at 1.2 V vs. RHE while the potential of the generator microband electrode is swept in the cathodic direction. Figure 254 shows that the collector microband signal starts to rise above the background between 0.5 and 0.6 V (generator potential) vs. RHE. This indicates that in the DMBE experiment described, H_2O_2 production starts to occur between 0.5 and 0.6 V (generator potential) vs. RHE. The collector microband signal continues to climb as the generator microband electrode potential is swept in the cathodic direction. This result seems consistent with RRDE work with a poly-crystalline electrode conducted by Paulus et al.[97] [18]. Paulus et al. showed that the ring current obtained for RRDE voltammetry in O_2 saturated 0.1 M $HClO_4$ did not start to rise until the disk potential was below 0.4 V vs. RHE. The ring current obtained in this work increased significantly as the disk potential was swept in the cathodic direction. The collector microband electrode current also continues to rises in a similar fashion as the electrode at which the ORR takes place is swept in the cathodic direction. The main difference in the results is that the DMBE current does not approach a well defined limiting current plateau. This, however, is understood in terms of the nature of quiescent conditions that lead to less well defined mass transfer characteristics in the DMBE experiment than in the RRDE experiment. The results presented here are promising in the sense that the DMBE device is capable of demonstrating an ORR current which results in a H_2O_2 detection current, even when relying on only the process of physical diffusion. The DMBE will be extended to vapor-equilibrated conditions in order to simulate more realistic PEMFC operating conditions.

CONCLUSION: Peroxide Transport and DMBE Studies

The diffusivity of H_2O_2 was examined in order to aid in the development of a microband electrode device for studying the ORR and H_2O_2 production under realistic PEMFC operating conditions. H_2O_2 oxidation was shown to be under appreciable mass transfer control above 1.2 V vs. RHE. The aqueous H_2O_2 diffusivity was determined to be 1.1×10^{-5} cm^2/sec. The oxidation of H_2O_2 is a complicated, sluggish process on Pt. This is evidenced by an additional anodic feature, and a zero-current value of the potential, 0.82 V vs. RHE, being more than 150 mV than the predicted thermodynamic value, 0.67 V vs. RHE. The diffusivity of H_2O_2 in a film of Nafion 117 on a Pt RDE was calculated to be 6×10^{-7} cm^2/sec.

A DMBE device was fabricated and tested in aqueous acid solution. The cyclic voltammetry behavior recorded for the generator and collector microband electrodes was similar to that expected for a poly-crystalline Pt electrode. However, the H^+ adsorption/desorption portion of the voltammograms did not mimic the usual behavior of clean well-defined Pt surface.. The area of the generator microband electrode was estimated to be 6×10^{-3} cm^2 , which is about 33% larger than its geometric area, 4×10^{-3} cm^2. The cause of the observed behavior, leading to a larger

than expected calculated area, is unknown.. Linear sweep of the generator microband electrode in the cathodic direction resulted in the demonstration that this device is capable of producing an ORR current. The ORR current observed appeared to tend toward mass transfer limitation between 0.2 and 0.3 V vs. RHE. This current reached a peak value of -2.25 μA. A H_2O_2 detection signal at the collector microband electrode was also shown to rise appreciably above background levels. This current increased steadily after about 0.4 V (generator potential) vs. RHE. The collector microband electrode current continued to increase, to a value of 0.5 μA, as the generator microband electrode potential was swept in the cathodic direction. These results are consistent with the ORR/H_2O_2 detection behavior observed by other researchers employing the much more robust RRDE experiment. Since an appreciable ORR current and H_2O_2 detection signal that rely strictly on physical diffusion have been demonstrated, the DMBE device will be employed utilizing a vapor-equilibrated polymer electrolyte to study the OR under more realistic PEMFC operating conditions.

4.2: In Situ Studies of Peroxide Generation, Transport and Reaction

Hydrogen peroxide has been postulated to form under various conditions in polymer electrolyte membrane fuel cells (PEMFC), and it has been implicated in the premature aging of the polymer electrolyte membrane. However, there is conflicting evidence regarding its source and quantity. It is expected from the work in *4.1: Ex Situ Studies of Peroxide Generation, Transport and Reaction* and other work that peroxide can be formed at both anode and cathode in the fuel cell under certain conditions. Rotating ring-disk electrode studies of Pt supported electrodes show that peroxide is formed:

6. When oxygen is present at a Pt electrode at a potential of roughly 0 to 0.2 V vs. NHE (i.e. under anodic conditions).

7. As a side product of the oxygen reduction reaction below ~0.7 V.

These conclusions are derived from solution-phase studies. In the actual fuel cell environment, it possible that the reaction is modified, particularly under low RH conditions. Mechanisms[98] above also depends strongly on the oxygen access to the anode via cross-over. We sought to improve on the understanding of these processes in the fuel cell by developing appropriate in situ methods to probe peroxide production.

Among the reports in the literature, Ref.99 claims to have detected peroxide in–situ in a 25cm^2 PEMFC at 60^oC. In this work Pt micro wires of 25um in diameter were used as in-situ probes for detecting the peroxide in a sandwich cell configuration. As is well known in the literature, in a PEMFC operated with H_2/Air (O_2), reactant gases are known to cross over to the opposite side and therefore, hydrogen and oxygen gases permeate through the membrane, creating the conditions for H_2O_2 formation on the catalysts. Thus, in a PEMFC at the point where H_2O_2 is produced there will be H_2 present. Platinum is known to be very active for the oxidation of both H_2 and H_2O_2, and hence, the use of Pt as an in-situ probe in the membrane may not be a good choice due to the interference of H_2. This is demonstrated by fact that the same Pt electrode is 5 times more active toward H_2O_2 oxidation in the presence of H_2 as opposed to its activity for H_2O_2 oxidation in the presence of O_2 in acid (Figure 279 vs. Figure 276 in Ref.[99]). Therefore, we decided to use a probe material that is only active for H_2O_2 oxidation at high potentials, but much

less active toward H_2 oxidation. For this purpose, we have chosen gold micro wires as in-situ probes.

Before starting the in-situ experiments in a PEMFC, we determined, using chronoamperometry, the H_2O_2 oxidation calibration curves for the 25um gold wire in H_2 (and Air) saturated 0.5M H2SO4 at room temperature. For a working electrode, we used 12cm of this wire from the spool that will be used later as probes in the fuel cell. As expected, Au wire is indeed less sensitive to the presence of H_2 when H_2O_2 is oxidized at 1.46V/SHE in acid, as evidenced by the similarity of the two calibration curves in H_2 and Air saturated acid Figure 273.

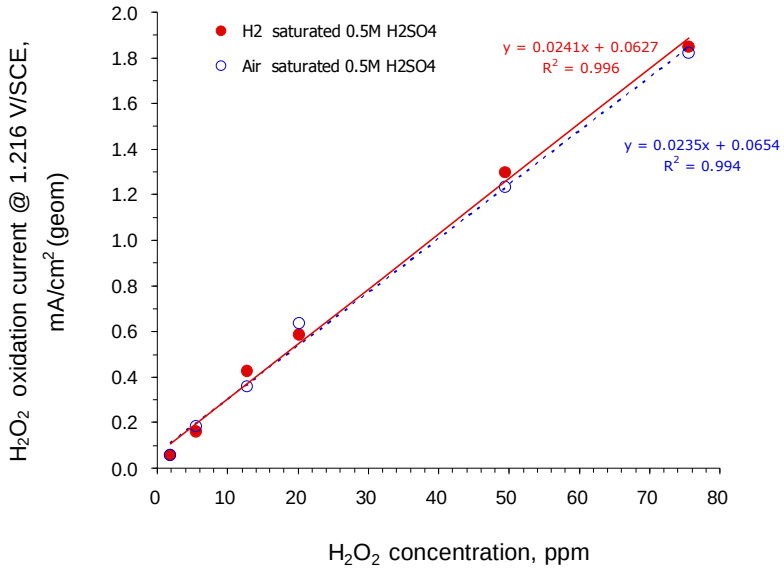

Figure 273. Calibration curve for H2O2 detection in 0.5 M sulfuric acid (H2 or Air saturated) using 25um gold wire as working electrode, a gold gauze as counter electrode, and saturate calomel electrode as reference. (current was read at 10 second of chronoamperometry curves potentiostated at 1.216 V/SCE = 1.458V/SHE)

This result encouraged us in using gold wire as in-situ probes for H_2O_2 detection in a PEMFC. We further discovered another property of a gold electrode toward H_2O_2 oxidation in the presence of H_2 in acid. As shown in Figure 274, in the low voltage region (I.e. below 0.6V/SHE) H_2 oxidation is apparently promoted in the presence of H_2O_2. At such a low potential, one would not expect oxidation of peroxide on gold if only peroxide is present, as demonstrated by air-saturated curves in Figure 274. An extensive literature search indicates that this phenomenon had not been reported before and we call it peroxide-assisted H_2 oxidation on gold in acid.

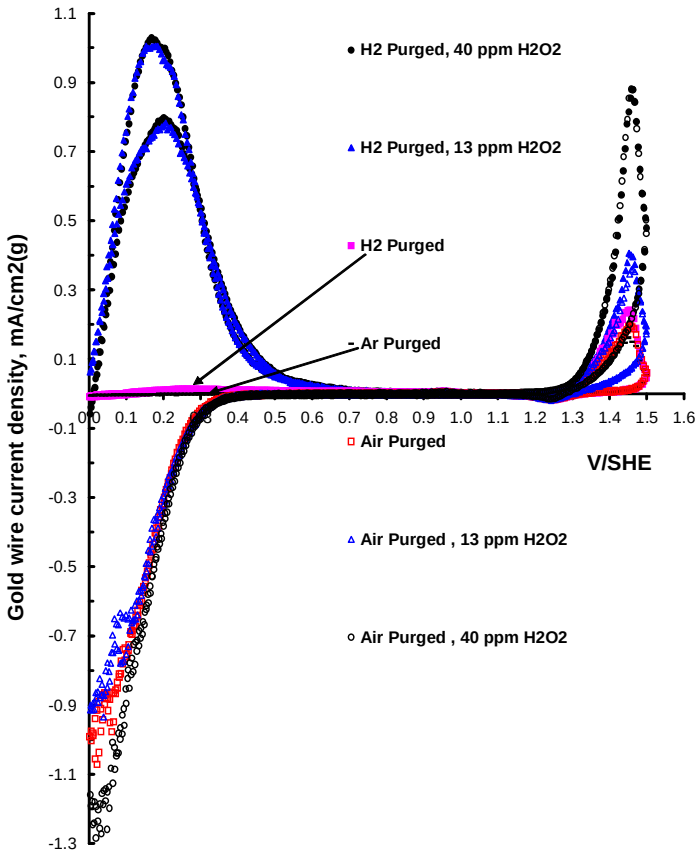

Figure 274. 20mV/s CV (20 oC) H2O2 oxidation on 25um Au wire in Ar, Air & H2 saturated 0.5M H2SO4

A careful inspection of Figure 274 indicates that the height of the low voltage H_2 oxidation peaks in the presence of H_2O_2 does not have a linear relationship with H_2O_2 concentration. Thus the presence of such peaks only can be used as qualitative indicator for the presence of both H_2 and H_2O_2. These peaks are very sensitive to low concentration of H_2O_2, e.g., 2ppm H_2O_2 gives a peak current at 0.2V/SHE which is about half of 75ppm H_2O_2. However, in a PEMFC, whether it is on-load or in OCV condition, H_2 and O_2 are everywhere due to the intrinsic gas permeability of the membrane. Polycrystalline Au is known to reduce O_2 to H_2O_2 at low potentials, such as shown in Figure 274 This means that the low voltage signal from Au probe in a PEMFC with H_2/Air(O_2) could be obscured by the generation of H_2O_2 on the probe itself. Thus, only the high potential oxidation peaks of H_2O_2 on Au can be used to determine H_2O_2 that comes from the fuel cell electrodes.

Furthermore, the non-linear behavior of the response as a function of peroxide concentration could be interpreted to indicate that a surface mediated reaction is taking lace and that the relative transport rates, i.e. the permeation rates D X C, controls the response.

Having determined the suitability of 25um gold wire as an in-situ probe under some conditions, we built a 50cm^2 cell, adopting a sandwich cell configuration similar to that reported in Ref.4. The sketch of the sandwich cell is shown in Figure 275with the following configuration:

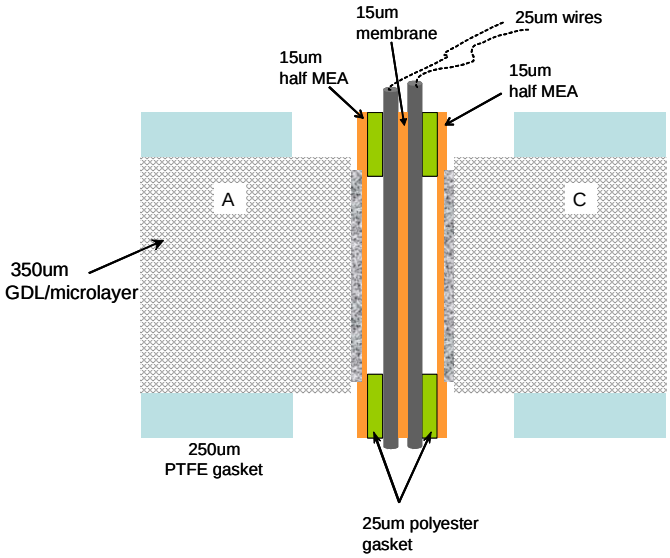

Figure 275. Schematics of the 50cm2 fuel cell, scaled in x direction before compression.

The probe distance from both electrodes in our cell correspond to the configuration (b) of Ref. 99, i.e., probes are 30um away from FC electrode/GDL interface. Both anode and cathode half MEAs have a Pt loading of 0.4 mg/cm2. The two gold wires were about 2mm apart in their placement in the membrane close to the gas inlet region, similar to that in Ref. 99.

The cell was broken in by cycling the cell (up to 0.8 Amps/cm2), until the voltage difference between two consecutive curves at 0.8A/cm^2 is 5 mV. The I-V performance of this cell after break-in is shown in Figure 276.

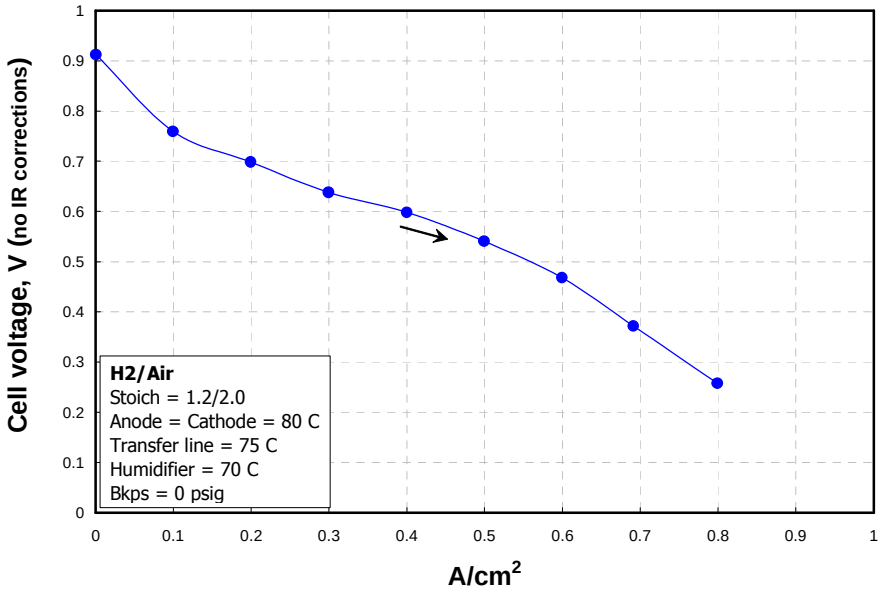

Figure 276. cell#1: I-V Curve for cell#1 with 25um Gold probes.

In order to determine that the H_2O_2 formed at the anode which could migrate toward the cathode side, for the on-load condition we selected cell voltage levels where the cathode is expected to generate negligible H_2O_2 and yet maintain the cell performance without cathode electrode degradation. We selected 0.5A/cm^2, 0.54V and corresponding flow rate at a stoich of H_2/Air=1.2/2.0 for all of our studies. The anode probe failed for cell#1, so the results of cathode probe for cell#1 will be presented below.

Before starting any other tests, the H_2 crossover for the cell, and H_2 sensitivity of the cathode (probe) were measured using 5 different H_2 concentrations at the anode and 100% N_2 at the cathode. The results in Figure 277 show that probe responses track that of the fuel cell cathode, indicating the probe is functional.

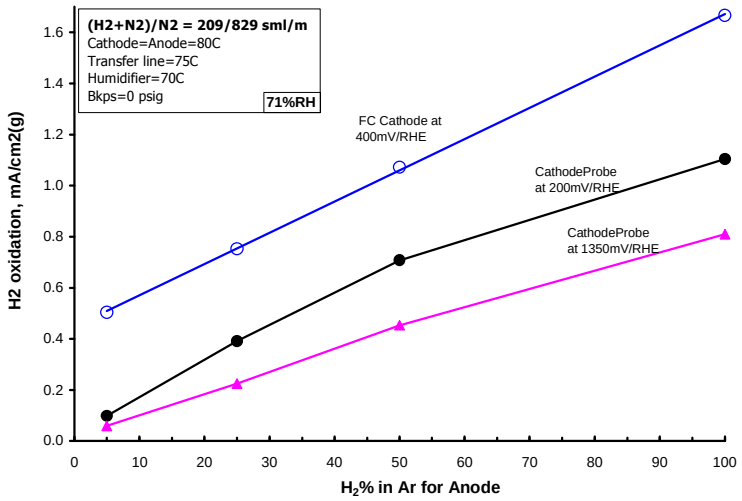

Figure 277. cell#1: H2 Crossover to fuel cell cathode and Au cathode probe as function of H2% at Anode, 80C, 71%RH

Cyclic voltammograms and chronoamperometry for the gold cathode probe:

The 20mV/s cyclic voltammograms of the cathode probe at fixed temperature, 80^{o}C and 71%RH and fixed flow rate of A/C=209/829smlm are shown for three different conditions in Figure 278

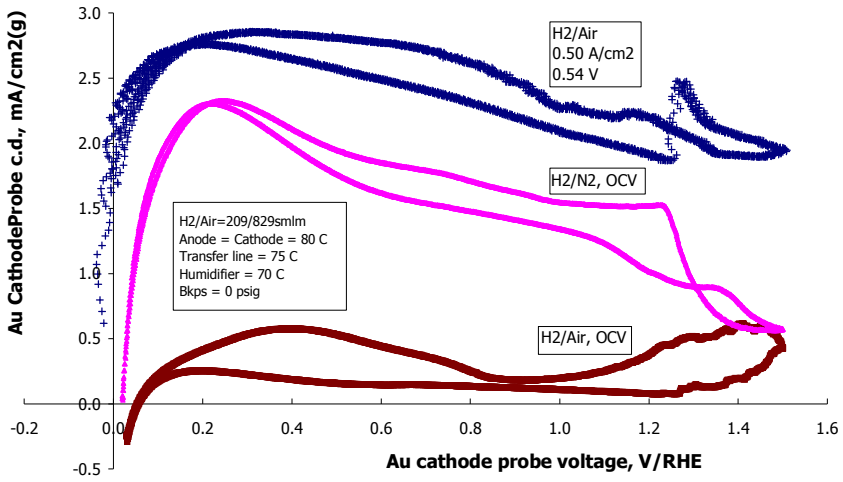

Figure 278. cell#1: Au cathode probe 20mV/s CVs at H2/Air(N2)=209/829sml/m, 80C, 71%RH (Note: the jump at ~1.3V for the on-load curve is most likely due to electrical noise)

We found that scan rate of 20mV/s or lower and/or higher do not normally produce stable cyclic voltammetric response. Curves with acceptable response characteristics do not show any evidence of the presence of H_2O_2 at the cathode probe (Figure 277). We carried out 15 min chronoamperometry over the entire potential range and sampled currents from the stable region of the I-t curve, where the time is at least 6 minute or greater, i.e. a steady state condition. The I-V curves of the Au cathode probe under those three conditions constructed from the chronoamperometry with a 15min sampling time are shown in Figure 279.

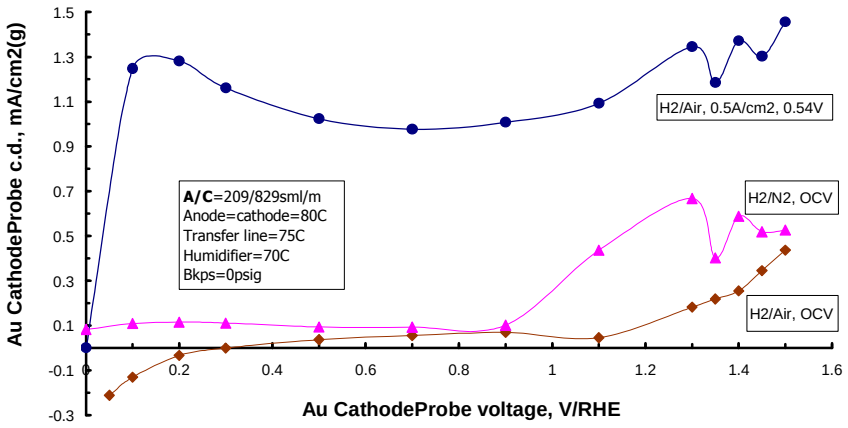

Figure 279. cell#1: Au cathode probe I-V curves from the chronoamps for 0.5A/cm2, H2/Air and H2/Air(N2), OCV.

Comparison of CVs and I-V curves from chronoamperometry indicated that the trends seen in the CVs under three different conditions are followed by the chrono I-V curves. But there is one important difference between CVs and chronoamperometry I-V curves at high voltage regions.

The chronoamperometry I-V current don't decrease at high voltage regions like it does in CVs under all three conditions. Since we saw this current increase even under H_2/N2 condition, it cannot used as evidence for the presence of H_2O_2. However, the reason for this difference between CV and chronoamperometry I-V curves is not clear at this time. Based on those observations we thought that 20mV/s CVs are not a reliable indicator of micro probe behavior inside the cell, so from now on we report only I-V curves from 15min chronoamperometry.

Since we did not detect H_2O_2 in the fuel cell either at on-load or H_2/Air, OCV conditions, we wanted to find out if the Au cathode probe can respond to the presence of externally fed H_2O_2. A separate experiment in our group had demonstrated that if one feeds 500ppm H_2O_2 in the cathode of 5cm^2 PEMFC at room temperature, about 10% makes it to a large surface area probe electrode which is ~15um away from the cathode. We conducted similar experiments to see if the 25 um gold wire probe can detect any peroxide that may survive decomposition at the cathode and diffuse to the Au probe. As the result in Figure 280 shows, indeed the Au cathode probe can detect H_2O_2 if it is present.

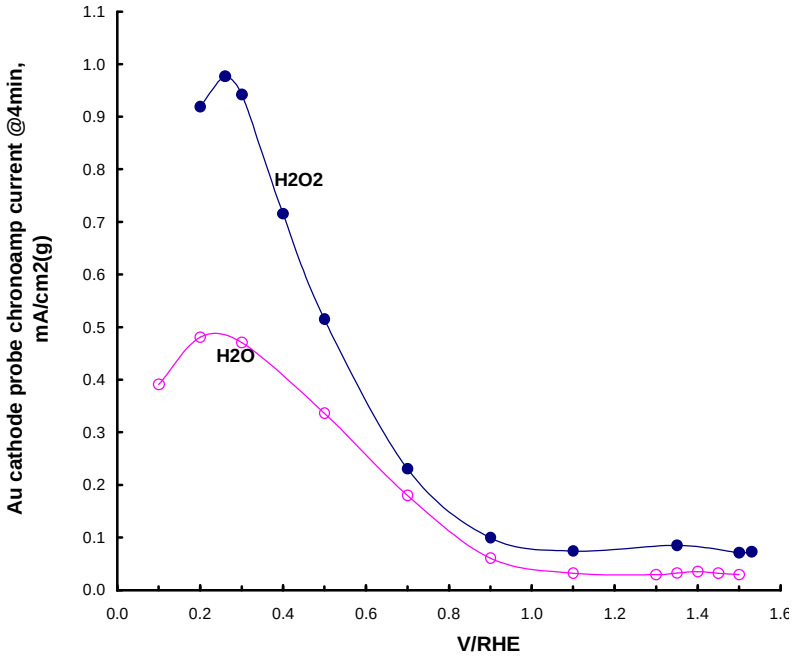

Figure 280. cell#1: Chronoamp currents at 4min for the Au cathode probe with anode=H2(209 sml/m), cathode=water(N2) or 500 ppm H2O2 (4 ml/m) at 19°C.

Cell#1 failed at this stage of the experiment, so another cell (cell#2) was built with the same type of materials and broken-in in the same fashion. The H_2/Air performance of cell#2 and the cathode and Au cathode probe sensitivities for H_2% at anode (Au anode probe was not functional) at 80^{o}C and 71%RH are very similar to that for cell#1 under the same conditions, as shown in Figure 281 and Figure 282

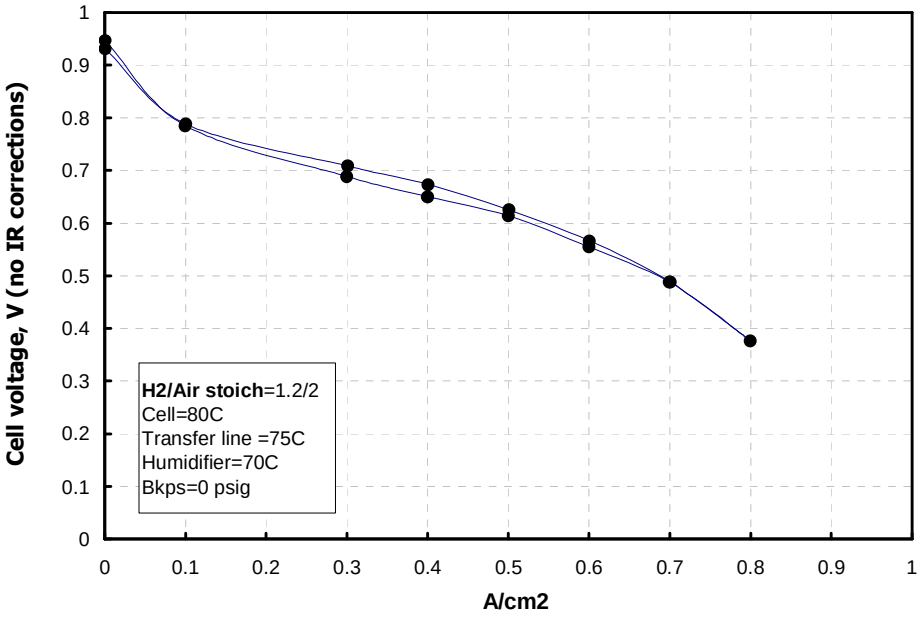

Figure 281. cell#2: I-V curve at 71%Rh, 80C

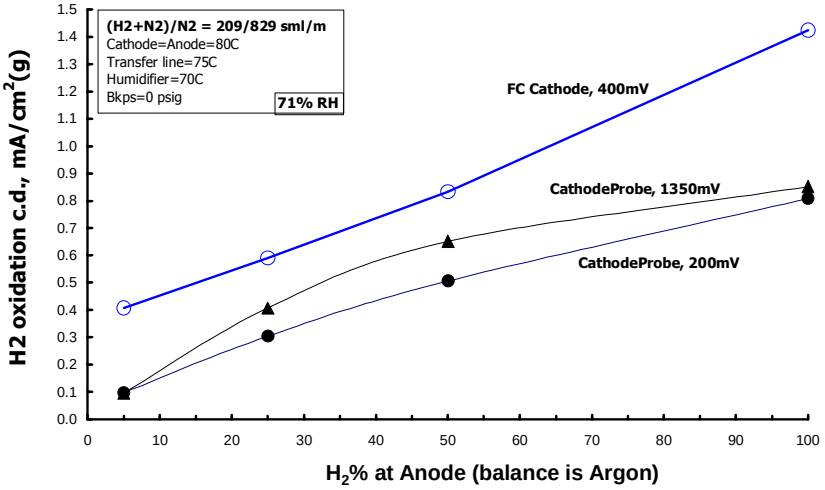

Figure 282. cell#2: H2 sensitivity of the Au probe.

For cell#2, the I-V performance is a little better. However, the Au cathode probe chronoamperometry I-V curves for cell#2 under the same conditions has a different trend, shown in Figure 283, from that for cell#1 (cf. Figure 279).

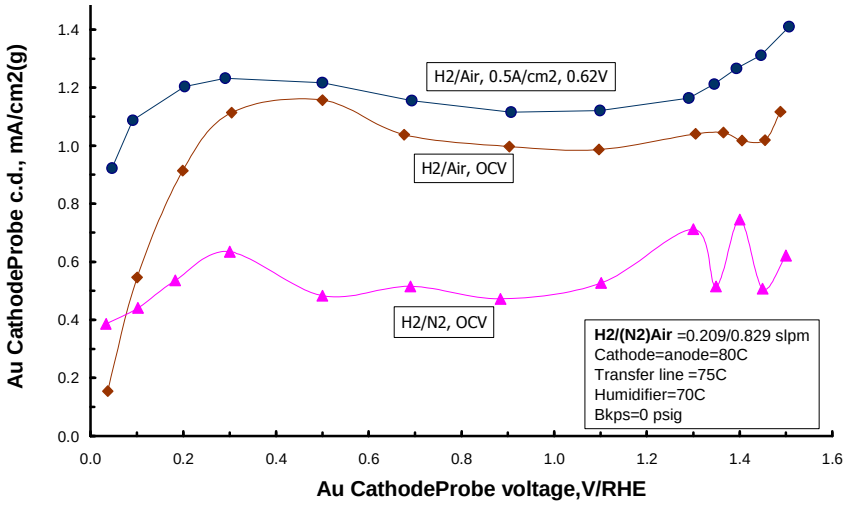

Figure 283. cell#2: Au cathode probe I-V curves from the chronoamps for 0.5A/cm2, H2/Air and H2/Air(N2), OCV .

Now, the observations can be summarized as follows:

under the conditions: Anode/Cathode = 80 ^{o}C = 0.209/0.829 sl/m; the Au probe potential scanned from 0 – 1.5 V/RHE,

the relative order of Au cathode probe currents are:

at 71%RH

cell#1: H_2/Air (0.5A/cm2, 0.54V) > H_2/N2, OCV > H_2/Air, OCV

cell#2: H_2/Air (0.5A/cm2, 0.62V) > H_2/Air, OCV > H_2/N_2, OCV

at 100%RH cell#2: H_2/N_2, OCV > H_2/Air (0.5A/cm2, 0.63V) > H_2/Air, OCV

No clear evidence regarding the presence of H_2O_2 either at the anode or the cathode can be gleaned from the above results for cell#1 and cell#2. However, there is one consistent trend for both cells: the H_2/Air on-load curve is always higher than that at H_2/Air, OCV under the same conditions. There is no doubt that there exists a favorable condition for the formation of peroxide at the anode. Since peroxide concentration should be greater at H_2/Air OCV condition due to higher O_2 crossover than under the on-load condition, the crossover H_2 could be consumed by the incipient H_2O_2, and therefore, the H_2 oxidation current at OCV would be suppressed compared to that under the on-load condition. To find out if that were the case, we fed the anode inlet with H_2-saturated water and H_2-saturated 50ppm H_2O_2, respectively. Indeed, that was the case as shown in Figure 284(a) and (b), -- H_2O_2 can consume the H_2 or vice versa, as one would expect based on the simple chemistry of these two species on Pt.

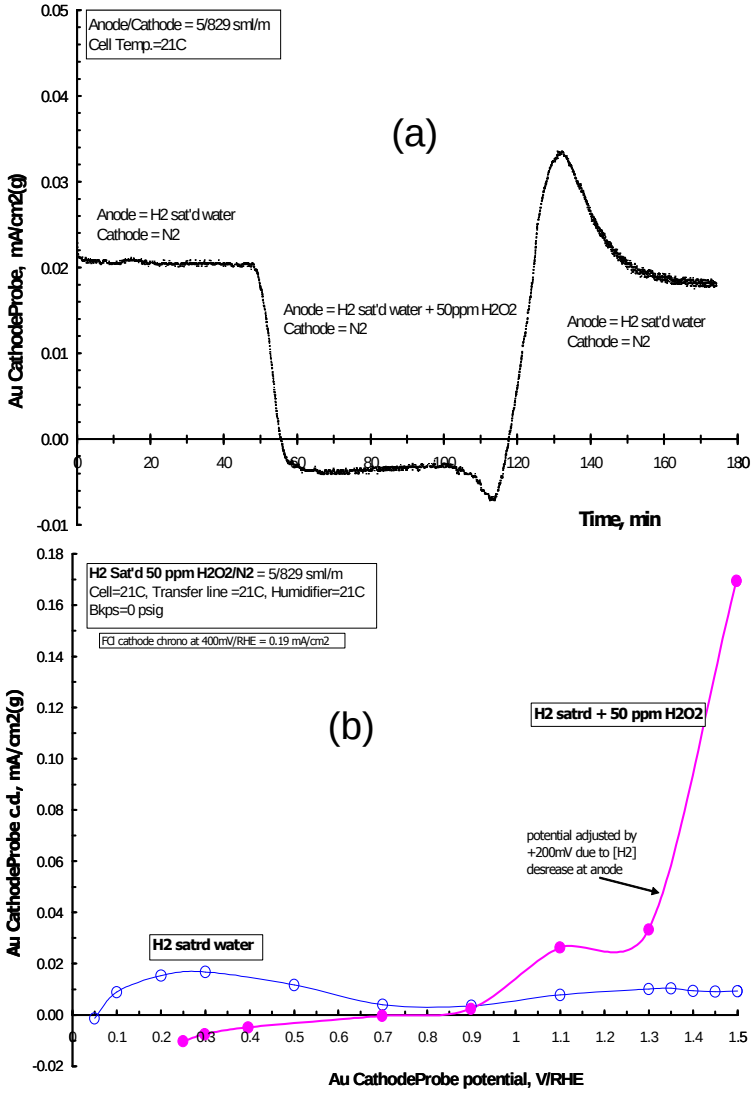

Figure 284. (a) Au cathode probe chronoamps with or without H2O2 at the anode, (b) the I-V curves extracted from chronoamps, both at 21oC.

In Figure 284 (a) it is clear that there is no H_2 left from the anode that can make it to the probe. Otherwise we would have seen a peroxide assisted H_2 oxidation peak like that in Figure 274. In Figure 284 (b) it is evident that the Au cathode probe can detect the leftover H_2O_2 in the high potential region, and can reduce the O_2 that comes from the partial decomposition of H_2O_2 at the anode catalyst.

Based on this observation we reasoned that the crossover O_2 concentration is not enough to generate sufficient H_2O_2 at the anode to diffuse to the cathode probe, and/or H_2 concentration is too high to overwhelm the H_2O_2 response at the cathode probe. We also thought that since Au is not as active as Pt, perhaps we are missing the H_2O_2. So we put both Pt and Au 25um wires as in-situ probes, side-by-side in cell#3. The Pt and Au probes on each side is only ~2mm apart. For this cell, we investigated first the effect of H_2 concentration at the anode on the probe responses.

H_2 and O_2 sensitivities of the Pt and Au probes:

The H_2/Air performance of cell#3 and the fuel cell cathode and cathode probe for H_2 sensitivity trends at 60°C and 100%RH are very similar to that for cell#2. Since Ref. 99 reported results for 60°C using cyclic voltammetry, we used the same condition and CVs for different concentration of H_2 at the cell anode. As shown in Figure 285 there is no evidence of H_2O_2 on these CVs, even if H_2 concentration is reduced such that the O_2 concentration dominates at the anode Pt probe.

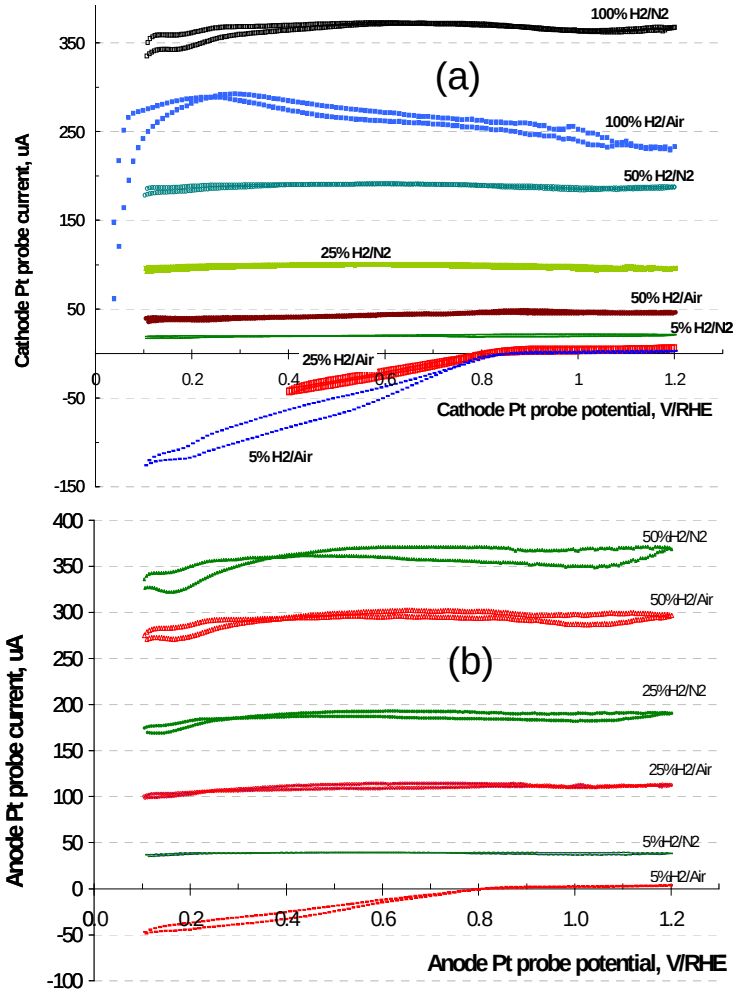

Figure 285. 13 cell#3: (a) cathode Pt probe and (b) anode Pt probe 20mV/s CV, x%H2/N2(Air), OCV, 60C, 100%RH, flow rate A/C=209/829 sml/m

The cell#3 probe I-V curves extracted from the 15min chronoamperometry for both anode and cathode probes are shown in Figure 286 and Figure 287, and they do not show any evidence for the presence of H_2O_2 either at anode or at cathode at 71%RH and 100%RH at 80°C.

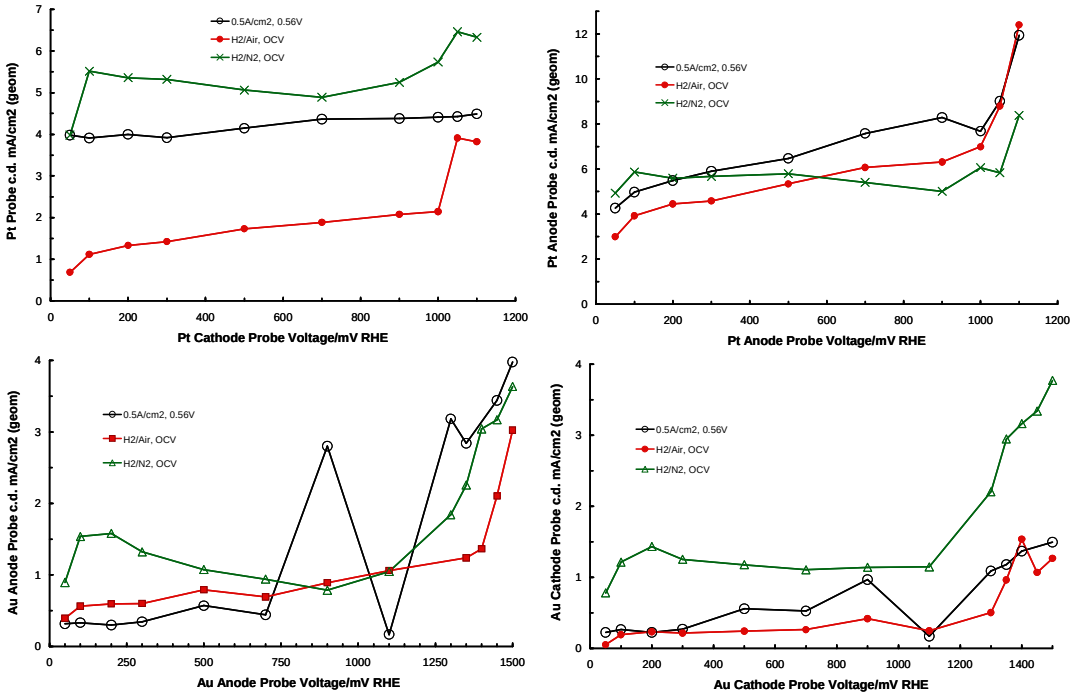

Figure 286. cell#3: probe I-V curves extratced from the 15min chronoamps at 100%RH, 80C, flow rate A/C=209/829 sml/m.

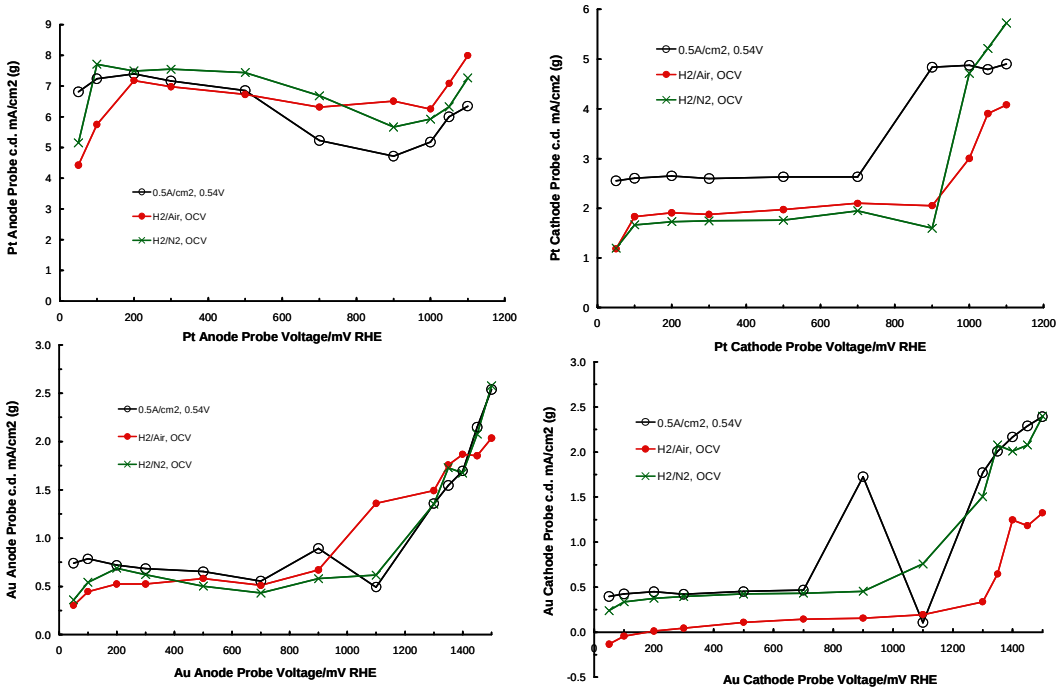

Figure 287. cell#3: probe I-V curves extratced from the 15min chronoamps at 71%RH, 80C, flow rate A/C=209/829 sml/m.

Before we have a chance to investigate the O_2 concentration effect, the cell#3 probes failed, i.e., they made contact to the cell electrode. Hence, cell#4 was built using the same materials and hardware, and both Pt and Au 25um wires as probes, as in cell#3. The H_2/Air performance of this cell and H_2 crossover after break-in is comparable to that of cell#3. For this cell, we conducted 60 min chronoamperometry for each probe at H_2/(N_2, O_2) OCV conditions. For example, the anode (cathode) Au probe was held at 300mV for one hour under H_2/N_2, OCV, at which time the cathode feed was switched to O_2 and held at the same voltage for another one hour. If there were peroxide formation under H_2/ O_2, OCV condition, due to H_2O_2 assisted H2 oxidation at this potential one would expect a jump in current from N_2 to O_2. Similar experiments were done for Pt probes, but they were held at 1.0V/RHE to detect the incipient H_2O_2.

The results shown in Figure 288 indicate that no direct evidence for peroxide detection is presented by either type of probes.

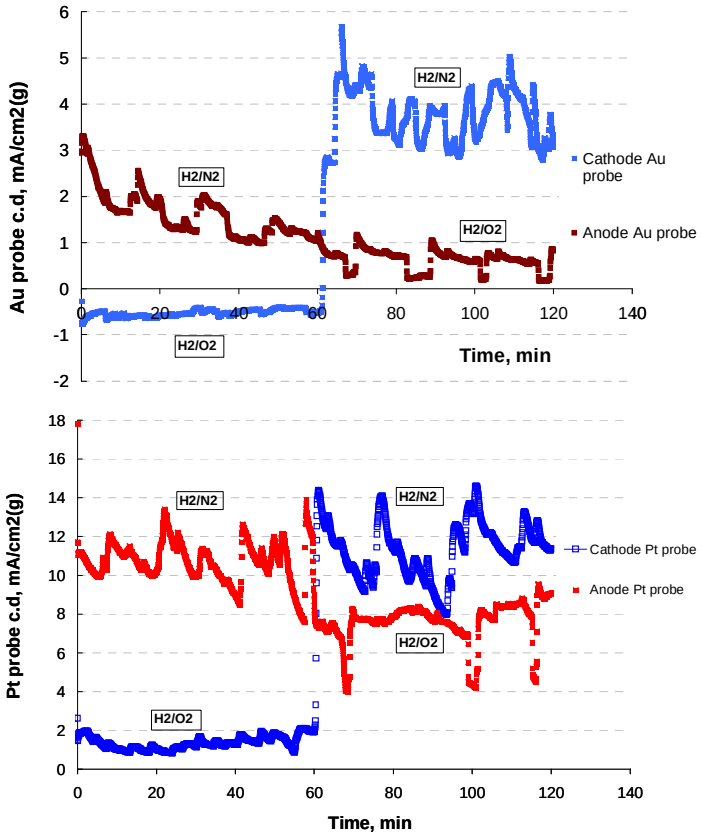

Figure 288. cell#4: Chronoamps at 300 mV for Au probes, 1000 mV for Pt probes, under the condition of H2/N2(O2), 60°C, 100%RH, each gas for 1 hr hold.

The only consistent trend is that the presence of O_2 greatly suppresses the H_2 oxidation current on the cathode probes for both Pt and Au. For Au probes it seems to suggest that O_2 reduction occurs without peroxide generation, because we did not see a H_2O_2 assisted H_2 oxidation peak. For Pt probes it means that the H_2 crossover rate is diminished due to its consumption by the crossover O_2 at the anode catalyst/membrane interface, because at 1.0V/RHE one does not expect O_2 reduction.

Overall conclusions

(iii) In 50cm^2 PEMFCs built with 3M 15um membrane and Pt/Au wire probes (dia. 25um) sandwiched between two 15um half MEAs, total thickness 45um, due to low gas crossover, no detectable amount of peroxide, less than 1ppm, present either at anode probe or cathode probe. This is in sharp contrast to the reported ~10 ppm H_2O_2 seen at the anode in a comparable PEMFC in Ref.99 (Figure 287 curve b). However, our rather extensive tests cast some doubt on the applicability of this methodology to reliably yield results on peroxide concentration.

(iv) A new mechanism, though seems obvious, for peroxide elimination at anode, and perhaps elsewhere in the cell is demonstrated -- peroxide is reduced by H_2.

(v) On Pt or Au, the CV behavior at high voltage, >1V, is completely different from the chronoamperometric behaviors for the probes, indicating that the probe CVs are not a reliable way for quantitatively determining H_2O_2 concentration in a PEMFC.

4.3 Acknowledgments

Rey Sidik, Michael Pelsozy, Arun Agarwal, Uziel Landau, Ramachandran Subbarraman, J. Adin Mann, Robert Edwards, Vladimir Gurau and Thomas A. Zawodzinski Jr.

4.4 References

[81] T. J. Schmidt, H. A. Gasteiger, O. D. Staeb, P. M.Urban , D. M. Kolb, and R. J. Behm, *J. Electrochem. Soc.*, **145**, 2354 (1998).
[82] U.A. Paulus, T.J. Schmidt, H.A. Gasteiger and R.J. Behm, *J. Electroanal. Chem.*, **495**, 134 (2001).
[83] E.B. Yeager, Electrochim. Acta, 29, 1527, (1984).
[84] U.A. Paulus, A. Wokaun, G.G. Scherer, T.J. Schmidt, V. Stamenkovic, V. Radmilovic, N.M. Markovic, P.N. Ross, J. Phys. Chem. B 106, 4181 (2002).
[85] U.A. Paulus, A. Wokaun, G.G. Scherer, T.J. Schmidt, V. Stamenkovic, V. Radmilovic, N.M. Markovic, P.N. Ross, Electrochimica Acta 47, 3787 (2002).
[86] M. Lefevre and J. Dodelet, *Electrochimica Acta*, **48**, 2749 (2003)
[87] O. Antoine & R. Durand, *J. Appl. Electrochem.,* **30**, 839 (2000)
[88] L. Geies, R. Faure and R. Durand, *Electrochimica Acta*, **44**, 1317 (1998)
[89] P. Stonehart, *Berichte der Bunsengesellschaft/Physical Chemistry Chemical Physics*, **9**, 913 (1990)
[90] M. Watanabe, H. Sei and P. Stonehart, *J. Electroanal. Chem.*, **261,** 375 (1989)
[91] J. C. Huang, R. K. Sen and E. Yeager, *J. Electrochem. Soc.*, **126**, 786 (1979)
[92] N. M. Markovic, H. A. Gasteiger, P. N. Ross, Jr., *J. Phys. Chem.* **99**, 3411 (1995)
[93] Z. Liu, J. S. Wainright, R. F. Savinell, J. Electrochem. Soc., In Press
[94] F. Porchet, P. Javet, Electrochim. Acta, 40, 2569, (1995)
[95] Z. Liu, Ph.D, Thesis. Case Western Reserve University, 2004
[96] P. Westbroek, E. Temmerman, J. Electroanal. Chem., 482, 40 (2000)
[97] U. A. Paulus, A. Wokaun, G.G. Scherer, T.J. Schmidt, V. Stamenkovic, N.M. Markovic, P.N. Ross, Electrochim. Acta, 47, 3787 (2002)
[98] A. B. LaConti, M. Hamdan and R. C. McDonald, *Handbook of Fuel Cells: Fundamentals, Technology and Applications*, Vol.3, Chap.49, W. Vielstich, A. Lamm and H. A. Gasteiger, Editors, Wiley, New York (**2003)**
[99] V. O. Mittal, H. R. Kunz, and J. M. Fenton, *Electrochemical and Solid-State Letters*, **9**(6) A299-A302(**2006**).

Section 5. Application of Accelerated Testing and Statistical Lifetime Modeling to MEA Development

5.1 Introduction

Accelerated testing and statistical lifetime modeling are important tools in the development of durable membrane electrode assemblies (MEAs). There are several reasons for using accelerated tests and three of the main reasons are:

1. Marketing – "Our product last X times longer than the competition" is a powerful statement.
2. Customers – Reliability and durability are key requirements that need to be met in order to supplant an existing technology with an emerging technology.
3. Product development – Real time testing is not practical for products that last many years. In order to continue to develop products with improved durability an accurate estimate of lifetime is necessary within a short period of time.

The field of accelerated testing can be loosely divided into three types of tests: screening tests, mechanistic tests and lifetime tests[1]. Screening tests are typically *ex-situ* component (a component is any item that is assembled into the final product, *e.g.*, a membrane is a component of an MEA) tests designed to quantify incremental improvements during component development. Screening tests are very useful in determining the relative durability of one component design to another. Mechanistic tests are designed such that the degradation pathway and kinetic parameters can be determined. Mechanistic tests are useful when it is important to know the exact degradation pathway in order to mitigate it. Lifetime tests are typically performed on the final product in order to determine its durability and reliability under a given set of operating conditions. When combined with statistical lifetime analysis, it may be possible to predict the lifetime of the product under various operating conditions. Of the three types of accelerated tests, screening tests are the easiest to set-up and most widely used; whereas lifetime tests often take long periods of time and are difficult to administer properly and consistently. There is one cardinal rule that needs to be followed in all accelerated tests – the failure mode in the accelerated test **must be** the same as the failure mode in 'normal' operating conditions; otherwise the test results will be misleading and possibly useless.

5.2 Accelerated Testing

Before developing accelerated tests, the performance of the product over time must be determined. An example of MEA performance over time is shown in Figure 289. Once the time dependant performance is established, the next step is to postulate failure modes followed by appropriate accelerated tests designed to mimic the failure mode. For example, the loss in cell voltage at 0.05 A/cm^2 may be due to increasing H_2 crossover, the loss in current at 0.8 V may be due to loss of catalyst activity or surface area, and the loss in current at 0.4 V may be due to increasing mass transport resistance from gas-diffusion layer flooding. Once the failure mode is understood, the next step is to establish an accelerated test to accelerate that particular failure mode.

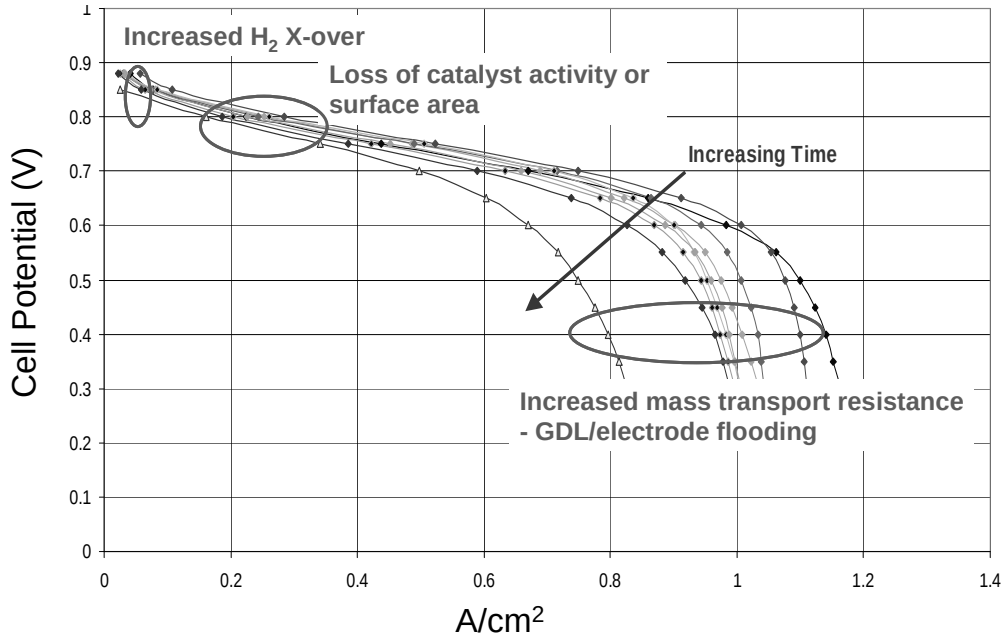

Figure 289. Typical MEA performance over time.

5.2.1 Screening Tests

Screening tests are exactly what name implies – a 'brute-force' method to 'screen' numerous components quickly and efficiently to determine relative component durability. Screening tests do not provide insight into the failure kinetics or mechanism. The following will discuss examples of various screening tests for membranes, catalysts and GDLs (gas diffusion layer). Detailed discussion on the accelerated tests used in the development of membrane, GDL and electrode can be found in sections *2.1 Membrane*, *2.2 GDL Development*, and 2.3 Catalyst/Electrode Development respectively. The following is a simple summary of appropriate accelerated tests for MEA development

Membrane

The primary failure mode for membranes is hole formation, which can be caused by chemical degradation, material fatigue due to mechanical stresses or a combination of chemical and mechanical stresses. The Fenton's test is a common *ex-situ* test to measure membrane chemical stability and involves soaking the membrane in a peroxide solution and measuring either the membrane weight loss or fluoride release over time. Another common test is the MEA OCV (open circuit voltage) test[2] to measure membrane chemical stability. Unlike the Fenton's test, the MEA OCV test is an *in-situ* test that uses an MEA instead of only a membrane. In the OCV test, an MEA is placed in a cell and exposed to H_2 on one electrode and O_2 (or air) on the other electrode. By holding the MEA at OCV, it is speculated gas crossover results in peroxide formation which in turn degrades the membrane. Just like the Fenton's test, fluoride release over time is the important metric to track (Figure 290a). The main difference between Fenton's test and the OCV test is that Fenton's test only measures chemical stability of the membrane while the OCV test measures both the membrane's ability to inhibit the production of peroxide (by affecting the gas crossover rates) and the chemical stability of the material. As a result, while the OCV test may be more realistic in terms of fuel cell operation, it is also more difficult to interpret the results due to the two mechanisms in comparison to one in the Fenton's test.

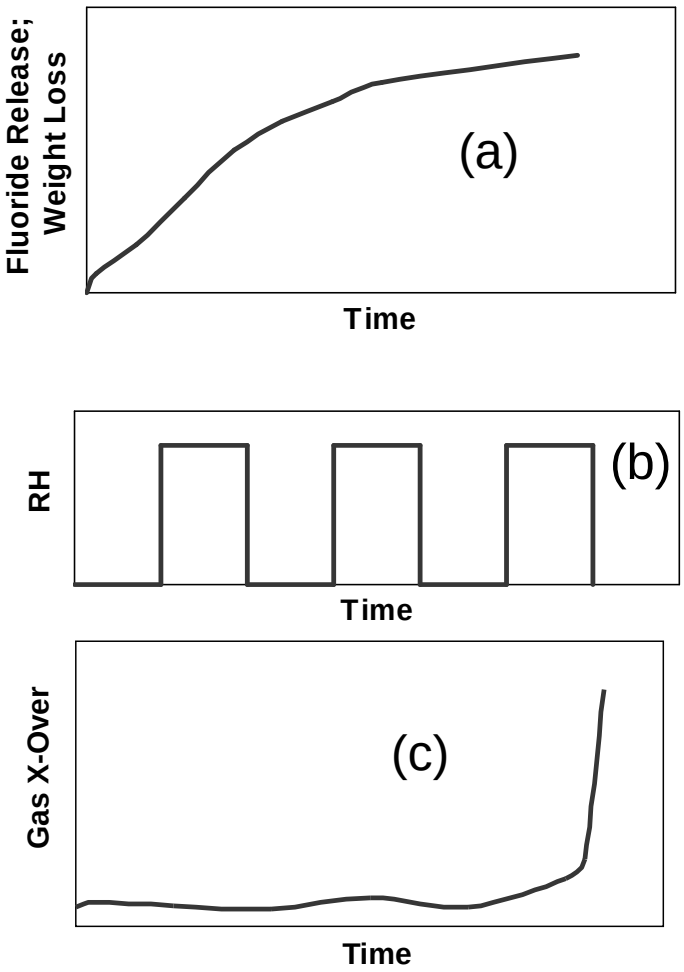

Figure 290. Examples of membrane screening tests. (a) Typical Fenton's test results; (b) Relative humidity cycle profile; (c) typical gas crossover data resulting from relative humidity test.

A humidity cycle[3] is an example of a simple test to mechanically stress the membrane. In this test, the membrane or MEA is placed in a cell and both electrodes are exposed to humidified N_2. The humidity level of the N_2 gas varies over time from 0% RH to 100% RH, or even supersaturated conditions (Figure 290b). The rapid change in humidification causes the membrane to swell or shrink which introduces mechanical stresses in the membrane. Periodically, gas crossover from one electrode to another is measured as a function of time in order to determine when membrane breech occurs (Figure 290c). Since the feed gas is N_2, no chemical degradation occurs during this test. By changing the gas feed to H_2 on one electrode and O_2 on the other electrode and introducing and load profile cycle on top of the humidity cycle, the membrane can be exposed to chemical and mechanical stresses simultaneously. In this coupled test, fluoride release, gas crossover and OCV decay are typically monitored over time.

Catalyst – There are three primary methods to age catalysts and each addresses different failure modes. The first method is an *ex-situ* thermal aging technique that measures support stability[4]. In this method, catalyst powder is weighed and placed in an oven. The weight loss of the powder is monitored over time (Figure 291a). This technique studies the stability of the support to Pt catalyzed chemical combustion and is very useful for determining the relative stability of different carbon supports. The second method is an *in-situ* technique to measure the electrochemical stability of the support at a given potential. In this test, an MEA is typically held at ~ 1.0 V under H_2/N_2. Periodically, the surface area is measured via cyclic voltammetry and the change in

surface area over time is recorded as a measure of the catalyst stability (Figure 291b). The time frame to observe a loss in surface area greatly depends on the carbon type and cell voltage. Typically, higher carbon support surface areas or the higher cell voltages, result in more easily observed changes in surface area.. The last method, potential cycling, is the most complex to analyze as it accelerates electrochemical degradation of the support, Pt agglomeration and Pt dissolution. The potential cycle is typically from 0.05 V to 1.0 or 1.2 V with the cell under H_2/N_2 gas feeds. The potential cycle causes the most damage to the catalyst because it accelerates three degradation pathways. Typically, a rapid decrease in catalyst surface area is observed (Figure 291c).

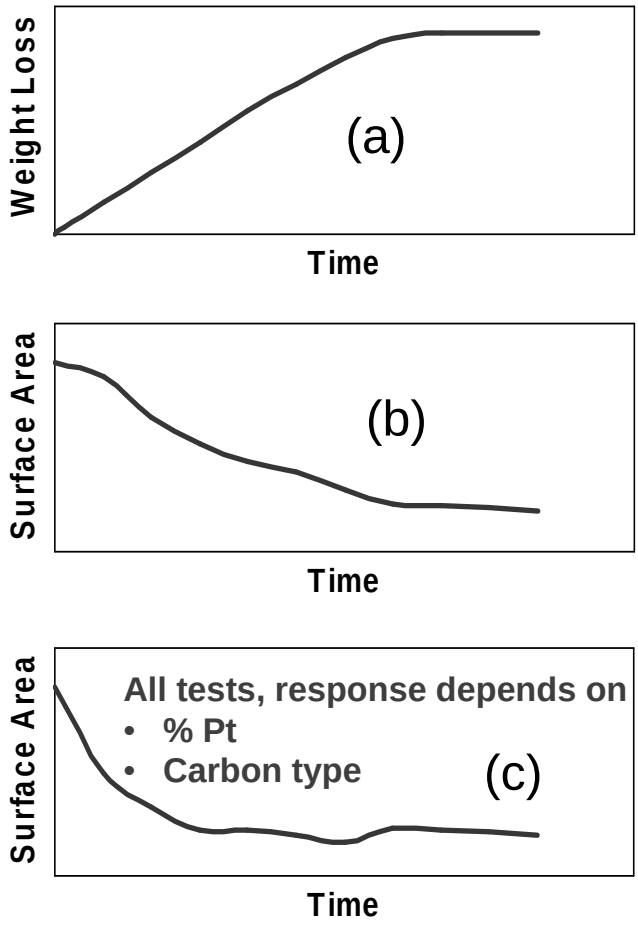

Figure 291. Examples of catalyst screening tests. Typical results from (a) thermal aging, (b) constant potential aging and (c) potential cycling.

GDL

The primary failure of the GDL is loss of hydrophobicity which results in increased mass transport resistance, typically referred to as MEA flooding. Three different screening tests have been used to accelerate this failure mode[5]. The first test studies carbon chemical stability by soaking the GDL in a hydrogen peroxide solution at elevated temperature. The other two tests study carbon electrochemical stability via constant potential or potential cycling tests. In either electrochemical test, the GDL is placed in a sulfuric acid solution. For the constant potential tests, a voltage outside of normal fuel cell operation is applied to the GDL, generally the voltage is greater than 1 V. For the potential cycling test, the GDL voltage is cycled between 0.3 to 0.8 V (a voltage range within typical fuel cell operation). For either electrochemical test, the current or coulombs is

monitored and the higher the value, the more unstable the GDL. Throughout the chemical and electrochemical accelerated tests, the contact angle of the GDL is measured (see Figure 292). The material is considered to fail when there is a sudden drop in the contact angle or when the contact angle drops below a critical threshold. In order to quantify the effect of change in contact angle, the aged GDL can be assembled into an MEA and evaluated. In this manner, a relationship between contact angle and fuel cell performance may be established.

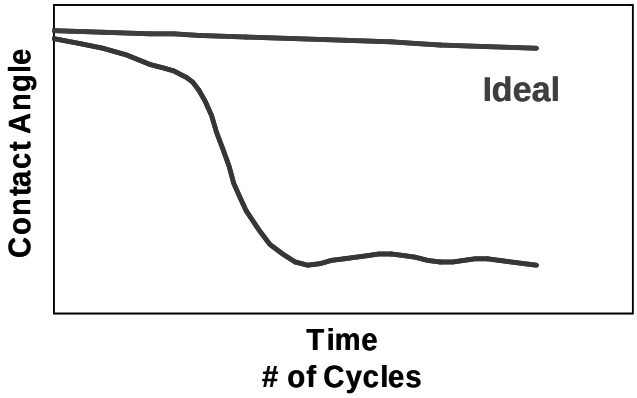

Figure 292. Typical results from GDL screening tests

5.2.2 Mechanistic Tests

Mechanistic test are very similar to screening tests with one important exception – mechanistic tests are designed to determine the failure kinetics and pathway whereas screening tests only compare the relative durability of two or more candates. Understanding the reason behind the difference in durability between component A and B is at the heart of any mechanistic test. Furthermore, mechanistic tests may even incorporate screening tests combined with detailed quantitative analysis of the component in order to determine failure kinetics and pathways.

Membrane Example

For a PFSA membrane, it is generally accepted that the primary degradation pathway is –COOH end group unzipping[6] due to attack from HO· or other radicals. However, this might not be the only degradation pathway. A plot of fluoride ion generation versus –COOH end group concentration (Figure 293)[7] results in a non-zero fluoride ion generation intercept which strongly suggests that there is a secondary degradation mechanism. In order to investigate a secondary membrane failure mode, a mechanistic test was implemented using small model compounds with representative functional groups found in the polymer electrolyte membrane[8,9]. Studying the small model compounds offer two main advantages over the polymer – (1) It is relatively easy to track chemical/structural changes in small molecules in comparison to a polymer. (2) By utilizing small molecules, one can isolate and better study the reactivity of various functional groups. Through the use of the model compound mechanistic tests, a better understanding of membrane degradation resulted; namely, that there is a secondary failure mechanism centering on the ether linkage in the side chain[8,9]. For more detailed information on the model compound study, see section *2.1.3 Model Compound studies.*

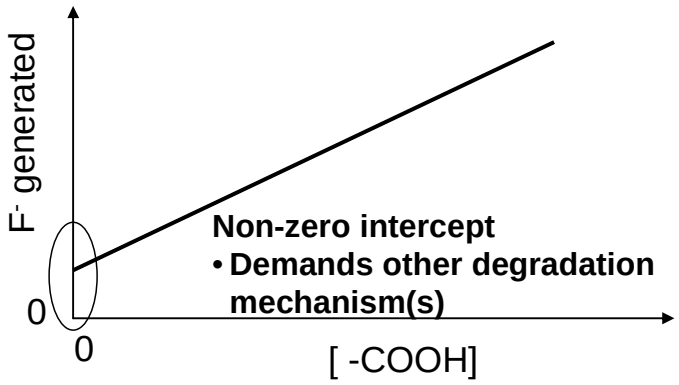

Figure 293. Impact of –COOH end group concentration on fluoride ion generation[7].

5.2.3 Lifetime Tests

As the name implies, lifetime tests are designed to determine the final product's (not the individual components) lifetime under a given set of operating conditions. The operating conditions can be 'end-use' conditions or 'accelerated' conditions. 'End-use' refers to the desired operating conditions of the product: for example, 70℃ cell temperature and 100% inlet gas relative humidity are often used for stationary power use conditions. 'Accelerated' refers to any condition different from the 'end-use' that will accelerate the product failure modes and thereby shorten the lifetime of the product during the test: for example, 90℃ cell temperature and 50% inlet gas relative humidity. The first step in establishing lifetime tests is to define the variables involved. A partial list of fuel cell system variables is listed in Table 1. The list is by no means all inclusive and it will vary based upon fuel composition and system design. After generating the variable list, the next step is to identify the one to three most important variables to investigate. Then a series of experiments can be designed around the selected variables before testing is started. Since lifetime tests can have high sample-to-sample variability, multiple replicas (> 5) of each sample at each condition must be run. A post mortem analysis can help identify or confirm failure modes. For example, if there is a particular MEA that died earlier than expected it would be important to look for an edge failure as opposed to a hole in the active area.

Load Profile Experiment Example

One of the important variables affecting MEA/system lifetime is load setting. In order to determine the effect of load on lifetime, three different load profiles were investigated (Figure 294). In the load profile A, the current is cycled from 0.01 to 0.51 A/cm^2 in 0.25 A/cm^2 increments. In load profile B, the load is held constant at 0.35 A/cm^2. In load profile C, the load is cycled from 0.26 to 0.51 A/cm^2 in 0.25 A/cm^2 increments. By comparing lifetimes from load profiles A and C, one can determine the impact of near-OCV operation on lifetime. By comparing the lifetimes from load profiles B and C, one can determine the impact of load cycling on lifetime. The results of the load profile lifetime test example are shown in Figure 295. Clearly, the load profile has a significant impact on MEA/system lifetime.

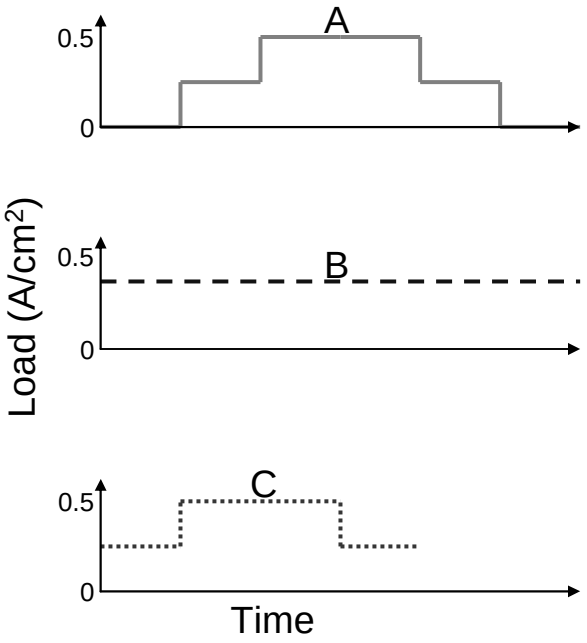

Figure 294. MEA accelerated lifetime tests load profile.

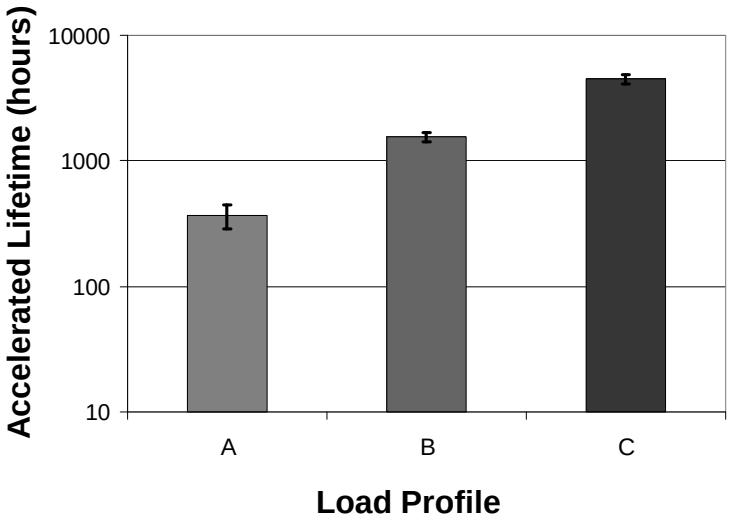

Figure 295. Effect of load profile on MEA lifetime. Cell conditions: 90℃ cell temperature, 70℃ gas inlet dew points, H_2/Air, 7 psig anode overpressure.

5.3 Statistical Lifetime Analysis and Modeling

A significant amount of data was generated during the lifetime tests. A comprehensive table summarizing these tests is attached at the end of this section Table 40. Because of the significant investment of time and the complexity of this type of work it is extremely important to analyze the data correctly. To illustrate this fact, the following example is provided (Figure 296). Six identical samples were tested to failure and lasted 391, 525, 658, 919, and 994 hours respectively. The average lifetime of the six samples is 695 hours and the standard deviation is 295 hours as shown in Figure 296a. But what does this mean? If a seventh sample is tested, will it last 695 hours? It's impossible to say, because the wrong analysis was performed. Lifetime is not defined by a single data point; lifetime is a statistical distribution. As such, the data in this example must be analyzed in terms of probability – what is the probability that a sample will fail at any point in time? The probability analysis using a Weibull distribution is shown in Figure 296b.

Using the probability plot, it is clear that the average of 695 hour is not the lifetime of the samples; instead, 695 hours represents the time by which 50% of the samples will have failed. In other words, if a fuel cell stack consists of 100 MEAs, fifty of them will have failed by 695 hours. Since it only takes one failed MEA to mark the end of the fuel cell stack lifetime, a more realistic definition of lifetime for the 100 MEA fuel cell stack occurs at a percent failure of 1 % which corresponds to a lifetime of ~ 225 hours.

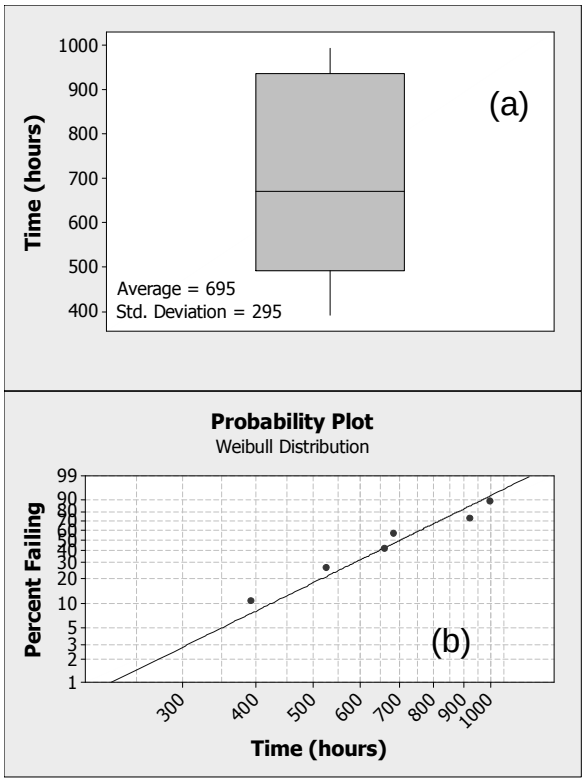

Figure 296. Analysis of lifetime data using (a) average and standard deviation and (b) statistical probability distribution.

Another benefit of using statistical analysis is the ability to incorporate censored data, or test data that is still ongoing. When using statistical analysis, it is just as useful to the analysis to know that a sample failed at 2,000 hours as it is to know that a sample didn't fail at 2,000 hours and is still under test.

A lifetime model is needed to predict lifetimes under 'end-use' conditions from the 'accelerated' lifetime test results. In the model, it is important to use the correct mathematical relationships to fit system variables listed in Table 38 between the different operating conditions. For example, the Arrhenius relationship can be used to account for the impact of temperature at the different test conditions. To predict the lifetime distribution at 'end-use' conditions from 'accelerated' lifetime test conditions, multivariate-nonlinear statistical methods need to be utilized. One such program is SPLIDA which is built within an S-PLUS platform[1]. SPLIDA can account for non-linear data, censored data and also separate failure modes.

Table 38. Example List of Key System Variables

- Cell temperature
- Gas dew point (inlet and outlet)
- Load setting

- Gas pressure
- Flow field design
- Contaminants
- Gas composition
- Cell compression

Previously, the data presented in Figure 295 was analyzed in terms of averages and standard deviations in order to determine lifetime. However, averages and standard deviations don't capture the entire lifetime picture, the data needs to be analyzed using SPLIDA. The results of the SPLIDA analysis are shown in Figure 297. Not only can SPLIDA provide a lifetime probability distribution for the data in Figure 295, it can also predict the lifetime of the samples at 'end-use' conditions (70℃ cell temperature and 100% inlet gas relative humidity). When using SPLIDA for statistical analysis, the following relationships were selected: Weibull distribution for lifetime data, Arrhenius relationship for temperature, class relationship for load profile, and humidity transformation for humidity effects. In Figure 297, the solids lines represent load profile A, the dashed lines represent load profile B and the dotted lines represent load profile C. The symbols represent actual data points and the lines are the statistical model fit to the data. The data on the left of Figure 297 were taken under highly accelerated conditions (hot and dry cell operation) and the data on right of the figure are model predictions at end use conditions. At the end use conditions, at a failure probability of 1%, the predicted lifetime of the samples under load profile C is ~ 20,000 hours.

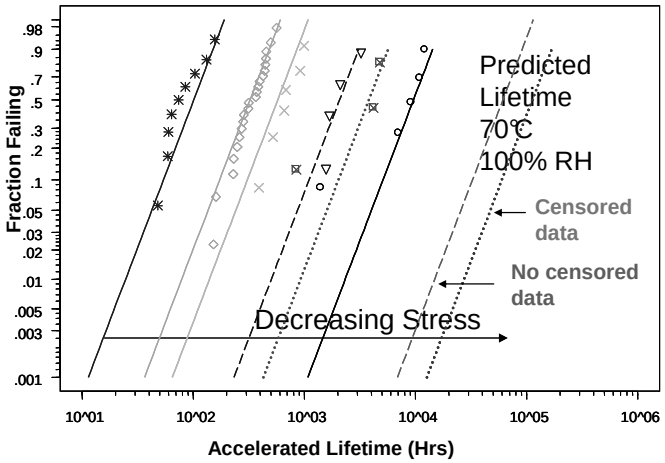

Figure 297. Statistical MEA lifetime predictions from accelerated test data using SPLIDA.

An extensive predictive, statistical model has been developed which combines the probability distributions in Figure 297 with the dependence of lifetime on initial fluoride ion release rate (Figure 298).

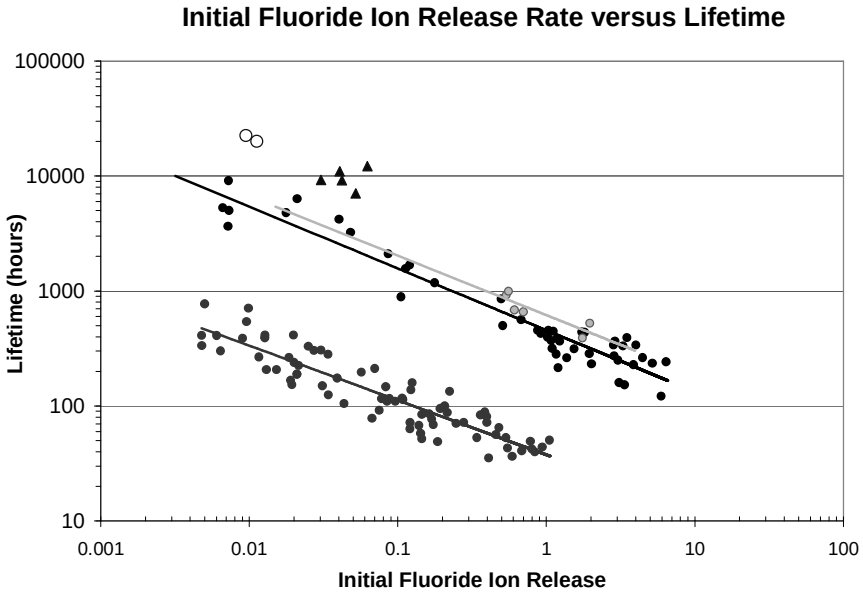

Figure 298. Accelerated Lifetime vs. Initial Fluoride Release Rate

The following predictive equation was developed.

Equation (1)
$$Lifetime = \frac{A}{T+273} + H * LN\left(\frac{RH}{100-RH}\right) + F * LN(FRR) + I$$

Where:

- A = Arrhenius Constant
- H = Humidity Constant
- F = Fluoride Release Constant
- I = Intercept

* Load cycle differences not included yet

Application of this equation provided accurate predictions of lifetime only within the conditions studied and is not universal to all conditions of interest. The first three conditions shown in Table 39 are the cell temperature (CT), anode dew point (AD) and cathode dew points (CD), CT/AD/CD, that were used to derive the model. For these conditions the agreement between the predicted and actual lifetimes is very good. However, the 90/90/90 condition was not run and the predicted lifetimes are clearly incorrect.

Table 39. Predicted vs. Actual Lifetimes for Equation 1

Conditions	Fluoride Release	Equation Prediction Lifetime (hrs)	95% Lower Confidence Interval (hrs)	95% Upper Confidence Interval (hrs)	Actual Lifetime (hrs)
90/60/60	0.457	63	56	70	56
90/70/70	1.11	329	291	372	347
70/70/70	0.042	9,272	11,314	13,817	10,984

90/90/90	0.5	5,633,891	1,079,697	29,410,394	Not Run

Relative humidity is confined to values between 0 and 100% and has a strong influence on model predicted lifetimes. One consequence of this is that the transformation used, (RH/(RH-100), become infinitely small and infinitely large at the boundaries. Instability at the boundary of 100% RH was especially problematic. In most of our analysis we used 93%RH as representative of saturated conditions. This resulted in reasonable predictions but the predicted values can be easily skewed because of the instability at this boundary. To develop a better model an improved representation of RH was made by using the resistance as measured by impedance spectroscopy. The model predictions given from the reciprocal of the impedance measurement as well as the reciprocal of the cell temperature provided a more robust model. The predicted lines and the data match better than with Equation (1). The resulting improved predictive Equation (2) is:

Equation (2)
$$Lifetime = \frac{A}{T} + \frac{H}{R} + F * LN(FRR) + I$$

Where:

- A = Cell Temperature Constant
- H = Humidity Constant
- R = Resistance from Impedance Measurement
- F = Fluoride Release Constant
- I = Intercept

The following two figures show the results of a statistical analysis using this new term for humidity. Figure 299 shows the analysis with the 70/70/70 (non-accelerated conditions) omitted and Figure 300 shows the same analysis with the points included. Notice that the line predicted for the 70/70/70 condition (right most line) virtually the same in both analyses (note: line colors are different in figure). This indicates that the accelerated conditions are able to predict non accelerated results with reasonable accuracy.

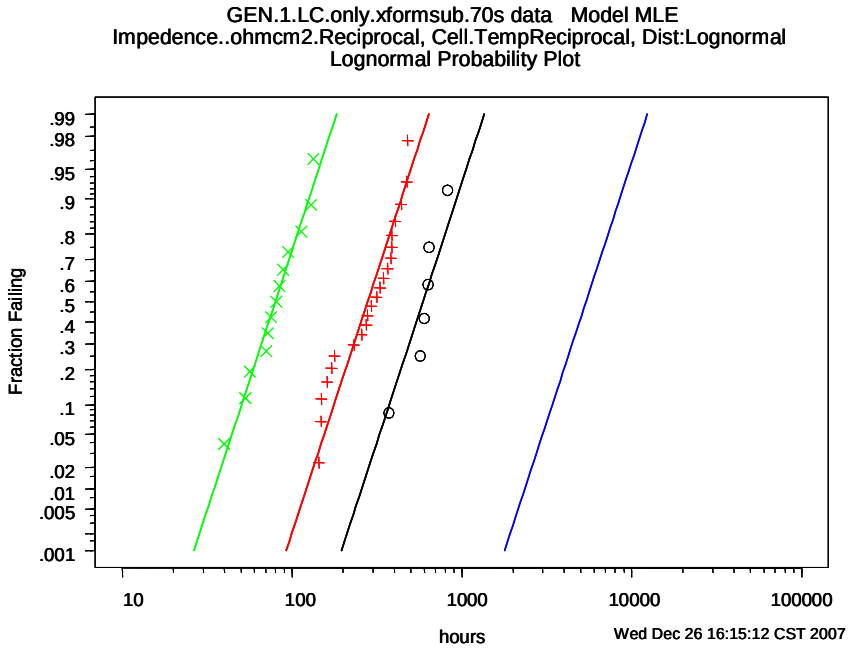

Figure 299. Statistical Analysis for MEA lifetime. 70/70/70 data omitted.

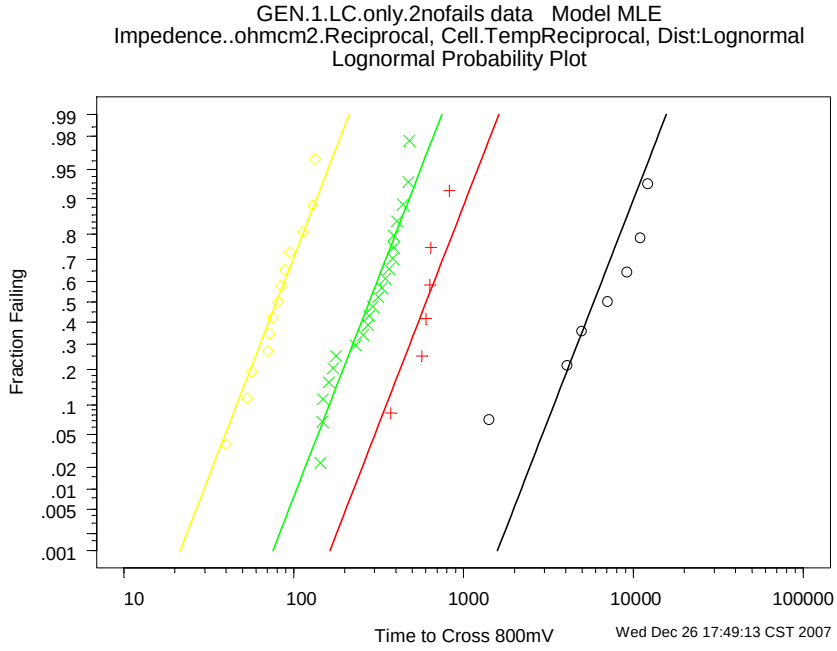

Figure 300. Statistical Analysis for MEA lifetime. 70/70/70 included (black circles).

In addition to the new transformation given in Equation 2 a lognormal distribution was used to fit the data instead of a Weibull distribution. The lognormal distribution gives slightly lower life predictions and results in more conservative prediction. While the model from Equation 2 still

does not predict perfectly in conditions that where not tested, it does fit well for conditions that have lifetime data.

MEAs made with the final design materials were started testing at 70/70/70℃ and 90/70/70℃ conditions. All of these samples are still alive at the end of the contract and have low fluoride release rates. Predicted lifetime from Equation (2) are approximately 26,000 hours lifetime (95% confidence interval is 12,000 hours-60,000 hours). Similarly using the fluoride mapping in Figure 10 the final design samples give a fluoride release rate that corresponds to a 30,000-40,000 hour lifetime.

5.4 Summary

Using tools such as accelerated tests and statistical lifetime modeling allow for early estimates of durability. There are three basic types of accelerated tests: (1) Screening tests are appropriate for measuring incremental improvements in component durability. (2) Mechanistic tests are designed to provide a fundamental understanding of the degradation pathway. (3) Lifetime tests are used to determine the product's lifetime under a given set of operating conditions.

Lifetime is a probability distribution and therefore the data analysis needs to account for this fact. When the results of lifetime tests are combined with statistical lifetime analysis, it is possible to predict product lifetime at 'end-use' conditions from 'accelerated' degradation conditions. This can often lead to faster development of MEAs and components because critical lifetime information can be learned without waiting for lengthy lifetime tests to complete under 'end use' conditions.
A reasonable lifetime model was developed using fluoride release data and a multivariable statistical analysis program. The model predicts lifetimes for conditions where data exists and is not as robust for predicting lifetime on conditions where there is little or no lifetime data. Samples running with final design materials show good potential and given the initial fluoride release have predicted lifetimes over 20,000 hours with the possibility of lasting 40,000 hours.

Table 40. Summary of all single cell durability tests

FC Number	Conditions*	MEA	Time to Cross 800mV	Ave. F- Ion at equilibrium (ug/min)
FC048153	90/70/70 LC	3M Commercial MEA - 2	171	3.04
FC048154	90/70/70 LC	3M Commercial MEA - 2	178	2.86
FC048439	90/70/70 CJ	3M Commercial MEA - 1	1453	0.086
FC048440	70/70/70 LC	3M Commercial MEA - 1	10984	0.041
FC048441	70/70/70 LC	3M Commercial MEA - 1	9181	0.042
FC048442	70/70/70 LC	3M Commercial MEA - 1	12207	0.062
FC048443	90/70/70 LC	3M Commercial MEA - 1	278	1.54
FC048444	90/70/70 CJ	3M Commercial MEA - 1	1452	0.113
FC048445	90/70/70 CJ	3M Commercial MEA - 1	1582	0.120
FC048446	90/70/70 LC	3M Commercial MEA - 1	257	1.37
FC048447	90/70/70 CJ	3M Commercial MEA - 1	1704	0.048
FC048449	70/70/70 LC	3M Commercial MEA - 1	7069	0.052
FC048450	80/70/70 LC	3M Commercial MEA - 1	372	1.75
FC048451	90/70/70 LC	3M Commercial MEA - 1	148	3.09
FC048452	80/70/70 LC	3M Commercial MEA - 1	570	0.70
FC048453	90/70/70 LC	3M Commercial MEA - 1	144	3.36
FC048454	70/70/70 LC	3M Commercial MEA - 1	1414	0.065
FC048455	80/70/70 LC	3M Commercial MEA - 1	641	0.61
FC048456	90/70/70 LC	3M Commercial MEA - 1	161	3.86

FC048457	80/70/70 LC	3M Commercial MEA - 1	826	0.54
FC049237	90/70/70 LC	3M Commercial MEA - 2	231	1.09
FC049238	90/70/70 LC	3M Commercial MEA - 2	315	1.02
FC049991	90/70/70 LC	3M Commercial MEA - 2	149	2.01
FC049992	90/70/70 LC	3M Commercial MEA - 2	405	1.73
FC050001	80/70/70 LC	3M Commercial MEA - 1	633	0.56
FC050002	90/70/70 LC	3M Commercial MEA - 1	388	0.87
FC050008	90/70/70 LC	3M Commercial MEA - 1	480	0.51
FC050094	90/70/70 LC	Additive Experiment - 4	6640	0.021
FC050095	70/70/70 LC	3M membrane	9252	0.030
FC050177	90/70/70 LC	Exp. 33 micron 3M membrane	133	6.40
FC050178	90/70/70 LC	Exp. 33 micron 3M membrane	112	5.17
FC050179	90/70/70 LC	Exp. 33 micron 3M membrane	181	3.49
FC050180	90/70/70 LC	Exp. 33 micron 3M membrane	207	4.00
FC050181	90/70/70 LC	Exp. 33 micron 3M membrane	250	4.45
FC050184	90/70/70 LC	Exp. 36 micron Nafion™	62	5.93
FC050185	90/70/70 LC	Exp. 36 micron Nafion™	188	2.84
FC050186	90/70/70 LC	Exp. 36 micron Nafion™	152	1.81
FC050187	90/70/70 LC	Exp. 36 micron Nafion™	269	2.90
FC050188	90/70/70 LC	Exp. 36 micron Nafion™	171	3.28
FC052281	70/70/70 LC	3M Commercial MEA - 1	4078	0.047
FC052619	90/70/70 LC	3M Commercial MEA - 1	387	1.23
FC052621	90/70/70 LC	3M Commercial MEA - 1	347	1.11
FC052625	80/70/70 LC	3M Commercial MEA - 1	601	1.96
FC052633	90/70/70 MLC	3M Commercial MEA - 1	8194	0.007
FC052634	80/70/70 MLC	3M Commercial MEA - 1	1621	0.008
FC052635	70/70/70 LC	3M Commercial MEA - 1	4968	0.030
FC052636	70/70/70 MLC	3M Commercial MEA - 1	4959	0.05
FC052637	70/70/70 MLC	3M Commercial MEA - 1	4684	0.043
FC052638	80/70/70 CJ	3M Commercial MEA - 1	1413	0.019
FC052639	70/70/70 MLC	3M Commercial MEA - 1	7600	0.068
FC052640	80/70/70 MLC	3M Commercial MEA - 1	1663	0.008
FC052641	70/70/70 CJ	3M Commercial MEA - 1	3539	0.072
FC052642	80/70/70 CJ	3M Commercial MEA - 1	1476	0.015
FC053843	70/70/70 LC	Saratoga	935	0.014
FC053844	70/70/70 LC	Saratoga	1778	0.009
FC053845	90/70/70 LC	Saratoga	6142	0.00662
FC053846	70/70/70 LC	Saratoga	1610	0.015
FC053847	90/70/70 LC	Saratoga	5019	0.0073
FC053848	70/70/70 LC	Saratoga	4375	0.009
FC053849	90/70/70 LC	Saratoga	3652	0.0072
FC053850	70/70/70 LC	Saratoga	3481	0.011
FC054929	80/70/70 LC	Saratoga	1645	0.005
FC054930	70/70/70 LC	Saratoga	1796	0.010
FC054931	90/70/70 MLC	Saratoga	2360	0.0141
FC054932	90/70/70 MLC	Saratoga	1249	0.0165
FC054935	80/70/70 LC	Saratoga	4582	0.006
FC054936	80/70/70 LC	Saratoga	2652	0.008
FC054937	90/70/70 MLC	Saratoga	1588	0.0161
FC054940	80/70/70 LC	Saratoga	893	0.015

FC055542	90/70/70 LC	3M Commercial MEA - 1	586	0.793
FC055543	90/70/70 LC	3M Commercial MEA - 1	2448	0.052
FC055544	90/70/70 LC	3M Commercial MEA - 1	955	0.130
FC056440	80/70/70 CJ	3M Commercial MEA - 1	3128	0.064
FC056442	80/70/70 MLC	3M Commercial MEA - 1	3478	0.0104
FC056443	80/70/70 CJ	3M Commercial MEA - 1	6503	0.005
FC057827	70/70/70 LC	Final Design - A	6200	0.0030
FC057828	90/70/70 LC	Final Design - A	1423	0.0340
FC057830	70/70/70 LC	Final Design - A	6000	0.0043
FC057832	70/70/70 LC	Final Design - B	5900	0.0022
FC057833	90/70/70 LC	Final Design - B	3220	0.0177
FC10077	90/60/60 LC	Additive Experiment - 13	638	0.005
FC10087	90/60/60 LC	Reinforced Experiment - 3	23.9	0.293
FC10088	90/60/60 LC	Reinforced Experiment - 1	33	0.065
FC10101	90/60/60 LC	Reinforced Experiment - 2	116	0.053
FC10102	90/60/60 LC	Reinforced Experiment - 2	55	0.160
FC10103	90/60/60 LC	Reinforced Experiment - 2	117.6	0.039
FC10120	90/60/60 LC	Reinforced Experiment - 1	103	0.212
FC10121	90/60/60 LC	Reinforced Experiment - 1	77	1.894
FC10125	90/60/60 LC	Reinforced Experiment - 2	146.5	0.349
FC10136	90/60/60 LC	3M membrane	28.9	0.986
FC10137	90/60/60 LC	Reinforced Experiment - 5	38.5	0.792
FC10235	90/60/60 LC	3M membrane	74	0.065
FC10236	90/60/60 LC	3M membrane	61	0.513
FC10371	90/60/60 LC	Additive Experiment - 14	374	0.0060
FC10418	90/60/60 LC	Additive Experiment - 4	333	0.025
FC10560	90/60/60 LC	Exp. 30 micron Nafion™	280	0.034
FC10562	90/60/60 LC	Exp. 30 micron Nafion™	98	0.107
FC10567	90/60/60 LC	3M membrane	189	0.017
FC10568	90/60/60 LC	3M membrane	406.9	0.009
FC10628	90/60/60 LC	3M membrane	216	0.030
FC10628	90/60/60 LC	3M membrane w/ Additive	216	0.030
FC10632	90/60/60 LC	3M membrane	488.5	0.010
FC10632	90/60/60 LC	3M membrane w/ Additive	488.5	0.010
FC10763	90/60/60 LC	Additive Experiment - 14	278	0.0272
FC11902	90/60/60 LC	Reinforced Experiment - 5	218.7	0.067
FC11903	90/60/60 LC	Reinforced Experiment - 5	195	0.092
FC12226	90/60/60 LC	Exp. 30 micron Nafion™	79	0.174
FC12227	90/60/60 LC	Exp. 30 micron Nafion™	107	0.120
FC12313	90/60/60 LC	3M membrane	115	0.033
FC12334	90/60/60 LC	3M membrane	128.5	0.033
FC12432	90/60/60 LC	Catalyst Experiment	271	0.038
FC12435	90/60/60 LC	Catalyst Experiment	232	0.031
FC12437	90/60/60 LC	Catalyst Experiment	134	0.095
FC12438	90/60/60 LC	Catalyst Experiment	120.6	0.154
FC12855	70/70/70 LC	Final Design - B	3100	0.0234
FC12856	70/70/70 LC	Final Design - B	3000	0.0047
FC12857	90/70/70 LC	Final Design - B	2743	0.0097
FC48026	90/60/60 LC	3M membrane	95	0.193
FC48027	90/60/60 LC	3M membrane	39.9	0.836

FC48030	90/60/60 LC	3M membrane	84.4	0.145
FC48036	90/60/60 LC	3M membrane	53.2	0.341
FC48039	90/60/60 LC	3M membrane	110.1	0.085
FC48041	90/60/60 LC	3M membrane	72	0.398
FC48047	90/60/60 LC	3M membrane	113.7	0.108
FC48048	90/60/60 LC	3M membrane	72	0.278
FC48052	90/60/60 LC	3M membrane	70.6	0.247
FC48056	90/60/60 LC	3M membrane	56.5	0.457
FC48057	90/60/60 LC	3M membrane	78.2	0.067
FC48063	90/60/60 LC	3M membrane	80.9	0.397
FC48068	90/60/60 LC	3M membrane	109.8	0.096
FC48151	90/60/60 LC	3M membrane	197	0.057
FC48152	90/60/60 LC	3M Commercial MEA - 2	104.6	0.043
FC48152	90/60/60 LC	3M membrane	105	0.043
FC48458	90/70/70 MLC	3M Commercial MEA - 1	521	0.497
FC48511	90/60/60 LC	3M membrane	43.2	0.549
FC48516	90/60/60 LC	3M membrane	49.4	0.781
FC48521	90/60/60 LC	3M membrane	40.8	0.683
FC48530	90/60/60 LC	3M membrane	36.4	0.589
FC49244	90/60/60 LC	3M Commercial MEA - 2	88.6	0.385
FC49993	90/70/70 LC	3M Commercial MEA - 2	330	1.08
FC49996	90/70/70 LC	3M Commercial MEA - 2	274	1.94
FC50003	90/70/70 MLC	3M Commercial MEA - 1	4790	0.018
FC50004	90/70/70 MLC	3M Commercial MEA - 1	4200	0.040
FC50005	95/70/70 LC	3M Commercial MEA - 1	655	0.5494
FC50006	95/70/70 LC	3M Commercial MEA - 1	910	0.556
FC50007	100/70/70 LC	3M Commercial MEA - 1	657	0.2112
FC50009	100/70/70 LC	3M Commercial MEA - 1	447	0.4401
FC50010	95/70/70 LC	3M Commercial MEA - 1	656	0.6185
FC50079	90/60/60 LC	3M 700 EW Ionomer	65	0.480
FC50082	90/60/60 LC	3M 700 EW Ionomer	85.5	0.163
FC50091	90/60/60 LC	3M membrane w/ Additive	650	0.010
FC50096	90/60/60 LC	3M membrane w/ Additive	361	0.013
FC50101	90/60/60 LC	Additive Experiment - 11	147	0.083
FC50102	90/60/60 LC	3M membrane	52	0.405
FC50108	90/60/60 LC	End Group Experiment -2	125	0.034
FC50109	90/60/60 LC	End Group Experiment -2	239	0.020
FC51607	90/60/60 LC	3M Commercial MEA - 2	133.8	0.454
FC51614	90/60/60 LC	End Group Experiment -1	68.8	0.174
FC51620	90/60/60 LC	End Group Experiment -1	63.3	0.121
FC51627	90/60/60 LC	3M Commercial MEA - 2	129.7	0.100
FC51628	90/60/60 LC	3M Commercial MEA - 2	75.5	0.379
FC51765	90/60/60 LC	Eq. Weight Study - 1	44	0.940
FC51767	90/60/60 LC	Eq. Weight Study - 1	50.5	1.050
FC52289	90/60/60 LC	3M Commercial MEA - 2	173	0.144
FC52343	90/70/70 LC	3M Commercial MEA - 3	216	1.200
FC52344	90/70/70 LC	3M Commercial MEA - 3	900	0.105
FC52345	90/70/70 LC	3M Commercial MEA - 3	1167	0.1772
FC52463	90/70/70 LC	3M Commercial MEA - 2	293	1.166
FC52624	90/70/70 LC	3M Commercial MEA - 1	440	0.92

FC52626	90/70/70 LC	3M Commercial MEA - 1	383	0.68
FC52627	90/70/70 LC	3M Commercial MEA - 1	475	1.03
FC52632	90/70/70 LC	3M Commercial MEA - 1	365	1.19
FC54598	90/60/60 LC	3M membrane	50	0.075
FC54599	90/60/60 LC	3M membrane	138.2	0.015
FC54608	90/60/60 LC	3M Commercial MEA - 4	295	0.013
FC54609	90/60/60 LC	3M Commercial MEA - 4	474	0.0066
FC55090	90/60/60 LC	Reinforced Experiment - 4	92	0.186
FC55091	90/60/60 LC	Reinforced Experiment - 4	106	0.207
FC55094	90/60/60 LC	Reinforced Experiment - 4	334	0.009
FC55099	90/60/60 LC	Reinforced Experiment - 4	267	0.023
FC55738	90/60/60 LC	Reinforced Experiment - 3	47	0.308
FC55739	90/60/60 LC	Reinforced Experiment - 3	26	0.856
FC56390	90/60/60 LC	Reinforced Experiment - 4	170	0.047
FC56392	90/60/60 LC	Reinforced Experiment - 4	237	0.100
FC56401	90/60/60 LC	Reinforced Experiment - 5	2	0.052
FC56928	90/60/60 LC	Reinforced Experiment - 5	525.5	0.003
FC58150	70/42/42 LC	Commercial MEA - 1	330	0.018
FC58151	80/51/51 LC	3M Commercial MEA - 1	698	0.007
FC58152	70/42/42 LC	3M Commercial MEA - 1	244	0.015
FC58153	80/51/51 LC	3M Commercial MEA - 1	981	0.008
FC58154	70/42/42 LC	3M Commercial MEA - 1	206	0.013
FC9019	90/60/60 LC	Additive Experiment - 4	224.7	0.021
FC9021	90/60/60 LC	Additive Experiment - 1	412.1	0.012
FC9022	90/60/60 LC	Additive Experiment - 3	57.9	0.143
FC9023	90/60/60 LC	Additive Experiment - 5	266.9	0.012
FC9235	90/60/60 LC	3M membrane	159.6	0.125
FC9236	90/60/60 LC	3M membrane	71.8	0.121
FC9237	90/60/60 LC	Additive Experiment - 1	167.3	0.019
FC9312	90/60/60 LC	Additive Experiment - 2	35.3	0.409
FC9313	90/60/60 LC	Additive Experiment - 2	53.16	0.534
FC9343	90/60/60 LC	Additive Experiment - 8	264.4	0.018
FC9379	90/60/60 LC	Additive Experiment - 5	153.5	0.019
FC9380	90/60/60 LC	Additive Experiment - 4	301	0.006
FC9381	90/60/60 LC	Additive Experiment - 3	77	0.169
FC9408	90/60/60 LC	Additive Experiment - 8	335.7	0.01
FC9742	90/60/60 LC	Additive Experiment - 6	42.3	0.798
FC9743	90/60/60 LC	Additive Experiment - 9	100	0.207
FC9744	90/60/60 LC	Additive Experiment - 9	87.7	0.215
FC9745	90/60/60 LC	Additive Experiment - 7	175	0.039
FC9746	90/60/60 LC	Additive Experiment - 7	138.7	0.122
FC9854	90/60/60 LC	Additive Experiment - 10	134	0.223
FC9855	90/60/60 LC	Additive Experiment - 10	83.5	0.360
FC9909	90/60/60 LC	Additive Experiment - 11	189	0.021
FC9909	90/60/60 LC	Additive Experiment - 11	189.2	0.021
FC9910	90/60/60 LC	Additive Experiment - 11	116.3	0.088
FC9910	90/60/60 LC	Additive Experiment - 11	115.7	0.078
FC9964	90/60/60 LC	Additive Experiment - 12	212	0.070
FC9965	90/60/60 LC	Additive Experiment - 12	150	0.031
FC9983	90/60/60 LC	Additive Experiment - 12	389	0.009

FC9984	90/60/60 LC	3M membrane w/ Additive	201	0.013

* Conditions defined in terms of cell temp, anode dew point, cathode dew point and load cycle $T_{cell}/T_{anode\ D.P.}/T_{cathode\ D.P.}$ LC = Load Cycle, MLC =Modified Load Cycle, CJ = Constant Current

5.5 Acknowledgements

Thoughtful discussions with Prof William Meeker of Iowa State University are acknowledged.

5.6 References

1. W.Q. Meeker and L.A. Escobar, Statistical Methods for Reliability Data, John Wiley and Sons, Inc. (1998).
2. G. Escobedo, “Enabling Commercial PEM Fuel Cells with Breakthrough Lifetime Improvements,” 2006 DOE Hydrogen Program Review, May 2006.
3. G. Gittleman, Y-H. Lai and D. Miller, “Durability of Perfluorosulfonic Acid Membranes for PEM Fuel Cells,” Fall AIChE Meeting, October 2005.
4. D. Stevens, M. Hicks, G. Haugen, J. Dahn, “Ex situ and in situ stability studies of PEMFC catalysts: Effect of carbon type and humidification on degradation of the carbon,” *J. Electrochem. Soc*., 152 (12), A2309 (2005).
5. J. Frisk, W. Boand, M. Hicks, M. Kurkowski, A. Schmoeckel and R. Atanasoski, “How 3M developed a new GDL construction for improved oxidative stability,” 2004 Fuel Cell Seminar, San Antonio, TX, November 2004.
6. D. Curtin, R. Lousenberg, T. Henry, P. Tangeman and M. Tisak, “Advanced materials for improved PEMFC performance and life,” *J. Power Sources*, 131 (1-2) 41 (2004).
7. K. Schwiebert, K. Raiford, G. Nagarajan, F. Principe and G. Escobedo, “Strategies to Improve the Durability of Perfluorosulfonic Acid Membranes for PEM Fuel Cells,” Fuel Cell Durability, December 2005
8. D. Schiraldi, “Perfluorinated polymer electrolyte membrane durability,” *Polymer Reviews*, 46 (3), 315 (2006).
9. D. Schiraldi, C. Zhou and T. Zawodzinski, “Model Studies of Perfluorinated PEM Membrane Degradation,” 232nd ACS Meeting, San Francisco, September 2006.

Section 6. MEA Performance Characteristics in Stacks and Systems

6.1 MEA Product Design Requirements & Verification

Membrane, electrodes and GDL are all equally important to a functional unit of a fuel cell. Superior reliability each of these subcomponents is crucial; equally important is the necessity to perform as a single optimized unit with maximized performance and its intended durability. Optimization includes clear understanding of the performance window and latitude against operating extremes. At the beginning of this program, Plug Power had already started manufacturing and installing systems with Gen 1 MEA's in the PEMFC stack design. So it was crucial to understand the degradation profiles using real world conditions. Hence to quantify the critical parameters for a new design, Plug Power took on activities around data mining of the first generation systems. This also enabled key system level understanding to further improve stack life.

6.1.1 Data-Mining of first-generation reformer based systems

Plug Power started analyzing field data from over 20 fuel cell systems (the stacks were built using commercial MEAs) for stack decay mechanisms including data recording (such as system operating parameters and environmental parameters) and data processing. Neural Networks and CART (Classification and Regression Trees) were used to identify underlying relationships and higher order interactions in large data sets. Field systems have the highest complexity and run under non-ideal conditions. Failure modes that do not occur in single cells, modules, and even stacks when operated in the laboratory setting could occur in field systems. Accordingly, information from existing field systems would be very valuable in designing any new systems.

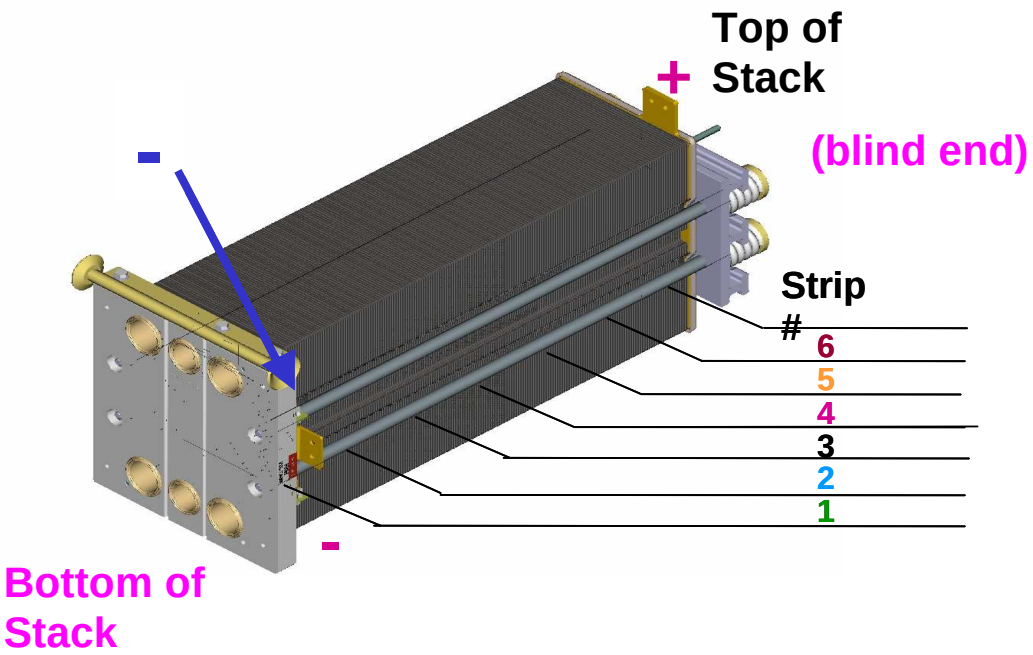

Figure 301. Stack Stratification Scheme – Layout of Early design

At Plug Power, 256 parameters are recorded for each system for data gathering for on-site diagnostics and monitoring. Through 2004 Q1, the Plug Power team performed data mining on 4 SU1-type systems operated at a US Military location in upstate New York. These systems were operated to output a constant power of 2.5 kW at 220VAC. Natural gas was reformed and a fixed air bleed was used to mitigate CO in the reformed fuel. Each stack was separated into 6 zones for ease of data recording, with 13 cells in Zone 1 and 15 cells in Zones 2-6. Accordingly, the behavior of each zone could be studied independently. The reactant and coolant inlets and outlets were located at the bottom of the stack. Figure 301 shows the Zone layout and reactant inlets and outlets for the SU1-type stack.

Cathode ΔT effect on stack performance degradation

Figure 302 shows the effect of cathode ΔT on stack degradation rate in Plug Power's field systems. Cathode ΔT is defined as the normalized stack cathode air outlet temperature minus the cathode air inlet temperature. It is clear from the general trend in Figure 1 that a higher cathode ΔT led to a higher stack performance degradation rate. The plot indicates a 50% reduction in degradation rate when the cathode ΔT is decreased by 22% (reduced ΔT correlates with increased cathode humidity at the outlet). The degradation rate was calculated based on one-month operation of more than 40 Plug Power's fuel cell systems in the field.

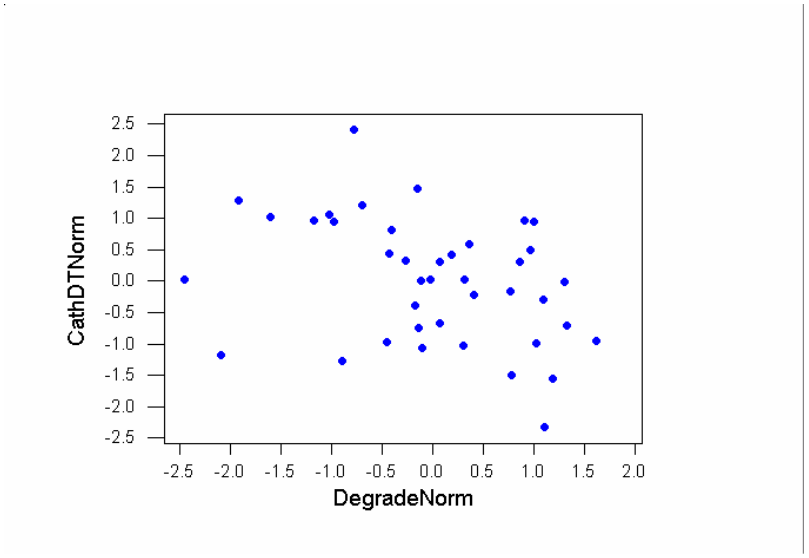

Figure 302. Cathode d T impact on degradation

Cathode inlet temperature effect on stack performance in systems

Figure 303 shows cathode inlet temperature effect on stack performance and degradation rate in systems. With the increase of cathode inlet temperature of 25%, the average stack voltage increased by11%, while the stack performance degradation rate dropped an order of magnitude (cathode inlet temperature correlates with humidity level at the inlet). The results shown in Figure 303 illustrate linear relationships between cathode inlet temperature and stack performance/stack performance degradation rate.

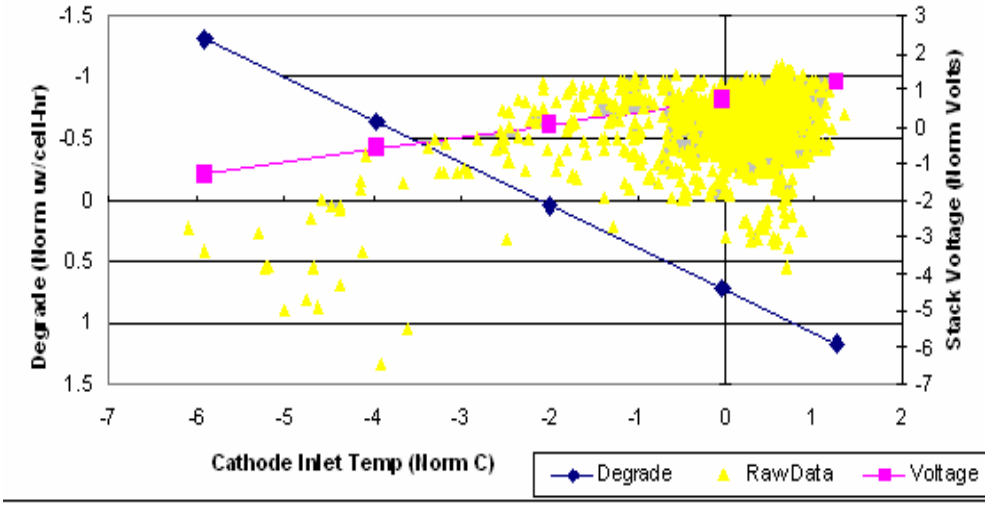

Figure 303. Cathode Inlet Temperature effects on Degrade rate and Instantaneous Performance (normalized data)

Stack Top to bottom stratification

Figure 304, Figure 305, Figure 306 and Figure 307 show the average cell voltage of each of the 6 zones for 4 systems. It can be seen that the top cells, Zone 6, had lower performance and they decreased faster near end of life. It can also be seen that the performance of all the zones decreased with time and that most system shutdown or trips could recover part of the lost performance. It has been correlated to the 3 – 5 ^{0}C increase in cell temperature at the top of the stack. After shutdown, while restarted, the cell-to-cell variability seems to be small, while as they run longer the variability increases with time.

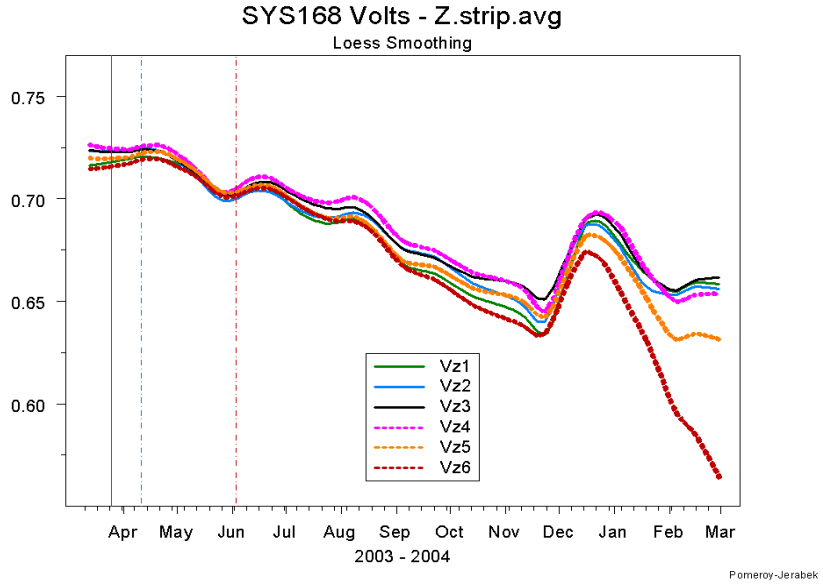

Figure 304. Stack Degradation with Zone stratification –System 168

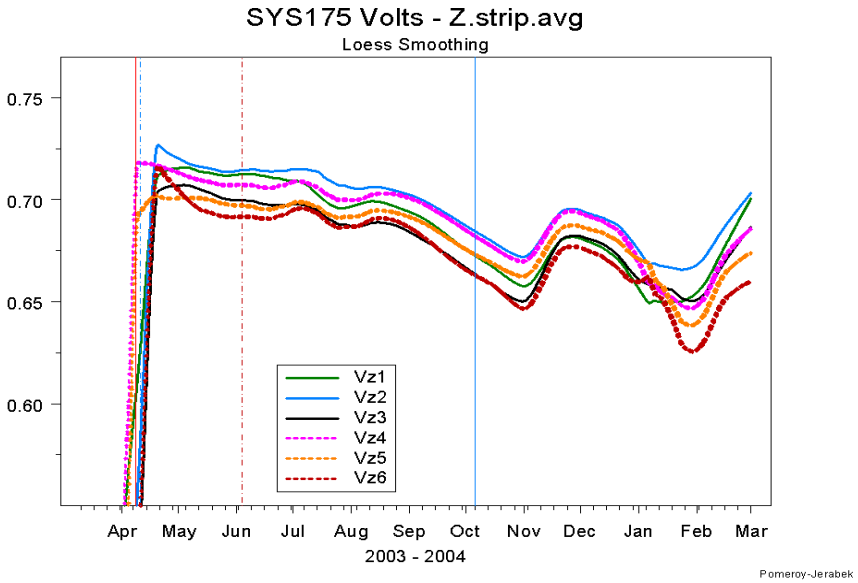

Figure 305. Stack Degradation with Zone stratification –System 175

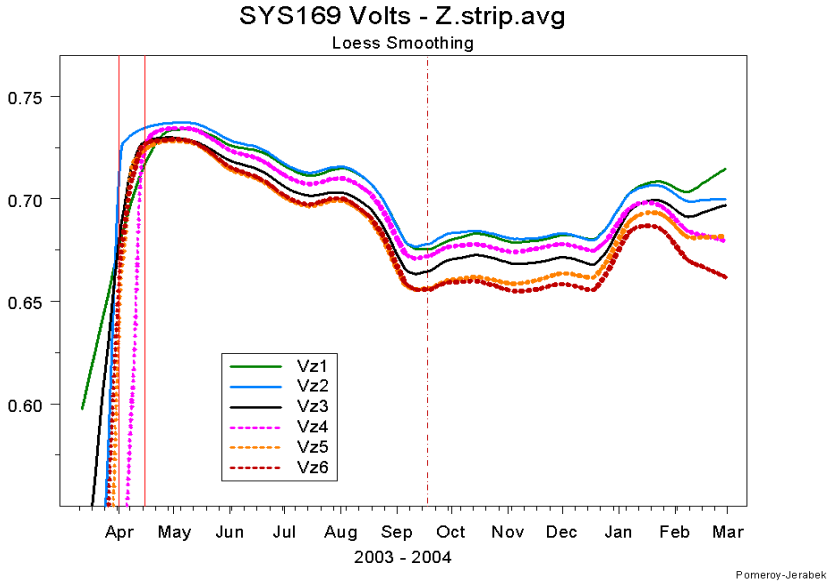

Figure 306. Stack Degradation with Zone stratification –System 169

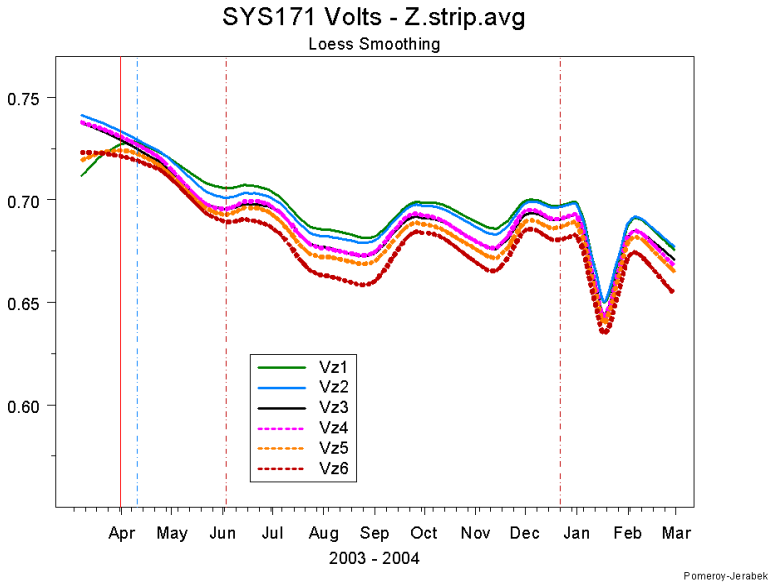

Figure 307. Stack Degradation with Zone stratification –System 171

Conclusions

1. Cathode ΔT has a significant impact on stack degradation rate in systems. Data mining results from more than 20 systems show a trend that the stack degradation rate increases with cathode ΔT and outlet humidity.
2. Reducing the difference between the cathode inlet temperature and the coolant inlet temperature (inlet humidity) improves both stack performance and stack lifetime.
3. Temperature variations from bottom to top of the stack need to be minimized in stack design.

Plug Power autopsied many stacks of this generation 1 and found the following two failure modes to recur and these were the drivers for system improvement and robust MEA requirements.

a) **Membrane crossover leakage** - This mode is addressed with the improved membrane developed under the 3M/DOE project. When the 3M/DOE MEAs were operated in the system testing planned, comparisons were drawn with respect to the behavior reported for various 3M MEAs in this report. CO and air bleed effects have been understood along with other interactions such as drying and gasket material interactions. In addition to that several controls modifications were completed on the coolant temperature gradient control and stack inlet temperature controls.

b) **Cathode Electrode Damage** -Stacks have failed due to cathode damage attributed to repeated startup and shutdown activity. This was found to be due to the presence of an H2/Air interface that propagates on the anode side during startup and shutdown. This leads to severe carbon corrosion in the cathode electrode, resulting in significant activation loss of the catalyst layer. The startup and shutdown procedures have been improved through several changes. Also some new tools have been developed to characterize these failures.

6.1.2 Effect of Operating Conditions on Cell life and Performance

Introduction

Task 5 specifically emphasized on developing the relationship of performance and degrade rate to operating conditions such as current density (power), cell temperature, reactant pressure, varying levels of CO with Air bleed, relative humidity were also studied during 2004 – 2005 timeframe. In this report we concentrate on the critical parameters that control the fuel cell performance. In addition to the operating conditions, Plug Power also quantified the impact of cations on cell performance, since all of these contribute to extrinsic factors leading to degradation. Intrinsic degradation rates are due to subcomponent specific failure modes. However intrinsic degradation is accelerated due to extremes in operating conditions, contamination and other extrinsic factors. Most of the testing was performed in 50-cm^2 test stations. Plug Power purchased a 6-cell Precision Flow Technologies (PFT) station in January 2004 as shown in Figure 308, which unfortunately got partially functional in October 2005. Most of the initial characterization studies were performed in internally Plug Power developed stations. Several gage R&R measurements were conducted and measurement system analysis was performed on cell temperature, humidifier temperature, mass flow meters, voltage and current. The station error was documented and reported out in quarterly summaries. A regular calibration has been conducted to ensure reliable data from these stations.

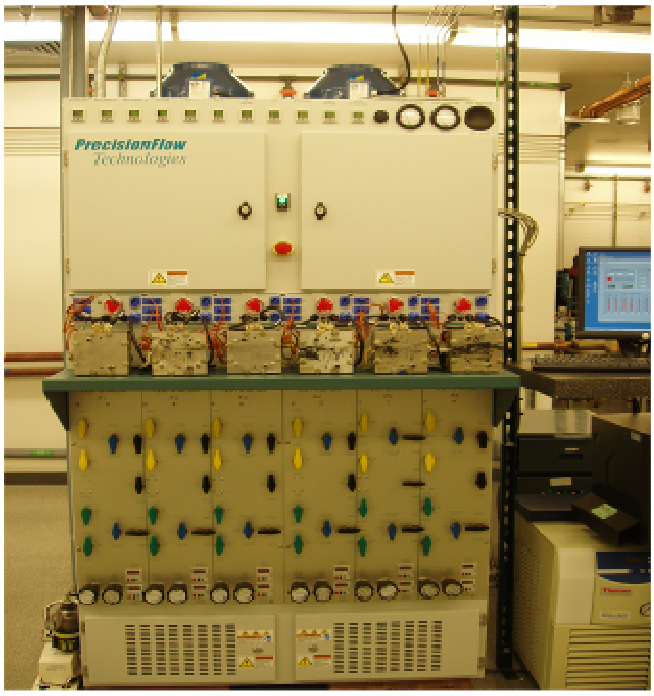

Figure 308. Precision Flow Technologies 6-cell station

3M Gen I MEA's with an active area of 50cm^2 were used for this test at different current densities using reformate/air at 1.2/2.0 stoichiometry, cell temperature 65°C, 100% anode and cathode relative humidity and 2% air bleed. The reformate was composed of 10 ppm CO, 49% H_2, 17% CO_2, and balanced by N_2. The beginning-of-life (BOL) performance was collected at different current densities. The cells were then operated at each current density (OCV, 0.05, 0.1, 0.2, 0.3, 0.4, 0.6, and 0.7A/cm^2) for 1000 hours and the degradation rates were calculated based on the performance from 100 hours to the end of this testing period. The fluoride release was monitored throughout the entire testing period.

Current Density Effects: (Steady State)

Current density is an important factor that influences the voltage degradation rate and lifetime of an MEA because the water and heat transport profiles, and the cell voltage (especially the cathode voltage) are functions of current density. Due to iterative process of design improvements in MEA, we fixed Gen 1 MEA for most of our studies. This obviously can be extended to the improvements we had over the years. More specifically, at lower current density, the higher cathode voltage may cause higher carbon oxidation/corrosion and catalyst oxidation rates, leading to faster cell performance degradation; while at higher current density, water management may become difficult and anode drying as well as local high temperature spots may become more likely, resulting in higher cell degradation too; then the minimum degradation rate may be in the intermediate current density region. Figure 309 shows our initial mental model of degradation rates dependence on the stack current.

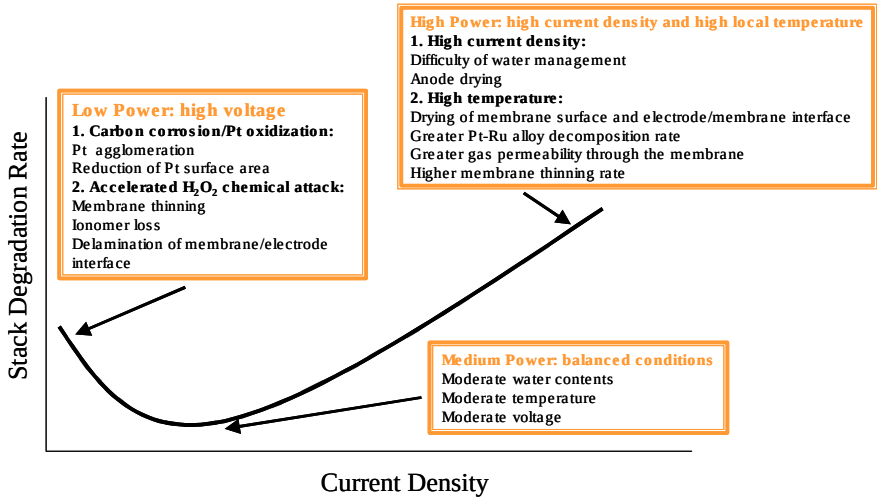

Figure 309. Degradation dependence on current density

General performance loss relationships

There are three main types of performance loss during a fuel cell operation: ohmic loss mainly contributed by membrane and MEA interface resistances, catalyst activity loss mainly contributed by cathode ORR (Oxygen Reduction Reaction), and mass transport loss contributed by electrodes and GDL's. The total voltage loss can be expressed by the following equation:

$$E_{cell} = E_o - (i + i_n)R - A\ln\left(\frac{i + i_n}{i_0}\right) - B\ln\left(\frac{i + i_n}{i_l} - 1\right) - \text{Anode loss}$$

Ideal voltage; IR loss; Cathode activation (ORR) loss; Cathode mass transport loss; Total anode loss

Equation 56

If the internal current density i_n (crossover current) is negligible, then the above equation can be written as:

$$E_{cell} = E_o - iR - A\ln(\frac{i}{i_0}) - B\ln(\frac{i}{i_l} - 1) - \text{Anode loss}$$

Determined by Nernst equation

R: resistance Determined from impedance

i_O:exchange current density, determined by modeling or experiment

i_L:limiting current, determined by experiment

Determined by reformate pumping

Equation 57

Table 41 show the three major voltage loss of 3M Gen 1 MEA's. The actual MEA performance at each current density was at constant stoichiometry. It is clear that the cathode ORR loss and cathode mass transport loss were the major performance losses (over 80% of the total voltage loss at 0.60 A/cm^2) for 3M Gen 1 MEA. These two kinds of losses increased slightly with current density from 0.2 to 0.6 A/cm^2. Meanwhile, the IR loss was much smaller, changed from 12 mV at 0.2 A/cm^2 to 36 mV at 0.60 A/cm^2.

Table 41. 3M MEA performance losses

Type of performance loss	Current density (A/cm^2)		
	0.2	0.4	0.6
ORR loss (mv)	226	246	272
Mass transport loss (mv)	128	145	156
IR loss (mv)	12	24	36

These losses are depicted graphically in Figure 310

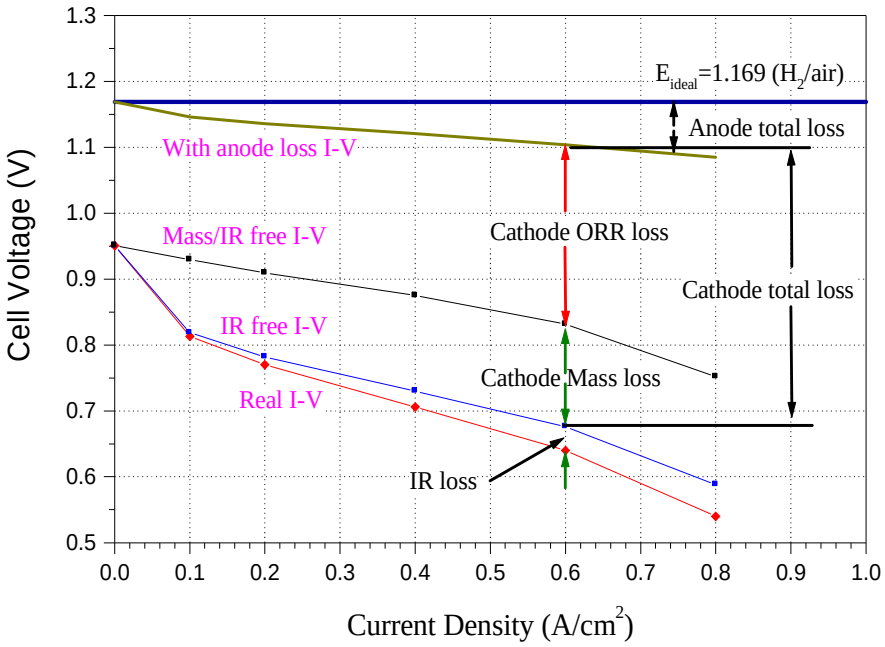

Figure 310. Voltage Losses as a function of current density

In 2004 Q1, Plug Power reported the 1000-hour endurance studies about the effect of current density on performance and durability of 3M Gen I MEAs. During 2004 Q2, Plug Power team finished 2,000 hours endurance test and the results were updated in this report. 3M Gen I MEAs with an active area of 50cm^2 were used for this test at different current densities using reformate/air at 1.2/2.0 stoichiometry (for OCV cell, the reactants flow was set at 0.05A/cm^2), cell temperature 65°C, 100% anode and cathode relative humidity and 2% air bleed. The reformate was composed of 10 ppm CO, 48% H_2, 17% CO_2, and balanced by N_2. The beginning-of-life (BOL) performance was collected at different current densities. The cells were then operated at each current density (OCV, 0.05, 0.1, 0.2, 0.3, 0.4, 0.6, and 0.7 A/cm^2) for 2000 hours (one cell at 0.2 A/cm^2 for 3000 hours) and the degradation rates were calculated based on the performance from 100 hours to the end of this testing period. The voltage degrade rate along with fluoride release rates were monitored throughout the entire testing period. The voltage degrade rate at current densities of 0.0, 0.05, 0.10, 0.20, 0.30, 0.40, 0.60, and 0.70 A/cm^2 are plotted in Figure 311 along with the fluoride release rates. The fluoride released into the anode and cathode exhaust water was measured using ICP. This information was useful to understand the life expectancy under different operating points.

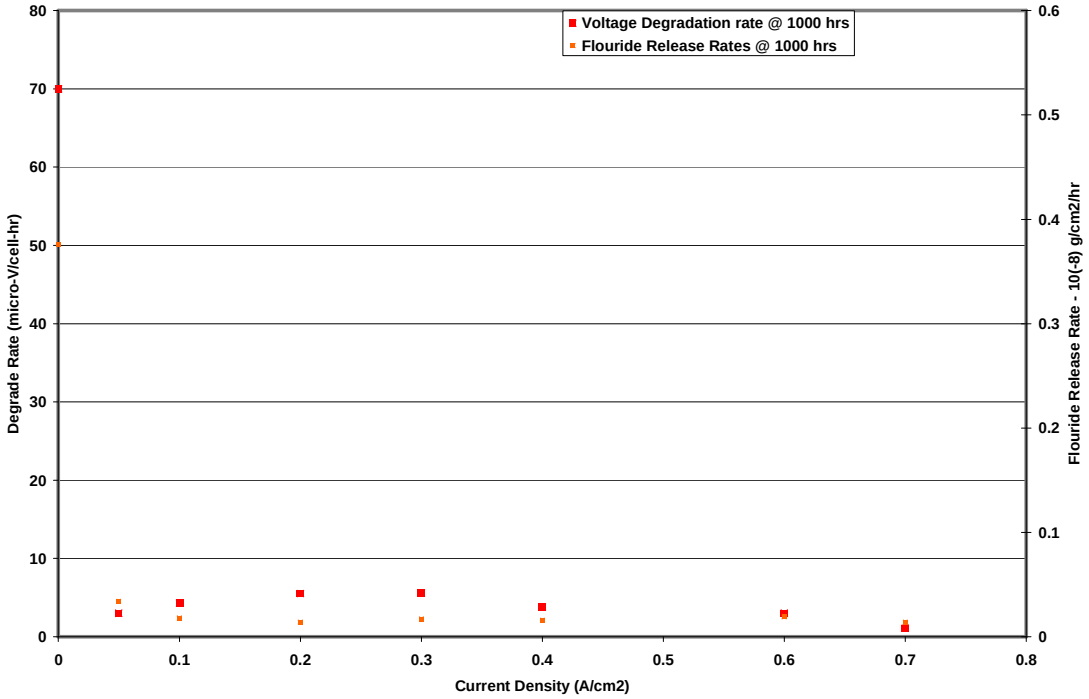

Figure 311. Degradation metrics as a function of current density

Cell Temperature Effects: (Steady State)

a) Performance:

3M Gen I MEAs with an active area of 50cm^2 were used for this test at different temperatures using reformate/air at 1.2/2.0 stoichiometry, 100% anode and cathode relative humidity and 2% air bleed. The reformate was composed of 10 ppm CO, 49% H_2, 17% CO_2, and balanced by N_2. The beginning-of-life (BOL) performance with hydrogen and reformate were collected at different temperatures using one cell in the same test station to minimize station and MEA variations.

In constant stoichiometry performance measurements, voltage meter was used to read the cell performance and the estimated overall error bar from test station was ±3mV. The polarization curves were developed over the cell temperature of 40 – 80 ^{0}C as shown in Figure 312. The histogram plots in figure 10 clearly shows the cell performance is more sensitive to temperature when reformate is used as fuel. This is due to the fact that 10 ppm CO, the contaminant adsorbs more at lower temperature and affects available electrochemical sites for hydrogen oxidation. Table 42 shows the effect of temperature on active area and exchange current density. The temperature sensitivity to active area may be explained away due to inadequacies in controlling to a specific water content – the area calculated from cyclic voltammograms are always lower if relative humidity of the gas streams are lower. The apparent exchange current density calculated from electrochemical impedance spectroscopy increases beyond 28 %. The temperature also affects the ionic conductivity of the membrane which will in-turn show up in high frequency impedance. This change can be seen in polar curve slope change again in Figure 312.

Several cells were operated at different temperatures from 40 to 80°C at 0.6 A/cm^2 for over 1000 hours. The degradation rates were calculated based on the performance from 100 hours to the end of the testing period by using linear curve fitting on the raw data. The fluoride release was monitored throughout the entire testing period. The end-of-life (EOL) performance was collected at the end of the testing.

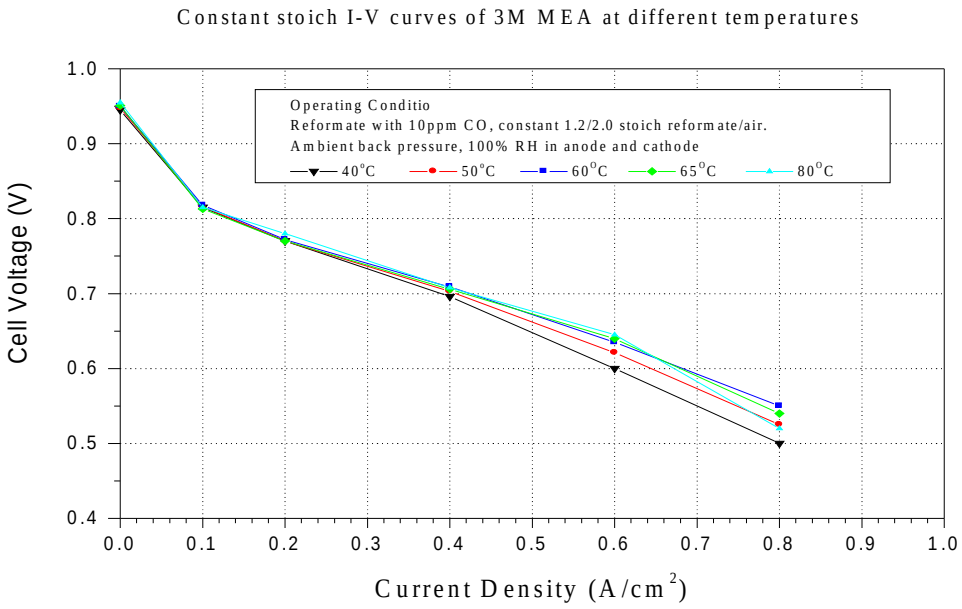

Figure 312. Constant Stoichiometry Polarization curves

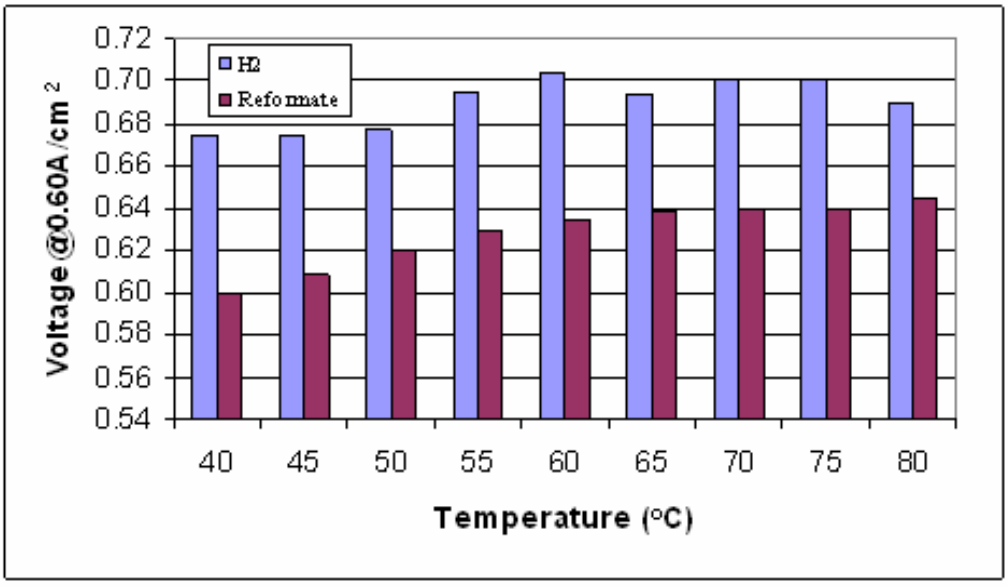

Figure 313. Histogram Plots with hydrogen and reformate as fuel

Table 42. Temperature effect on BOL electrochemical active area and exchange current density

Temperature (°C)	40	50	60	65	70	80
Anode active area (C/50 cm^2)	0.75	0.73	0.72	0.70	0.69	0.68
Cathode active area (C/50 cm^2)	1.87	1.70	1.75	1.67	1.67	1.57
Cathode exchange current density (mA/cm^2)	2.7	2.8	2.9	3.1	3.4	3.7

b) Endurance:

Six 3M Gen1 MEAs were tested over 1000 hours at 0.60A/cm^2 at temperatures of 40, 50, 60, 65,70 and 80°C, respectively, to study the performance degradation rate. The endurance results were summarized in Table 43. The degradation rate at temperatures from 40 to 70°C was about 5 μV/hr. The high degradation rate at 80°C (100 μV/hr) was probably due to flooding and the cell was only tested for 300 hours. The fluoride release rate was lowest at 40°C, and no significant difference was observed from 50 to 70°C within 1000 hour of testing. This behavior could not be explained as we were expecting Arrhenius relationship of fluoride release to temperature.
After 1000 hours of testing, cathode lost about 20 to 35% of its original electrochemical active area at all the temperatures, but anode active area loss was minimal at 60 and 65 °C, and was about 25, 10 and 17% at 40, 50, and 70°C, respectively (Table 42).

The temperature dependence for the degradation rate helped understand the life expectancy under a wide range of operating temperature. The ambient temperature will fix the stack temperature and hence it was crucial to understand the relationship to performance and life trade-off's.

Table 43. Temperature effect on cell degradation

Temperature (°C)	**40**	**50**	**60**	**65**	**70**	**80***
Active area loss after 1,000 hrs testing, anode (%)**	25	10	0	0	17	0
Active area loss after 1,000 hrs testing, cathode (%)**	34	25	22	35	30	26
Degradation rate (μv/hr)	5	6	2	6	5	100
Total fluoride released in 1,000 hrs (μg/cm^2)	15	25	32	26	29	N/A

Reactant Pressure Effects: (Steady State)

The performance of a fuel cell is affected by many factors. One of the factors is the reactant pressure. A higher pressure normally results in better fuel cell performance. But the auxiliary power consumption will be increased in order to create a higher pressure. It is then important to figure out under what kind of condition a net power gain will be achieved. Cathode mass transport is a major voltage loss contributor to 3M Gen 1 MEA. So a performance gain is expected if the cell is operated with cathode reactant being pressured and this can be predicted using (3). When the cell's backpressure was changed from a lower pressure P_1 to a higher pressure P_2, the voltage gain due to the pressure change could be expressed as:

$$\Delta V_{gain} = \alpha \frac{RT}{4F} \ln\left(\frac{P_2}{P_1}\right) = C \ln\left(\frac{P_2}{P_1}\right)$$

Equation 58.

Where α is a constant, R is the gas constant, T is temperature (K), and F is the Faraday constant.

3M Gen I MEAs with an active area of 50cm2 were used for this test at different cathode pressures using reformate/air at 1.2/2.0 stoichiometry, cell temperature 65°C, 100% anode and cathode relative humidity and 2% air bleed. The reformate was composed of 10 ppm CO, 49% H_2, 17% CO_2, and balanced by N_2. The cell was incubated according to Plug Power's standard procedure. After the incubation, the cell was tested for 50 to 100 hours to reach its stable performance. The cell performances under different cathode backpressures (0, 5, 10, 15, 20 and 30 psig) were measured using voltage meter. The anode was under ambient pressure during the testing. Experimental results with different cathode backpressure are presented in Figure 314 and the voltage gains are listed in Table 44. The cathode backpressure was set at 0, 5, 10, 15, 20, and 30 psig with operating current density of 0, 0.1, 0.2, 0.4, 0.60, 0.80, and 1.0A/cm^2, respectively. The voltage gain at a specific backpressure is almost constant when the current density is lower than 0.2A/cm^2. When the current density is larger than 0.40A/cm^2, this voltage gain increased significantly with current density. There are two major contributions to the voltage gain under pressurized condition: one is cathode catalyst activation improvement and the other is cathode mass transport property improvement. At low current density (0 to 0.2A/cm^2), almost all the voltage gain is coming from the catalyst activation improvement. At higher current density (larger than 0.40A/cm^2), some of voltage gain is also coming from mass transport improvement, and the higher the current density, the more the contribution from mass transport improvement.

Table 44. Voltage gain (m V) of 3M Gen 1 MEA under different cathode back pressures

Current density (A/cm2)	Pressure				
	5 psi	10 psi	15 psi	20 psi	30 psi
0	10	20	24	28	33
0.1	9	18	23	28	34
0.2	9	16	24	28	35
0.4	13	21	29	37	47
0.6	16	25	33	39	49
0.8	18	35	44	56	71
1	25	45	59	70	92

Pressure effect co-efficient is calculated from the gain data set (d V/ d ln (P)) and this clearly shows the change is minimal from 0 – 0.2 A/cm^2, whereas from 0.2 – 0.6 A/cm^2 the coefficient increases and is above the theoretical limit that can be obtained from (3) associated with the Nernst gains. A summary of this is plotted in Figure 309 and depicts a minimum from the summation of activation and Nernst gains. Obviously to achieve higher reactant pressure, one may need a compression device and to recover lost energy, a bottoming cycle may be needed to improve the net efficiency. However we have limited our system design to close to ambient pressure conditions.

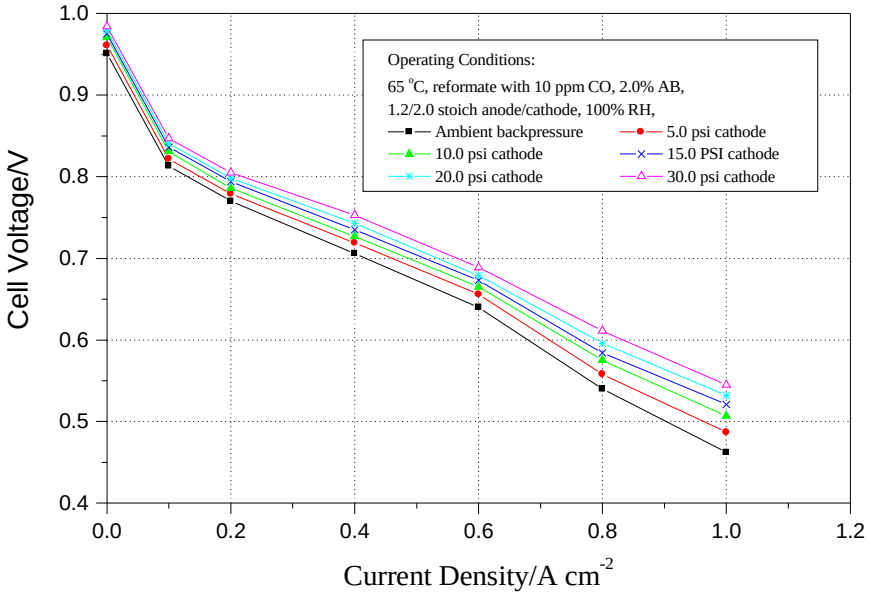

Figure 314. Reactant Pressure effects on Polarization curve

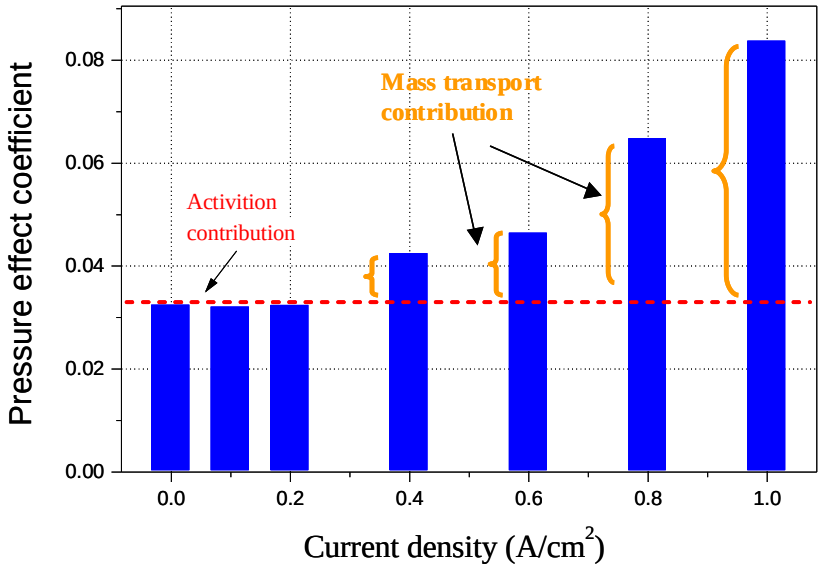

Figure 315. Pressure effect coefficient as a function of current density

CO and Air Bleeding effects: (Steady State)

Air bleed is routinely used at the anode side of PEM fuel cells operating with a CO-containing reformate in order to alleviate the anode overpotential loss from CO poisoning. The amount of air bleed, expressed as a volumetric percentage of air bled in to the hydrogen content in a reformate, depends on both CO and H_2 concentrations for a given anode. Typically this amounts to approximately 200:1 stoichiometry for O_2/CO and tends to be slightly higher for reformate with

low CO concentration. In addition to the consumption of valuable H_2 due to excessive stoich O_2, air bleed also is believed to contribute to membrane and ionomer degradation at the anode side due to the generation of hydrogen peroxide radicals. It was thus important to find out experimentally the optimal air bleed level for a particular reformate and to establish a relationship between air bleed/CO level and cell degradation rate/lifetime. 3M Gen I MEAs with an active area of 50 cm^2 were used for this study with a Plug Power standard single channel serpentine test rig. The stoichiometry is 1.2/2.0 for reformate/air at 0.6 A/cm^2. The cell operates at 65 °C, 100% RH at the inlets of both anode and cathode, and a fixed air bleed level. House reformate was used for 10 ppm CO/Air Bleed (AB) endurance tests, which is composed of 48% H_2, 17% CO_2, and balanced by N_2 and bottled gases were used for 100 ppm CO. The fluoride release was monitored throughout the entire testing period. The air bleed sensitivity results for 10 and 100 ppm CO reformates are plotted in Figure 316

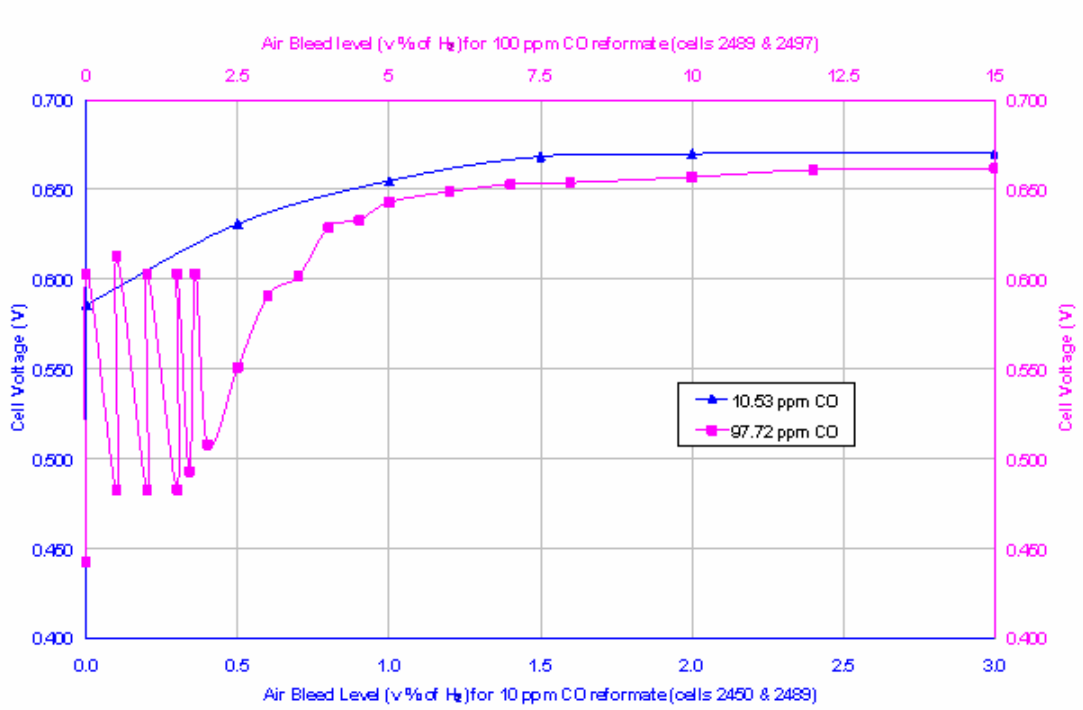

Figure 316. Air bleeding effect on performance with varying amounts of CO.

For example, 1% and 1.5% air bleeds were selected for the 10 ppm CO reformate endurance tests. For 100 ppm CO reformate, air bleed levels were set at 5, 7.5, and 10% to represent the sweet spot range. Substantial performance loss was observed without air bleed, with the 40% H_2 reformate experiencing more voltage drop than the 48% H_2 reformate. There was not a substantial voltage improvement going from 1% to 2% air bleed: + 5 mV at 1.5% AB and another + 1 mV at 2% (Measurement Systems Analyses shows +/-3 m V error on these stations). Through endurance test results, cells with lower air bleed have lower fluoride release rates and appear to have lower voltage degradation rates However, cells running with lower air bleed were more sensitive to transient CO effect. These factors must be balanced when selecting the air bleed setting.

Figure 317 shows the results in the red sections from the endurance tests using100 ppm CO reformate (cylinder) at 8 % air bleed levels (note: the blue sections are tests using 10 ppm CO house reformate). The tests were carried out for 600-700 hours each. The initial air bleed levels were set at 8, 10, and 12%, respectively. The cell with 12% air bleed was switched to 6% air

bleed after 166 hours of testing because the cell could not maintain a stable voltage. This is likely due to the low actual anode fuel stoich as a result of the very high air bleed level. With a 12% air bleed (i.e., 12% of H_2 input), the actual H_2 stoich was only 1.06 when the H_2 input flow was set at 1.2 stoich.

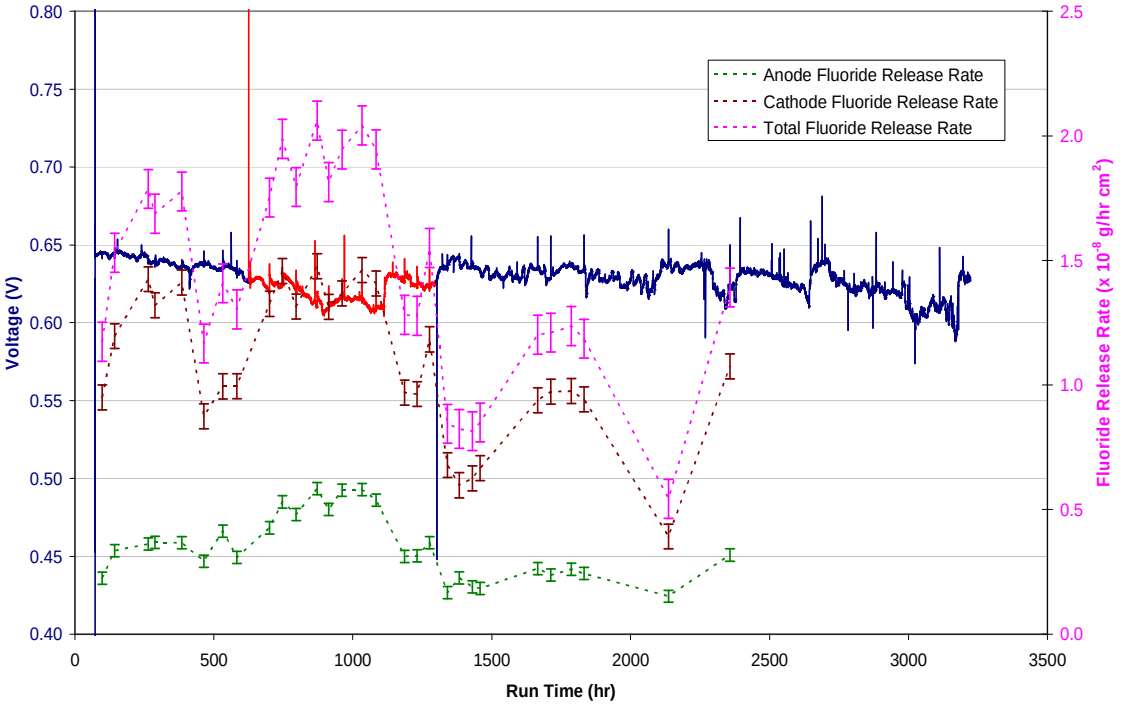

Figure 317. 100 ppm CO with 8 % AB Conditions

All three cells experienced accelerated voltage decays (red sections) as compared to the performances of the same cells using 10 ppm CO reformate (2% air bleed, blue sections). However for the most part, these voltage losses were not permanent. They could be recovered either through a purging or a startup/shutdown. This suggests that there could be a slow CO accumulation at the anode electrodes resulting in recoverable voltage decay, a phenomenon often associated with insufficient air bleed. The apparent voltage decay trend is depicted in Figure 318. The apparent voltage decay rate decreases as air bleed level increases until the air bleed level hits a certain level (~ 10%). Afterwards, the voltage decay increases dramatically probably because the low actual anode (under) stoich now plays a more important role. Although there is no significant difference in voltage performance at the beginning of life for air bleed levels higher than 5%, stable long term cell performance requires a much higher air bleed level.

Figure 5. Voltage decay at different Air bleed level

0.6 A/cm^2, 1.2/2.0 ref/air, 100% RH, 65^{o}C; 100 ppm CO, 48% H_2, 15% CO_2, balance N_2

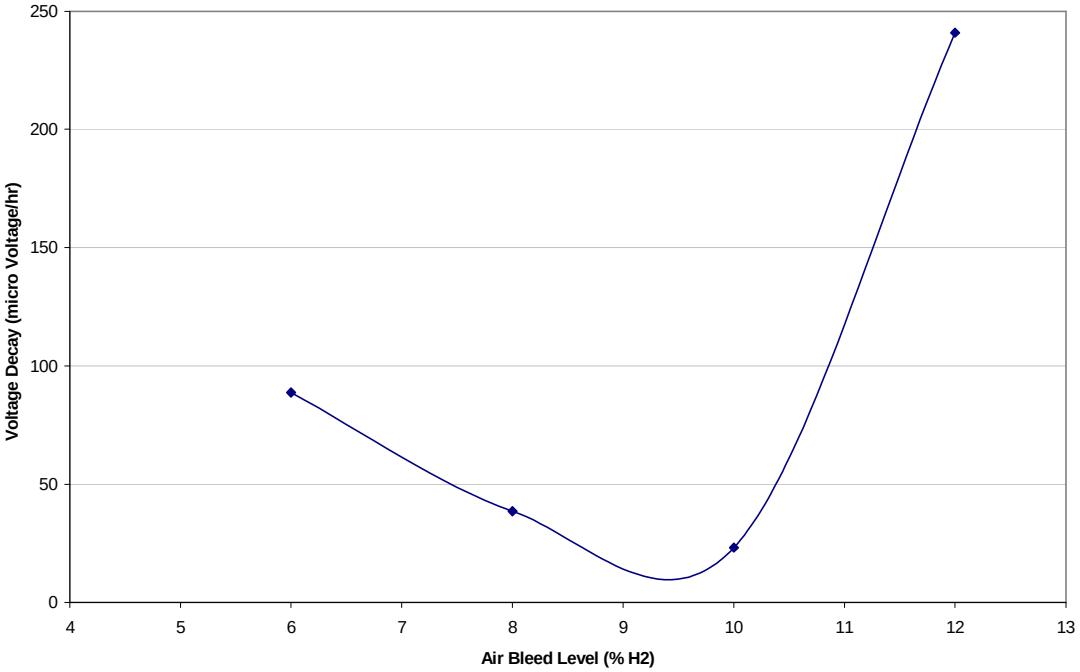

Figure 318. Temporary Voltage degrade rates as a function of air bleeding

Except for the 12% air bleed data point, the fluoride release rate follows the general trend of higher air bleed leading to higher fluoride release rate (Figure 319). The abnormal data point for 12% air bleed test could be a facility issue since this cell also showed unusually low anode exhaust water for both 12% and 6% air bleed tests. One intriguing observation is that the changes on the anode side also affect the cathode side fluoride release rate, which follows essentially the same trend as the anode side as seen in Figure 320. Such synergetic effect has been observed elsewhere where a change in either anode or cathode side causes in the same direction a change in the opposite side of the membrane. It is not clear whether this is due to cross-membrane transport of certain species such as H_2O_2 and HF, or a combination of them. This is useful in optimizing CO levels and air bleed percentages to minimize performance losses, but also to gain tolerance during transients where CO levels could reach a maximum of 500 ppm. Also this gives an indication of the nominal CO concentration. All of our system points have been designed for nominally around 10 ppm CO with 2 % Air bleed. However typically excursions are seen and recorded in our database.

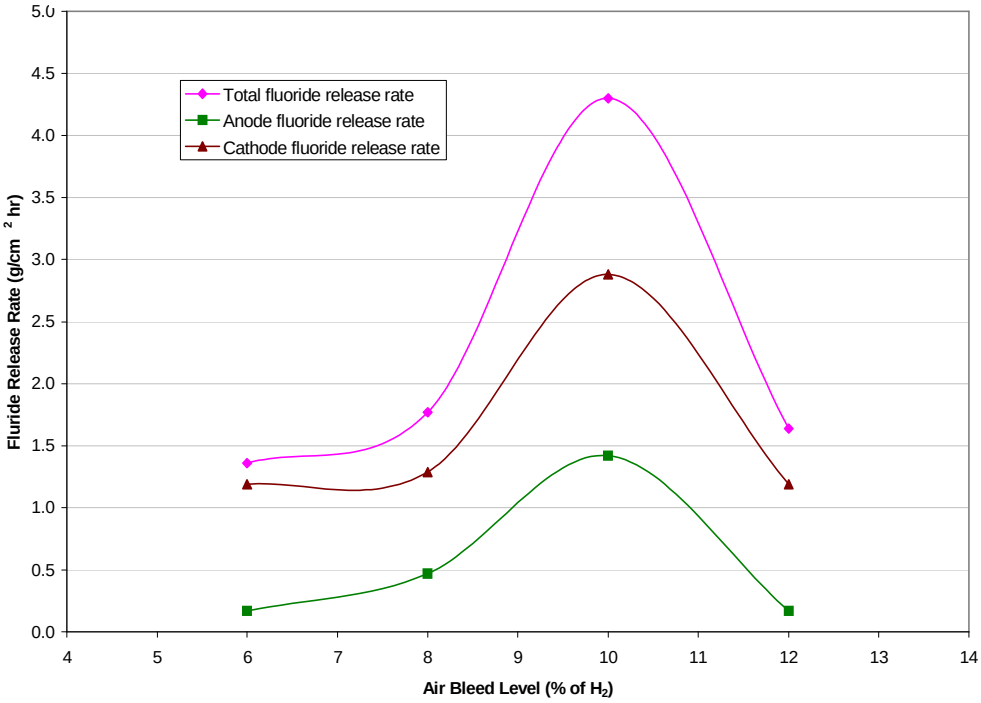

Figure 319. Fluoride release rates as a function of air bleeding at fixed CO level

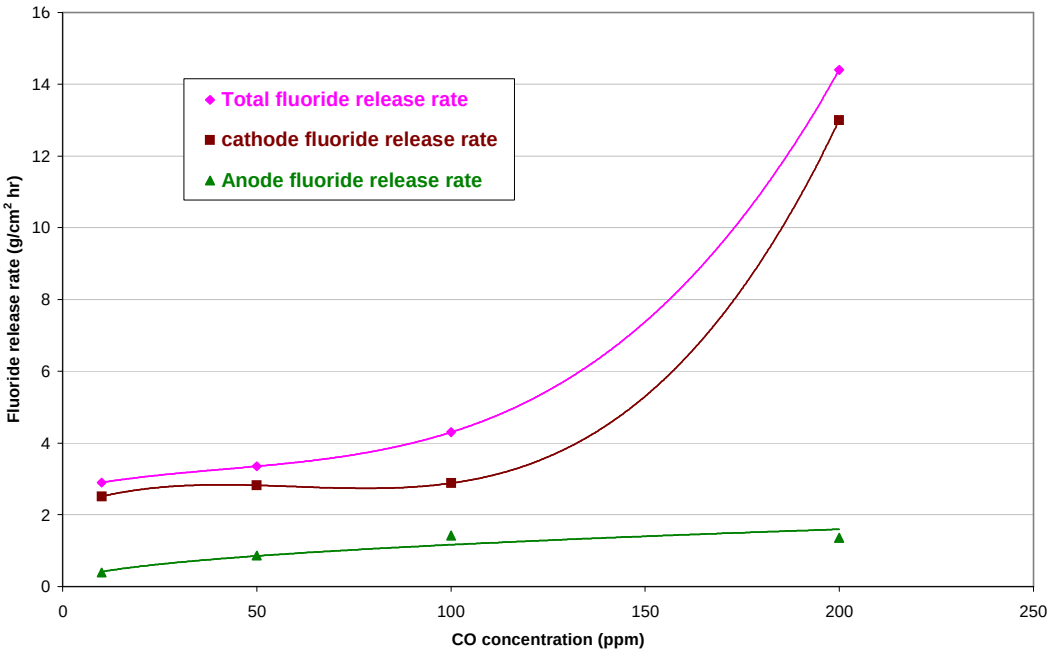

Figure 320. Fluoride release rates as a function of CO level

Reactant Relative Humidity Effects: (Steady State)

RH is an important factor that may influence the voltage degradation rate and lifetime of an MEA because membrane dry out causes ionomer loss and electrode/membrane interface delamination. Maintaining 100% RH at both the anode and cathode is nominally desired. However, in real system, it is very difficult to maintain the RH exactly at 100%RH. In the Plug Power system, since we reform the fuel to produce H_2 we also produce water to create enough water on the anode side, however on the cathode side, the product water is expected to humidify the cathode side. This means the relative humidity at the cathode will be impacted by several factors including flow, inlet temperature, coolant inlet and outlet of a fuel cell. It is thus useful to examine how much effect a lower RH will have on a fuel cell. There is no significant impact on initial performance as shown in Figure 321, however as time develops, the degradation rates become critical. It is desired to develop this relationship to understand the capability of systems to handle such exposure. So in all our experiments, the anode was retained at 100 % R.H and the cathode stream was varied.

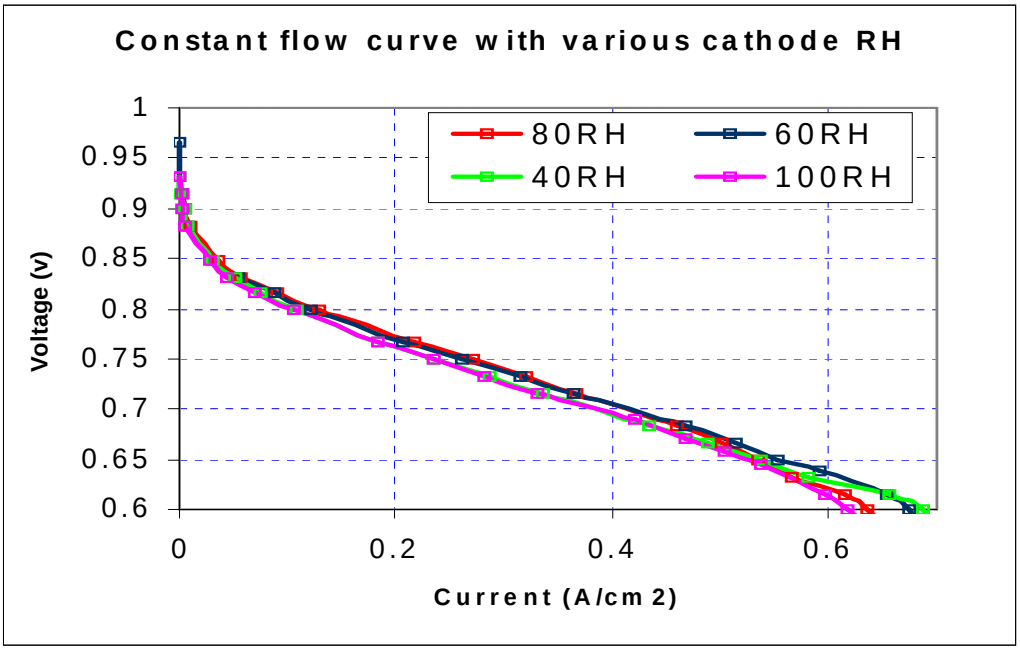

Figure 321. Polarization curves at different cathode RH

The cell 1 KHz impedance increases and the membrane ionic conductivity decreases with the decrease in RH, especially at RH lower than 80%. Overall the degradation rate increases with the decrease in RH as shown in Table 45. The fluoride release rate increases when RH decreases from 100% RH to 40%RH as shown in Table 46. It is clear that the time at low RH will significantly impact stack life and when autopsy was performed, a 10 – 20 % membrane thinning was measured when using < 60 % RH cathode inlet conditions. Typically in systems, high efficiency methods are used for transferring water back into the cathode inlet stream and evaporative methods are used to maximizing water by retaining the water in the vapor phase.

Table 45. Voltage degradation as a function of RH in the cathode streams.

RH (%)	Testing hours	Current density (A/cm^2)	Degradation rate (µv/hr)
40	1000	0.6	40±3
60	1200	0.6	17±4
80	1050	0.6	20±2
100	1300	0.6	3±2
120	1050	0.6	1±3

Table 46. Fluoride release rates as a function of cathode RH

RH (%)	Current density (A/cm^2)	Total fluoride release rate 10^{-8} g/hr.cm^2	Cathode fluoride release rate 10^{-8} g/hr.cm^2	Anode fluoride release rate 10^{-8} g/hr.cm^2
40	0.6	4.89	4.07	0.82
60	0.6	3.54	3.25	0.29
80	0.6	3.52	3.02	0.50
100	0.6	2.85	2.25	0.60
120	0.6	2.67	2.37	0.31

Cation Contamination effects:

During a fuel cell operation, cations could leach out from difference sources, such as the catalysts, GDLs, plates, gaskets, insulation materials and other stack components, humidifiers, fuel processor, and connection tubing and pipes. The common cations to contaminate a fuel cell generally include alkali metals (e.g., Li^+, Na^+, K^+, Rb^+, Cs^+), alkaline earth metals (e.g., Mg^{2+}, Ca^{2+}), transition metals (e.g., Ag^+, Ni^{2+}, Mn^{2+}, Cu^{2+}, Zn^{2+}, Cr^{3+}, Al^{3+}), ammonium (NH_4^+) and its derivatives. Those cations could get into the proton-exchange membrane and the ionomer within the electrodes to replace out the protons and thus lowering the proton conductivity. The incorporation of cations could also affect the membrane structure and thus its other properties, such as the mechanical strength, cross linking, water content, and proton osmotic drag numbers. Subtask 6.2 focuses on the identification of system contamination. Based on our experience, fuel cell contamination is dominated by cations. In this report, we report the physical properties and performance changes of 3M Gen I MEAs after being contaminated by different cations.

1) Contamination Procedure: For each cation contaminated aqueous solution, two 3M Gen I MEAs were soaked in for 15 min at 80^{o}C. The solution was then cooled down naturally to room temperature and let it stay over night to make sure that the ion exchange between the proton and the cation reached equilibrium. The MEA was then taken out of the solution and dried at 80^{o}C for 30 min. One of the MEA was used for ICP analysis to determine how much of the cation was exchanged into the edge membrane, GDL, and the catalyst-coated membrane (CCM), respectively; and the other MEA was assembled into a 50-cm^2 single cell fixture for fuel cell testing.

2) Fuel Cell Performance Evaluation: The MEA was incubated using Plug Power's standard procedure and was tested at 65 ^{0}C using reformate/air at 1.2/2.0 stoichiometry and 2% air bleed at100% RH for both the anode and cathode. The reformate was composed of 10 ppm CO, 48% H_2, 17% CO_2, and balanced by N_2. Cyclic voltammetry (CV) and AC impedance were acquired to help identify the reasons causing the fuel cell performance and other physical property changes after contamination.

3) Results

a. Membrane Property Change

When some of the protons in the membrane are exchanged with other metal cations, the membrane microstructure may change. Table 47Table 7 lists the change of ion exchange capacity, water uptake, cluster diameter, number of fixed charge sites, and cluster surface charge density change associated with Na^+ and Ca^{2+} contamination, respectively. The parameters shown in Table 7 were calculated based on Nafion cluster model from the literature.

Table 47. Membrane Property Change Associated with Cation Contamination

Ion exchange extent	Ion exchange capacity (mol/g)	Water uptake at 70^{o}C	Cluster Diameter (Å)	Number of fixed charge sites (for 50 cm^2) N_{SO3-H}(x10^{20})	Cluster surface charge density (Q/mol)
100% H^+	1.0	35	27.5	1.84	0.527
20% Na^+	0.8	30	22.5	1.62	0.490
30% Ca^{2+}	0.7	28	22.5	1.42	0.476

Ion exchange capacity was calculated from ICP analysis result. The number of the fixed charge reflects the total sites available for the proton conductance, and it is directly related to the proton conductivity and proton transport in the membrane. The cluster is another factor reflecting the membrane microstructure such as the localized membrane situation.

Number of fixed charge site is calculated by the following equation

$$N_{So3} = \frac{\rho_{dry} V_{dry} L_A}{EW}$$

Equation 59

where

N_{So3}: number of fixed charge sites

ρ_{dry} : dry membranes density

V_{dry} : dry membrane volume

L_A : Avogadro's number

Cluster surface density was obtained by first calculating the total number of sulfonate groups in the membrane, and then divide this number by the total amount of pore surface area:

$$\sigma = \frac{\rho_{dry}(1-\theta)\alpha F}{2\theta EW} \quad (5)$$

where

σ : surface charge density
θ : membrane porosity
EW: equivalent weight
F: Faraday's constant
A: pore radius (m)

It can be concluded based on the data shown in Table 47 that the water uptake, the cluster diameter, the fixed charge sites, and the cluster charge density were reduced after the membrane was contaminated with the metal ions.

b. Amounts of Contaminants Exchanged into MEAs

After the MEAs had been contaminated by the method described above, the metal ion concentrations in the GDL, the edge membrane, and the catalyst-coated membrane (CCM) were analyzed by ICP. The results are shown in Table 48. It was found that the highest concentration of the metal ion was in the edge membrane and the lowest was in the GDL. Also, the CCM picked up much lower metal ions than the edge membrane.

Table 48. Metal Ion Concentrations in the edge Membrane, GDL, and CCM

Contaminates	Conc. in GDL(ppm)	Conc. in CCM (ppm)	Proton exchanged by metal ion in CCM (%)	Proton exchanged by metal ion in edge membrane (%)
25ppm Fe^{2+}	305	3961	14	44
25ppm Al^{3+}	301	2917	20	63
75 ppm Na^{+}	330	1734	15	51
25ppm Ca^{2+}	320	2950	20	60

c. CV, Impedance, OCV and Performance

Table 49 summarizes the electrochemical active surface area, 1 kHz impedance, OCV and cell performance after the MEAs were contaminated with different metal ions. After the MEAs were contaminated with Al^{3+}, Ca^{2+} and Na^{+}, the cells showed similar OCV as the baseline MEA; however, the one contaminated with Fe^{2+} showed a 30-40 mV lower OCV. No obvious crossover was found after a crossover leakage check. Two other repeat Fe^{2+} cells showed similar result regarding the OCV. It is possible some redox reaction could be occurring at the electrode site. All the contaminated MEAs showed lower performance than the baseline MEA, and the one contaminated with Al^{3+} suffered the most, while the one contaminated with Na^{+} lost the least amount of performance. The 1 kHz impedance that reflects the total ohmic resistance of the cell increased significantly for the MEAs contaminated by Ca^{2+} and Al^{3+}, but that of the other two MEAs contaminated by Na^{+} and Fe^{2+} did not show much change.

Table 49. Effects of Contaminants on CV, Impedance, OCV and Performance

Contaminants	OCV (V)	Voltage at 0.6A/cm^2 (V)	1kHz Impedance	Cathode and anode ECSA

			(mohm/50cm^2)	mC/50cm^2
Baseline	0.968	0.648	1.32-1.45	C:1864 A: 650
25 ppm Fe (II)	0.900- .942	0.601	1.32-1.42	C:1590- A: 720
25ppm Ca (II)	0.95-0.970	0.594	1.75-2.01	C:1685 A:761
25ppm Al (III)	0.950-0.960	0.589 (at 0.4 A/cm^2)*	1.75-2.00	C:1562 A: 583
75 ppm Na (I)	0.965-0.975	0.624	1.40-1.58	C:1400 A: 677

* MEA contaminated by Al^{3+}, the cell could not reach a current density of 0.6 A/cm^2.

The mass transport of the MEAs illustrated by the impedance spectra in Figure 322 increased in the following sequence: $Na^+ < Fe^{2+} < Ca^{2+} < Al^{3+}$. The cathode electrochemical active surface areas of all the contaminated MEAs were lower than that of the baseline MEA, while the anode electrochemical active surface areas did not show any trend. Some of the failed stacks were later autopsied, but no significant contamination was found from failed MEA's from stacks in reliability fleet.

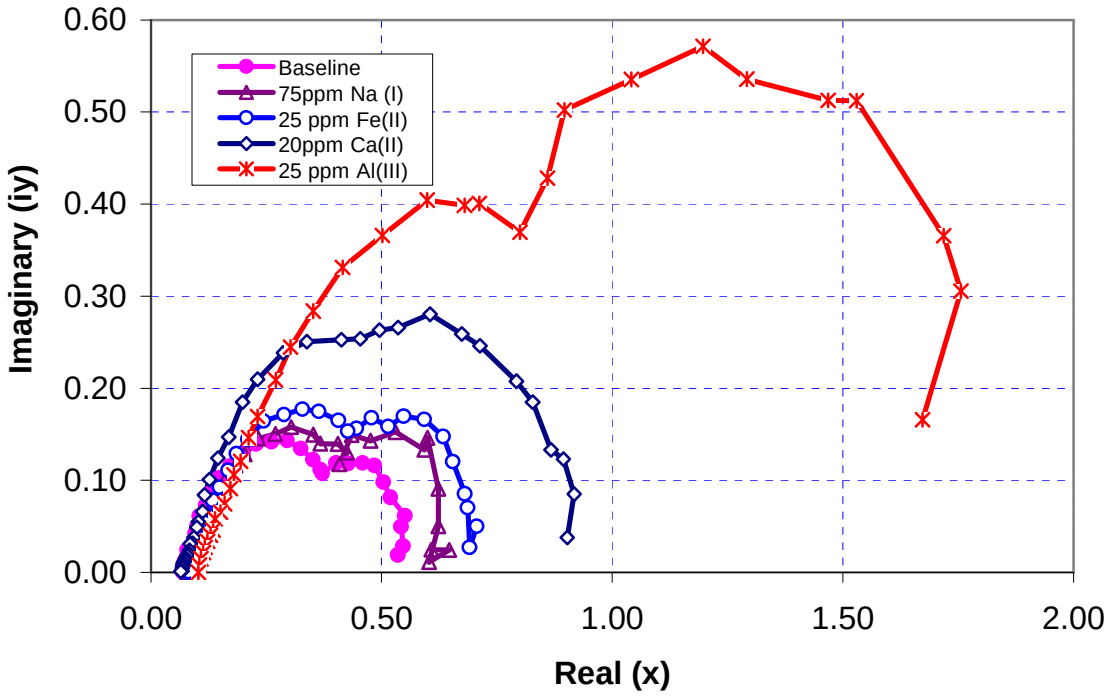

Figure 322. Nyquist signatures of various cation contaminants

6.1.3 Stack Failure Analysis & Signatures

In order to understand and correct life limiting stack failures, twenty-five failed stacks from laboratory and field testing have undergone failure analysis (FA). The FA included stack

operation diagnostic tests, visual inspection and SEM analysis. These stacks had running hours from 1100 to 3800 and the average stack life is around 2400 hours. All stacks analyzed to date form a baseline for perfluorosulfonic acid membrane based MEAs tested. This analysis allowed the correction of several MEA life limiting failures to be corrected. The FA results are summarized in Table 50. The primary failure mechanisms observed are cell #1 failure, membrane crossover leakage, MEA activation loss and GDL/plate electrical shorting. The various failure modes discovered through this analysis have been addressed through design modifications for the DOE4 final stack testing. This activity is an important step to ensure that failure modes that are independent of MEA design have minimum impact on the final MEA tests.

About half of stacks failed due to a high voltage degradation rate of cell #1. For all cell #1 failures, corrosion products were found in the coolant ports. The coolant port gasket was damaged and underwent anomalously high compression stress relaxation. This resulted in cell shorting due to plate edge contact. As a containment action, a coolant polishing filter has been installed in the system and a significant improvement in cell #1 durability has been observed.

Membrane crossover leakage is the second most often observed failure mode. This mode is addressed with the improved membrane developed under the 3M/DOE project. When the 3M/DOE MEAs are operated in the system testing planned, comparisons will be drawn with respect to the behavior reported for the 3M MEAs in this report.

Several stacks failed due to cathode damage due to frequent startup and shutdown activity. This was found to be due to the presence H2/Air interface that propagates on the anode side during inappropriate startup and shutdown. This leads to severe carbon corrosion in cathode electrode, resulting in significant activation loss of the catalyst layer. The startup and shutdown procedures have been improved through several changes.

Electrical shorting due to plate-to-plate or electrode-to-electrode contact is another failure mode that has been observed. To contain this problem, an insulation layer has been applied on the plate edge surface. Also, studies are underway intended to determine if a reduction of the compression force will significantly reduce electrode-to-electrode shorting.

Reliability growth planning for the fuel cell stack has been formalized as part of the effort to ensure maximum MEA operating life. The effort is focused on identifying both known and potential failure modes and mechanisms from development testing experience and failure analysis data. A Design Failure Modes & Effects Analysis (DFMEA) approach is being used to catalog and prioritize the failure modes and their causes. Reliability has been quantified for the development fleet as base-lining continues in preparation for testing of MEAs developed under the 3M/DOE project.

Table 50. Stack Failure Causes Identified by Autopsy

Stack Name	Cell#1 Failure	Cathode Electrode Damage	Other Individual Cell Failures					Run Hours (I>2A)
			Electrical Shorting	Crossover Leakage	Electrode Damage	Mass Transport Loss	No Defect Found	
95T	□					□		1841
X3		□						2211
S20B03	□	□						2576
DIP1				□				2712

S20B06	□							2560
S20B04		□						3800
X4		□						1935
S32B03	□							2011
S20B05	□	□						1831
S28B11	□							1700
X2		□						1100
S28B07					□			2200
S28B09							□	2200
S28B10	□		□	□				3170
S32B04	□							2800
S28B05	□							1600
S28B03	□							2700
S28B12			□	□				2700
S28B02			□	□				2600
S24B03	□							1200
S28B14			□	□				2700
S28B13			□	□				2500
S32B02	□			□				3500
S28B08				□				3300
S24B02	□			□				2750
Total: 25 stacks	13	6	5	9	1	1	1	average:2400

Design initiatives have been developed based on identified failures. The Plug Power reliability test fleet is being used to demonstrate the expected MEA reliability improvement due to these design improvements and results to date are positive. Pareto shows once the cell 1 failure was fixed, the crossover (39 %) and the electrode damage (21%) would dominate as the life-limiters. The cell 1 failure was addressed in the later iterations due to some critical changes in the thermal management system and also due to eliminating air gap between the cell plates at the corner locations.

6.2 Design Mitigation and Verification:

6.2.1 Membrane Cross-over:

Early indications showed pinholes developing inside the active area and also around the edges of the membrane in the outside perimeter – around 30 – 60 mils from the visible GDL edge. Plug Power attributed this behavior mostly due to membrane hydration management along with interaction with silicone gaskets that are injection molded on the plates. Since then, Plug Power and 3M collaborated on the edge protection since most of the preliminary failures were due to the membrane embrittlement near the edges of the exposed membrane. The long-term membrane failures inside the active area were addressed through 3M's Rev 3 membrane development program. Plug Power evaluated edge-protection based on silicone-based, epoxy-based UV cure and also film sub-gasket materials from 3M. Though we had initial success with silicone based edge protection systems, early analysis showed high activation and mass-transport losses at all current densities within 1200 hrs of test as shown in Figure 323. The polarization curve shows a beginning of life (BOL) comparison with end of life (EOL) at 1200 hrs.

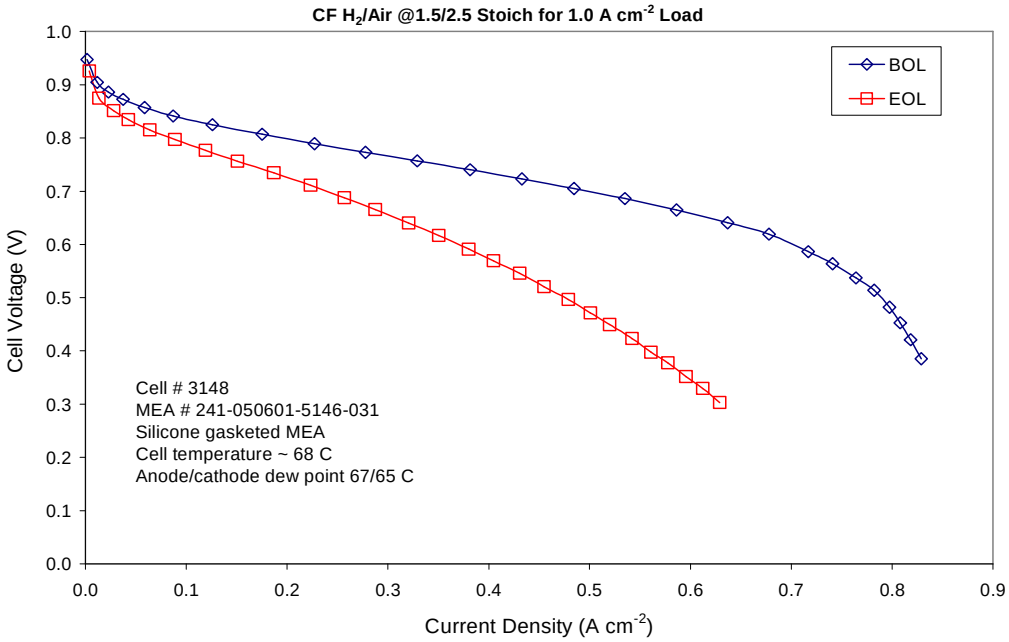

Figure 323. Edge Protection using silicone sub-gaskets

This provided the motivation to shift focus to UV cured epoxy systems and discontinue the development with silicone based sub-gaskets. In 2006 Q1, the Plug Power team started evaluating 3M sub-gasketed MEAs in four 8-cell modules B, C, D, and E. In addition, 3 stacks were also run in accelerated protocol. Module B was removed from testing after 500-hr to inspect the sub-gasket layer and an autopsy/visual inspection was complete. The other three modules have completed 1500-hr endurance tests as shown in Figure 324 and some end of life autopsy. It was interesting to note that the modules passed the leak test given that they ran through an accelerated protocol developed internally at Plug Power – subsaturated anode and cathode with H2/Air as the reactants with Propylene glycol /DI as the coolant.

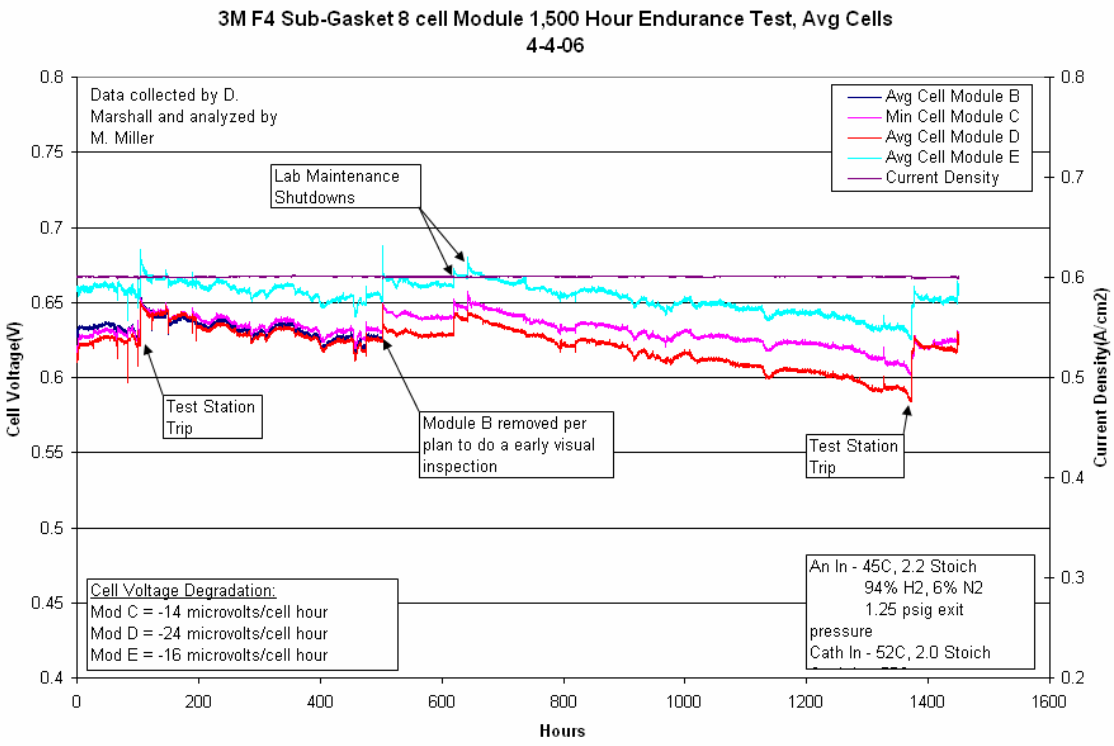

Figure 324. Edge Protection using UV cured epoxy systems (F4) – 8 Cell Modules

The 500-hr inspection showed some fracture in the F4 (UV cured epoxy) sub-gasket. These fractures were found only under the region compressed by the stack-plate gaskets. This was suspected to be due to excessive gasket forces causing failure of the sub-gasket material in this region; the plate-gaskets had not been optimized for introduction of the additional thickness associated with the sub-gasket. To ensure that the fracture was not due to some other factor such as chemical damage, it was decided that modules run to 1500 hours would be inspected to determine if there was additional deterioration of the sub-gasket.

Figure 325. shows a comparison of sub-gasket fracture after approximately 500 and 1500 hours of module operation. After 1500 hours fractures were found only in the region under the plate-gasket, as observed after 500 hours.

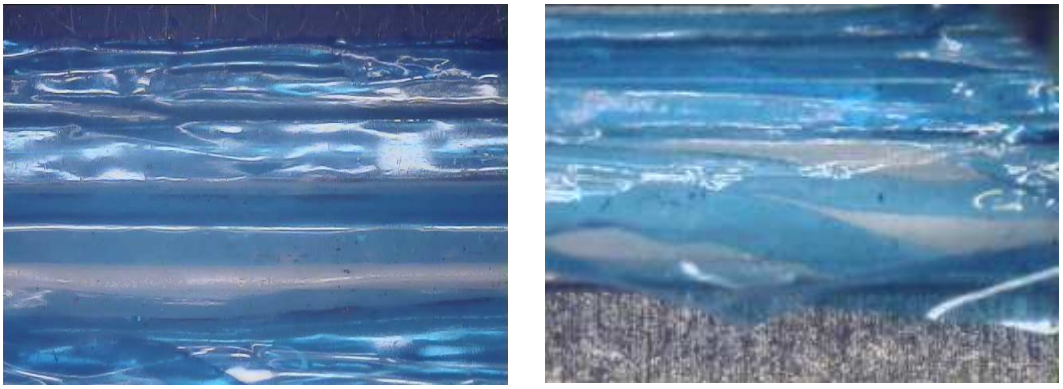

Figure 325. Comparison of Sub-gasket Fracture from 8 cell modules at ca. 1500 hours (left) and at ca. 500 hours (right)

Similar behavior was observed for subgasket fracture in full stacks as seen in Figure 301Figure 326 Only one example of a fracture of the subgasket was observed in the membrane border region between the plate-gasket and the GDL; more than 3000 cm of gasket perimeter was inspected. This leads us to conclude that gasket overload plays the primary role in the fractures observed and that the subgasket system provides excellent protection of the membrane border region. However, Figure 326 also shows that there is a tendency for subgasket adhesion to the plate-gasket (this was observed in both modules and stacks). This adhesion is expected to exacerbate the tensile stresses in the plane of the subgasket. This indicates that adhesion must be taken into account during gasket/subgasket system design.

Figure 326. Subgasket Fracture at ca. 1100 Hours from Full Stacks. Typical Border Region Fracture (left) and Gasket Adhesion Example (right).

Film barrier seems the most likely candidate due to favorable scenarios associated with both mechanical and chemical properties. 3M has built DOE4 MEAs with PEN sub-gaskets. A 1-mil PEN with 0.5 mil adhesive was applied to both sides of standard membrane and the MEA was prepared in 3M. Samples were shipped to Plug Power and were evaluated for performance and durability. Initially the performance at the same compression seemed to be lower for the MEA's with the PEN gaskets. Then we realized that some active area was lost due to the cell construction. Once we corrected for this dead-band of active area, this compensation resulted in a performance equivalent to the unsub-gasketed DOE catalyst module. The polarization curve comparison is shown in Figure 327 and the conditions are listed in the figure.

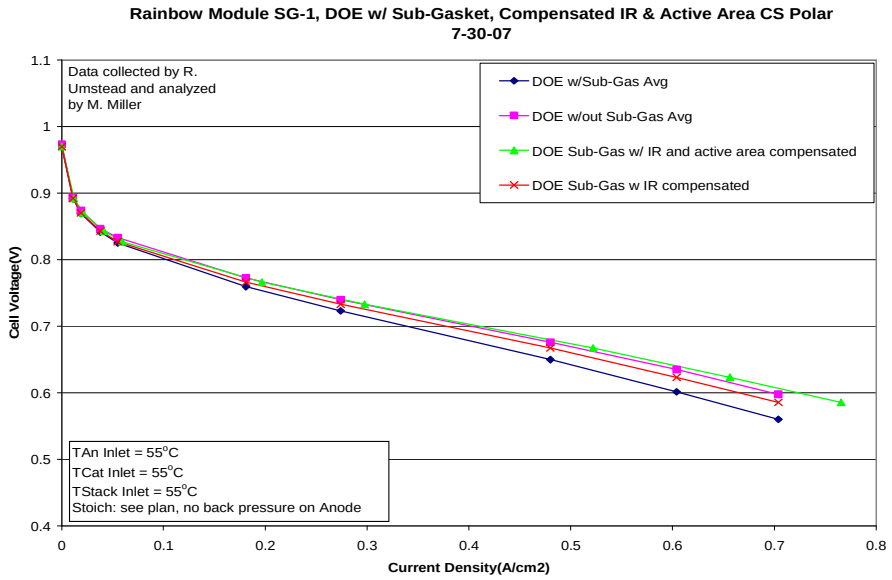

Figure 327. Film Subgasketed MEA Polarization curves.

Adding this rigid layer did affect the compression in the active area. It was crucial to understand the effect of this film thickness and properties on the active area loading. The active area loading is crucial to retain good performance. In addition, the loading will shift to the gasket area. From the gasket design perspective, it is equally important to define the maximum stress at the edge location. Plug Power purchased Topaq Imaging equipment under the DOE funding and pressurex films to record the transference of pressure under baseline conditions and with these sub-gaskets. This will help us to optimize the gasket design and also the film thickness requirements. Under similar loading of 4000 lbs, one could see the difference between the baseline in Figure 328 and the subgasketed MEA in Figure 329

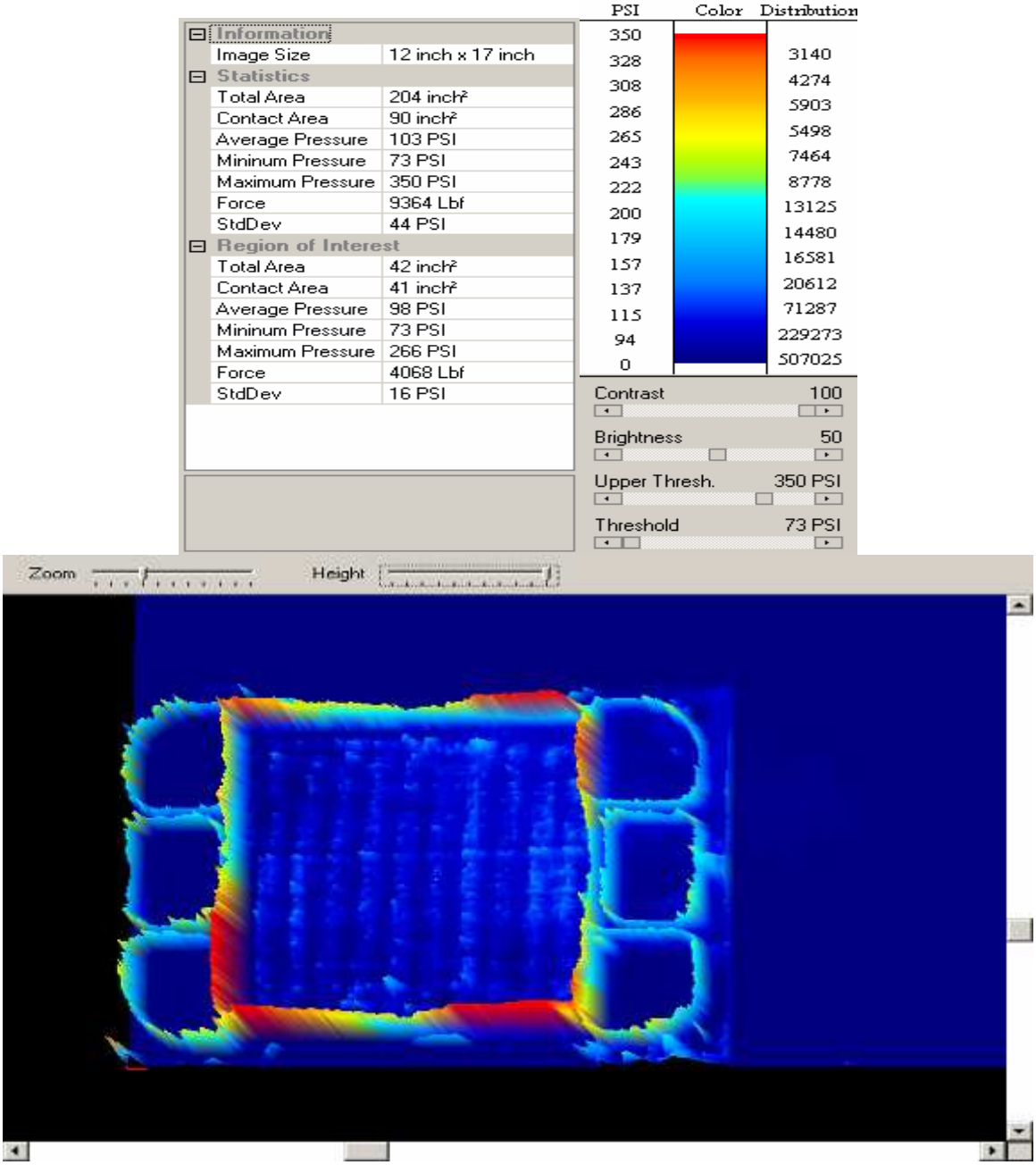

Figure 328. Pressure Scan of Baseline MEA against a 264-cm2 plate

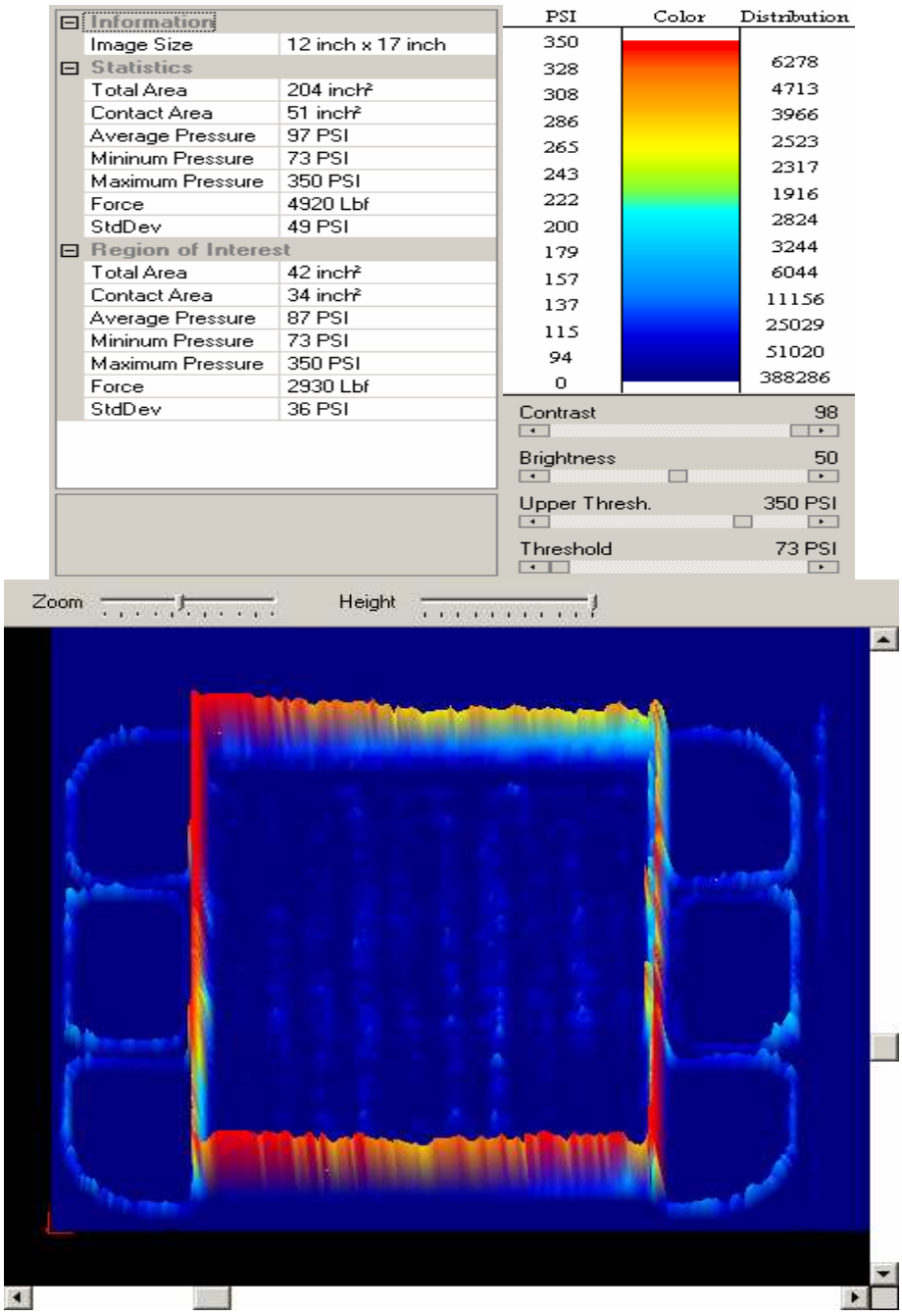

Figure 329. Pressure Scan of subgasketed MEA against a 264-cm2 plate

Currently endurance tests are ongoing to ascertain the fix effectively at the edge location. Meanwhile future improvements are under discussion for this design. This includes decreasing the dead-band around the edge area and also possibly avoiding a 3-mil step at the gasket with extended design around the coolant and reactant ports.

6.2.2 Plug Power Accelerated Module Summary: (Rev 2 vs. Rev 3 with final DOE-4)

Four 8-cell modules were built and were operated under conditions known to accelerate MEA damage. Two modules were testing in accelerated condition 1 (Condition 1): 1.4/2.0 Ref/Air Stoich, 10ppm CO w/air bleed, anode inlet dew point = 75 Celsius, cathode inlet dew point = 64 and 75 Celsius switching with a 12 hour period, anode and cathode dry bulb temperature = 75 Celsius. The current is cycled on an approximate daily basis and is operated at 0.3, 0.4, 0.5 and 0.6 amps/cm^2. Two remaining modules followed the condition 2 (Condition 2): 1.4/2.0 (Reformate/Air) Stoich, 10ppm CO w/air bleed, anode inlet dew point = 75 Celsius, cathode inlet dew point = 64 and 75 Celsius switching for two days and five days, respectively (note that during the two day period, current density is held at 0.05 amp/cm2 and during the 5 day period the current is cycled through the other current densities). The anode and cathode dry bulb temperature = 75 Celsius.
Figure 330 shows the outcome of the test with respect to crossover failure mode. Rev 3 clearly outperformed Rev 2 MEA outlasting a statistically significant 1800 hours and 2 cells failed due to material interaction with the gaskets. It is also interesting to note that the DOE 4 final module outlasted Rev 2 MEA under the normal condition and a linear fit showed a 4 micro-volts/cell-hr degradation. The module did not exhibit **ANY** crossover at that point of the test.

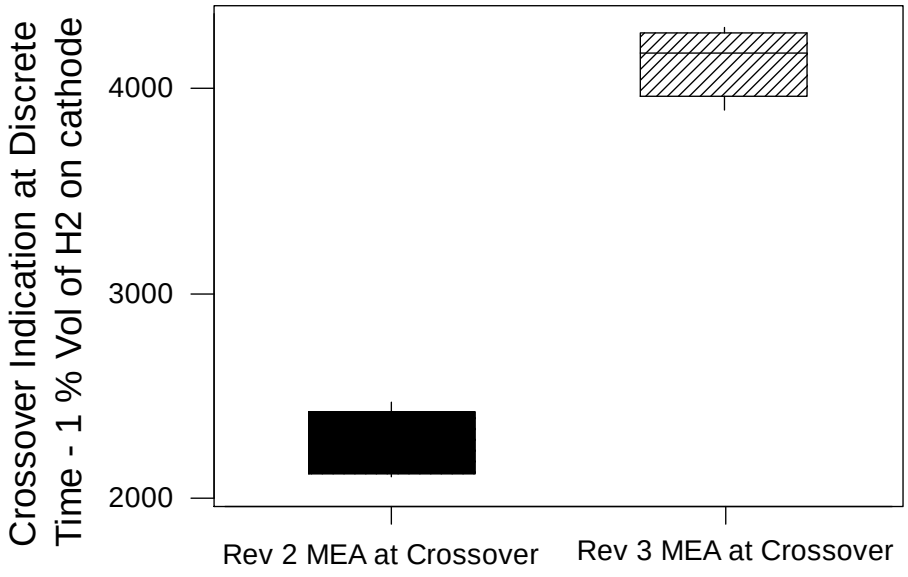

Figure 330. Box Plot of Rev 2 vs. Rev 3 MEA Crossover Metric

Between the edge protection and the modifications with DOE Final membrane, it is expected that we outperform any prior system endurance. From the 50-cm^2 single cell and also full scale active area with 8-cell modules has shown improvement. It is interesting to note that the DOE final iteration module actually showed no cells > 1 % vol of H_2 on the cathode side.

6.2.3 Cathode Electrode Damage:

Starting and stopping of fuel cells have recently been extensively studied and many operational strategies can be deployed to mitigate carbon corrosion during startup/shutdown. The magnitude of carbon corrosion has to be fully understood in order to improve the design for specific operational requirements. This requires developing an understanding of the requirements for an MEA to be robust to starting and stopping.

Start/Stop Modeling Analyses:

In this report, the cathode carbon corrosion during the start/stop is investigated by modeling a corrosion cell under different conditions. Some preliminary experiments were also conducted to quantify the improvement of the DOE-4 final catalyst over the Rev 2 CCB version. The purpose of this work is to assess the magnitude and extent of carbon corrosion and to develop effective mitigation strategies. A 3D model that describes the interrelated electrochemical reactions and transport of species and charges is developed to predict the carbon corrosion current density distribution and the effect of water present at the cathode.

In the simulations, single-channel geometry is employed where the half-cell is modeled with symmetric boundary conditions, as shown in Figure 331. The conservation equations of mass, momentum, species and charges coupled with electrochemical reactions kinetics are solved using commercial CFD software STAR-CD by implementing user-defined subroutines.

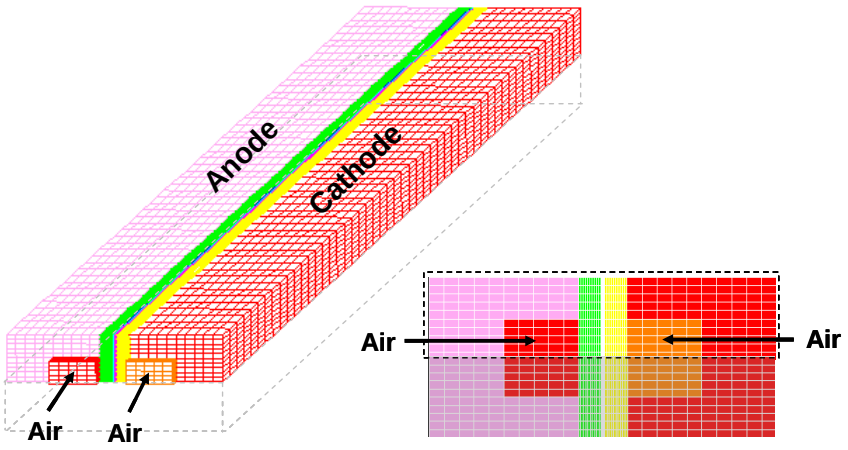

Figure 331. Mesh Used in Simulation

A reverse current is applied on the corrosion cell to simulate the current imposed by the hydrogen oxidation during fuel cell startup/shutdown. Current densities ranging from 2 mA/cm^2 to 100 mA/cm^2 are studied using the present model where cell voltages on the corrosion cell and carbon corrosion rates with different RH conditions are predicted. In the first case, a constant current density of 100 mA/cm^2 is applied on the corrosion cell with fully humidified inlet condition. The concentration distributions of O_2 and H_2O are plotted in Figure 332and Figure 333, respectively. In order to consume the electrons released from the hydrogen oxidation, in this case from the supplied current, an oxygen reduction reaction (ORR) occurs at the anode. The anode oxygen concentration decreases due to the oxygen consumption and water concentration increases due to the water production. To supply the protons required for the anode ORR reaction, carbon will be oxidized on the cathode side. If enough water is present at the cathode, water will be oxidized to share part of the current. In this water oxidation reaction (WOR) or oxygen evolution reaction (OER), oxygen is produced at the cathode and hence the cathode oxygen concentration

increases and meanwhile the water concentration decreases as can be seen from Figure 333. The current distribution is plotted in Figure 336 ; here the current is negative to reflect a reverse current compared with normal fuel cell operations. The current distribution along the flow direction is mainly determined by the oxygen concentration on the anode and the lateral variation is due to the electron transport. However, the small range of current density variation indicates that the impact of both species concentration and electron transport is small.

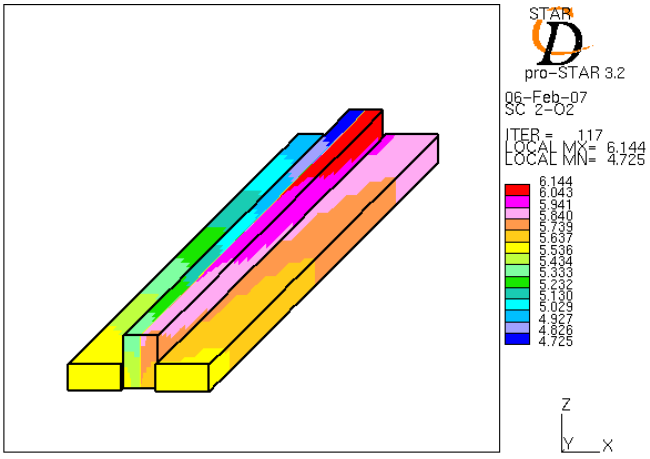

Figure 332. O2 Concentration (mole/m3) Distribution at 100 mA/cm2 with 100% RH

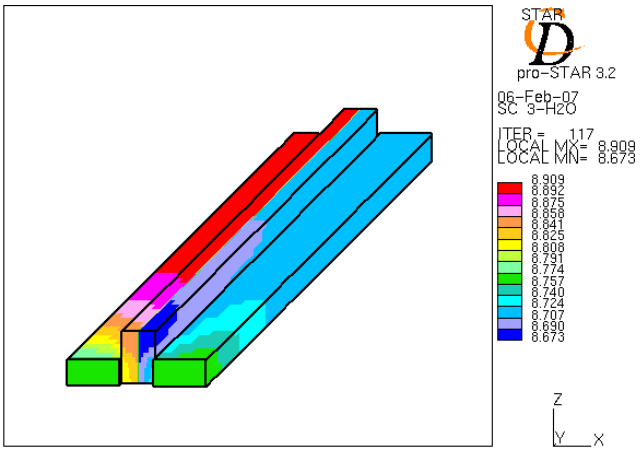

Figure 333. Water Concentration [mole/m3] Distribution at 100 mA/cm2 with 100% RH

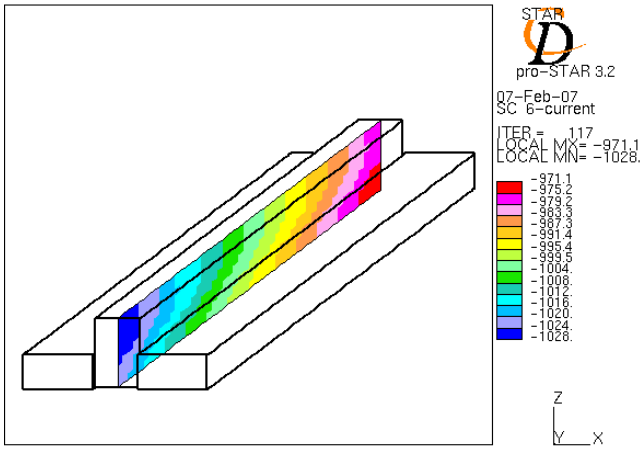

Figure 334. Current Density Distribution [A/m2] at 100 mA/cm2 with 100% RH

Figure 335 shows the electrolyte phase potential distribution (1.0+Φe) in the membrane of a corrosion cell where the reference point at the anode bipolar plate is set at 1.0 V. FromFigure 335, the electrolyte phase potential is about -0.82 V. The cell voltage, or the cathode electronic potential, is 0.69 V from the simulation, therefore an interfacial potential difference of about 1.5 V is exerted on the cathode; this potential drives carbon corrosion.

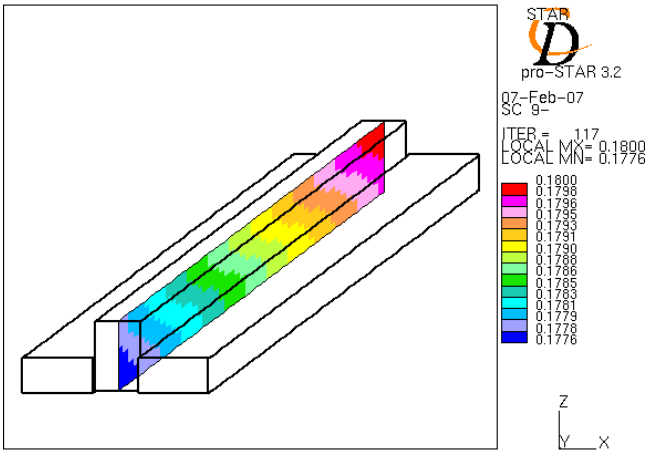

Figure 335. Electrolyte Phase Potential (1.0+Φe) [V] at 100 mA/cm2 with 100% RH

The carbon corrosion rate in catalyst layer is shown in Figure 336.. A volumetric corrosion rate of 9.6 g/m^3-sec results under the specific condition modeled; this is equivalent to a 9.6×10^{-6} mg/cm^2-sec for a 10 μm thick catalyst layer.

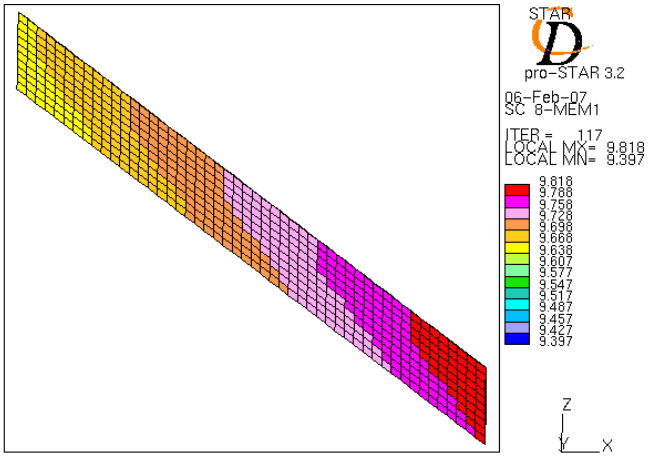

Figure 336. Carbon Corrosion Rate [g/m3] at 100 mA/cm2 with 100% RH

When a small current of 2 mA/cm^2 is applied with fully humidified conditions, the cell voltage drop to 0.45 V and the membrane potential is -0.43 V which results in a potential difference of 0.88 V on the cathode. A corrosion rate of 3.2×10^{-6} mg/cm^2-sec is obtained in this case, as shown in Figure 337. The decrease of the corrosion rate indicates that the corrosion current decreases with a smaller total current. However, the carbon corrosion current change is much smaller than the total current change (3 times vs. 50 times). The reason is because the WOR (or OER) takes most of the current during both cases due to the relative fast kinetics compared to carbon oxidation reaction COR. Therefore, the WOR current changes dramatically, corresponding to the total current change, while the COR current is less affected.

To investigate the effect of RH a simulation with RH as low as 10% at 100 mA/cm^2 is performed. With less water present at the cathode, WOR current is greatly reduced and carbon corrosion current has to increase compensate the total current. In this case, the cell voltage is 0.86 V and the electrolyte potential is -0.82 V, which imposes a 1.7 V potential difference on the cathode. The carbon corrosion rate increases to 2.1×10^{-5} mg/cm^2-sec, as shown in Figure 338.

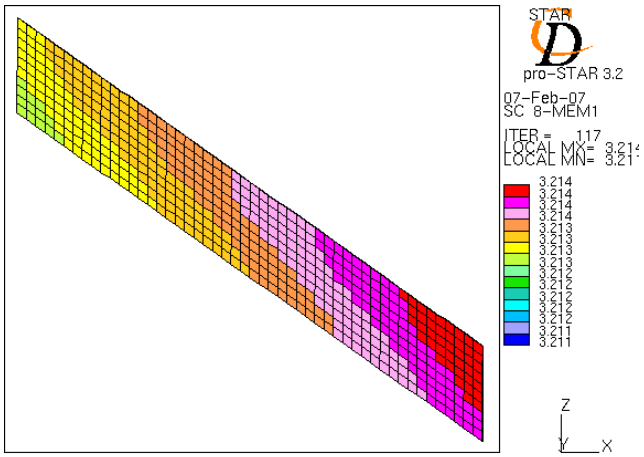

Figure 337. Electrolyte Phase Potential [V] at 2 mA/cm2 with 100% RH

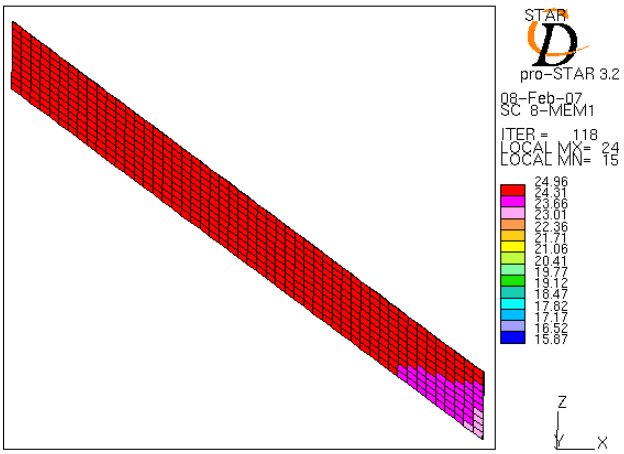

Figure 338. Electrolyte Phase Potential [V] at 100 mA/cm2 with 10% RH

In conclusion, a 3D model has been developed to estimate the carbon corrosion rate and the effect of RH on carbon corrosion. The carbon corrosion rate increases exponentially with the interfacial potential difference between the electronic phase and the electrolyte phase. Therefore, a high potential difference across this interface should be avoided to minimize carbon corrosion. Once a fuel cell is fully humidified, the WOR can share most of the current and the total current change has a small effect on the corrosion rate. However, under a low RH condition, most current needs to be taken by the carbon oxidization reaction, which leads to a fast carbon consumption rate. This also depends on the catalysts that are chosen in the fuel cell cathodes. To limit the COR, the exchange current density of the WOR should exceed in few orders of magnitude over the COR for the selected catalyst.

Accelerated Testing

Currently a station is modified to perform start/stop testing. To study the fix effectivity of DOE-4 Final catalysts with respect to starting and stopping of a fuel cell, we performed an accelerated potentiostatic experiment and held the fuel cell at 0.6 V with air on both anode and cathode electrodes for a fixed period of time. This was done with 3 M Rev 2 MEA's and DOE-4 Final MEA's sandwiched between Plug Power flow fields. We believe during shutdown, air takes-over the anode chamber. During start-up this air is available to create fronts with the hydrogen that is moving into the anode chamber. During these fronts, we believe the fuel cell cathode can reach as high as 1.4 V – 1.8 V depending on the conditions on the anode electrode, membrane and the cathode electrode. A typically 0.6 V with air/air electrode could mean as high 1.4 V on the cathode assuming the anode electrode is at 0.8 V. We wish to further confirm the exact electrode potential using a reference electrode set-up in the near future. Please refer to Figure 339 and Figure 340 which shows the effect of 0.6 V air/air at different time intervals on the electrochemical active area measured in coulombs.

The performance was clearly affected post 10 min accelerated test conditions for Rev 2 MEA and the DOE-4 Final MEA could go beyond the 30 min at similar stress conditions and still retain sufficient performance to address system steady state requirements. Please refer Figure 341 and Figure 342 where performance polarization curves are generated for the Rev 2 and the DOE-4 MEA.

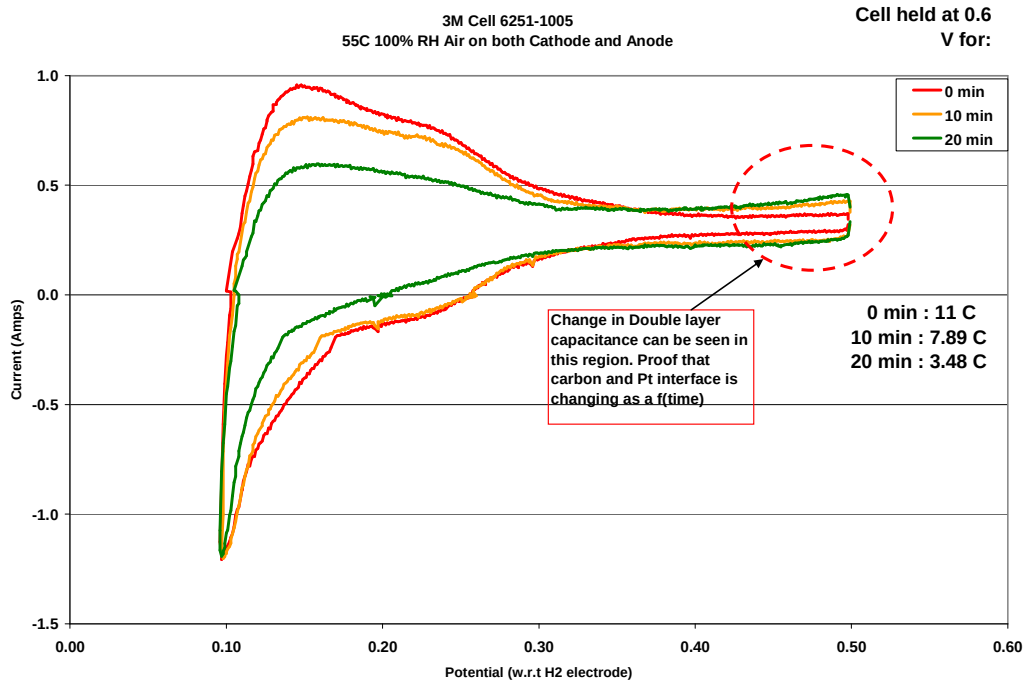

Figure 339. Cyclic Voltammograms using 3 M Rev 2 MEA

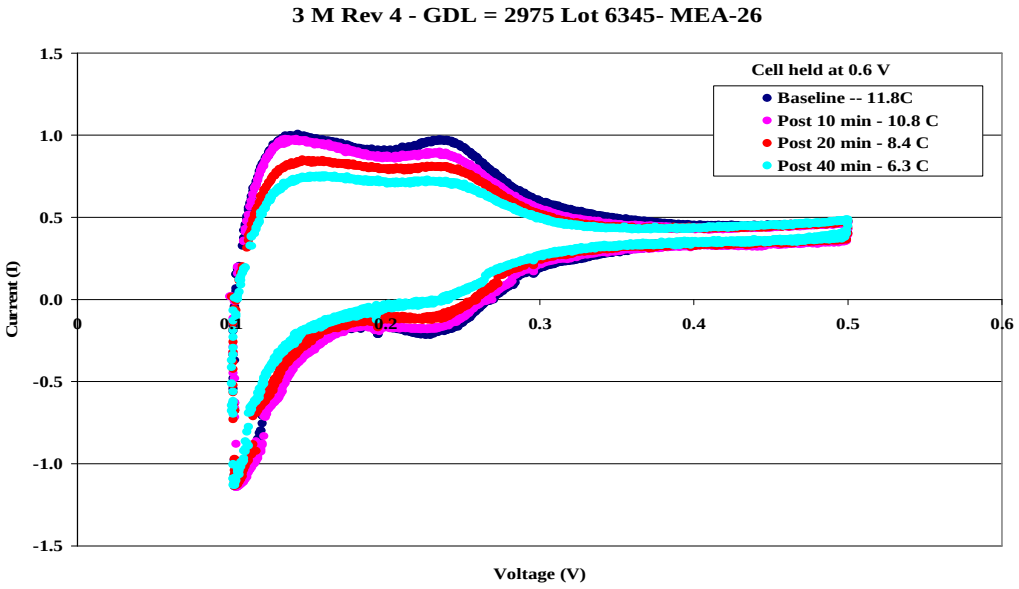

Figure 340. Cyclic Voltammograms using 3 M DOE-4 – 0, 10 min, 20 min and 40 min

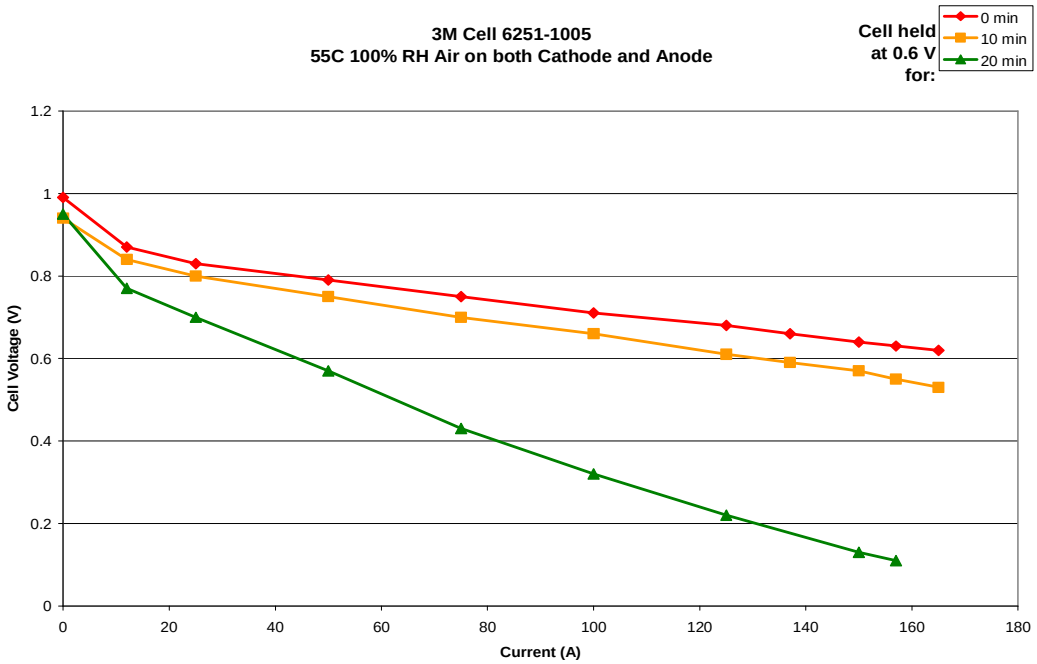

Figure 341. Performance Curves Using 3 M Rev 2 MEA's – 0, 10 min, 20 min

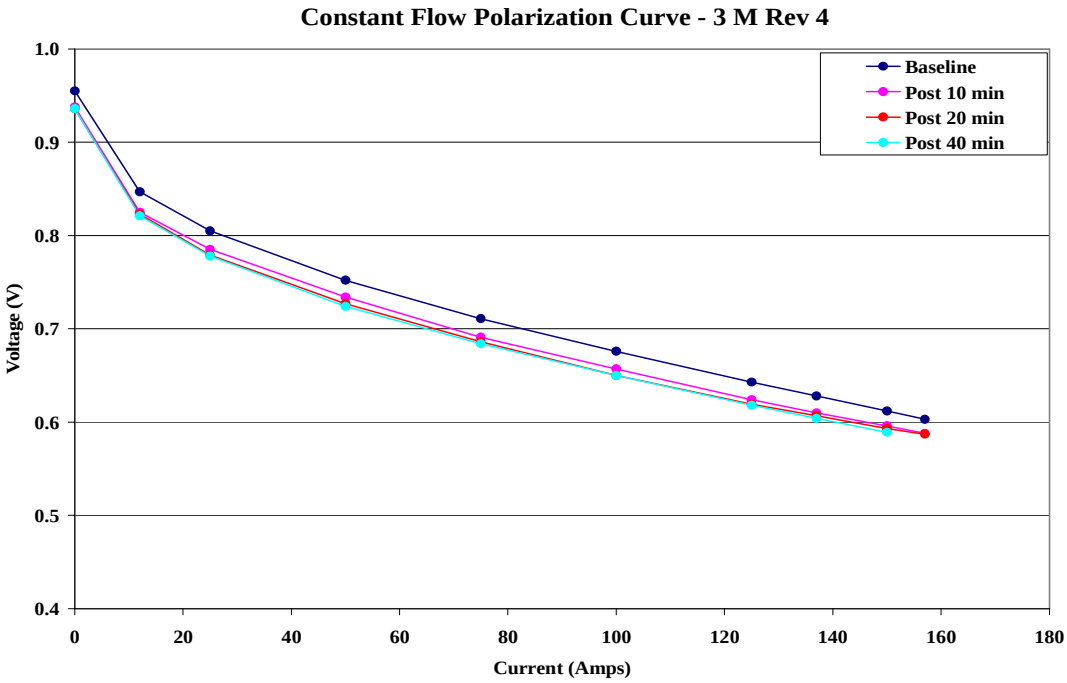

Figure 342. Performance Curves Using 3 M DOE-4 MEA's - 0, 10 min, 20 min and 40 min

8-cell modules were built and we used a protocol as illustrated in
Figure 343 to simulate hydrogen pushing air and air pushing hydrogen – so 5 such cycles are completed before a polar curve is initiated. When the average goes below 0.5 V, it is considered to be the point at which failure has occurred.

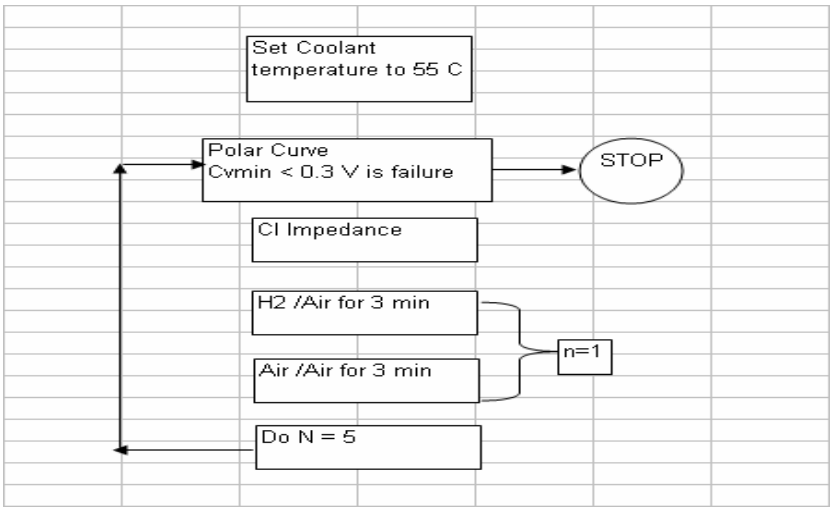

Figure 343. Accelerated Starting and Stopping Test Flow-Chart.

As can be seen fromFigure 344, the DOE4 Final version catalyst and 2975 GDL (235 cycles) outperforms the current Rev 2 baseline (40 cycles) significantly – about 6 X improvement in starting and stopping capability. It is interesting to note that the 2975 GDL has also had an effect on improving start-stop capability. In 2004 Q3, Plug Power and 3M did an accelerated aging of the GDL using high voltages in liquid electrolytes and studying the limiting current density of the resulting MEA with the subjected GDL. 3M Gen I MEAs with an active area of 50 cm^2 were used for this test.

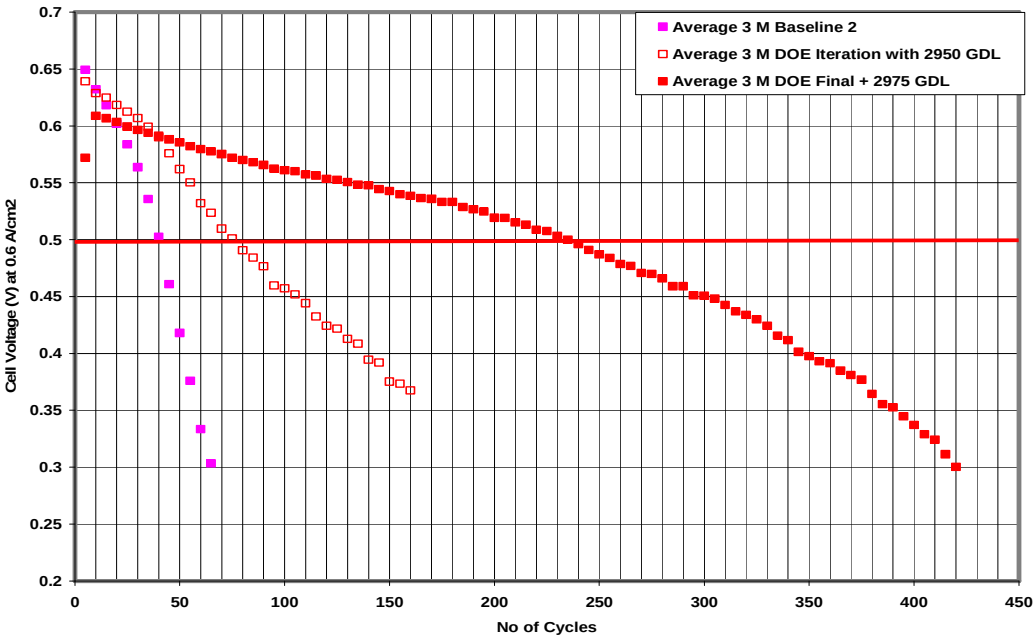

Figure 344. 8-cell module accelerated start-stop cycling

Before the assemblies of the MEAs, the cathode GDL was aged at 0.80, 1.4, 2.0 and 2.6V for 10minutes, respectively. All other MEA components, such as anode GDL, anode/cathode electrodes and membrane, are the same with standard 3M Gen 1 MEA. Performance curves can be seen in Figure 345

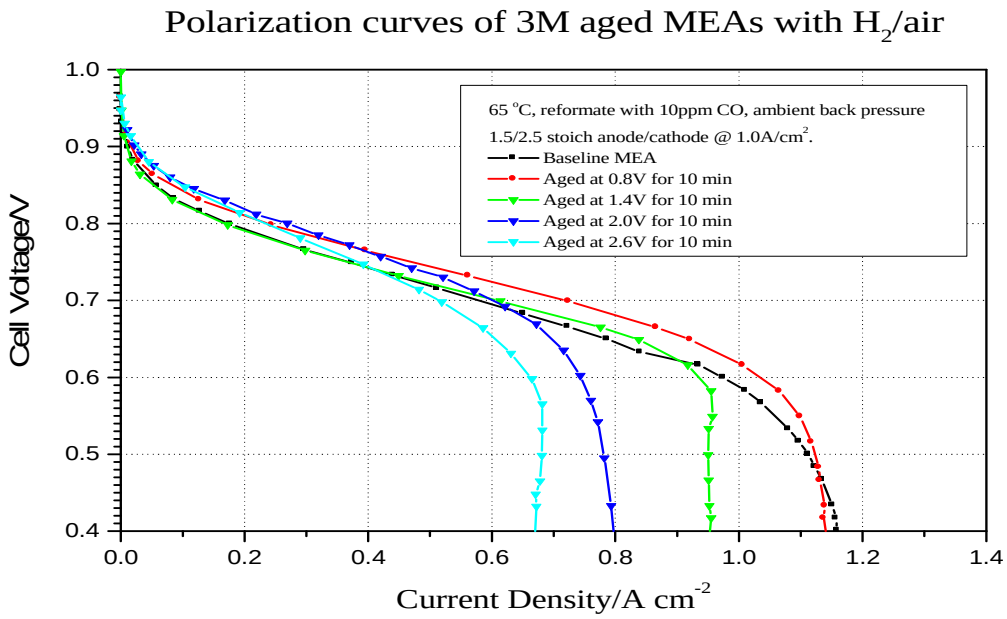

Aging voltage (V)	Baseline	0.8	1.4	2.0	2.6
Limiting current (A/cm^2)	1.16	1.14	0.95	0.80	0.68

Figure 345. 8-cell module accelerated start-stop cycling

So far we have discussed the material solutions associated with carbon corrosion. Understanding the damage in-situ in a system is key to developing system level strategies. In order to develop engineering solutions, further validation of high potentials in-situ was demonstrated using hydrogen reference electrode similar to the one developed and described by W. He et al.[1] A critical difference in our study is the use of integrated membrane, which is an extension of the membrane in the cell. This eliminates the need to make an electrolyte junction, and avoids junction potential problems possible with other methods. The location of the reference electrode is shown in the Figure 346 below. Hydrogen was bubbled at this location where it contacts with a catalyst coated GDL.

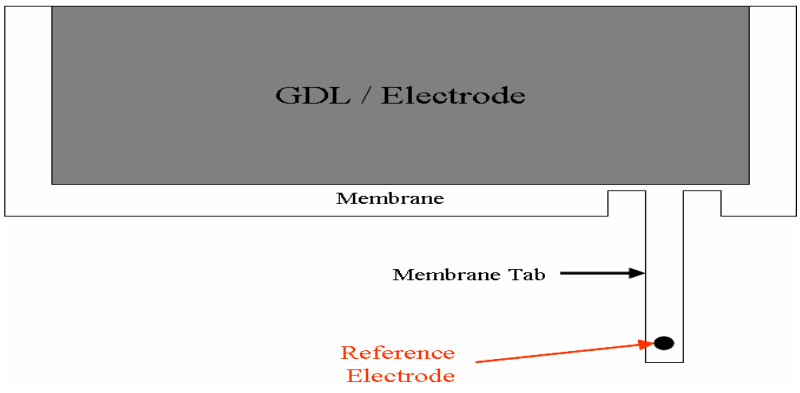

Figure 346. Reference Electrode location on the MEA.

Startup/shutdown transient tests were performed on a full size stack with reference electrodes installed at the anode inlet and anode outlet locations of cell 5. The stack was operated under

simulated uncontrolled startup/shutdown transient conditions, and the reference electrodes were used to measure the resulting interfacial potentials within the cell. As shown in Figure 347, a startup transient is captured using reference electrode measurements. During this startup transient a front of hydrogen moves through the cell from anode inlet to anode outlet. As this is happening the reverse-current mechanism depresses the membrane potential at the anode outlet to – 0.84 V with respect to the membrane potential at the anode inlet. This depressed membrane potential causes the cathode interfacial potential to reach 1.58 V, which in turn drives the carbon corrosion reaction at the cathode electrode.

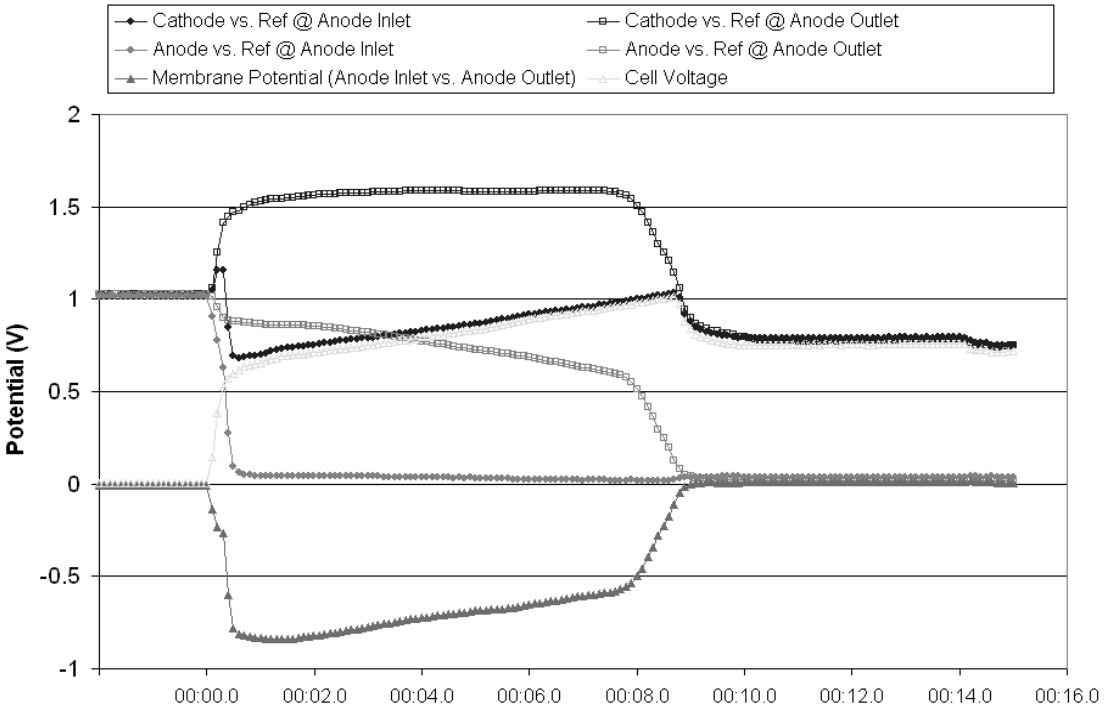

Figure 347. System startup transient with reference electrodes installed at cell 5 anode inlet and anode outlet.

The carbon corrosion rate was calculated using

$$i_C = i_{0,C} \exp\left[\frac{\alpha_a F}{RT}\left(\Phi_1 - \Phi_2 - U_C\right)\right]$$

Equation 60

where the exchange current density, $i_{0,C}$ and the anodic transfer coefficient, α, are assumed to be 2.5 nA/cm2 and 0.275 respectively as published by J.P.Meyers et al.[2] The Langmuir adsorption term used in this publication is ignored here because we are only concerned with interfacial potentials elevated above 1 V, caused by startup/shutdown transients at which rapid carbon corrosion occurs. Φ_1 is the potential in the solid phase at the cathode electrode, and Φ_2 is the potential in the membrane adjacent to this electrode. For these calculations of cathode carbon corrosion the cathode potential vs. reference electrode measurement is used for the Φ_1 - Φ_2 term.

For the carbon corrosion reaction

$$C + 2H_2O \rightarrow CO_2 + 4H^+ + 4e^-$$

Equation 61

a standard electrode potential (vs. SHE) of 0.207 V was used for U_C (6) .
If we know the current system capability, engineering solutions can be characterized using reference electrodes and predictions can be made without further testing. So when the flow was increased by 15 times, the time of elevated interfacial potential dropped from 8 – 12 seconds to < 4 seconds. This estimated a carbon corrosion loss reduction of 6 X. Using this model, the prediction for start-stop capability should increase by 72 %. With accelerated experiments as discussed earlier, Plug Power did see a 70 % improvement in the new condition when experimented at the module level. This improvement is shown in Figure 348

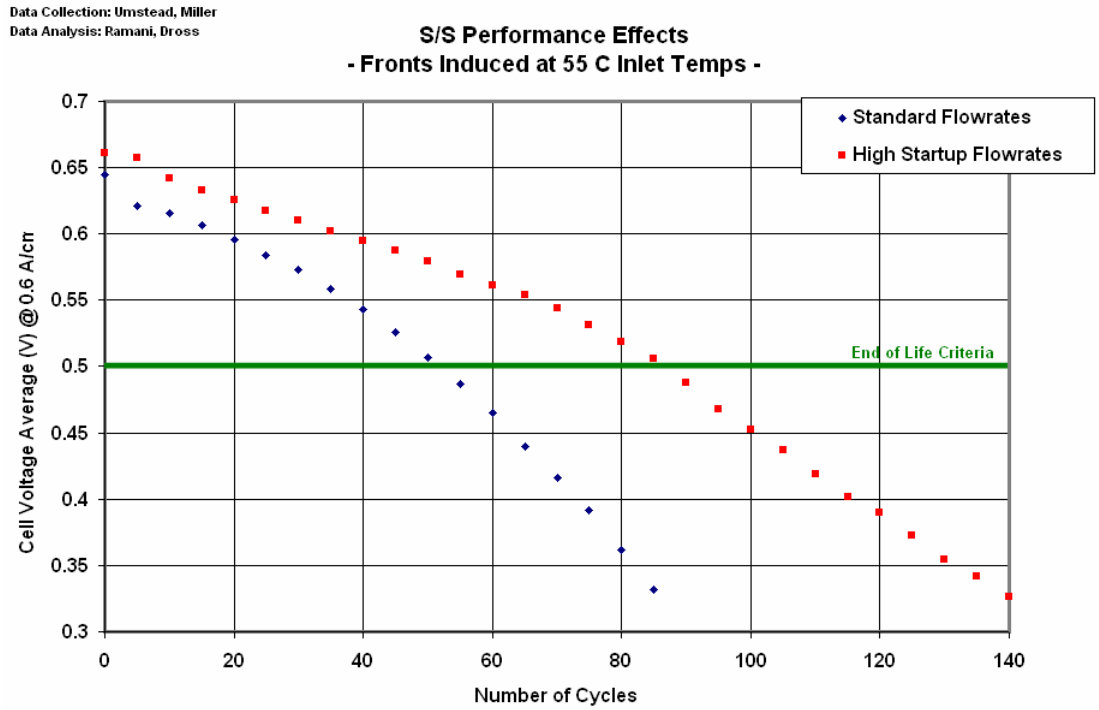

Figure 348. Accelerated testing – Showing engineering solution of 15 X reactant flows during start-up improves start-stop capability by 70 %.

6.2.4 Segmented Cell Tool Development

When stacks are decommissioned, they have failed either due to low cells or due to low average of the stack. Single cell failures still dominate stack failures. These failures have been randomly located from bottom through top of the stack. In order to understand more about these failures, we need to perform careful analysis of the stack after it is decommissioned. In Q2 2006, Plug Power studied the in-plane cell voltage development as the cell ages. Cell voltage has been observed to vary by the location (inlet, middle and outlet) of measurement. This behavior is especially notable for cells in stacks that have been operated for many hours. Cell voltage differences within a single of several hundred millivolts have been observed in used stacks. While for new stacks, the differences observed are typically only 10 to 20 millivolts. The cell voltage distribution for a stack having run approximately 2500 hours shows a behavior results when there is in-plane current flow; the voltage change is due to this flow in the presence of the cell in-plane resistance. For a used stack, individual cells degrade locally and local increases in resistance can occur. The through-plane current in such a region is thus reduced and has to be redistributed to

adjacent cells through in-plane current. Both experiments and modeling have been conducted to confirm the hypothesis. An multi-cell module was built and tested with through-plane current blocked near the outlet region of cell number four. It is hypothesized that when the MEA is blocked locally, the through-plane current will have to bypass the region through in-plane current flow. The adjacent cells then will have low through-plane current in the same region due to the bypassed current. This explains why the adjacent cells have high local voltage. This cell voltage variation phenomenon brings uncertainty to the monitoring of the cell voltage through single location voltage measurement. The random failures have some relationship to intrinsic MEA properties, which varies over the length and width of the MEA. Process variables impact the uniformity of the MEA and adding on the flow-field effects creates non-uniformity on the MEA surface. In order to understand the local relationships, 3M worked on a segmented cell approach using PCB boards, which could be integrated into Plug Power hardware. Using this characterization tool, the desire is to understand the nature of current generation, voltage separation at local sites at spatial resolution of 3 –4 cm^2 per segment. This will further help us separate the beginning of life performance and intrinsic failure mechanisms dependency on flow-field vs. MEA manufacturing variables. Here we discuss the segmented design and also some of the preliminary data that has been gathered in Q4 2007.

Segmented Cell Characterization:

Plug Power installed the segments in a fuel cell module at the cell 7 cathode and the cell 8 anode locations as shown in Figure 349. This module was connected to a load-bank and controlled through Plug Power Interface. However the data was also gathered using the 3M PXI NI interface, especially the data from the segmented cell as shown in Figure 350. Current, voltage and impedance from each segment is collected and stored. The PCM boards were connected together to sustain the current path, however as explained in the design section, the current was collected through 10 mohm resistors at 52 segments, the segments closer to inlets are 13 and 40 and the segments closer to outlets are 1 and 52 as shown in Figure 351. At a stack current of 120 Amps, an average of 2.29 amps is collected per segment and the standard deviation collected at discrete time is around 0.4 amps. This indicates current distribution at the interface in the lower and upper segments of the interface. In this report, we only cover preliminary work that was possible under the time constraints.

Figure 349. Fuel Cell Module showing segmented approach at cell 7/8 interface.

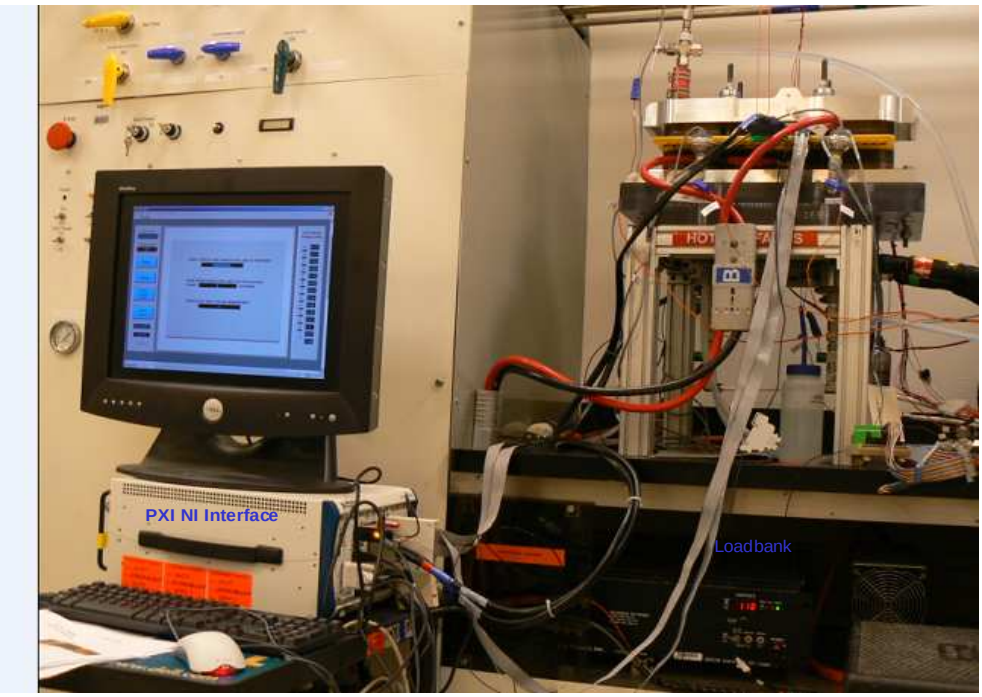

Figure 350. Fuel Cell Module Interface with PXI NI Interface

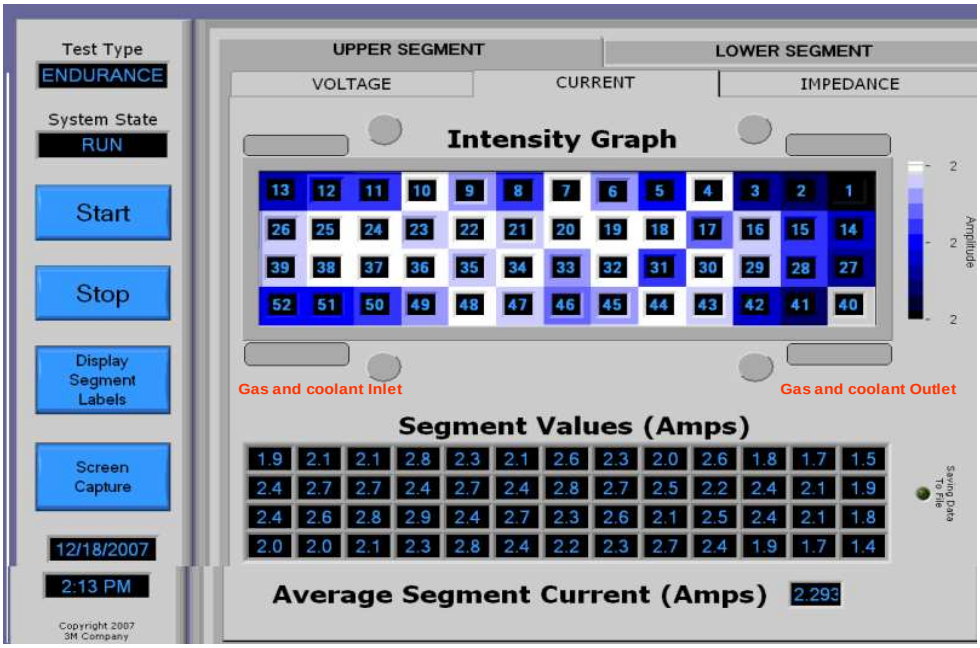

Figure 351. Software Interface showing 52 segments – Inlets and outlets are marked. Snapshot taken at 119 – 120 Amps.

Apart from the display in the screen, a 3D dynamic imaging functionality for the voltages is also available and can be seen in Figure 352. It maps the voltage spatially from inlet to outlet. Visual display enables easier understanding of dynamics during both steady state and transients.

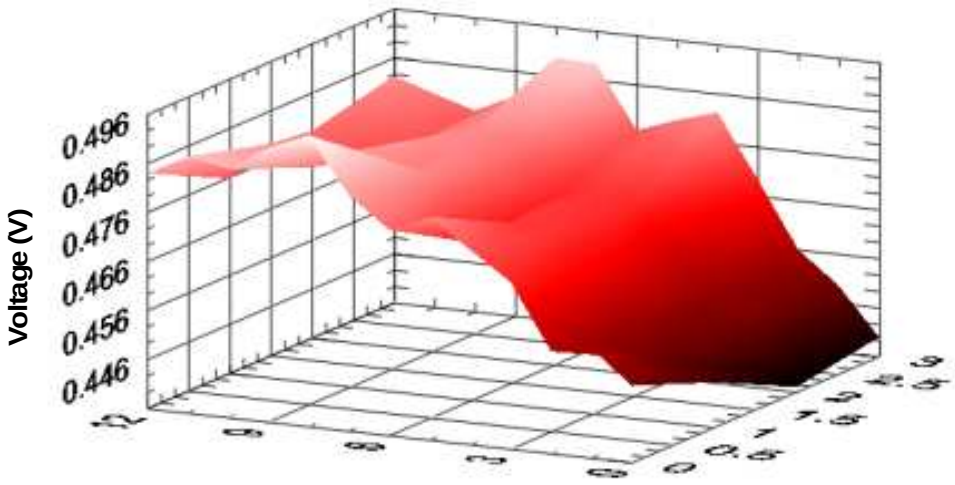

Figure 352. 3D- Dynamic View of segment voltages from inlet to outlet at stack current of 120 Amps

The dynamic view also shows the effect of increasing cathode flow real time. The voltage at the inlet and outlet improve dramatically and the current distribution evens up, reducing the current at the inlet. At each column, there are 4 segments – these are averaged and plotted from inlet to outlet in Figure 353 for two different currents. The behaviour is identical; the current goes down as it nears the outlet. The current increases at the center of the MEA and then decreases at the outlet for both 73 and 120 Amps. Obviously this can change over a function of time. Local de-activation of catalyst at the center may push current to other locations that are capable of handling the additional current. As the current decreases at the outlet, the local impedance also increases at the location as can be seen from Figure 354. As shown in Figure 355, it is interesting to note that when the cathode flows are lowered, the outlet current drops significantly, but the net current has to remain the same at an average of 2.31 Amps for a total of 120 Amps across the interface of cell 7 and 8. The decrease in current at the outlet is compensated by the increase in current at the stack inlet. This indicates current generation will be shifted where more favorable conditions exist.

In summary, there are various possibilities with this tool. This tool can be used to study how local defects propagate with time and how they result in performance loss. This can also be used as a tool in failure analysis to understand where the MEA has sustained major loss in properties. All of this when mapped in real time, can help further refine MEA process variables, MEA properties, flow-field parameters. Plug Power and 3M intend to use this tool beyond the DOE project to sustain critical learning to enable new designs moving the industry forward.

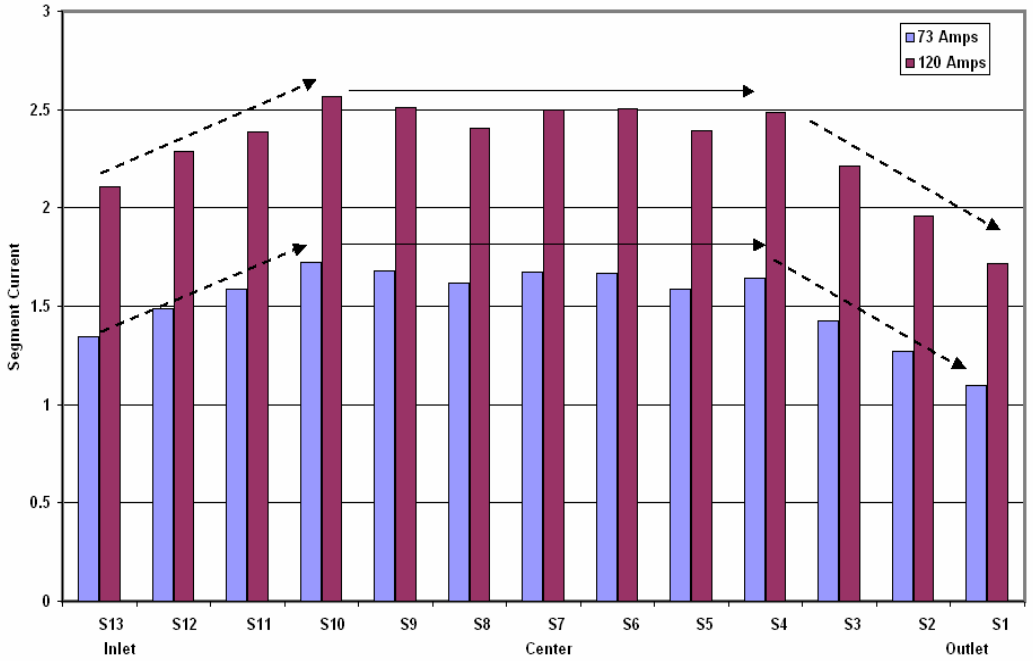

Figure 353. Inlet to Outlet Averaged Current Distribution at two different currents.

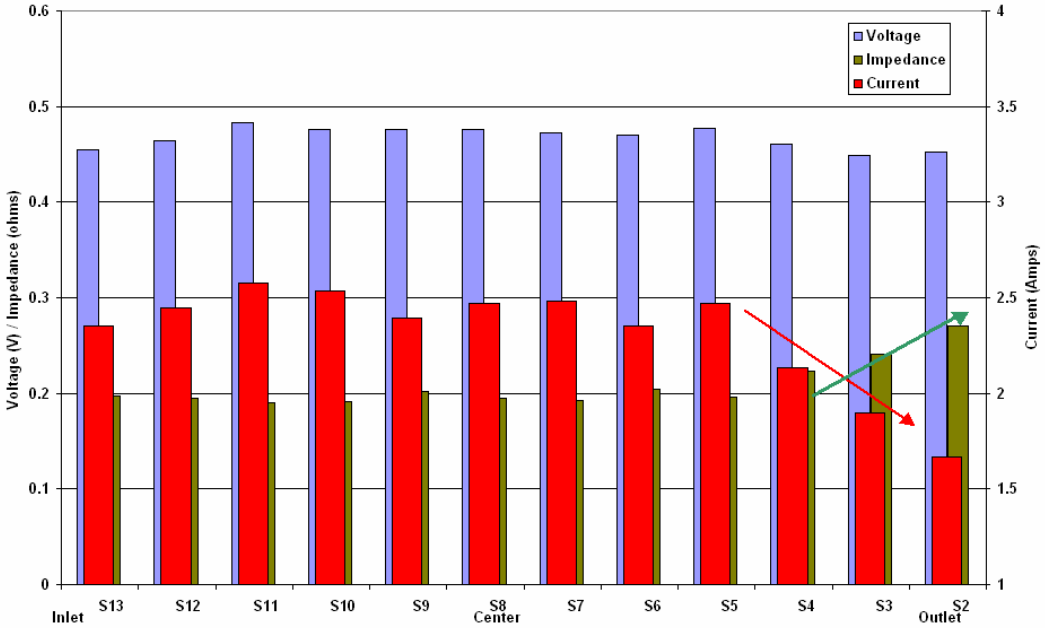

Figure 354. Inlet to Outlet Averaged Distribution at 120 Amps for current, voltage and impedance

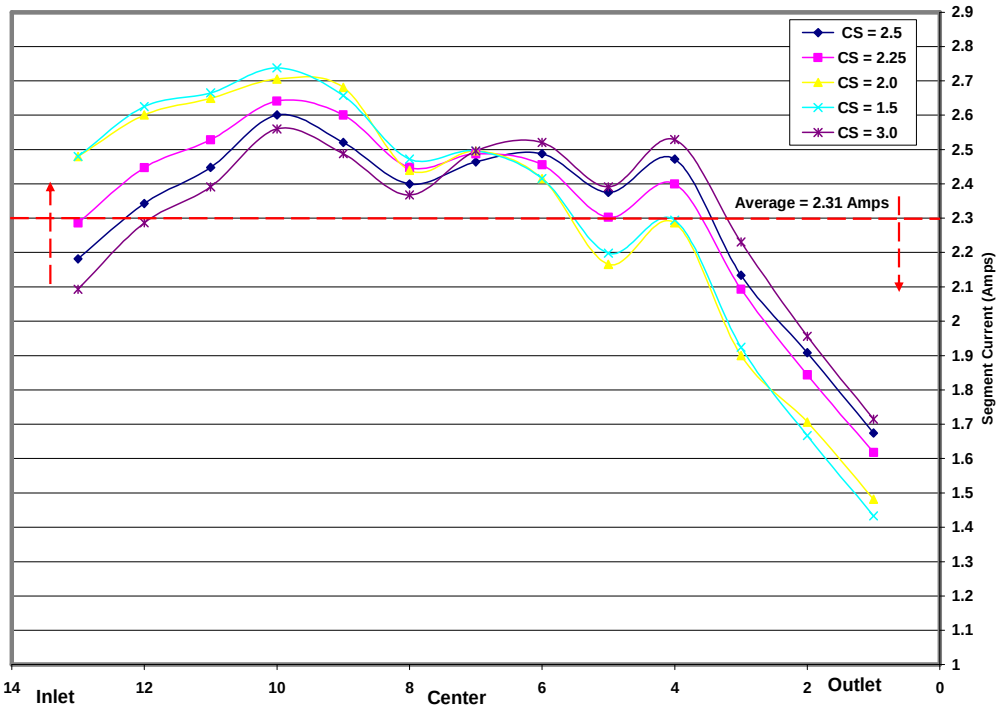

Figure 355. Effect of cathode stoic on segment current

6.2.5 System Improvements

In addition to transient system improvements, several steady state parameters have also been improved for increasing system reliability.

Thermal Management Module Ringing

Implementation of thermal management module temperature ringing controls modifications, described in the 2Q 2006 report have been carried out. These changes prevented the need to reconfigure certain stack coolant input and output mechanical configurations. Performance before and after the modifications are shown in Figure 356 through Figure 358. It can be seen that the severe temperature ringing shown in Figure 356 is substantially reduced by controls tuning alone. However, the performance was deemed insufficient to ensure stack stability and maximum durability. Feed-forward control algorithms were designed and resulted in substantial improvement in the time decay characteristics of the stack temperature after a load change; the improvements in performance are evident in Figure 358.

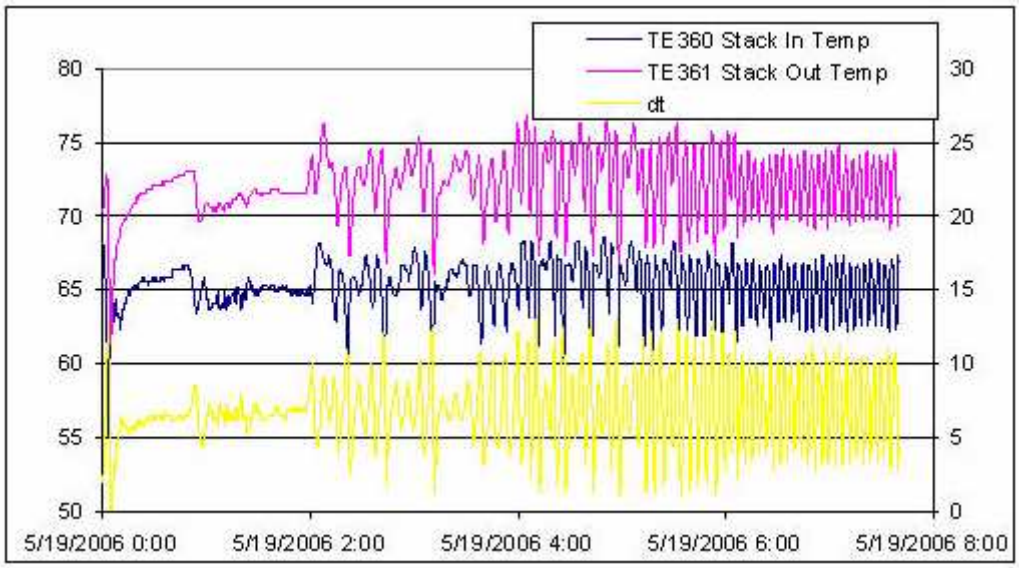

Figure 356. Stack Temperature Ringing Before Controls Modification

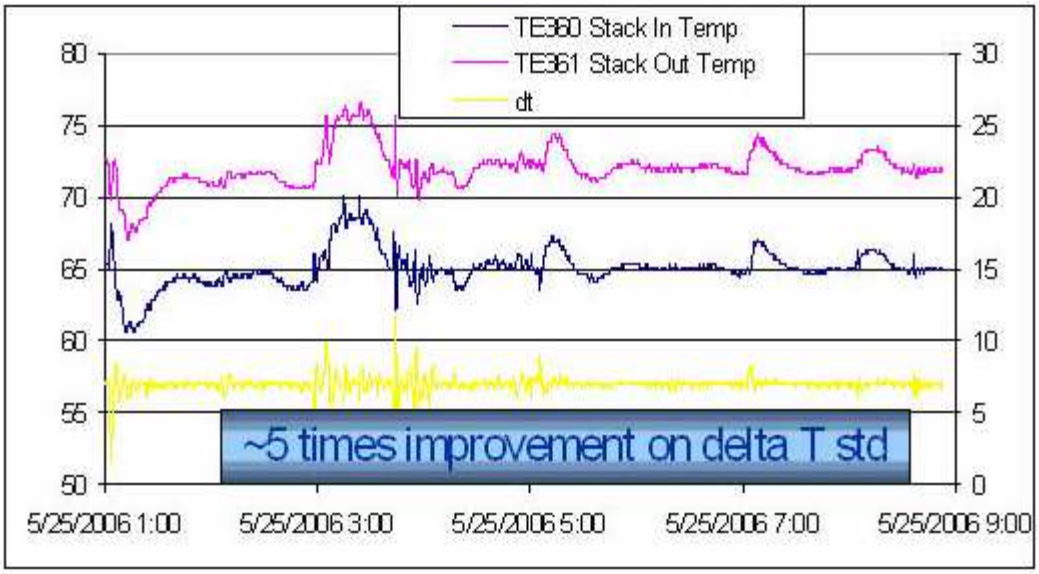

Figure 357. Stack Temperature Behavior after Controls Tuning. (Temperature peaks and subsequent critically damped decay occur with stack load changes.)

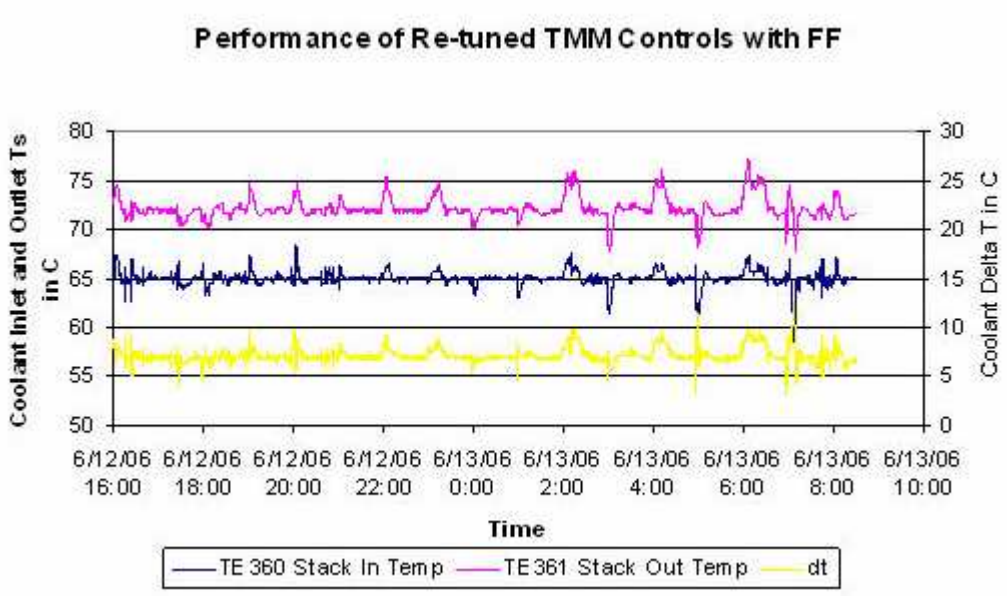

Figure 358. Stack Temperature Behavior after Controls Tuning and Feed-Forward Control Algorithm Implementation (Temperature peaks and subsequent decay occur with stack load changes.)

Float Valve Improvements

Failures of the float valves utilized as a part of the stack manifold have occurred due to contamination. Also, the flow performance has been found to be sub optimal. When the float valve under performs, there can be shutdowns due to different conditions (such as high levels of CO or CH_4 slip) stemming from water ingestion into elements of the reformer. An improved design that has higher flow capability and is less sensitive to contaminants has been carried out. This design implementation will improve the performance of the stack and enhance the durability of the MEA due to improved gas quality and a reduction of unplanned shutdowns.

Auto-Thermal Reformer Thermal Well Studies

Control of the auto-thermal reformer (ATR) temperature is critical to delivery of high quality reformate to the stack. This control is critically dependent on the response speed and accuracy of the temperature measurement. In order to optimize the speed and accuracy of the temperature measurement, study of several thermal well configurations has been carried out. Currently, the results are being analyzed and will form the basis for recommendations relative to the current design of the ATR thermal well.

Auto-Thermal Oxidizer Light-Off Optimization

If auto-thermal oxidizer (ATO) light-off/startup occurs too slowly, damage of the reformer will occur. Such damage will reduce the reformate quality over time and reduce the life of the stack. A designed experiment was carried out using a Taguchi robust design protocol in order to determine the optimum settings for ATO light-off. This experiment included four control factors with three levels each; noise inputs were also introduced to represent ATR condition and startup state (cold or hot). Based on the analysis of the ATO light-off experiments new startup control set points have been defined. These set points reduce the ATO light-off time by ca. 34% and will result in improved gas quality delivered to the stack over time.

Weak Cell Handling

A weak cell identification algorithm was developed and coded. The weak cell identification algorithm and the control actions taken upon weak cell detection continued to be tested and improved. The weak cell identification algorithms have been running under test since April 14, 2006 and are found to accurately identify weak cells that match certain criterion. Controls actions taken upon detection of weak cells have been modified several times based upon machine operation data mining. A separate health criterion was established for the weak cells that links system action to stack reactant stoichiometry, stack power demand and system efficiency. Weak cells whose voltage drops below a threshold voltage level will trigger system stack recovery action to prevent stack shutdown, while protecting the cells from being driven to negative voltages.

Improved CO Destruction of the LTS Reactor Enhanced Insulation Design (Wong)

The system design was found to have insufficient latitude to consistently bring CO to a low enough level. It is known that cell voltage performance will suffer in the presence of excess CO and that excess CO exposure over long periods of operation will reduce MEA life. A measure of the consistency of the level of CO delivered to the stack is variability of the cell to cell voltage level. One measure of this variability in the cell ratio: This is defined as the lowest cell voltage divided by the average cell voltage for a stack. Root cause analysis led to the finding that the reaction temperature of the low temperature shift (LTS) reactor was too low. An improved LTS reactor insulation package was designed to raise the LTS reactor temperature. This design was tested and implemented for 3M/DOE MEA test systems.

6.3 MEA Durability in System

6.3.1 System Reliability Demonstration

Three demonstration stacks were built and run over the course of this program. Two stacks used MEAs that were made using interim improvements (“Rev 2” and “Saratoga”) and implemented system improvements identified to date. The last stack used the final construction MEA (“DOE4”) and final system improvements.

Operation of the first Rev3 MEA based stack in system 2B209 has continued without incident with the stack accumulating ca. 8876 hours of operation as of date. Figure 359 shows the evolution of the average cell voltage in time for the Rev 3 stack. The rate of voltage performance loss of this stack is still approximately 7-8 μVolt/cell/hour if end to end method is used. The machine is still extremely stable and appears to be the strongest stack at its life used in the fleet based on its performance at this stage of runtime. This stack has not had a single low cell voltage shutdown in its entire duration of run in the fleet. Least maintenance has been required for this system post installation of this stack and the stack is still performing at a min cell ratio of 0.97 at 8876 hrs. Currently the stack along with its system is being returned back to Plug Power site for further continuance of the reliability test. This stack has about 60 % of its life left and already collected invaluable data-set.

System SU1B270 has accumulated approximately 8000 hours of operation; the voltage versus time behavior for the stack in this system is shown in Figure 360. The average cell degradation rate during the operation of this system is ca. 6 microvolts/cell/hour. The stack in this system is constructed with DOE4 – “Saratoga” MEAs which are similar to the DOE4-Final MEAs except the system was the first generation systems. The stacks are being operated at approximately 3.2 kilowatts (constant power). On a similar scope, system SU1B301 has accumulated approximately 9200 hours of system operation; the voltage versus time behavior for the stack in this system is shown in Figure 361. The average cell degradation rate during the operation of this system is ca. 3 microvolts/cell/hour. The stacks are being operated at approximately 3.2 kilowatts (constant

power). The cell voltage degradation rate is approximately linear over the operating periods. The cell ratio for both stacks is remaining at approximately constant at 0.95. A cell ratio of this magnitude is fairly typical for a new stack, so this is a positive finding for stack wear as a dispersion of voltage with time is expected as stacks age.

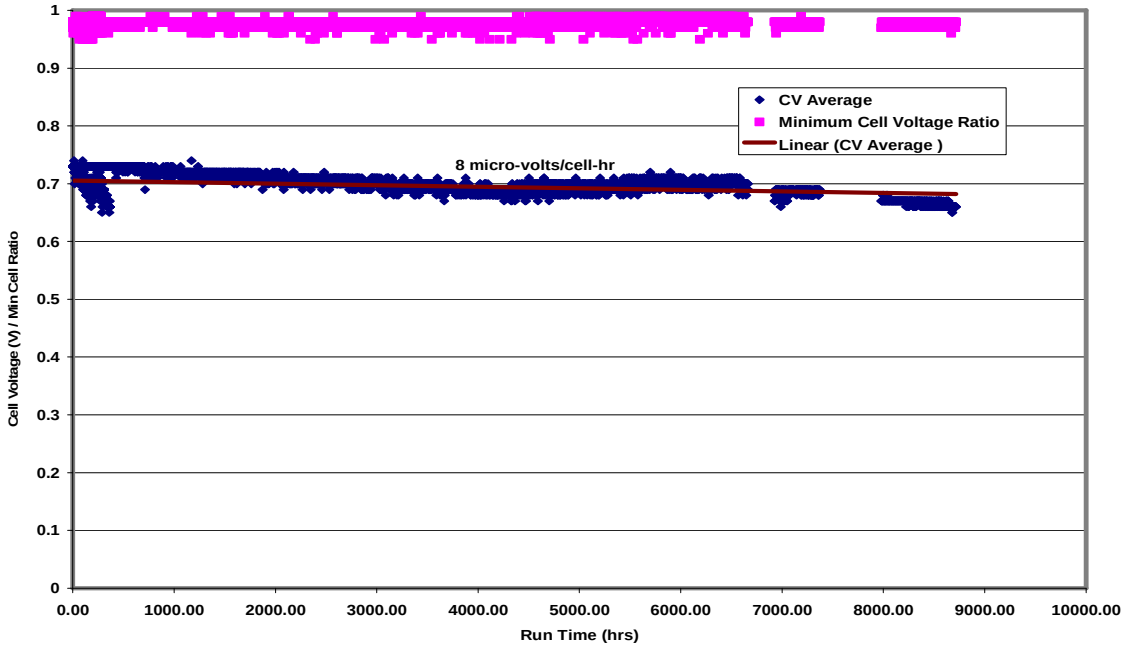

Figure 359. 2B209 Rev 3 stack at 8.2 micro-volts/cell-hr at > 8876 hrs.

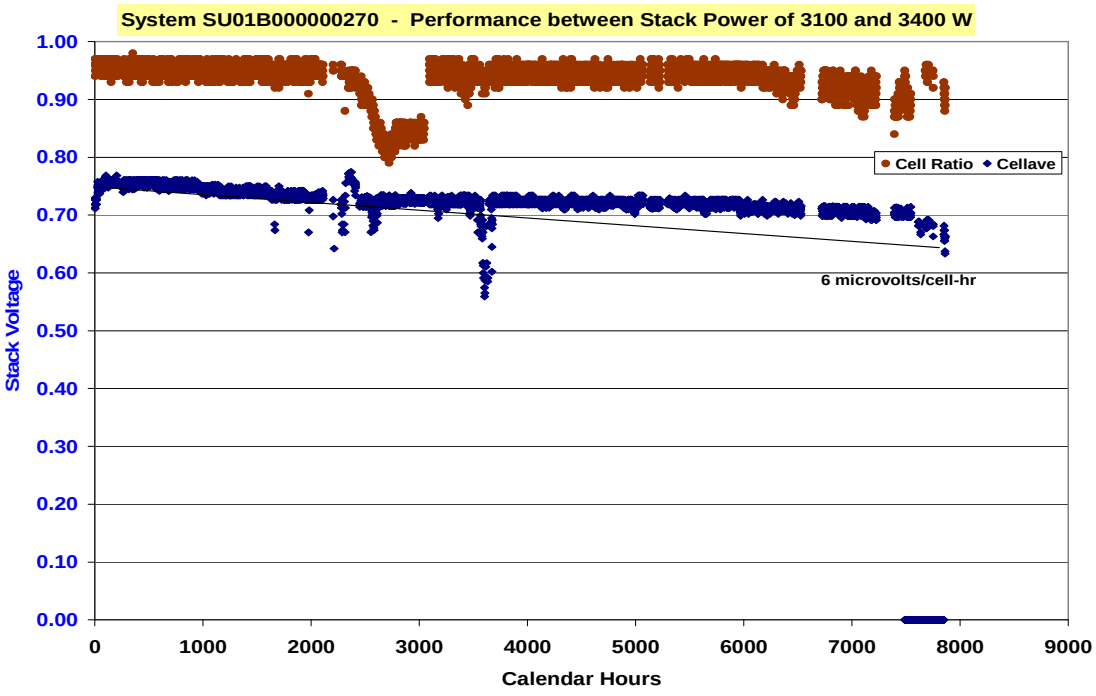

Figure 360. SU1B270 DOE4 Iteration stack at 6 micro-volts/cell-hr at close to 8000 hrs.

System 2B304 is running with a DOE4-Final MEA version and it is currently gathering data in the Plug Power fleet. This system is currently operating at a steady power or 3.2 – 3.4 kW for about 2080 hrs and the stack degradation as reported to be extremely low at around 3.5 microvolts/cell-hr (end to end method). The stack is meeting its efficiency requirement until there was a high CO event – the reformer was fixed after some gas measurements were taken. The stack did recover from this event and gain the performance back. Please refer to Figure 362 for durability plots. One of the goals for this project was that we run at least for 2000 hrs with this stack and we have met the target time for demonstrating low degradation rates during this 2000 hr system run time with minimum cell trips – CO event was not counted as a cell trip during this duration. Please refer to table 11 for system statistics against a set of metrics.

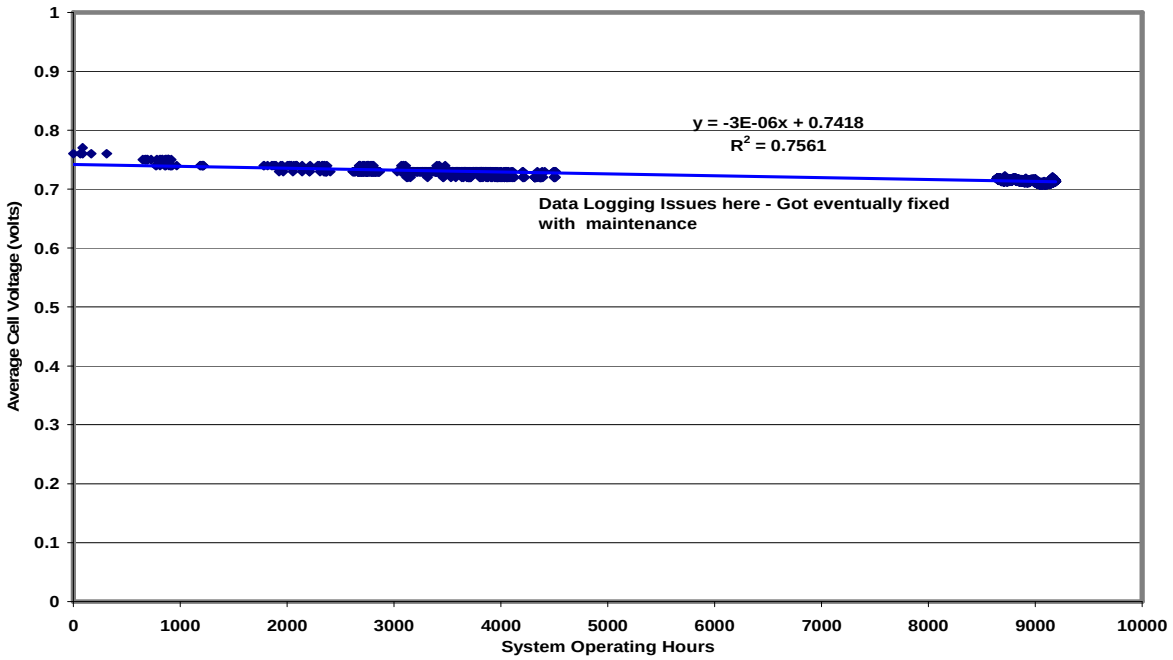

Figure 361. SU1B301 DOE4 Iteration stack at 3 micro-volts/cell-hr at close to 9000 hrs.

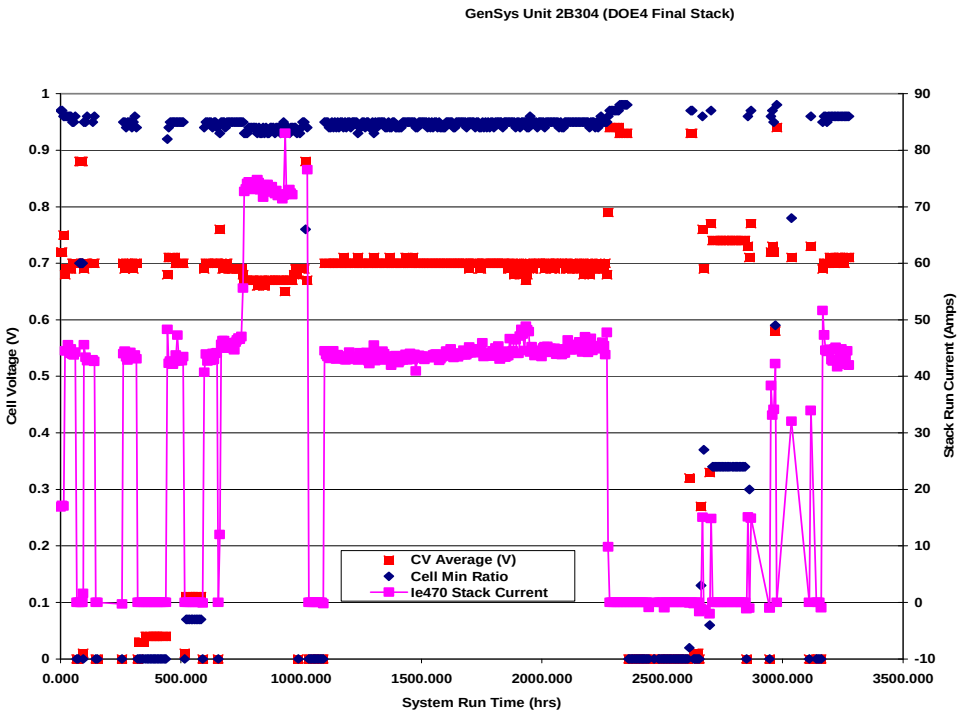

Figure 362. 2B304 DOE 4Final stack at 3.5 micro-volts/cell-hr at > 2080 hrs.

Table 51. System Metrics / Statistics for 2B304 with DOE4 Final Stack

System Stat Summary	Feb-07	Mar-07	Apr-07 to June 18 07	Cumulative	Goal
Total Unit Run Hours (excludes days down awaiting parts but includes troubleshooting time)	360	670	1156	2187	3321
Unit Availability (unit run hours/total hours possible)	54%	90%	61%		100%
Total kWh DC exported - min and max	962	2413	3142	6516	3321
Simple Efficiency (Total DC/Total Fuel)	28%	29%	26%		30%
Number of Starts	17	7	27	51	0
Startup Reliability (Number of attempted starts/number successful)	53%	71%	56%		100%
Stack Hours Accumulated	336	660	1081	2078	3321
Stack Loaded/Unit Available Hours	93%	99%	93%	95%	100%
Total Cell Trips	6	4	0	10	0

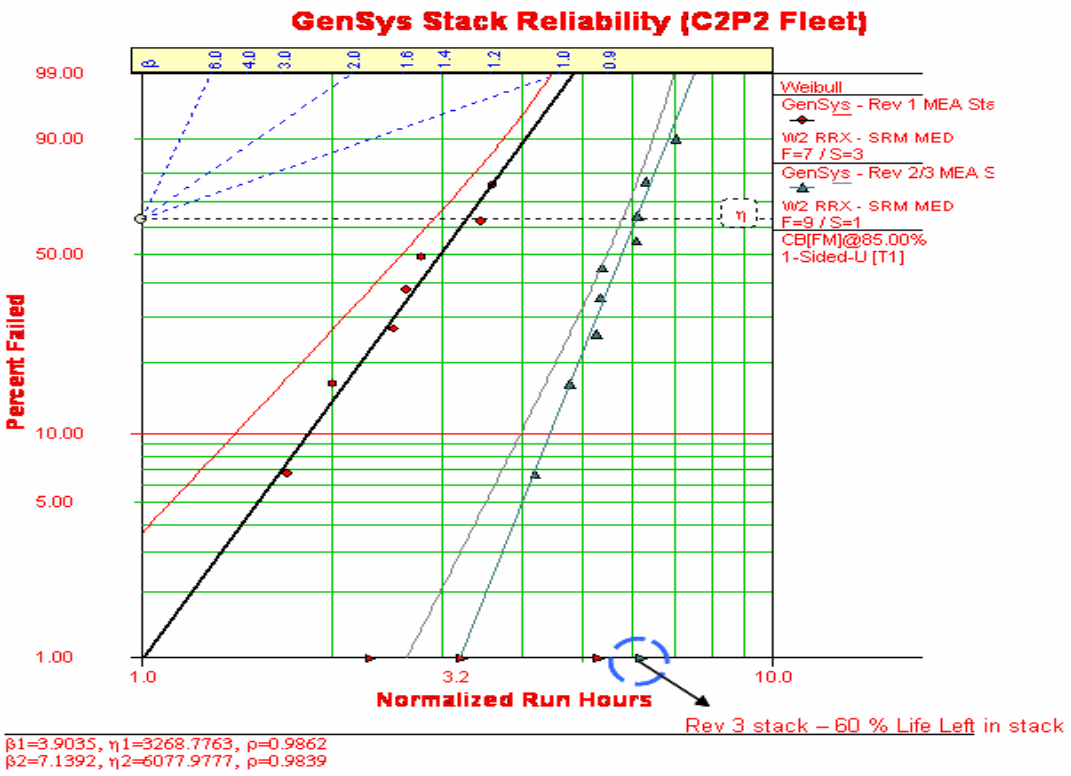

Figure 363. Weibull distribution of Rev 2/ Rev 3 MEA's in C2P2 fleet.

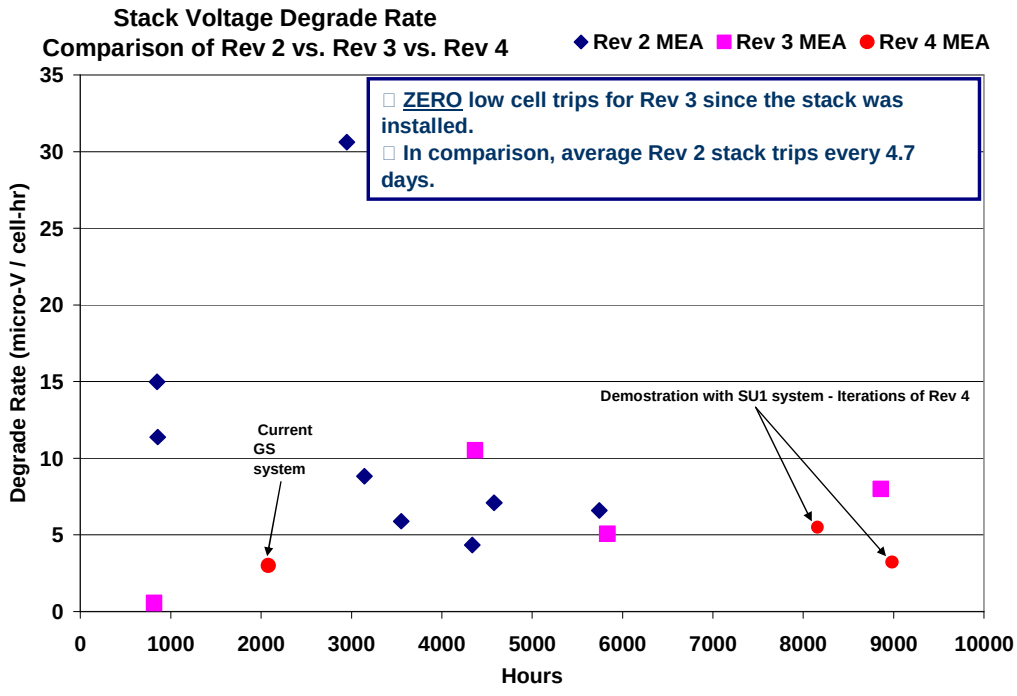

Figure 364. Degrade rate distribution as a function of time at discrete points for various MEA designs.

Summary For Stack Demonstration

In summary, the various MEA designs over the duration of this project have increased reliability in system significantly – the weibull distribution in Figure 363 reflects the improvement over the Rev 2 MEA's under close to identical system conditions. If we normalize stack life using 1 % failures, the Rev 3 shows > 70 % life improvement. It is known that degradation rates vary as a function of time and it is interesting to note in Figure 364 that the final MEA Rev 4 design showed a fixed degradation rate of 3 – 6 micro-volts/cell-hr (N=2+1) during most of its run. Rev 4 MEA's are also capable of withstanding starting and stopping applications making them even more reliable in real world applications.

6.4 Acknowledgements

Plug Power would like to acknowledge many associates at 3 M for their contributions in technical discussions and lab support. These associates include Mike Yandrasits, Mike Hicks, Phil Miller, Karl Kropp and Pinar E Serim. We also acknowledge Department of Energy's contribution in advancing the technology forward. This research supported in part by Department of Energy, Cooperative Agreement No. DE-FC36-03G013098. DOE support does not constitute an endorsement by DOE of the views expressed in this presentation.

6.5 List of Publications/Presentations based on this research

1. Guoqing Wang, Manikandan Ramani and Chev Eldrid, Plate In-Plane Electrical Resistance Impact to Stack Performance, ECS 210th meeting, Cancun,Mexico
2. In-situ Reference Electrode Technique for Accelerated Start/Stop Testing
   4th Annual International Fuel Cell Testing Workshop 2007, September 12-13, 2007
   National Research Council Canada Institute for Fuel Cell Innovation in Vancouver, BC
3. R. Dross, B. Maynard, In-Situ Reference Electrode Testing for Cathode Carbon Corrosion ECS Trans. 11, 1059 (2007)

6.4 References

1. W. He and T. V. Nguyen, *J. Electrochem. Soc.*, **151,** A185 (2004)
2. J. P. Meyers and R. M. Darling, *J. Electrochem. Soc.*, **8**, A1432 (2006)

Section 7. External Communications

Section 6 contains a list of presentations, publications and patents on topics studied under this project.

7.1 Presentations

- M. T. Hicks, "MEA and Stack Durability for PEM Fuel Cells", 2004 Hydrogen Fuel Cells Infrastructure and Technology Review, Philadelphia, PA, May (2004).
- C. Zhou, T. Zawodzinski, Jr., D. Schiraldi, "Chemical changes in Nafion® membranes under simulated fuel cell conditions," 228th ACS Meeting, Philadelphia, PA, August 2004.
- M.T. Hicks, "Accelerated testing – Application to fuel cells", 2004 Fuel Cell Testing Workshop, Vancouver BC, Canada, September 2004.

- A. Agarwal, U. Landau and T. Zawodzinski, Jr., “Hydrogen peroxide formation during oxygen reduction on high surface area Pt/C catalysts,” 206th ECS Meeting, Honolulu, HI, October 2004.
- C. Zhou, T. Zawodzinski, Jr., D. Schiraldi, “Chemical changes in Nafion® membranes under simulated fuel cell conditions,” 206th ECS Meeting, Honolulu, HI, October 2004.
- M. Pelsozy, J. Wainright and T. Zawodzinski Jr., “Peroxide production and detection in polymer films,” 206th ECS Meeting, Honolulu, HI, October 2004.
- A. S. Agarwal, U. Landau and T. Zawodzinski, Jr., “Hydrogen peroxide formation during oxygen reduction on a high surface area Pt/C catalyst,” 206th ECS Meeting, Honolulu, HI, October 2004.
- J. Frisk, W. Boand, M. Hicks, M. Kurkowski, A. Schmoeckel, and R. Atanasoski, “How 3M developed a new GDL construction for improved oxidative stability,” 2004 Fuel Cell Seminar, San Antonio, TX, November 2004.
- D. Schiraldi, “Chemical durability studies of model compounds and Nafion® under mimic fuel cell conditions,” Advances in Materials for Proton Exchange Membrane Fuel Cells, Pacific Grove, CA, February 2005.
- S. Hamrock, “New membranes for PEM fuel cells”, Advances in Materials for Proton Exchange Membrane Fuel Cells, Pacific Grove, CA, February 2005
- C. Zhou, T. Zawodzinski, Jr., D. Schiraldi, “Chemical durability studies of model compounds and Nafion® under mimic fuel cell conditions,” 229th ACS Meeting, San Diego, CA, March 2005.
- M. T. Hicks, “MEA and Stack Durability for PEM Fuel Cells”, 2005 Hydrogen Fuel Cells Infrastructure and Technology Review, Washington, DC, May 2005.
- D. Schiraldi and C. Zhou, “Model compound studies of fuel cell degradation”, High Temperature Membrane Working Group, 2005 Hydrogen Fuel Cells Infrastructure and Technology Review, Washington, D.C., May (2005).
- M. Yandrasits, “Mechanical property measurements of PFSA membranes at elevated temperatures and humidities”, 2nd International Conference on Polymer Batteries and Fuel Cells, Las Vegas, NV, June 2005.
- D. Schiraldi and C. Zhou, “Chemical durability studies of PFSA polymers and model compounds under mimic fuel cell membrane conditions,” 230th ACS Meeting, Washington, D.C., August 2005.
- M. Hicks, D. Pierpont, P. Turner, T. Watschke, M. Yandrasits, “Component Accelerated Testing and MEA Lifetime Modeling,” 2005 Fuel Cell Testing Workshop, Vancouver, BC, September 2005.
- J. Dahn, D. Stevens, A. Bonakdarpour, E. Easton, M. Hicks, G. Haugen, R. Atanasoski, M. Debe, “Development of Durable and High-Performance Electrocatalysts and Electrocatalyst Support Material,” 208th Meeting of The Electrochemical Society, Los Angeles, CA, October 2005.
- D. Pierpont, M. Hicks, P. Turner, T. Watschke, “Accelerated Testing and Lifetime Modeling for the Development of Durable Fuel Cell MEAs,” 208th Meeting of The Electrochemical Society, Los Angeles, CA, October 2005.
- M. Hicks, K. Kropp, A. Schmoeckel, R. Atanasoski, “Current Distribution Along a Quad-Serpentine Flow Field: GDL Evaluation,” 208th Meeting of The Electrochemical Society, Los Angeles, CA, October 2005.
- G. Haugen, D. Stevens, M. Hicks, J. Dahn, “Ex-situ and In-situ Stability Studies of PEM Fuel Cell Catalysts: the effect of carbon type and humidification on the degradation of carbon supported catalysts,” 2005 Fuel Cell Seminar, Palm Springs, CA, November 2005.
- D. Pierpont, M. Hicks, P. Turner, T. Watschke, “New Accelerated Testing and Lifetime Modeling Methods Promise Development of more Durable MEAs,” 2005 Fuel Cell Seminar, Palm Springs, CA, November 2005.
- M. Hicks, R. Atanasoski, “3M MEA Durability under Accelerated Testing,” 2005 Fuel Cell Durability, Washington, DC, December 2005.

- Z. Qi, Q. Guo, B. Du, H. Tang, M. Ramani, C. Smith, Z. Zhou, E. Jerabek, B. Pomeroy, J. Elter, "Fuel Cell Durability for Stationary Applications - From Single Cells to Systems," 2005 Fuel Cell Durability, Washington, DC, December 2005.
- M. T. Hicks, "MEA and Stack Durability for PEM Fuel Cells", 2006 Hydrogen Fuel Cells Infrastructure and Technology Review, Washington, DC, May 2006.
- M. Hicks, " Investigation of Current Distribution in a 50 cm^2 Quad Serpentine Flow Field via a 121-Channel Segmented Cell", Gordon Research Conference; Fuel Cells, July 2006, Smithfield, RI.
- C. Zhou, D. Schiraldi, T. Zawodzinski Jr., "Model Studies of Perfluorinated PEM Membrane Chemical Durability", 2nd MEA Manufacturing Symposium, August 22 – 24, 2006, Dayton, OH.
- M. Hicks, "The Application of Accelerated Testing and Statistical Lifetime Modeling to MEA Development", 2nd MEA Manufacturing Symposium August 22 – 24, 2006, Dayton, OH.
- C. Zhou, D. Schiraldi, T. Zawodzinski Jr., "Chemical Degradation Study of A Perfluorinated Ionomers: Nafion®", American Chemical Society 232nd National Meeting, September 10 - 14, 2006 San Francisco, CA.
- D. Schiraldi, C. Zhou, T. Zawodzinski Jr., "Model Studies of Perfluorinated PEM Membrane Degradation" American Chemical Society 232nd National Meeting, September 10 - 14, 2006, San Francisco, CA.
- M. Yandrasits and S. Hamrock, "3M Membrane Technology" Fluoropolymers 2006, October 17th 2006, Charleston SC.
- R. Subbaraman, T. Zawodzinski, M. Pelsozy, R. Sidik, A. Agarwal, U. Landau, C. Zhou, D. Schiraldi, B. Edwards, "The Origin and Fate of Peroxide in PEM Fuel Cells" 2006 Joint International Meeting , October 30-November 1, 2006, Cancun, Mexico.
- Z. Qi, "Fundamental Issues of PEM Fuel Cell Durability and Performance", Fuel Cells Durability & Performance 2006, December 6-8, 2006, Miami Beach, Florida.
- M. Hicks, "Application of Accelerated Testing and Statistical Lifetime Modeling to MEA Development", Advances in Materials for Proton Exchange Membrane Fuel Cell Systems, February 19, 2007, Asilomar, CA.
-
- M. A. Yandrasits, "MEA and Stack Durability for PEM Fuel Cells", 2007 Hydrogen Fuel Cells Infrastructure and Technology Review, Washington, DC, May 2007.

7.2 Publications

- A. Agarwal, U. Landau and T. Zawodzinski, Jr., "Hydrogen peroxide formation during oxygen reduction on high surface area Pt/C catalysts," 206th ECS Meeting, Honolulu, HI, October 2004.
- M. Pelsozy, J. Wainright and T. Zawodzinski Jr., "Peroxide production and detection in polymer films," 206th ECS Meeting, Honolulu, HI, October 2004.
- A. S. Agarwal, U. Landau and T. Zawodzinski, Jr., "Hydrogen peroxide formation during oxygen reduction on a high surface area Pt/C catalyst," 206th ECS Meeting, Honolulu, HI, October 2004.
- D. Stevens, M. Hicks, G. Haugen, J. Dahn, "Ex situ and in situ stability studies of PEMFC catalysts: Effect of carbon type and humidification on degradation of the carbon," *J. Electrochem. Soc*., 152 (12), A2309 (2005).
- D. Pierpont, M. Hicks, P. Turner, T. Watschke, "Accelerated Testing and Lifetime Modeling for the Development of Durable Fuel Cell MEAs," *ECS Transactions*, Vol 1, 2006.
- M. Hicks, K. Kropp, A. Schmoeckel, R. Atanasoski, "Current Distribution Along a Quad-Serpentine Flow Field: GDL Evaluation," *ECS Transactions*, Vol 1, 2006.
- M. Hicks and D. Pierpont, "Application of Accelerated Testing and Statistical Lifetime Modeling to MEA Development", *Proton Exchange Fuel Cells Durability*, M. Inaba, T. Schmidt and F. Buchi editors, 2007 (to be published).

7.3 Patents

US7214740 “Fluorinated ionomers with reduced amounts of carbonyl end groups”

US2006-0222840-A1 “Oxidatively Stable Microlayers of Gas Diffusion Layers”